Conference Proceedings of the Society for Experimental Mechanics Series

Helena Jin · Cesar Sciammarella · Sanichiro Yoshida
Luciano Lamberti *Editors*

Advancement of Optical Methods in Experimental Mechanics, Volume 3

Conference Proceedings of the Society for Experimental Mechanics Series

Springer

Conference Proceedings of the Society for Experimental Mechanics Series

Series Editor
Tom Proulx
Society for Experimental Mechanics, Inc.,
Bethel, CT, USA

For further volumes:
http://www.springer.com/series/8922

Helena Jin • Cesar Sciammarella • Sanichiro Yoshida
Luciano Lamberti
Editors

Advancement of Optical Methods in Experimental Mechanics, Volume 3

Conference Proceedings of the Society for Experimental Mechanics Series

Springer

Editors
Helena Jin
Sandia National Laboratories
Livermore, CA
USA

Cesar Sciammarella
Illinois Institute of Technology
Chicago, IL
USA

Sanichiro Yoshida
Department of Chemistry and Physics
Southeastern Louisiana University
Hammond, LA
USA

Luciano Lamberti
Politecnico Di Bari, Bari
Italy

ISSN 2191-5644 ISSN 2191-5652 (electronic)
ISBN 978-3-319-00767-0 ISBN 978-3-319-00768-7 (eBook)
DOI 10.1007/978-3-319-00768-7
Springer Cham Heidelberg New York Dordrecht London

Library of Congress Control Number: 2011929511

Printed on acid-free paper

Springer is part of Springer Science+Business Media (www.springer.com)

Preface

Advancement of Optical Methods in Experimental Mechanics, Volume 3: Proceedings of the 2013 Annual Conference on Experimental and Applied Mechanics represents one of eight volumes of technical papers presented at the SEM 2013 Annual Conference & Exposition on Experimental and Applied Mechanics organized by the Society for Experimental Mechanics and held in Lombard, IL, June 3–5, 2013. The complete Proceedings also includes volumes on: *Dynamic Behavior of Materials; Challenges in Mechanics of Time-Dependent Materials and Processes in Conventional and Multifunctional Materials; Mechanics of Biological Systems and Materials; MEMS and Nanotechnology; Experimental Mechanics of Composite, Hybrid, and Multifunctional Materials; Fracture and Fatigue; Residual Stress, Thermomechanics & Infrared Imaging, Hybrid Techniques and Inverse Problems*.

Each collection presents early findings from experimental and computational investigations on an important area within Experimental Mechanics, Optical Methods being one of these areas.

With the advancement in imaging instrumentation, lighting resources, computational power, and data storage, optical methods have gained wide applications across the experimental mechanics society during the past decades. These methods have been applied for measurements over a wide range of spatial domains and temporal resolutions. Optical methods have utilized a full range of wavelengths from X-ray to visible lights and infrared. They have been developed not only to make two-dimensional and three-dimensional deformation measurements on the surface, but also to make volumetric measurements throughout the interior of a material body.

Livermore, CA, USA — Helena Jin
Chicago, IL, USA — Cesar Sciammarella
Hammond, LA, USA — Sanichiro Yoshida
Politecnico Di Bari, Bari, Italy — Luciano Lamberti

Contents

Chapter 1
Super-Resolution in Ultrasonic NDE

Shanglei Li, Anish Poudel, and Tsuchin Philip Chu

Abstract This paper discusses the use of an iterative back projection (IBP) super-resolution (SR) image reconstruction technique on the carbon epoxy laminates with simulated porosity defects. In order to first validate and evaluate the application of the proposed method, three artificially simulated delamination defects in carbon epoxy laminates were considered. Based on the preliminary results, it was verified that the contrast signal-to-noise ratio (CNR) of the SR image was higher than the bi-cubic interpolation image. Further, the peak signal-to-noise ratio (PSNR) value of SR result had an average increase of 5.7088 dB compared to the bi-cubic interpolation method. This validates the proposed approach used to generate the reconstructed SR images with image quality similar to the original simulated UT images. After the validation, the UT image reconstruction algorithm was applied to the ultrasonic C-scan amplitude images of a porosity sample. Based on the results, it was demonstrated that the SR image achieved better visual quality with an improved image resolution. It was also demonstrated that this method was capable of detecting the defects with more confidence by recovering the defect outline compared to the LR C-scan image. The defect outline in SR images is more distinct to recognize, allowing post-processing work such as measurement of defect size, shape, and location to be much easier.

Keywords NDE • Ultrasound • Image reconstruction • IBP • Super-resolution

1.1 Introduction

The magnitude of damage detection and prevention in existing infrastructures such as highways, bridges, aircraft, railroads, gas and liquid transmission pipelines, waterways and ports, and buildings are of great importance today. This problem has increased dramatically in the last three decades and is likely to keep increasing. Further, an entire new generation of civil, mechanical, and aerospace structures are being developed that are using composites as their main building blocks. These include commercial and military aircraft, space vehicle panels, composite bridges, and other machines that use composites in some form or another. In order to prevent the occurrence of catastrophic failures, it is imperative to develop an intelligent damage detection technique that is simple, robust, and capable of accurately characterizing the extent and location of existing damage in a composite structure. Ultrasonic testing (UT) is a proven NDE method which is predominantly applied during the inspection of composites [1–9]. The main reasons behind this are its large surface, speed, and non-contact testing capabilities. Industrial applications of ultrasonic imaging technology have grown rapidly in past decades as a practical tool for research, development, and health monitoring. Since typical industry applications involve single transducer signal acquisition and translation, improvements in speed are true cost savers and can open the door for new applications where image capture time is limited. Resolution improvements of ultrasonic images are typically achieved by increasing signal frequency and using focused beams. Frequencies from the kHz to GHz ranges are being employed to generate digital images

S. Li (✉)
Department of Electrical and Computer Engineering, Southern Illinois University Carbondale,
1230 Lincoln Drive, Carbondale, IL 62901, USA
e-mail: shanglei@siu.edu

A. Poudel • T.P. Chu
Department of Mechanical Engineering and Energy Process, Southern Illinois University,
1230 Lincoln Drive, Carbondale, IL 62901, USA

H. Jin et al. (eds.), *Advancement of Optical Methods in Experimental Mechanics, Volume 3*,
Conference Proceedings of the Society for Experimental Mechanics Series,
DOI 10.1007/978-3-319-00768-7_1,

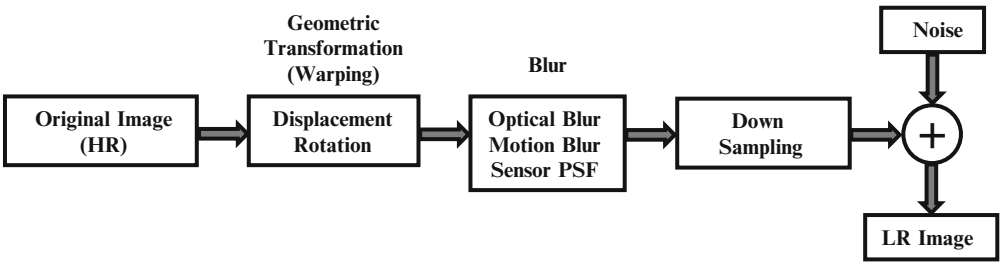

Fig. 1.1 Observation model of the LR image

of regions deep within a material, or at the surface. Details regarding the influences of the focusing lens, pulse frequency, and material properties on the final image resolution have been skillfully reviewed by Gilmore [10]. However, ultrasonic images have lower resolution and poor imaging quality due to the speckle noise produced by the interference of backscattered signals [11–13]. Image data sets obtained from ultrasonic C-scans may not provide satisfactory images for correlation. UT C-scan contrast and detection of defects in composite materials is limited by inhomogeneous density and anisotropic properties of the composites. Moreover, the C-scan image resolution depends on the physical characteristics of ultrasonic transducers (sensor). This makes ultrasonic C-scan inspection difficult to qualitatively and quantitatively evaluate region of interest (ROI). A key NDE goal is to obtain images having the best possible spatiotemporal resolution by limiting the effects of ultrasonic transducers, the uncertainty principles, and the diffraction limits [14]. Super-resolution (SR) image reconstruction is an approach to overcome the inherent resolution limitations of the ultrasonic system. It attempts to solve the problem with software rather than hardware.

This paper discusses an implementation of a SR image reconstruction algorithm based on the lower resolution (LR) image fusion. For this, a micro-scanning imaging technique is utilized to obtain an LR image sequence with sub-pixel displacement. This SR algorithm fuses a set of LR images to form an image with the same resolution as the desired higher resolution (HR) image, and interpolates a LR image as the initialization guess for the iterative restoration algorithm. These images are used to find the HR image by utilizing the iterative back projection (IBP) algorithm.

1.1.1 Super-Resolution Image Reconstruction

Super-resolution image reconstruction is a digital signal processing approach which uses a number of frequency domain aliasing, blurred, and additive noise effect lower resolution images to get high frequency information and more pixel values to overcome the inherent resolution limitations of the existing imaging system. The concept of super-resolution based on a sequential image was firstly introduced by Tsai and Huang [15]. They implemented the frequency domain based approach to reconstruct one improved resolution image from several blurred, down-sampled, and noisy images. After that, various literatures have reported on the use of super-resolution and related topics [16–24].

A typical observation model of the LR image is depicted in Fig. 1.1.

The observed LR image y is assumed to have been deformed during the image acquisition process by geometric transformation (warping), optical blur, motion blur, sensor point spread function (PSF), and downsampling performed on the original HR image X, resulting in a decline in LR image quality. Accordingly, the mathematical model is expressed as:

$$\mathrm{y} = \mathrm{DPRX} + \mathrm{V} \tag{1.1}$$

Where: y is the LR image with resolution of $L_1L_2 \times 1$
D is the downsampling (decimation) matrix $L_1L_2 \times M_1M_2$
P is the blurring matrix of size $M_1M_2 \times M_1M_2$
R is the warping matrix of size $M_1M_2 \times M_1M_2$
X is the original HR image with the size of $M_1M_2 \times 1$
V is the additive noise during the image acquisition process of size $L_1L_2 \times 1$

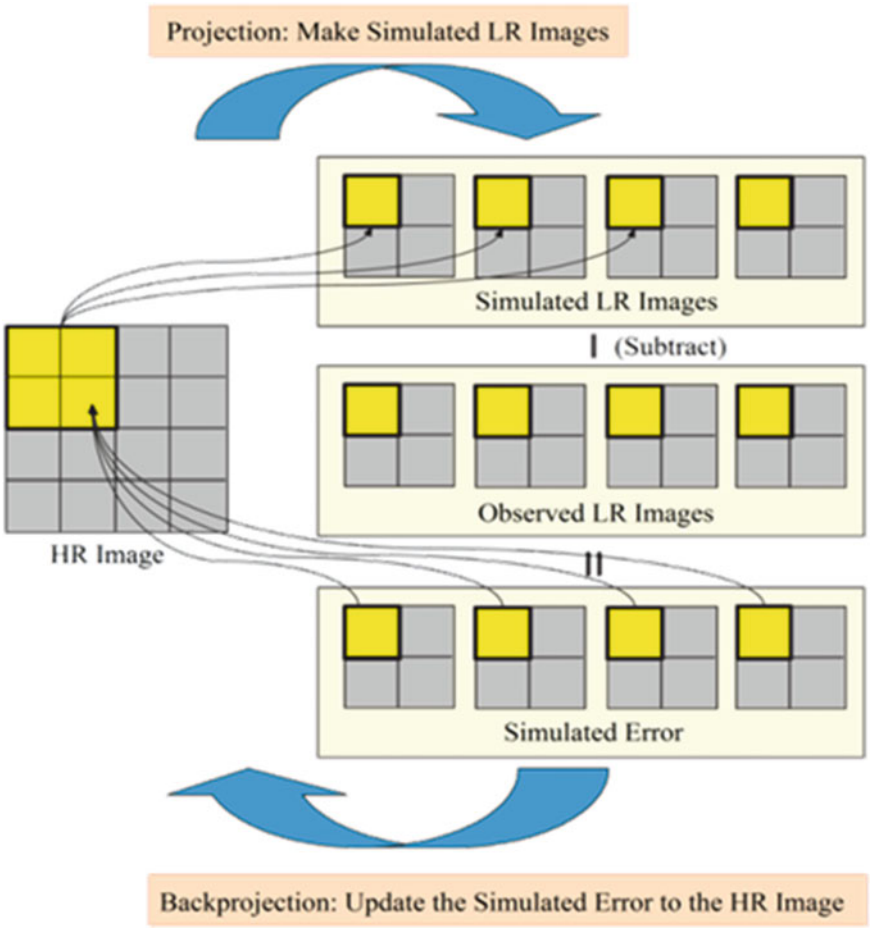

Fig. 1.2 A pictorial example of the IBP method [25]

Thus, the reconstruction of SR image can be considered as solving an ill-posed and ill-conditioned inverse problem that utilizes a set of LR images y_1,y_2,. . .,y_n with a resolution of $L_1 \times L_2$ to solve the HR images $X_1, X_2, \ldots, X_n$ with a resolution of $M_1 \times M_2$.

1.1.2 Iterative Back Projection (IBP) Algorithm

The IBP is a classical algorithm that is based on the back projection technique which is commonly used in computed tomography. This algorithm proposed by Irani and Peleg [17, 18] is based on the idea that the recovered higher resolution (HR) image should produce the same image as the one observed if passing it through the lower resolution (LR) image generation model. The HR image is estimated by back projecting the error (difference) between the simulated LR images and the observed LR images. The process is repeated iteratively until some stopping criteria are met, such as the minimization of the energy of the error or the maximum number of allowed iterations. However, the main limitation of this method is that it usually requires several LR images to recover a high quality HR image. The schematic diagram of IBP method is shown in Fig. 1.2.

1.2 Experimental Setup and Procedure

The material used in this study was a carbon epoxy laminate with simulated porosity defects as shown in Fig. 1.3. This panel had dimensions of 200 × 300 × 3.36 mm. The sample had five simulated porosity defects of varied diameter (15 and 30 mm). These defects were artificially created by controlling the pressure during the curing process. The range of porosity was from 1 % to 5 %.

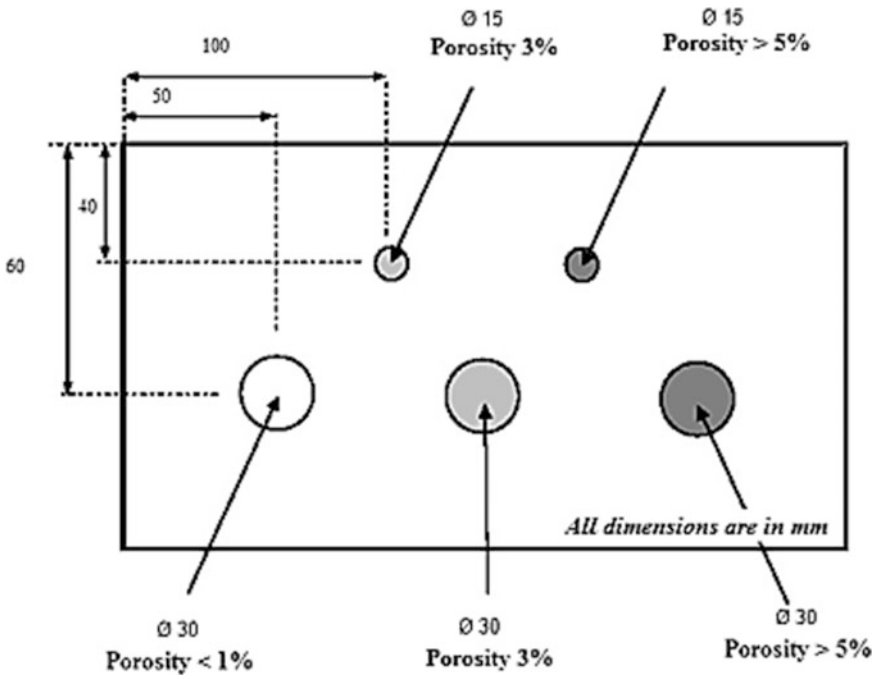

Fig. 1.3 Defect maps in carsimulated porosity defectssimulated porosity defect

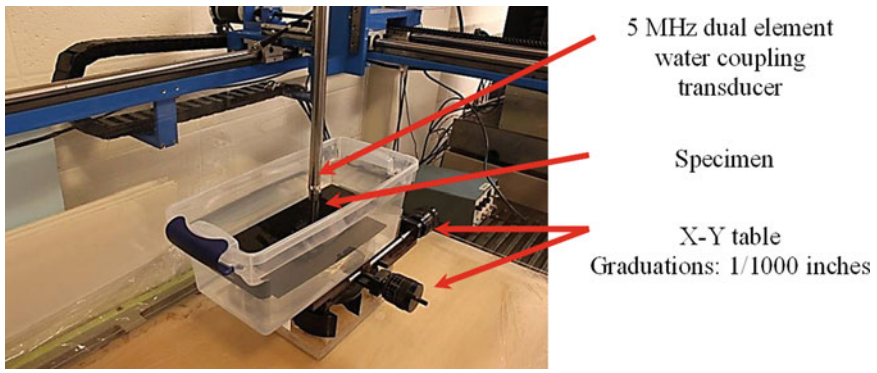

Fig. 1.4 Ultrasonic micro-scanning setup for the carbon epoxy laminates

The pulse-echo ultrasonic C-scans were conducted in an immersion tank using an immersion ultrasonic system as shown in Fig. 1.4. A 5 MHz dual element transducer with a 2 in. focal length was driven by a Panametric 5,072 pulser/receiver. The UT scan increment was 0.01 in.. In pulse-echo (reflection) mode, the transducer performs both the transmitting and the receiving of the pulsed waves as the ultrasonic wave is reflected back to the device. The measured ultrasound is reflected from material interfaces, such as the back wall of the object or from an imperfection within the object. The C-scan machine displays these results in the form of a signal with amplitude representing the intensity of the reflection, and the distance representing the arrival time of the reflection. The micro-scanning method is utilized to obtain multiple sub-pixel displacement LR UT images for the optimum performance of the UT image resolution. This approach is similar to that described in our outside work [26]. For this study, a micro-scanning technique was employed by setting the displacement of 0.003 in. Figure 1.4 depicts an X-Y table with micro-scanning technique to obtain the sub-pixel displacement. The graduation of the X-Y table is 1/1,000 in..

1.3 Results

In order to first validate and evaluate the application of super-resolution UT image reconstruction, three artificially simulated delamination defects were considered. These defect images were generated from ultrasonic 3D data to simulate delaminations in a carbon epoxy laminate. Details on the method used to generate these images are described in our

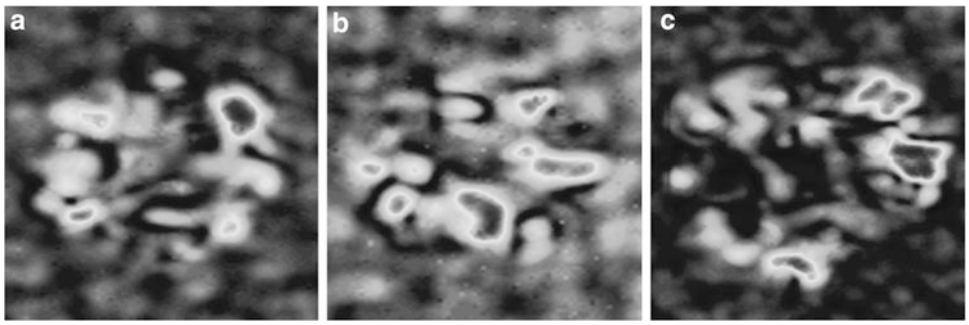

Fig. 1.5 Simulated UT delamination defects (**a**) Defect I, 456 × 432 pixels (**b**) Defect II, 464 × 396 pixels (**c**) Defect III, 508 × 492 pixels

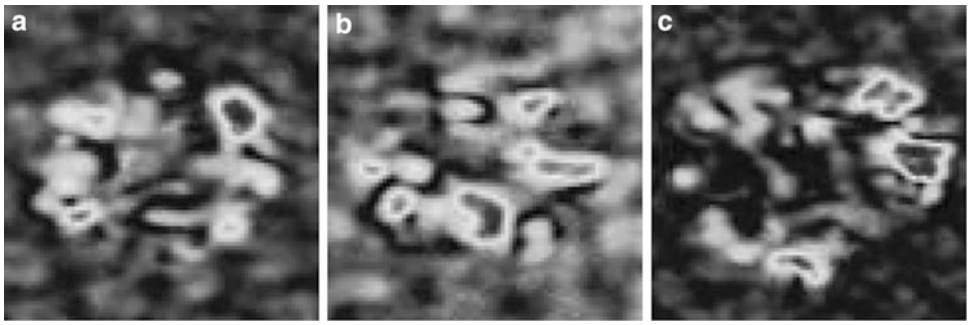

Fig. 1.6 One of the generated subsampled images for each defect (**a**) Defect I, 114 × 108 pixels (**b**) Defect II, 116 × 99 pixels (**c**) Defect III, 127 × 123 pixels

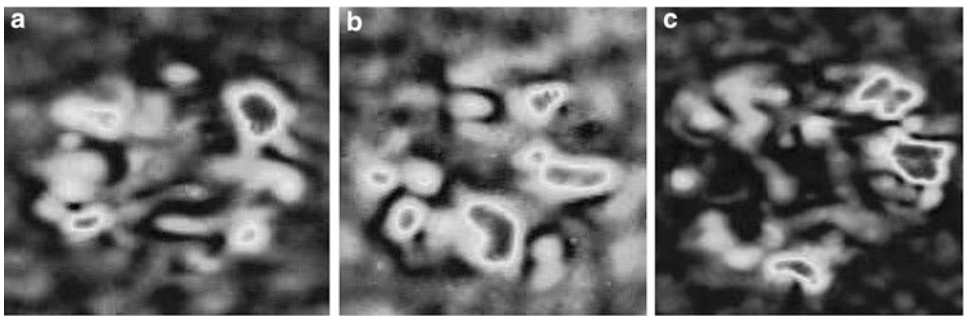

Fig. 1.7 Reconstructed SR image from 9 LR images (**a**) Defect I, 456 × 432 pixels (**b**) Defect II, 464 × 396 pixels (**c**) Defect III, 508 × 492 pixels

outside work [24]. The test images were 456 × 432, 464 × 396, and 508 × 492 pixels, and plotted in 8 bit grayscale images (256 Gy levels) as shown in Fig. 1.5.

In order to simulate the LR image sets obtained with micro-scanning technique, each defect image (shown in Fig. 1.5) was subsampled to 16 LR images with resolutions 114 × 108, 116 × 99, and 127 × 123 pixels for defects I, II, and III respectively. Considering the performance of the super-resolution reconstruction and the computational complexity, the best balance was found using 9 LR images for the super-resolution image reconstruction. Thus for this study, 9 of 16 subsampled LR images for each defect are used for SR image reconstruction. For each defect, one of the generated subsampled images is shown in Fig. 1.6. These subsampled images are scaled to the same size as the simulated UT images only for the purposes of displaying and comparing detail.

Then, the IBP SR method was applied to the subsampled LR images. Figure 1.7 shows the reconstructed SR images from 9 LR images for each type of defects as described earlier. The reconstructed SR image resolution were 456 × 432, 464 × 396, and 508 × 492 pixels for defects I, II, and III respectively.

Table 1.1 Experimental comparison of CNR & PSNR

		CNR (dB)	PSNR (dB)
Defect I	*Bi-cubic interpolation*	0.9515	19.4450
	IBP SR reconstruction	1.1027	23.9556
Defect II	*Bi-cubic interpolation*	0.5907	18.3682
	IBP SR reconstruction	0.6133	24.2702
Defect III	*Bi-cubic interpolation*	1.8549	24.8207
	IBP SR reconstruction	1.9799	29.8042

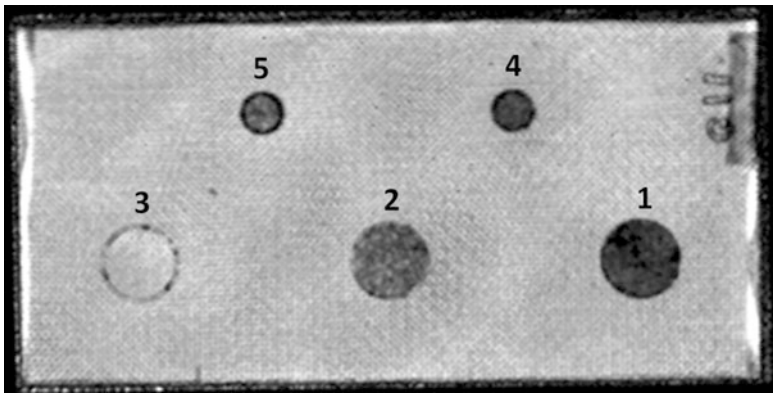

Fig. 1.8 Pulse-echo amplitude C-scan image for carbon epoxy laminates with simulated porosity defects

For subjective evaluation, the subsampled images (shown in Fig. 1.6) were used to reconstruct SR images (as shown in Fig. 1.7) with four times the resolution of the individual subsampled images. Pixel blocking effects were evident from images in Fig. 1.6 due to the low spatial resolution. In contrast, SR images (shown in Fig. 1.7) had smoother and clearer edges than the studied subsampled images.

Furthermore, to test the reconstructed image quality and robustness of the IBP method, the SR result and bi-cubic interpolation result were compared with the original simulated UT image results respectively. For this, peak signal-to-noise ratio (PSNR) and contrast signal-to-noise ratio (CNR) were employed for quantitative assessment.

The PSNR is given as:

$$PSNR = 10 \cdot \log_{10}\left(\frac{{MAX_I}^2}{MSE}\right) \tag{1.2}$$

Where: MAX_I is the maximum possible pixel value of the image. In this study, all pixels are represented using 8 bits gray level, here MAX_I is 255.

MSE is the mean squared error between two compared images.

The CNR is given as:

$$CNR = \frac{S_i - S_o}{\sqrt{\sigma_i^2 + \sigma_o^2}} \tag{1.3}$$

Where: S_i and S_o are the mean values inside and outside the ROI respectively

σ_i and σ_o are the standard deviations respectively

From Table 1.1, it can be verified that the CNR of the SR image is higher than bi-cubic interpolation image. Further, note that the PSNR value of SR result has an average increase of 5.7088 dB compared to bi-cubic interpolation method. The IBP method provides better performance in PSNR, indicating the quality of the reconstructed SR image is close to the original simulated UT image, which can verify that the IBP method is robust and reliable. Since the proposed method provides good performance in both of CNR and PSNR, we can see that the proposed super-resolution reconstruction method is effective in resolution enhancement.

After the validation procedure, the IBP method was applied on the ultrasonic C-scan images obtained by micro-scanning technique for carbon epoxy laminate with simulated porosity defects. Figure 1.8 shows the 5 MHz ultrasonic pulse-echo

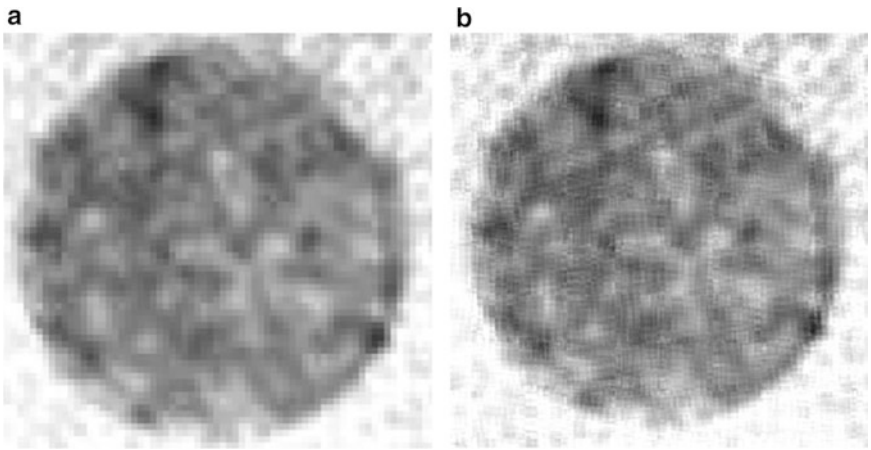

Fig. 1.9 Comparison of micro-scan UT image and SR result images (**a**) One of the micro-scan UT images (**b**) Reconstructed SR image

amplitude C-scan results for carbon epoxy laminates with porosity defects. As shown in Fig. 1.8, the ultrasonic imaging resolution capability becomes poorer for the lower percentage of the porosity. Therefore, super-resolution imaging can be a great tool for resolution improvement to detect lower percentage porosity.

To demonstrate the feasibility of implementing the IBP method on porosity samples, ultrasonic C-scan image (back wall amplitude data) obtained for defect two was considered. The C-scan image for defect two is normalized and plotted in 8 bit grayscale images (256 Gy levels) as shown in Fig. 1.9a, where defect areas are represented by dark shade of gray, i.e. a significant drop in pulse-echo signal amplitude.

Image in Fig. 1.9a is one of the nine images obtained by the micro-scanninchesmethod with the displacement of 0.003 in., approximately 1/3 pixel of the UT image. The resolution of the obtained UT images is 180×180 pixels. For the pre-processing, a 3×3 Wiener filter is applied on UT images to reduce the noise. From the super-resolution results obtained in Fig. 1.9b, comparison indicates that SR image shows better visual quality. The reconstructed SR image's resolution is 720×720 pixels, and it has the capability of detecting defects with more confidence by recovering the defect outline which is not as clear in the LR C-scan image. The defect outline in SR images is more distinctly recognizable, allowing post-processing work such as the measurement of defect size, shape, and location to be much easier.

1.4 Conclusions

The iterative back projection (IBP) super-resolution ultrasonic image reconstruction algorithm was applied to the 5 MHz ultrasonic pulse-echo amplitude C-scan results for carbon epoxy laminates with simulated porosity defects. The experimental results obtained have demonstrated the effectiveness of the applied method. Super-resolution image reconstruction can be utilized to overcome the inherent limitations of the existing ultrasonic C-scan system. For the future work, since the C-scan time is proportional to the desired resolution, to double the resolution in both x and y direction, four times the original scanning time may be required. If a C-scan system is equipped multiple ultrasound transducers with known displacement from each other, the system can offer a SR result with a resolution four times larger than the original UT image while maintaining the same scanning time; or the same resolution image can be achieved with a quarter of the original time.

References

1. Li S, Poudel A, Chu TP (2012) An image enhancement method for ultrasonic NDE of CFRP panels. In: 21st annual research symposium and spring conference, ASNT, Dallas, 19–23 Mar 2012
2. Poudel A, Chu TP, Filip P (2012) Application of ultrasonic non-destructive evaluation in braking materials. In: Proceeding SAE annual brake colloquium, 30th, Society of Automotive Engineers, San Diego
3. Poudel A, Chu TP (2012) Intelligent nondestructive testing expert system for aircraft carbon/carbon composite brakes using infrared thermography and air-coupled ultrasound. Mater Eval 70(10):1219–1229

4. Poudel A, Lane M, Li S, Chu TP (2012) NDE of commercial C/C brake disks standards using air-coupled ultrasonic testing. In: Proceeding nondestructive evaluation of aerospace materials and structures III, St. Louis
5. Chakrapani SK, Dayal V, Hsu DK, Barnard DJ, Gross A (2011) Characterization of waviness in wind turbine blades using air-coupled ultrasonics. In: Thompson DOCDE (ed) Review of progress in quantitative nondestructive evaluation, Vols 30a and 30b, San Diego, pp 956–962. http://proceedings.aip.org/resource/2/apcpcs/1335/1/956_1
6. Hsu DK, Hughes MS (1992) Simultaneous ultrasonic velocity and sample thickness measurement and application in composites. J Acoust Soc Am 92(2):669–675
7. Jeong H, Hsu DK (1995) Experimental analysis of porosity-induced ultrasonic attenuation and velocity change in carbon composites. Ultrasonics 33(3):195–203
8. Livings RA, Dayal V, Barnard DJ, Hsu DK Flaw detection in a multi-material multi-layered composite: using FEM and air-coupled UT. In: Proceeding 37th annual review of progress in quantitative nondestructive evaluation (QNDE), San Diego, pp 942–949. http://proceedings.aip.org/resource/2/apcpcs/1335/1/956_1
9. Nair SM, Hsu DK, Rose JH (1989) Porosity estimation using the frequency dependence of the ultrasonic attenuation. J Nondestruct Eval 8 (1):13–26
10. Gilmore RS (1996) Industrial ultrasonic imaging and microscopy. J Phys D Appl Phys 29(6):1389–1417
11. Hong SK, Ohr YG (1998) Ultrasonic speckle pattern correlation interferometry using a pulse-echo method. J Phys D Appl Phys 31(11):1392–1396
12. HongMei Z, MingXi W, JinJin W, XuLei Q (2010) Super-resolution reconstruction of deformable tissue from temporal sequence of ultrasound images. In: 2010 International conference on artificial intelligence and computational intelligence (AICI 2010), vol 1,Sanya, pp 337–342. http://ieeexplore.ieee.org/xpls/abs_all.jsp?arnumber=5656514&tag=1
13. Kouame D, Ploquin M (2009) Super-resolution in medical imaging: an illustrative approach through ultrasound. In: 2009 IEEE international symposium on biomedical imaging: from Nano to Macro, vols 1 and 2, Boston, pp 249–252. http://ieeexplore.ieee.org/xpls/abs_all.jsp?arnumber=5193030
14. Clark G, Jackson J (2006) Super-resolution algorithms for ultrasonic nondestructive evaluation imagery. J Acoust Soc Am 120(5):3140–3140
15. Tsai RY, Huang TS (1984) Multiframe image restoration and registration. Adv Comput Vis Image Process 1:101–106
16. Stark H, Oskoui P (1989) High resolution image recovery from image plane arrays, using convex projections. J Opt Soc Am A Opt Image Sci Vis 6(11):1715–1726
17. Irani M, Peleg S (1990) Super resolution from image sequences. In: Proceedings 10th international conference on pattern recognition (Cat. No.90CH2898-5), vol 112, Atlantic City, pp 115–120. http://ieeexplore.ieee.org/xpl/articleDetails.jsp?arnumber=479905
18. Irani M, Peleg S (1991) Improving resolution by image registration. CVGIP-Graph Models Image Process 53(3):231–239
19. Schultz RR, Stevenson RL (1995) Improved definition video frame enhancement. In: 1995 international conference on acoustics, speech, and signal processing – conference proceedings, vols 1–5, Detroit, pp 2169–2172
20. Schultz RR, Stevenson RL (1995) Video resolution enhancement. In: Technol, E. Soc Photo Opt Instrumentat (eds) Proceeding conference on image and video processing III, San Jonse, pp 23–34
21. Schultz RR, Stevenson RL (1996) Extraction of high-resolution frames from video sequences. IEEE Trans Image Process 5(6):996–1011
22. Schultz RR, Stevenson RL (1996) Motion-compensated scan conversion of interlaced video sequences. In: Technol, E. Soc Photo Opt Instrumentat (eds) Proceeding conference on image and video processing IV, San Jose, pp 107–118. http://proceedings.spiedigitallibrary.org/proceeding.aspx?articleid=1014864
23. Kang MG, Chaudhuri S (2003) Super-resolution image reconstruction. IEEE Signal Process Mag 20(3):19–20
24. Li S, Chu TP (2012) Ultrasonic 3D reconstruction of CFRP panel delamination. In: ASNT fall conference, ASNT, Orlando, 29 Oct–1 Nov 2012
25. Park SC, Park MK, Kang MG (2003) Super-resolution image reconstruction: a technical overview. IEEE Signal Process Mag 20(3):21–36
26. Li S, Poudel A, Chu TP (2013) Super-resolution image reconstruction for ultrasonic NDE of carbon composites. In: Accepted for proceedings of 22nd annual research symposium and spring conference, Memphis, 18–21 Mar 2013

Chapter 2
Nanoparticle and Collagen Concentration Measurements Using Scanned Laser Pico-projection

Chin-Ho Chuang, Ti-Wen Sung, Chih-Ling Huang, and Yu-Lung Lo

Abstract The images projected by scanned laser pico-projectors (SLPPs) contain speckle noise caused by the reflection of the high coherent laser light source from the projection screen. A speckle pattern can be used to detect the concentration of liquid solution with nanoparticle. Three samples: solid solution, liquid solution, and collagen solution are tested. The experimental results show that the green laser within the SLPP provides a better sensitivity and resolution than the red or blue lasers. In solid solution measurement, different concentrations of nanoparticles embedded in a poly (methyl methacrylate) (PMMA) matrix are tested. In liquid solution measurement, different concentrations of nanoparticles dissolved in deionized water are also tested. Finally, the system shows ability to measure the collagen concentrations from 0.125 % to 0.025 %. Accordingly, the proposed system provides a viable, low-cost solution for high-sensitivity in biomedical, chemical and environmental applications.

Keywords Nanoparticle concentration • Speckle • Scanned laser pico-projector • Collagen

2.1 Introduction

Scanned laser pico-projectors (SLPPs) are an emerging solution for projecting large-scale images using compact portable devices such as notebooks or cell phones. SLPPs comprise red/green/blue laser, each with a lens near the laser output which collects the light from the laser and provides a collimated beam. The projected image is created by modulating the three lasers synchronously with the position of the scanned beam [1]. SLPPs have lots of important practical benefits, including an inherently high image contrast and an infinite focus [1, 2]. Various methods have been proposed for measuring volume roughness directly by means of an ultrafast pulsed laser [3, 4] or the third-order laser speckle frequency correlations of a tunable laser [4, 5] in solid solution. However, these methods are costly and complex. Recently, Curry et al. [6] proposed a study to directly determine diffusion properties of random media from speckle contrast by using a femtosecond pulse laser with controlled bandwidth. In addition, UV/VIS/NIR spectrometers use the Beer-Lambert law to measure the absorbing molecular concentration. However, this method has some limitations that the absorbing medium needs to be homogenous and does not scatter the radiation [7]. Accordingly, the present study exploits the inherent speckle noise characteristics to realize a simple yet highly precise relative nanoparticle concentration measurement in both solid and liquid solutions by only a commercial SLPP device and a digital camera. Finally, it demonstrates the concentration measurements of collagen witch is an important role in the biomedical field, particularly for wound healing, controlled drug delivery and tissue regeneration [8].

C.-H. Chuang • T.-W. Sung • C.-L. Huang • Y.-L. Lo (✉)
Department of Mechanical Engineering, National Cheng Kung University, Tainan 701, Taiwan
e-mail: loyl@mail.ncku.edu.tw

H. Jin et al. (eds.), *Advancement of Optical Methods in Experimental Mechanics, Volume 3*,
Conference Proceedings of the Society for Experimental Mechanics Series,
DOI 10.1007/978-3-319-00768-7_2,

2.2 Experimental Setup and Nanoparticle Solution Preparation

In the present study, the measurement system was constructed using a commercial SLPP purchased from MicroVision. Four different projection images were created using the red laser, green laser, blue laser, and white light (all lasers on) within the SLPP, respectively. Silica nanoparticles were synthesized by hydrolysis and condensation of TEOS in an ethanol and ammonia by a modified Stöber method [9]. PMMA composite samples containing silica nanoparticles in various concentrations were prepared for solid solution using an in situ polymerization method. The resulting solution was homogeneous, without any phase separation or precipitation. Silica nanoparticles were then added to the PMMA solution in concentrations of 0, 1, 2, 3, 4 and 5 wt%, respectively. The PMMA/silica nanoparticle solutions were dripped onto a Teflon sheet and left to dry under ambient conditions. Following the evaporation of the toluene content, polymeric composite sheets of PMMA/silica nanoparticles with a thickness of approximately 2 mm were obtained.

In liquid solution, the silica nanoparticles were dissolved in deionized water at six different concentrations (0, 0.001, 0.002, 0.003, 0.004 and 0.005 M). The resulting solution was homogeneous without phase separation or precipitation. Subsequently, the nanoparticle solution was put into a quartz cuvette for further experiments (Fig. 2.1).

2.3 Concentration Measurements

2.3.1 Measurement in Solid Solution

Figure 2.2 shows the experimental results obtained for the variation of the speckle contrast with the nanoparticle concentration given green/red/blue/white (all lasers on) illumination light, respectively. It is seen that for a given nanoparticle concentration, the green image has a greater speckle contrast than the red or blue images. Consequently, the green laser is better suited to volume roughness measurement than the red or blue lasers. Figure 2.2 shows that the maximum sensitivity of the measurement system is equal to −8.59 ((speckle contrast %)/(wt%)). The average standard deviation of the speckle contrast in the green image over three repeated experiments was found to be 0.11 (speckle contrast %). Thus, the resolution of the measurement system (using the green image) was determined to be 0.013 (wt%).

2.3.2 Measurement in Liquild Solution

Figure 2.3 shows the experimental results obtained for the variation of the speckle contrast with the nanoparticle concentration given green/red/blue/white illumination light, respectively. It is seen that for a given nanoparticle concentration, the green image has a greater speckle contrast than the red or blue images as observed in solid solution measurement.

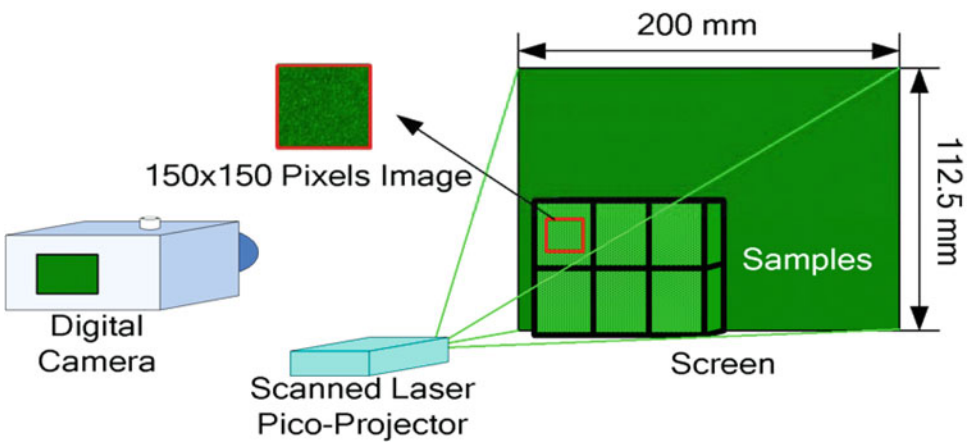

Fig. 2.1 Experimental setup of nanoparticle concentration measurement [10]

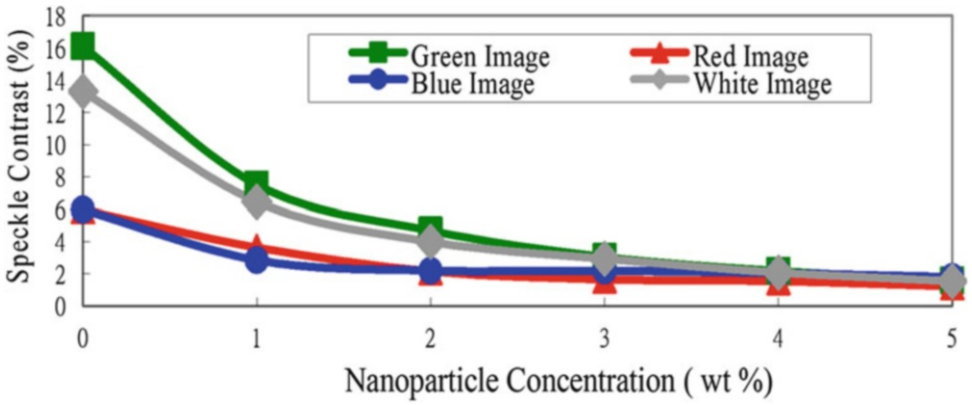

Fig. 2.2 Speckle contrast versus nanoparticle concentration in PMMA matrix

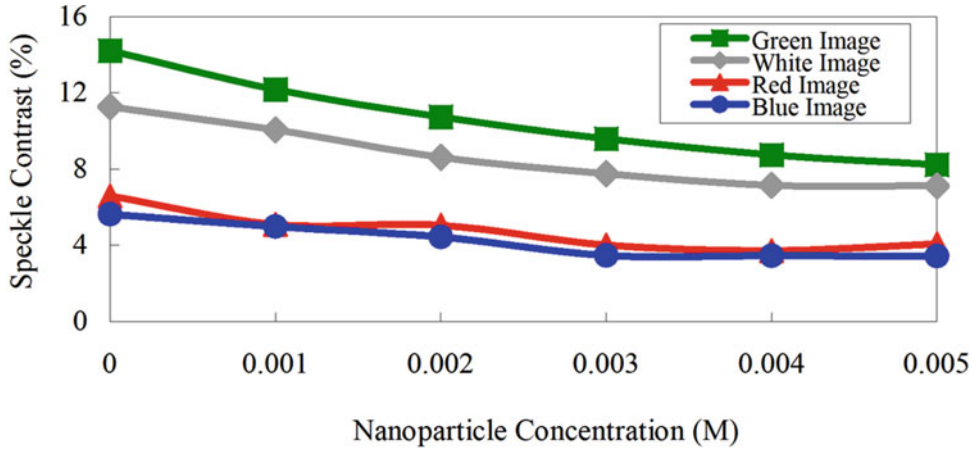

Fig. 2.3 Speckle contrast with nanoparticle concentration

However, the green image speckle contrast of a quartz cuvette with 0 M nanoparticle concentration is about 14.22 %. Figure 2.3 shows that the maximum sensitivity with green image is equal to −2050 (speckle contrast %/M). The resolution of the measurement system (using the green image) was determined to be 7.51×10^{-5} M.

2.3.3 Measurement in Collagen Solution

Collagen from calf skin (Sigma C9719) was dissolved in 0.1 M acetic acid solution (Fluka) under moderate magnetic stirring for 3 h at room temperature. The resulting solution was homogeneous, without any phase separation or precipitation. Collagen powder was prepared as a 0.5 % collagen type I solution in 0.1 M acetic acid (i.e., 5 mg collagen/1 ml 0.1 M acetic acid) and diluted in concentrations of 0.125, 0.100, 0.075, 0.050 and 0.025 wt%, respectively. Subsequently, the collagen type I solution was put into a quartz cuvette for further experiments. Figure 2.4 shows the experimental results obtained for the variation of the speckle contrast with the collagen concentration given green illumination light. It shows that the biomaterial concentration is successfully demonstrated.

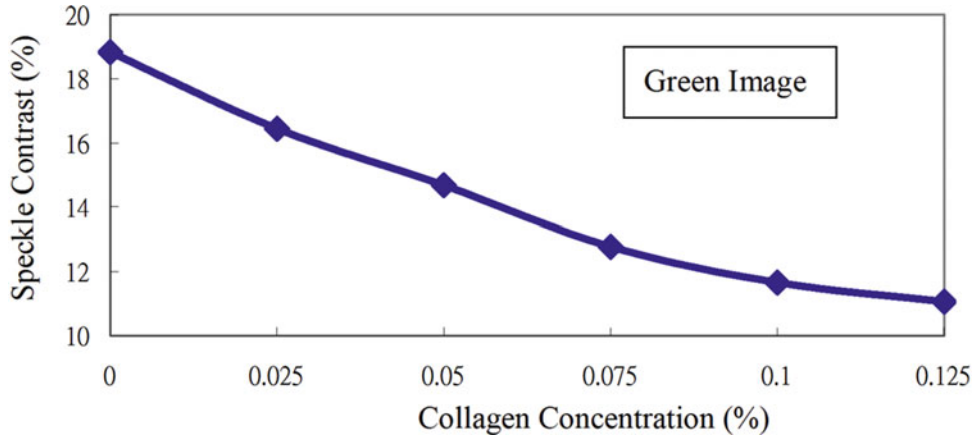

Fig. 2.4 Speckle contrast with collagen concentration under green light illumination

2.4 Conclusions

The experimental results have shown that a higher sensitivity and resolution are obtained when the sample is illuminated using the green laser within the SLPP. As a result, it provides an effective tool for a variety of nanoparticle concentration measurements in solid and liquid solutions, and the new expectations including biomedical, chemical and environmental applications can be explored. The collagen concentration measurement is an important demonstration in this study.

Acknowledgements The financial support provided to this study by the National Science Council of Taiwan, R.O.C., under contract no. NSC 99-2221-E-006-034-MY3 is gratefully acknowledged. This work has been partially published in Chuang C-H et al. (2012) Relative two-dimensional nanoparticle concentration measurement based on scanned laser pico-projection. *Sensors and Actuators B: Chemical* **173**: 281–287.

References

1. Freeman M, Champion M, Madhavan S (2009) Scanned laser pico-projectors: seeing the big picture (with a small device). Opt Photonic News 20:28–34
2. Chellappan KV, Erden E, Urey H (2010) Laser-based displays: a review. Appl Opt 49:F79–F97
3. Riechert F, Glockler F, Lemmer U (2009) Method to determine the speckle characteristics of front projection screens. Appl Opt 48:1316–1321
4. Webster MA, Webb KJ, Weiner AM (2003) Temporal response of a random medium from speckle intensity frequency correlations. J Opt Soc Am A 20:2057–2069
5. Webster MA, Webb KJ, Weiner AM (2002) Temporal response of a random medium from third-order laser speckle frequency correlations. Phys Rev Lett 88:033901
6. Churry N, Bondareff P, Leclercq M, van Hulst NF, Sapienza R, Gigan S, Gresillon S (2011) Direct determination of diffusion properties of random media from speckle contrast. Opt Lett 36:3332–3334
7. Ingle JDJ, Crouch SR (1988) Spectrochemical analysis. Prentice Hall, New Jersey
8. Wolfgang F (1998) Collagen–biomaterial for drug delivery. Eur J Pharm Biopharm 45:113–136
9. Stöber W, Fink A, Bohn E (1968) Controlled growth of monodisperse silica spheres in the micron size range. J Colloid Interface Sci 26:62–69
10. Chuang C-H, Sung T-W, Huang C-L, Lo Y-L (2012) Relative two-dimensional nanoparticle concentration measurement based on scanned laser pico-projection. Sensors and Actuators B: Chemical 173:281–287

Chapter 3
High-speed Shape Measurement with 4 kHz Using Linear LED Device

Motoharu Fujigaki, Yohei Oura, Daisuke Asai, and Yorinobu Murata

Abstract High-speed shape measurement is required to analysis the behavior of a breaking object, a vibrating object or a rotating object. A shape measurement by a phase shifting method can measure the shape with high spatial resolution because the coordinates can be obtained pixel by pixel. A light source stepping method (LSSM) using linear LED array was proposed by authors. Accurate shape measurement can be performed by a whole space tabulation method (WSTM). The response speed of the LED array is more than 12 kHz. In this paper, high-speed shape measurement is performed with a high-speed camera by WSTM and LSSM using a linear LED array. The phase shifting is performed in 12,000 Hz and the shape measurement of a rotating fan is performed in 4,000 Hz.

Keywords High-speed shape measurement • Linear LED device • Light source stepping method • Whole space tabulation method • Phase shifting method

3.1 Introduction

Accurate 3D shape measurement is requested in industry. High-speed shape measurement is also required to analyze the behavior of a breaking object, a vibrating object or a rotating object. A shape measurement by a phase shifting method can measure the shape with high spatial resolution because the coordinates can be obtained pixel by pixel.

This method needs phase shifting mechanism in the projector as a primary function. High stability, high brightness, high-speed response and low cost are required for a projector for shape measurement. In conventional method, a mechanical grating panel movement method [1, 2], an LCD (liquid crystal display) projector [3, 4] and a DLP (digital light processing) projector using DMD (digital micro-mirror device) [5–7], a MEMS (microelectromechanical system) scanner grating projector [8, 9], and a projector with a free-form mirror [10] are employed to project phase-shifted grating patterns. Especially, high-speed shape measurement was performed using a DLP projector [6, 7].

Authors proposed a light source stepping method (LSSM) using linear LED array [11, 12]. The basic idea was also mentioned in a patent description around 10 years ago [13]. The shape measurement using this idea was not apparently realized at that time. The disadvantage of LSSM is that shifted phase varies according to the z position. However, as the z coordinate and the obtained phase using an algorithm of a phase-shifting method have a one-to-one relationship, accurate shape measurement can be realized using a whole space tabulation method (WSTM) proposed by authors [14, 15]. The shape measurement equipment can be produced with low-cost and compact without any phase-shifting mechanical systems by using this method. Also it enables us to measure 3D shape in very short time by switching the light sources quickly.

M. Fujigaki (✉) • Y. Murata
Department of Opto-Mechatoronics, Wakayama University, 930, Sakaedani, Wakayama 640-8510, Japan
e-mail: fujigaki@sys.wakayama-u.ac.jp

Y. Oura
Graduate School of Systems Engineering, Wakayama University, 930, Sakaedani, Wakayama 640-8510, Japan

D. Asai
HIKARI Co., Ltd., 418-4 Minaminoda, Tohon, Ehime 791-0297, Japan

H. Jin et al. (eds.), *Advancement of Optical Methods in Experimental Mechanics, Volume 3*,
Conference Proceedings of the Society for Experimental Mechanics Series,
DOI 10.1007/978-3-319-00768-7_3,

In this paper, the response speed of the linear LED array produced by authors is verified and high-speed shape measurement is realized. The LSSM with the linear LED array and the WSTM are applied to the high-speed shape measurement with a high-speed camera. The experimental trial to measure the height distribution of a rotating fan in 4,000 Hz with shifting phase in 12,000 Hz is performed.

3.2 Principle

3.2.1 Light Source Stepping Method (LSSM)

Figure 3.1 shows a schematic illustration of projected grating pattern with a point light source and a grating plate such as a Ronchi ruling. A grating plate is placed between a light source and an object. When the light source is assumed to be a point light source, the shadow of the grating plate is projected on the object. As shown in this figure, the projected phase $\phi(x_p, z_p)$ at point P(x_p, z_p) on the object becomes the same phase at point G(x_g, z_g) on the grating plate. Point G is a intersection of a line connecting the point of light source S(x_s, z_s) and point P with the grating plate.

The phase ϕ on the grating plate is expressed in Eq. 3.1,

$$\phi(x, z_g) = \frac{2\pi x}{p} + \phi_0, \tag{3.1}$$

where p is a pitch of the grating and ϕ_0 is an intercept value at $x = 0$. The x coordinate at point G is calculated from the coordinates of point S and point P as shown in Eq. 3.2,

$$x_g = \frac{x_p - x_s}{z_p - z_s}(z_g - z_s) + x_s = \frac{z_g - z_s}{z_p - z_s}x_p + \frac{z_p - z_g}{z_p - z_s}x_s. \tag{3.2}$$

The projected phase $\phi(x_p, z_p)$ at point P is obtained as shown in Eq. 3.3,

$$\phi(x_p, z_p) = \phi(x_g, z_g) = \frac{2\pi x_g}{p} + \phi_0. \tag{3.3}$$

Figure 3.2 shows a schematic illustration of phase-shifted projected grating patterns using a light source stepping method. The projected grating pattern is changed with stepping the light source position as shown in Fig. 3.2. The projected phase at point P on an object is also changed according to the position of the light source. When the position of light source is stepped from S to S′ with a distance Δx, the intersection of a line connecting the point of light source and point P with the grating plate is changed from G to G′ with a distance Δx_g as shown in Eq. 3.4,

$$\Delta x_g = \frac{z_p - z_g}{z_p - z_s}\Delta x. \tag{3.4}$$

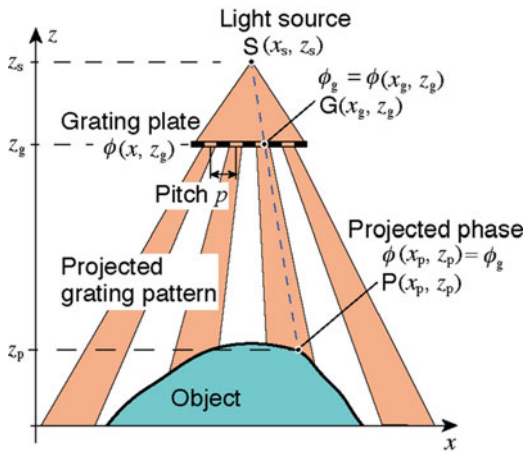

Fig. 3.1 Projected grating pattern with a point light source and a grating plate

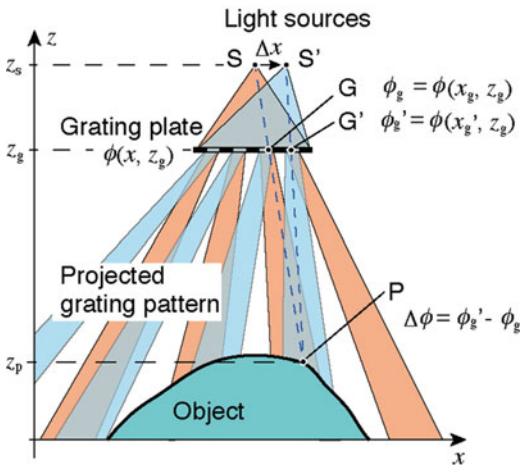

Fig. 3.2 Phase-shifted projected grating pattern using a light source stepping method

The projected phase at point P is shifted with $\Delta\phi$ as shown in Eq. 3.5,

$$\Delta\phi = \frac{2\pi}{p} \cdot \frac{z_p - z_g}{z_p - z_s} \Delta x. \tag{3.5}$$

This equation means that the projected phase is shifted in proportion as the light source stepping distance Δx and the proportionality coefficient is determined by the grating pitch of the grating plate and z positions of the light sources, grating plate and point P on the object. As the grating pitch of the grating plate, z position of the light sources and z position of the grating plate are fixed, the proportionality coefficient is corresponding to the z position of the object surface.

Actually, the light source is not a point but it has spatially spread. The light diffracts at the grating plate. So, the projected phase is exactly different from the right side of Eq. 3.3. However, when the grating pitch is around 1 mm, the influence of the diffraction is so small that the difference from Eq. 3.3 is small.

3.2.2 Whole-Space Tabulation Method (WSTM)

In the LSSM, shifted phase varies according to the z position as mentioned above. As the z coordinate and the obtained phase using an algorithm of a phase-shifting method have a one-to-one relationship.

We proposed a calibration method for an accurate and high-speed shape measurement using multiple reference planes. Figure 3.3 shows the principle of the calibration method. The reference plane oriented vertically to the z-direction is translated in the z-direction by small amount. A camera and a projector are arranged and fixed above the reference plane. The grating is projected from the projector onto the reference planes. The phase of the projected grating can be easily obtained using the phase-shifting method. A pixel of the camera takes an image on the ray line L in Fig. 3.3a. The pixel contains images of the points $P_0, P_1, P_2 \ldots P_N$ on the reference planes $R_0, R_1, R_2 \ldots R_N$, respectively. At each point, the grating phases $\theta_0, \theta_1, \theta_2 \ldots \theta_N$ can be calculated by the phase-shifting method. Therefore, the correspondence between the heights $z_0, z_1, z_2 \ldots z_N$ and the phases $\theta_0, \theta_1, \theta_2 \ldots \theta_N$, respectively, is obtained. From these phase-shifted images, the calibration tables are formed to obtain the z coordinate from the phase θ at each pixel as shown in Fig. 3.3b.

This method excludes a lens distortion and the intensity warping of the projected grating from measurement results theoretically. Tabulation makes short-time measurement possible because the z coordinate can be obtained by looking at the calibration tables from the phase at each pixel point and it does not require any time-consuming complex calculation.

3.3 Experiment

3.3.1 Experimental Setup

Figure 3.4a shows a photograph of a linear LED array device. There are nine parallel lines with 0.5 mm pitch. Each line has 30 LED chips connected in series. The size of a chip is a square of 350 μm by 350 μm. In Fig. 3.4a, the first left line is switched on and the other lines are switched off. Figure 3.4b shows a driver circuit for the linear LED array. Each line has a transistor (Toshiba, 2SC2240) as a switching device.

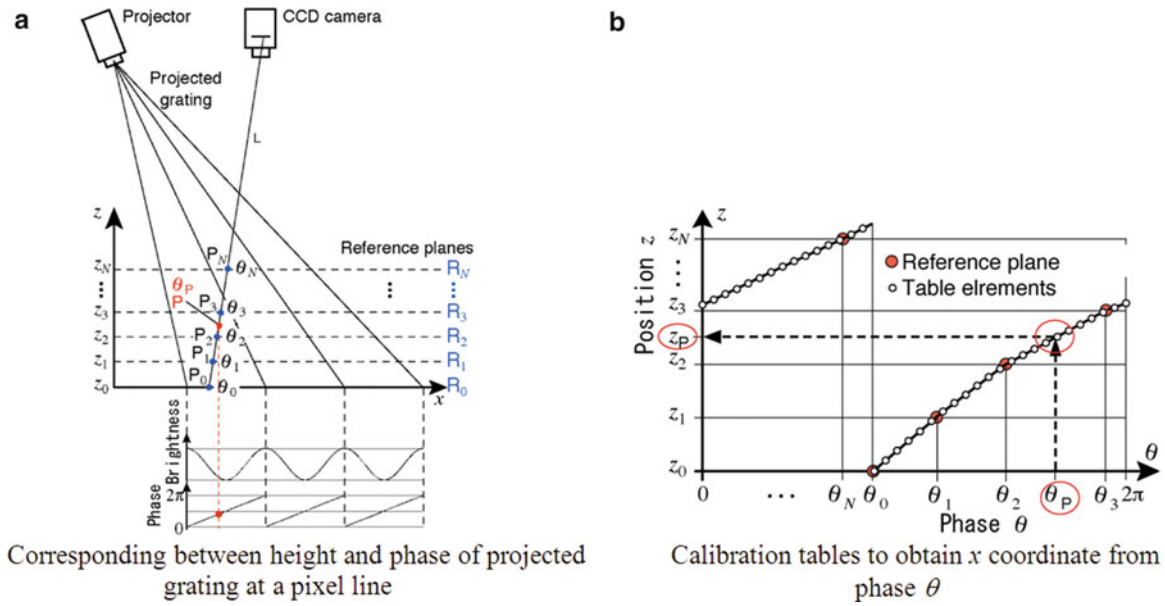

Fig. 3.3 Principle of whole-space tabulation method (**a**) Corresponding between height and phase of projected grating at a pixel line (**b**) Calibration tables to obtain x coordinate from phase θ

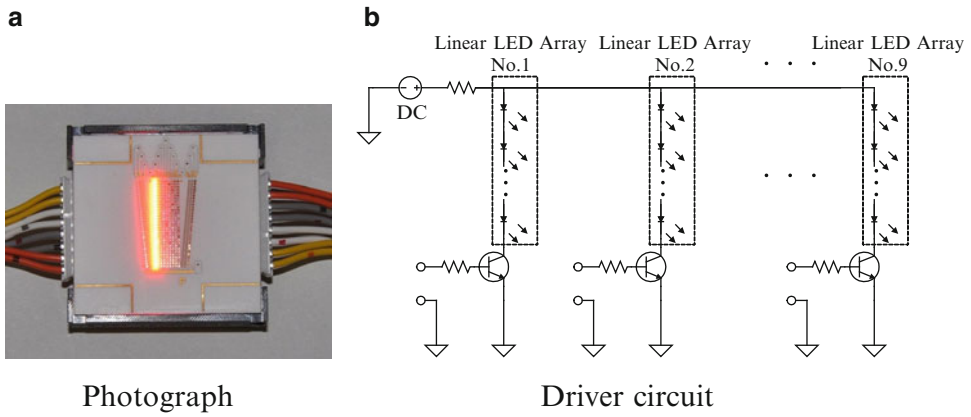

Fig. 3.4 Linear LED array device

Figure 3.5a shows a block diagram of an experimental setup. A high-speed camera (Redlake, Motion Xtra HG-100 K) is used. The orientation angle of the projector composed of the linear LED array device, a grating plate and a lens from the axis of the high-speed camera is 35°. The distance between the linear LED array device and the grating plate is 25 mm. The pitch of the grating plate is 1.02 mm. The distance between the grating plate and a lens is 15 mm. The projected grating pitch on the object can be reduced into 2.8 mm by this lens. It is necessary to increase the brightness to capture image in high speed. The measuring range is 4.0 mm in this case. A reference plane is translated from 0 to 5.0 mm at every 0.1 mm. The relationship between the phases of the projected gratin onto the reference plane and the z position was recorded to produce the phase-height tables for the WSTM. The calibration tables were produced at every $2\pi/1{,}000$ in phase.

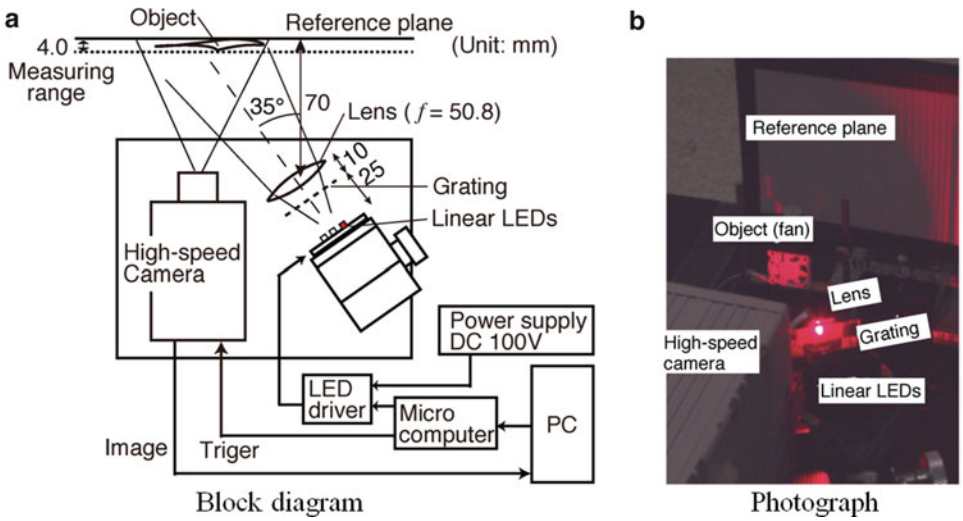

Fig. 3.5 Experimental setup

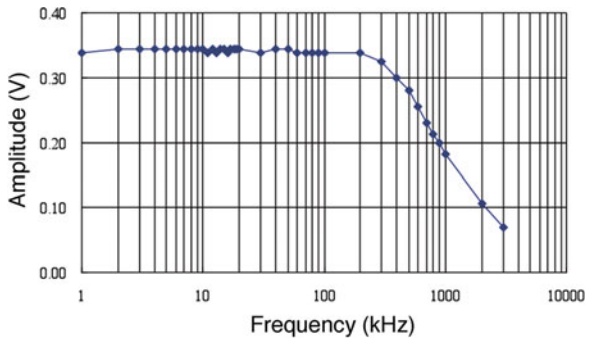

Fig. 3.6 Amplitude characteristic with changing the frequency of a rectangular wave from 1 to 3,000 kHz

3.3.2 Verification of Response Speed of Linear LED Array

Verification of the response speed of a linear LED array is performed. A pulse generator produces a square wave and it is applied to the base electrode of a transistor used as a switching device as shown in Fig. 3.5b. The voltage of power supply was 117 V and the lighting current is 113 mA. The response speed of a photo sensor and the amplifier is 100 MHz. The change of lighting power of the linear LED array is detected by the photo sensor. The amplitude of the input square wave and output wave is recorded by an oscilloscope simultaneously in time series. The frequency of input square wave is changed from 1 to 3 MHz.

The result of response speed of linear LED array is shown in Fig. 3.6. The output amplitudes of the photo sensor are almost same from 1 to 200 kHz. The output amplitude of the photo sensor in 1 MHz becomes half of the output amplitude in 200 kHz. This result shows that the linear LED array has enough ability to be applied for a high-speed shape measurement.

3.3.3 Experimental Results

A fan rotating with 29 times per second is used as an object. The phase shifting speed is 12,000 Hz. The grating images are grabbed by the high-speed camera synchronized with the phase shifting. Figure 3.7a shows a grating image projected onto the rotating fan. A phase shifting with three steps is performed in this experiment. The phase map of three phase shifted

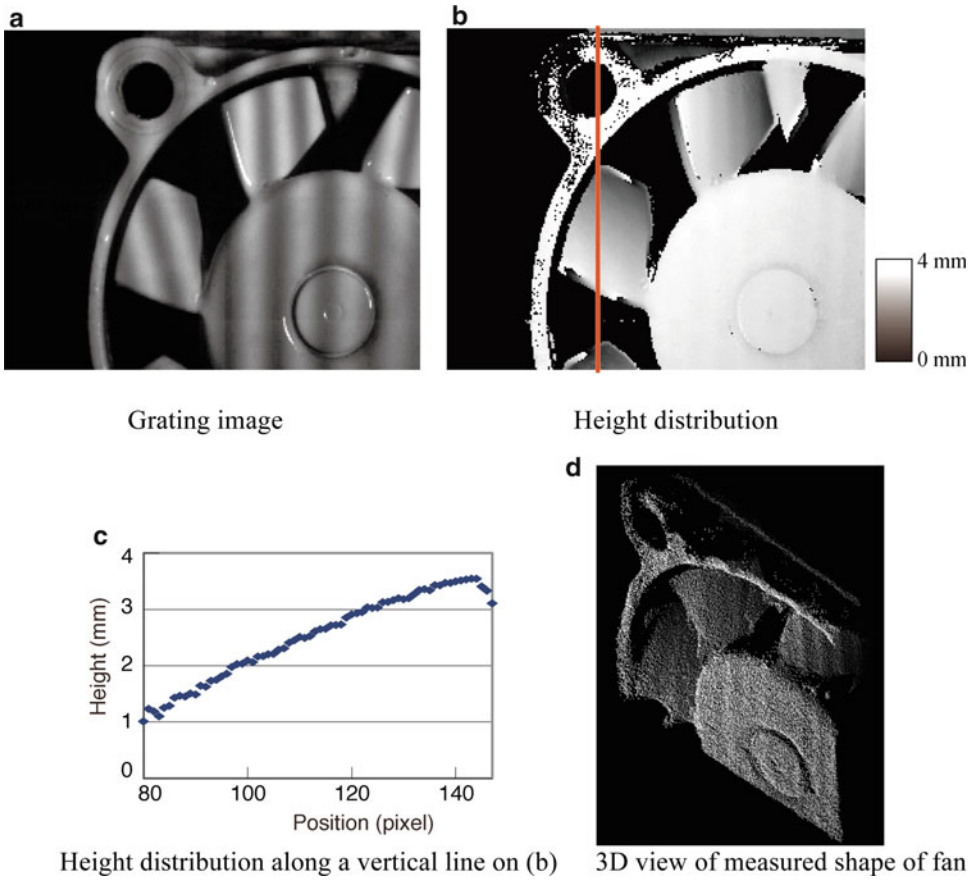

Fig. 3.7 Measured result of a rotating fan (**a**) Grating image (**b**) Height distribution (**c**) Height distribution along a vertical line on (**b**) (**d**) 3D view of measured shape of fan

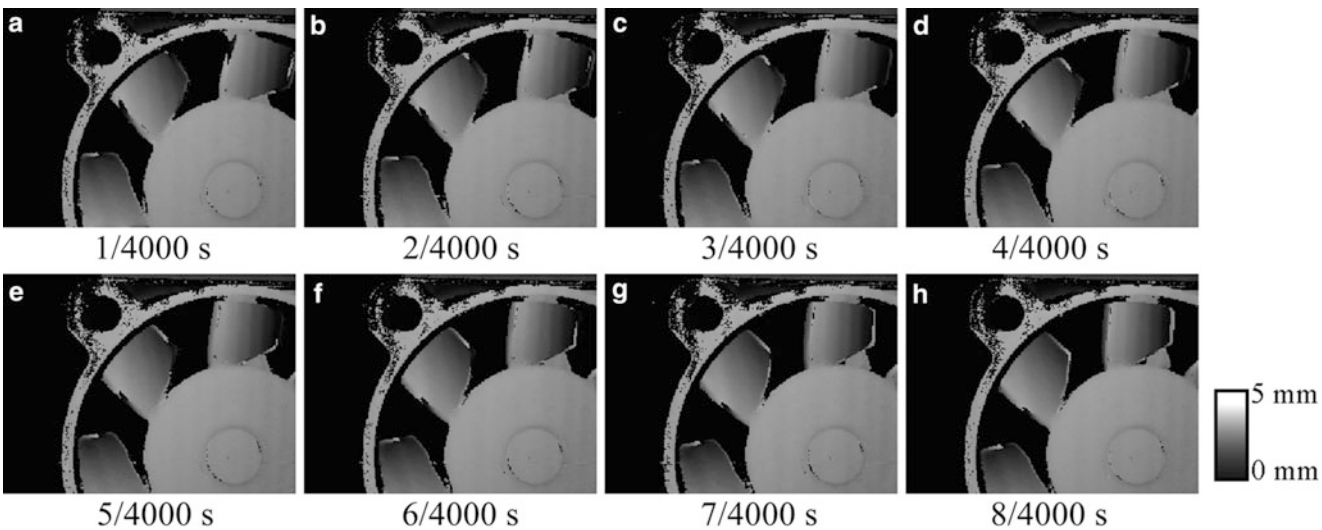

Fig. 3.8 Measured height distributions of a rotating fan in time series (**a**) 1/4,000 s (**b**) 2/4,000 s (**c**) 3/4,000 s (**d**) 4/4,000 s (**e**) 5/4,000 s (**f**) 6/4,000 s (**g**) 7/4,000 s (**h**) 8/4,000 s

grating images is obtained in every 1/4,000 s. The height distribution also obtained in every 1/4,000 s. Figure 3.7b shows a height distribution measured by this experimental setup. The cross section of the height distribution along a vertical line on Fig. 3.7b is shown in Fig. 3.7c. Figure 3.7d shows a 3D view of measured shape of the fan. Figure 3.8 shows the measured height distributions of a rotating fan in time series at intervals of 1/4,000 s.

3.4 Conclusions

High-speed shape measurement with a phase-shift grating projection method using a high-speed camera was performed in this paper. The LSSM using a linear LED array was employed as a grating projection method. The WSTM was employed to analyze the height distribution from obtained phase distribution. The WSTM is suitable for the LSSM. It was experimentally verified that the response speed of the linear LED array produced by authors was more than 200 kHz. In this experiment, the phase-shifting projection was performed in 12,000 Hz and the shape measurement of a rotating fan was performed in 4,000 Hz with three-steps phase shifting method.

Acknowledgement This research was supported by Hyogo COE program.

References

1. Morimoto Y, Fujigaki M, Toda H (1999) Real-time shape measurement by integrated phase-shifting method. Proc SPIE 3744:118–125
2. Fujigaki M, Matsumoto S, Masaya A, Morimoto Y, Murata Y (2012) Development of shape measurement system using mirrors for metallic objects. J JSEM 2(Special Isssue):194–197
3. Yen HN, Tsai DM, Yang JY (2006) Full-field 3-D measurement of solder pastes using LCD-based phase shifting techniques. IEEE Trans Electron Pack Manuf 29–1:50–57
4. Chan CS, Asundi AK (1994) Phase-shifting digital projection system for surface profile measurement. Proc SPIE 2354:444–452
5. Huang PS, Zhang C, Chiang F-P (2003) High-speed 3-D shape measurement based on digital fringe projection. Opt Eng 42–1:163–168
6. Zhang S, Weide DVD, Oliver J (2010) Superfast phase-shifting method for 3-D shape measurement. Opt Express 18–9:9684–9689
7. Gong Y, Zhang S (2010) Ultrafast 3-D shape measurement with an off-the-shelf DLP projector. Opt Express 18–19:19743–19754
8. Yoshizawa T, Wakayama T, Takano H (2007) Application of a MEMS scanner to profile measurement. Proc SPIE 6762:67620B-1-5
9. Asai D, Miyagi T, Fujigaki M, Morimoto Y (2010) Application to bin-picking of shape measurement using whole-space tabulation method with MEMS scanner grating projector. J JSEM 10(Special Issue):186–191
10. Zwick S, Fessler R, Jegorov J, Notni G (2012) Resolution limitations for tailored picture-generating freeform surfaces. Opt Express 20–4:3642–3653
11. Oura Y, Fujigaki M, Masaya A, Morimoto Y (2011) Development of linear LED device for shape measurement by light source stepping method. Opt Meas Model Metrol 5:285–291
12. Morimoto Y, Masaya A, Fujigaki M, Asai D (2012) Shape measurement by phase-stepping method using multi-line LEDs. In: Md. Zahurul Haq (ed) Applied measurement systems, InTech, Chapter 7, pp 137–152, http://www.intechopen.com/books/applied-measurement-systems; http://cdn.intechweb.org/pdfs/29356.pdf
13. Horikawa Y (2010) Japanese unexamined patent application publication no 2002-286432
14. Fujigaki M, Morimoto Y (2008) Shape measurement with grating projection using whole-space tabulation method. J JSEM (Japanese) 8(4):92–98
15. Fujigaki M, Takagishi A, Matui T, Morimoto Y (2008) Development of real-time shape measurement system using whole-space tabulation method, SPIE international symposium. Proc SPIE 7066:706606

Chapter 4
Deconvolving Strain Maps Obtained with the Grid Method

M. Grédiac, F. Sur, C. Badulescu, and J.-D. Mathias

Abstract The use of various deconvolution techniques to enhance strain maps obtained with the grid method is addressed in this study. Since phase derivative maps obtained with this measurement technique can be approximated by their actual counterparts convolved by the envelope of the kernel used to extract phases and phase derivatives, non-blind restoration techniques can be used to perform deconvolution. Six deconvolution techniques are compared here in order to restore a synthetic phase derivative map. Obtained results are analyzed and discussed.

Keywords Deconvolution • Displacement • Grid method • Strain measurement • Metrological performance

4.1 Introduction

Full-field measurement techniques are now wide spread in the experimental mechanics community. One of the reasons is their ability to measure heterogeneous states of strain and to detect localized events that often occur in specimens under test. Assessing the metrological performances of full-field measurement techniques remains an open issue. Recent papers published in this field mainly deal with digital image correlation [1, 2] for instance. One of the problems is that these performances depend on various parameters whose individual contribution is generally difficult to estimate [3].

Another problem is the fact that metrological performances depend on two conflicting concepts: resolution and spatial resolution. The first one is defined here by the smallest strain or displacement that can be detected, the second one by the smallest distance between independent measurements. It is well known that the better resolution, the worst spatial resolution. In addition, displacement is generally the physical quantity which is provided by many techniques but strain is the physical quantity involved in constitutive equations of engineering materials, so it often needs to be calculated. Since displacement maps are generally noisy, they are smoothed before differentiation which is performed to obtain strain components [4]. In conclusion, the number of parameters influencing the metrological performance is significant. This leads to confused ideas on the actual metrological performances of full-field measurement techniques, especially when strain components are considered instead of displacements.

M. Grédiac (✉)
Institut Pascal, UMR CNRS 6602, Clermont Université, Université Blaise Pascal, BP 10448, Clermont-Ferrand 63000, France
e-mail: Michel.Grediac@univ-bpclermont.fr

F. Sur
Laboratoire Lorrain de Recherche en Informatique et ses Applications, UMR CNRS 7503, Université de Lorraine, CNRS, INRIA projet Magrit, Campus Scientifique, BP 239, Vandoeuvre-lès-Nancy, Cedex 54506, France

C. Badulescu
Laboratoire Brestois de Mécanique et des Systèmes, ENSTA Bretagne, 2 rue François Verny, Brest, Cedex 9 29806, France

J.-D. Mathias
Laboratoire d'Ingénierie pour les Systèmes Complexes, IRSTEA, Campus universitaire des Cézeaux, 24 avenue des Landais, BP50085, Aubière, Cedex 63172, France

H. Jin et al. (eds.), *Advancement of Optical Methods in Experimental Mechanics, Volume 3*,
Conference Proceedings of the Society for Experimental Mechanics Series,
DOI 10.1007/978-3-319-00768-7_4,

This paper is devoted to the problem of the actual strain determination in case of localized phenomena which occur for instance when heterogeneous materials are tested. It is well known that with any measurement technique, smoothing performed to limit the impact of noise impairs both the size of the details in strain maps and the strain amplitude in these zones: details are generally enlarged due to blurring and the amplitude of the identified strain value is lower than the actual one.

The measurement method employed here is the grid method, which relies on a regular bi-directional marking of the surface under investigation. Images of this grid are taken while testing the specimens. These images are then processed to retrieve the in-plane displacement and strain components. This surface preparation is in general more difficult to obtain than a speckle, which is the typical marking used for digital image correlation. The big advantage of grids is however that a regular marking is much easier to duplicate or to control than a random one. In addition, a regular marking makes it possible to use powerful image processing techniques based on the Fourier transform for which a broad literature is available [5].

It has been recently shown that displacement and strain maps obtained with the grid method can be approximated with their actual counterparts convolved by the envelope used to extract the phase and phase derivatives from the grid images by windowed Fourier transform [6]. The idea is therefore to use deconvolution technique in order to restore displacement and strain fields and obtain actual distributions of these quantities. This paper is solely devoted to phase derivative. Indeed the change of this quantity during a test is directly proportional to strain maps. Finding phase derivatives is more critical than finding phases only. The reason is that spatial differentiation requires a smoothing stage to reduce the impact of noise. This procedure induces more severe convolution for phase derivatives than for phases.

Deconvolution techniques have only seldom been employed in the field of mechanics [7, 8]. Concerning displacement and strain measurement, one of the main reasons is certainly that the "classic" procedure to find strain maps, which consists in finding first displacement maps, smoothing them and differentiate the obtained result, involves several non-linear steps and numerous parameters. Consequently, the retrieved displacement and strain components do not appear as the convolution of the corresponding actual quantities in this case.

In this context, the aim of this paper is to show that deconvolution can be applied to restore strain maps obtained with the grid method. The main steps of the grid method are first recalled. The basics of deconvolution are then described along with the characteristics of various deconvolution algorithms. The performance of these algorithms is then briefly illustrated through the deconvolution of a synthetic phase derivative map.

4.2 The Phase and Phase Derivatives Provided by the Grid Method as the Convolution of Their Actual Counterparts

The grid method consists first in depositing a crossed grid on the surface under investigation in order to track the change in the geometry of the grid while loading increases, and to deduce the 2D strain fields from these images. The typical value of the pitch (denoted p) is 0.2 mm. The procedure for depositing the grids is given in [9].

Processing grid images consists first in extracting the phases along directions x and y both in the reference and in the current images. The displacement is obtained from the phase changes along both directions using the following equation:

$$\tilde{u}_i = -\frac{p}{2\pi}\Delta\,\tilde{\Phi}_i,\ \ i = x, y \tag{4.1}$$

for the displacements and

$$\tilde{\varepsilon}_{ij} = -\frac{p}{4\pi}\Delta\left(\frac{\partial\tilde{\Phi}_i}{\partial x_j} + \frac{\partial\tilde{\Phi}_j}{\partial x_i}\right),\ \ i, j = x, y \tag{4.2}$$

for the strain components. It has been recently demonstrated in [6] that each of the quantities $\tilde{X}$ defined above ($\tilde{X} = \tilde{\Phi}_i, \frac{\partial\tilde{\Phi}_i}{\partial x_j}, \tilde{u}_i, \tilde{\varepsilon}_{ij},\ i,j = x, y$) is nearly equal to the convolution of its actual counterpart X by the envelope of the kernel denoted g used in the windowed Fourier transform. Thus

$$\tilde{X} \approx X\ ^{*}\ g \tag{4.3}$$

where the symbol * denotes convolution.

This property has two important consequences. The first one is that any sudden variation of the actual displacement (resp. strain) distribution is smoothed by the phase (resp. phase derivative) extraction procedure. Hence the maps obtained after applying this procedure are automatically blurred in zones featuring high strain gradients. The quantities provided by the grid image processing exhibit systematically a lower amplitude than the actual ones in these zones. In addition, the geometry of these details in the maps is also spread by convolution. The second consequence is that since such maps can be considered as maps of the actual quantity convolved by g, one can restore them and try to find the actual quantity by deconvolution.

The remark concerning deconvolution is especially true for strain maps. Indeed in this case, function g generally defines a wide window in order to limit noise effect on the phase derivative. The classic route for finding the phase derivatives, namely finding first the displacements, smoothing them and differentiating the obtained result is slightly changed here by merging the first two steps. Thus enlarging the window when extracting the phases reduces noise effect, so no further smoothing is necessary prior to differentiation to obtain phase derivatives. The main advantage of this procedure is that the link between phase derivatives and grid image is straightforward, thus deconvolution can be performed.

4.3 Phase and Phase Derivatives Restoration by Deconvolution

Deconvolution of noisy maps is an ill-posed inverse problem which is prone to noise amplification and artefacts such as the so-called ringing artifact [5]. Solving this type of problem can only be efficiently performed by using suitable strategies which generally rely on various assumptions which enable us to add some a priori information, and therefore to reduce the abovementioned problems.

Various deconvolution techniques have been tested in this study in order to observe and quantify their ability to restore correctly strain maps. These techniques are direct deconvolution, regularized (Tikhonov) deconvolution, Rirchardson-Lucy deconvolution and Wiener filtering, with two different variants concerning the last two. Full details concerning the application of these techniques to strain map restoration can be found in Ref. [10].

All these techniques have been tested in turn to deconvolve a synthetic phase derivative image containing a wide range of frequencies. The image of the synthetic $\frac{\partial \Phi_y}{\partial y}$ distribution is shown in Fig. 4.1a. As may be seen, the phase derivative amplitude is constant throughout the phase derivative map. It is equal to 10^{-3}, which is a usual value for phase derivatives in deformed structures. The maximum frequency of the $\frac{\partial \Phi_y}{\partial y}$ distribution is located on the left-hand side of this figure. It is equal to half the frequency of the grid to avoid aliasing. All these quantities linearly evolve from the left- to the right-hand side, the maximum period being equal to 16 times that of the grid on the right-hand side. The idea is to observe at a glance both the effect of convolution due to phase derivative extraction and the ability of the deconvolution techniques listed above to restore the phase derivative distribution.

The corresponding phase derivative Φ_y is merely obtained by integration and the other phase Φ_x is assumed to be null. This information is used to modulate a grid whose pitch is equal to 5 pixels, and build a synthetic image for which the gray level is modelled as follows

$$s(x,y) = \frac{A}{2}\left[2 + \sin^3(2\pi fx) + \sin^3(2\pi fy + \Phi_y)\right] \tag{4.4}$$

where A is the amplitude and f the spatial grid frequency. Cubic sine functions are used here instead of pure sine functions to illustrate the fact that only the first harmonic of the periodic encoding is used to retrieve the phase and its derivatives as mentioned in [6]. It must finally be pointed out that a Gaussian white noise with various amplitude values has been added to this synthetic grid image to assess the robustness of the procedure.

Figure 4.1b shows the difference between the reference phase derivative and that obtained by applying the windowed Fourier transform. In this case, a noise (amplitude 5 pixels) has been added to the synthetic grid image modulated with the phase obtained by integrating the phase derivative distribution shown in Fig. 4.1a. A Gaussian window is employed in the windowed Fourier transform performed to retrieve the phase and phase derivatives. Its amplitude is equal to 5 pixels, which is a typical value employed in practice. It can be seen that the higher the frequency, the greater the error between identified and reference phase derivatives.

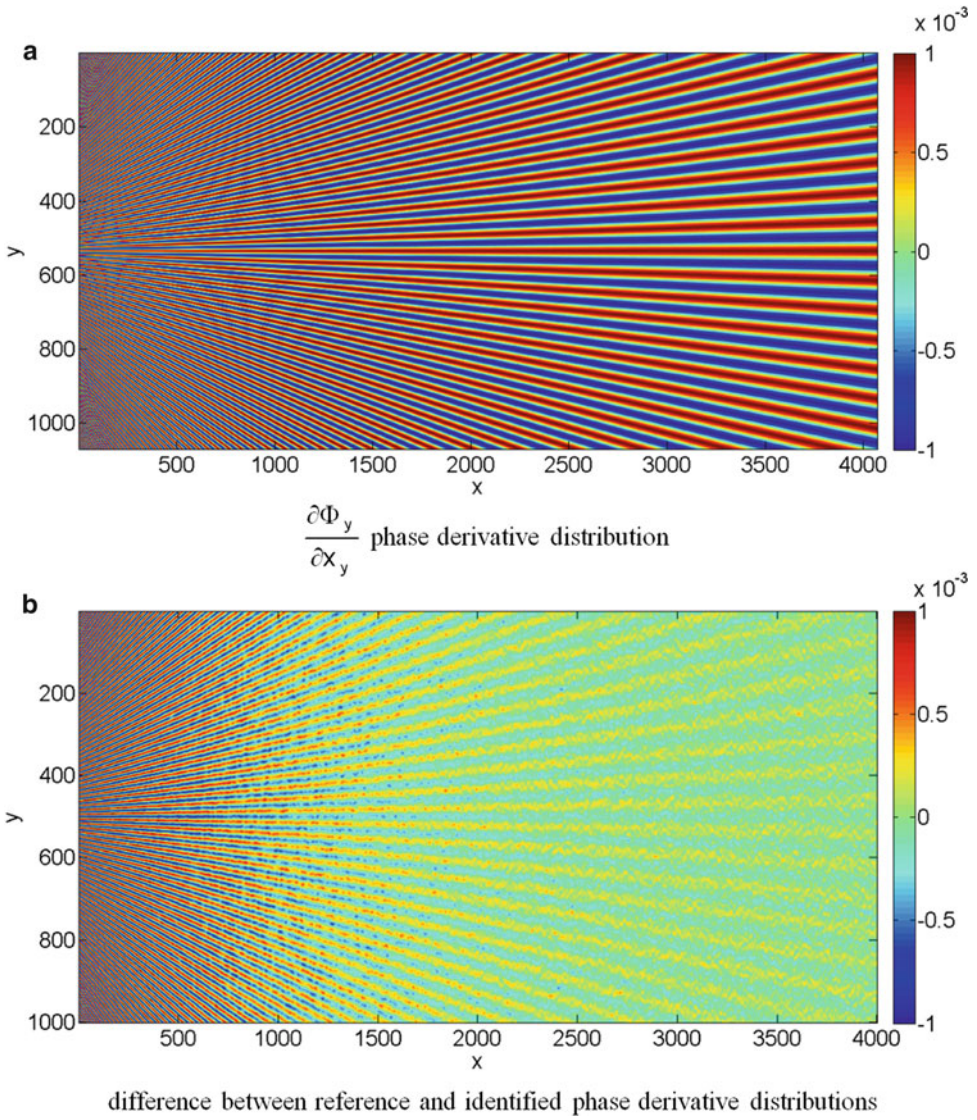

Fig. 4.1 Synthetic distribution of the phase used to test various deconvolution techniques [10]. (**a**) $\frac{\partial \Phi_y}{\partial x_y}$ phase derivative distribution, (**b**) difference between reference and identified phase derivative distributions

4.4 Typical Results

Typical examples of phase derivative maps restored with some deconvolution techniques are shown in Fig. 4.2. It can be seen that regularized deconvolution is unstable whereas it can be checked that this technique is able to restore very efficiently phase derivative maps when no noise is added (results not shown here). This illustrates the fact that deconvolution is an ill-posed problem which must be solved with care.

Figure 4.2b shows that the Richardson-Lucy algorithm restores high frequencies but significant noise amplitude is visible. Since this algorithm only restores images containing positive quantities and since we deal here with phase derivatives which can be negative, deconvolution is performed on the exponential of the phase derivative map. The logarithm of the result is then taken to obtain the restored distribution.

The phase derivative map deconvolved with Wiener filtering in shown in Fig. 4.2c. Comparing this map with that shown in Fig. 4.1b shows that this is a good compromise between high frequencies restoration and noise level in the phase derivative deconvolved map. A more refined analysis of the results obtained with the latter technique shows that Wiener filtering outperforms the Richardson-Lucy algorithm if the noise in the maps to be deconvolved is correctly characterized [10]. It has indeed been demonstrated in [6] that this noise is spatially correlated, thus deconvolution benefits from taking its autocorrelation function into account.

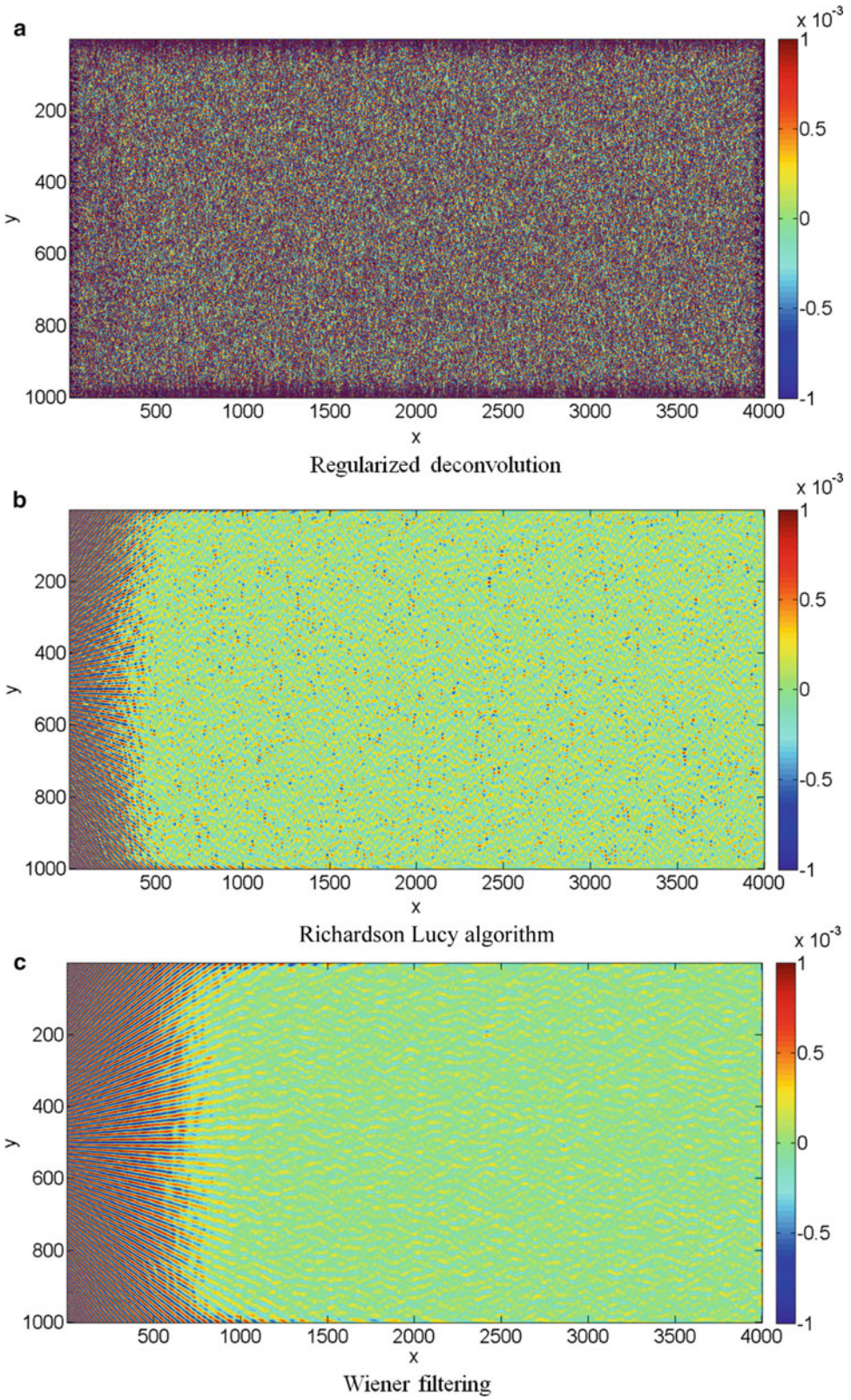

Fig. 4.2 Example of phase derivative maps obtained after deconvolution with various techniques [10]. (**a**) Regularized deconvolution, (**b**) Richardson Lucy algorithm, (**c**) Wiener filtering

4.5 Conclusion

Various deconvolution techniques were used to restore strain fields obtained with the grid method. A synthetic example is used to assess the performance of these deconvolution techniques. The influence of noise on the quality of the deconvolved maps is a major issue since some techniques are totally unstable when noise is taken into account whereas they give good results without noise in the grid images. Numerical simulations show that the Richardson-Lucy algorithm and Wiener filtering give good results in terms of compromise between noise level in the restored maps and ability to restore rather high frequencies.

References

1. Bornert M, Brémand F, Doumalin P, Dupré J-C, Fazzini M, Grédiac M, Hild F, Mistou S, Molimard J, Orteu J-J, Robert L, Surrel Y, Vacher P, Wattrisse B (2009) Assessment of digital image correlation measurement errors: methodology and results. Exp Mech 49(3):353–370
2. Lava P, Cooreman S, Coppieters S, De Strycker M, Debruyne D (2009) Assessment of measuring errors in DIC using deformation fields generated by plastic FEA. Opt Lasers Eng 47:747–753
3. Wang YQ, Sutton MA, Bruck HA, Schreier HW (2009) Quantitative error assessment in pattern matching: effects of intensity pattern noise, interpolation, strain and image contrast on motion measurements. Strain 45:160–178
4. Meng LB, Jin GC, Yao XF (2007) Application of iteration and finite element smoothing technique for displacement and strain measurement of digital speckle correlation. Opt Lasers Eng 45(1):57–63
5. Gonzalez RC, Woods RE (2006) Digital image processing, 3rd edn. Prentice-Hall, Upper Saddle River, NJ
6. Sur F, Grédiac M (2013) Towards deconvolution to enhance the grid method for in-plane strain measurement, Inverse Problems and Imaging (In revision)
7. Maas AM, Somers PAAM (2006) Two-dimensional deconvolution applied to phase-stepped shearography. Opt Lasers Eng 26:1594–1602
8. Dhanasekar B, Ramamoorthy B (2010) Restoration of blurred images for surface roughness evaluation using machine vision. Tribol Int 43:268–276
9. Piro JL, Grédiac M (2004) Producing and transferring low-spatial-frequency grids for measuring displacement fields with moiré and grid methods. Exp Tech 28(4):23–26
10. Grédiac M, Sur F, Badulescu C, Mathias JD (2013) Using deconvolution to improve the metrological performance of the grid method. Opt Lasers Eng 51:716–734

Chapter 5
Advanced Test Simulator to Reproduce Experiments at Small and Large Deformations

Marco Rossi, Michele Badaloni, Pascal Lava, Dimitri Debruyne, Gianluca Chiappini, and Marco Sasso

Abstract Full field measurements and inverse methods can be conveniently used to identify the constitutive properties of materials. Several methods are available in the literature which can be applied to many different types of materials and constitutive models (linear elasticity, elasto-plasticity, hyper-elasticity, etc.). The effectiveness of the identification procedure is related to the specimen geometry and the quality of the optical measurement technique. A method to improve and optimize the identification procedure is to numerically simulate the whole process. In such a way it is possible to compare different configurations and chose the one that shows the lowest identification error.

A test simulator was already developed by the authors and, in this paper, an improved version is presented. The simulator is now able to deal with small deformations thanks to a super-sampling algorithm which allows to reduce the numerical artefacts introduced during the image deformation. The simulated experiments are compared with actual ones. A series of experiments has been performed using aluminium specimens. The reliability of the simulated experiments is evaluated looking at the simulated and experimental displacement and strain maps and comparing the obtained identification errors

Keywords Full-field measurements • Error assessment • Test simulator • Inverse methods

5.1 Introduction

The use of full-field measurement techniques, such as Digital Image Correlation (DIC), is getting more and more widespread thanks to the improvements in the digital camera performances, computational power and correlation algorithms. The computational time has been remarkably reduced and user friendly GUIs are now available to perform the analysis. All these reasons and the moderate cost of the required equipment are gradually bringing DIC the status of standard measurement tool in mechanical testing laboratories.

The displacement and strain maps coming from full-field measurement may have a lot of different applications, e.g. characterizing defects, measuring the maximum deflection of a panel etc., however one of the most interesting applications is the identification of the mechanical properties of materials.

Standard mechanical tests, like uniaxial tensile, are designed to produce a uniform state of stress within the specimen. Therefore, several experiments are required to identify, for instance, the elastic stiffness components of orthotropic

M. Rossi (✉) • M. Badaloni • G. Chiappini • M. Sasso
Università Politecnica delle Marche, via brecce bianche, Ancona 60131, Italy
e-mail: m.rossi@univpm.it; m.badaloni@univpm.it; g.chiappini@univpm.it; m.sasso@univpm.it

P. Lava
Department of Mechanical Engineering, Catholic University College Ghent, Association K.U. Leuven, Gebroeders Desmetstraat 1, Ghent B-9000, Belgium
e-mail: pascal.lava@kahosl.be

D. Debruyne
Department of Mechanical Engineering, Catholic University College Ghent, Association K.U. Leuven, Gebroeders Desmetstraat 1, Ghent B-9000, Belgium

Department MTM, Katholieke Universiteit Leuven, Kasteelpark Arenberg 44, Leuven (Heverlee) B-3001, Belgium
e-mail: dimitri.debruyne@kahosl.be

H. Jin et al. (eds.), *Advancement of Optical Methods in Experimental Mechanics, Volume 3*,
Conference Proceedings of the Society for Experimental Mechanics Series,
DOI 10.1007/978-3-319-00768-7_5,

materials. Using full-field measurements, a mechanical test can be designed in order to produce heterogeneous stress-strain fields. In this way, richer information about the material behaviour can be obtained in a single test because the material is submitted to different stress conditions at different locations of the test specimen.

Different methods are available to extract the mechanical properties of materials from full-field measurements, for instance the finite element updating [1, 2], the virtual fields method [3] and many others. A review of these methods can be found in [4]. Although by then an extended literature is available on the different types of identification methods, much less papers have been dedicated to the study of the interactions between the identification procedure and the full-field optical technique used to obtain the strain data. So far, the error assessment has most of the time been focused only on the full-field optical measurement [5, 6]. In order to study the interactions between measurement and identification technique, a test simulator aimed to reproduce the whole measurement chain was firstly proposed in [7]. In this paper the simulated test was the Unnotched Iosipescu shear test [8] using the grid method [9] as full-field optical technique and the virtual fields method [3] as identification technique. Simulated experiments allowed to define the best specimen geometry which minimize the identification error.

In this paper the simulator was adapted to simulate DIC measurements [10]. Then a comparison with actual experiments was accomplished to evaluate the reliability of the simulator to reproduce the experimental errors.

5.2 Test Simulator and Image Deformation

The test simulator is aimed to reproduce an experimental test that involves full-field measurements. The flow chart of Fig. 5.1 illustrates the different steps of the simulation procedure. The input parameters describe the features of the test that has to be simulated, that are: the test geometry (e.g. shape of the specimen, thickness, type of applied load, etc.) the stiffness components, and the CCD camera characteristics (e.g. dynamic range, pixel resolution, fill factor etc.).

First a finite element model of the experimental test is built up with the appropriate specimen geometry, loads and boundary conditions. It is important to check that a suitable mesh refinement is employed. The computed displacement field will be used indeed to deform an image so it is necessary to know the displacement which occurs at each pixel position. The stiffness components adopted in the FE model are the reference value for the material investigated during the experiments. In this case an aluminium specimen is used with Young's modulus of 70 GPa and Poisson's ration 0.33.

The displacement field in the zone of the FE model framed by the camera in the actual experiment is used to numerically deform a reference image. The reference image is here a picture of the speckle pattern painted in the specimen surface. The image deformation algorithm represents a very critical part of the simulation procedure because it will unavoidably introduce numerical artefacts. It is important to minimize such errors. Different techniques can be used to numerically deform an image as, for instance, numerical binning (only for rigid shift), various types of grey level interpolation, FFT. The different types have been compared in [11] where it turns out that the FFT approach produce the more accurate results. In this paper the image is deformed using interpolation functions of the grey level and adopting a supersampling/undersampling algorithm to reduce the numerical errors.

As first step, a picture of the experimental speckle pattern is used to generate a "high resolution" (HR) reference image. This image is obtained by interpolating the grey level value at sub-pixel position using a cubic interpolation. An actual pixel is subdivided in a matrix of 3×3 sub-pixels. The HR reference image is deformed using the FEM displacement data. The deformation algorithm is illustrated in Fig. 5.2. The displacement field from FEM is interpolated onto the sub-pixel

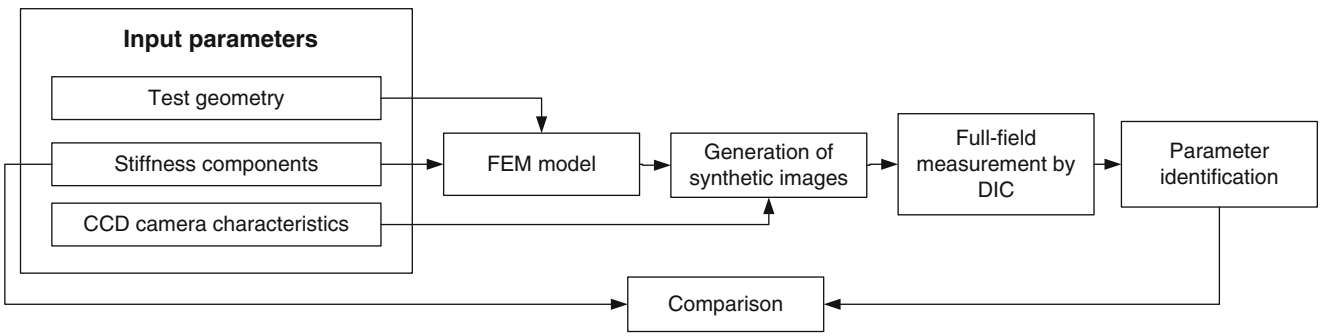

Fig. 5.1 Flow chart of the simulation process

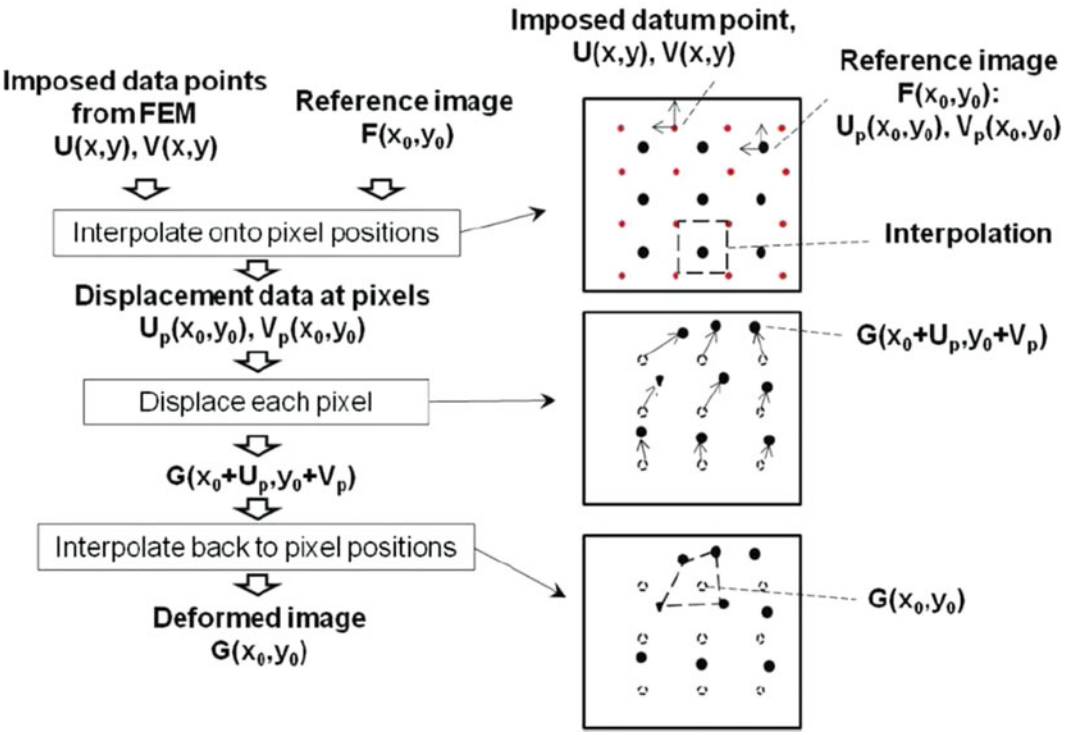

Fig. 5.2 Scheme of the image deformation routine

positions. The deformed position of the sub-pixel is thus achieved adding the displacement field to the position coordinates. Finally the grey level value at the sub-pixel position of the deformed image is obtained by interpolation.

The interpolations are performed using the "TriScatteredInterp" Matlab® function which allows to perform an interpolation on a scattered dataset. Such routine uses Delaunay triangulation to deal with the scattered data, the used interpolation method is C0 continuous.

The synthetic images are finally obtained by pixel under-sampling of the corresponding HR images. The super/under-sampling procedure is rather time consuming but allows to generate accurate synthetic images starting from real acquired images of the speckle pattern. Synthetic noise can be added to the syntactic image using a Gaussian random noise function where the standard deviation is the one measured during the experiments.

5.3 Experiments

The experiments consisted in a series of tensile tests performed with an electromechanical tensile machine (Zwick®Z050 model). The experimental set-up is illustrated in Fig. 5.3. One CMOS cameras with a resolution of 1280 × 1024 pixels (Pixelink® B371F model) was employed. The camera, with a lens of 200 mm, was aligned with the axis perpendicular to the specimen surface and placed at distance of around 1,750 mm from it to reduce the effect of out-of-plane movements. This camera was used to acquire the images to be processed with the 2D DIC program. The camera is synchronized with the tensile machine and, in the performed experiments, takes a picture every 2 s. A green-light (Banner® Led high-Intensity Ring Light) was pointed on the specimen to give an uniform illumination.

The specimen was cut from a sheet metal of aluminium 6,061 with a 4 mm thickness. In the area of measurement of the specimen a white layer of paint was applied, then black stains were sprayed onto the surface to generate a speckle pattern. Three types of tests were made. First, noise measurements were conducted taking subsequent pictures of the same fixed specimen. Then a constant vertical rigid body movement was imposed to the specimen, namely 1.43 mm. At last a tensile test was performed using force control, the load was varied from a minimum preload value of 0.1 kN to a maximum load of 12 kN. Such maximum force was chosen so that the yield limit of the material is not exceeded. The present research deals indeed only with the elastic part of the material behaviour. The same test was repeated several times in order to have statistical information. During each test, the maximum and minimum load was held for 5 s in order to have at least two

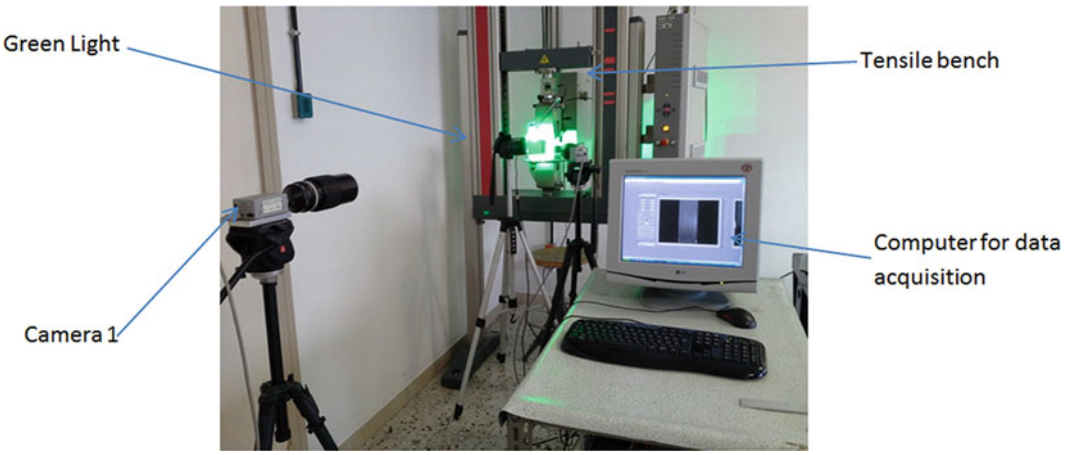

Fig. 5.3 Experiment set-up

Table 5.1 MatchID parameters

MatchID parameters	
Subset	21
Stepsize	5
Strain window	15

images for each level of force, since the acquisition frame rate is 0.5 fps. From the acquired images, a reference (at minimum force) and a deformed images (at maximum force) were selected. The displacement and strain maps were computed using MatchID [12]. The settings used in the DIC program are listed in Table 5.1.

5.4 Results and Discussions

The performed experimental tests have been then reproduced with the simulator, the results are discussed in this section. As preliminary analysis, the level of noise in terms of grey level was computed. Two images of the same target were acquired and the noise level was computed as the standard deviation of the difference of the grey level, at each pixel, divided by $\sqrt{2}$. After some repetitions, an average standard deviation of 1.75 grey levels was identified. A Gaussian noise with such a standard deviation was used in the simulation procedure. The noise is directly introduced in the grey level of the generated images, as explained before.

The reference image for the simulated tests was obtained from the actual picture of the experimental tests. Only a portion of the image was used, i.e. the zone of the specimen used to perform the DIC analysis. In this way, the simulated images have the same speckle pattern and the same pixel resolution of the experimental ones. The used portion of the image has a size of 391×904 pixels.

In the first test, the specimen was kept fixed, so that no displacement or strain should be measured by the DIC analysis. For each test repetition around 15,000 measurement points are obtained from DIC. In the second test a constant displacement in the vertical direction was imposed, in this case the measured strain field should be zero too. Means and standard deviations from the experimental and simulated tests are presented in Tables 5.2 and 5.3.

The obtained standard deviations are rather small both for displacement and strain fields, similar results are also obtained in other papers [13]. The simulator correctly reproduces the experiments. An increase of the strain standard deviation is obtained in the translated specimen. It is interesting noting that this effect is reproduced by the simulator, although the amount of noise input in the images is the same used for the fixed test. An example of experimental and simulated measured strain fields are shown in Fig. 5.4.

From these results it turns out that the simulator is able to reproduce the DIC error when the only source of error is the camera noise. In the second part of the paper, the simulator was employed to reproduce a tensile test aimed to identify the stiffness parameters of the aluminium, i.e. the Young's modulus E and the Poisson's ratio ν. Dealing with uniaxial tensile tests the parameters can be retrieved by:

Table 5.2 Noise measurement and simulation, fixed specimen

Experiments (5 repetitions)					
	u_x [pixels]	u_y [pixels]	ε_{xx}	ε_{yy}	ε_{xy}
Mean	-1.31×10^{-1}	-7.36×10^{-2}	8.11×10^{-5}	2.28×10^{-4}	-1.20×10^{-5}
Standard deviation	1.34×10^{-2}	4.88×10^{-2}	1.58×10^{-4}	1.71×10^{-4}	8.73×10^{-5}
Simulated experiments (10 repetitions)					
	u_x [pixels]	u_y [pixels]	ε_{xx}	ε_{yy}	ε_{xy}
Mean of the	-1.32×10^{-1}	-7.26×10^{-2}	8.80×10^{-5}	2.27×10^{-4}	-1.09×10^{-5}
Standard deviation	1.33×10^{-2}	4.74×10^{-2}	1.50×10^{-4}	1.69×10^{-4}	8.77×10^{-5}

Table 5.3 Noise measurement and simulation, translated specimen

Experiments (7 repetitions, mean translation: 1.43 mm)					
	u_x [pixels]	u_y [pixels]	ε_{xx}	ε_{yy}	ε_{xy}
Mean	-3.01×10^{-1}	-3.07×10^{1}	2.53×10^{-5}	1.31×10^{-4}	-2.20×10^{-5}
Standard deviation	4.12×10^{-2}	5.00×10^{-2}	2.80×10^{-4}	3.47×10^{-4}	2.46×10^{-4}
Simulated experiments (7 repetitions, input translation: 1.43 mm)					
	u_x [pixels]	u_y [pixels]	ε_{xx}	ε_{yy}	ε_{xy}
Mean	-2.62×10^{-4}	-3.03×10^{1}	1.29×10^{-6}	5.90×10^{-6}	-2.03×10^{-5}
Standard deviation	1.81×10^{-2}	1.89×10^{-2}	2.23×10^{-4}	2.40×10^{-4}	3.43×10^{-4}

$$E = \frac{\sigma_y}{\bar{\varepsilon}_y} = \frac{F}{A\bar{\varepsilon}_y} \tag{5.1}$$

$$\nu = -\frac{\bar{\varepsilon}_x}{\bar{\varepsilon}_y} \tag{5.2}$$

where $\bar{\varepsilon}_x$ and $\bar{\varepsilon}_y$ are the average value of the strain field, F is the applied force and A is the area of the specimen. The displacement field used to deform the images is obtained from a FE model of the specimens and a reference value of 70 GPa and 0.33 is used for E and ν, respectively. The results are shown in Table 5.4.

The accuracy of the simulated experiments, in terms of standard deviation of the identified values, is much higher compared to the one obtained experimentally. The mean value of E is also lower than the one expected for the used material, although in this case a direct comparison with the experiments is not possible since it is not known the exact value of the Young's modulus of the material. The present study is indeed focused on the standard deviation of the identified parameters which can be quantitatively compared with the standard deviation obtained in the experiments.

From this results it turns out that the grey level noise due to the camera is not the major source of error which influence the experiments. For instance in the FE model the clamps were supposed to be rigid while in the real case this is not true. Moreover that could be out-of-plane movements which influence the identification as explained in [13]. The presence of out-of-plane movements is testified in Fig. 5.5 where the experimental strain fields is compared with the simulated one. An unexpected strain gradient is clearly visible in the experimental measurements. This is probably due to a rotation of the specimen. Rigid in plane and out-of-plane movements can be introduced in the simulator by modifying the input displacement:

$$u_x = u_x^{FE} + C_x + \frac{\Delta z}{z} \cdot x \tag{5.3}$$

$$u_x = u_y^{FE} + C_y + \frac{\Delta z}{z} \cdot y \tag{5.4}$$

where C_x and C_y are constant values which indicates rigid body movement in the horizontal and vertical directions, Δz is the out-of-plane movement and z is the distance of the lens from the specimen surface. The constants used in the simulation for the rigid movement are $C_x = 0.05$ mm; $C_y = 0.5$ mm, this values are deduced from the experiments. The distance between lens and specimen is z = 1,750 mm. Since no data are available about the magnitude of the out-of-plane movement a tentative constant value of 0.012 mm was used. The new results are listed in Table 5.5.

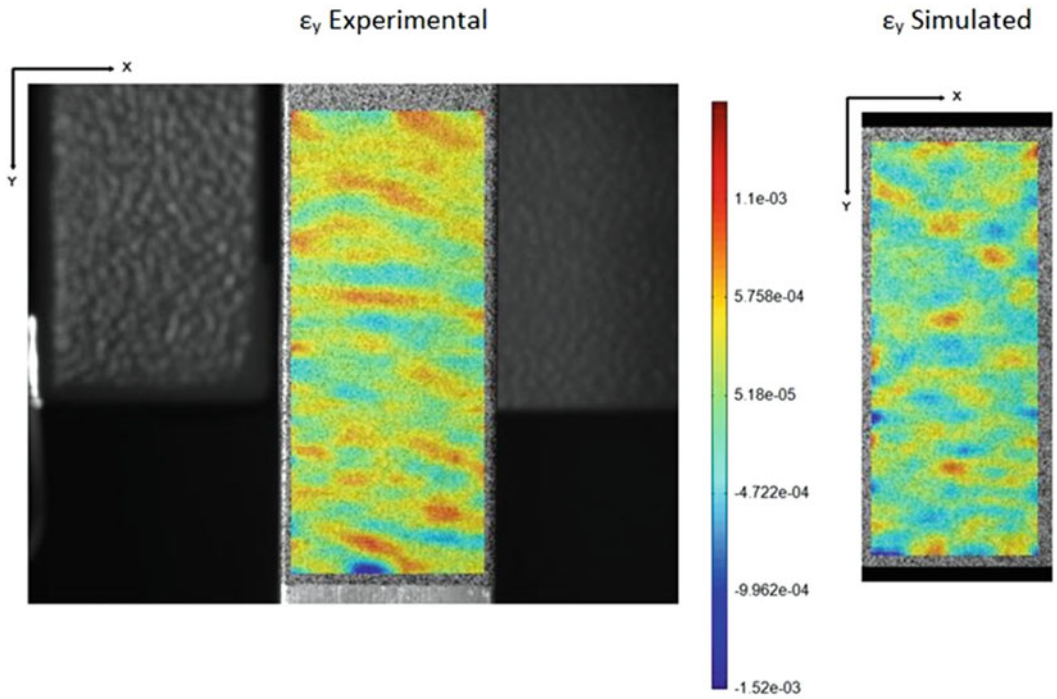

Fig. 5.4 Comparison between experimental and simulated strain maps in the translation test

Table 5.4 Identification results

Experiments (20 repetitions)				
	Mean(E) [MPa]	Std(E) [MPa]	Mean(ν) [MPa]	Std(ν) [MPa]
	62,483.72	3,111.61	0.3098	0.0700
Simulated experiments (20 repetitions, reference values: E = 70000 MPa ν = 0.33)				
	Mean(E) [MPa]	Std(E) [MPa]	Mean(ν) [MPa]	Std(ν) [MPa]
FE displacement	70,597.50	252.35	0.3292	0.0033

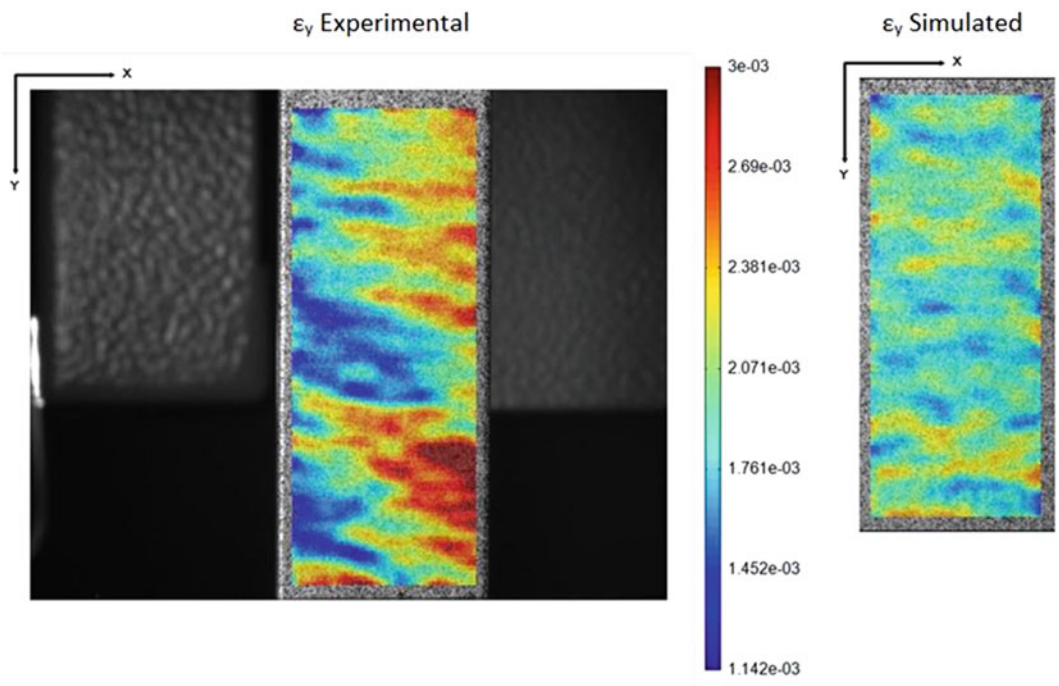

Fig. 5.5 Comparison between real experiments and simulated ones in terms of strain maps

Table 5.5 Identification results

Experiments (20 repetitions)				
	Mean(E) [MPa]	Std(E) [MPa]	Mean(ν) [MPa]	Std(ν) [MPa]
	62,483.72	3,111.61	0.3098	0.0700
Simulated experiments (20 repetitions, reference values: E = 70000 MPa ν = 0.33)				
	Mean(E) [MPa]	Std(E) [MPa]	Mean(ν) [MPa]	Std(ν) [MPa]
FE displacement	70,597.50	252.35	0.3292	0.0033
+ in-plane movement	70,583.75	543.93	0.3271	0.0064
+ out-of-plane movement	68,087.85	270.55	0.2864	0.0044
FE + in-plane + out-of-plane	68,846.10	302.68	0.3063	0.0036

Looking at the simulated results, adding in-plane and out-of-plane movements modify the mean value of the identified results but not large differences are obtained in the standard deviations. There still is a large variation between the standard deviation of the experiments and the simulated tests. In order to improve the likelihood of the simulator, a variance should be introduced in the applied in-plane and out-of-plane movements. In this way, using a sort of Monte Carlo simulation, the simulator should be able to produce numerical experiments which approximate what happens in real ones.

5.5 Conclusions

A simulator able to reproduce experiments which involves DIC measurement is presented and used to simulate tensile test on aluminium specimens. The simulator is first validated using fixed specimen and then rigid body movements. In this case the simulator correctly describes the experimental behaviour. When a tensile test is simulated, however, a much larger standard deviations of the identification parameters is obtained in the experiments compared to the simulated tests. This can be explained because of the out-of-plane movements that has to be considered in the simulator. The simulator has to be enriched including more source of errors to fit the experimental tests. After a calibration of the simulator using simple tensile tests, it can be used to correctly reproduce more complex experimental tests which involves heterogeneous strain fields and inverse methods to identify the constitutive parameters.

References

1. Cooreman S, Lecompte D, Sol H, Vantomme J, Debruyne D (2008) Identification of mechanical material behavior through inverse modeling and DIC. Exp Mech 48(4):421–433
2. Lecompte D, Smits A, Sol H, Vantomme J, Van Hemelrijck D (2007) Mixed numerical–experimental technique for orthotropic parameter identification using biaxial tensile tests on cruciform specimens. Int J Solid Struct 44(5):1643–1656
3. Pierron F, Grédiac M (2012) The virtual fields method. Springer, New York
4. Avril S, Bonnet M, Bretelle A-S, Grédiac M, Hild F, Ienny P, Latourte F, Lemosse D, Pagano S, Pagnacco E, Pierron F (2008) Overview of identification methods of mechanical parameters based on full-field measurements. Exp Mech 48:381–402
5. Bornert M, Brémand F, Doumalin P, Dupré J-C, Fazzini M, Grédiac M, Hild F, Mistou S, Molimard J, Orteu J-J, Robert L, Surrel Y, Vacher P, Wattrisse B (2009) Assessment of digital image correlation measurement errors: methodology and results. Exp Mech 49:353–370
6. Wang Y, Lava P, Coppieters S, De Strycker M, Van Houtte P, Debruyne D (2012) Investigation of the uncertainty of DIC under heterogeneous strain states with numerical tests. Strain 48(6):453–462
7. Rossi M, Pierron F (2012) On the use of simulated experiments in designing test for material characterization from full-field measurement. Int J Solid Struct 49:420–435
8. Pierron F, Vert G, Burguete R, Avril S, Rotinat R, Wisnom M (2007) Identification of the orthotropic elastic stiffnesses of composites with the virtual fields method: sensitivity study and experimental validation. Strain 43:250–259
9. Surrel Y (1996) Design of algorithms for phase measurements by use of phase-stepping. Appl Opt 35:51–60
10. Sutton MA, Orteu JJ, Schreier HW (2009) Image correlation for shape, motion and deformation measurements. Springer, New York
11. Reu PL (2011) Experimental and numerical methods for exact subpixel shifting. Exp Mech 51:443–452
12. http://www.matchid.org
13. Sutton MA, Yan JH, Tiwari V, Schreirer HW, Orteu JJ (2008) The effect of out-of-plane motion on 2D and 3D digital image correlation measurements. Opt Laser Eng 46:746–757

Chapter 6
The Eigenfunction Virtual Fields Method

Sankara J. Subramanian

Abstract The Virtual Fields Method (VFM, Pierron and Grediac, 2012) is an inverse technique for computing mechanical properties of materials from full-field deformations obtained from techniques such as Digital Image Correlation (DIC). VFM is based on the principle of virtual work, which is a weak statement of the equations of motion. Central to VFM is the appropriate choice of virtual fields, which in prior work, have been assumed to be polynomials that are continuously differentiable, either piece-wise or over the entire domain of interest. In this work, we propose a new method for systematically identifying virtual fields by performing a principal component analysis (PCA) of the strain field measured from experiments. The virtual strain components to be used in VFM are then chosen to be the eigenfunctions so determined. In addition to being a physically meaningful set of virtual fields, such a choice exploits the orthogonality of the computed eigenfunctions while simultaneously eliminating computation of a large number of coefficients that define the virtual fields in prior approaches. In the case of linear elastic behaviour, we show that this new approach, named the Eigenfunction Virtual Fields Method (EVFM), leads to a compact system of equations that can be solved for the unknown material parameters.

Keywords Full-field measurement • Constitutive equations • Principle of virtual work • Principal components analysis • Virtual Fields Method

6.1 Introduction

The Virtual Fields Method (VFM; [1]) is an inverse-computation technique based on the Principle of Virtual Work (PVW; [2]), used to estimate mechanical properties of materials from full-field strain measurements. In the context of infinitesimal deformations, if inertial effects and body forces are small enough to be neglected, PVW may be stated as

$$\int_V \sigma : \epsilon^* \mathrm{d}V = \int_{S_T} t \cdot u^* \mathrm{d}A, \tag{6.1}$$

where V is the volume occupied by the solid of interest, S_T is the portion of the exterior surface of the solid where tractions are prescribed, σ is any statically admissible stress field, t is the (true) traction vector specified on S_T, u^* is any kinematically admissible virtual displacement field and $\epsilon^* = \frac{1}{2}(\nabla u^* + \nabla u^{*T})$ is the virtual strain field obtained by differentiating the virtual displacement field u^* with respect to the current configuration [2]. In the literature, the left hand side of Eq. (6.1) is commonly referred to as the *internal virtual work* and the right hand side the *external virtual work*.

Linear VFM, i.e. applications of VFM to linear elastic material parameter estimation, is the topic of concern in this article. A good review of methods for solving this problem is found in [3]. The treatment herein is restricted to in-plane deformations of homogeneous, but possibly anisotropic, materials and plane-stress deformation of specimens made of such

S.J. Subramanian (✉)
Department of Engineering Design, Indian Institute of Technology Madras, Chennai, India
e-mail: shankar_sj@iitm.ac.in

H. Jin et al. (eds.), *Advancement of Optical Methods in Experimental Mechanics, Volume 3*,
Conference Proceedings of the Society for Experimental Mechanics Series,
DOI 10.1007/978-3-319-00768-7_6,

materials, as is customary in VFM. Thus, in these materials, the stress tensor σ is related to the strain ε through a uniform fourth-order elasticity tensor C:

$$\sigma = C\epsilon \tag{6.2}$$

Following Voigt notation, $(\sigma_{11}, \sigma_{22}, \sigma_{12}) \equiv (\sigma_1, \sigma_2, \sigma_3); (\epsilon_{11}, \epsilon_{22}, 2\epsilon_{12}) \equiv (\epsilon_1, \epsilon_2, \epsilon_3)$, Eq. (6.1) may be written in indicial form as

$$C_{ij} \int_V \epsilon_i \epsilon_j^* \mathrm{d}V = \int_{S_T} t_i u_i^* \mathrm{d}A \tag{6.3}$$

In VFM, advantage is taken of current experimental techniques such as Digital Image Correlation (DIC; [4]), which generate spatially dense measurements of strain components ε_i over the specimen area of interest. For each choice of virtual field, the integrals on the left hand side and right hand side of Eq. (6.3) are explicitly computed, generating one linear equation in the unknown material parameters. If N independent material constants p_α, $(\alpha = 1,\ N)$, feature in C, then these p_α are computed in VFM by generating a sufficient number of linear equations for the unknowns by employing various virtual displacement fields $u^{*\,k}$, $k = 1,\ d$; $d \geq N$ and solving the resulting system of equations $PQ = R$. Details of application of VFM to estimation of constitutive parameters of various material models, both linear and non-linear (e.g. elasto-plasticity, damage), may be found in the recent book on VFM [1].

The choice of virtual fields plays a vital role in the successful computation of the materials parameters p_α. In the earliest works, the virtual fields were chosen based on intuition and trial-and-error [5], but these were not guaranteed to yield independent equations for the unknown material parameters. For this reason, so-called 'special' virtual fields were defined [6] to yield fully decoupled equations for the unknowns. These fields were called special since they rendered the matrix of virtual work coefficients (P) equal to the identity matrix. However, a large number of unknown coefficients are introduced to define the virtual fields in this approach, which becomes computationally expensive. While [6] employed special virtual fields that were continuous over the entire domain of interest, piece-wise virtual fields with virtual nodal displacements akin to those commonly used in the finite-element method were introduced by Toussaint et al. [7]. Virtual fields have also been chosen to be those that are least sensitive to experimental noise; this was investigated for the case of virtual fields continuous over the whole domain by Avril et al. [8], and later extended to the case of piecewise virtual fields by Avril and Pierron [3].

In this work, a novel method of choosing virtual fields is presented. This approach differs markedly from that presented in the literature to date in that the form of the virtual fields is not determined a priori. Rather, the virtual fields are determined from the measured displacement field; they are, in fact, based on the eigenfunctions of the measured strain fields and hence, the method proposed herein is called the Eigenfunction Virtual Fields Method (EVFM). Since actual measured strain fields are used in the computations, EVFM provides a physically-based and systematic means of selecting virtual strain fields and solving the resulting VFM equations for the unknown material parameters. Another significant advantage of EVFM is that no unknown coefficients (as in the case of full-domain or piece-wise virtual fields) are introduced to define the virtual fields since the eigenfunctions are completely defined by the measured strain fields to begin with. The proposed choice of virtual fields leads to enormous algebraic simplification compared to existing VFM approaches, resulting in a compact system of equations to be solved.

6.2 Computation of Eigenfunctions of Strain Fields

EVFM is built around eigenfunctions of the measured strain components ε_1, ε_2 and ε_3 and therefore, computation of these eigenfunctions is discussed before the method itself is presented. It is assumed that the three strain components have been obtained from experiments on a grid of $(m+1) \times (n+1)$ points, from the centroids of whose cells a new grid of $m \times n$ points is obtained. Let the three strain components be generated on this new grid by simple averaging of the four surrounding values on the original grid and stored in the three $m \times n$ matrices E_1, E_2, and E_3 respectively. This averaging operation is introduced merely to simplify the algebra that appears later in this article, and is not essential to the efficacy of the method. Although this operation also introduces interpolation error into the original data, this is not expected to be a significant issue since the measurement grid is typically quite fine.

From the generated strain component grids, two augmented matrices E^r and E^c of sizes $3m \times n$ and $m \times 3n$ respectively are formed as follows:

$$E^r = \begin{bmatrix} E_1 \\ E_2 \\ E_3 \end{bmatrix}; \quad E^c = [\, E_1 E_2 E_3 \,] \tag{6.4}$$

Principal Component Analysis (PCA, [9]) is used to investigate E^r and E^c, whose eigenfunctions are obtained by performing Singular Value Decomposition (SVD). Thus, one obtains the decompositions:

$$E^r_{(3m\times n)} = L^r_{(3m\times 3m)} S^r_{(3m\times n)} (R^r)^T_{(n\times n)}; \quad E^c_{(m\times 3n)} = L^c_{(m\times m)} S^c_{(m\times 3n)} (R^c)^T_{(3n\times 3n)}, \tag{6.5}$$

where

- The columns of L^r and L^c contain the left eigenvectors of E^r and E^c (i.e. those of $E^r(E^r)^T$ and $E^c(E^c)^T$);
- S^r and S^l are diagonal matrices that contain the singular values of E^r and E^c;
- The columns of R^r and R^c contain the right eigenvectors of E^r and E^c (i.e. those of $(E^r)^T E^r$ and $(E^c)^T E^c$)

respectively. A significant benefit of this decomposition is that each set of eigenvectors forms a complete orthonormal basis; thus, the right eigenvectors form an orthonormal basis for the row space of each augmented matrix, while the left eigenvectors form an orthonormal basis for the column space [10].

Denote by l^r and r^r the left and right eigenvectors of E^r, and by and r^c the left and right eigenvectors of E^c, of length $3m$, n, m, and $3n$ respectively. It is also assumed that the singular values of E^r and E^c are E^c are arranged in decreasing order. Then, the number of principal eigenvectors for each augmented matrix may be obtained by identifying the knee in the respective logarithmic plots of singular values [9, 11]. The principal left and right eigenvectors of each augmented matrix show the dominant spatial patterns in each composite strain field along the X_1- and X_2-directions respectively and the contribution of the ith pattern to each matrix is reflected in the magnitude of the corresponding singular value λ_i [11].

Since the left and right eigenvectors form an orthonormal basis for column and row spaces of the composite matrices respectively, the columns and rows of the strain matrices E_1, E_2, and E_3 may be expanded in terms of these eigenvectors. It is frequently found that full-field strain data are highly redundant and only a small number $p \ll \min(m, n)$ eigenvectors are *dominant*. Therefore, it is sufficient to reconstruct the strain matrices in terms of the p-dimensional subspace of the row and column spaces spanned by these p dominant left and right eigenvectors. If $\tilde{E}^r_1$ is the matrix of strain values ε_1 reconstructed using the p right eigenvectors of E^r, then

$$\tilde{E}^r_1 = \tilde{A}^r_1 (\tilde{R}^r)^T = E_1 \tilde{R}^r (\tilde{R}^r)^T, \tag{6.6}$$

where $\tilde{R}^r$ is the $n \times p$ matrix whose columns contain the p dominant right eigenvectors of E^r and $\tilde{A}^r_1 = E_1$ is an $m \times p$ matrix of components of the rows of E_1 along the columns of $\tilde{R}^r$ from which it is seen that the kth row $(\tilde{E}^r_1)^{(k,-)}$ of $\tilde{E}^r_1$ is given by

$$(\tilde{E}^r_1)^{(k,-)} = (\tilde{A}^r_1)^{(k,-)} (\tilde{R}^r)^T \tag{6.7}$$

Similarly, $\tilde{E}^c_1$, the matrix of ε_1 values reconstructed from the p dominant left eigenvectors of E^c is written as

$$\tilde{E}^c_1 = \tilde{L}^c (\tilde{A}^c_1)^T = \tilde{L}^c (\tilde{L}^c)^T E_1, \tag{6.8}$$

with $\tilde{L}^c$ is the $m \times p$ matrix whose columns contain the p left eigenvectors of E^c and $\tilde{A}^c_1 = (E_1)^T \tilde{L}^c$ is a $p \times n$ matrix of components of the columns of E_1 along the columns of along the columns of $\tilde{L}^c$. Similar reconstructions are defined for the other two strain component matrices.

6.3 The Eigenfunction Virtual Fields Method

In this article, the Eigenfunction Virtual Fields Method is introduced, in which the virtual strain fields are constructed from the dominant right eigenvectors of E^r (of length n) and dominant left eigenvectors of E^c (of length m). Since the constitutive equations (6.2) relate the true stress component fields to the true strain fields, which in turn can be reconstructed in terms of the right or left eigenvectors, these choices of virtual strain fields, coupled with the fact that each set of eigenvectors is orthonormal, lead to very simple forms for the internal work term in Eq. (6.3). These virtual fields also enable simple forms for the virtual displacements on S_T, from which the external virtual work term can be calculated.

To make these ideas clear, the problem of determining the elastic constants of an isotropic, linear elastic solid using full-field strain data from a uniaxial tension of a plate is studied. The objective in choosing this model problem is to highlight the various steps involved in EVFM; a more formal development of the method and its application to more general constitutive equations will be taken up elsewhere. Let the thickness h of the plate be small enough for plane stress conditions to prevail and the area of interest be a rectangular region (as is common in many experiments) of extent $L_1 \times L_2$ as shown in Fig. 6.1. Further, let a tensile load P be applied on the boundaries at $X_2 = 0,\ X_2 = L_2$ while those at $X_1 = 0,\ X_1 = L_1$ remain traction-free. Note that the exact distribution of the tractions on S_T is unknown, and as discussed by Grediac et al. [6], this exact distribution is not required, but knowledge of the total load P is sufficient to compute the external virtual work. For the purpose of illustration, the area of interest is assumed to be far enough away from the points of application of load so that one may assume that a uniform state of stress prevails therein.

Under these conditions, the stress-strain relations have the form [12]:

$$\sigma_1 = (Q_1\epsilon_1 + Q_2\epsilon_2);\ \sigma_2 = (Q_2\epsilon_1 + Q_1\epsilon_2);\ \sigma_3 = (\frac{Q_1 - Q_2}{2})\epsilon_3, \tag{6.9}$$

where two material constants $Q_1 = \frac{E}{1-\nu^2}$ and $Q_2 = \nu Q_1 = \frac{E\nu}{1-\nu^2}$ have been defined. Using Eq. (6.9), the virtual work equations can be written as

$$\int_V \left[(Q_1\epsilon_1 + Q_2\epsilon_2)\epsilon_1^* + (Q_2\epsilon_1 + Q_1\epsilon_2)\epsilon_2^*\right] \mathrm{d}V = \int_{S_T} \left(t_1 u_1^* + t_2 u_2^*\right) \mathrm{d}S \tag{6.10}$$

The true strain fields for the problem at hand are uniform:

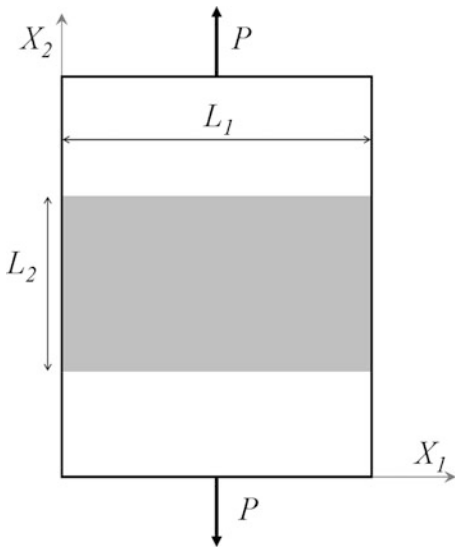

Fig. 6.1 Boundary conditions and geometry for the plane-stress unaxial tension problem studied; *shaded region* shows the area of interest

$$E_1 = e_1 \underset{(m\times n)}{\begin{bmatrix} 1 & 1 & \cdots & 1 & 1 \\ 1 & 1 & \cdots & 1 & 1 \\ \vdots & \vdots & \ddots & \vdots & \vdots \\ 1 & 1 & \cdots & 1 & 1 \\ 1 & 1 & \cdots & 1 & 1 \end{bmatrix}}; \; E_2 = e_2 \underset{(m\times n)}{\begin{bmatrix} 1 & 1 & \cdots & 1 & 1 \\ 1 & 1 & \cdots & 1 & 1 \\ \vdots & \vdots & \ddots & \vdots & \vdots \\ 1 & 1 & \cdots & 1 & 1 \\ 1 & 1 & \cdots & 1 & 1 \end{bmatrix}}; \; E_3 = e_3 \underset{(m\times n)}{\begin{bmatrix} 0 & 0 & \cdots & 0 & 0 \\ 0 & 0 & \cdots & 0 & 0 \\ \vdots & \vdots & \ddots & \vdots & \vdots \\ 0 & 0 & \cdots & 0 & 0 \\ 0 & 0 & \cdots & 0 & 0 \end{bmatrix}}, \tag{6.11}$$

where e_1 and e_2 are the measured transverse and axial strains respectively. For these true strain fields, E^r and E^c consist of only one dominant singular value each and therefore, only one dominant left and right eigenvector each. Of these, the dominant right eigenvector of E^r and left singular eigenvector of E^c, which are used in constructing the virtual strain fields, are expressed respectively as:

$${}^1r^r = \frac{1}{n^{\frac{1}{2}}} \underset{(1\times n)}{\begin{bmatrix} 1 & 1 & \cdots & 1 & 1 \end{bmatrix}}; \quad {}^1l^c = \frac{1}{m^{\frac{1}{2}}} \underset{(1\times m)}{\begin{bmatrix} 1 1 \end{bmatrix}}. \tag{6.12}$$

The boundaries at $X_1 = 0,\ X_1 = L_1,\ X_2 = 0,\ X_2 = L_2$ constitute the areas for computation of the external virtual work. As pointed out in [6], the distribution of tractions on these boundaries is not known in an experiment; only the total force is known. Therefore, it is essential to choose virtual fields that are uniform on the boundary S_T so that the external virtual work can be computed.

Before the actual virtual fields are described, the following piece-wise continuous versions of the discrete eigenvectors obtained in the previous section are defined:

$$f_n(X_1; r) = \sum_{k=1}^{n} N_k(X_1) r_k; \quad N_k(X_1) = \begin{cases} 1, \text{ if } (X_1)_k - \frac{\Delta X_1}{2} < X_1 < (X_1)_k + \frac{\Delta X_1}{2} \\ 0, \text{ otherwise} \end{cases}, \tag{6.13}$$

where $\Delta X_1 = \frac{L_1}{n}$, $(X_1)_k$ is the X_1 value at the kth grid location and r_k is the kth component of the right eigenvector r. A similar function f_m (with $\Delta X_2 = \frac{L_2}{m}$) is defined for a left eigenvector l as

$$f_m(X_2; l) = \sum_{k=1}^{m} N_k(X_2) l_k; \quad N_k(X_2) = \begin{cases} 1, \text{ if } (X_2)_k - \frac{\Delta X_2}{2} < X_2 < (X_2)_k + \frac{\Delta X_2}{2} \\ 0, \text{ otherwise} \end{cases}. \tag{6.14}$$

Note that due to orthonormality of the eigenvectors, the following results for the inner products between ith and jth hold:

$$\int_0^{L_1} f_n(X_1; {}^i r) f_n(X_1; {}^j r) \mathrm{d}X_1 = \delta_{ij} \Delta X_1; \quad \int_0^{L_2} f_m(X_2; {}^i l) f_m(X_2; {}^j l) \mathrm{d}X_2 = \delta_{ij} \Delta X_2, \tag{6.15}$$

where δ_{ij} is the Kronecker delta.

A set (say, Set 1) of p virtual fields may be constructed using the p dominant right eigenvectors of E^r:

$$(i = 1, p): \quad {}^i\epsilon_1^* = f_n(X_1, {}^i r^r); \quad {}^i\epsilon_2^* = 0; \quad {}^i\epsilon_3^* = 0; \tag{6.16}$$

Here ${}^i r^r$ is the ith dominant right eigenvector of E^r. Note that the virtual strain fields constructed vary only along the 1-direction and are uniform along the 2-direction. Virtual displacement fields compatible with these virtual strain fields may be obtained straightforwardly for any $X_1 \mid (X_1)_j - \frac{\Delta X_1}{2} < X_1 < (X_1)_j + \frac{\Delta X_1}{2}$ as

$$(i = 1, p): \quad {}^i u_1^* = \int_0^{X_1} \epsilon_1^*(s) \mathrm{d}s = \left[\sum_{k=1}^{j-1} {}^i r_k^r \right] \Delta X_1 + {}^i r_j^r (X_1 - (X_1)_j); \quad {}^i u_2^* = 0, \tag{6.17}$$

where ${}^{i}r_k{}^{r}$ is the kth component of the ^{i}th right eigenvector of E^r. These virtual displacement fields are also uniform along the 2-direction.

Likewise, a second set of virtual fields, denoted Set 2, which vary only along the 2-direction may be constructed from the dominant left eigenvectors of E^c:

$$(i = 1, p): \quad {}^{i}\epsilon_1^* = 0; \quad {}^{i}\epsilon_2^* = f_m(X_2, {}^{i}l^c); \quad {}^{i}\epsilon_3^* = 0 \tag{6.18}$$

with the virtual displacement fields for any $X_2 \mid (X_2)_j - \frac{\Delta X_2}{2} < X_2 < (X_2)_j + \frac{\Delta X_2}{2}$ given by

$$(i = 1, p): \quad {}^{i}u_1^* = 0; \quad {}^{i}u_2^* = \int_0^{X_2} \epsilon_2^*(s)\mathrm{d}s = \left[\sum_{k=1}^{j-1} {}^{i}l_k^c\right]\Delta X_2 + {}^{i}l_j^c(X_2 - (X_2)_j), \tag{6.19}$$

6.4 Results and Discussion

For the uniaxial tensile test considered here, the elastic constants are easily obtained in terms of applied load and measured strains as

$$E = \frac{P}{L_1 h e_2}; \quad \nu = \frac{-e_1}{e_2} \Longrightarrow Q_1 = \frac{P e_2}{L_1 h (e_2^2 - e_1^2)}; \; Q_2 = \frac{-P e_1}{} L_1 h (e_2^2 - e_1^2) \tag{6.20}$$

It will be shown in this section that the proposed virtual fields yield this answer in a straightforward manner.

With the virtual fields as in Eqs. (6.16) and (6.17), the virtual work Eqs. (6.10) read

$$\int_V (Q_1\epsilon_1 + Q_2\epsilon_2)\epsilon_1^* \mathrm{d}V = \int_{S_T} \left(t_1 u_1^* + t_2 u_2^*\right)\mathrm{d}S \tag{6.21}$$

The boundary S_T consists of the four surfaces at $X_1 = 0,\ X_1 = L_1,\ X_2 = 0,\ X_2 = L_2$. On the first two surfaces, $t_i = 0$ and on the last two, tractions are applied only along the 2-direction, while the only non-zero virtual displacement is ${u_1}^*$; therefore, the total external virtual work is zero. Thus, the principle of virtual work, with the substitution of Eq. (6.16) can be stated as

$$\int_V (Q_1\epsilon_1 + Q_2\epsilon_2)\epsilon_1^* \mathrm{d}V = 0 \tag{6.22}$$

The internal virtual work integral on the left hand side can be evaluated as

$$\int_V (Q_1\epsilon_1 + Q_2\epsilon_2)\epsilon_1^* \mathrm{d}V = \sum_{k=1}^{m} \left[\int_{V_k} (Q_1\epsilon_1 + Q_2\epsilon_2)\epsilon_1^* \mathrm{d}V\right], \tag{6.23}$$

where V_k is the volume of a slice of width $\Delta X_2 = L_2/m$ and length L_1 centred around $X_1 = (X_1)_k$. The integral over the kth slice is now considered.

$$\begin{aligned} I_k &= \int_{V_k} (Q_1\epsilon_1 + Q_2\epsilon_2)\epsilon_1^* \mathrm{d}V \\ &= h\ \Delta X_2 \int_0^{L_1} (Q_1\epsilon_1 + Q_2\epsilon_2)_{X_2 = (X_2)_k} f_n(X_1, {}^{i}r^r)\mathrm{d}X_1 \end{aligned} \tag{6.24}$$

Along each horizontal strip, $X_2 = (X_2)_k = \text{constant}$ and ε_1 and ε_2 can be expressed as linear combinations of the piecewise-continuous p dominant right eigenvectors:

$$\epsilon_1(X_1,(X_2)_k) = \sum_{l=1}^{p} (\tilde{A}_1^r)^{(k,l)} f_n(X_1, {}^l r^r); \quad \epsilon_2(X_1,(X_2)_k) = \sum_{l=1}^{p} (\tilde{A}_2^r)^{(k,l)} f_n(X_1, {}^l r^r) \tag{6.25}$$

Then, I_k becomes

$$\begin{aligned} I_k &= h\Delta X_2 \int_0^{L_1} \left[Q_1 \left(\sum_{l=1}^{p} (\tilde{A}_1^r)^{(k,l)} f_n(X_1, {}^l r^r) \right) \right. \\ &\quad \left. + Q_2 \left(\sum_{l=1}^{p} (\tilde{A}_2^r)^{(k,l)} f_n(X_1, {}^l r^r) \right) \right] f_n(X_1, {}^i r^r) \mathrm{d}X_1 \\ &= h\Delta X_2 \sum_{l=1}^{p} \left[Q_1 (\tilde{A}_1^r)^{(k,l)} \int_0^{L_1} f_n(X_1, {}^l r^r) f_n(X_1, {}^i r^r) \mathrm{d}X_1 \right. \\ &\quad \left. + Q_2 (\tilde{A}_2^r)^{(k,l)} \int_0^{L_1} f_n(X_1, {}^l r^r) f_n(X_1, {}^i r^r) \mathrm{d}X_1 \right] \end{aligned} \tag{6.26}$$

which, upon using Eq. (6.15) simplifies to

$$I_k = h\Delta X_1 \Delta X_2 \left[Q_1 (\tilde{A}_1^r)^{(k,i)} + Q_2 (\tilde{A}_2^r)^{(k,i)} \right], \tag{6.27}$$

and the principle of virtual work can be written as the system of linear equations

$$(i = 1, p): \quad \left[Q_1 \sum_{k=1}^{m} (\tilde{A}_1^r)^{(k,i)} + Q_2 \sum_{k=1}^{m} (\tilde{A}_2^r)^{(k,i)} \right] = 0 \tag{6.28}$$

A similar procedure using the virtual fields of Set 2 and integrating along columns leads to the system of equations:

$$(i = 1, p): \quad h\Delta X_1 \left[Q_1 \sum_{k=1}^{n} (\tilde{A}_2^c)^{(i,k)} + Q_2 \sum_{k=1}^{n} (\tilde{A}_1^c)^{(i,k)} \right] = P \sum_{t=1}^{m} i l_t^c \tag{6.29}$$

Since there is just one dominant eigenvector in the case of uniaxial tension, setting $p = 1$ in the above systems leads to one equation each. From Eqs. (6.6) and (6.12) $(\tilde{A}_1^r)^{(k,1)} = n^{\frac{1}{2}} e_1, (\tilde{A}_2^r)^{(k,1)} = n^{\frac{1}{2}} e_2,$ for $k = 1, m$; $(\tilde{A}_1^c)^{(1,k)} = m^{\frac{1}{2}} e_1, (\tilde{A}_2^c)^{(1,k)} = m^{\frac{1}{2}} e_2,$ for $k = 1, n$. Using these and $1 l_t^c$ given by Eq. (6.12), Eqs. (6.28) and (6.29) yield the system of equations

$$\begin{bmatrix} e_2 & e_1 \\ e_1 & e_2 \end{bmatrix} \begin{Bmatrix} Q_1 \\ Q_2 \end{Bmatrix} = \begin{Bmatrix} P/hL_1 \\ 0 \end{Bmatrix}, \tag{6.30}$$

from which the desired results of Eq. (6.20) follow.

Although this model problem provides simple strain fields with just one eigenvector each, it nevertheless illustrates the main features of EVFM and how a linear system of equations may be assembled and solved for the unknown material parameters. Strain data from actual experiments are expected to be more spatially heterogeneous due to a larger number of dominant eigenvectors and experimental noise. However, the larger number of dominant eigenvectors does not pose any difficulties for application of EVFM as one simply obtains more equations to be solved in a least-squares sense. Experimental noise, on the other hand, has been shown in [11] to infiltrate the eigenvectors; the more the noise in the measured strain fields, the more noise one sees in the eigenvectors, and the more the less-dominant eigenvectors are affected. Thus, if experimental conditions are controlled such that noise is minimal and a significant number of dominant eigenvectors of

comparable singular values are obtained i.e. one simultaneously activates a bunch of dominant eigenvectors, then one would expect that these eigenvectors will be free of noise and EVFM may be applied as presented here without any significant modifications.

This article is intended to be a brief introduction to EVFM. Issues such as the effect of including noisy eigenvectors in EVFM, as well as extension of the method to other constitutive laws, both linear and non-linear will be dealt with in the future. Although the application presented in the present work is simple, EVFM allows for more complicated boundary conditions and anisotropic material behaviour, and these directions will be pursued elsewhere. An important issue in VFM is material parameter *identifiability* [8], an issue that is intimately tied to noise in the experimental measurements. Every eigenfunction chosen as the basis of a virtual field is orthogonal to every other eigenfunction into which the true strain fields are decomposed and therefore the virtual work corresponding to these components of the true field vanishes. Since many of these eigenfunctions correspond to noise in the measured strain fields, the internal virtual work integrals receive no contribution from the noise in the measured strain fields. Thus, the eigenfunction decomposition employed in EVFM directly results in reducing the effect of experimental noise on material parameter identifiability and this will be investigated formally in the future.

6.5 Conclusions

1. In this work, EVFM, a novel implementation of conventional VFM, is proposed. The central idea in EVFM is the systematic generation of virtual displacement and strain fields using the eigenfunctions of two strain matrices that are composites of the three measured in-plane strain component fields. The eigenfunctions are identified by performing SVD of these matrices and the measured strain component fields are reconstructed in terms of only these principal eigenvectors.
2. It is shown that eigenvector decomposition of the measured strain fields and subsequent use of eigenvectors for the virtual fields allows one to interpret the internal virtual work integral as a sum of inner products between the eigenvectors. Since these eigenvectors are orthonormal, enormous simplification of the virtual work integrals is obtained, leading to two simple systems of linear equations in the unknown material parameters.
3. The orthonormality of the eigenfunctions acts to eliminate from teh virtual work integral the effect of all eigenvectors except the one on which the virtual fields are based. Since experimental noise typically corresponds to lower order eigenvectors, eigenvector orthonormality automatically reduces the effect of noise on the virtual work equations, and therefore, on the computed material parameters.
4. The proposed technique has been applied to a model problem, plane-stress uniaxial tension, and the exact solution recovered in terms of the measured axial and transverse strains, applied load and specimen geometry.
5. Several future extensions of EVFM have been identified and will be pursued in the near future.

References

1. Pierron F, Grediac M (2012) The Virtual Fields Method: extracting constitutive mechanical parameters from full-field deformation measurements. Springer, New York
2. Malvern LE (1977) Introduction to the mechanics of a continuous medium. Prentice-Hall, Englewood Cliffs
3. Avril S, Pierron F (2007) General framework for the identification of constitutive parameters from full-field measurements in linear elasticity. Int J Solids Struct 44:4978–5002
4. Sutton MA, Orteu J-J, Schreier HW (2009) Image correlation for shape, motion and deformation measurements. Springer, New York
5. Grediac M, Pierron F, Surrel Y (1999) Novel procedure for complete in-plane composite characterization using a single T-shaped specimen. Exp Mech 39(2):142–149
6. Grediac M, Toussaint E, Pierron F (2002) Special virtual fields for the direct determination of material parameters with the Virtual Fields Method. 1 – principle and definition. Int J Solids Struct 39(10):2691–2705
7. Toussaint E, Grediac M, Pierron F (2006) The Virtual Fields Method with piecewise virtual fields. Int J Mech Sci 48(3):256–264
8. Avril S, Grediac M, Pierron F (2004) Sensitivity of the Virtual Fields Method to noisy data. Comput Mech 34(6):439–452
9. Jolliffe IT (2002) Principal component analysis. Springer, New York
10. Strang G (2006) Linear algebra and its applications. Cengage Learning
11. Grama SN, Subramanian SJ (2012) Computation of full-field strains using principal components analysis. Manuscript under review.
12. Timoshenko SP, Goodier JN (2010) Theory of elasticity. McGraw-Hill, Singapore

Chapter 7
The Kinematics and Dynamics of 3-D Displacement Fields

C.A. Sciammarella, L. Lamberti, F.M. Sciammarella, and A. Boccaccio

Abstract In the last few decades Experimental Mechanics, helped by advanced technologies to gather 3-D spatial information in non-transparent media, has evolved into a very general tool. It has become possible to observe the internal volume of engineering materials and in the area of biomechanics living internal tissues. This paper contains a brief review of Continuum Mechanics mathematical models that are available to formulate problems in 3-D including large deformations. The extension of the experimental methods that measure displacements in 2-D to 3-D is presented. Two important cases are considered: (a) use of deterministic signals, (b) use of random signals. In order to separate the complexity of the subject of 3-D analysis from the difficulties that arise from the use of random signals, the connection between mathematical models and their experimental determination is presented utilizing deterministic signals. The extension of the use of random signals to the determination of displacements in 2-D to 3-D is outlined. A new method to extract displacement information from random signals is developed and an example of application is provided. Two methods to extract displacement information in 3-D, the classical method based on displacement projections and discrete image correlation (DIC) based on following gradients of intensities are compared. There are many complex steps involved in data processing aside the basic approach, this circumstance makes difficult a comparison between the two methods, however it is possible to conclude that the results are in fair agreement.

Keywords 3-D continuum kinematics • 3-D continuum dynamics • Large deformations • Experimental 3-D displacement measurements opaque media • 3-D displacement measurement (deterministic, random signals) • 3-D displacement analysis discrete image correlation (DIC)

7.1 Introduction

The analysis of deformations, strains and stresses in the 3-D continuum is a well developed methodology based on the kinematics and the dynamics of the continuum. In Experimental Mechanics, a vast array of techniques have been developed to measure 3-D strains and stresses utilizing different forms of the photoelastic effect for elastic, viscoelastic fields and some plasticity problems. There is also an extensive array of methods based on the measurement of displacements in 3-D fields, starting with moiré, holography, speckle interferometry, speckle photography, and, more recently, digital image correlation (DIC) that can be applied to any of the above mentioned methods but is particularly useful in the analysis of random carriers and hence is very often associated with random carriers although it may also be applied to deterministic carriers. All these

C.A. Sciammarella (✉)
College of Engineering and Engineering Technology, Northern Illinois University, DeKalb, USA

Department of Mechanical, Materials and Aerospace Engineering, Illinois Institute of Technology, Chicago, USA
e-mail: csciammarella@niu.edu

L. Lamberti • A. Boccaccio
Dipartimento di Meccanica, Matematica e Management, Politecnico di Bari, Bari, Italy
e-mail: lamberti@poliba.it; a.boccaccio@poliba.it

F.M. Sciammarella
College of Engineering and Engineering Technology, Northern Illinois University, DeKalb, USA

H. Jin et al. (eds.), *Advancement of Optical Methods in Experimental Mechanics, Volume 3*,
Conference Proceedings of the Society for Experimental Mechanics Series,
DOI 10.1007/978-3-319-00768-7_7,

methods have been applied to the 3-D analysis of transparent media in an extensive number of publications. These techniques have also been extended to non-transparent media by utilizing adequate forms of radiation that can penetrate a given solid medium and with an adequate sensor can produce an image where the displacement information is encoded in gray levels [1, 20]. This paper focuses on these applications since they can help solve problems of great technical interest in important areas of material properties related to the structure of the material under investigation, also with the derivation of constitutive equations, and also in the damage analysis of materials [1–10]. These techniques provide a powerful tool to the biological applications of Experimental Mechanics [11–20]. We will also concentrate on the applications that deal with the inside volume of bodies rather than the outside surfaces. The inclusion of the words kinematics and dynamics in the title is due to the fact that in many experimental methods constitutive equations are involved in the analysis of deformations. It must be pointed out that there are no methods to measure stresses, it is always displacements or displacement derivatives that are measured and constitutive equations are introduced to extract stress information. The selection of particular constitutive equations is guided by the selected kinematic variables.

In the topic of non-transparent media, there are numerous applications of computed X-ray tomography applied to granular media at two different scales, at the continuum scale and at the micro-scale. In these applications, 3-D discrete image correlation (DisIC) is utilized as a tool to obtain displacement information. A basic motivation is to correlate features obtained in the stress-load relations with the full 3-D field deformation. Numerous examples and references can be found in [1]. For example, Ref. [2] presents an application of the same idea to wood. In [3], Laue micro-diffraction and DIC are combined for improved measurements of the elastic strains with spatial resolution of micrometers. DIC is utilized to evaluate the displacements of the Laue spots. In [4], microtomographic images obtained on the BM05 beam line at the European Synchrotron Radiation Facility (ESRF) in Grenoble (France) are utilized in conjunction with DIC to investigate the process of compacting foam by impact. In [5], the selected kinematics to extract displacement information is based on continuous finite-element shape functions with enrichment to account for the presence of discontinuities in the analyzed displacement fields. The introduced derivations are applied to analyze one loading cycle of a fatigue-cracked nodular graphite cast iron sample by using computed tomography. An investigation of the phenomenon of crack closure using similar technology is found in [6]. In [7], a complex internal structure is analyzed. A three-dimensional DIC technique is applied for strain measurements in open-cell structures such as trabecular bone. High-resolution computed tomography images for displacement measurements are combined with DIC and FEM. In order to determine the local strain-state within single bone trabecula, a special mesh is generated to fill the solid structure. In [8], the mechanical behavior of nano-structured W/Cu thin films deposited on Kapton under controlled biaxial loadings is studied utilizing 2-D synchrotron x-ray diffraction and DIC techniques. In [9, 10], fundamental aspects of the utilization of techniques of 3-D analysis in opaque media utilizing DIC methodology are addressed.

The preceding references provide a spectrum of applications where x-rays tomography has been applied to solid mechanics and material properties problems and that utilize DIC as displacement decoding technique. There is another area where 3-D imaging of opaque substances plays a fundamental role: bio-mechanics. The tool of preference is the Magnetic Resonance Imaging (MRI) technique. A MRI scanner is a device in which an object under observation is inside a powerful magnetic field that aligns the spins of the nucleons (positrons, neutrons) in the volume of the object. Separate radio-frequency magnetic fields are applied to systematically modify the spin of the nucleons and the effect of these additional electromagnetic signals is to modify the spins. This modification depends on the particular composition of the volume under observation and is detectable by the scanner. Spatial information is recovered using Fourier analysis of the recorded signals. By using gradients in different directions, 2-D images in gray levels or in 3-D volumes can be obtained in any arbitrary orientation. An additional effect called tagging can be produced if the electromagnetic signals are modulated resulting in changing the gray levels of the gathered signals. In this way, line carriers can be inscribed in the volume for example of the tissue of an observed organ (see Fig. 7.1). The change in the magnetic spin is a characteristic property of the observed tissue, and the tagged regions follow the motion of the tissue. The alignment of the spins is subjected to processes of decay but the duration in time is in many cases long enough to follow the motion of the tissue. Heart motion is one of the more important applications that utilize this methodology.

The quality of the created carriers is high in Fig. 7.1 and as such when performing the analysis of these carriers it allows the reconstruction of the heart kinematics. Details of this 3-D method of displacement measurement in non transparent media can be found in [11–20].

In this paper, the 3-D analysis of bodies will be approached from the point of view of the fundamental aspects of the required methodology to gather the information that is directly available from images. The kinematics and associated dynamics will be briefly reviewed.

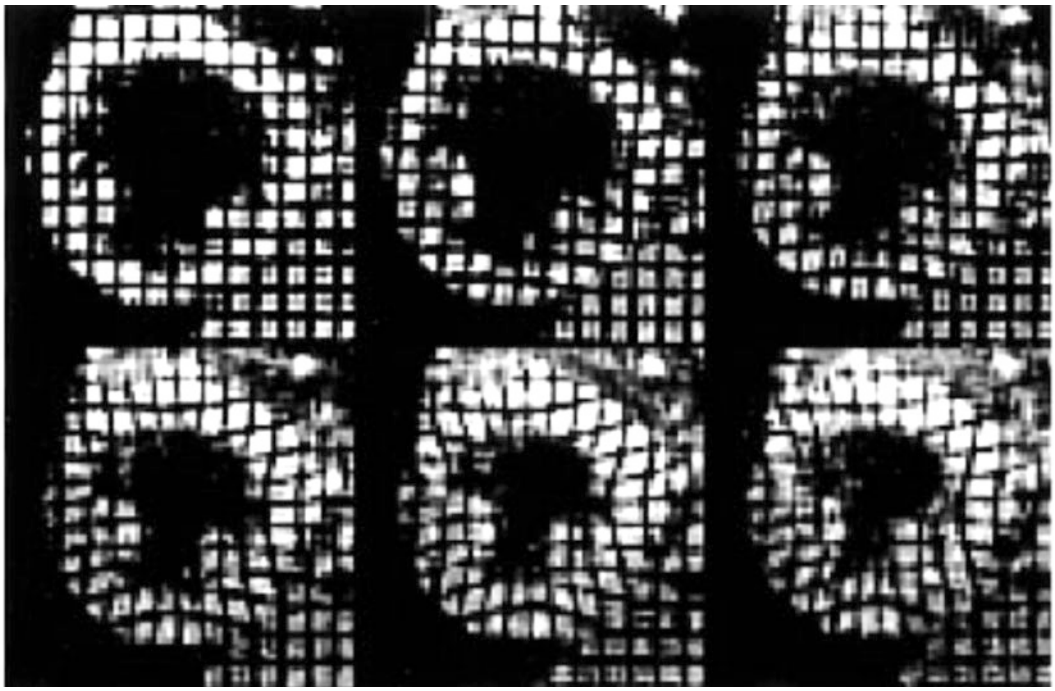

Fig. 7.1 Tagged images of the left ventricle of a healthy heart trough a complete systole [16]

7.2 Description of Motion in the Continuum

Figure 7.2 illustrates the motion of a point in the 3-D space. From the position P_o it moves to the position P undergoing a displacement that is called **u** or **U** depending on the utilized reference system. One reference system, X_1-X_2-X_3 symbolically indicated $[X_i]$ corresponds to the initial or undeformed configuration. This system is called the Lagrangian system or material reference system and utilizes the selected body configuration, called base configuration, to represent the different variables that define the deformation of the body. It is particularly suitable to describe bodies with limited ranges of deformations.

The system x_1-x_2-x_3 corresponds to deformed configurations of the body and is called the Eulerian system or also spatial system. The Eulerian system follows the different configuration of the body as the body is deformed. If one follows the deformation of a body as a function of a certain parameter, for example the time t, and wants to refer the different variables of the problem to the deformed configurations at time intervals Δt, the spatial reference configuration must then be modified at each time interval Δt. The analyzed body will have given configurations at a chosen time interval Δt, the Eulerian coordinate will be changing with the time intervals Δt.

In order to get a basic understanding of the 3-D kinematics, the analysis will be started with a very general case (see Fig. 7.2): the Eulerian reference system is given a translation and a rotation. It must be understood that reference systems are chosen keeping in mind a selected final objective, which in general is to get the simplest path to the final results.

The basis vectors of the coordinate system are related through the equations $\boldsymbol{l}_i \cdot \mathbf{e}_j = \alpha_{ij}$ where $\boldsymbol{l}_i$ and $\mathbf{e}_j$, respectively, are the base vectors of the reference systems $[X_i]$ and $[x_j]$. Parameters α_{ij} are the directions cosines that fulfill the orthogonality conditions $\alpha_{ik}\alpha_{kj} = \delta_{ij}$. The vectorial relationship that defines the variable displacement can be derived from Fig. 7.2:

$$\mathbf{u}(\mathbf{X}) = \mathbf{X}(O_e) + \mathbf{x}(P) - \mathbf{X}(P_o) \tag{7.1}$$

Also,

$$\mathbf{u} = \mathbf{U} \tag{7.2}$$

In order to insure the continuity of the deformation that is built in the theory of the continuum, the following determinant must be different from zero. This determinant is called the Jacobian of the coordinate change and the fact that is different from zero provides the reversibility of the transformation.

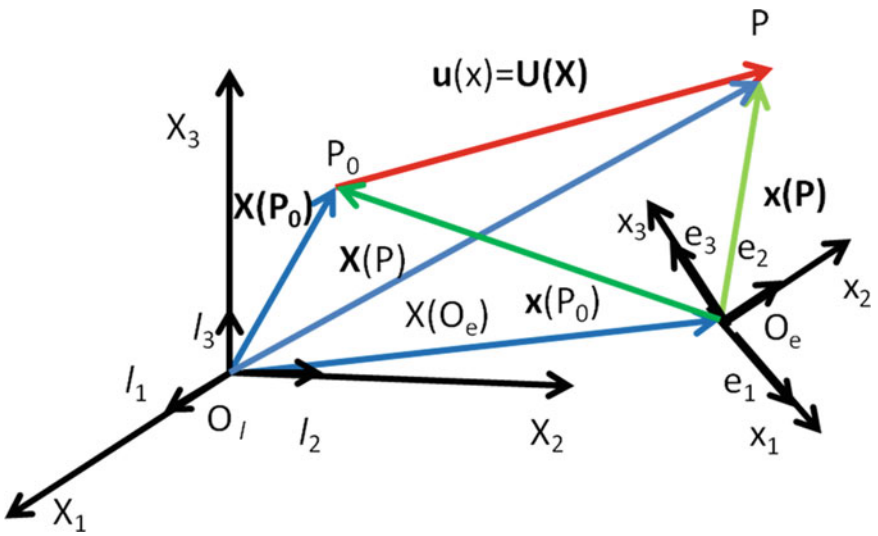

Fig. 7.2 Motion of a point in the Continuum with indication of two systems of reference: $\mathbf{X}_l$ (Lagrangian) and $\mathbf{x}_e$ (Eulerian)

$$J = \det \begin{vmatrix} \frac{\partial x_1}{\partial X_1} & \frac{\partial x_1}{\partial X_2} & \frac{\partial x_1}{\partial X_3} \\ \frac{\partial x_2}{\partial X_1} & \frac{\partial x_2}{\partial X_2} & \frac{\partial x_2}{\partial X_3} \\ \frac{\partial x_3}{\partial X_1} & \frac{\partial x_3}{\partial X_2} & \frac{\partial x_3}{\partial X_3} \end{vmatrix} = \det \left| \frac{\partial x_i}{\partial X_j} \right| \tag{7.3}$$

7.2.1 Deformation Gradient Tensors

By introducing the Continuum Mechanics basic assumption that the deformation in the neighborhood of a point is an affine transformation, one arrives to the fundamental tensors that define the deformation of the continuum. In Lagrangian coordinates, the deformation gradient tensor is expressed as:

$$[F] = \left| \frac{\partial x_i}{\partial X_j} \right| = \begin{bmatrix} \frac{\partial x_1}{\partial X_1} & \frac{\partial x_1}{\partial X_2} & \frac{\partial x_1}{\partial X_3} \\ \frac{\partial x_2}{\partial X_1} & \frac{\partial x_2}{\partial X_2} & \frac{\partial x_2}{\partial X_3} \\ \frac{\partial x_3}{\partial X_1} & \frac{\partial x_3}{\partial X_2} & \frac{\partial x_3}{\partial X_3} \end{bmatrix} \tag{7.4}$$

The relationship between the above indicated matrix and the Jacobian is:

$$\det[F(X)] = J(X) \tag{7.5}$$

Switching to Eulerian coordinates, the inverse relationship is represented

$$[F]^{-1} = \left| \frac{\partial X_i}{\partial x_j} \right| = \begin{bmatrix} \frac{\partial X_1}{\partial x_1} & \frac{\partial X_1}{\partial x_2} & \frac{\partial X_1}{\partial x_3} \\ \frac{\partial X_2}{\partial x_1} & \frac{\partial X_2}{\partial x_2} & \frac{\partial X_2}{\partial x_3} \\ \frac{\partial X_3}{\partial x_1} & \frac{\partial X_3}{\partial x_2} & \frac{\partial X_3}{\partial x_3} \end{bmatrix} \tag{7.6}$$

Introducing the definition of displacement given in Eq. 7.1 in the above relationships, one arrives to define the [G] tensor in Lagrangian coordinates:

$$G = \begin{bmatrix} \frac{\partial U_1}{\partial X_1} & \frac{\partial U_1}{\partial X_2} & \frac{\partial U_1}{\partial X_3} \\ \frac{\partial U_2}{\partial X_1} & \frac{\partial U_2}{\partial X_2} & \frac{\partial U_2}{\partial X_3} \\ \frac{\partial U_3}{\partial X_1} & \frac{\partial U_3}{\partial X_2} & \frac{\partial U_3}{\partial X_3} \end{bmatrix} = \begin{bmatrix} \frac{\partial x_1}{\partial X_1} - 1 & \frac{\partial x_1}{\partial X_2} & \frac{\partial x_1}{\partial X_3} \\ \frac{\partial x_2}{\partial X_1} & \frac{\partial x_2}{\partial X_2} - 1 & \frac{\partial x_2}{\partial X_3} \\ \frac{\partial x_3}{\partial X_1} & \frac{\partial x_3}{\partial X_2} & \frac{\partial x_3}{\partial X_3} - 1 \end{bmatrix} \tag{7.7}$$

Symbolically, the above equation is represented by,

$$[G] = [F] - [I] \tag{7.8}$$

where [I] is the identity tensor.

In the Eulerian system, the above relationships are represented by

$$[J] = [I] - [F]^{-1} = \begin{bmatrix} 1 - \frac{\partial X_1}{\partial x_1} & \frac{\partial X_1}{\partial x_2} & \frac{\partial X_1}{\partial x_3} \\ \frac{\partial X_2}{\partial x_1} & 1 - \frac{\partial X_2}{\partial x_2} & \frac{\partial X_2}{\partial x_3} \\ \frac{\partial X_3}{\partial x_1} & \frac{\partial X_3}{\partial x_2} & 1 - \frac{\partial X_3}{\partial x_3} \end{bmatrix} = \begin{bmatrix} \frac{\partial u_1}{\partial x_1} & \frac{\partial u_1}{\partial x_2} & \frac{\partial u_1}{\partial x_3} \\ \frac{\partial u_2}{\partial x_1} & \frac{\partial u_2}{\partial x_2} & \frac{\partial u_2}{\partial x_3} \\ \frac{\partial u_3}{\partial x_1} & \frac{\partial u_3}{\partial x_2} & \frac{\partial u_3}{\partial x_3} \end{bmatrix} \tag{7.9}$$

The tensors [F] and [G] and the inverse $[F]^{-1}$ and [J] are fundamental tensors in the development of strain measures in Continuum Mechanics. The above quantities can be extracted from any of the methods that provide displacements encoded in levels of gray. The goal of this paper is to illustrate the processes required to transform levels of gray information recorded in 2-D images into the above 3-D tensors required by the kinematics of the continuum.

7.3 The Deformation Tensors and Strain Tensors

There is another important step in describing the kinematics of the continuum: the introduction of the concepts of stretch and strain and the separation of displacements caused by rigid body motions from those due to changes of dimensions. The kinematics of solids deals with relative changes of position of points, hence translations are not considered and the only rigid body motions of interest are rotations. The required relationships between displacement components generated by deformation and displacements due to rigid body rotations can be derived directly from a general property of square matrices, the polar decomposition theorem that separates the stretch component of a displacement from rigid body rotations:

$$[F] = [R][U] = [V][R] \tag{7.10}$$

In the above equation, [U] is called the right stretch tensor and [V] is called the left stretch tensor, referring to their position with respect to the rotation tensor. These tensors are symmetric positive definite tensors. That is $[U]^T = [U]$ and $[V]^T = [V]$, where the upper script "T" indicates the transposed matrix. The rotation tensor [R] satisfies the identity $[R][R]^T = [I]$.

Since the notion of deformation implies the relative change of distances between two neighbor points P and Q, the changes of coordinates produced by rotations must be eliminated from the deformation tensor. Therefore, the deformation tensor must be invariant upon rigid body motions. Taking into consideration the above explained criterion, from Eq. 7.10 it follows

$[F]^T = [[R][U]]^T = [U][R]^T$. Then, multiplying $[F]^T[F]$ one gets:

$$[C_R] = [F]^T[F] = [U]^2 \tag{7.11}$$

or in indicial notation, $C_{Rij} = \frac{\partial x_k}{\partial X_i}\frac{\partial x_k}{\partial X_j}$.

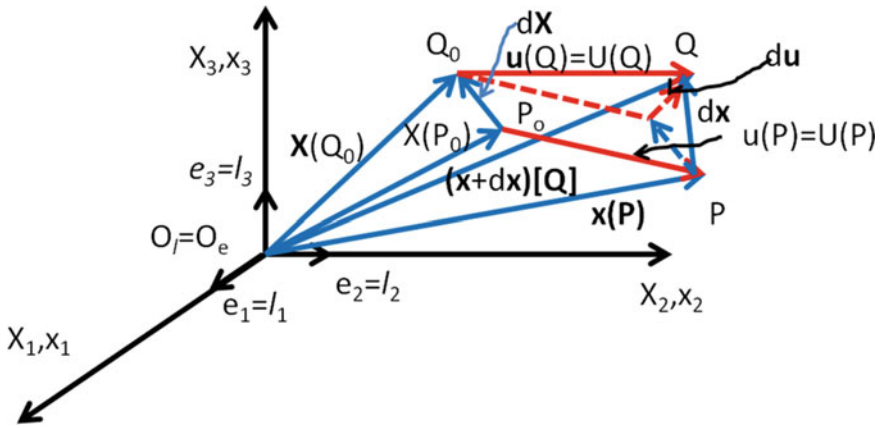

Fig. 7.3 The change of the distance **dx** between two neighbor points P and Q is represented. For simplicity of the analysis, the Lagrangian and the Eulerian coordinates are taken as coaxial

The tensor given by Eq. 7.11 is called the right Cauchy-Green tensor and physically represents the square of the vector **dx** (see Fig. 7.3), that in the deformed continuum is the distance between the two neighboring points P(**x**) and Q(**x**).

By similar procedures, the left Cauchy-Green deformation tensor can be obtained:

$$[C_L] = [F][F]^T = [V]^2 \tag{7.12}$$

or in indicial notation, $C_{Lij} = \dfrac{\partial x_i}{\partial X_k}\dfrac{\partial x_j}{\partial X_k}$.

This deformation tensor is denoted also as the Finger deformation tensor:

$$[B] = [F][F]^T = [V]^2 \tag{7.13}$$

or in indicial notation, $B_{ij} = \dfrac{\partial x_k}{\partial X_i}\dfrac{\partial x_k}{\partial X_j}$.

The quantity $\lambda_N = \mathbf{dx/dX}$ that gives the ratio of a differential element d**x** in the deformed condition to its the initial length d**X** is called the stretch ratio. Introducing the definition of Lagrangian strain, it can be written:

$$e_N^L = \frac{dx - dX}{dX} = \lambda_N - 1 \tag{7.14}$$

The above definition is the classical definition of strain used in engineering problems. If we introduce the definition of Eulerian strain, it can be written:

$$e_n^E = \frac{dX\text{-}dx}{dx} = \frac{1}{\lambda_N} - 1 \tag{7.15}$$

By combining Eqs. 7.14 and 7.15, the relationships between strain definitions are derived:

$$e^L = \frac{e^E}{1 - e^E},\ e^E = \frac{e^L}{1 + e^L} \tag{7.16}$$

The natural strain or Henky's strain is defined as:

$$e^h = \ln\left(\frac{1}{1 - e^E}\right) = \ln(1 + e^L) \tag{7.17}$$

By computing the eigen-values of the Cauchy-Green tensor, the principal stretches to the square λ_i^2 are obtained. Knowing these quantities, it is possible to compute other forms of strain tensors through tensor transformations.

In the preceding paragraphs the notion of strain was connected to the deformation tensors through the concept of stretch λ. Direct measures of strain are introduced utilizing the derivatives of the displacements. There are several tensors that have been introduced in the literature such as the Green-Lagrange strain tensor. It can be shown that the Lagrangian definition of strain $e_N^L = \frac{dx-dX}{dX}$ leads to an expressions of the form,

$$e_{x_1}^{L} = \sqrt{1 + 2\frac{\partial u_1}{\partial X_1} + \left(\frac{\partial u_1}{\partial X_1}\right)^2 + \left(\frac{\partial u_2}{\partial X_1}\right)^2 + \left(\frac{\partial u_3}{\partial X_1}\right)^2} - 1 \tag{7.18}$$

The above equation can be written as:

$$\left(e_{x_1}^{L} + 1\right)^2 = 1 + 2\frac{\partial u_1}{\partial X_1} + \left(\frac{\partial u_1}{\partial X_1}\right)^2 + \left(\frac{\partial u_2}{\partial X_1}\right)^2 + \left(\frac{\partial u_3}{\partial X_1}\right)^2 \tag{7.19}$$

The above expression if $\left(e_{x_1}^{L}\right)^2 << 1$ can be simplified by neglecting terms whose contributions to the total value are negligible.

$$\varepsilon_{x_1}^{L} = \frac{\partial u_1}{\partial X_1} + \frac{1}{2}\left[\left(\frac{\partial u_1}{\partial X_1}\right)^2 + \left(\frac{\partial u_2}{\partial X_1}\right)^2 + \left(\frac{\partial u_3}{\partial X_1}\right)^2\right] \tag{7.20}$$

Similarly, for the shear strains, adopting the same assumptions applied to the normal strains and assuming also that $\arcsin\gamma = \gamma$, one obtains:

$$\varepsilon_{x_1 x_2}^{L} = \frac{1}{2}\left(\frac{\partial u_1}{\partial X_2} + \frac{\partial u_2}{\partial X_1}\right) + \frac{1}{2}\left[\frac{\partial u_1}{\partial X_1}\frac{\partial u_1}{\partial X_2} + \frac{\partial u_2}{\partial X_1}\frac{\partial u_2}{\partial X_2} + \frac{\partial u_3}{\partial X_1}\frac{\partial u_3}{\partial X_2}\right] \tag{7.21}$$

Similar expressions can be obtained for the other components of the simplified strain tensor that is called the Green-Lagrangian tensor. This tensor can be connected to the deformation gradient tensor [F] as follows:

$$[E]^{L} = \frac{1}{2}\left[[F]^{T}[F] - [I]\right] \tag{7.22}$$

In the same way, for the Eulerian strain tensor one can obtain:

$$[E]^{E} = \frac{1}{2}\left[[I] - [F]^{T}[F]^{-1}\right] \tag{7.23}$$

The above relationship leads to the following expression:

$$\varepsilon_{x_1}^{E} = \frac{\partial u_1}{\partial x_1} - \frac{1}{2}\left[\left(\frac{\partial u_1}{\partial x_1}\right)^2 + \left(\frac{\partial u_2}{\partial x_1}\right)^2 + \left(\frac{\partial u_3}{\partial x_1}\right)^2\right] \tag{7.24}$$

And for the shear strain,

$$\varepsilon_{x_1 x_2}^{E} = \frac{1}{2}\left(\frac{\partial u_1}{\partial X_2} + \frac{\partial u_2}{\partial X_1}\right) - \frac{1}{2}\left[\frac{\partial u_1}{\partial X_1}\frac{\partial u_1}{\partial X_2} + \frac{\partial u_2}{\partial X_1}\frac{\partial u_2}{\partial X_2} + \frac{\partial u_3}{\partial X_1}\frac{\partial u_3}{\partial X_2}\right] \tag{7.25}$$

With either the tensors [F] and [G] or the tensors $[F]^{-1}$ and [J] all the necessary information to develop the kinematics of the continuum is available. This also includes the necessary information to compute the strain tensors so that one goes back to the classical definitions of strains and hence to the formulation of stress–strain relationships that define the constitutive equations.

In Eqs. 7.24 and 7.25, if one neglects the products of the derivatives of the displacements such that $\frac{\partial u_i}{\partial x_j} << 1$ and $\frac{\partial u_k}{\partial x_i}\frac{\partial u_k}{\partial x_j} << 1$, that is if small deformations and rotations are present, one returns to the linear infinitesimal tensor.

7.4 Dynamics of the Continuum

While the kinematics of the continuum is straight forward, the dynamics is far more complex than the kinematics. The reason for this feature of the dynamics of the continuum is that the dynamics involves the realm of modeling the behavior of solids and this covers an extremely wide spectrum of behaviors. The most general approach is to define for a given medium an internal energy function. This function will contain thermodynamic variables such as temperature, entropy etc. as well as kinematic variables that depend on the tensors [F] and [G] or the tensors $[F]^{-1}$and [J] or on forms of the finite strain tensors defined in preceding sections. It should be remembered that constitutive equations depend on an adopted definition of deformation as well as on constants or functions that must be obtained by experiments where the adopted tensor variables can be measured and applied forces are also measured. The strain energy function can be expressed as a function of the adopted deformation tensor or a strain tensor that has been chosen and at the same time as a function of a measure of stress that is compatible with the adopted kinematic variables. If the internal energy $W(\mathbf{E}_{ij})$ is defined as a function of a given strain tensor $[E_{ij}]$, and assuming that the internal energy depends on the deformation gradient only and if one ignores thermodynamic variables and energy dissipation processes, it can be written:

$$S_{ij} = \frac{\partial W(E_{ij})}{\partial E_{ij}} \tag{7.26}$$

where S_{ij} are the components of a stress tensor and E_{ij} are the components of a strain tensor.

Associated with the adopted strain measure E_{ij}, there is a stress tensor S_{ij} which is the conjugate of the strain in the definition of virtual work. A simple extension of the classical elastic medium is the Saint Venant-Kirchhoff elastic medium defined by the energy function,

$$W(E) = \frac{C_{1L}}{2}\left(\mathrm{tr}[E]^{L}\right)^{2} + C_{2L}\left(\mathrm{tr}[E]^{L}\right)^{2} \tag{7.27}$$

In Eq. 7.27, C_{1L} and C_{2L} are constants that play the role of the Lamé elastic constants in linear elasticity and $[E]^{\mathbf{L}}$ is the Lagrangian-Green tensor defined in Eq. 7.22.

Then,

$$\mathbf{S}^{\mathbf{PK2}} = \frac{\partial W(\mathbf{E}^{L})}{\partial \mathbf{E}^{L}} = C_{1L}\mathrm{tr}(\mathbf{E}^{L})I + 2C_{2L}\mathbf{E}^{L} \tag{7.28}$$

where $\mathbf{S}^{PK2}$ is called the second Piola-Kirchhoff stress tensor. In indicial notation, we can write:

$$\mathbf{S}^{\mathbf{PK2}}_{\mathbf{ij}} = \frac{\partial W(E^{L}{}_{ij})}{\partial E^{L}{}_{ij}} \tag{7.29}$$

The above example shows that from experimental observations one must select the type of adequate kinematic variables that fit experimental data to a constitutive equation. This is one example of a extremely large realm of possibilities to represent the behavior of materials of scientific and or engineering interest. The point to emphasize is the kinematics and the dynamics are closely related and this relationship should not be overlooked.

7.5 Experimental Determination of the Deformations in 3-D

In the preceding sections a basic summary of the continuum kinematics was presented. It is necessary to analyze the experimental techniques that can be utilized to retrieve the deformation tensors, [F] and [G] or $[F]^{-1}$ and [J], from a continuum 3-D medium. The problem will be approached from the point of view of methods that measure displacements.

As mentioned in the introduction, there are a large number of optical techniques to measure displacements on the surfaces of non-transparent bodies or inside transparent bodies. Optical techniques that measure displacements were developed separately although occasionally connections between them were pointed out. In chronological order, moiré was the first technique to be developed. Moiré was followed by holography, speckle interferometry, speckle photography. The next

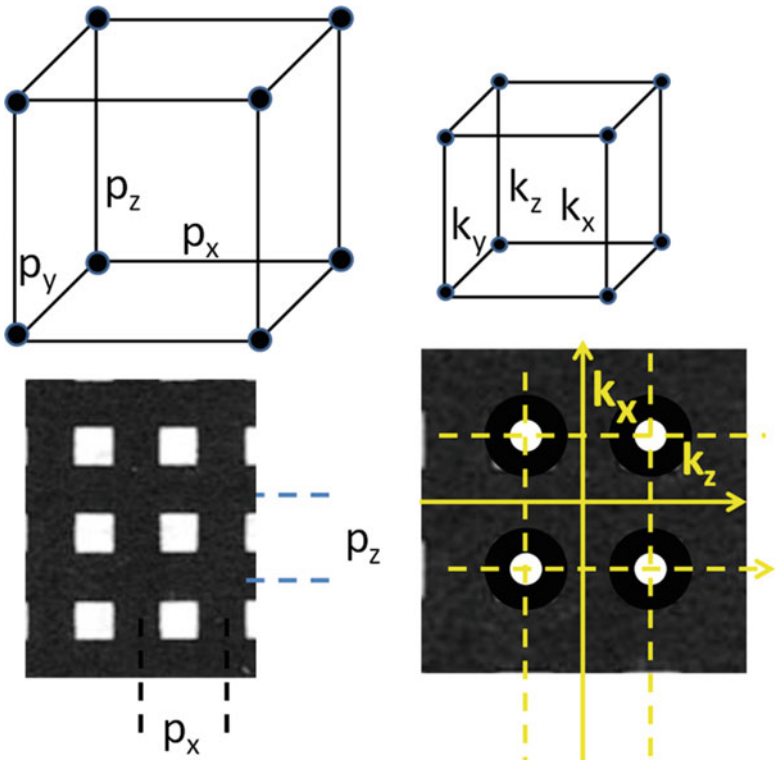

Fig. 7.4 Carrier in the 3-D space, physical space basic pitch p, basic frequencies k_x, k_y and k_z in the frequency space

technique to be developed was the numerical correlation of speckles either produced by coherent illumination or by printed random patterns also known as DIC. All these methods have been applied to the 3-D analysis of transparent media. As shown in the Introduction, these techniques have also been extended to non-transparent media by utilizing forms of radiation that can penetrate a given solid medium and with a system of sensors, electronic circuitry and through algorithms can produce images that encode displacement information as gray levels.

The first step in the process of generating displacement data is to have a carrier on the volume under observation. A carrier is a known signal that upon changes of the body will be modified from a certain known configuration, called the reference configuration or base configuration, to another configuration, the perturbed configuration. Since one is dealing in the most general case with a deformation process, a reference parameter is required, for example the time or any other monotonically increasing parameter that is connected with the problem under analysis. We will start with a very general scheme without referring to any particular method since the aim of the paper is to connect experimental observations to the kinematics of the continuum. The displacement information may be extracted from a deterministic signal or from a random signal. The analysis will start with a deterministic signal to simplify the understanding of the basic steps involved without introducing the additional complications arising from the use of a random carrier. What is of interest is the basic mathematical framework that is independent of the type of signal utilized.

Let us assume that the volume of 3-D space under investigation is tagged with a carrier system that can be identified to have a specific spatial frequency. The frequency can be defined in the physical space by the pitch of the carrier p or by a frequency in the reciprocal space $f_{xi} = 1/p$. Figure 7.4 provides the 3-D scheme for spatial and frequency analysis of displacements. The base spatial distances are $p_x = p_y = p_z = p$ and in the frequency space the base spatial frequencies are $k_x = k_y = k_z = k_o$. At this point it is not necessary to specify how the reference system is introduced to the medium under analysis. Only the existence of this reference the system must be acknowledged. For reasons of simplicity on the developments to be introduced, the reference system is associated with a Cartesian system of coordinates. Figure 7.4 illustrates the concept for the case of a 3-D prismatic body.

It is assumed that one has tagged the volume of the body with a carrier system of planes in 3-D. The points of the tagged carrier planes are attached to the material of the body so that upon deformation the points in the most general case have trajectories that are 3-D curves but in view of the theory of the continuum the carrier planes remain continuous surfaces whose intersection with the reference system of coordinates give continuous curves that provide information concerning the position of the points in the space as the body deforms. In Fig. 7.5, a point A of projections in the coordinate planes A_i ($i = 1,2,3$) is identified by its coordinates X_{A1}, X_{A2} and X_{A3}. The objective of the deformation analysis is to follow the

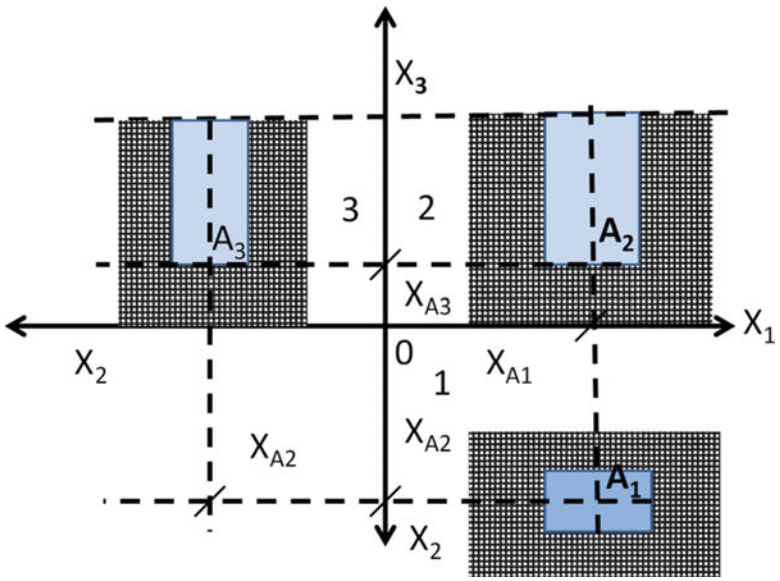

Fig. 7.5 Descriptive Geometry representation of a 3-D prismatic shape body whose volume has been tagged with an orthogonal system of carrier planes represented in 3-D by orthogonal lines

trajectories of the points of the body as it deforms as a function of a parameter that grows monotonically, for example the time t. Utilizing the nomenclature of the preceding sections, Fig. 7.5 is the reference base and the deformation of the body will be analyzed by following the shapes of the body at certain intervals of time.

The coordinate system X_1, X_2 and X_3 is the material system of reference. The spatial system of reference x_1, x_2 and x_3 can be selected keeping in mind certain particular purpose: for example, it can be selected in coincidence with the material system. In most cases, only relative motions of points are of interest. Hence, only relative displacements will be involved in the process of following the deformation of the studied body.

7.6 Tracking Point Displacements

In the developments of this section and in the following sections the Eulerian approach will be adopted. The focus of the paper is in the most general case of deformation. Since we are looking at large deformations, there will be considerable changes on the geometry of the analyzed specimen. There are several procedures that can be followed to track a point located inside a 3-D body or at the boundary of the body. At a given point of the continuum the displacement of the point is encoded in gray levels. The position and the displacement can be connected to the notion of fringe order n, where n is a real number [21]. One has to remember that coordinate positions can be transformed into angular variables trough the concept of phase [22]. The actual value of the phase at a given point depends on the selection of the marker corresponding to the order zero, which provides the reference from which the orders are determined. Since we are referring to relative displacements, the zero order reference is arbitrary and is selected by the operator analyzing the deformation process. The usefulness of the transformation of distances into angles is based on an important relationship that separates the levels of gray at a given point into two variables through a procedure that is applied in digital signal processing. A signal can be represented by a phasor [23]:

$$\vec{I}\,(X,t) = I(X,t)e^{i\phi(x,t)} \tag{7.30}$$

where: $\vec{\mathbf{I}}\,(\mathbf{x},\ t)$ is the gray level intensity at a given point of the 3-D space represented by the phasor; I(**x**,t) is the amplitude of the phasor in gray levels; **x** is the Eulerian position vector at the time t; $\boldsymbol{\phi}$(**x**,t) is a angular variable called the phase. Since I (**x**,t) depends on many factors that are independent of the motion, following the approach of the vast majority of optical methods, the amplitude of the phasor is disregarded and the displacement is related to the phase [24] trough the relationship:

$$\mathbf{u}(\mathbf{x},\mathrm{t}) = \frac{\Phi(\mathbf{x},\mathrm{t})}{2\pi}\mathrm{p} \tag{7.31}$$

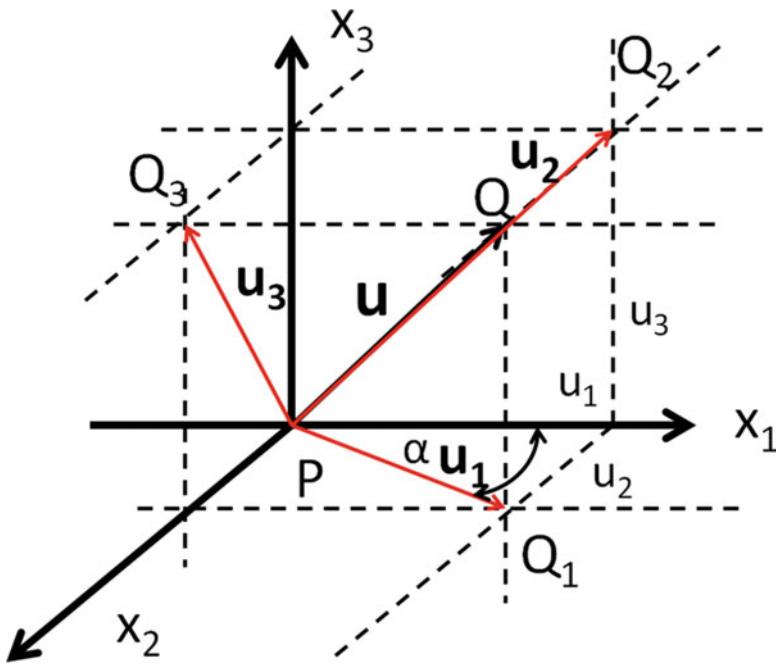

Fig. 7.6 Relative displacement between two points at times t_m and t_{m+1}

Figure 7.6 shows the displacement vector of a point P at time t_m, that moves to the position Q corresponding to the time t_{m+1}.

The following vectorial equation is satisfied by the displacement vector:

$$\boldsymbol{u}(x, t_m) = \boldsymbol{u}_1(x, t_m) + \boldsymbol{u}_2(x, t_m) + \boldsymbol{u}_3(x, t_m) \tag{7.32}$$

where the $\mathbf{u_i}(\mathbf{x},t_m)$ are the components of the displacement vector in each of the reference planes at some reference time t_m. These component vectors satisfy the following equations:

$$\begin{cases} \mathbf{u}_1(\mathbf{x}, t_m) = u_1(x_1, x_2, t_m)\,\mathbf{e}_1 + u_2(x_1, x_3, t_m)\,\mathbf{e}_2 \\ \mathbf{u}_2(\mathbf{x}, t_m) = u_1(x_1, x_2, t_m)\,\mathbf{e}_1 + u_3(x_2, x_3, t_m)\,\mathbf{e}_3 \\ \mathbf{u}_3(\mathbf{x}, t_m) = u_2(x_2, x_3, t_m)\,\mathbf{e}_2 + u_3(x_2, x_3, t_m)\,\mathbf{e}_3 \end{cases} \tag{7.33}$$

These components are given by:

$$\begin{cases} u_1(x_1, x_2, t_m) = \dfrac{p\phi_1(x_1, x_2, t_m)}{2\pi} = n_1(x_1, x_2, t_m)\,p \\ u_2(x_1, x_3, t_m) = \dfrac{p\phi_2(x_1, x_3, t_m)}{2\pi} = n_2(x_1, x_3, t_m)\,p \\ u_3(x_2, x_3, t_m) = \dfrac{p\phi_3(x_2, x_3, t_m)}{2\pi} = n_3(x_2, x_3, t_m)\,p \end{cases} \tag{7.34}$$

The vector $\mathbf{u}(\mathbf{x}, t_m)$ can be represented by the vector $\Phi(\mathbf{x}, t_m)$ defined in Eq. 7.31. The above relationships are general and are valid for any carrier defined by gray levels. If the carrier is sinusoidal or it has been filtered to get the first harmonic or another harmonic and is defined by a multiple of a given frequency as shown in Fig. 7.4, the displacement vector in 3-D is proportional to the phase vector. To find the successive configurations of a body that it is deformed it is equivalent to follow the phase vector. This approach reduces the noise contamination that is brought by the amplitude modulation as it is well known in signal analysis and its practical application to FM radio as compared to AM radio. Consequently, to track a point in space is reduced to tracking the phase of the point.

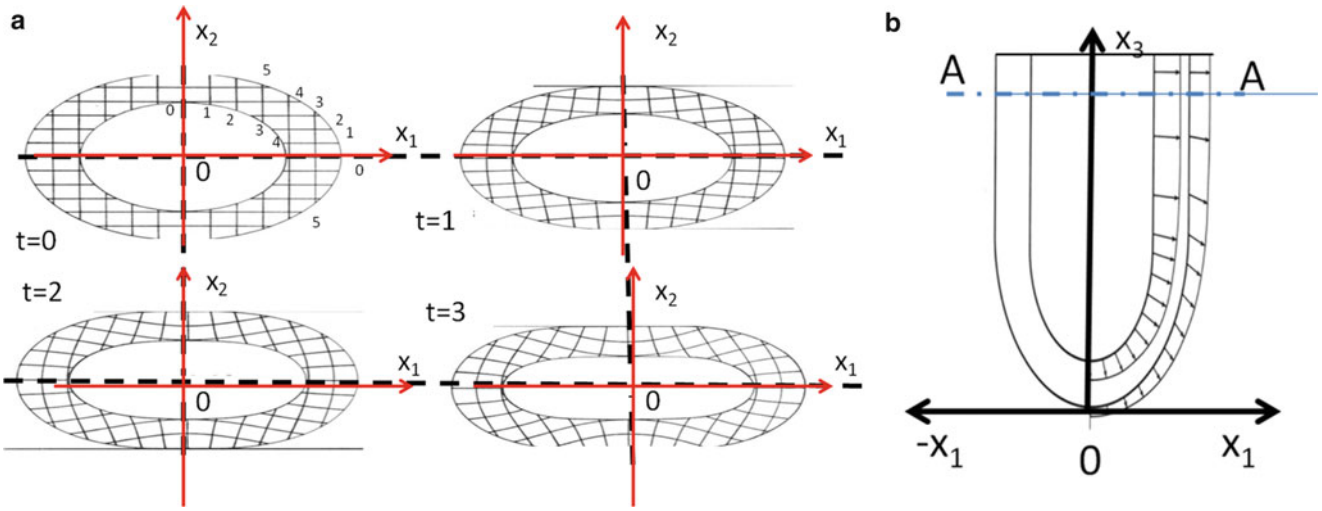

Fig. 7.7 (**a**) Sections A-A and orthogonal family of tagged lines to retrieve the displacement field components in the plane x_1-x_2 in successive time intervals; (**b**) Elevation of the body in the plane x_1-x_3 indicating position of plane A-A and the displacement vectors of the boundary of the body that because of the symmetry of deformations are contained in the x_1-x_3 plane

In the problem being considered, the phase of a given point of the continuum is a 3-D curve that is a function of the vector position "**x**" and a monotonically increasing parameter, the time "t". Considering configurations of the deformed body in time as in the case for many biomechanical problems, t will be the parameter of reference.

The problem must be solved by stepwise procedures. Let us consider a reference configuration of a point P corresponding to the vector position $\mathbf{x_s}(t_s)$, at the time t_{s+1} the point will have a position $\mathbf{x_{s+1}}(t_{s+1})$. Following the Descriptive Geometry representation of Fig. 7.5 and the vector projections of Fig. 7.6, it is possible to follow the evolution of the body in each of the three quadrants. To follow the process in a quadrant we will consider the vector:

$$\mathbf{u}_1(x, t_m) = \frac{p}{2\pi}[\phi_1(x_1, x_2, t_m)\mathbf{e}_1 + \phi_2(x_1, x_3, t_m)\mathbf{e}_2] \tag{7.35}$$

From Fig. 7.6, it can be seen that the angle made by this vector with the x_1 axis is:

$$\mathrm{tg}\alpha = \frac{\phi_1(x_1, x_2, t_m)}{\phi_2(x_1, x_3, t_m)} \tag{7.36}$$

The modulus of the displacement vector is:

$$\left\|\mathbf{u}_1(x, t_m)\right\| = \frac{p}{2\pi}\sqrt{\phi_1^2(x_1, x_2, t_m) + \phi_2^2(x_1, x_3, t_m)} \tag{7.37}$$

Figure 7.7 shows a tagged orthogonal carrier that allows to follow the displacements of the cross-section of a 3-D body in the plane x_1-x_2 for successive time intervals $\Delta t = 1$ from $t = 0$ to $t = 3$. In the initial position, corresponding to the time $t = 0$, the carrier raster utilized to follow deformations is in the reference or initial position. There are two orthogonal families defined by integer parameters $n = 0,1, 2\ldots$The lines parallel to the x_1 axis provide vertical displacement information and in view of the symmetry of the deformed body the orders are growing from zero corresponding to the line coinciding with x_1 to a maximum $n = 5$. In the case of the vertical lines that give the horizontal displacements, the zero order is given to the line that coincides with the x_2 axis and grows to $n = 5$. As the time parameter increases the shape of the cross-section changes. The difference between the initial carrier position and the deformed carrier position provides the displacement information.

7.7 Trajectory Lines

All the necessary elements to track the position of the points in a cross-section as a function of a monotonically increasing parameter (in this case, the time "t") are available. The displacement vector inclination and magnitude are defined by Eqs. 7.36 and 7.37. By taking selected time increments, one can define the trajectory of points in the 2-D space as it is shown in Fig. 7.8b. In two dimensions, the lines of equal inclination [25] given by Eq. 7.36 should not be confused with the traditional definition of isoclinics utilized in Photoelasticity. The isoclinics in Photoelasticity are the lines tangent to the principal strains and in homogeneous materials also to the principal stresses. The trajectory lines can be obtained from the lines of equal inclination of the displacement vector through the same process that isostatics are obtained from the isoclinics. Once the trajectory vectors are obtained in each plane the actual vector in the 3-D space can be determined (see Fig. 7.8a). With this information on the geometry of the body illustrated in Fig. 7.7, one can see, for example, the change of configuration of the body in the plane x_1-x_3 between times $t = 0$ and $t = 1$ (Fig. 7.7b).

By combining Eqs. 7.9 and 7.31, it can be written:

$$[J] = \frac{p}{2\pi}\begin{bmatrix} \frac{\partial \phi_1}{\partial x_1} & \frac{\partial \phi_1}{\partial x_2} & \frac{\partial \phi_1}{\partial x_3} \\ \frac{\partial \phi_2}{\partial x_1} & \frac{\partial \phi_2}{\partial x_2} & \frac{\partial \phi_2}{\partial x_3} \\ \frac{\partial \phi_3}{\partial x_1} & \frac{\partial \phi_3}{\partial x_2} & \frac{\partial \phi_3}{\partial x_3} \end{bmatrix} \tag{7.38}$$

That is, if the components of the vector $\boldsymbol{\phi}(\mathbf{x},t)$ are known:

$$\boldsymbol{\phi}(\mathbf{x},t) = \frac{p}{2\pi}\left[\boldsymbol{\varphi}_1(\mathbf{x},t) + \boldsymbol{\varphi}_2(\mathbf{x},t) + \boldsymbol{\varphi}_3(\mathbf{x},t)\right] \tag{7.39}$$

with:

$$\begin{cases} \boldsymbol{\varphi}_1(\mathbf{x},t) = \phi_1(x_1,x_2,t)\,\mathbf{e}_1 + \phi_2(x_1,x_3,t)\,\mathbf{e}_2 \\ \boldsymbol{\varphi}_2(\mathbf{x},t) = \phi_1(x_1,x_2,t)\,\mathbf{e}_1 + \phi_3(x_2,x_3,t)\,\mathbf{e}_3 \\ \boldsymbol{\varphi}_3(\mathbf{x},t) = \phi_2(x_1,x_3,t)\,\mathbf{e}_2 + \phi_3(x_2,x_3,t)\,\mathbf{e}_3 \end{cases} \tag{7.40}$$

it is possible to compute all the necessary derivatives to obtain a stretch tensor or strain tensor of our choice in the spatial coordinate system following the successive time intervals as shown in Fig. 7.7. Once the most convenient stretch or strain

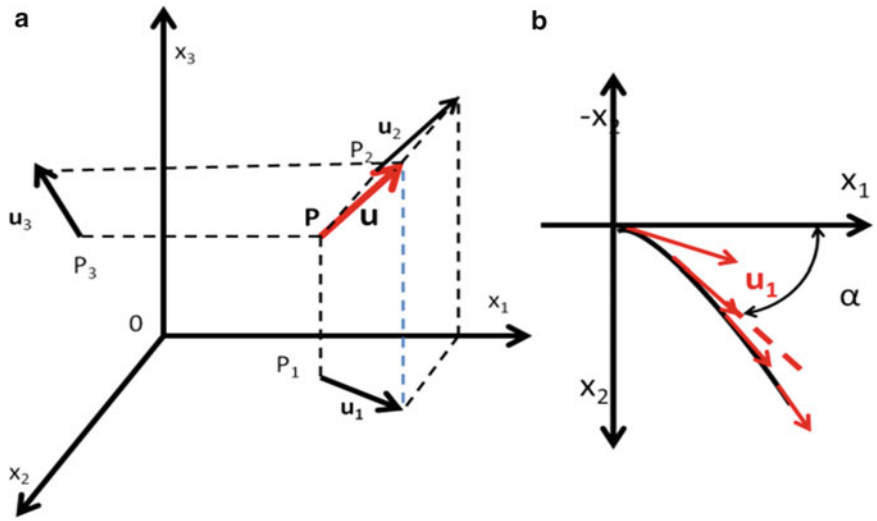

Fig. 7.8 (**a**) Displacement vector **u** in the 3-D space. (**b**) Displacement vector in the plane x_1-x_2, between $t = 0$ and $t = 1$(for example, see in Fig. 7.7 the change of the contour of the body in the plane x_1x_3) and successive positions of the displacement vectors of the points of the plane describing a trajectory line

tensor for a particular application are chosen, one can determine the stress vector that is the conjugate of the selected stretch or strain tensor according to the particular energy function found experimentally to apply to the particular material of the analyzed body.

7.8 Computation of the Components of the Deformation Tensor or the Strain Tensor of Our Choice

In many cases the analysis of a body that has experienced large deformations is limited to finding the components of the selected strain tensor. This task can be accomplished as outlined in the preceding section without unwrapping the phase information. Let us briefly look at some of the details of this operation. In Ref. [22], it is shown that in a plane, for example in the plane x_1-x_2, the derivative of the phase with respect to the coordinate x_1 is given by:

$$\frac{\partial \phi_1(x_1, x_2)}{\partial x_1} = \frac{1}{I_o}\sqrt{\left[\frac{\partial I_c(x_1, x_2)}{\partial x_1}\right]^2 + \left[\frac{\partial I_s(x_1, x_2)}{\partial x_1}\right]^2} - 2\pi f_{cx1} \tag{7.41}$$

where: $\phi_1(x_1,x_2)$ is the phase function of the projected displacement u_1 (see first equation of 7.34); I_o is the background intensity of the carrier; $I_c(x_1,x_2)$ is the amplitude of the in-phase component of u_1; $I_s(x_1,x_2)$ is the in-quadrature component of u_1, $f_{cx1} = 1/p$ is the carrier frequency as defined in Fig. 7.4. The above derivatives are computed in FT transform plane and do not require the unwrapping of the phase function.

In a similar way, the derivatives of functions $\phi_2(x_1,x_2)$, and $\phi_3(x_2,x_3)$ can be computed. Knowing the phase derivatives it is possible to compute a selected stretch or strain tensor.

7.9 Computation of the Spatial Trajectories of the Points

In some particular cases one may be interested in determining the trajectory of a point or a collection of points of the body under analysis. In the preceding sections, the process to obtain the phases that are the components of the displacement vector was outlined. That is, by utilizing Eq. 7.36 it is possible to compute the inclination α of the displacement vector and by applying Eq. 7.37 it is possible to compute the modulus of the vector $\mathbf{u}_1$ shown in Fig. 7.6.

By similar operations we can obtain the other two vectors $\mathbf{u}_2$ and $\mathbf{u}_3$. All these operations depend on the application of Eq. 7.36 which provides the wrapped phases ϕ_i. This means that the phase is defined in an interval 2π. Figure 7.9 shows the process of getting the components of the vector $\mathbf{u}_1$. At the point under consideration, one of the components, ϕ_1, is at the end of a period. The wrapped phase and the unwrapped phase are related by the relationship:

$$\phi_{1unw} = \phi_{1w} + n\ 2\pi \tag{7.42}$$

where n indicates the order of the 2π cycle. With the presence of noise in the signal it is not possible to establish exactly where a given order ends and the next order begins. However, there is a procedure that can be utilized to remove this

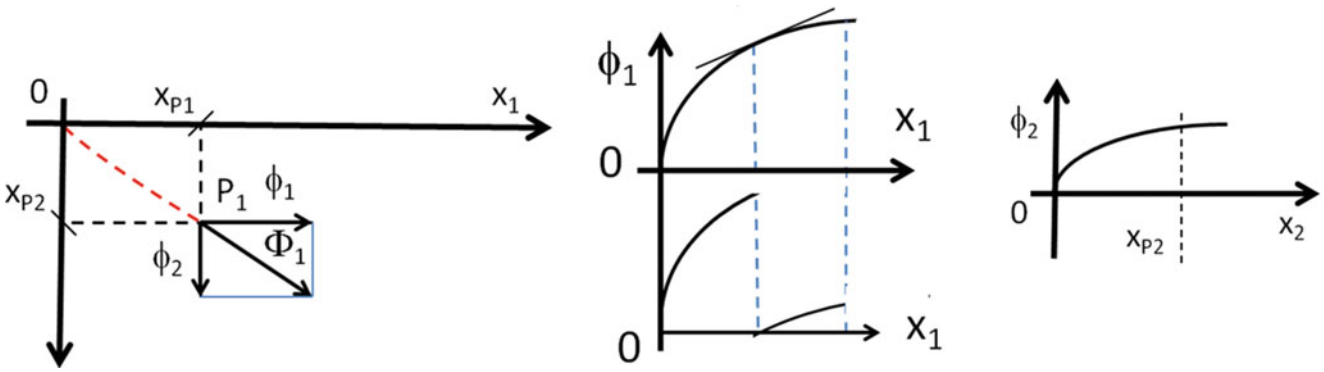

Fig. 7.9 The process of phase unwrapping brings a jump of 2π to one of the vector displacement components

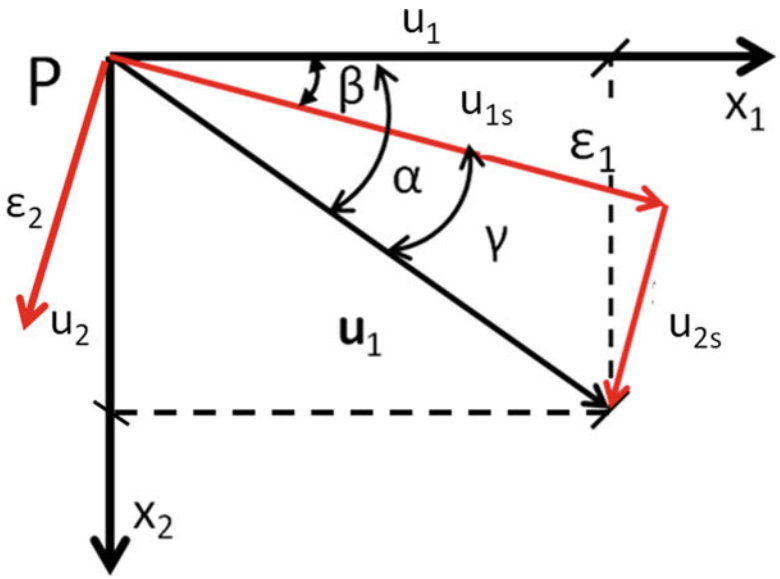

Fig. 7.10 Displacement vector at a point P of a trajectory line represented in Fig. 7.8: ε_1 and ε_2 are the principal strains of a selected strain tensor. Principal strains are coaxial with the principal stresses S_1 and S_2 of a tensor that is compatible with the adopted strain tensor

indetermination. There is an important property of the phase [26] that has been utilized before to compute the deformation or the strain tensors: the phase gradient can be obtained directly from the wrapped phase. That is:

$$\nabla_x \varphi_{unw} = \nabla_x \phi_w \tag{7.43}$$

This property can be utilized to remove the discontinuity of the unwrapping though the following considerations.

Figure 7.10 represents a displacement vector tangent to a displacement trajectory as depicted in Fig. 7.8. ε_1 and ε_2 are the principal strains of a selected strain tensor. S_1, S_2 are the components of the principal stresses of a tensor that is compatible with the adopted strain tensor.

The angle β is the isostatic angle of the principal strains (stresses); α is the angle that vector displacement makes with the axis x_1 defined previously as isoclinic of the displacement trajectories; γ is the angle between the displacement vector and the isostatics. From Fig. 7.10, it follows:

$$\mathrm{tg}\alpha = \mathrm{tg}(\beta + \gamma) \tag{7.44}$$

Strains are obtained independently of the unwrapping process. The angle β can be computed by finding the principal strains of the tensor in the plane x_1-x_2. By knowing one component of the displacement vector at the end of a cycle, the other component can be obtained from the vectorial relationship that arise from Fig. 7.10.

In the example assumed in Fig. 7.9, the component u_1 is affected by the noise in the cyclic jump. However, u_2 is available and then:

$$u_1 = u_{1s} \cos\beta - u_{2s} \sin\beta \tag{7.45}$$

$$u_2 = u_{1s} \sin\beta + u_{2s} \cos\beta \tag{7.46}$$

where:

$$u_{1s} = \|\mathbf{u}_1\| \cos\gamma \tag{7.47}$$

$$u_{2s} = \|\mathbf{u}_1\| \sin\gamma \tag{7.48}$$

This information provides the required components to insure that the tangent of the trajectory is preserved as shown in Fig. 7.8. It is possible to see that this unwrapping procedure does not suffer from the problem of the classical unwrapping procedure. If in the point under analysis both components have a jump it is possible to use extrapolation procedures based in

the previously developed relationships in the neighborhood of the discontinuity to secure the continuity of the tangents of the two trajectories under consideration.

Summarizing previous developments the following steps in the analysis of the deformation of a body can be pointed out. The adopted strategy is to tag the continuum with reference planes that remains fixed to the continuum and deform with it. In Cartesian coordinates the intersection of the carrier planes with the coordinates planes form a system of orthogonal planes (Fig. 7.5). As the medium deforms, the tagging carrier deforms with it (Figs. 7.1 and 7.7). Following the conclusions expressed by Eq. 7.43 and outlined in more detail in Eq. 7.41, the derivatives of the displacements can be obtained from the unwrapped pattern. Practically, this means that the deformed carrier encodes the displacement information in the deformed shape and using Eulerian stretch or strain tensors one can directly utilize the actual geometry to represent the state of deformation of the analyzed body. In order to obtain the derivatives of the displacements, one resorts to the differentiation in the frequency space [26]. This method implies that the coordinates correspond to the final shape (Eulerian description). If one wants to follow the trajectory of the points of the medium then it is necessary to unwrap the phase and follow the rules given in Sect. 7.8.

7.10 3-D Analysis of a Random Signal

In the preceding sections, the 3-D analysis of displacements where deterministic signals are utilized was presented. These developments serve as a model to outline processes of 3-D displacements studies. In a great deal of cases random signals will be the only tagging available. This tagging will be due to the presence of random signals related to the structure of the medium that, through some type of radiation that the medium is transparent to, will generate random carriers similar to what occurs in 2-D cases where speckles, whatever their source is, are utilized as carriers of displacement information.

The general approach is exactly identical to that illustrated for a deterministic signal. All procedures outlined in the preceding sections will be followed and the only difference is the type of carrier being utilized. Consequently, in what follows, procedures that are connected to random signals will be presented along with an outline of possible approaches. As mentioned before, the emphasis will be in possible ways to extract displacement information from random 3-D signals. Since the spatial frequencies of the random signals will be determined by the structure of the analyzed material, procedures to increase the spatial resolution must be introduced. A process to increase spatial resolution will be presented and will be illustrated with an example.

The passage from the 2-D case to the 3-D case to get a formal model needs additional developments in the analysis of random signals processing. In the case of 2-D random signals, the distribution of gray levels when raster sensors are utilized has lead to developments that take care of the transition from the classical point-wise theory of speckles as presented in [27] to the "box car" model of [27–29]. Similar developments are required for the 3-D analysis of random signals.

In order to understand the derivations involved, let us consider in the 2-D case the effect of the relative size of the speckle with respect to the size of a pixel of a sensor. The intensity detected by a single pixel sensor is given by the expression:

$$I_{nm}(\text{sensor}) = \frac{1}{A_o}\int\limits_{\text{sensor}}\int S(x,y)I(x,y)\,dx\,dy \tag{7.49}$$

where: I_{nm} represents the intensity measured by a sensor located at the position (n,m), n indicating the rows and m the columns in the array sensor; A_o is the area of the sensor; S(x,y) is a very complicated function that provides the transformation of the received energy into units of intensity (this function depends on many variables); I(x,y) is the intensity provided by the first order statistics of a speckle field, the negative exponential distribution.

It is necessary to obtain the probability density function $p_{int}(I)$ of the integrated speckle field as well as a second order statistics. A model to solve this problem as it has been mentioned before is given by the "box-car" approximation. The speckle field is divided into statistically independent areas. The intensity is considered a constant in each of these areas also called correlation cells. The correlations cells are assumed to be squares of size ℓ and the sensor is assumed to be a square of size L. A variable given by the ratio L/ℓ of these two quantities is the quantity utilized to develop the statistics of the "box car model".

A similar type of statistical analysis must be developed in 3-D. However, in this case, one deals with voxels, short for volume pixel. The volume of the analyzed body has to be divided into elements of volume (voxels) and the gray level of a voxel must be statistically computed to get 3-D information. The selection of a voxel size poses a large number of problems that can only be statistically analyzed. It is necessary to create models that relate the number of statistically independent gray

levels recorded in the image to the voxel size in order to define the gray level of a voxel. There is a great deal of work that is required to facilitate the selection of parameters and variables to optimize the process of retrieving 3-D information. Some of these aspects are addressed in [9, 10].

A method to retrieve information in a 3-D problem will now be outlined utilizing natural random patterns. This method follows the procedures indicated in the preceding sections devoted to deterministic signals. We will operate with a data base given by the gray levels of the voxels of the reference system that we will designate I_{M1} while the corresponding gray levels for a deformed condition will be denoted as I_{M2}. It is assumed that sections similar to those outlined in Fig. 7.5 for a deterministic signal tagging are generated. We will then obtain projected displacements in the three reference planes that we can utilize as described in the case of a deterministic signal to characterize the deformation of the body and get the derivative of the displacements. The method is based on the developments presented in [30] implemented utilizing digital techniques that correspond to the optical operations also described in [30].

The first image of a plane of a body is recorded: there is a random distribution of gray levels corresponding to natural features of the material of the observed object in the particular analyzed section, intersection of a voxel with the selected plane. A second image is recorded after a deformation has been applied to the observed body. The steps applied in processing the acquired images are described in the following text and afterwards the derivations of the corresponding equations are given.

1. First step

Add to the image I_{M1}, that contains a random pattern of gray levels (speckle), a speckle pattern I_{SP}. This additional speckle pattern is introduced to increase the spatial resolution of the data processing. It is the equivalent in a moiré pattern to introduce a reference grating of higher frequency than the model grating. This speckle has a spatial frequency content much higher than the speckle of the image of the body that is analyzed. Let us call I_{R1} the corresponding distribution of gray levels of the resulting image obtained by superimposing the two distributions:

$$I_{R1} = I_{M1} + I_{SP} \tag{7.50}$$

2. Second step

A second image of the deformed object is recorded, I_{M2}, and the same speckle pattern I_{SP} is added to this image. The resulting intensity is:

$$I_{R2} = I_{M2} + I_{SP} \tag{7.51}$$

3. Third step

The patterns I_{R1} and I_{R2} are separately shifted. The shifts are applied in the directions parallel to the axis of a Cartesian system of coordinates, x-direction horizontal, y-direction vertical.

For each original pattern two patterns are generated by applying displacements in the horizontal or the vertical directions. Let us describe one of these two operations and assume that the shifts of each one of the two patterns include only the vertical displacement Δp. The number of pixels of the applied shift should be evaluated on the basis of the sought spatial resolution in the resultant images. Considering the undeformed image, the resulting image is:

$$S_1 = I_{R1} + I_{R1}(\Delta p) \tag{7.52}$$

The corresponding image for the deformed pattern is:

$$S_2 = I_{R2} + I_{R2}(\Delta p) \tag{7.53}$$

An image of deformed pattern plus its shifted image is obtained. The shifting produces the equivalent of a system of spatial carrier fringes that facilitate the process of getting displacement information from the recorded pattern.

4. Fourth step

In this step, the carrier fringes modulated by the applied deformation are obtained. Considering always the undeformed pattern, the FT of S_1 is computed as:

$$FT(S_1) = S_{f1} \tag{7.54}$$

A system of fringes are observed in the FT plane, these fringes are a function of the relative displacement experience by the two images of the specimen [30].

5. Fifth step
   In this step the carrier fringes are obtained. Two filters are simultaneously applied: a low pass filter that only allows passing the zero order and a band-pass filter that allows passing the first minimum of the fringes observed in the FT. The filtered pattern contains the vertical displacement pattern encoded in a horizontal carrier. The horizontal carrier has a pitch that depends on the applied shift in the y-direction. The same operation can be performed by a shift in the horizontal direction. The identical process is applied to the deformed image; the carrier will be modulated by the applied displacement field.
6. Sixth step
   By subtracting from the deformed pattern phase the undeformed pattern phase, it is possible to obtain the corresponding displacement components.

7.10.1 Derivation of the Equations

First step
The gray levels distribution of the first image corresponding to the gray levels of the undeformed image can be represented by a phasor:

$$\vec{I}_{M1r}(x,y) = I_{AM1r}(x,y)\exp[i\phi_{M1r}(x,y)] \tag{7.55}$$

where the symbol $\Rightarrow$ represents a phasor, I_{AM1r} is a random amplitude term and ϕ_{M1r} is a random phase.

The added speckle pattern can be represented as follows:

$$\vec{I}_{spr}(x,y) = I_{spr}(x,y)\exp[i\phi_{spr}(x,y)] \tag{7.56}$$

Second step
The two phasors representing two fields of gray levels are added. The result is another speckle field produced by the vectorial addition of the two fields:

$$\vec{I}_{R1}(x,y) = I_{r1}(x,y)\exp[i\phi_{r1}(x,y)] \tag{7.57}$$

The addition corresponding to the deformed pattern yields another random pattern:

$$\vec{I}_{R2}(x,y) = I_{r2}(x,y)\exp[i(\phi_{r1}(x,y) + \phi_d(x,y))] \tag{7.58}$$

where $\phi_d(x,y)$ is the phase change produced by the displacement field.

The common assumption behind Eq. 7.58 is the following. When a deterministic signal is added to a random pattern, the phasor representing the resulting signal will only change the phase (that phase corresponds to the added displacement) while the amplitude is preserved.

Third step
To account for the displacement between images, the delta function $\delta(x,y)$ is introduced. For the second image, the delta function $\delta(x,y - y_o)$ is introduced to represent the shifted image. For the undeformed pattern it can be written:

$$\vec{S}_1 = \vec{I}_{R1}(x,y) \otimes \delta(x,y) + \vec{I}_{R1}(x,y) \otimes \delta(x,y - y_o) \tag{7.59}$$

where the symbol $\otimes$ denotes the convolution integral.

Taking $\vec{I}_{R1}$ as a common factor, it is obtained:

$$\vec{S}_1 = \vec{I}_{R1}(x,y) \otimes [\delta(x,y) + \delta(x,y - y_o)] \tag{7.60}$$

Fourth step
Taking the FT of Eq. 7.55, it follows:

$$FT\left[\vec{S}_1\right] = FT\left\{\vec{I}_{R1}(x,y) \otimes [\delta(x,y) + \delta(x, y - y_o)]\right\} \tag{7.61}$$

Applying the convolution theorem, we can write:

$$FT\left[\vec{S}_1\right] = FT\left[\vec{I}_{R1}(x,y)\right] FT[\delta(x,y) + \delta(x, y - y_o)] \tag{7.62}$$

The FT of the random speckle is another random function in the frequency space:

$$\vec{I}_{fR1}(f_x, f_y) = I_{fr1}(f_x, f_y) \exp[i\phi_{fr1}(f_x, f_y)] \tag{7.63}$$

The following identity can be introduced:

$$\frac{1}{2}[\delta(x,y) + \delta(x, y - y_o)] = \delta(x, y + y_o/2) + \delta(x, y - y_o/2) \tag{7.64}$$

Recalling the properties of FT, it follows:

$$FT\,[\delta(x, y + y_o/2) + \delta(x, y - yo/2)] = \cos\frac{\pi}{\Delta y} f_y \tag{7.65}$$

where $\Delta y = y - y_o$.
By combining Eqs. 7.62 and 7.65, it is derived:

$$FT\left[\vec{S}_1\right] = I_{fr1}\,(f_x, f_y) \exp\{i[\varphi_{fr1}(f_x, f_y)]\} \cos\frac{\pi}{\Delta y} f_y \tag{7.66}$$

In the frequency plane, there is a speckle pattern modulated by the Young's fringes produced by the shift of the two patterns. For the sake of simplicity, the presence of a halo effect has not been included in the derivation [31].

Fifth step
In this step the pattern in the frequency plane is filtered and the inverse FT of the filtered pattern is computed. The second filter is located at the location of the first zero of the Young's fringes observed in the FT.
The filter at the frequency zero passes $\delta(0)$ and the inversion gives in the physical space a constant background term I_o. To this constant background a first order term is added. As shown in [33], the filtering and inversion operations produce fringes that correspond in this particular case to a carrier of an equivalent pitch,

$$p = \Delta y \tag{7.67}$$

Finally, it is obtained in the physical space a system of carrier fringes modulated by a random pattern limited in frequency by the applied filter [34]. The intensity profile of these fringes is:

$$I(x,y) = I_o + I_1 \cos\frac{2\pi}{\Delta y} y \;\left[I_{sp} \cos\varphi_{sr}\right]_F \tag{7.68}$$

In Eq. 7.68 $\left[I_{sp} \cos\varphi_{sr}\right]_F$ is a symbolic representation of the filtered and inverted random pattern.
If the same procedure is applied to the image of the deformed specimen it is important to consider that another term must be added to the phase term corresponding to the carrier as shown by Eq. 7.68. Hence, to the phase term of Eq. 7.68 it is necessary to add the term $\phi_d(x,y)$. Furthermore the filtered random pattern will modulate the carrier. That is:

$$I(x,y) = I_0 + I_1 \cos\left[\frac{2\pi}{\Delta y} y + \varphi_d\right] \;\left[I_{sp} \cos\varphi_{sr}\right]_F \tag{7.69}$$

Sixth step

Computing the unwrapped phases of the signals 7.68 and 7.69 and subtracting the phase in Eq. 7.68 from the phase in Eq. 7.69 one obtains the corresponding displacements with the correct signs.

Knowing $\phi_d(x,y)$ one can get the derivatives to obtain the tensors [F] and [G] or the inverse $[F]^{-1}$ and [J] as described in Sect. 7.2.

7.11 Application of the Proposed Procedure for Random Signals

An example of the method outlined in the preceding sections is described in what follows, the determination of the vertical displacements and strains produced by a simulated uniform compression of a granite stone selected as a natural random structure. The region under analysis is 65.177×65.177 mm^2 region. The compression was simulated by contracting the image by -0.01 %. The contraction of the specimen is $\Delta v = 65.177 \times (-0.01) = -0.65177$ mm. A 512×512 pixels image was utilized; the value in mm of 1 pixel is $\Delta p = 65.177/512 = 0.1273$ mm

The applied shift is 7 pixels that produces fringes of pitch $p_y = 7 \times 0.1273 = 0.891$ mm.

Steps 1–6 were applied to the initial and the deformed images. Figure 7.11 shows the three images involved in the analysis of the deformed specimen.

Figure 7.12a shows the FFT of the image of Fig. 7.11c. The figure also shows the Young's fringes in the frequency space modulated by the halo of the filter aperture. In Fig. 7.12, it is also shown the filtered order and the resulting carrier fringes. The HoloStrain program [32] was applied to perform all the operations involved in the six steps of data processing. From the

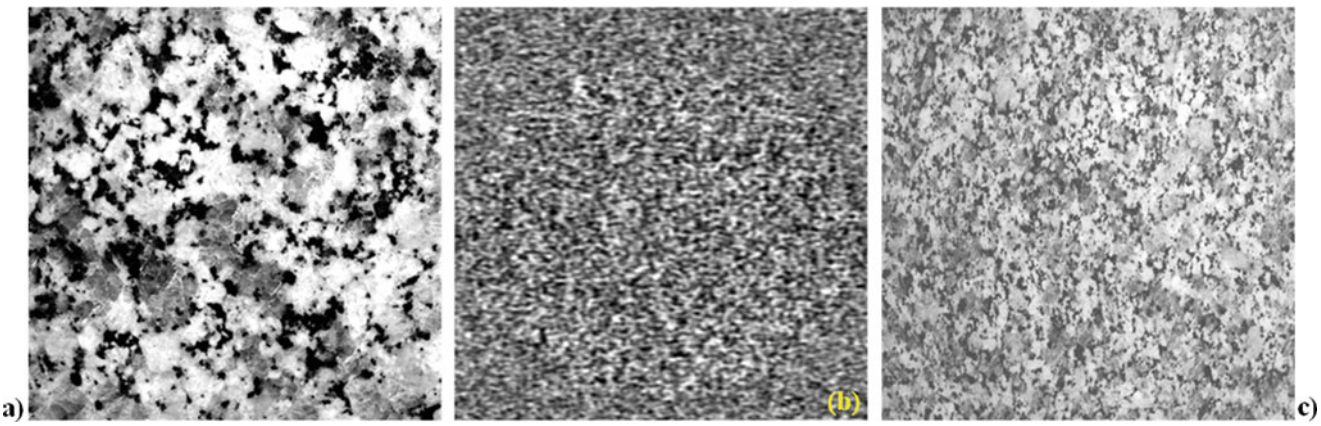

Fig. 7.11 (**a**) Initial random pattern of the natural granite stone; (**b**) speckle pattern added to the pattern shown in Fig. 7.10a; (**c**) final pattern showing the addition of the two patterns

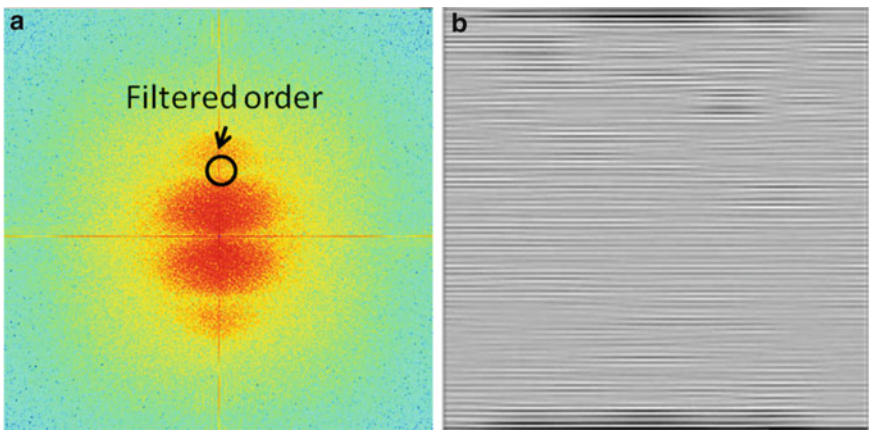

Fig. 7.12 (**a**) FT of the loaded image and filtered order; (**b**) carrier fringes that contain the displacement information of the deformed specimen

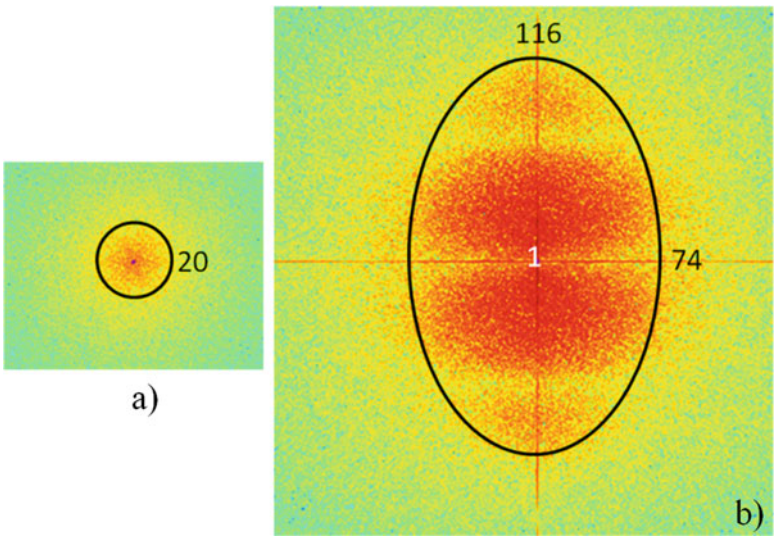

Fig. 7.13 Relative frequencies recorded in the FT plane: (**a**) FT of the pattern shown in Fig. 7.11b; (**b**) FT pattern of Fig. 7.11c

HoloStrain program the average strain in the area of interest was computed, $e^E = -0.01012$. The average stain e^E can be computed also from the input data as

$$e^E = \frac{L_f - L_i}{L_f} = \frac{-0.65117}{64.525} = 0.0101$$

with $L_i = 65.177$ and $L_f = 64.525$. The difference of the computed input strain and the measured strain is 20με.

Although this is a simple example as it deals with a uniform strain field, it sheds light on several important aspects on the application of random gray levels (i.e. speckles) to the 3-D analysis. There two important aspects that need to be stressed: (i) the introduction of an additional speckle pattern with a higher spatial resolution; (ii) the addition of a system of carrier fringes.

The FT of a random speckle pattern produces a speckle pattern in the frequency plane with maximum intensity at the center and decaying intensity towards a circle (assuming circular symmetry). Figure 7.13 shows the relative sizes of the regions in the frequency space that record the presence of the speckle spectrum. Since the speckles are carriers of information only areas that have spectral components above the random noise background can provide information. These regions provide the limit to the spatial frequencies available to get displacements and their derivatives. In Fig. 7.13a, the speckle pattern signal of the natural stone above the noise background is approximately recorded up to at the frequency of 20 pixels while in Fig. 7.13b the signal of the added patterns is visible up to the frequency of 74 pixels in the x-direction and in the y-direction of the shift up to 110 pixels. Hence, the addition of a random speckle pattern to the random pattern of the stone levels of gray makes it possible to measure frequencies 74/20 = 3.7 times higher than for the original pattern.

The second point is related to the feasibility of extracting information from the obtained patterns. In [34], it is shown that although theoretically equivalent the in-quadrature method and the phase stepping method to retrieve phase from fringe patterns, in practice they are not. The frequency modulation of the phase influences the spectrum of the signal. As the modulation increases the spread of the spectrum also increases. The spread of harmonics of the signal is such that the separation of harmonics required by the in-quadrature technique becomes extremely difficult to achieve. The carrier fringes by reducing the frequency modulation of the signal make it possible to apply the in-quadrature method and obtain reliable results. This is a procedure that is built in the HoloStrain program [32] and has proven to be effective in all the cases that we have applied it. Phase retrieval by phase-stepping requires multiple exposures thus making the analysis far more complex.

Going back to the voxel size, in the example that has been presented the voxel size is related to the introduced shift. Since a 7 pixel shift was introduced, the location of the points is known with the spatial resolution of 0.9 mm.

7.12 Relationships Between the Different Approaches to Handle 3-D Data Recovery

In Sects. 7.5 through 7.7 the kinematics of 3-D displacement fields has been outlined using deterministic signals and basic properties of 3-D displacement fields and their geometrical representation. In Sects. 7.10 and 7.11 the use of random carriers was introduced and a method for practical application was developed along the classical lines of speckle methods. In the current literature of Experimental Mechanics most of the work on 3-D analysis as it is shown in Sect. 7.1 is based on DIC applied to random carriers. In Ref. [16], another technique for 3-D analysis based on an assumption similar to that utilized in DIC is applied. It is interesting to connect different approaches presented in this paper to a common framework.

In Sect. 7.6, the displacement signal 7.30 represented as levels of gray was separated into two components: the amplitude component and the phase component. Through Eq. 7.31, displacements were connected to the vectorial function $\boldsymbol{\phi}(\mathbf{x},t)$ thus removing the effect of the amplitude factor in the signal. Traditionally, the methods that measure displacements utilize the argument that points that have multiple values of the same projected displacement have the same gray (phase) level. This property results in the case of two dimensional deformations in two families of fringes providing the projected displacements.

DIC applies a similar idea based on the concept of optical flow to the lines of equal displacement or trajectories as defined in Sect. 7.7 and assumes that a given point that has a position x_m at time t_m and has a gray level $I(x_m,t_m)$, at the position x_{m+1} and time t_{m+1} has the gray level $I_m(x_m,t_m) = I_{m+1}(x_{m+1},t_{m+1})$, or, equivalently, it holds $I_m(x_m,t_m) - I_{m+1}(x_{m+1},t_{m+1}) = 0$. This equation is the starting point of DIC.

In [16] the same assumption utilized in DIC was adopted. At the same time, the classical approach of separating gray levels into an amplitude and a phase components is assumed leading to the equation

$$\varphi(x_{m+1},t_{m+1}) - \varphi(x_m,t_m) = 0 \tag{7.70}$$

Along a similar path to DIC in [16] the approximate solution of the above equation is obtained on the basis of an iteration procedure utilizing the Newton-Raphson method. The result of the n^{th} iteration is,

$$\mathbf{x}^{(n+1)} = \mathbf{x}^{(n)} - \frac{\varphi(\mathbf{x}^{(n)},t_{m+1}) - \varphi(\mathbf{x}_m,t_m)}{\nabla_{\mathbf{x}}\varphi(\mathbf{x}^{(n)},t_m)} \tag{7.71}$$

Since unlike DIC that operates with levels of gray levels the problems of phase retrieval are solved by utilizing Eq. 7.43 and additional algorithms that solve the problem of noise outlined in Sect. 9 and phase determination analyzed in Sect. 10. Basically, the motion is followed in successive intervals of time corresponding to tagged images. Consequently, the method introduced in Ref. [16] has the same basic starting assumption as DIC, uses also the Newton–Raphson method. However, in place of tracking intensities the proposed method in Ref. [16] tracks phases and consequently additional algorithms required to convert gray level signals into displacement information are different.

7.13 Computation of the Strains of the Myocardium

The strain analysis of a cross-section of the myocardium carried out in Ref. [16] falls in the general methodology outlined in this paper. In [16], it is mentioned that Eulerian strains were computed from the displacement data obtained from the CINE Harmonic Phase (HARP) method. Since displacement derivatives were computed from phase data by utilizing the finite difference method, no unwrapping was required to perform such operation. The derivatives were utilized to compute Eulerian strains. However, it is not fully explained by the authors of Ref. [16] which definition of the tensor they selected and the tensor transformations required to compute strains plotted in Figs. 2 and 3 of Ref. [16]. The definition given in the Appendix B of Ref. [16] for the Eulerian strain tensor is not a standard definition of Continuum Mechanics and not all of the involved symbols in the definition of Eulerian strain are explained.

Some of the images presented in [16] have been processed by utilizing the method outlined in this paper and the two dimensional version of the tensorial equations. The original images of Ref. [16] are shown in Fig. 7.1. Since the reference image corresponding to the undeformed body was not available, each pattern was compared with the first pattern of Fig. 7.1 which represents itself a deformed configuration (see Fig. 7.14a). Special cares were taken in cropping the region of interest of the different patterns in order to avoid fictitious displacements caused by artificial image shifts. Hence, displacement maps extracted from image processing operations were fully representative of the actual motion of the heart. The pixel size (about

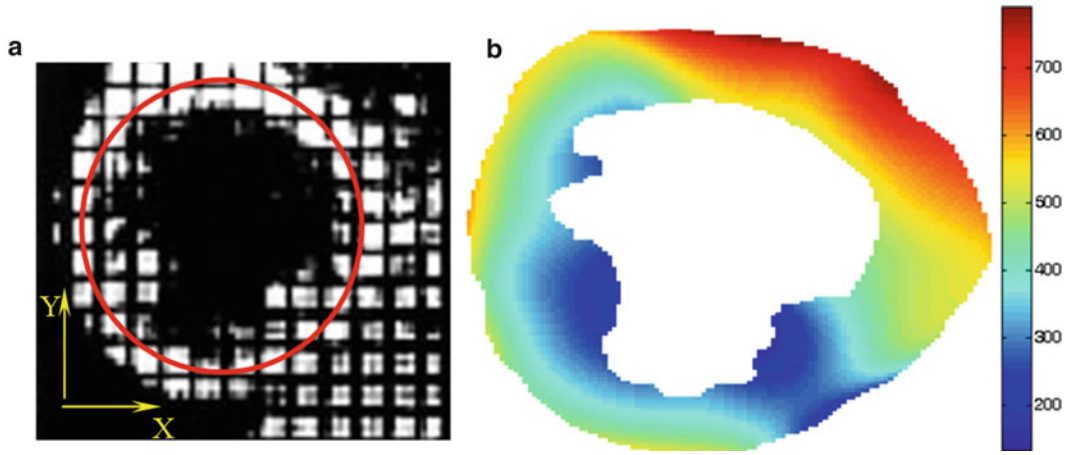

Fig. 7.14 (**a**) Tagged image of the lower ventricle short-axis view throughout systole in a healthy volunteer (reference system and heart baseline are indicate in the figure); (**b**) magnitude of the total displacement vector in the wall of the ventricle (scale microns)

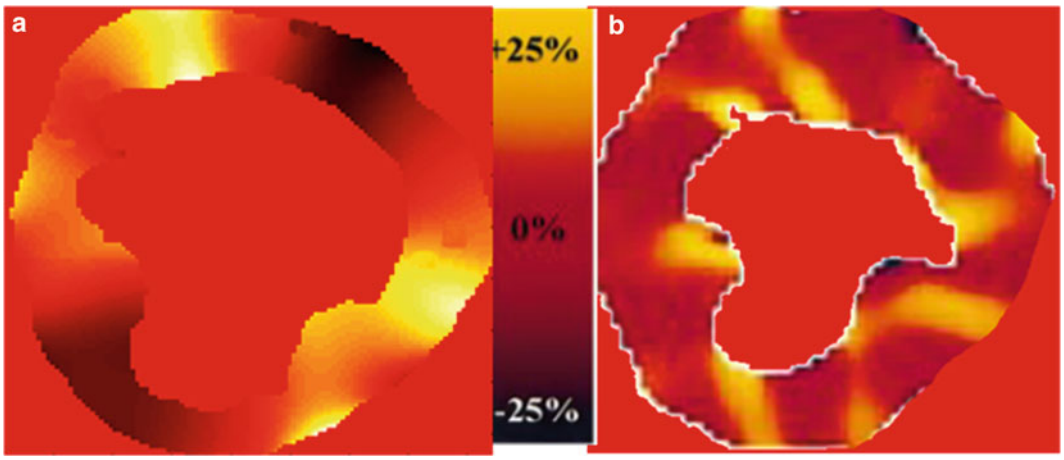

Fig. 7.15 (**a**) Strains obtained by applying the Holostrain program; (**b**) strains as given in [17]. *Yellow* indicates positive strains (stretching) *black* indicates negative strains (shortening)

700 μm) was calibrated by reporting the average length of the heart baseline image (the baseline is sketched in red in Fig. 7.14a) measured in the circumferential direction to the values usually indicated in literature. Once the pixel size was determined, it was possible to determine the pitch of the cross grating tagging the image (about 7,000 μ m).

The frequency modulation of the system of lines in the horizontal and vertical directions was analyzed in the FT domain. By properly selecting frequencies it was possible to obtain the displacement components u and v, respectively in the coordinate directions X and Y (also indicated in Fig. 7.14a). The displacement components u_1 and u_2 along the coordinate axes X and Y were then summed up to obtain the total displacement:

$$\|u_1(x, t_m)\| = \sqrt{u_i^2(x_1, x_2, t_m) + u_2^2(x_1, x_2, t_m)} \tag{7.72}$$

Figure 7.14b represents the magnitude of the displacement vector of the points of the image which corresponds to the second image of the original sequence of patterns considered in Ref. [16] and shown in Fig. 7.1 of the present article.

The derivatives of displacement components were obtained by differentiating fringes in the frequency space. Derivatives were smoothed out in order to remove discontinuities, especially near boundaries. The Eulerian components of the strain tensor were computed utilizing the definitions given in Eqs. 7.24 and 7.25. The slope of the baseline of the deformed profile of the heart was computed from the processed image and strain components were projected on it in order to determine the total strain in the circumferential direction. Figure 7.15 compares the Eulerian strains in the circumferential direction

determined in the present study (Fig. 7.15a) with the results shown in [16] (see Fig. 7.15b). In view of the possible differences in actual procedures to arrive to the final results, a fair agreement exists between the two strain distributions particularly in the order of magnitude of the strains at the recorded time.

7.14 Summary and Conclusions

The availability of methods to obtain information from inside optically non-transparent media either by creating tags or by utilizing random gray levels distributions has opened a very important and vast field of research in the actual behavior of real materials of scientific or engineering interest. Also bioengineering has been provided with a very powerful tool of research. In this paper the necessary background in Continuum Mechanics for 3-D displacement and strain analysis has been reviewed and all the processes involved in data gathering and processing have been presented. The cases of deterministic and random signal processing have also been considered. Finally, the classical approach utilizing displacement components and a method that is an extension DIC have been compared in their application to a deterministic signal and the results show a fair agreement in spite of the very different procedures applied.

References

1. Viggiani G, Hall SA (2012) Full-field measurements in experimental geomechanics: historical perspective, current trends and recent results. In: Viggiani G, Hall SA, Romero E (eds) ALERT Doctoral School 2012: advanced experimental techniques in geomechanics. ALERT Geomaterials, pp 3–68, ISBN 978-3-00-039683-0
2. Clouet B, Muszynski L, Pommier R (2008) Optical measurement of local strains development in finger-jointed wood subjected to static and sustained load. In: Proceedings of the 8th world congress in computational mechanics, Venice
3. Petit J, Bornert M, Hofmann F, Robach O, Micha JS, Ulrich O, Le Bourlot C, Faurief D, Korsunsky AM, Castelnau O (2011) Combining Laue micro diffraction and digital image correlation for improved measurements of the elastic strain field with micrometer spatial resolution. In: Proceedings of the IUTAM symposium on full-field measurements and identification in solid mechanics, Cachan. Elsevier: Procedia IUTAM, vol 4, pp 133–143
4. Roux S, Hild F, Viot P, Bernard D (2008) Three dimensional image correlation from X-ray computed tomography of solid foam. Compos Appl Sci Manuf 39(8):1253–1265
5. Réthoré J, Tinnes JP, Roux S, Buffière JY, Hild F (2008) Extended three-dimensional digital image correlation (X3D-DIC). Comptes Rendus Mécanique 336(8):643–649
6. Yusof F, Withers PJ (2009) Real-time acquisition of fatigue crack images for monitoring crack-tip stress intensity variations within fatigue cycles. J Strain Anal Eng 44(2):149–158
7. Verhulp E, Van Rietbergen B, Huiskes R (2004) A three-dimensional digital image correlation technique for strain measurements in microstructures. J Biomech 37(9):1313–1320
8. Djaziri S, Faurie D, Le Bourhis E, Goudeau P, Renault PO, Mocuta C, Thiaudière D, Hild F (2013) Deformation modes of nanostructured thin film under controlled biaxial deformation. Thin Solid Films 530:30–34
9. Leclerc H, Périé J, Roux S, Hild F (2011) Voxel-scale digital volume correlation. Exp Mech 51(4):479–490
10. Roux S, Taillandier-Thomas T, Bouterf A, Leclerc H, Morgeneyer TF, Hild F (2012) Digital volume correlation from tomographic images: results and challenges. In: Proceedings of the 2012 IUTAM symposium on advances of optical methods in experimental mechanics, Taipei
11. Zerhouni EA, Parish DM, Rogers WJ, Yang A, Shapiro EP (1988) Human heart: tagging with MR imaging–a method for noninvasive assessment of myocardial motion. Radiology 169(1):59–63
12. Mosher TJ, Smith MB (1990) A DANTE tagging sequence for the evaluation of translational sample motion. Magn Reson Med 15(2):334–339
13. Bolster BD, McVeigh ER, Zerhouni EA (1990) Myocardial tagging in polar coordinates with striped tags. Radiology 177(3):769–772
14. Guttman M, Prince J, McVeigh ER (1994) Tag and contour detection in tagged MRI images of the left ventricle. IEEE Trans Med Imaging 13 (1):74–88
15. Osman NF, Kerwin WS, McVeigh ER, Prince JL (1999) Cardiac motion tracking using CINE harmonic phase (HARP) magnetic resonance imaging. Magn Reson Med 42(6):1048–1060
16. Garot J, Bluemke DA, Osman NF, Rochitte CE, McVeigh ER, Zerhouni EA, Prince JL, Lima JAC (2000) Fast determination of regional myocardial strain fields from tagged cardiac images using harmonic phase MRI. Circulation 101(9):981–988
17. Wyman BT, Hunter WC, Prinzen FW, McVeigh ER (1999) Mapping propagation of mechanical activation in the paced heart with MRI tagging. Am J Physiol Heart Circ Physiol 276:881–891
18. O'Dell WG, Schoeniger JS, Blackband SJ, McVeigh ER (1994) A modified quadrupole gradient set for use in high resolution MRI tagging. Magn Reson Med 32(2):246–250
19. Huang J, Qian Z, Huang X, Metaxas D, Axel L (2008) Tag separation in cardiac tagged MRI. In: Proceedings of the 11th international conference on medical image computing and computer-assisted intervention – Part II, New York
20. Rutz AK (2008) Advances in whole-heart MRI tagging for the assessment of myocardial motion. Ph.D. dissertation, Swiss Federal Institute of Technology, Zurich

21. Sciammarella CA (1965) Basic optical law in the interpretation of moiré patterns applied to the analysis of strains – Part 1. Exp Mech 5:154–160
22. Sciammarella CA, Sciammarella FM (2012) Experimental mechanics of solids. Wiley, Chichester, p 406, Chapter 13.2.1
23. Sciammarella CA, Sciammarella FM (2012) Experimental mechanics of solids. Wiley, Chichester, p 170, Chapter 7.4.6
24. Sciammarella CA, Sciammarella FM (2012) Experimental mechanics of solids. Wiley, Chichester, p 261, Chapter 16.3
25. Durelli AJ, Parks VJ (1970) Moiré analysis of strain. Prentice-Hall, Englewood Cliffs
26. Sciammarella CA, Sciammarella FM (2012) Experimental mechanics of solids. Wiley, Chichester, p 404, Chapter 13.8.2
27. Goodman JW (1984) Statistical properties of laser speckle patterns. In: Dainty JC (ed) Topics in applied physics, vol 9. Springer, Berlin
28. Lehmann M (1998) Statistical theory of two-wave speckle interferometry with unresolved speckle and its application to the optimization of deformation measurements. Ph.D. thesis, Swiss Federal Institute of Technology, Lausanne
29. Lehmann M (1996) Phase-shifting speckle interferometry with unresolved speckles: a theoretical investigation. Opt Commun 128 (4–6):325–340
30. Burch JM, Tokarski JMJ (1968) Production of multiple beam fringes from photographic scatterers. Opt Acta 15(2):101–111
31. Sciammarella CA, Sciammarella FM (2012) Experimental mechanics of solids. Wiley, Chichester, pp 584–585, Chapter 19.2
32. General Stress Optics Inc. (2007) Holo-Moiré strain analyzer version 2.0, Chicago http://www.stressoptics.com
33. Sciammarella CA, Sciammarella FM (2012) Experimental mechanics of solids. Wiley, Chichester, p 408, Chapter 13.8.3
34. Sciammarella CA, Sciammarella FM (2012) Experimental mechanics of solids. Wiley, Chichester, p 275, Chapter 10.4.3

Chapter 8
Shape Measurement Using a New 3D-DIC Algorithm That Preserves Sharp Edges

Jacques Harvent, Benjamin Coudrin, Ludovic Brèthes, Jean-José Orteu, and Michel Devy

Abstract Digital Image Correlation is widely used for shape, motion and deformation measurements. Basically, the main steps of 3D-DIC for shape measurement applications are: off-line camera calibration, image matching and triangulation. The matching of each pixel of an image to a pixel in another image uses a so-called subset (correlation window). Subset size selection is a tricky issue and is a trade-off between a good spatial resolution, achieved with small subsets that preserve image details, and a low displacement uncertainty achieved with large subsets that can smooth image details.

In this paper, we present a new multi-step DIC algorithm specially designed for measuring the 3D shape of objects with sharp edges. With this new algorithm an accurate 3D reconstruction of the whole object, including the sharp edges that are preserved, can be achieved.

Keywords Shape measurement • Stereovision • Digital image correlation (DIC) • Edge preservation • Accurate 3D reconstruction

8.1 Introduction

We address the problem of providing an accurate 3D reconstruction of a complex object by using a DIC-based shape measurement technique. The DIC technique requires choosing a correlation criterion, the size of the correlation window (also called subset) and the window transformation model (subset shape function). The choice of the subset size is a tricky issue [1, 2] and is a trade-off between a good spatial resolution, achieved with small subsets that preserve image details, and a low displacement uncertainty achieved with large subsets that can smooth image details.

In order to increase the accuracy of the shape reconstruction, several authors have proposed to use a multi-view stereo method that exploits a large number of images [3–6] and that allows using a small subset size.

In this paper, we address the problem of providing an accurate 3D reconstruction of an object by using the classical two-views 3D-DIC technique.

In the classical DIC-based matching technique, discontinuities (e.g. cracks in 2D-DIC-based displacement/strain measurements, sharp edges in stereo-DIC-based shape measurements) are difficult to handle and several authors have proposed new DIC formulations specially designed for DIC matching in presence of discontinuities [7–10]. Most of these work deal with 2D discontinuities and few work have been done on the handling of 3D discontinuities like sharp edges in the DIC process.

J. Harvent • B. Coudrin • L. Brèthes
NOOMEO, 425 rue Jean Rostand, F-31670 Labège, France
e-mail: ludovic.brethes@noomeo.eu

J.-J. Orteu (✉)
Université de Toulouse, Mines Albi, ICA (Institut Clément Ader), Campus Jarlard, F-81013 Albi, France
e-mail: jean-jose.orteu@mines-albi.fr

M. Devy
CNRS, LAAS, 7 avenue du colonel Roche, F-31400 Toulouse, France

Université de Toulouse, LAAS, F-31400 Toulouse, France

H. Jin et al. (eds.), *Advancement of Optical Methods in Experimental Mechanics, Volume 3*,
Conference Proceedings of the Society for Experimental Mechanics Series,
DOI 10.1007/978-3-319-00768-7_8,

The extraction of edges can be performed after the 3D shape measurement, using a 3D mesh like in [11]. An analysis of the 3D mesh allows a fine extraction of the surface discontinuities, then of the edges. In our method, sharp edges are obtained using DIC and are extracted directly from the 3D points cloud generated by the stereo-DIC-based method, without building a 3D mesh.

We propose a new DIC method, based on a new correlation criterion and a new window transformation model, specially designed to preserve the sharp edges that can be present on some machined objects.

8.2 Overview

The presented method is an extension to the standard stereo-vision 3D reconstruction. It aims to refine points near sharp edges. These points are generally badly estimated due to an over-smoothing effect. Standard stereo-vision uses the approximation that the observed surface is locally continuous and almost planar. This assumption becomes false near sharp edges causing a false estimation of the surface. Due to the planar approximation, standard stereo-vision tends to measure edges as curves.

To achieve the sharp edges preservation, our proposed method performs an iterative refinement of the areas where the planar approximation fails. It starts from an initial 3D reconstruction of an object. The 3D reconstruction step estimates a 3D point-cloud representation of the surface, normals and confidence values of the measured points.

First the algorithm detects regions with high curvature. These regions are considered candidates to the edge refinement. Next, the method estimates the possible location of edges for each area and reorganize normals around the edges. Then every considered point is estimated using a bi-plane transformation based correlation model.

At the end of the process, the results are compared to the initial reconstruction and the best result is chosen. This validation step ensures that high curvature areas not representing actual sharp edges would not be "sharpened" by error.

8.3 Problem Formulation and Notation

In the following, we consider a stereo-vision system with two digital cameras. Cameras are calibrated and the rigid transformation between them is known. Images are considered distortion free – i.e. the images are provided by a perfect distortion free system or the images have been corrected from their distortion using the calibration parameters. Moreover, images and transformations are considered in the epipolarly rectified space.

The rigid body transformation which transforms a 3D point X in the first camera coordinate frame to the second camera coordinate frame is given by a 3×4 matrix $[R|t]$ with $R \in SO(3)$ and $t \in \mathbb{R}^3$. Intrinsic parameters are given by K_0 and K_1 with $K_i \in \mathbb{R}^{3 \times 3}$. A 3D point and its normal are written respectively X and $n = (n_x, n_y, n_z)$. 2D images points are noted x_0 and x_1 for camera 0 and camera 1. We define the left image as I_0 and the right image as I_1. $I(x)$ refers to the gray level value of a point x in the image I.

8.4 Initial Reconstruction

Standard stereo-vision is a pixel-matching process between images acquired from two strongly calibrated cameras. Pixels are matched by correlation of their neighborhoods in images. To obtain a better correlation, one need to estimate the deformation of the neighborhoods of matched pixels between the images. This deformation is caused by the orientation of the observed surface. This is equivalent to estimate the normal to the surface at the correlated point. Assuming the surface can be considered locally planar around the correlated point, the estimated deformation is an homography (Fig. 8.1).

This homography is expressed as:

$$H = K_1[R|t]SK_0^{-1} \tag{8.1}$$

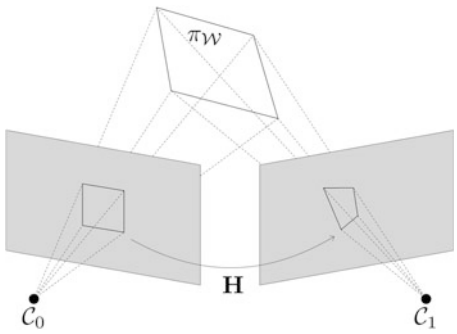

Fig. 8.1 An homography is a projective transformation relating the projections of a plane in two images

$$S = \begin{bmatrix} -1 & 0 & 0 \\ 0 & -1 & 0 \\ 0 & 0 & -1 \\ n_x & n_y & n_z \end{bmatrix} \tag{8.2}$$

In Eq. (8.2) S is a representation of the tangent plane to the observed surface. The vector n_x, n_y, n_z is the normal to the tangent plane.

The correlation of a region between stereo images I_0 and I_1 is the minimization of the function

$$min \sum_{x \in W} [I_0(x) - I_1(H(x))]^2 \tag{8.3}$$

If the surface is not locally-planar, the homography is not a representative model of the surface and does not allow a correct measurement of the surface. The following section proposes to extend the correlation function and homography estimation in sharp edges region, where the planar approximation fails.

8.5 Edge Detection

Detection of 3D edges highly depends on the quality of the initial 3D reconstruction, which gives accurate results for flat areas but not along the edges. Patch based methods tend to smooth discontinuities because they approximate the local surface. After the initial 3D reconstruction, the measured 3D points of a sharp edge can have the same shape as a curvy part. This means that classical curvature estimation methods are not sufficient to discern an edge from a curve. This is not an issue as accuracy of our algorithm does not rely on detection. We only detect edges in order to avoid processing irrelevant points.

For each 3D point, the standard deviation to the average normal is computed. When the deviation is higher than an arbitrary threshold, the 3D point is possibly an edge and will be processed. This detection method is based on the observation that points near edges are not correctly estimated. This is due to the use of a wrong surface model in the correlation function. In consequence the correlation confidence for these points is low.

8.6 Edge Initial Estimation

For each selected points, we compute an initial estimate of the edge model that we will refine later. The initial estimate consists in two mean normals which describe the two faces of an edge. In order to compute these two normals, we consider a region around an edge and modify normals so that they model the shape of the edge. Figure 8.2 presents the process using a side view of the result of an initial 3D reconstruction. Normals do not represent a sharp edge and tend to model a curve. Normals are modified by replacing those with the highest deviation by those with the lowest deviation. Then the two mean normals (green) are computed as the means of normals estimated on each side of the edge.

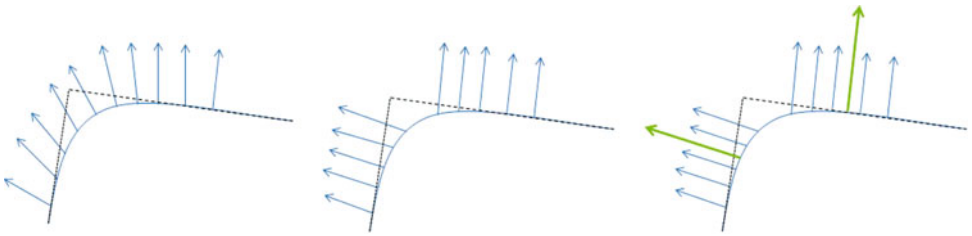

Fig. 8.2 Side view of a 3D reconstruction along an edge. *Blue* surface and normals are the result of the initial reconstruction. *Dotted black line* is the actual edge. Normals are filtered and classified. High deviation normals are suppressed and replace with lower deviation normals. *Green* normals are the means of the two identified groups of normals

When dealing with noisy 3D points and normals, curvature estimation may not be accurate. The algorithm may replace a normal from a face of the edge with a normal from the other face. This introduces errors in the estimation of the mean normals. To avoid this, we weight the deviation values using a Gaussian function centered on the currently processed point. This penalizes normals from other side of the edge and results in a better correction.

8.7 Edge Preservation

8.7.1 Edge Matching

In order to refine points along edges, we introduce a new model represented by two planes which intersects as a 3D line (the edge). The intersection of two planes can be expressed as Plucker coordinates and depends on six parameters which are the components of the two normals of the two planes, i.e. the two faces of the edge. They define two homographies which are applied according to the side of the line where image points are located. We write the new cost function as

$$\min \sum \alpha(I_0(x) - I_1(H_0(x)))^2 + (1-\alpha)(I_0(x) - I_1(H_1(x)))^2 \tag{8.4}$$

with

$$\alpha = \left\{ \begin{array}{l} 0 \text{ if } f(x)<0 \\ 1 \text{ otherwise} \end{array} \right\} \tag{8.5}$$

where

$$f(x) = l \cdot x \tag{8.6}$$

with

$$[l]_\times = K_0[R|t]L(K_0[R|t])^t \tag{8.7}$$

and

$$L = n_1 {n_2}^t - n_2 {n_1}^t \tag{8.8}$$

8.7.2 Edge Consistency

The proposed edge model produces good results along sharp edges made of two faces. However, problems may occur when the edge model is used on surfaces with chamfers, and spikes.

Both chamfers and spikes are composed of more than two planes. When more than one edge is included in the correlation window, our edge model cannot fit the surface perfectly. In order to discard wrong results produced by the edge optimization, we compare results obtained by standard criterion to results obtained by edge optimization and choose the better one. This works as both methods minimize a sum of squared differences on pixel intensity.

8.8 Results

The results presented in this section have been processed from images of a home-made stereo-vision system. It is composed of two 1, 024 $\times$768 CCD cameras with 8 mm lenses and a pattern projector. The stereoscopic baseline is 140 mm long and the cameras are oriented with a 15° angle. The working distance is about 400 mm and the pixel size is about 0.23 mm. During the image correlation process, 11 $\times$11 pixels correlation windows are used, leading to a spatial resolution of about 2. 5 $\times$2. 5 mm^2. The whole setup has been described and evaluated by Coudrin et al. [5]. The cameras and the projector are synchronized. We use a pattern projection to provide a dense 3D information from the pair of cameras, whatever the texture on the object surface. When the system is triggered, the pattern is projected on the scene. Then the two cameras acquire images simultaneously. The pair of images is used in a reconstruction algorithm, providing a 3D point cloud by a stereo-vision surface growing method. Points are expressed with respect to the frame $\mathcal{C}_0$ of the principal camera.

Figure 8.3 presents a comparison of the improvement brought by our method on a mechanical part reconstruction. On the left, one can see the result of the initial reconstruction. The part contains both sharp edges and curvy edges. On the right one can note that the sharp edges have been corrected and are sharper. Curvy edges have not been modified.

Figure 8.4 shows a cylindrical gauge block. It is composed of a section of a cylinder with flat surfaces on the top and the bottom and perfectly circular surface on the inside. The CAD model of this part is known and accurate up to 1 µm. Figure 8.4 shows the initial reconstruction of the cylinder. Figure 8.5 presents the qualitative result of edge optimization. The edge at the intersection of the inner cylinder and the top surface has been sharpened. The other edges have not been altered since they are not actual sharp edges.

Since the CAD model is known for this part, we have evaluated the accuracy of our method by comparing the 3D reconstruction results to the theoretical surface. We have used the Geomagic Qualify™ software to align and compare our result to the CAD model ground truth. The software gives a comparison by projecting orthogonally each point of our 3D reconstruction to the surfaces of the CAD model. The result of the comparison is a distance map. Small projection distances are displayed in green, and tend to dark red or dark blue when the distance increases.

Figure 8.6 shows the distance map of the initial 3D reconstruction to the CAD model. The error increases strongly on the edge. Indeed, the initial reconstruction over-smooth this sharp edge. Consequently, the points have been estimated far behind the actual surface. After the edge optimization process, Fig. 8.7 shows the improved result. The edge has been accurately reconstructed and all the points on the edge are not in the acceptable green range.

As a side effect of our method, one can note that the top surface contains a certain amount of error in Fig. 8.6 that is minimized in Fig. 8.7. This is due to the alignment step of the Geomagic Qualify software. Since the initial reconstruction contains more error, it is harder to align with the actual surface. With the edge improvement, the 3D reconstruction is more accurate and can be easily aligned to the CAD model.

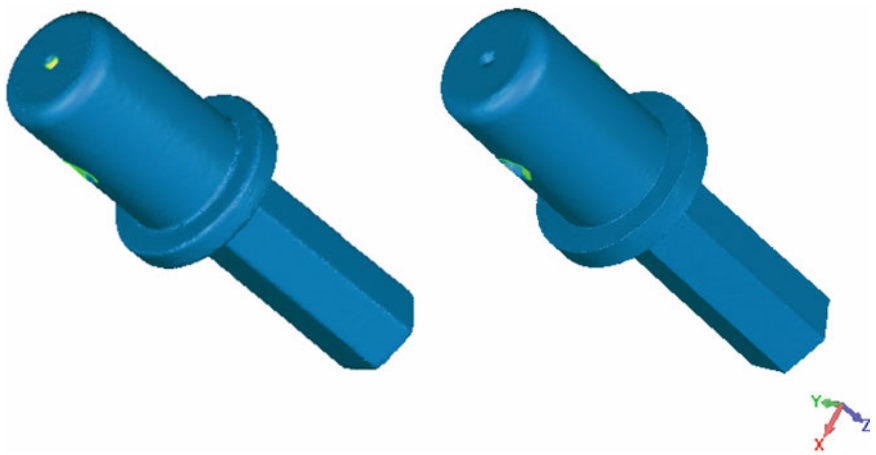

Fig. 8.3 Result of standard 3D reconstruction (*left*) and edge-optimized 3D reconstruction (*right*)

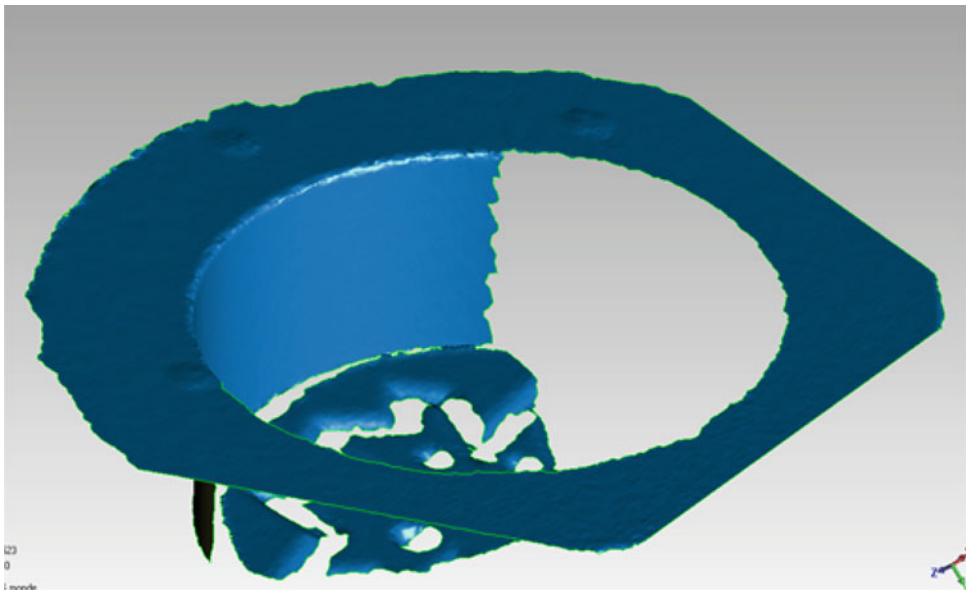

Fig. 8.4 Initial 3D reconstruction of a cylinder

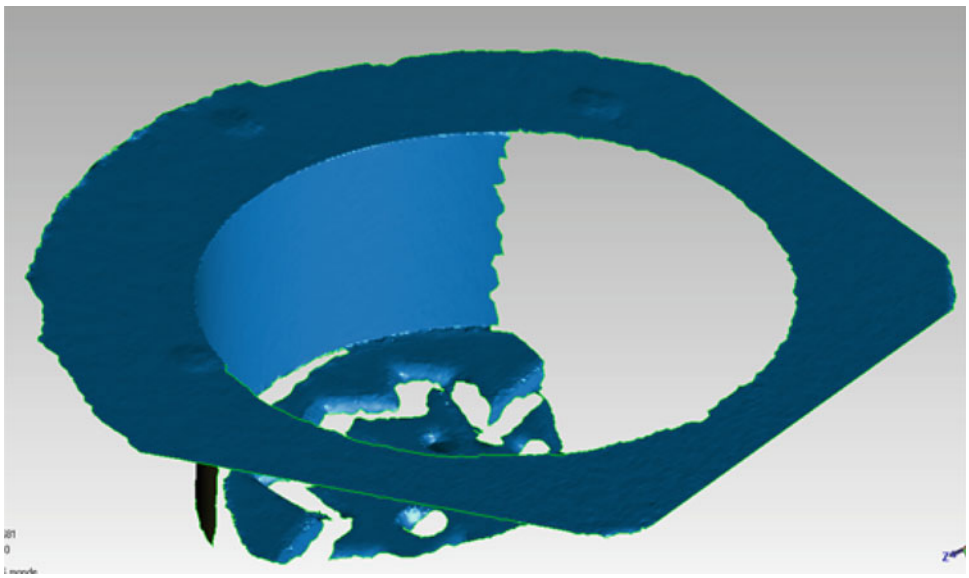

Fig. 8.5 Edge-optimized 3D reconstruction of the cylinder

It should be noted that we have shown in [6] that the standard stereo-DIC approach does not perform well with a small window size (3 ×3 or 5 ×5 pixels). Indeed, reducing the window size increases ambiguities in correlation and causes drifts in the stereo matching process, causing noise and holes in the 3D reconstruction. On the contrary, with a 11 ×11 pixels window, the noise is reduced and no holes appear, but the window becomes too large compared to the size of some small details, causing a smoothing effect (see Fig. 10 in [6]). With the new multi-step stereo-DIC method proposed in this paper, a 11 ×11 pixels window can be used while reducing the smoothing effect.

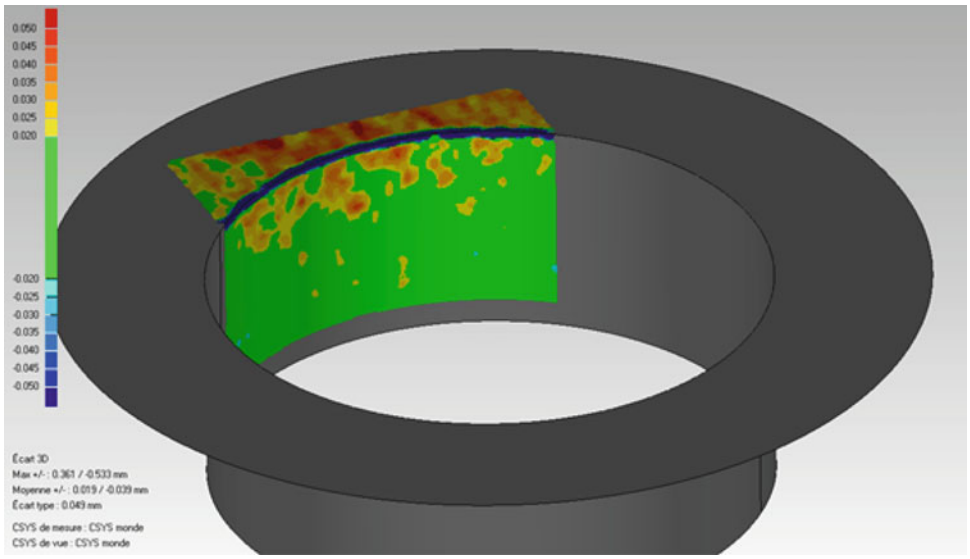

Fig. 8.6 Distance map of the initial 3D reconstruction to the CAD model

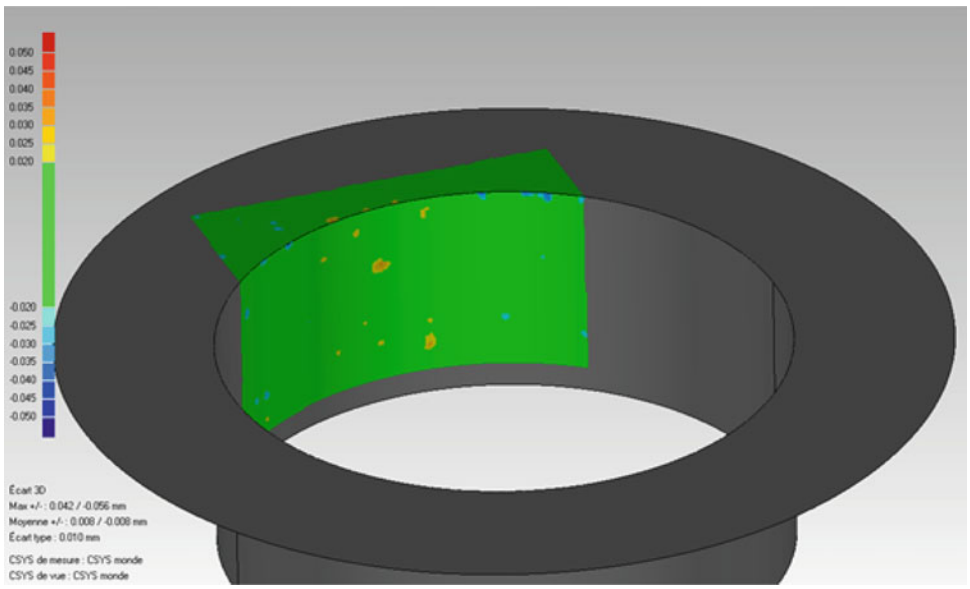

Fig. 8.7 Distance map of the edge-optimized 3D reconstruction to the CAD model

8.9 Conclusions and Future Work

We have developed a new multi-step stereo-DIC algorithm, based on a new correlation criterion and a new window transformation model, specially designed for measuring the 3D shape of machined objects with sharp edges.

With a standard stereo-DIC-based shape measurement technique, sharp edges are generally smoothed. This effect can be minimized by choosing small size subsets but this increases the stereo matching uncertainty.

With our new method, reducing the subset size to avoid smoothing sharp edges is not necessary.

Results on real machined objects show that, with our new method, an accurate 3D reconstruction of the whole object, including the sharp edges that are preserved, can be achieved.

Many methods for 3D reconstruction are iterative and multi-resolution, improving an initial low-resolution model up to a representation with the required resolution and accuracy. Future work will be devoted to such a method, including using a priori knowledge provided by the object CAD model when available, in order to make simpler and more accurate the modeling process.

References

1. Pan B, Xie H, Wang Z, Qian K, Wang Z (2008) Study on subset size selection in digital image correlation for speckle patterns. Opt Express 16(10):7037–7048
2. Sutton MA, Orteu J-J, Schreier HW (2009) Image correlation for shape, motion and deformation measurements – basic concepts, theory and applications. Springer, New York. ISBN:978-0-387-78746-6
3. Seitz SM, Curless B, Diebel J, Scharstein D, Szeliski R (2006) A comparison and evaluation of multi-view stereo reconstruction algorithms. In: 2006 IEEE computer society conference on computer vision and pattern recognition, New York, pp 519–528
4. Furukawa Y, Ponce J (2010) Accurate, dense, and robust multi-view stereopsis. IEEE Trans Pattern Anal Mach Intell 32(8):1362–1376
5. Coudrin B, Devy M, Orteu J-J, Brèthes L (2011) An innovative hand-held vision-based digitizing system for 3D modelling. Opt Lasers Eng 49 (9–10):1168–1176
6. Harvent J, Coudrin B, Brèthes L, Orteu J-J, Devy M (in press) Multi-view dense 3D modelling of untextured objects from a moving projector-cameras system. Mach Vis Appl, doi:10.1007/s00138-013-0495-z
7. Helm JD (2008) Digital image correlation for specimens with multiple growing cracks. Exp Mech 48:753–762
8. Sjödahl M (2010) Image and complex correlation near discontinuities. Strain 46(1):3–11
9. Poissant J, Barthelat F (2010) A novel "subset splitting" procedure for digital image correlation on discontinuous displacement fields. Exp Mech 50:353–364
10. Pan B, Wang Z, Lu Z (2010) Genuine full-field deformation measurement of an object with complex shape using reliability-guided digital image correlation. Opt Express 18(2):753–762
11. Attene M, Falcidieno B, Rossignac J, Spagnuolo M (2003) Edge-sharpener: recovering sharp features in triangulations of non-adaptively re-meshed surfaces. In: ACM symposium on geometry processing, Aachen

Chapter 9
Three-dimensional Underwater Measuring by Structured Light Projection

R. Rodriguez-Vera, J.E. Pinto-Preciado, Daniel D. Aguayo, and J.A. Rayas

Abstract Structured light projection is a fast and flexible optical method for measuring the 3D shape of objects. The measurement is performed within a few seconds. The result is a dense cloud of points that accurately describes the shape of the surface. The information could be used e.g. to generate CAD models from an item designed by hand, or it could be used for product quality inspection. The desired information, such as distances, angles, profiles, etc. can conveniently be extracted from the measurement results. It is also possible to calculate and visualize the deviation between a measurement and a CAD model. Most of the research work made with this technique has been carried out in a terrestrial normal environment. However sometimes it is convenient to make measurements inside hazardous or wet media, such as fogy, cloudy, raining, scattering, or underwater, or even biologic and toxic media. In this paper are presented the first steps toward obtain 3D inform shape information of a structure which is immersed inside water. Two of the most important steps are the optical setup characterization and the study optical properties of the environment. Both give us mainly conditions of illumination and restrictions on the object surface texture. In order to characterize the CCD optics, experiments related to fringe visibility varying distance to target and density and absorption of the media are carrying out. The first experimental results are presented.

Keywords Underwater measurements • Turbidity • Structured light • Fringe projection • Light absorption • 3D measuring

9.1 Introduction

Search out of lost objects located under the oceans such as shipwrecks, submarine treasures, and even oil excavations has forced to engineers and researchers to use instruments like sonar mounted on underwater vehicles and submarines [1–3]. Another difficult activity is the rescue of people which implies several limitations due to skills physical and abilities of the persons involved, this implies the use of several tools like lamps, cameras, lighters, diving wearing, reanimation equipment, helicopters, and faster aquatic motor vehicles that cover all the security norms [4]. The sub-aquatic artificial vision also has been applied in science areas such as submarine archeology to measure and recover antiques under the water. This process is really complex and delicate since any error can destroy the pieces if they are taken out of the water [5].

Looking for a solution to recover the topography and full-shape of these objects should be used the well-known non-destructive techniques, which are normally used in a terrestrial environment condition. These techniques involve several optical techniques used to measure the 3D shape of mechanical or biological samples. Some of these are structured

R. Rodriguez-Vera (✉) • J.A. Rayas
Centro de Investigaciones en Óptica, A.C., Loma del Bosque No. 115, Col. Lomas del Campestre, León, GT, Mexico
e-mail: rarove@cio.mx

J.E. Pinto-Preciado
Instituto Tecnologico de Tuxtla Gutierrez, Carretera Panamericana Km. 1080, Tuxtla Gutierrez, Chiapas
C.P. 29050, Apartado Postal: 599, Mexico

D.D. Aguayo
ITESM Campus León, Eugenio Garza Sada s/n, Col. Cerro Gordo, León, GT C.P. 37190, Mexico

H. Jin et al. (eds.), *Advancement of Optical Methods in Experimental Mechanics, Volume 3*,
Conference Proceedings of the Society for Experimental Mechanics Series,
DOI 10.1007/978-3-319-00768-7_9,

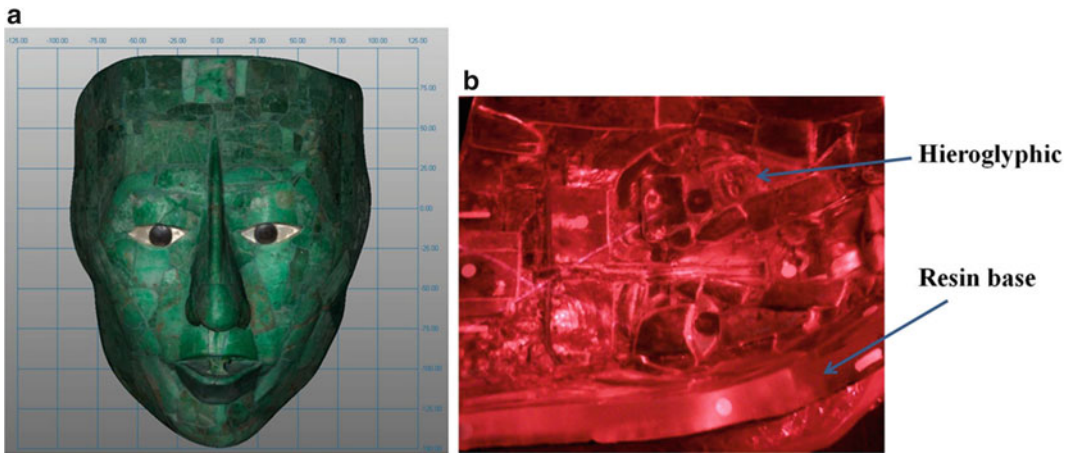

Fig. 9.1 Pakal's mask. (**a**) Front view of the digitized result. (**b**) A section of back view showing the transparent resin base and some mosaic's hieroglyphics

light projection, speckle interferometry, and holographic interferometry [6–8]. All these methods provide high accuracy and precision measurements. Among them, structured light projection is a versatile technique, which has advantages such as easy and fast perform; as well as, high accuracy, and the delivered information should be used to replicate a CAD model or reproduced it using CNC equipment [9–12].

Recently some of the authors of this paper have been involved in the use of structured light projection for digitizing and replicating archeological pieces. One of the most important projects is a trousseau replication of a Mayan King: K'inich Janaab' Pakal (or only Pakal) [13, 14]. The most important piece of Pakal's trousseau is its mask. When archaeologists discovered the Pakal's tomb in 1952 in the Mayan city of Palenque, Chiapas State of Mexico, they found the mask made bits. Each one of these bits is a mosaic made of green jade of approximately 1 mm thickness. The total of mosaics that constitutes the actual mask is 320. The mask restorers from the National Anthropology Museum of Mexico (NAMM) invested approximately 8 years in making such a restoration. The restoration technique was quite handmade. On a frame or base of transparent resin of 1 cm of thickness they were placing the mosaics one by one until having that is exhibited in a gallery of the NAMM. To digitize the back part of the mask and to detect under-relief hieroglyphics incrusted on some of the mosaics, optical distortion caused by the transparent base resin is present. Figure 9.1 shows two views of Pakal's mask. Figure 9.1a belongs to a front view from the cloud 3D points as delivered the structured light projection technique. Whereas Fig. 9.1b is a section of the real back view showing some mosaic's hieroglyphics and the resin base thickness. As a result, cloud points and resolution delivered by the structured light projection technique were affected. This is the reason from which the authors began to investigate the use of the structured light projection to digitize solids inside different depth, turbidity, and absorption media. In this paper are presented the first steps toward obtain 3D shape information of a structure which is immersed inside water. Two of the most important steps are the optics CCD camera characterization and the study of optical properties of the environment.

9.2 Theory

Measuring 3D surface under different environments than that of controlled conditions in a laboratory is complicated. This is a reason to look for alternatives methods, or modify the conventional techniques with the help of new technologies. The motivation of the present work is to perform 3D measurements on a sample that could be located inside of a participant media (such as fogy, cloudy, raining, scattering, underwater, and even a toxic or biological media), which should be difficult if a traditional contact instrument is used [15–17]. Several techniques using laser scanning, photogrammetric, computer vision, 3D modeling, and 3D reconstruction have been performed in rivers, estuaries, and oceans [18, 19]. Most of them to carry out underwater research principally for understanding geomorphology conduct, biodiversity deterioration, autonomous navigation, rescue, inspection, and experimental mechanics, among others [4, 20, 21].

Apart of considering the geometrical parameters involved in the experimental setup of the structured light projection technique, it is necessary to mention those of the medium, such as, light absorption, reflection, and refraction [22]. Since the object is located under water it has to be considered the absorption of the medium, which can be calculated by Beer–Lambert

law [23] that relates the incident light intensity with the outgoing light after the absorption by the medium, which is described by the equation:

$$\frac{I_t}{I_o} = e^{-A}. \tag{9.1}$$

Where I_o and I_t are the intensity of the incident and transmitted light, respectively. The absorbance is $A = \alpha lc$, and is related to absorption coefficient of the substance, α; the distance that light travels through the media, l; and the concentration of the medium, c; while the factor α is defined as

$$\alpha = \frac{4\pi k_\lambda}{\lambda}. \tag{9.2}$$

Where k_λ is the extinction coefficient and λ is the absorbed light wavelength. The light reflection and refraction can be explained using the concepts involved in the Snell's law [22], while the method to recover the information recorded with structured light projection technique using a phase-stepping method [24]. The phase-stepping fringe analysis using four steps requires capture four fringe patterns with phase displacement of $\pi/2$ between each of them. Then, the four fringe images are modelled as follows:

$$I_1(x,y) = a + b\cos[\phi(x,y)] \tag{9.3a}$$

$$I_2(x,y) = a + b\cos\left[\phi(x,y) + \frac{\pi}{2}\right] \tag{9.3b}$$

$$I_3(x,y) = a + b\cos[\phi(x,y) + \pi] \tag{9.3c}$$

$$I_4(x,y) = a + b\cos\left[\phi(x,y) + \frac{3\pi}{2}\right] \tag{9.3d}$$

Where $I_1(x, y)$, $I_2(x, y)$, $I_3(x, y)$ and $I_4(x, y)$ are the captured intensity fringe patterns, $a(x, y)$ represents the background, $b(x,y)$ the fringe contrast, and $\phi(x, y)$ is the optical phase. From the fringe patterns detected, the wrapped phase map $\phi(x, y)$ is calculated by:

$$\phi(x,y) = \tan^{-1}\left[\frac{I_4(x,y) - I_2(x,y)}{I_1(x,y) - I_3(x,y)}\right]. \tag{9.4}$$

This wrapped phase is worked ahead in order to have an unwrapped one [25]. Finally, mapping and scaling from the unwrapped phase, ϕ_u, the local height of the surface is obtained from next equation

$$z(x,y) = \frac{d_x}{2\pi\tan\theta}\phi_u(x,y), \tag{9.5}$$

where $z(x, y)$ represents the height of the object measured from the reference plane, d_x is the fringe pattern period, while θ is the angle between the projection and observation direction. In next section will be described the experimental test performed applying the theoretical concepts mentioned above.

9.3 Experimental Setup and Results

Figure 9.2 shows a clay object which is used as the target. It is notorious that the surface target object contains some under-relief protuberances which must be detected by the experimental system of fringe projection. The target object is placed inside a plastic container. An experimental scheme is shown in Fig. 9.3a. After filled with pure water the container which in is immersed the clay target, it was proceeded to fringe image capture through the use of a CCD camera. In the experimental

Fig. 9.2 Clay sample placed inside the plastic container

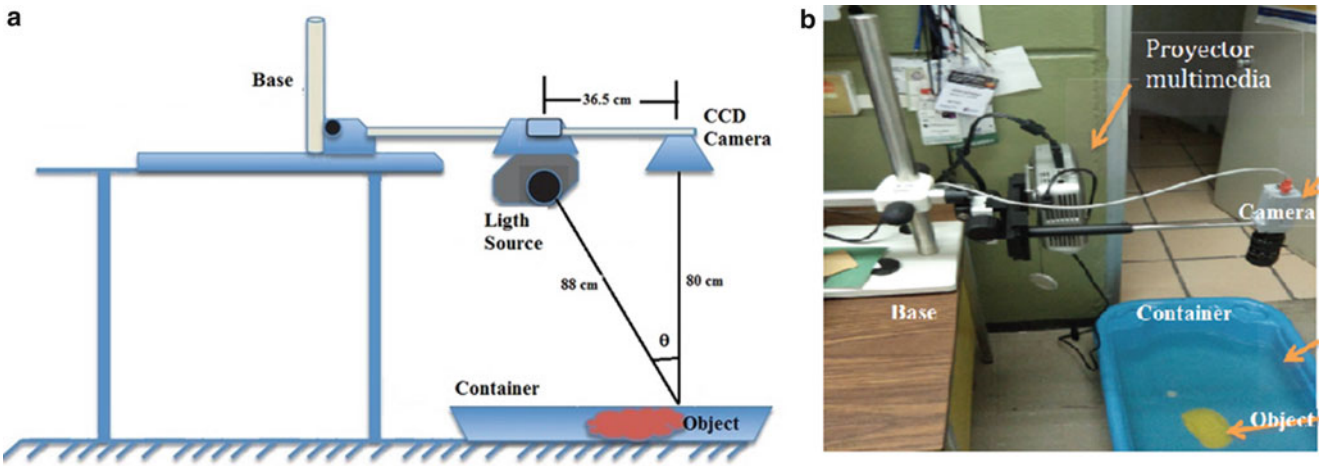

Fig. 9.3 Fringe projection setup: (**a**) Schematic and (**b**) Physical setup. Actually the container is a baby's bathtub

setup shown in Fig. 9.3b, a Dell multimedia projector and Pixelink CCD camera are employed. Focus adjust, exposition time, contrast, brightness, and projection angle were taking care in order to obtain the best measurement conditions. Once the clay object under test is placed inside the plastic container filled with 20 l of pure water, the fringe patterns generated by computer (see Eqs. 9.3a, 9.3b, 9.3c, and 9.3d) are projected over the interface air-water and then transmitted to the surface clay object; the four fringe images are recorded.

Four different tests were performed in different scattering conditions, by using a concentration of water and milk. First test, Test1, was recorded without any forced scattering in the water. In successive tests were carried out adding 10 ml of milk each time to produce simulated scattering conditions inside milky media. The first test served as a base to compare with the results of the other ones; that means, adding 10, 20, and 30 ml, respectively. The images recorded are digitally processed to obtain the wrapped phase maps and the unwrapped phase map respectively, to finally get and mapping the measured 3D topography. Figure 9.4a–d show images for the projected fringes over the object surface and Fig. 9.5a–d present the 3D topography reconstructed after each test for the corresponding images in Fig. 9.4.

From the images of Fig. 9.4a–d it is possible to construct the profiles shown in Fig. 9.6. That profiles where obtained taken a same object region for the different scattering and turbidity conditions of the media. Then, these profiles on Fig. 9.6 display the visibility behaviour of the projected fringes for the media cited conditions. This way, the red colour profile corresponds

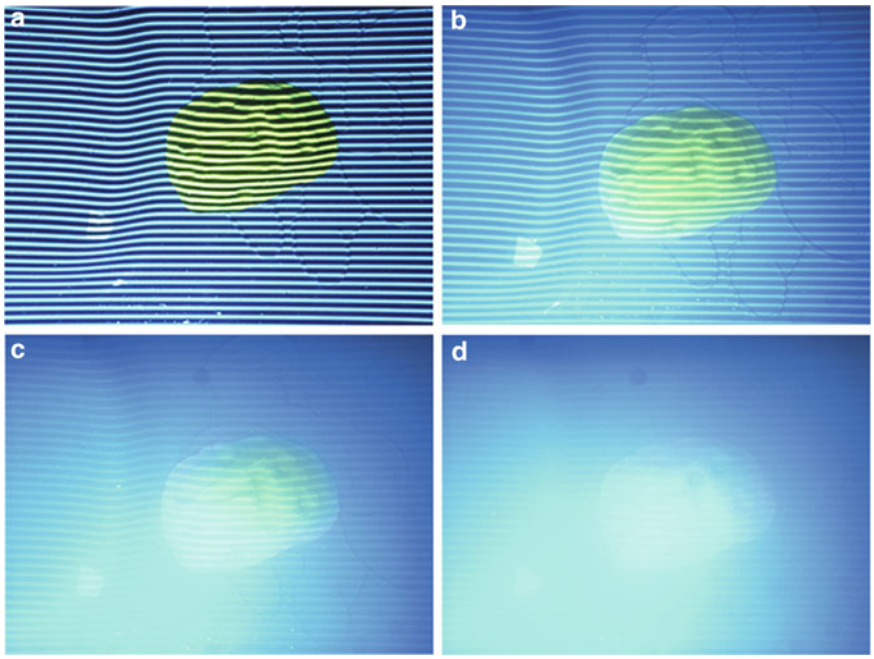

Fig. 9.4 Fringe patterns projected (**a**–**d**) over the clay surface object during the four tests using 0, 10, 20 and 30 ml of milk respectively to produce the scattering and turbidity in the water

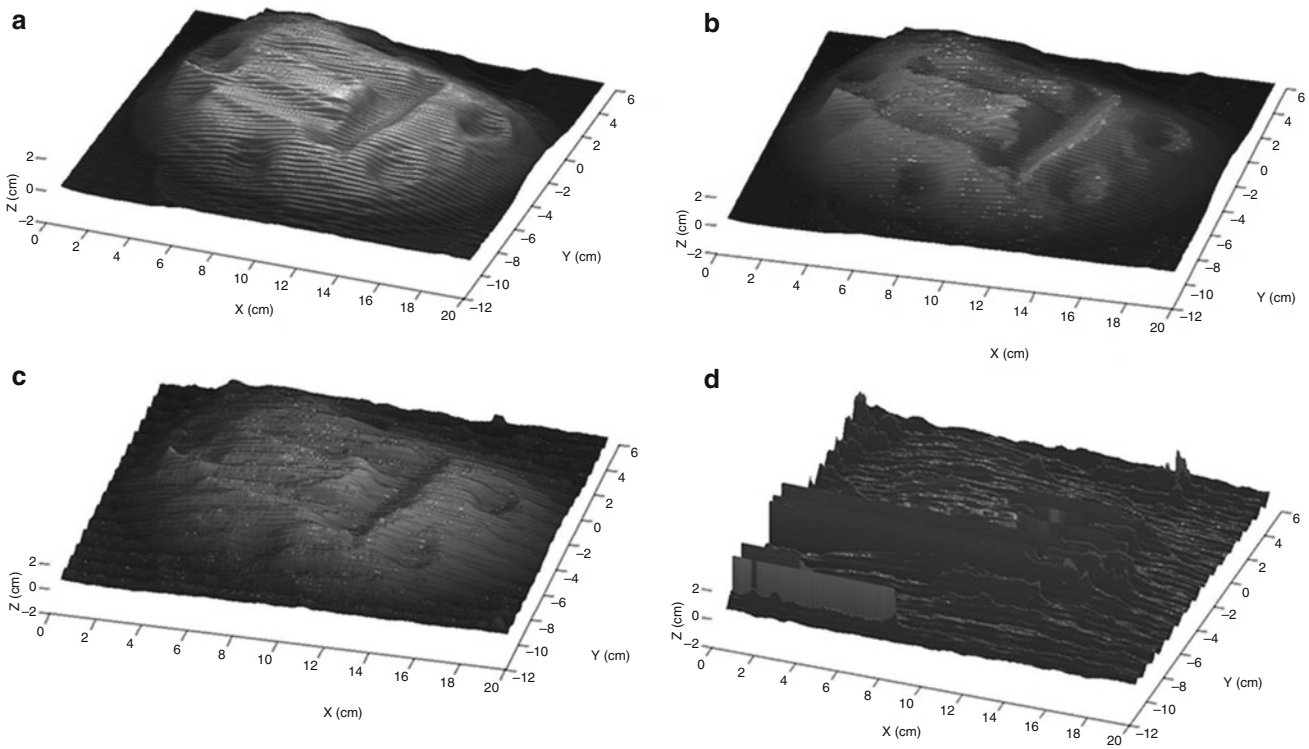

Fig. 9.5 Images (**a**–**d**) shows the object topography reconstructed from to the corresponding images shown in the Fig. 9.4

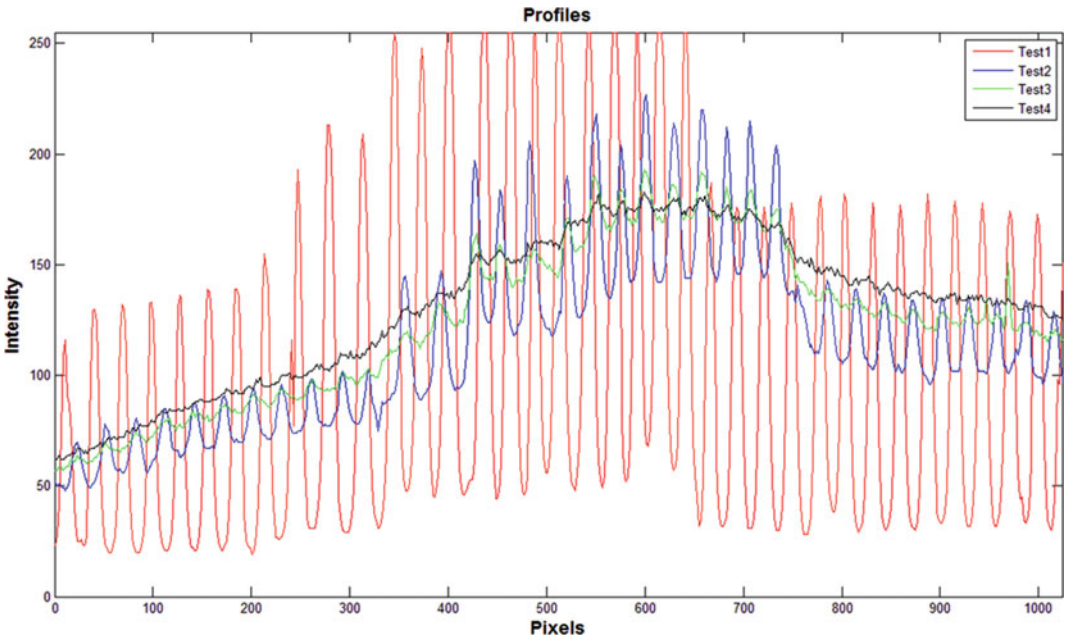

Fig. 9.6 Profiles obtained from the four tests with the conditions of no turbidity, and the turbidity caused by 10, 20, and 30 ml of the milk added to water

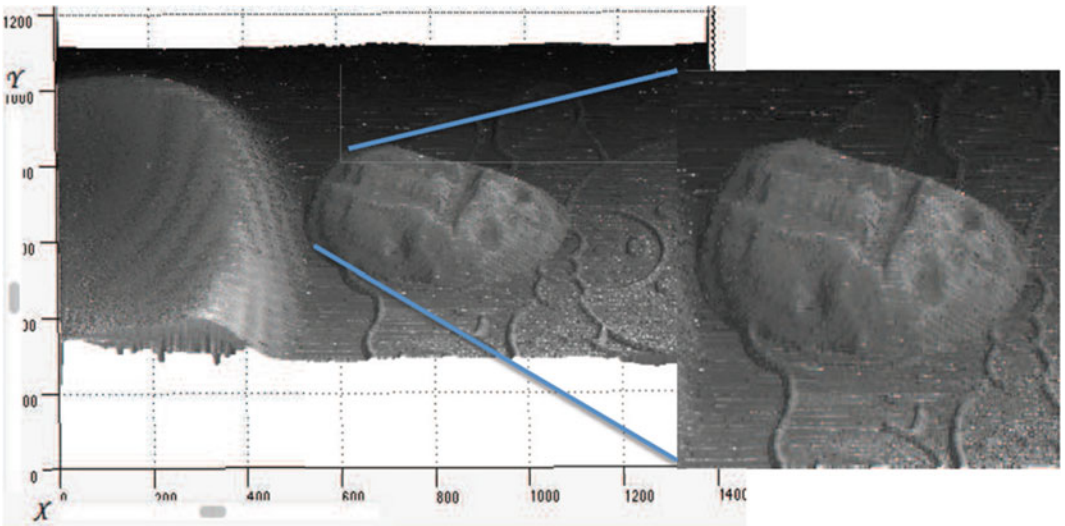

Fig. 9.7 Clay object topography zoomed image

to the medium with pure water. The blue plot is for the test performed with 10 ml milky water. It is noticed that the profile maintains a similar one to the first test, but presents a displacement and a minor intensity value. While the other tests (20 and 30 ml) were is clearly visible that the turbidity and scattering affects the intensity value. This is reflected in the 3D topography reconstruction.

Finally, the image shown in the Fig. 9.7 presents a zoom view where the detail of the technique can be appreciated since is possible to observe the 3D reconstruction of some marks in relief grabbed on the bottom of the plastic container.

9.4 Conclusions

The use of non contact measurement techniques are widely known nowadays they are used in controlled environment. However, the present work represents an alternative that could be helpful to recover data of objects located in a different media than the terrestrial. The experimental results reported here were obtained for an object in a scattered media using the non contact fringe projection technique. The reconstruction of the 3D surface of the object is possible, but certainly, the resolution of the system is affected by the absorption provoked by milk added to the water. The profiles obtained from the images of the projected fringes over the object shown the effects of the scattering and turbidity in the reconstruction of the 3D surfaces. The experimental setup must be improved and modified to perform several tests with different materials, shape and different media to demonstrate the potentiality of the technique for future application in several technology and science areas.

Acknowledgements Authors would like to thank the partial technical support given by Martin Olmos-Lopez, technician at CIO. Also, one of us RRV, appreciate the useful help at the very beginning of this project by Christian I. Gutierrez-Macias, student of Electronic Engineering Faculty, Universidad LaSalle, Leon.

References

1. Bingham B, Foley B, Singh H, Camilli R, Delaporta K, Eustice R, Mallios A, Mindell D, Roman C, Sakellariou D (2010) Robotic tools for deep water archaeology: surveying an ancient shipwreck with an autonomous underwater vehicle. J Field Robot 27(6):702–717
2. Williams DP (2012) AUV-enabled adaptive underwater surveying for optimal data collection. Intel Serv Robot 5(1):33–54
3. El-Fakdi A, Carreras M (2013) Two-step gradient-based reinforcement learning for underwater robotics behavior learning. Robot Auton Syst 61(3):271–282
4. Chill RG (1981) Lifesaving and marine safety. New Century United States, Piscataway, Lifesavingassociation
5. Haralick RM, Shapiro LG (1992) Computer and robot vision, vol II. Addison-Wesley, Reading
6. Gasvik KJ (2002) Optical metrology, 3rd edn. Wiley, Chichester
7. Rastogi PK (2001) Digital speckle pattern interferometry and related techniques. Wiley, Chichester
8. Kreis T (1996) Holographic and speckle interferometry. Akademie Verlag, Berlin
9. Martɲnez A, Rayas JA, Flores JM, Rodriguez-Vera R, Aguayo DD (2005) Técnicas ópticas para el contorneo de superficies tridimensionales. Revista Mexicana de Física 51(4):431–436 (In Spanish)
10. Múnera N, Lora GJ, Garcia-Sucerquia J (2011) Técnicas De Proyección De Franjas Y De Escaneo Láser Para La Reconstrucción 3D: Generación de Archivos CAM de Piezas dentales. Revista Colombiana de Física 43(3):909–912 (In Spanish)
11. Lanman D, Taubin G (2009) Build your own 3D scanner: 3D photograhy for beginners. In: SIGGRAPH Asia'09: ACM SIGGRAPH 2009 courses, New Orleans, pp. 1–87
12. Cheng J, Chung R, Lam EY, Fung KS, Wang F, Leung WH (2005) Three-dimensional reconstruction of wafer solder bumps using binary pattern projection. In: Price JR, Meriaudeau F (eds) Machine vsion applications in industrial inspection XIII. Proceedings of SPIE, Boston, 5679:212–222
13. Rodriguez Vera R (2010) Reproducción de piezas arqueológicas mediante proyección de luz estructurada (Reproduction of archaeological pieces by structured light projection), Gaceta CyT México, CONACYT, 3(36) (In Spanish). Electronic paper can be readied linking to http://www.gacetacyt.org//index.php?option=com_content&task=view&id=1092&Itemid=154
14. Rodriguez Vera R (2011) Reproducción del ajuar del rey maya Pakal mediante proyección de luz estructurada (Trousseau reproduction of the Mayan King Pakal by structured light projection). Diseres 4(18):24–25 (In Spanish). Electronic paper can be readied linking to http://diseres.com.mx/index.php?option=com_content&view=article&id=166:suicidio&catid=35:ejemplares&Itemid=29
15. Narasimhan SG, Nayar SK (2002) Vision and the atmosphere. Int J Comput Vis 48(3):233–254
16. Cerezo E, Perez F, Pueyo X, Seron FJ, Sillion FX (2005) A survey on participating media rendering techniques. Visual Comput 21(5):303–328
17. Jaffe JS, Moore KD, McLean J, Strand MR (2001) Underwater optical imaging: status and prospects. Oceanography 14(3):64–75
18. Sanchez F, Serrano A, Gomez Ballesteros M (2009) Photogrammetric quantitative study of habitat and benthic communities of deep Cantabrian Sea hard grounds. Cont Shelf Res 29:1174–1188
19. Dong N, Jia Z, Shao J, Li Z, Liu F, Zhao J, Peng P-Y (2011) Adaptive object detection and visibility improvement in foggy image. J Multimedia 6(1):14–21
20. Haile MA, Ifju PG (2012) Application of elastic image registration and refraction correction for non-contact underwater strain measurement. Strain 48(2):136–142
21. Arora H, Hooper PA, Dear JP (2012) The effects of air and underwater blast on composite sandwich panels and tubular laminate structures. Exp Mech 52(1):59–81
22. Malacara D (1989) Óptica básica (Basic optics). Fondo de Cultura Económica, México (In Spanish)
23. Ingle JDJ, Crouch SR (1998) Spectrochemical analysis. Prentice-Hall, Englewood Cliffs
24. Malacara D, Servin M, Malacara Z (2005) Interferogram analysis for optical shop testing, 2nd edn. Taylor & Francis, Boca Raton
25. Ghiglia DC, Pritt MD (1998) Two- dimensional phase unwrapping. Wiley, New York

Chapter 10
Implementation and Evaluation of Single Frame Recording Techniques for Holographic Measurements of the Tympanic Membrane In-Vivo

I. Dobrev, C. Furlong, J.J. Rosowski, J.T. Cheng, and E.J. Harrington

Abstract We are developing an advanced computer-controlled digital holographic system (DHS) with the ability to measure both shape and acoustically induced deformations of the tympanic membrane of several species, including humans. The DHS has been deployed in the clinic and is currently being optimized for in-vivo measurements.

The clinical environment presents numerous challenges such as disturbances due to patient's heartbeat, breathing, patient's tremor as well as environmentally induced mechanical vibrations of several orders of magnitude larger (1–10 Hz, 0.1–100 μm) than the nanometer measuring resolution of the system. Biological samples and the tympanic membrane in particular represent numerous challenges for optical systems including non-uniform light scattering, random internal and external reflections as well as low reflectivity (<10 %) and high transparency (>50 %). Design and optimization of the system for clinical use includes the development and implementation of various acquisition strategies and algorithms for minimization of measurement disturbances in clinical conditions as well as in-vivo measurements.

In this work we show implementation of several single frame acquisition algorithms based on both lens and lensless optical holographic configurations. We also evaluate their performance in terms of acquisition speed, external mechanical disturbance tolerance, appropriate depth of field, as well as tolerance to non-uniform light scattering typical in biological samples.

Keywords Digital holography • In-vivo measurements • Light scattering • Otology • Single frame holography

10.1 Introduction

Understanding the human hearing process and associated disorders depends largely on the quantification of the mechanical properties of the human eardrum, also known as tympanic membrane (TM), and its role in transforming the sound waves from the outer-ear into vibrations of the middle-ear. However, methods to examine the physical health as well as to study

I. Dobrev (✉) • E.J. Harrington
Center for Holographic Studies and Laser micro-mechaTronics – CHSLT, Worcester, USA

Department of Mechanical Engineering, Worcester Polytechnic Institute, Worcester, MA 01609, USA
e-mail: ivo_d@wpi.edu

C. Furlong
Center for Holographic Studies and Laser micro-mechaTronics – CHSLT, Worcester, USA

Department of Mechanical Engineering, Worcester Polytechnic Institute, Worcester, MA 01609, USA

Eaton-Peabody Laboratory, Massachusetts Eye and Ear Infirmary, Boston, MA 02114, USA

Department of Otology and Laryngology, Harvard Medical School, Boston, MA, USA

J.J. Rosowski • J.T. Cheng
Eaton-Peabody Laboratory, Massachusetts Eye and Ear Infirmary, Boston, MA 02114, USA

Department of Otology and Laryngology, Harvard Medical School, Boston, MA, USA

H. Jin et al. (eds.), *Advancement of Optical Methods in Experimental Mechanics, Volume 3*,
Conference Proceedings of the Society for Experimental Mechanics Series,
DOI 10.1007/978-3-319-00768-7_10,

specific pathological conditions of the ear are performed by qualitative visual observations by otoscope-based procedures. These procedures provide limited quantitative data to physicians who in many cases have to make decisions based on partial information and subjective judgments.

We are developing full-field-of-view digital holographic methods to quantitatively measure the steady state and transient acousto-mechanical responses of the human TM in-vivo to help in the diagnosis and treatment of common hearing losses. To achieve such measurements one has to overcome important technological challenges imposed by the dimensions of the TM, its confined location, and the disturbances produced by the patient's heartbeat, breathing, as well as environmentally induced vibrations. In addition, the amplitude of the motions induced by acoustic excitation of the TM (i.e. <1 μm) is several orders of magnitude smaller than those produced by external disturbances (i.e. >500 μm). To overcome these challenges we are developing holographic methods to be able to perform measurements at high speeds (i.e., $>25{,}000$ fps), high temporal resolution (<10 μs) and in full-field-of-view with nanometer scale resolutions to be able to quantify the acousto-mechanical steady state and transient responses of the TM in-vivo.

In this paper we present our work on the development of several single frame phase sampling methods as well as appropriate acquisition techniques and their application for high speed measurement of the steady state and transient response of the human TM in-vivo.

10.2 Methods

We are developing a digital holographic system (DHS) as a tool for the quantification of the acoustically induced response of the TM. The system has already been deployed in the clinic for in-vitro testing and is currently being optimized for in-vivo measurements in-vitro [1–4] and we are currently optimizing its acquisition and phase sampling methods for in-vivo measurements [5]. In order to reduce the effect of external disturbances in in-vivo conditions such as those produced by the patient's heartbeat, breathing, and environmentally induced vibrations, the overall acquisition time of the TM's response is to be minimized (<1 ms), as indicated by previous research [6]. In this paper, we outline our work on the development and implementation of phase measurement algorithms with high temporal resolution (<10 μ) to record and quantify the rapidly (up to 20 kHz) developing full-field-of-view deformation patterns on the surface of the TM in-vivo in order to quantify the acousto-mechanical response of the TM.

10.2.1 Overview of the Digital Holographic System (DHS)

A digital holographic system (DHS), as shown in Fig. 10.1, provides control system architecture capable of single frame acquisition and synchronizing between the excitation, illumination and acquisition during a steady state or transient measurements. Based on physiological restrictions on the geometry of system for otology applications, the measurement and acoustic excitation systems are physically combined within a compact otoscope head module [7, 8], as shown in Fig. 10.1, where its stability and orientation are maintained by a mechatronic otoscope positioner.

10.2.2 Acquisition Techniques

We present two single frame acquisition techniques, pulsed double exposure and continuous high speed acquisition, and their use with various single frame phase sampling methods for high-speed acquisition and measurement. The continuous high-speed acquisition method allows for capture of a reference state of the object and its comparison to a series of deformed states recorded with a high speed camera (i.e., $>25{,}000$ fps) after the application of a pulsed acoustic excitation. This allows for detailed measurement of the transient acousto-mechanical response of the TM. The synchronization of the camera exposure, acoustic excitation and laser illumination is governed by the control system through an acousto optic modulator (AOM) in sync with the object excitation, as shown in the timing diagram of Fig. 10.2.

Since no acoustic excitation is provided during the reference state, we apply a temporal phase sampling of the reference state in combination with single frame evaluation of the deformed state [9]. This is achieved by dynamically adjusting the frame rate of the high-speed camera in synchronization with the acoustic excitation, laser illumination and PZT driven temporal phase shifter, as shown in the timing diagram of Fig. 10.2. To minimize the sampling time of the reference state, we

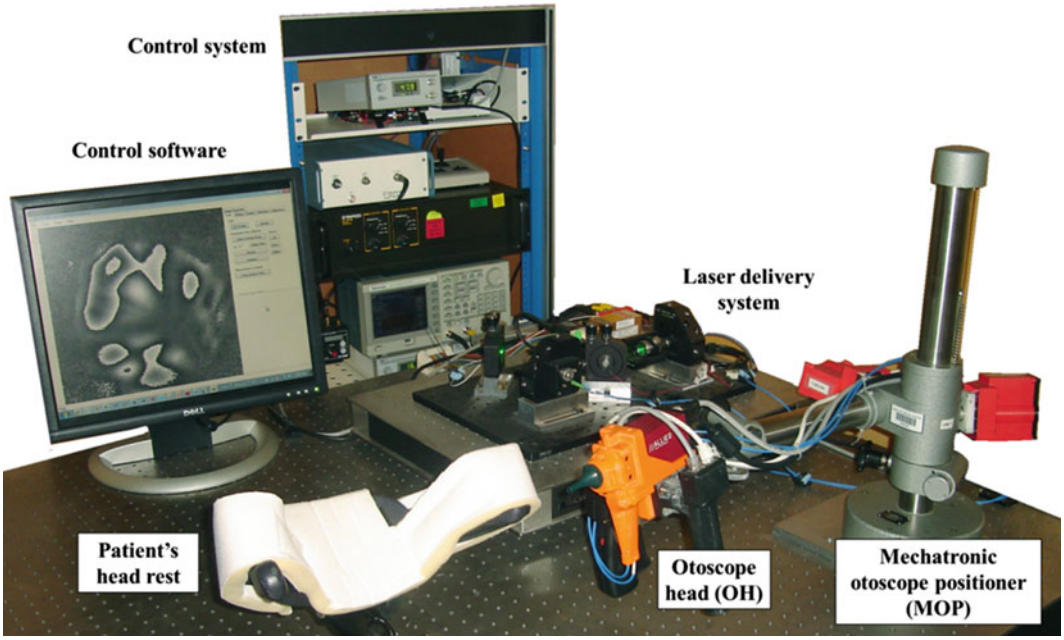

Fig. 10.1 Full system overview

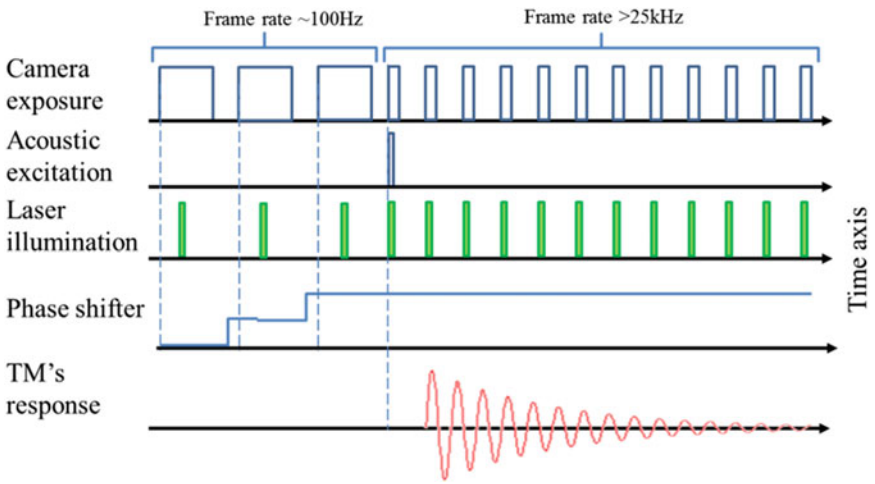

Fig. 10.2 Timing diagram of a continuous high speed acquisition method

sample only two reference images, which can be achieved by either discrete phase stepping or preferably by a continuous phase shifting [10] to minimize any acquisition delay associated with the response time of the phase shifter.

The modified version of the continuous high speed acquisition, pulsed double exposure acquisition method, can be applied with a regular video-rate (10–100 Hz) camera by capturing only two frames in a quick succession ($<$1 ms) per acoustic excitation pulse [11]. One frame is captured at a reference state and one at a deformed state of the TM with a controlled delay between the application of the pulsed acoustic excitation and the acquisition of the deformed state. By controlling the separation between any pair of double exposure and by repeatedly exciting the TM, the method allows for the sequential capture of the full duration of the acousto-mechanical response of the TM.

10.2.3 Phase Sampling Methods

10.2.3.1 Digital Lensless Fourier Holography

The DHS utilizes lensless digital holography for measurements of the displacement of the acoustically induced motion of the TM. The digital holographic reconstruction algorithm is based on the approximation of the wave front propagation described by the Fresnel-Kirchhoff transform integral [12]. Accounting for the digitization parameters of the CCD and using the Fresnel approximation the reconstruction algorithm can be written in the following discrete form using the computationally optimized fast Fourier transform (FFT):

$$\Gamma(\xi,\eta) = z(k,l)FFT^{-1}(h(k,l)R(k,l)w(k,l)), \tag{10.1}$$

where k and l are the pixels on the CCD plane (hologram plane), $h(k,l)$ is the hologram function in CCD coordinate system, $R(k,l)$ is the reconstruction reference wave, and $w(k,l)$ is a chirp function used for reconstruction of the complex wavefront The reconstructed light field $\Gamma(\xi,\eta)$ is a complex function that contains both intensity (modulation) as well as phase information about the object. The chirp function $w(k,l)$ can be expressed as:

$$w(k,l) = exp\left[-i\frac{\pi}{\lambda d}(k^2\Delta x^2 + l^2\Delta y^2)\right], \tag{10.2}$$

where Δx and Δy are the pixels size in the CCD plane, λ is the laser wavelength, and d is the reconstruction distance. The coefficient $z(k,l)$ in Eq. 10.1 adds a constant phase change to the reconstructed hologram $\Gamma(\xi,\eta)$ and is often omitted from computation of the phase change due to deformation of the object.

At the time of recording, the hologram contains information about all three components – the DC component and the conjugate twin images, however only one of the twin images is of interest. To extract the desired component, we apply the spatial phase shifting method [13] that allows for separation of these components in the recording stage and filtration of the desired component in reconstruction process.

10.2.3.2 Local Phase Sampling Method

The local phase sampling method [14] allows for measurement of the phase information of the deformed object without the need of augmentation of the setup (i.e. introduction additional of spatial frequency components) in the recording stage. The method also allows for a hybrid approach for phase sampling of the deformed state of the TM, by combining the information from a single frame of the deformed state with several phase shifted frames of the reference state. The method is based on relation between the phase change between two interferograms, ϕ, and the correlation of their intensities, ρ, defined as follows [15]:

$$\rho(\phi) = \frac{1 + r^2 + 2r\cos\phi}{(1+r)^2}, \tag{10.3}$$

where r is the beam ration between the reference and object beam that create the interferometric pattern. In typical acoustical loading conditions the deformation of the surface of the TM is small (<1 μm) with a fringe density ~ $2\frac{ln}{mm}$ [16], thus the resulting spatial variation of the phase change, ϕ, is small relative to the initial random phase difference of the reference and object beams. Based on that, we can assume that ϕ is similar within a spatial neighborhood of measurement points and based on that we estimate the correlation between the reference and deformed state by correlating their intensities within a small kernel (i.e. 3 × 3 or 5×5 pixels). This allows for approximation, within a constant C, of the phase ϕ modulated by a cosine function [14]:

$$q_1 = Ccos(\phi), \tag{10.4}$$

$$q_2 = Ccos(\phi + \pi/2) = Csin(\phi), \tag{10.5}$$

where q_1 and q_2 are the Pearson's coefficient of correlation for finite discrete sets applied to the illumination data within the kernel of the two reference and one deformed interferogram, respectively. The phase shift $\pi/2$ between the two reference states can be generated by temporal phase shifting. Equations 10.4 and 10.5 allow for evaluation of the phase ϕ without ambiguities within a 2π range.

10.3 Results

10.3.1 Representative Results of Local Phase Sampling Method

To facilitate the development of our high-speed holographic methods for quantification of the transient response of a human TM in-vivo, we investigate the acousto-mechanical responses of artificial membranes subjected to transient acoustic stimuli and acquired through a continuous high speed (>85,000 fps) acquisition, as shown in Fig. 10.3. The sound source is a 50 μs pulse wave produced by a speaker mounted 10 mm to the left of the membrane at an angle of 45° relative to the membrane surface normal.

For this application we used a local phase sampling method with a combination of temporal phase sampling of the reference state and single frame sampling phase sampling of the deformed states. This allows for quantification of the every acquired instance of the transient response of the sample, as shown in Fig. 10.4. By analyzing the consecutive deformation states of the sample, the estimated in-plane surface wave speed is 29 m/s.

10.3.2 Representative Results of Single Frame Lensless Digital Holography

After verification of the performance of DHS system for capture of the transient response of artificial samples, we tested the measurement capabilities of our system for the quantification of the transient response of a human TM, as shown in Fig. 10.5. The temporal resolution shown is 20 μs and allows for sequential capture of the response of the tympanic membrane comparable to continuous high-speed digital holography measurements at 50,000 fps.

The single frame captured instances of the transient response of the TM are quantified, as shown in Fig. 10.6. Analysis of temporal variation in the displacement pattern indicates that this human TM specimen has an averaged time-constant of 5 ms, which has a spatial dependency.

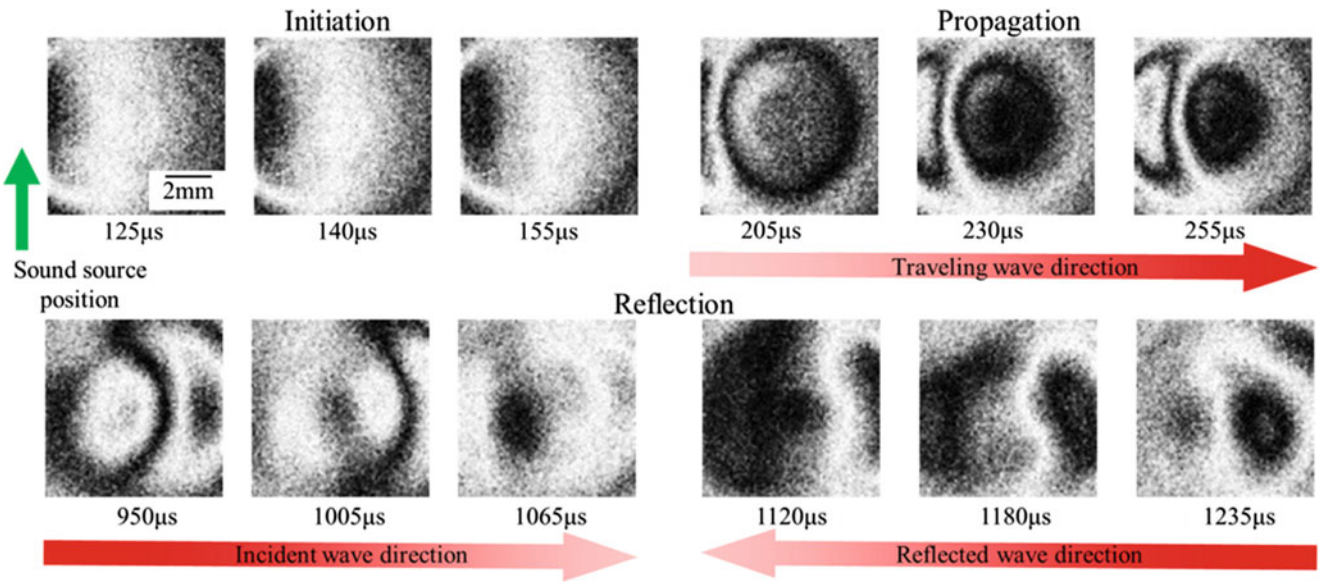

Fig. 10.3 Representative results of continuous high-speed digital holography measurements of the response of a 12 mm diameter latex membrane. Measurements have duration of 1.2 ms. The sample is excited by an impulse acoustic stimulus positioned on the right of the membrane that triggers surface waves that initiate, develop, and reflect across the sample. Acquisition speed is 87,500 fps and exposure time is 10 μs

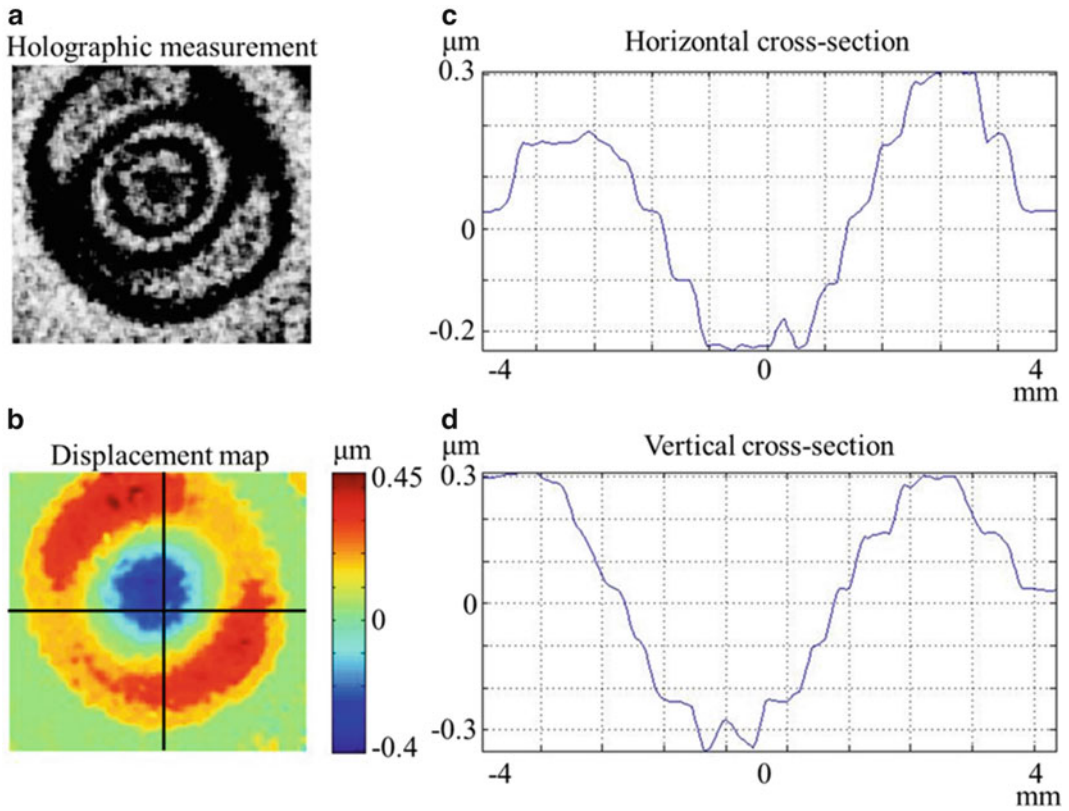

Fig. 10.4 Representative results of the quantification of a membrane deformation obtained by local phase sampling method: (**a**) modulation map of the holographic measurement; (**b**) displacement map; (**c**) and (**d**) *horizontal* and *vertical* cross-section of the displacement map. The deformation pattern corresponds to the response of the membrane 745 µs after the beginning of the transient acoustic excitation indicating a response of 0.85 µm amplitude p-p

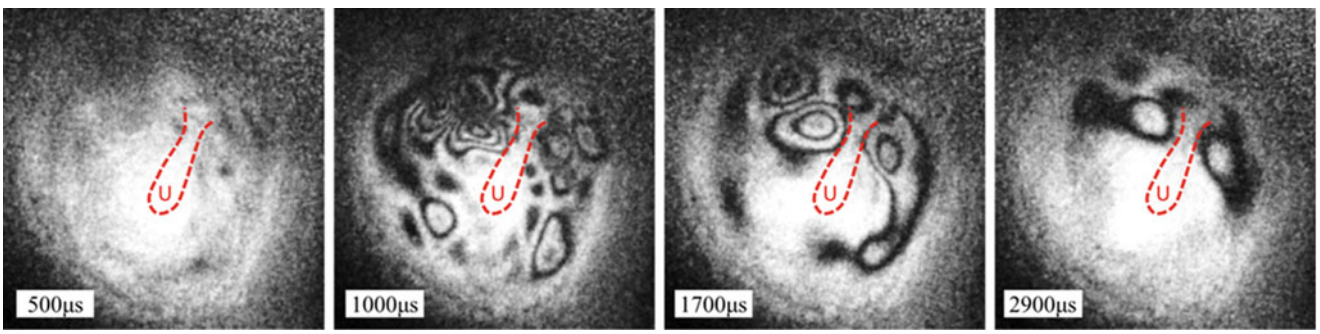

Fig. 10.5 Representative lensless digital holography measurements of the mechanical response of a human TM due to transient acoustic stimulus. The time stamp shown is referenced with respect to the beginning of the acoustic stimulus. The handle, or manubrium, of the malleus is outlined. The umbo at the end of the handle near the center of the TM is labeled with a "U"

10.4 Conclusions and Future Work

The DHS provides new and versatile means to quantitatively characterize the dynamics of the TM and can further aid in the treatment of conductive hearing disorders. Future work will be focused on development of methods to analyze the significance of the transient response of the TM, including the measurement of its mechanical and dynamic properties such as damping and response time in-vivo.

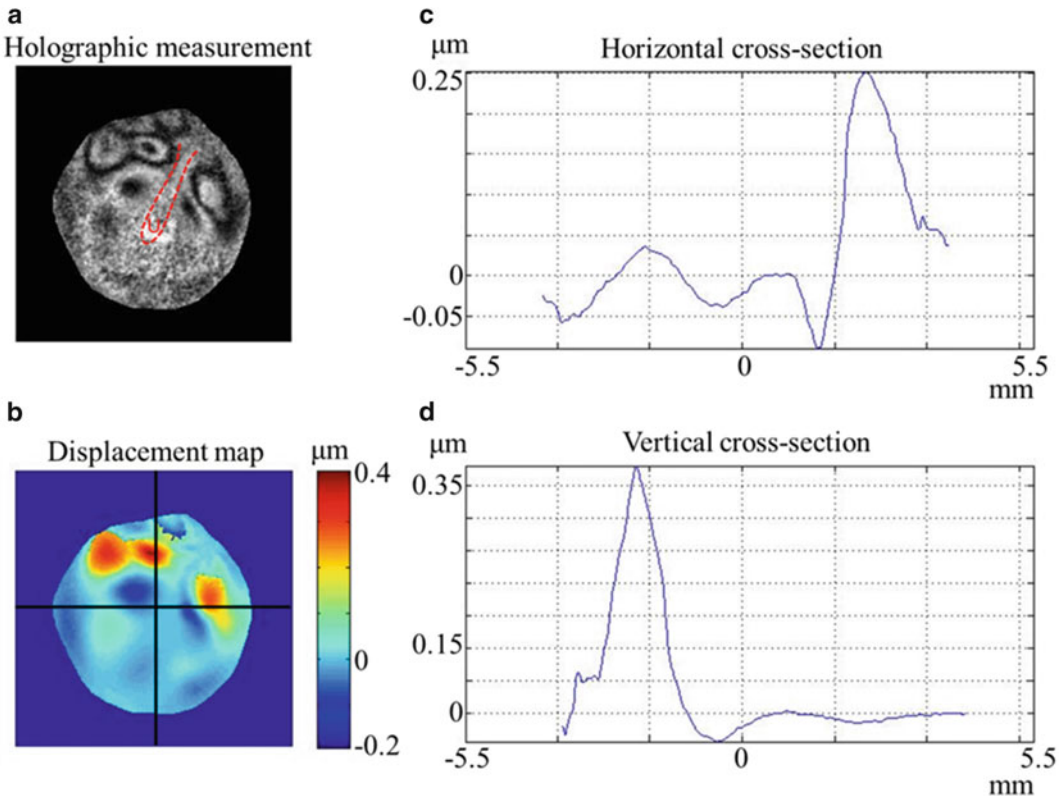

Fig. 10.6 Representative of the quantification of the TM's deformation obtained by lensless digital holography and spatial phase sampling methods: (**a**) modulation map of the holographic measurement; (**b**) displacement map; (**c**) and (**d**) are *horizontal* and *vertical* cross-section of the displacement map. The deformation pattern corresponds to the transient response of the TM 2.5 ms after the beginning of the transient acoustic excitation indicating a response of 0.57 μm amplitude p-p

Acknowledgements This work has been funded by the National Institute on Deafness and Other Communication Disorders (NIDCD), the National Institute of Health (NIH), the Massachusetts Eye and Ear Infirmary (MEEI), and the Mittal Fund. The authors also gratefully acknowledge the support of the NanoEngineering, Science, and Technology (NEST) program at the Worcester Polytechnic Institute, Mechanical Engineering Department.

References

1. Hernández-Montes M, Furlong C, Rosowski JJ, Hulli N, Harrington E, Cheng JT, Ravicz ME, Santoyo FM (2009) Optoelectronic holographic otoscope for measurement of nanodisplacements in tympanic membranes. J Biomed Opt 14(3):034023. doi:10.1117/1.3153898
2. Rosowski JJ, Cheng JT, Ravicz ME, Furlong C (2009) Computer-assisted time-averaged holograms of the motion of the surface of the mammalian tympanic membrane with sound stimuli of 0.4–25 kHz. Hear Res 253(1–2):83–96
3. Rosowski JJ, Dobrev I, Khaleghi M, Lu W, Cheng JT, Harrington E, Furlong C (2013) Measurements of three-dimensional shape and sound-induced motion of the chinchilla tympanic membrane. Hear Res 301:44–52. doi:10.1016/j.heares.2012.11.022
4. Khaleghi M, Lu W, Dobrev I, Cheng JT, Furlong C, Rosowski JJ (2013) Digital holographic measurements of shape and 3D sound-induced displacements of tympanic membrane. Opt Eng 52(10) (in-press)
5. Dobrev I, Furlong C, Cheng JT, Rosowski JJ (2013) Optimization of a digital holographic otoscope system for in-vivo measurements. Opt Las Eng (in preparation)
6. Løkberg OJ, Høgmoen K, Holje OM (1979) Vibration measurement on the human tympanic membrane in vivo. Appl Opt 18:763–765
7. Dobrev I, Harrington EJ, Cheng JT, Furlong C, Rosowski JJ (2013) Digital holographic otoscope for measurements of the human tympanic membrane in-vivo. In: Proceedings of SEM, Costa Mesa, 3:39–45, June 2012
8. Furlong C, Dobrev I, Harrington EJ, Hefti P, Khaleghi M (2012) Miniaturization as a key factor to the development and application of advanced metrology systems. Proc SPIE 84130T-1:12. doi:10.1117/12.981668
9. Kao CC, Yeh GB, Lee SS, Lee CK, Yang CS, Wu KC (2002) Phase-shifting algorithms for electronic speckle pattern interferometry. App Opt 41(1):46–54
10. Dubois A (2001) Phase-map measurements by interferometry with sinusoidal phase modulation and four integrating buckets. JOSA A 18(8):1972–1979

11. Cernadas D, Trillo C, Doval AF, López JC, Dorrío BV, Fernández JL, Pérez-Amor M (2002) Non-destructive testing with surface acoustic waves using double-pulse TV holography. Meas Sci Tech 13(4):438–444
12. Schnars U, Jüptner WPO (2002) Digital recording and numerical reconstruction of holograms. Meas Sci Tech 13:R85. doi:10.1088/0957-0233/13/9/201
13. Takeda M, Ina H, Kobayashi S (1982) Fourier-transform method of fringe-pattern analysis for computer-based topography and interferometry. JOSA 72:156–160
14. Georgas PJ, Schajer GS (2012) Modulo-2pi phase determination from individual ESPI images. Opt Las Eng 50(8):1030–1035
15. Jones R, Wykes C (1983) Holographic and speckle interferometry: a discussion of the theory, practice and application of the techniques. Cambridge University Press, New York
16. Furlong C, Rosowski JJ, Hulli N, Ravicz ME (2009) Preliminary analyses of tympanic-membrane motion from holographic measurements. Strain 45(3):301–309

Chapter 11
A Mechano-regulation Model to Optimize Design of Minimally Invasive Percutaneous Fixation Devices for Treatment of Fractured Vertebrae

A. Boccaccio, D.J. Kelly, and C. Pappalettere

Abstract Minimally invasive percutaneous fixation techniques play a role of crucial relevance in the clinical practice. In spite of their consolidated use, little is reported in the literature to provide a mechanobiological explanation on how design of fixation devices can affect the healing process within fractured vertebrae.

The aim of the study is to develop a multi-scale mechano-regulation model capable of predicting how the patterns of tissue differentiation within a vertebral fracture change in the presence or in the absence of fixation devices and how the dimensions of the device, and the materials it is made from, can affect the outcome of the healing process.

To this purpose, a multi-scale mechano-regulation model is developed that combines a macro-scale model representing the spinal segment L3-L4-L5 including the fractured body of the L4 vertebra, and a micro-scale model of a fractured portion of cancellous bone. The macro-scale model includes also a minimally invasive percutaneous fixation device. The above mentioned model allows us to investigate how spatial and temporal patterns of tissue differentiation in the fracture gap change for different dimensions of the fixation device components and for different materials (Ti-6Al-4V alloy and Co-Cr alloy). Furthermore, the model provides information on the stress state in the fixation device and hence allows the risk of failure of the device itself to be estimated.

The mechanical properties of the forming tissue change as the healing process progresses. In order to validate the mechano-regulation model, displacement fields will be measured with moiré and holography and compared with numerical computations.

The model predicts that fixation devices significantly shorten healing times. Increasing values of the rod diameter D and decreasing values of its radius of curvature R lead to shorter durations of the healing period. Manufacturing the rods in Cobalt-Chrome alloy is predicted to reduce slightly the healing period by providing greater mechanical stability within the fracture callus.

Keywords Mechanobiology • Vertebral fracture • Tissue differentiation • Minimally invasive percutaneous fixation • Moiré

11.1 Introduction

Many vertebral compression fractures can be safely treated in a conservative way [1, 2]. Numerous studies have demonstrated the successful application of conservative treatments for some vertebral fractures, for example bed rest followed by external orthesis, exercise in extension etc. [1, 3–8]. However, the treatment should continue for at least 3/4 months during which the collaboration of the patient is of crucial importance. The problems related to an excessively long bed rest period are numerous and it can be very difficult to quantify them [9]. On the other hand, treating a vertebral fracture (that could be submitted to a conservative treatment) with a traditional open surgery may be an overtreatment. In this

A. Boccaccio (✉) • C. Pappalettere
Dipartimento di Meccanica, Matematica e Management, Politecnico di Bari, Viale Japigia 182, Bari 70126, Italy
e-mail: a.boccaccio@poliba.it; c.pappalettere@poliba.it

D.J. Kelly
Centre for Bioengineering, Department of Mechanical Engineering, Trinity College Dublin, Dublin2, Ireland
e-mail: kellyd9@tcd.ie

H. Jin et al. (eds.), *Advancement of Optical Methods in Experimental Mechanics, Volume 3*,
Conference Proceedings of the Society for Experimental Mechanics Series,
DOI 10.1007/978-3-319-00768-7_11,

context, a good compromise may be the percutaneous minimally invasive fixation surgery. Such a technique is useful every time a conservative treatment cannot be applied and a posterior open arthrodesis may represent an overtreatment.

Different numerical models have been proposed which relate the tissue differentiation process occurring during healing of long and flat bones and osteochondral defects to the mechanical environment within the mesenchymal tissue [10–19]. By using the mechanobiological model of Claes and Heigele [12], Shefelbine et al. [20] demonstrated that the mechano-regulation principles regulating the healing process of diaphyseal fractures hold in case of fracture repair within trabecular bone.

In a previous study by the present authors [21] a multi-scale mechano-regulation model was developed simulating the healing process occurring within the trabecular bone of a wedge vertebral fracture. In the present study we expanded this model to include the effect of Minimally Invasive Percutaneous Fixation Devices (MIPFD). The objectives of the study are to evaluate: (i) how the spatial and temporal patterns of tissue differentiation change in presence or in absence of a MIPFD; (ii) how these patterns change for different geometrical parameters of MIPFD or for different materials with which such devices can be fabricated and (iii) the von Mises stress distribution within the MIPFD towards the end of the healing phase.

11.2 Materials and Methods

Two different finite element models of the spinal segment L3-L4-L5 were created (Fig. 11.1). The first one includes the fractured body of the L4 vertebra (Fig. 11.1a), the second one, in addition to the fractured vertebra, includes the model of a minimally invasive fixation device (Fig. 11.1b). The finite element code ABAQUS was utilized. CT scan data have been utilized for the generation of the finite element mesh of the entire L3 and L5 vertebrae and the posterior processes of the L4 vertebra. A simplified model of the body of the L4 vertebra as well as the intervertebral discs located above and below was developed in CAD environment.

The body of the fractured L4 includes the cortical shell with a thickness of 0.5 mm, the cancellous bone and the fracture gap (Fig. 11.1e–h). The cancellous and the cortical bone have been modelled as biphasic poroelastic materials possessing transversely isotropic elastic properties. Further details regarding the values of the mechanical properties utilized for the cancellous and cortical bone as well as the user defined Fortran subroutine utilized to model the heterogeneous distribution of cancellous bone material properties are reported in [21–23].

The minimally invasive percutaneous fixation devices include two principal components: the screws and the rods. Different dimensions for each component have been modelled in this study. All the simulations presented in the manuscript

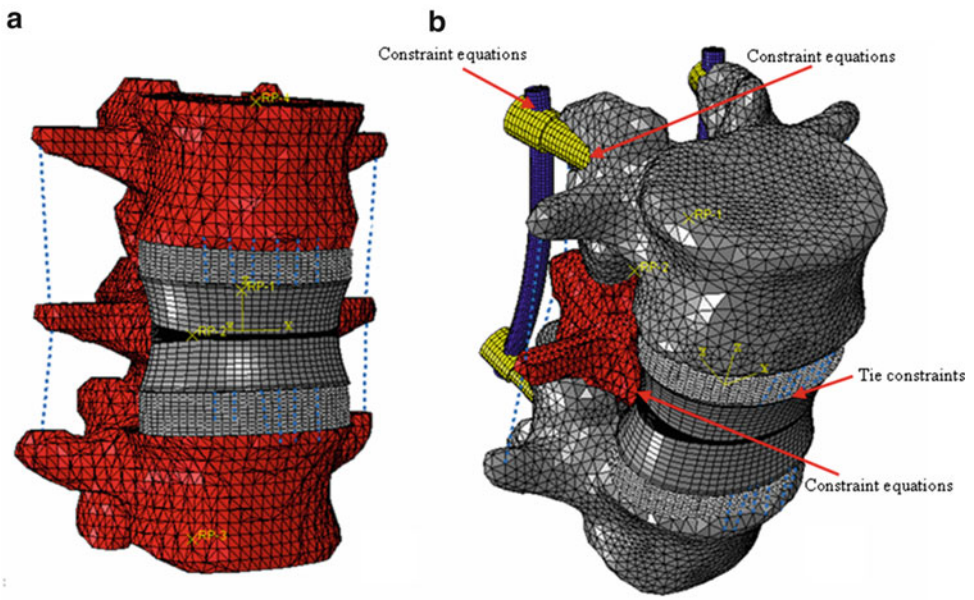

Fig. 11.1 Finite element model of the spinal segment with the fractured vertebra L4 in the presence (**b**) or in the absence (**a**) of MIPFD

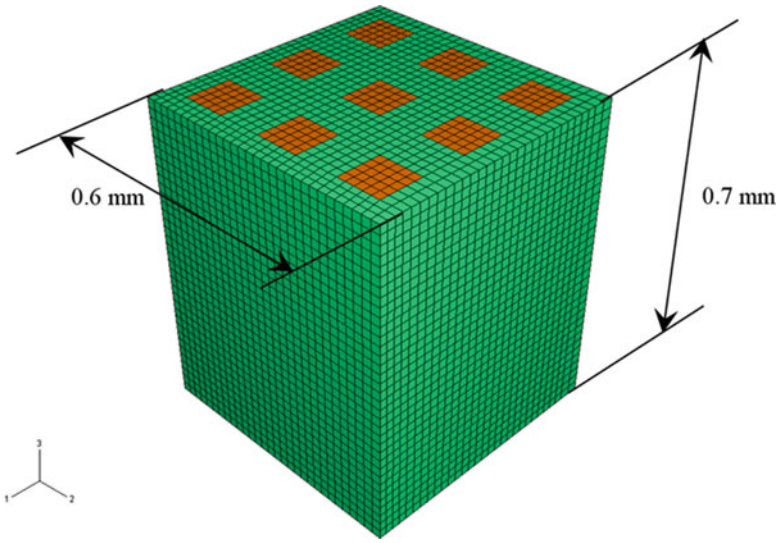

Fig. 11.2 Micro-scale model of the portion of fractured trabecular bone

refer to the case, screw diameter $D_S = 8.5$ mm. The typical value of rod diameter D for devices available on the market is $D = 5.5$ mm. The proposed mechano-regulation model has been utilized to predict how the patterns of tissue differentiation change if the diameter D increases or decreases by 40 %. Another important geometrical parameter for the rod is the radius of curvature R. The radius of curvature R is typically $R = 90$ mm. As in the case of the rod diameter, three different radii of curvature have been considered in the present study: $R = 90$ mm, $R = 126$ mm and $R = 54$ mm. The material of which the screws are typically realized is the Ti-6Al-4V alloy while the rods are realized both, in Ti-6Al-4V alloy or, very recently, in Cobalt Chrome alloy. In the case of MIPFD implanted, 18 cycles of analyses have been performed, 9 for the case of rods in Ti-6Al-4V alloy and 9 for the case of rods in Cobalt Chrome alloy. In the case of MIPFD absent, just one cycle of analysis has been run.

The micro-scale model of the trabecular bone is the same as that utilized by Shefelbine et al. [20] (Fig. 11.2). Further details about the micro-scale finite element model of trabecular bone are reported in [21, 23].

A multi-scale approach was adopted [21]. The equations describing tissue differentiation were implemented into an algorithm, a graphical summary of which is depicted in Fig. 11.3. The time period investigated corresponds to the first 100 days after the fracture event. The macro-scale model of the spinal segment with and without MIPFD was utilized to determine the elastic and poroelastic boundary conditions acting on eight different micro-scale models which were hypothesized to represent different regions in the fractured cancellous bone located in the neighbourhood of eight points. The micro-scale model, in turn, served to predict the local patterns of the tissues differentiating during the fracture repair process. Further details regarding the algorithm are reported [21, 23].

11.3 Results

In either the presence or the absence of MIPFD, the bone repair process is predicted to follow a similar pathway with significant temporal differences. Bone initially forms at the fractured trabecular ends, replacing a cartilaginous template through the process of endochondral bone formation. Then, bone resorption leads to rapid reorganization of the repair tissue thus favoring the formation of bony bridges linking the trabeculae spicules (Fig. 11.4).

The duration of the healing period -defined as the number of days necessary to have 30 % of the available space occupied by remodeled bony tissue-, decreases significantly when a fixation device is implanted. Furthermore, shorter healing periods are predicted for increasing values of the rod diameter D (for a fixed radius of curvature R) and for decreasing radii of curvature R (for a fixed rod diameter D). Finally, the greater stiffness of the Cobalt Chrome rods, allows slightly faster (than those predicted for the Ti-6Al-4V alloy rods) healing processes to occur.

The maximum value of the von Mises stresses within the device and computed at the end of the healing process was predicted to be localized in correspondence of the point where the rod is attached to the screw. The predicted magnitude of stress is sensitive to both the rod diameter D and the radius of curvature R. For increasing rod diameters D (for a fixed radius of curvature R) and radii of curvature R (for a fixed rod diameter D), smaller values of the maximum von Mises stress are

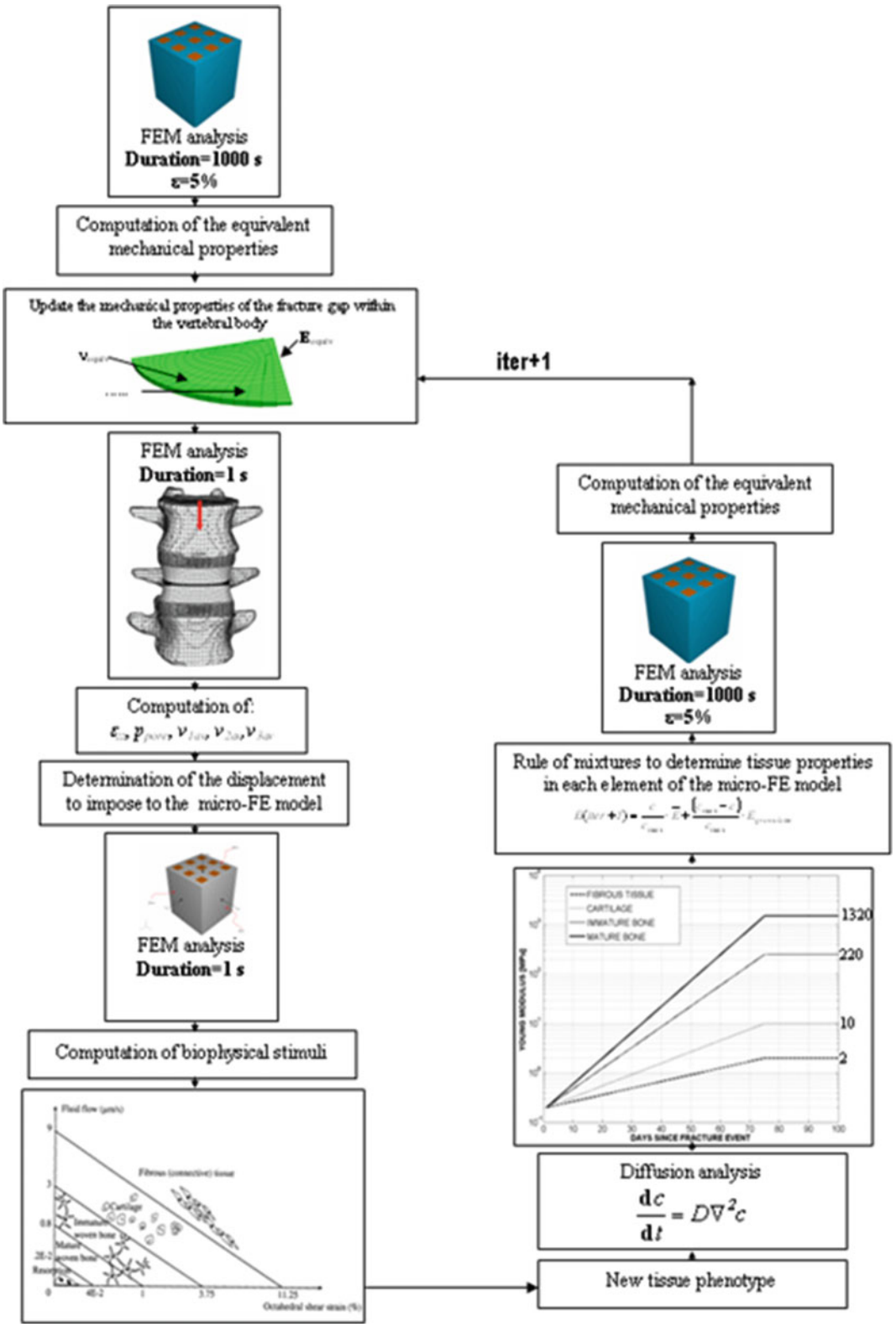

Fig. 11.3 Schematic of the algorithm (implemented in the FORTRAN environment) utilized to predict the fracture repair process within the vertebral fracture

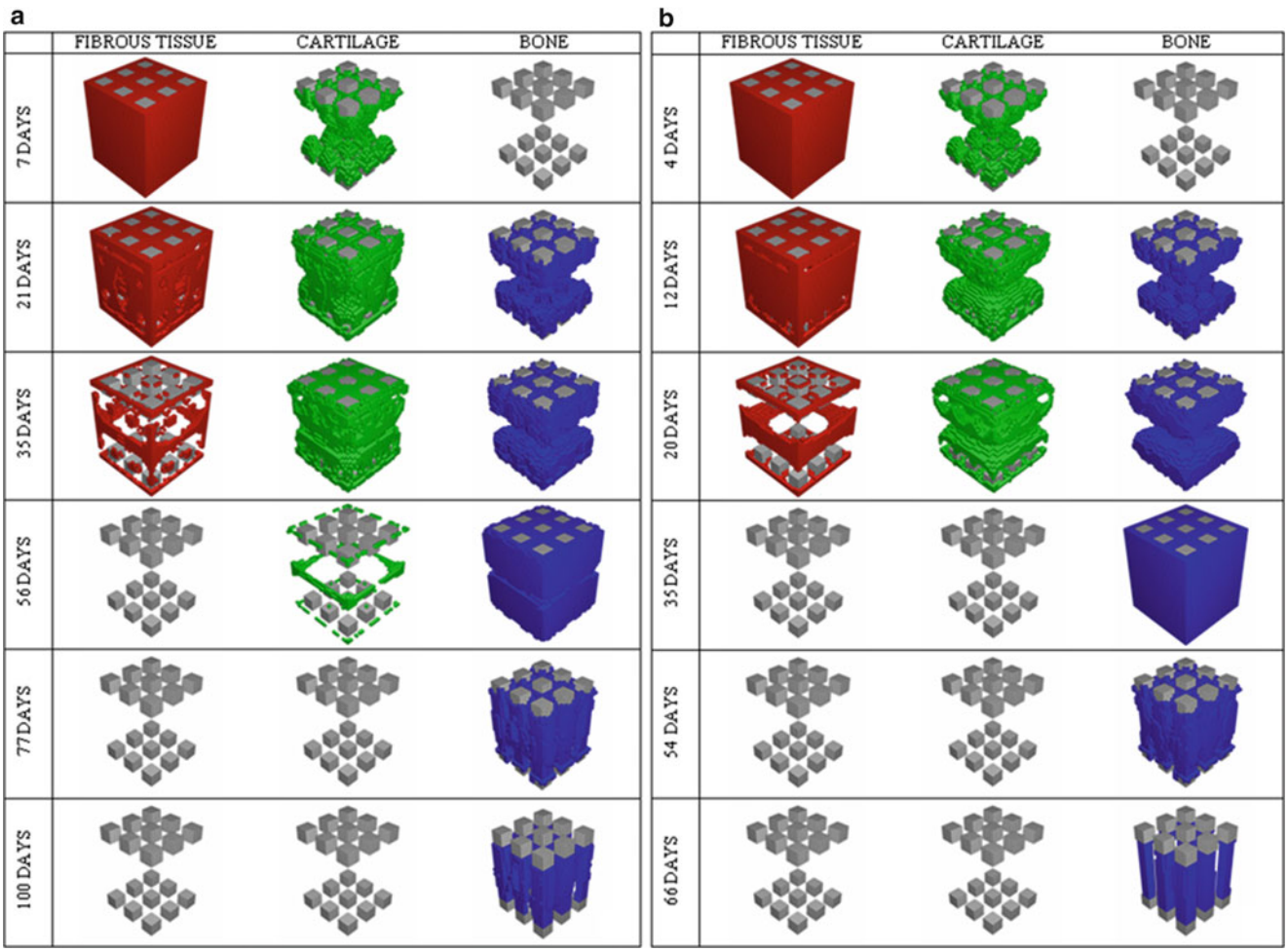

Fig. 11.4 Patterns of tissue differentiation predicted by the mechano-regulation model in the presence (**b**) and in the absence (**a**) of MIPFD

calculated. The predicted maximum von Mises stress is more sensitive to changes in the material with which the rods are realized. In the case of the Cobalt Chrome alloy, the model computes values of the maximum von Mises stress that are about 1.5 times higher than those predicted in the case of the Ti-6Al-4V alloy.

11.4 Conclusions

In this paper, by using a mechano-regulation model, the process of tissue differentiation and bone remodelling in a vertebral fracture treated with a fixation device have been simulated. Analyses revealed that the dimension of the screw diameter has negligible effects on the predicted patterns of tissue differentiation. More interesting appeared the effects of the rod diameter D as well as of its radius of curvature R. Increasing values of D and decreasing values of R lead to predictions of shorter durations of the healing period. However, for decreasing values of R, if D remains constant, higher von Mises stress peaks are predicted. Finally, the analyses carried out revealed that realizing the rods in Cobalt-Chrome alloy allows slightly shorter healing periods to be obtained (with respect to the case of rods in Ti-6al-4V) as well as heavier loads to be applied on the spinal segment.

The mechanical properties of the forming tissue change as the healing process progresses. In order to validate the mechano-regulation model, displacement fields will be measured with moiré and holography and compared with numerical computations. Alternatively, the mechanical properties of the tissues forming during the healing process could be measured via nano-indentation and in that case the approach adopted in [24] will be followed.

The computational model presented in this paper seems to be a promising tool able to predict how the choice of the different components of the fixation device and the modalities with which the device is implanted on the fractured spinal segment can affect the outcome of the healing process.

References

1. Mumford J, Weinstein JN, Spratt KF et al (1993) Thoracolumbar burst fractures. The clinical efficacy and outcome of nonoperative management. Spine 18:955–970
2. Shen WJ, Shen YS (1999) Nonsurgical treatment of three-column thoracolumbar junction burst fractures without neurologic deficit. Spine 24:412–415
3. Shen WJ, Liu TJ, Shen YS (2001) Nonoperative treatment versus posterior fixation for thoracolumbar junction burst fractures without neurologic deficit. Spine 26:1038–1045
4. Wood K, Buttermann G, Mehbod A et al (2003) Operative compared with nonoperative treatment of a thoracolumbar burst fracture without neurological deficit. A prospective, randomized study. J Bone Joint Surg Am 85-A:773–781
5. Wang ST, Ma HL, Liu CL et al (2006) Is fusion necessary for surgically treated burst fractures of the thoracolumbar and lumbar spine? A prospective, randomized study. Spine 31:2646–2452
6. Seybold EA, Sweeney CA, Fredrickson BE et al (1999) Functional outcome of low lumbar burst fractures. A multicenter review of operative and nonoperative treatment of L3-L5. Spine 24:2154–2161
7. Been HD, Poolman RW, Ubags LH (2004) Clinical outcome and radiographic results after surgical treatment of post-traumatic thoracolumbar kyphosis following simple type A fractures. Eur Spine J 13:101–107
8. Chow GH, Nelson BJ, Gebhard JS et al (1996) Functional outcome of thoracolumbar burst fractures managed with hyperextension casting or bracing and early mobilization. Spine 21:2170–2175
9. Pape HC, Giannoudis P, Krettek C (2002) The timing of fracture treatment in polytrauma patients: relevance of damage control orthopedic surgery. Am J Surg 183:622–629
10. Lacroix D, Prendergast PJ (2002) A mechano-regulation model for tissue differentiation during fracture healing: analysis of gap size and loading. J Biomech 35:1163–1171
11. Carter DR, Blenman PR, Beaupré GS (1988) Correlations between mechanical stress history and tissue differentiation in initial fracture healing. J Orthop Res 6:736–748
12. Claes LE, Heigele CA (1999) Magnitudes of local stress and strain along bony surfaces predict the course and type of fracture healing. J Biomech 32:255–266
13. Isaksson H, Wilson W, van Donkellaar CC et al (2006) Comparison of biophysical stimuli for mechano-regulation of tissue differentiation during fracture healing. J Biomech 39:1507–1516
14. Gòmez-Benito MJ, Garcìa-Aznar JM, Kuiper JH et al (2005) Influence of fracture gap size on the pattern of long bone healing: a computational study. J Theor Biol 235:105–119
15. Kelly DJ, Prendergast PJ (2005) Mechano-regulation of stem cell differentiation and tissue regeneration in osteochondral defects. J Biomech 38:1413–1422
16. Boccaccio A, Pappalettere C, Kelly DJ (2007) The influence of expansion rates on mandibular distraction osteogenesis: a computational analysis. Ann Biomed Eng 35:1940–1960
17. Boccaccio A, Prendergast PJ, Pappalettere C et al (2008) Tissue differentiation and bone regeneration in an osteotomized mandible: a computational analysis of the latency period. Med Biol Eng Comput 46:283–298
18. Boccaccio A, Lamberti L, Pappalettere C (2008) Effects of aging on the latency period in mandibular distraction osteogenesis: a computational mechano-biological analysis. J Mech Med Biol 8:203–225
19. Boccaccio A, Ballini A, Pappalettere C et al (2011) Finite element method (FEM), mechanobiology and biomimetic scaffolds in bone tissue engineering. Int J Biol Sci 7:112–132
20. Shefelbine SJ, Augat P, Claes L et al (2005) Trabecular bone fracture healing simulation with finite element analysis and fuzzy logic. J Biomech 38:2440–2450
21. Boccaccio A, Kelly DJ, Pappalettere C (2011) A mechano-regulation model of fracture repair in vertebral bodies. J Orthop Res 29:433–443
22. Boccaccio A, Vena P, Gastaldi D et al (2008) Finite element analysis in cancellous bone failure in the vertebral body of healthy and osteoporotic subjects. Proc Inst Mech Eng H 222:1023–1036
23. Boccaccio A, Kelly DJ, Pappalettere C (2012) A model of tissue differentiation and bone remodelling in fractured vertebrae treated with minimally invasive percutaneous fixation. Med Biol Eng Comput 50:947–959
24. Boccaccio A, Frassanito MC, Lamberti L, Brunelli R, Maulucci G, Monaci M, Papi M, Pappalettere C, Parasassi T, Sylla L, Urini F, De Spirito M (2012) Nanoscale characterization of the biomechanical hardening of bovine zona pellucida. J R Soc Interface 9:2871–2882

Chapter 12
The Optical Methods of Caustics and Photoelasticity: A Comparison

E.E. Gdoutos

Abstract The optical methods of photoelasticity and caustics have extensively been used for the determination of stress intensity factors (SIFs) in static and dynamic crack problems. Both methods present their potentialities and limitations. In crack problems the state of stress in the neighborhood of the crack tip changes from plane strain near the tip to plane stress away from the tip through an intermediate three-dimensional region. This affects the determination of SIFs using experimental methods. In the present work the methods of photoelasticity and caustics applied to crack problems are briefly presented and compared regarding the following criteria: the optical set-up, the efficiency in the determination of stress intensity factors, the effect of crack tip radius, the effect of plate boundaries, the location of the crack tip and the changing state of stress near the crack tip.

Keywords Photoelasticity • Caustics • Cracks • Stress intensity factors • Plane-stress • -Strain

12.1 Introduction

Photoelasticity is a well established optical method for the solution of two- and three-dimensional problems of stress analysis [1–3]. The method is based on the phenomenon of optical birefringence under load of transparent materials and the wave nature of light. It appeared at the turn of the twentieth century and reached full maturity in the second half of the century. The method has been applied to the determination of stress intensity factors in crack problems by a number of researchers [4–7].

The method of caustics is a relatively new method for the study of the state of affairs in problems of stress singularities. The method is based on geometrical optics and uses the phenomenon of optical birefringence when applied to transparent materials. It first appeared in 1965 and has been applied for the solution of crack problems under a variety of loading conditions and geometrical configurations [8–13].

In the following we will first give the relations that govern the intensity of light rays that emerge of the front or rear faces of a transparent specimen when it is illuminated by a light beam. We will then present the stress optical relations for light rays traversing the specimen or reflected from its rear and emerging from its front face. The basic principles of the methods of photoelasticity and caustics will be briefly presented. The state of stress in the vicinity of the crack tip as it changes from plane strain at the tip to plane stress at a critical distance from the tip through an intermediate three-dimensional region will be presented. A comparison of both methods will take place with regard to the following criteria: the optical set-up, the efficiency in the determination of stress intensity factors, the effect of crack tip radius, the effect of plate boundaries, the location of the crack tip and the changing state of stress near the crack tip.

E.E. Gdoutos (✉)
Office of Theoretical and Applied Mechanics of the Academy of Athens School of Engineering,
Democritus University of Thrace, GR-671 00 Xanthi, Greece
e-mail: egdoutos@civil.duth.gr

H. Jin et al. (eds.), *Advancement of Optical Methods in Experimental Mechanics, Volume 3*,
Conference Proceedings of the Society for Experimental Mechanics Series,
DOI 10.1007/978-3-319-00768-7_12,

12.2 Intensity of a Light Ray Illuminating a Transparent Specimen

A light ray incident on a transparent specimen passes several times through its thickness (Fig. 12.1). Considering such a ray part of it is reflected from the front face, while the other part passes through the thickness of the specimen. This ray meets the rear face and one part of it is reflected, while the other emerges from the rear face of the specimen. The successive reflections from the two faces of the specimen are repeated, so that an infinite number of rays emerge from the front and the rear face of the specimen.

The percentage of the intensity of the light is the same at each successive reflection from the front or the rear face of the specimen. Let us designate by β the reduction ratio. On the other hand, the reduction coefficient for the reflected light rays differs for the entering and the emerging rays. The intensity of a light ray emerging from the specimen is given by [3]

$$I_{r,t_{k,l}} = \beta^k (1-\beta)^1 I, \tag{12.1}$$

where $k = 1, l = 0, 2$ or $k = 3,5,7\ldots, l = 2$ for the rays that emerge from the front face of the specimen and $k = 0, 2, 4\ldots$ and $l = 2$ for the rays that emerge from the rear face of the specimen.

The value of the coefficient β is given by [3]

$$\beta = \left(\frac{n-1}{n+1}\right)^2, \tag{12.2}$$

where n is the refractive index of the specimen.

For $n = 1.5$, which corresponds approximately to most common glasses and plastics Eq. 12.2 yields β = 004. From Eq. 12.1 we obtain the intensities of the rays that emerge from the front face of the specimen $I_{r1,0} = 0.04\, I, I_{r1,2} = 0.03686\, I$, $I_{r3,2} = 0.00006\, I$ and for the rays that emerge from the rear face of the specimen $I_{t0,2} = 0.92160\, I, I_{t2,2} = 0.00147\, I$. From these values it is concluded that only $I_{r1,0}$, $I_{r1,2}$ *and* $I_{t0,2}$ are worthwhile considering.

12.3 Stress-Optical Equations

The stress-optical equations governing the variation of the optical path of a light ray traversing a transparent specimen or reflected from the front or the rear face of the specimen are derived. The cases of plane stress and plane strain are considered separately.

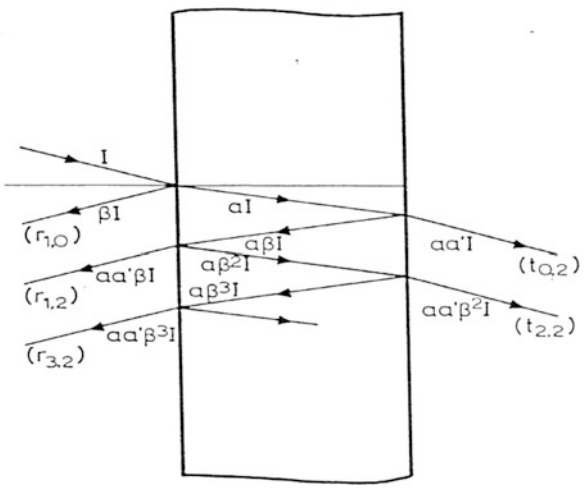

Fig. 12.1 Distribution of the intensity of light that emerges from the front and rear faces of a transparent specimen

12.3.1 Plane Stress

The variation of the optical path of a light ray normally traversing a specimen along the directions of principal stresses σ_1 and σ_2 is given by [3]

$$\Delta s_{t_{1,2}} = t\Delta n_{1,2} + (n - n_0)\Delta t \tag{12.3}$$

where t is the thickness of the specimen, $n_{1,2}$ the index of refraction along the directions of the principal stresses σ_1 and σ_2, n the index of refraction of the material of the specimen under no load, and n_0 the index of refraction of the surrounding medium. Δ denotes the variation of the respective quantity.

According to the Neumann-Maxwell stress-optical law for the case of linear elastic behavior, the variation of the refractive index $\Delta n_{1,2}$ due to loading along the directions of the principal stresses $\sigma_{1,2}$ is given by [3]

$$\Delta n_{1,2} = n_{1,2} - n = b_1\varepsilon_{1,2} + b_2\left(\varepsilon_{2,1} + \varepsilon_3\right) \tag{12.4}$$

where b_1 and b_2 are the strain optical constants and ε_1, ε_2, ε_3, the principal strains.

For generalized plane stress conditions ($\sigma_3 = 0$) introducing Hooke's law into Eq. 12.4 we obtain

$$\Delta n_{1,2} = n_{1,2} - n = C_1\sigma_1 + C_2\sigma_2 \tag{12.5}$$

where

$$C_1 = \frac{b_1 - 2\nu b_2}{E}, \qquad C_2 = \frac{b_2 - \nu(b_1 + b_2)}{E}. \tag{12.6}$$

with ν representing Poisson's ratio.

From Eqs. 12.3, 12.4, 12.5, and 12.6 we found that

$$\Delta s_{t1,2} = \left(\alpha_t\sigma_{1,2} + b_1\sigma_{2,1}\right)t \tag{12.7}$$

where

$$\alpha_t = C_1 - \frac{\nu}{\mathrm{E}}(n - n_0),\ b_t = C_2 - \frac{\nu}{\mathrm{E}}(n - n_0). \tag{12.8}$$

Equation 12.7 can be put in the form

$$\Delta s_{t1,2} = c_t[(\sigma_1 + \sigma_2) \pm \xi_t(\sigma_1 - \sigma_2)]t \tag{12.9}$$

where

$$c_t = \frac{\alpha_t + b_t}{2}, \quad \xi_t = \frac{\alpha_t - b_t}{\alpha_t + b_t}, \tag{12.10}$$

For optically isotropic materials ($\mathrm{b}_1 = \mathrm{b}_2 = \mathrm{b}$, $\xi_\mathrm{t} = 0$) Eq. 12.9 takes the form

$$\Delta s_{t1} = \Delta s_{t2} = c_t(\sigma_1 + \sigma_2)t \tag{12.11}$$

where

$$\alpha_t = b_t = c_t = \frac{1}{E}[b(1 - 2\nu) - \nu(n - n_0)]. \tag{12.12}$$

Consider now the case of a light normally incident on the specimen, passing through its thickness and reflected from the rear face of the specimen. The variation of the optical path of the light ray along the directions of the principal stresses σ_1 and σ_2 is given by [3]

$$\Delta s_{r1,2} = \left[\left(n_{1,2} - n\right)t + \left(n - \frac{n_0}{2}\right)\Delta t\right]. \tag{12.13}$$

For generalized plane stress conditions ($\sigma_3 = 0$) the Newman-Maxwell and Hooke laws can be applied to Eq. 12.13 rendering

$$\Delta s_{r1,2} = 2\left(\alpha_r \sigma_{1,2} + b_r \sigma_{2,1}\right)t \tag{12.14}$$

where

$$\alpha_r = C_1 - \frac{\nu}{E}\left(n - \frac{n_0}{2}\right),\ b_r = C_2 - \frac{\nu}{E}\left(n - \frac{n_0}{2}\right). \tag{12.15}$$

Equation 12.14 can be put in the form

$$\Delta s_{r1,2} = 2c_r[(\sigma_1 + \sigma_2) \pm \xi_r(\sigma_1 - \sigma_2)]t \tag{12.16}$$

where

$$c_r = \frac{\alpha_r + b_r}{2}, \quad \xi_r = \frac{\alpha_r - b_r}{\alpha_r + b_r}, \tag{12.17}$$

For optically isotropic materials ($b_1 = b_2 = b$, $\xi_t = 0$) Eq. 12.16 takes the form

$$\Delta s_{r1} = \Delta s_{r_2} = 2c_r(\sigma_1 + \sigma_2)t \tag{12.18}$$

where

$$\alpha_r = b_r = \frac{1}{E}\left[(1 - 2\nu)b - \nu\left(n - \frac{n_0}{2}\right)\right] \tag{12.19}$$

Finally, consider the case of a light ray normally incident on the specimen and reflected from its front face. The variation of the optical path of the light ray along the directions of the principal stresses σ_1 and σ_2 for generalized plane stress conditions is due to the thickness variation only and is given by

$$\Delta s_{t1} = \Delta s_{t2} = c_f(\sigma_1 + \sigma_2)t\ c_f = -\nu/E \tag{12.20}$$

12.3.2 Plane Strain

The variation of the optical path of a light ray normally traversing a specimen along the directions of the principal stresses σ_1 and σ_2 under plane strain conditions ($\varepsilon_3 = 0$, $\sigma_3 = \nu\ (\sigma_1 + \sigma_2)$) is obtained from Eq. 12.3 and Hooke' s law as

$$\Delta s_{t1,2} = \left(\alpha_t \sigma_{1,2} + b_1 \sigma_{2,1}\right)t \tag{12.21}$$

where

$$\alpha_t = \frac{1}{E}\left[\left(1 - 2\nu^2\right)b_1 - \nu(1 + \nu)b_2\right],\ b_t = \frac{1}{E}\left[-\nu(1 + \nu)b_1 - \left(1 - \nu^2\right)b_2\right]. \tag{12.22}$$

For a light ray normally incident on the specimen, passing through its thickness and reflected from the rear face of the specimen the variation of the optical path is given by

$$\Delta s_{r1,2} = \left(\alpha_r \sigma_{1,2} + b_r \sigma_{2,1}\right) t \tag{12.23}$$

where

$$\alpha_r = 2\alpha_t,\ b_r = 2\beta_t \tag{12.24}$$

Finally, the variation of the optical path of an optical ray reflected from the rear face of the specimen under plane strain conditions is zero.

12.4 The Basic Principles of the Methods of Photoelasticity and Caustics

In the following the basic principles of the methods of photoelasticity and caustics are briefly presented.

12.4.1 The Method of Two-Dimensional Photoelasticity

The method of two-dimensional photoelasticity is based on the temporary or artificial birefringent effect, according to which some transparent materials when subjected to a stress system behave like birefringent crystals. The birefringence of the material is retained only during the application of the loads and disappears when they are removed. According to the temporary birefringence effect, the principal birefringence axes of the model coincide with the principal axes of the induced two-dimensional state of stress, and the optical birefringence induced is proportional to the difference of the principal stresses. From the stress-optical Eqs. 12.9 and 12.16 we have

$$\delta_t = (\Delta s_{t1} - \Delta s_{t2}) = (C_1 - C_2)(\sigma_1 - \sigma_2)t = C_0(\sigma_1 - \sigma_2)t \tag{12.25}$$

for the transmitted light rays, and

$$\delta_r = (\Delta s_{r1} - \Delta s_{r2}) = 2(C_1 - C_2)(\sigma_1 - \sigma_2)t = 2C_0(\sigma_1 - \sigma_2)t = \frac{1+\nu}{E}(b_1 - b_2)(\sigma_1 - \sigma_2)\, d_{eff} \tag{12.26}$$

for the reflected light rays, with $C_0 = C_1 - C_2$.

The specimen under loading is placed in the optical field of a crossed pair of linear polarizers (plane polariscope) or a crossed pair of linear polarizers and quarter wave plates (circular polariscope). In the first case of the plane polariscope two superimposed families of fringes, the isochromatics and isoclinics are obtained, while in the second case of the circular polariscope only the isochromatics are obtained. Isochromatics represent the loci of equal difference of principal stresses and isoclinis the loci of equal difference of inclination of the principal stresses.

12.4.2 The Method of Caustics

In the optical method of caustics, a specimen is illuminated by a parallel, convergent or divergent light beam and the reflected and/or transmitted rays undergo an optical path change dictated by the stress field. The change of the optical path is generally caused by the variation of the thickness and the refractive index of the specimen as it is subjected to loading. Under stress gradients resulting around geometrical discontinuities, the reflected or transmitted rays generate an envelope in the form of a highly illuminated three-dimensional surface in space. When this surface is intersected by a reference screen, a bright curve, the so-called caustic curve is formed. In the case of transparent materials, three caustics are obtained. They are created by the light rays reflected from the front and rear surfaces and by rays that are transmitted through the specimen. In the case of opaque materials, only one caustic is formed by the light rays as they are reflected by the specimen surface. The dimensions of the caustic

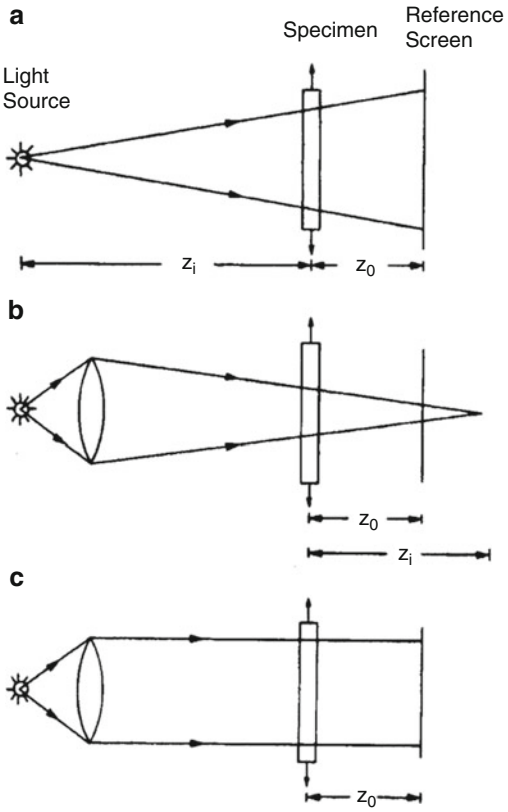

Fig. 12.2 Optical arrangement for divergent (**a**) convergent (**b**) parallel and (**c**) light

are quantitatively related to the state of affairs near the geometrical discontinuity and therefore, they can be used for the determination of the stress concentration or stress intensity factor. A schematic view of the optical arrangement for the method of caustics for divergent, convergent or parallel light is shown in Fig. 12.2. The caustic obtained on the reference screen is the image of the so-called initial curve on the specimen. For linear elastic crack problems, the initial curve is a circle centered at the crack tip. Thus, the evaluation of the caustic yields information on the stress conditions along the initial curve. For the case of a mode-I through-the-thickness crack the stress intensity factor K_{exp} is given by [1]

$$K_{\exp} = 0.0934 \frac{D^{5/2}}{Z_0 c t m^{3/2}} \tag{12.27}$$

where z_0 is the distance between the specimen and the viewing screen where the caustic is formed, c is the stress optical constant of the specimen under conditions of plane stress (c_t or $2c_r$ for the transmitted or reflected light rays), t is the specimen thickness, m is the magnification factor of the optical arrangement defined as the ratio of a length on the reference screen where the caustic is formed divided by the corresponding length on the specimen and D is the transverse diameter of the caustic at the crack tip. The above equation is valid when the state of stress in the vicinity of the crack tip is plane stress, so that the value of stress-optical constant under conditions of plane stress is used.

For optically isotropic materials, the caustic is created by the light rays reflected from the circumference of a circle, the so-called initial curve, which surrounds the crack tip. The radius of the initial curve is given by

$$r = 0.316 \text{ m } D \tag{12.28}$$

12.5 The State of Stress in the Vicinity of the Crack Tip

The state of stress in the neighborhood of the crack tip changes from plane strain very close to the tip to plane strain further away from the tip through an intermediate region where the stress field is three-dimensional. This has been documented by substantial analytical and experimental evidence. Levi et al. [14] using finite elements for a straight crack in a finite width

plate, found that the principal stress normal to the plane of the plate approaches zero at a distance from the crack tip equal to half the specimen thickness. This result indicates that at distances from the crack tip larger than half the specimen thickness, conditions of plane stress dominate, while at closer distances the stress situation is complex and generally cannot be idealized as plane stress or plane strain. The stresses vary through the plate thickness and the stress situation is three-dimensional.

This result was verified experimentally by Rosakis and Ravi-Chandar [11] who determined the extent of the region of three-dimensionality of the stress field in the neighborhood of the crack tip using reflected and transmitted caustics. They established that the stress state approaches that of plane stress at distances away from the crack tip greater than half the specimen thickness. **A** further investigation of the three-dimensional region around the crack tip was made by Meletis et al. [15] using the method of caustics. They performed experiments in double cantilever beam specimens of 2,090 Al alloy of different thicknesses. Analogous results were obtained in [16, 17]. It was established that the state of stress in the neighborhood of a crack tip is three-dimensional up to a limiting value, after which it becomes plane stress. This critical distance depends on the ratio of crack length to specimen thickness, t, and varies from t to 0.4t for plate thicknesses from 3 to 12.5 mm.

12.6 Comparison of the Methods of Photoelasticity and Caustics

12.6.1 Optical Set-up

Both methods of photoelasticity and caustics are based on light. Photoelasticity is based on the phenomenon of light interference, while the method of caustics is based on the law of reflection of geometrical optics. In both methods the optical arrangement is simple. In photoelasticity the specimen is inserted in a plane or circular polariscope and monochromatic or white light is used. In the method of caustics the specimen is illuminated by any type of light, monochromatic or white, coherent or not.

The method of caustics can be used in either a reflection or a transmission arrangement. Actually, for a transparent material three caustics are obtained, two from the light rays reflected from the front and rear faces of the specimen, and one from the light rays transmitted through the specimen. As it was previously referred to these three light rays carry most of the intensity of the infinite number of the light rays emerging from the front and rear faces of a transparent material. The intensity of the remaining light rays is insignificant. The method of photoelasticity is applied in transparent materials for transmission arrangements, while for opaque materials transparent coatings are used. In both methods transmission arrangements record changes of thickness and refractive index, while in the method of caustics reflection arrangements from the frony face of the specimen record only changes of thickness. In photoelasticity reflection arrangement records changes of thickness and refractive index.

12.6.2 Determination of Stress Intensity Factor

From Eq. 12.27 it is established that the value of stress intensity factor K, in the method of caustics is determined from a single measurement of a length, the diameter of the caustic. This makes the determination of stress intensity factor a simple matter. Information for evaluating stress intensity factor is obtained from a very small circular line, the initial curve surrounding the crack-tip. The radius of the initial curve r_0 is determined from Eq. 12.28 by measuring the transverse diameter D of the caustic, the magnification factor m being known from the optical setup. Thus, the region from which information is obtained is well localized. Values of K can also be obtained by measuring other geometrical dimensions of caustic and using simple evaluation formulas, analogous to Eq. 12.27. This allows determination of K, by a least squares technique. K is determined either by the light rays transmitted through the specimen or by the light rays reflected from the rear or the front face of the specimen. Thus, transparent and opaque specimens can be studied.

In photoelasticity determination of K from isochromatic patterns is not an easy task. There is a concentration of isochromatic loops near the crack tip due to the existing singularity at this point. Near the crack tip the isochromatic pattern is influenced by non linear elects. Thus, for the determination of K data should be taken from the isochromatic pattern at critical distances away from the crack tip. Dally and coworkers [7] developed a technique for obtaining K from data on isochromatics taken at distances from the tip where the influence of nonlinearities and crack tip effects is minimal.

12.6.3 Effect of Crack Tip Radius

Consider a plate with a slit of radius ρ which simulates a crack. The stress field in the vicinity of the tip of the slit is given according to Creager and Paris [18] by

$$\sigma_x = \frac{K_I}{(2\pi r)^{1/2}} \cos\frac{\theta}{2}\left(1 - \sin\frac{\theta}{2}\sin\frac{3\theta}{2}\right) - \frac{K_I}{(2\pi r)^{1/2}}\frac{\rho}{2r}\cos\frac{3\theta}{2} - \sigma_{0x}$$

$$\sigma_y = \frac{K_I}{(2\pi r)^{1/2}} \cos\frac{\theta}{2}\left(1 + \sin\frac{\theta}{2}\sin\frac{3\theta}{2}\right) + \frac{K_I}{(2\pi r)^{1/2}}\frac{\rho}{2r}\cos\frac{3\theta}{2} \tag{12.29}$$

$$\tau_{xy} = \frac{K_I}{(2\pi r)^{1/2}} \sin\frac{\theta}{2}\cos\frac{\theta}{2}\cos\frac{3\theta}{2} - \frac{K_I}{(2\pi r)^{1/2}}\frac{\rho}{2r}\sin\frac{3\theta}{2}$$

From the above equations it is established that the sum of the normal stresses is independent of the radius ρ of the slit. For optically isotropic or opaque materials the caustic curve depends only on the sum of the principal stresses, and, therefore, it is independent of the radius ρ. On the contrary, the isochromatic fringes in photoelasticity depend on the difference of the principal stresses, and, therefore, depend on the radius ρ. This dependence distorts the isochromatic patterns in the vicinity of the crack tip, and makes it mandatory to take measurements on the isochromatics at critical distances away from the tip of the slit that simulates a crack in experiments.

12.6.4 Effect of Plate Boundaries

The effect of plate boundaries on the stress field near the crack tip enters in the singular stresses through the constant term, σ_{0x} [19]. Since the caustic depends on the gradient of the sum of the principal stresses it is evident that it is independent of σ_{0x} which disappears in the differentiation, and therefore, the caustic is independent of the existence of boundaries. On the other hand, in photoelasticity, the isochromatic fringes depend on the difference of the principal stresses, and, therefore, on the existence of plate boundaries. The plate boundaries play a significant role on the form of the isochromatic loops and distort the direction of the loops either toward the crack or away from the crack.

12.6.5 Location of Crack Tip

The exact location of the crack tip is of major importance in problems of running cracks for the determination of crack speed. This task presents difficulties in photoelasticity due to high concentration of isochromatics near the crack tip. However, in the method of caustics the exact location of the crack tip can easily be determined. This is achieved by locating the points at which the caustic surrounding the crack tip intersects the crack line on both sides of the crack tip. From the geometry of the caustic, it is deduced that the crack tip is at a distance 0.421D from the point of intersection of the caustic and the crack, and at a distance 0.527D from the point of intersection of the caustic and the crack ligament.

12.6.6 Effect of Changing State of Stress

The state of stress in the neighborhood of the crack tip changes from plane strain near the crack tip to plane stress at a critical distance away from the tip. This distance is approximately equal to half the specimen thickness. Between the plane strain and plane stress region the state of stress is three-dimensional. In the optical method of caustics plane stress conditions are assumed to dominate near the crack tip. This implies that the initial curve which is mapped on lo the caustic should lie in the plane stress region. The optical path length in the method of caustics is proportional to the sum of the principal stresses and

the stress-optical constant which changes significantly from plane strain to plane stress. Thus for the correct determination of stress intensity factors the initial curve should lie in the plane stress region in order to use the plane stress value of the stress-optical constant.

In photoelasticity the isochromatic fringes depend on the difference of the optical path along the two principal stress directions. This difference for the light rays traversing the specimen or reflected from the rear face of the specimen is given by Eq. 12.25 or Eq. 12.26. In these equations b_1 and b_2 are material constants. Thus the difference of the optical path lengths along the principal stress directions is independent of the state of stress and it is the same for plane stress or plane strain conditions.

12.7 Conclusions

A comparison of the methods of photoelasticity and caustics as applied to crack problems was made relatively to six criteria, including the optical set-up, the efficiency in the determination of stress intensity factors, the effect of crack tip radius, the effect of plate boundaries, the location of the crack tip and the changing state of stress near the crack tip. Both methods use relatively simple optical arrangements. The method of caustics is superior compared to the method of caustics for the following criteria: determination of stress intensity factors, the effect of crack tip radius, the effect of plate boundaries, location of the crack tip. The method of photoelasticity is superior to the method of caustics for the criterion of changing the state of stress near the crack tip. This constitutes a great advantage of the method of photoelasticity compared to the method of caustics.

References

1. Coker EG, Filon LNG (1957) A treatise on photoelasticity. University Press, Cambridge
2. Frocht MM (1941/1948) Photoelasticity, vol 1, 2. Wiley, New York
3. Theocaris PS, Gdoutos EE (1979) Matrix theory of photoelasticity. Springer, Berlin/Heidelberg/New York
4. Post D (1954) Photoelastic stress analysis for an edge crack in a tensile field. Proc SESA 12(1):99–116
5. Wells A, Post D (1958) The dynamic stress distribution surrounding a running crack. A photoelastic analysis. Proc SESA 16(1):69–92
6. Dally JW (1979) Dynamic photoelastic studies of fracture. Exp Mech 19(10):349–361
7. Sanford RJ, Dally JW (1979) A general method for determining mixed mode stress intensity factors from isochromatic fringe patterns. J Eng Fract Mech 11:621–633
8. Theocaris PS (1891) Elastic stress intensity factors evaluated by caustics. In: Sih GC (ed) Mechanics of fracture, vol 7. Martinus Nijhoff, The Hague, pp 189–252
9. Theocaris PS, Gdoutos EE (1972) An optical method for determining opening-mode and edge sliding-mode stress intensity factors. J Appl Mech 39:91–97
10. Kalthoff JF (1994) Shadow optical method of caustics. In: Kobayashi AS (ed) Handbook on experimental mechanics, 2nd edn. Prentice-Hall, Eaglewood Cliffs, pp 407–476
11. Rosakis AJ, Ravi-Chandar K (1986) On crack tip stress state: an experimental evaluation of three-dimensional effects. Int J Sol Struct 22:121–134
12. Konsta-Gdoutos M, Gdoutos EE (1992) Some remarks on caustics in mode-I stress intensity factor evaluation. Theor Appl Fract Mech 17:47–60
13. Konsta-Gdoutos M, Gdoutos EE (1992) Guidelines for applying the method of caustics in crack problems. Exp Tech 16:25–28
14. Levi N, Marcal PV, Rice JR (1971) Progress in three-dimensional elastic–plastic stress analysis for fracture mechanics. Nucl Eng Des 17:64–75
15. Meletis EI, Huang W, Gdoutos EE (1991) A study of the three-dimensional region at crack tips by the method of caustics. Eng Fract Mech 39:875–885
16. Gdoutos EE (2009) Determination of SIFs in crack problems by caustics. In: Proceedings of the 2009 SEM international conference on experimental and applied mechanics, Albuquerque, p. 99, 1–3 June 2009 (full paper in conference CD)
17. Gdoutos EE (2012) The optical method of caustics applied to fracture mechanics problems. In: Silva Gomes JF, Mario Vaz AP (eds) Proceedings of the 15th international conference on experimental mechanics, Porto, pp 9–10, 22–27 July 2012 (full paper in conference CD)
18. Creager M, Paris P (1967) Elastic field equation for blunt cracks with reference to stress corrosion cracking. Int J Fract Mech 3:247–252
19. Gdoutos EE (2005) Fracture mechanics – an introduction, 2nd edn. Springer, Dordrecht

Chapter 13
Analysis of Portevin-Le Chatelier Effect of Al-Mg Alloy by Electronic Speckle Pattern Interferometry

Tatsuya Nakamura, Tomohiro Sasaki, and Sanichiro Yoshida

Abstract Displacement field in AA5052 alloy during tensile test was visualized using Electronic speckle pattern interferometry. The process of nucleation and propagation of Portevin-Le Chatelier deformation band during the plastic deformation were investigated by a dynamic observation of the images of displacement contours (fringe pattern). Various types of bands were observed depending on the applied strain rate and the total strain at which the deformation band (DB) appeared. The characteristics of nucleation and propagation of DBs were discussed being compared with the serrated curve in the load. Type A and B serration observed at the high strain rate was characterized by local strain in the DB, and it was found that the difference between type A and B arises from the increase in the local strain rate. Deformation band at low strain rate showed complicated change in response to the nucleation and propagation processes. The correlation between the band propagation and the serrated curve was discussed based on the variation in density and velocity of mobile dislocation.

Keywords Speckle interferometry • Aluminum alloy • Deformation measurement • Dislocation • Serration

13.1 Introduction

The Portevin-Le Chatelier (PLC) effect [1] is a well-known phenomenon observed in plastic deformation of many alloys. In metal forming, it is related to detrimental phenomena such as fracture by localization of plastic deformation into bands of intense shear or unacceptable visual appearance [2–5]. It is believed that the PLC effect is initiated at the microscopic level resulting from interaction between dislocations and obstacles such as solute atoms in solid solution or precipitates. The obstacles form atmospheres around the mobile dislocation, and cause pinning of the dislocations. In plastic deformation, the dislocations have to break away from these atmospheres and multiply. Tensile load increases in order to separate the pinned dislocation from the obstacles. Then the load drop is observed at the moment when the dislocations move. The effect described above is repeated periodically until the onset of necking of sample [6]. The intensity of this process, known as serrations, depends on various microstructural factors such as the heat treatment condition, grain size, solute atoms content, and the serration amplitude increases with an increase in strain. A considerable number of literatures on the PLC effect have been reported and the effect has been microscopically investigated by many researchers [7–19]. At the same time, it is closely connected to macroscopic phenomena such as the propagation of a localized, band-like strain (deformation band, DB) and the appearance of serrations in the stress–strain (S-S) curves. The DB can be characterized using parameters such as the critical strain where the DB appears, the magnitude of load drop, and the velocity of the moving DB. According to the characteristics in the S-S curve, serration has been qualitatively classified to three types of A, C and C by researchers [20–26]. Type A appears at large strain rates, and is characterized by weak pulsations on the S-S curve and a continuous

T. Nakamura • T. Sasaki (✉)
Department of Engineering, Niigata University (Japan), Niigata University, Ikarashin Ninocho 8050, Nishi-ku, Niigata-shi, Niigata 950-2181, Japan
e-mail: tomodx@eng.niigata-u.ac.jp

S. Yoshida
Department of Chemistry and Physics, Southeastern Louisiana University, SLU 10878, Hammond, LA 70402, USA
e-mail: syoshida@selu.edu

H. Jin et al. (eds.), *Advancement of Optical Methods in Experimental Mechanics, Volume 3*,
Conference Proceedings of the Society for Experimental Mechanics Series,
DOI 10.1007/978-3-319-00768-7_13,

propagation of the DB due to strong spatial correlations. Type B appears at intermediate strain rates, where the DB propagates accompanying regular serrations on the S-S curve. Type C appears at low strain rates, where the DB appears randomly in the sample surface with more prominent serrations on the stress–strain curves, compared with those of types A and B.

On the other hand, there are a numbers of experimental data on the temporal and spatial aspect of DB and the PLC effect observed using whole field measurement such as Electronic Speckle Pattern Interferometry (ESPI) [27–34] or Digital image correlation method (DIC) [35–39]. However, it still has not been clarified how the microscopic event is related to the macroscopic phenomena. In particular, the propagation mechanism of DB is a controversial subject. To investigate this question, we study macroscopic behavior of the DB varying the strain rate, and discuss the observation from the viewpoint of the PLC effect. In the present study, deformation process associated with the PLC effect during a tensile test for Al-Mg alloy has been visualized using ESPI. Much of the previous works on serrated flow has focused on the effects of test conditions and material composition and heat treatment condition. In this work, the serration characteristics are dynamically investigated for the entire plastic flow region and for three different strain rates. The onset of serration and the propagation of DB have been discussed.

13.2 Experimental Procedure

The material used in this study was Al-4.44mass%Mg binary alloy (industrial Aluminum alloy, AA5083-O) of 3 mm in thickness. Tensile specimen of 10 mm in gauge width and 25 mm gauge length was cut from the sheet by electronic discharge machining in rolled direction. The specimen was fully clamped at both ends and stretched under displacement control tensile machine at room temperature. Crosshead speeds in the tensile test were 5.0×10^{-2} mm/s 1.7×10^{-2} mm/s, 0.5×10^{-2} mm/s (strain rate: 2.0×10^{-3} s^{-1}, 6.7×10^{-4} s^{-1}, and 2.0×10^{-4} s^{-1}).

Deformation process until failure was measured using ESPI. The optical setup is the same as a previous paper [34] as shown in Fig. 13.1. Two optical configurations were arranged to vertical direction (*y-axis*) and horizontal (*x-axis*) direction to a tensile machine. Each optical configuration consisted of a dual beam ESPI setup described as follows. The light sources were semiconductor lasers with the wave length of 660 nm. The laser beam was expanded by optical lenses and split into two paths by a cube beam splitter. The two beams illuminated the surface of specimen at the same angle of incidence. The angle of incidence used in this study was 36°. The image of surface was captured using a CCD camera. Each pixels of the CCD received optical intensity resulting from coherent superposition of the surface due to the two laser beams. The horizontal configuration which the optical path is shown by solid line in Fig. 13.1 was sensitive to in-plane displacement component along only *x-axis*. Similarly, the vertical configuration shown by broke line was sensitive to displacement along *y-axis*.

Image of the specimen during the tensile test was captured by the CCD camera at 15–50 fps (frames per second). The light sources on the two optical configurations were alternatively turned on, being synchronized with the CCD camera at its frame

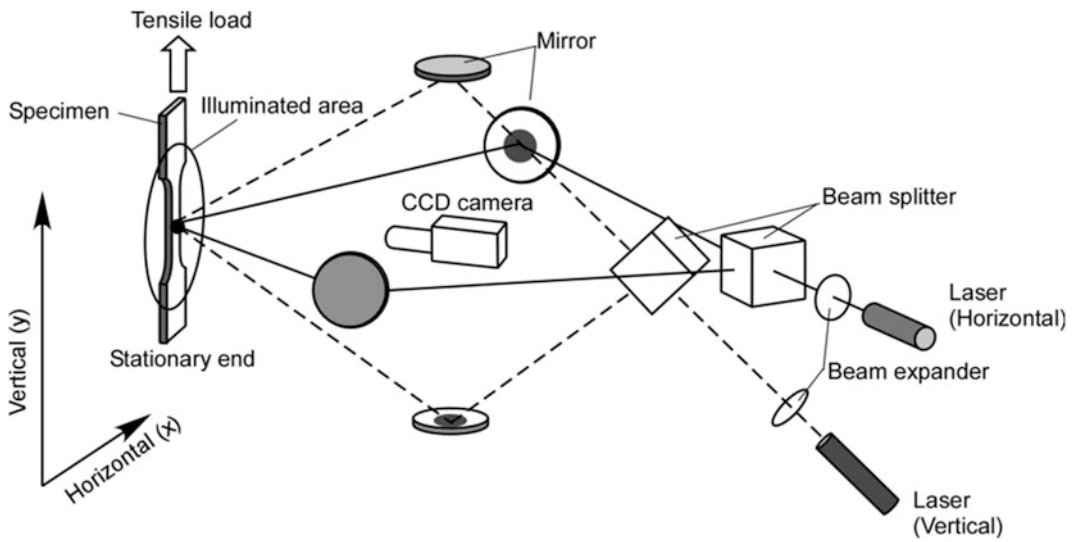

Fig. 13.1 Experimental arrangement

capture. Thus, images formed by the vertical and horizontal configurations were stored alternatively. The images were recorded into computer memory being sorted by the direction, and the change in the brightness of speckles was calculated numerically by subtracting each frame of image from a frame captured at a later frame. Consequently, the displacement distributions to *x-axis* and *y-axis* direction were individually observed as contours called the fringe.

13.3 Result and Discussion

13.3.1 Features of Deformation Band in Serrated Curve

Figure 13.2 shows load–displacement curves for the three crosshead speeds. The onset of serration is shown in the curve by arrows. The type of serration observed in the curves has strain rate sensitivity. With decrease in the tensile rate, the serration tends to start at large displacement of crosshead, while the observed load serrations are found to increase in amplitude. Features in nucleation and propagation behavior of DB are described below comparing to conventional classification.

13.3.1.1 DB at High Tensile Rate

At high tensile rate of 5.0×10^{-2} mm/s as shown in Fig. 13.2a, the curves begins to serrate immediately after the yielding. In the early stage of the plastic deformation (small total displacement), the serration is characterized by small load amplitude and large period. The ESPI fringe patterns and the corresponding load are indicated in Fig. 13.3. The displacement range is shown in Fig. 13.2 by an arrow "A". The subtracted images represent transverse displacement u and longitudinal displacement v resulting from a constant displacement interval of 0.3 s. The DB appears near the lower shoulder of specimen accompanied by a load drop as indicated in (Fig. 13.3a), then continuous propagation of DB occurs with increase in the load (Fig. 13.3b). This corresponds to type A serration observed by researchers [20–26]. When the DB reach a shoulder of specimen as shown in Fig. 13.3c, the DB stops and disappears with an increase in load. A new DB nucleates at the other of the specimen with a load rise (Fig. 13.3d). The interval of load popping is associated to the end of propagation and the nucleation of DB at the shoulder. With increase in the total displacement, the type of serration gradually changes to type B as described in the following section.

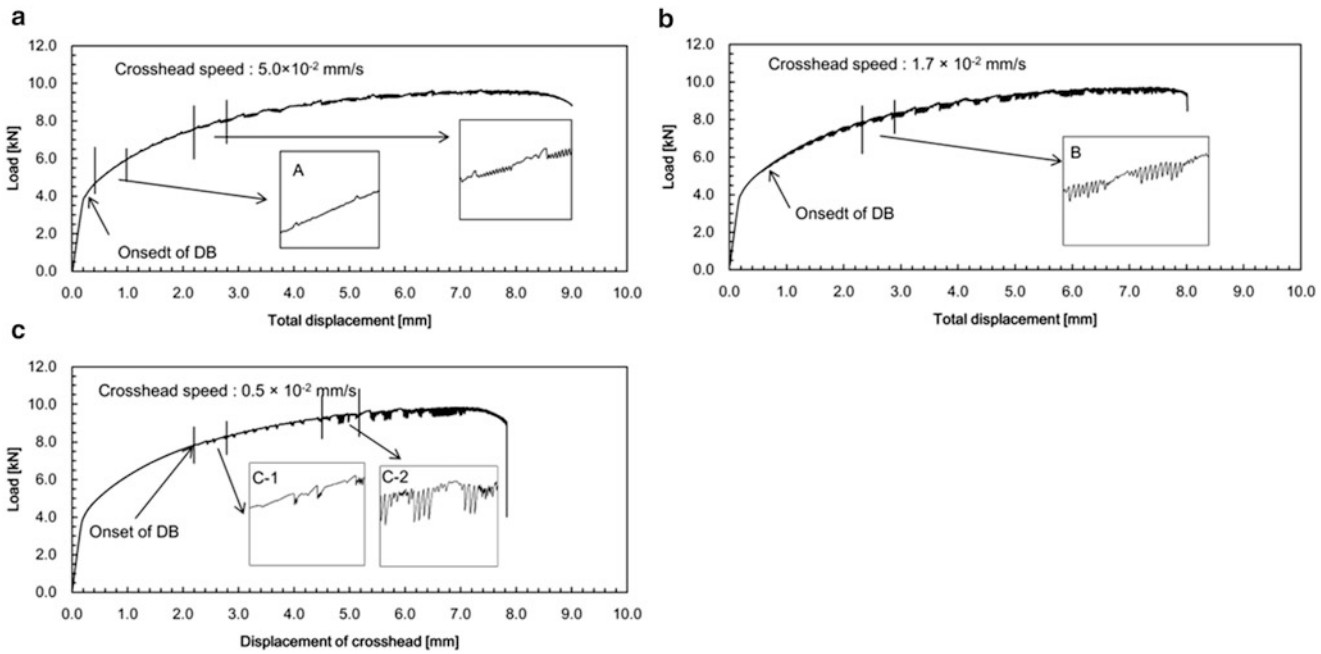

Fig. 13.2 Load–displacement curve

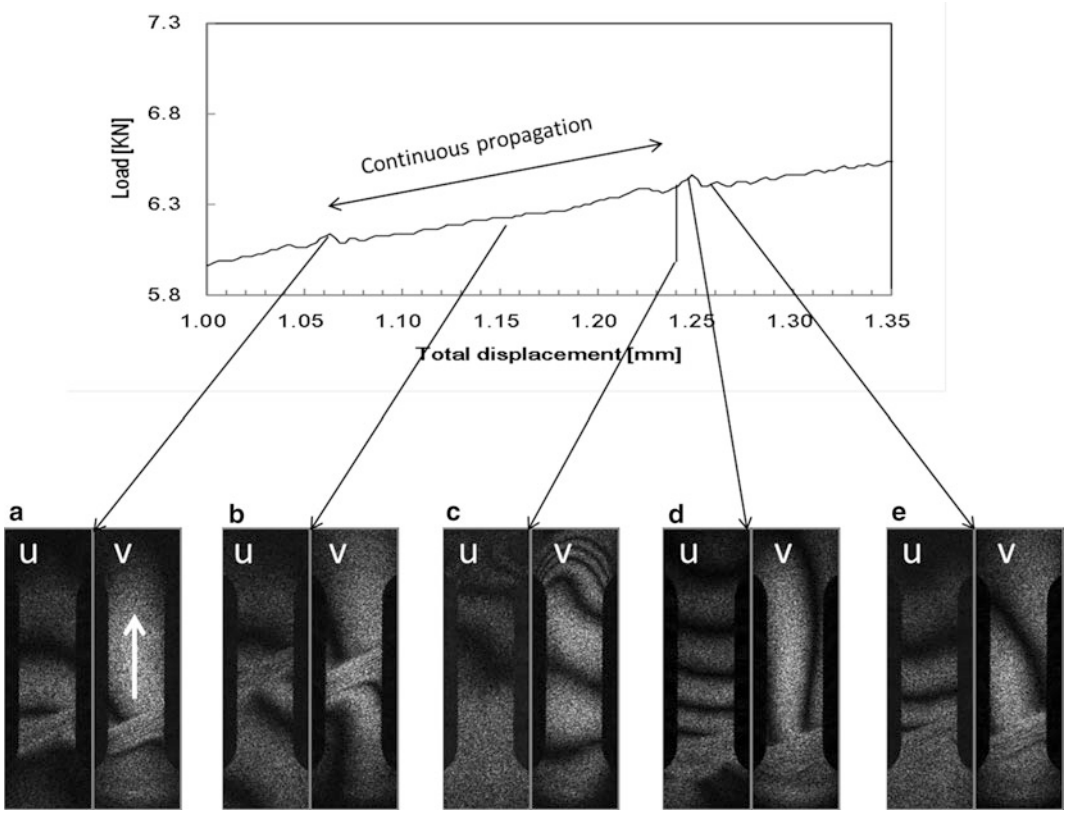

Fig. 13.3 Fringe pattern showing activity of DB observed in high tensile rate. Displacement range of *upper* graph are indicated in Fig. 13.2a by *arrow* "A"

13.3.1.2 DB at Intermediate Tensile Rate

Type B serration was observed in the late stage in the 5.0×10^{-2} mm/s tensile rate case (Fig. 13.2a) and the entire displacement range in 1.7×10^{-2} mm/s case (Fig. 13.2b). Figure 13.4 shows a typical change in the fringe pattern in type B observed at the total displacement range shown in Fig. 13.2b by an arrow "B". In this serration type, load pulsation periodically appeared. Change of fringe pattern in the pulsation is given by Fig. 13.4a–c. DB rapidly appears at each load peak by the rapid fringe concentration (Fig. 13.4b), then it disappears with a load drop (Fig. 13.4c). A new DB nucleates beside the previously disappeared DB, and the DB apparently propagates by this process that has been termed "discontinuous propagation" [20–26]. The fringes around the DB are parallel to the measurement direction as shown in Fig. 13.4b, i.e., the DB propagation accompanies rotation of the other part. The discontinuous propagation stops at the shoulder of specimen and the DB changes to a circular shape due to the shoulder geometry (Fig. 13.4c). Until a nucleation of a newer DB, a narrow deformation band as shown in Fig. 13.4e repeatedly appears near the other shoulder with a weak pulsation. The formation of narrow deformation band can be stated as the process for relaxation of rotation stored by the DB propagation. The narrow deformation band expands in the tensile direction, and grows to a new DB. Next propagation begins with a large load drop.

13.3.1.3 DB at Low Tensile Rate

At the low crosshead speed of 0.5×10^{-2} mm/s (Fig. 13.2c), change in fringe pattern during the serration was most complicated; the observed serration was classified into two types by the feature of the curve. Figure 13.5 shows the fringe pattern observed in an early stage of the serration at the low tensile rate. The displacement range was indicated in Fig. 13.2c by an arrow "C-1". The serrated curve consists of an increase and a weak pulsation of the load. In this type of serration, DB shows continuous propagation (Fig. 13.5a) with the increase of load similarly to type A serration. However, the propagation stops at the center of gauge part, then the DB gradually disappears with increase until a peak of the load (Fig. 13.5b, c).

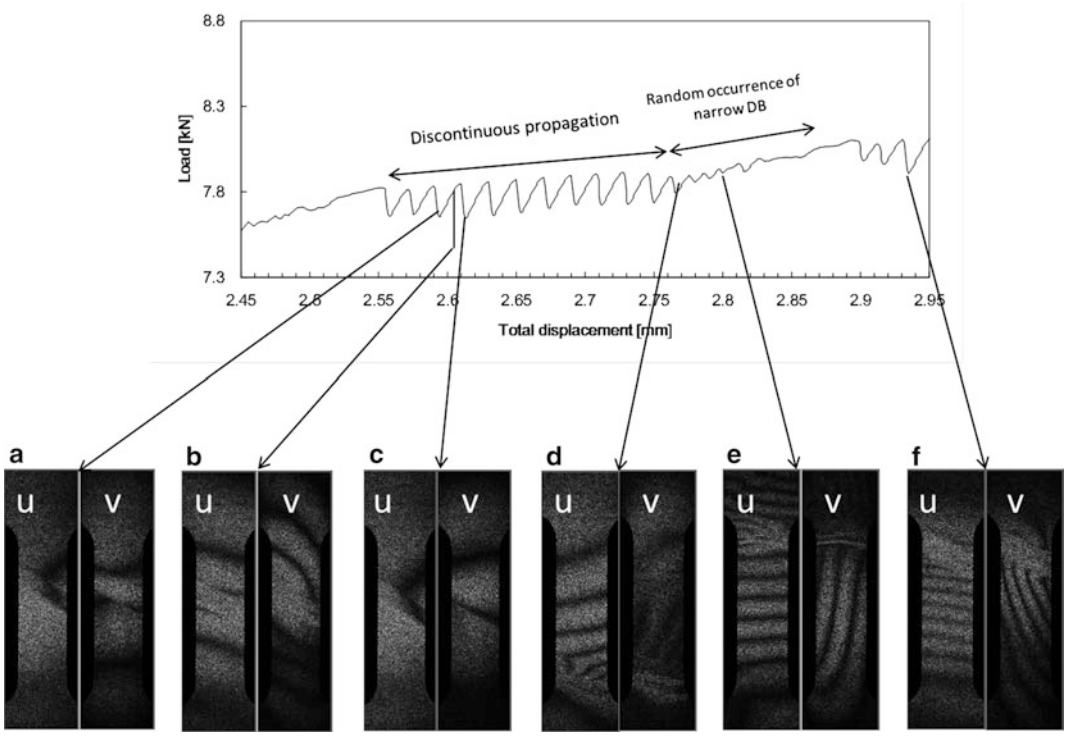

Fig. 13.4 Fringe pattern showing activity of DB observed in intermediate tensile rate at low displacement. Displacement range of *upper* graph are indicated in Fig. 13.2b by *arrow* "B"

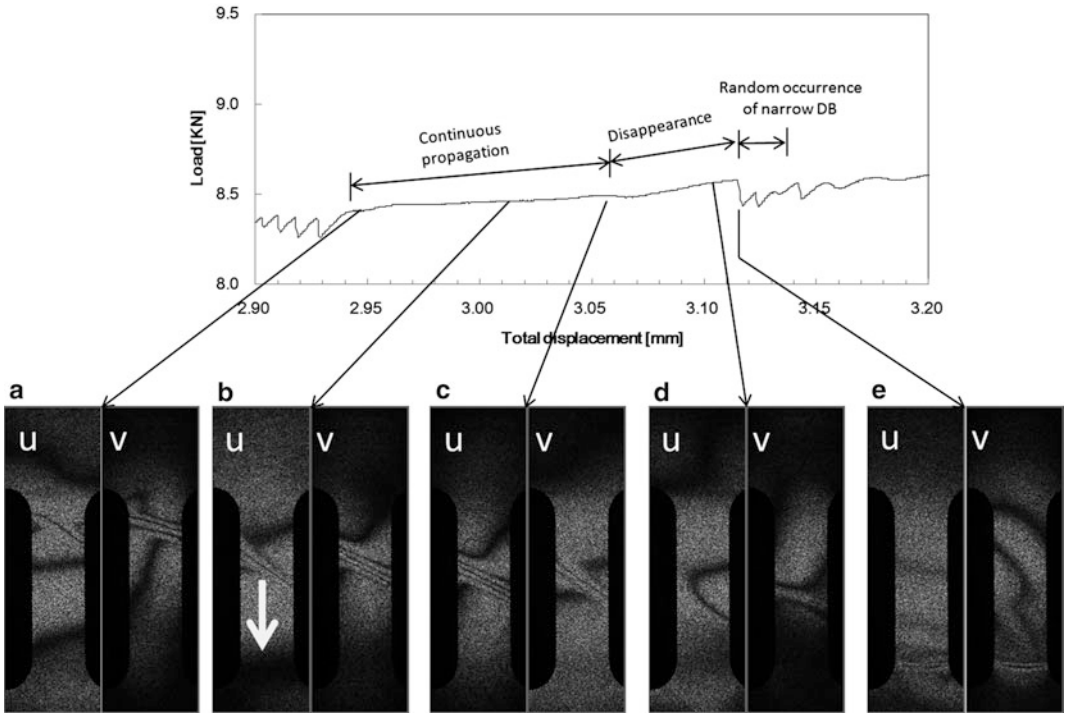

Fig. 13.5 Fringe pattern showing activity of DB observed in low tensile rate. Displacement range of *upper* graph are indicated in Fig. 13.2b by *arrow* "C-1"

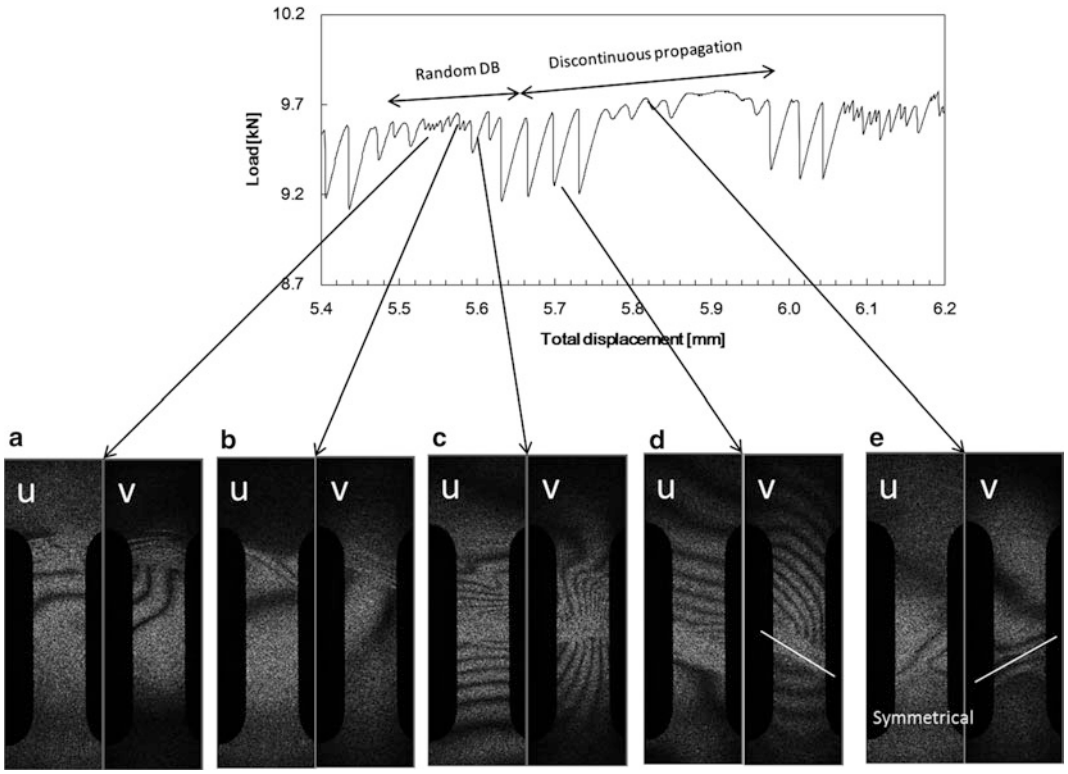

Fig. 13.6 Fringe pattern showing activity of DB observed in low tensile rate. Displacement range of *upper* graph are indicated in Fig. 13.2b by *arrow* "C-2"

With a load drop, narrow deformation band as shown in Fig. 13.5d, f randomly appears at both side shoulder with weak load pulsation. A new DB nucleates at the shoulder of specimen after the weak pulsation. These progresses seem to be different from the type C serration as observed in the low strain rate [20–26].

Figure 13.6 shows the fringe pattern observed in the late stage shown in Fig. 13.2c by an arrow "C-2". Relatively large load amplitude and random occurrence of DB agrees with the conventional type C serration. The amplitude of serration varies in the sequence. As shown in Fig. 13.6a, b, strain concentration characterized by a narrow deformation band at the shoulder with weak pulsation develops to DB nucleation, then DB randomly appears in the gauge part of specimen. Subsequently, discontinuous propagation of DB occurs with large pulsation by the same process as the type B serration. The angle of DB turns symmetrically at the center of specimen nucleated DB. The amplitude of load pulsation accordingly decreases with decrease in rotation around the DB. In this type of serration, the rotation induced by the DB propagation may be relaxed by changing the angle of DB. This fact indicates the load drop closely relates to the relaxation of the rotation induced by the shear deformation.

13.3.2 Local Strain Rate Inside DB

Figure 13.7 shows typical fringe patterns of DB observed in type A and type B serrations. Both images were obtained by subtracting images with same time interval of 0.04 s. For type B, five fringes can be observed inside the DB, while the number of fringe is smaller for type A than that in type B. Number of fringe represents local displacement during the subtracted time interval, thus the local strain rate inside the DB, $\triangle\varepsilon$, can be obtained by the number of fringe, n, the wave length of light source, λ, width of DB, w, and time interval $\triangle t$,

$$\Delta\varepsilon = n\lambda/w\Delta t \tag{13.1}$$

Variation of $\triangle\varepsilon$ with the total displacement at the high tensile rate of 5.0×10^{-2} mm/s is shown in Fig. 13.8. The initial $\triangle\varepsilon$ in the early stage is comparable to the applied tensile strain rate in gauge part (2.0×10^{-3} s^{-1}), then increases to higher

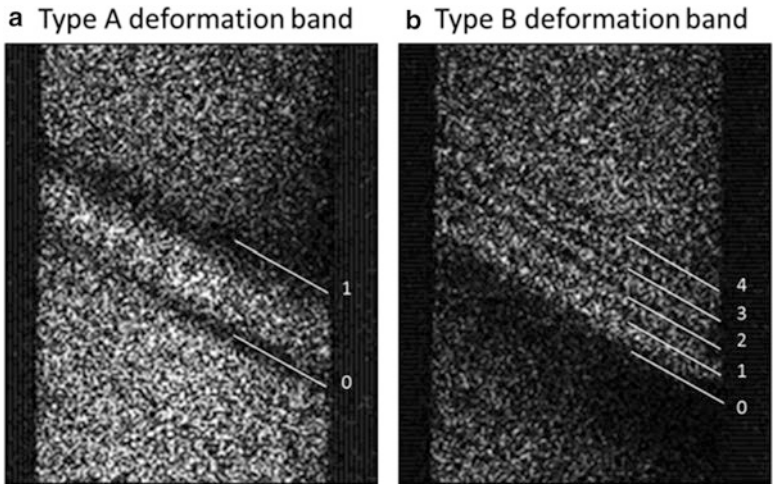

Fig. 13.7 Number of fringe in bands observed in type (**a** and **b**)

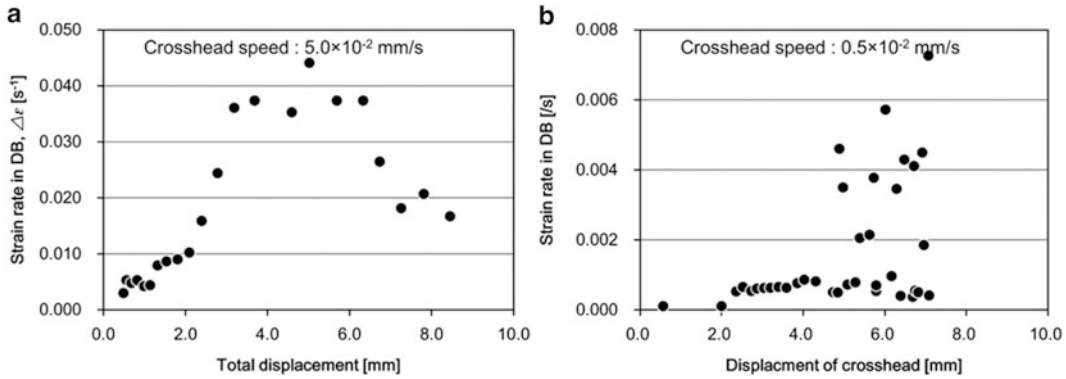

Fig. 13.8 Variation of local strain rate in DB with total displacement

values exceeding the tensile strain rate. This changes in the $\triangle\varepsilon$ are similarly to the transition from type A to B with total displacement observed in load–displacement curve as shown in Fig. 13.2a. The large local strain rate of the DB in type B serration has also been measured using high speed camera and DIC by Ait-Amokhtar et al. [37]. The local strain rate inside DB may result in the load drop. Therefore the result implies that the type A and type B serration are essentially due to a same propagation mechanism. On the other hand, correspondence of local strain rate to serration is also observed in low tensile rate given by Fig. 13.8b. The $\triangle\varepsilon$ in the early stage that shows continuous propagation is found to be relatively small. The strain rate in the DB can be connected to the density of the mobile dislocations, ρ_m, and their Burgers vector b and mean velocity v_d, according to Orowan's equation

$$\Delta\varepsilon = \Omega\rho_m b v_d \tag{13.2}$$

where Ω is the orientation factor usually set to 0.3. Assuming that v_d is equal to the width of DB observed in subtracted image ($=w$), ρ_m can be estimated by $\rho_m = \triangle\varepsilon/\Omega b v_d$. Figure 13.9 shows the mobile dislocation density at the occurrence of DB. For type B serration, the DB at the load drop where the maximum number of fringe is observed was measured. 0.286 nm was used for b in this study. From the viewpoint of dynamic strain aging, the load amplitude in the serration has been explained by interaction between the mobile dislocation and solute atom [7–11]. At the applied high strain rate, the mobility of solute diffusion cannot catch the dislocation motion, this lead to weak pulsation as type A serration. The pinning effect is enhanced with a decrease in strain rate, marked load pulsation thereby occurred by the unpinning process of dislocation. However, the ρ_m does not show significant increase in Fig. 13.9a, b. At the low tensile rate of Fig. 13.9c, though the ρ_m shows relatively

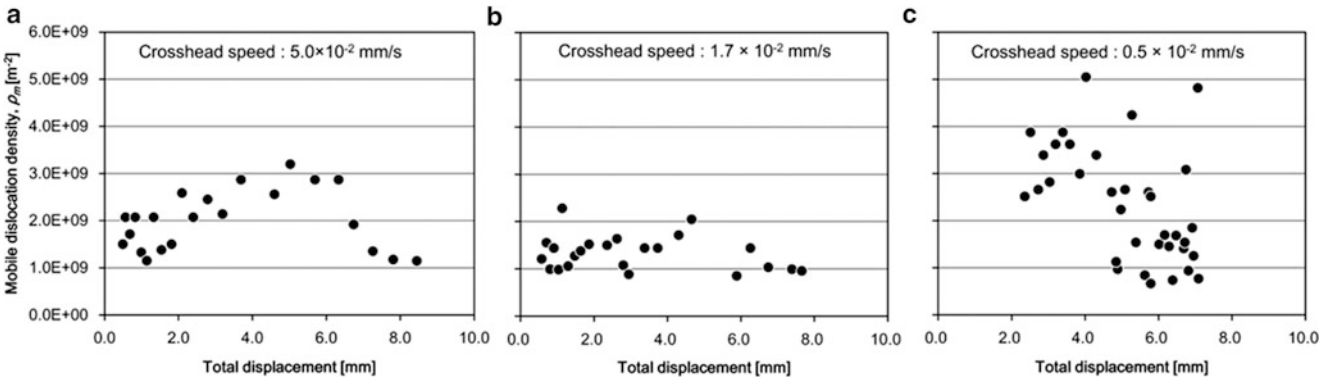

Fig. 13.9 Mobile dislocation density at the occurrence of DB

high values, it is found to be large at the small displacement in which the weak load pulsation appears. These results suggest that the pinning of dislocation does not be directly related to the load pulsation.

13.4 Summary

PLC effect during tensile test of Al-Mg alloy at various tensile rates was observed using two-dimensional ESPI system. Spatiotemporal characteristics of the DB have been discussed by ESPI fringe pattern being compared with the serrated curve. In this experiment, various types of serration involving type A and type B serration were observed in the load–displacement curve depending on the applied tensile rate and the total displacement where the DB occurs. The DB at low strain rate shows complicated change in response to the nucleation and propagation processes. The load drop in the serration is related to relaxation of rotation caused by DB propagation, the location where the DB nucleates, and local strain rate inside the DB. In particular, transition from type A to type B at the high tensile rate is resulting from the increase in local strain rate in the DB. The propagation of DB has been discussed based on density and velocity of the mobile dislocation.

References

1. Portevin A, Le Chatelier F (1923) Compt Rend Acad Sci Paris 176:507
2. Bird JE, Newman KE, Narasimhan K (1987) Heterogeneous initiation and growth of sample-scale shear bands during necking of Al-Mg sheet. Carlson JM Acta Metall 35:2971–2982
3. French IE, Weinrich PF (1975) The effects of hydrostatic pressure on the mechanism of tensile fracture of aluminum. Metall Trans A 6A:1165–1169
4. Chin GY, Hosford WF, Backofen WA (1964) Ductile fracture of aluminum. Trans Met Soc AIME 230:437–448
5. Korbel A, Embury JD, Hatherly M, Martin PL, Erbsloh HW (1986) Microstructural aspects of strain localization in Al-Mg alloys. Acta Metall 34:1999–2009
6. Cottrell AH (1953) A note on the PorteVin-Le Chatelier effect. Philos Mag 44:829
7. Sleeswyk AW (1958) Slow strain-hardening of ingot iron. Acta Metall 6:598
8. Ham RK, Jaffrey D (1967) Dislocation multiplication, vacancy accumulation, and the onset of jerky flow during forwaed and reverse 1strain in Cu-3.2 at.% Sn. Phil Mag 15:247
9. Worthington PJ, Brindley BJ (1969) Serrated yielding in substitutional alloys. Phil Mag 19:1175–1178
10. McCormick PG (1971) The Portevin-Le Chatelier effect in an Al-Mg-Si alloy. Acta Metall 19:463–471
11. Korbel A, Zasadzinski J, Sieklucka Z (1976) A new approach ti the Portevin-LeCatelier effect. Acta Metall 24:919–923
12. Brindley BJ, Worthington PJ (1981) Serrated yielding in aluminium-3 % magnesium. Scripta Metall 17:1357–1361
13. Korbel A, Dybiec H (1981) The problem of the negative strain-rate sensitivity of metals under the Portevin-Le Chatelier deformation conditions. Acta Metall 29:89–93
14. Kubin LP, Chihab K, Estrin Y (1988) The rate dependence of the Portevin-Le Chatelier effect. Acta Metall 36:2707–2718
15. Woo KD, Kim SW, Lou TP (2002) Mechanical properties and deformation behavior of Al-4Mg-0.4Sc-1.5Mn alloy at room temperature. Mater Sci Eng A 334:257–261
16. Tian B (2003) Ageing effect on serrated flow in Al-Mg alloys. Mater Sci Eng A349:272–278

17. Wen W, Morris JG (2003) An investigation of serrated yielding in 5000 series aluminum alloys. Mater Sci Eng A 354:279
18. Ziania L,∗, Boudrahema S, Ait-Amokhtara H, Mehennia M, Kedjarb B (2012) Unstable plastic flow in the Al-2%Mg alloy, effect of annealing process. Mater Sci Eng A 536:239–243
19. Wen W, Zhao Y (2005) The effect of Mg precipitation on the mechanical properties of 5xxx aluminum alloys. Mater Sci Eng A 392:136
20. Chihab K, Estrin Y, Kubin LP, Vergnol J (1987) kinetics of the Potevin-Le Chatelier bands in an Al-5at%Mg alloy. Scripta Metall 21:203
21. Robinson JM, Shaw MP (1992) The influence of specimen geometry on the Portevin-Le Chatelier effect in an Al-Mg alloy. Mater Sci Eng A159:159–165
22. Lebyodkin M, Brechet Y, Estrin Y, Kubin L (1996) Statistical behavior and strain localization patterns in the Portevin-Le Chatelier effect. Acta Mater 44:4531–4541
23. Chatterjee,A, Sarkar1 A, Barat ∗, P, Mukherjee P, Gayathri N (2009) Character of the deformation bands in the (A+B) regime of the Portecin-Le Chatelier effect in Al=2.5%Mg alloy. Mater Sci Eng A 508:156–160
24. Ziegenbein A, Hähner P, Neuhäuser H (2000) Correlation of temporal Instabilities and spatial localization during Potevin-Le Chatelier deformation of Cu-10at.% Al and Cu-15at.% Al. Comput Mater Sci 19:27–34
25. Reed JM, Walter ME (2003) Observations of serration characteristics and acoustic emission during serrated flow of an Al-Mg alloy. Mater Sci Eng A359:1–10
26. Ranca b,∗ N, Wagner D (2008) Experimental study by pyrometry of Portevin-Le Chatelier plastic instabilities-type A to type B transition. Mater Sci Eng A 474:188–196
27. Shabadi R, Kumar S, Roven H, Dwarakadasa E (2004) Characterisation of PCL band parameters using laser speckle technique. Mater Sci Eng A 364:140–150
28. Shabadi R, Kumar S, Roven H, Dwarakadasa E (2004) Effect of specimen condition, orientation and alloy composition on PCL band parameters. Mater Sci Eng A 382:203–208
29. Jiang Z, Zhang Q, Jiang H, Chen Z, Wu X (2005) Spatial characteristics of the Portevin-Le Chatelier deformation bands in Al-4 at%Cu polycrystals. Mater Sci Eng A 403:154–164
30. Jiang H, Zhang Q, Wu X, Fan J (2006) Spatiotemporal aspects of the Portevin-Le Chatelier effect in annealed and solution-treated aluminum alloys. Scripta Mater 54:2041–2045
31. Jiang H, Zhang Q, Chen X, Chen Z, Jiang Z, Wu X, Fan J (2007) Three types of Portevin-Le Chatelier effects. Acta Mater 55:2219–2228
32. Yoshida S (2008) Dynamics of plastic deformation based on restoring and energy dissipative mechanism in plasticity. Phys Mesomech 11:137
33. Yoshida S (2011) Scale-independent approach to deformation and fracture of solid-state materials. J Strain Anal 46:380
34. Sasaki T, Suzuki T, Yoshida S (2012) Proceedings of SEM XII International congress and exposition on experimental and applied mechanics, Costa Mesa, p 174
35. Yoshida S, Toyooka S (2001) Field theoretical interpretation on dynamics of plastic deformation-Portevin-Le Chatelie effect and propagation of shear band. J Phys Condens Matter 13:6741–6757
36. Tong W, Tao H, Zhang N, Hector LG Jr (2005) Time-resolved strain mapping measurements of individual Portevin-Le Chatelier deformation bands. Scripta Mater 53:87–92
37. Ait-Amokhtar H, Vacher P, Boudrahem S (2006) Kinematics fields and spatial activity of Portevin-Le Chatelier bands using the digital image correlation method. Acta Mater 54:4365–4371
38. Halim H, Wilkinson DS, Niewczas M (2007) The Portevin-Le Chatelier (PLC) effect and shear band formation in an AA5754 alloy. Acta Mater 55:4151–4160
39. Kang J et al (2006) On the sequence of inhomogeneous deformation processes occurring tensile deformation of strip cast AA5754. Acta Mater 54:209–218

Chapter 14
A Method for Overlapping Two DIC Views by Using a Two-Tone Speckle Pattern

Phillip L. Reu

Abstract Because both the accuracy and spatial resolution of digital image correlation (DIC) are directly related to the field-of-view and the number of pixels, it is sometimes advantageous to have a tight view for high resolution measurements and a wide view for overall object deformation. This approach will be demonstrated using a high-speed measurement of the deformation and strain of a riveted thin plate with an explosive loading. Overall plate deformation was provided by a wide-view stereo system, while a tight view of a section of the rivets was imaged with a second stereo pair to measure the strain around the rivet holes. The challenge is creating a speckle pattern which will work with both systems without creating holes in the overall measurement data. This was accomplished by creating a black/white course pattern for the wide view and a black/grey/white fine pattern for the tight view. The grey speckles were sized such that they are not resolved by the wide view and therefore do not compromise the full-field measurement. Details of the process and example results will be presented.

Keywords Digital image correlation • Uncertainty quantification • Photogrammetry • DIC • High-speed

14.1 Introduction

Digital Image Correlation (DIC) is a full-field photometric measurement technique. Fundamentally the resolution of the technique is related to the pixel size on the object. Therefore, to increase the displacement resolution it is important to maximize the number of pixels across the sample (all other things being equal). The use of DIC with widely available high-speed cameras has led to its increased use in explosive research. This technique has been used at Sandia National Laboratories to gain a more complete understanding of blast loading. To best quantify the loading on a plate, it is important to know both the overall deformation of the object, as well as be able to measure strain around small features. Due to limitations in the number of pixels available in high-speed imaging, this requires two radically different fields-of-view (FOV). This paper discusses a two-tone paint scheme with different speckle sizes to allow two overlapping views from two DIC stereo-systems. This maintains the primary measurement of the deformation of the entire paint surface, while allowing strain to be measured around rivets in the middle of the plate.

14.2 Experimental Setup

14.2.1 Explosive Test Stand and Stereo-rigs

Sandia National Laboratories has developed an explosive test stand for measuring the reaction of 1.2 m diameter plates to an explosive blast. The stand consists of a massive steel frame on which the plate can be bolted. The stand includes a large area around the plate for measurement of the stand movement, as well as delaying the arrival of the blast products into the

P.L. Reu (✉)
Sandia National Laboratories, PO Box 580087185 Albuquerque, NM 87185, USA
e-mail: plreu@sandia.gov

H. Jin et al. (eds.), *Advancement of Optical Methods in Experimental Mechanics, Volume 3*,
Conference Proceedings of the Society for Experimental Mechanics Series,
DOI 10.1007/978-3-319-00768-7_14,

Fig. 14.1 Stereo-rig setup behind protective wall

measurement area. Two DIC stereo-rigs were positioned approximately 6 m from the sample behind a protective wall with thru-holes for the cameras to observe the deformation of the plate surface during the blast loading. The camera position behind the wall provided adequate protection for the cameras, without the use of Lexan viewports. An analysis in Sect. 14.2.3 demonstrates why Lexan should be avoided if possible in DIC applications. The stereo-rig consisted of a beam on which all four cameras were rigidly mounted as shown in Fig. 14.1. The wide stereo-rig was composed of two Phantom v12 cameras with 35–80 mm zoom lenses and was run at a resolution of 368 × 360 pixels and 37,012 frames-per-second (fps). The tight stereo-rig used two v1610 cameras with 400 mm lenses, with a resolution of 1,280 × 720 pixels, and a frame rate of 18,500 fps. The sample area was shaded by a large tent structure to prevent shadows on the surface that greatly compromise the DIC results. Ambient light in the shade was still adequate to have an exposure of 15 μs for the wide view and 47 μs for the tight view.

14.2.2 DIC Speckling for Two Fields-of-View

The experimental design required that the displacement of the plate be maintained over the entire FOV to match the data acquired in previous tests, however, rivets on the plate, required a smaller FOV in order to capture their deformation and strain. The difficulty in doing this is that speckles optimized for one FOV are almost never adequate for a different size. This is because the goal is to have 3–5 pixels per speckle in order to optimize the spatial resolution of DIC by using the smallest effective subset size and step size, which leads to the smallest possible virtual gage size. The wide FOV had a pixel size on the object of 4 mm/pixel, which gives an optimal speckle size of between 12 and 20 mm. The tight FOV has a 0.4 mm/pixel size at the object, with an optimal speckle size of 1.2–2 mm. In this, case, because the pixel sizes at the object were so radically different, the small speckles for the tight view were small enough, ½-pixel or less in the wide view that they were not seen by the cameras – and appeared as a hazy area in the image (see left side and inset of Fig. 14.2). To create an appropriate speckle at the small FOV, a grey paint was used in order to have speckle contrast over both the large black speckles and the white areas between the speckles from the wide view speckle pattern. Of course, with this approach, there is a compromise in the contrast that may negatively impact the results. However, with 12-bit cameras and good lighting, there was plenty of dynamic range using the grey speckles, yielding 700 grey levels between the white and grey and another 700 grey levels between the grey and black. The match quality for this contrast was estimated by the DIC software to be 0.01 pixels.

14.2.3 The Effect of Lexan on DIC Results

There is no question that protecting expensive high-speed cameras during explosive testing is important, however, placing cameras behind Lexan *will* affect the results. This is due to the optical distortions caused by the Lexan and results from either the inherent optical defects of the material, or by bending the Lexan during mounting. It is important to quantify the influence of the Lexan on the results. For this experiment, the error was quantified by calibrating both with and without the Lexan in place, and acquiring images of a flat speckle target, translated in the FOV. The calibration using the same board yielded two different projection error scores; with Lexan it was 0.088 pixels and without Lexan it was 0.037 pixels. This is

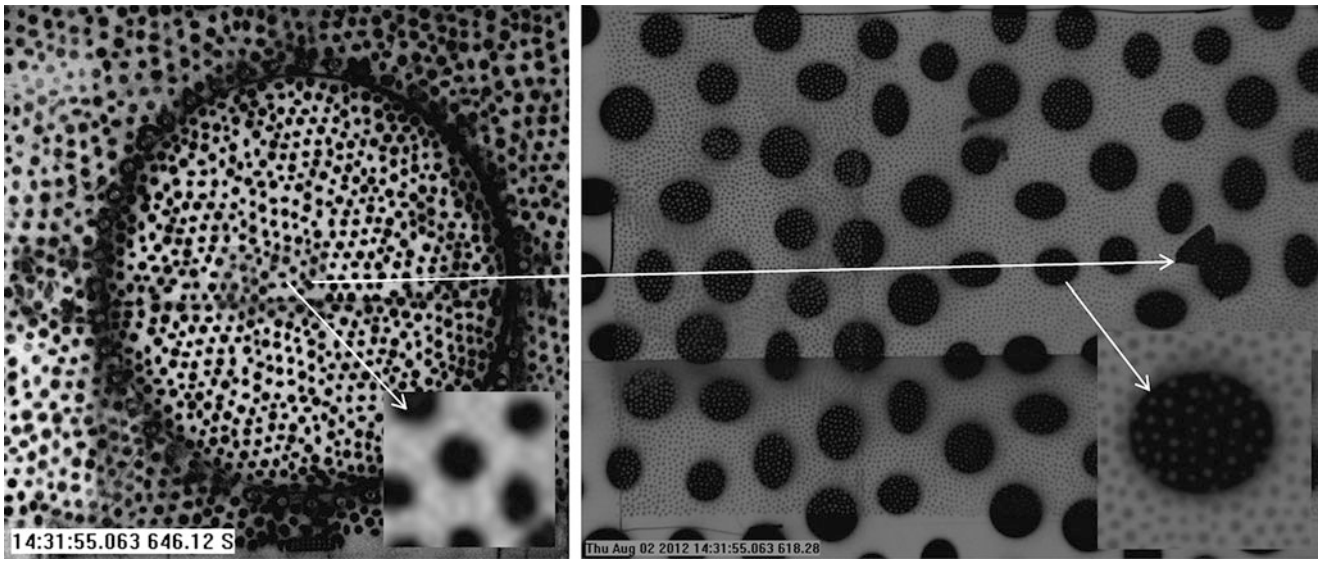

Fig. 14.2 Speckle patterns for both the (*left*) wide view showing unresolved small speckles as a hazy region and (*right*) tight view showing the resolved three-tone speckle pattern. Insets on both figures show a detailed region of the two-tone speckle region

Table 14.1 Error summary of Lexan

	Lexan	Lens Only
Average Projection	0.045	0.014
Max Projection	0.054	0.027
Average U Error 2σ	0.487	0.108
Average V Error 2σ	0.589	0.091
Average W Error 2σ	1.195	0.478
Max U Error	1.282	0.247
Max V Error	1.148	0.297
Max W Error	3.077	1.128

almost certainly caused by issues with fitting the non-radial lens distortions to the available radial distortion parameters during the bundle adjustment calibration. A flat board was then translated in the FOV and images were acquired both with and without the Lexan. The images were analyzed using DIC software, an average projection error of 0.05 pixels was obtained with the Lexan and 0.02 pixels without the Lexan. Again, indicating a compromise in the results due to the added optical distortions. A best-fit plane was used to transform the data from the camera coordinates to the flat plate, and then rigid-body motions were removed. For a flat plate that remains flat, this will primarily yield the errors due to the optical distortions. These errors are summarized in Table 14.1 and illustrated for the Z-direction in Fig. 14.3. The figure clearly shows that there is a 3 mm error in the out-of-plane direction caused only by the Lexan distortion. For reference – the pixel size at the object is 4 mm/pixel.

14.3 DIC Results

The plate with a lap rivet joint (6.35 mm rivets with 30 mm spacing) was loaded by an explosive charge behind the sample. The wide stereo-rig successfully captured the motion of the plate, with no loss of data in the high resolution region. The tight stereo-rig also yielded data throughout its FOV. The results from the two systems were compared using a line cut taken from the DIC data at a short period after the loading began. Figure 14.4 shows the out-of-plane results for two frames from the wide view and one from the tight view. The smoothing of the data over the lap joint is clearly seen in the wide view, because

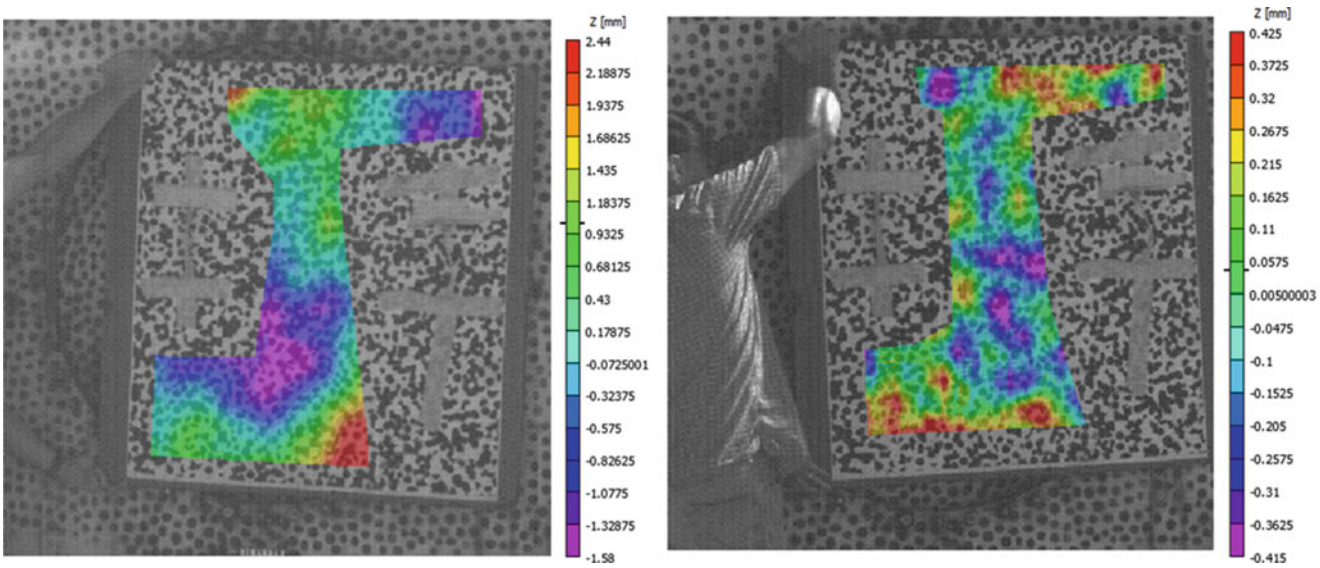

Fig. 14.3 (*Left*) False shape caused by Lexan distortions. (*Right*) DIC displacement noise

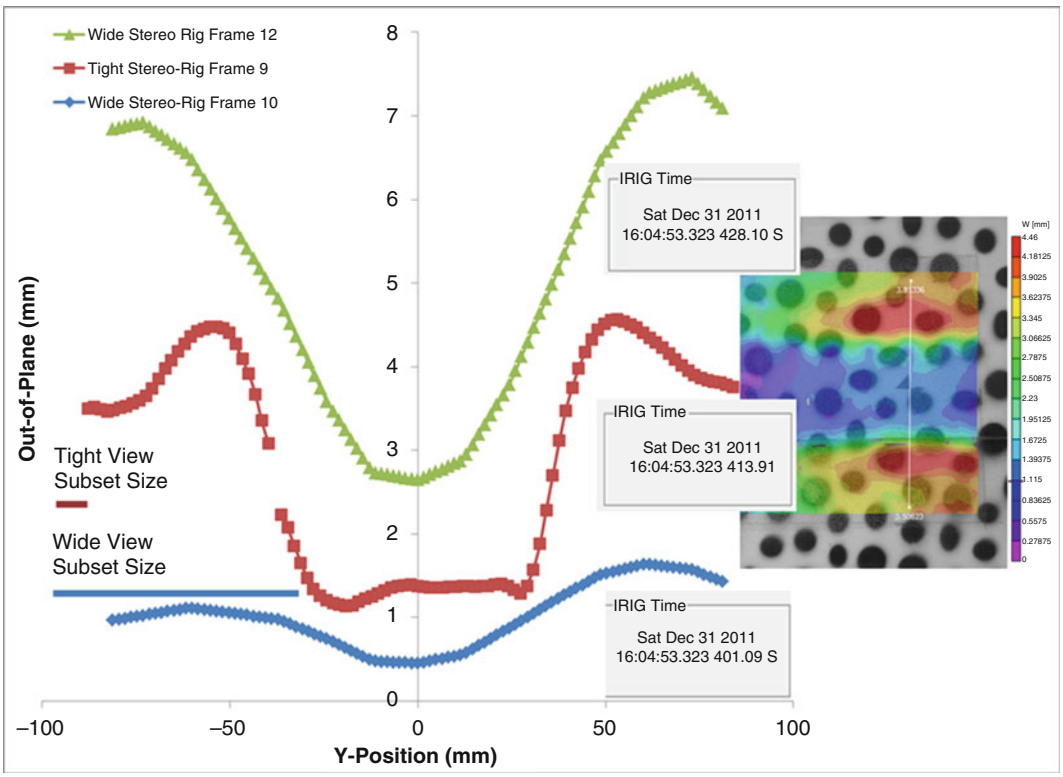

Fig. 14.4 Line cut comparing the out-of-plane displacement of the two FOVs along the illustrated line-cut. Also shown are the subset size on the same scale as the y-dimension

of the relatively large 68 mm subset size (illustrated in the figure), which bridges the high deformation gradient around the lap joint. The step size for the wide view was 3-pixels (12 mm), which yields only 16 data points across the dimension shown in Fig. 14.5. The added data points are interpolated. The tight view is better able to represent the displacements at the lap joint because the subsets are physically much smaller (11.6 mm) as illustrated in Fig. 14.5. This figure clearly illustrates the importance of spatial resolution on the accuracy of the DIC results.

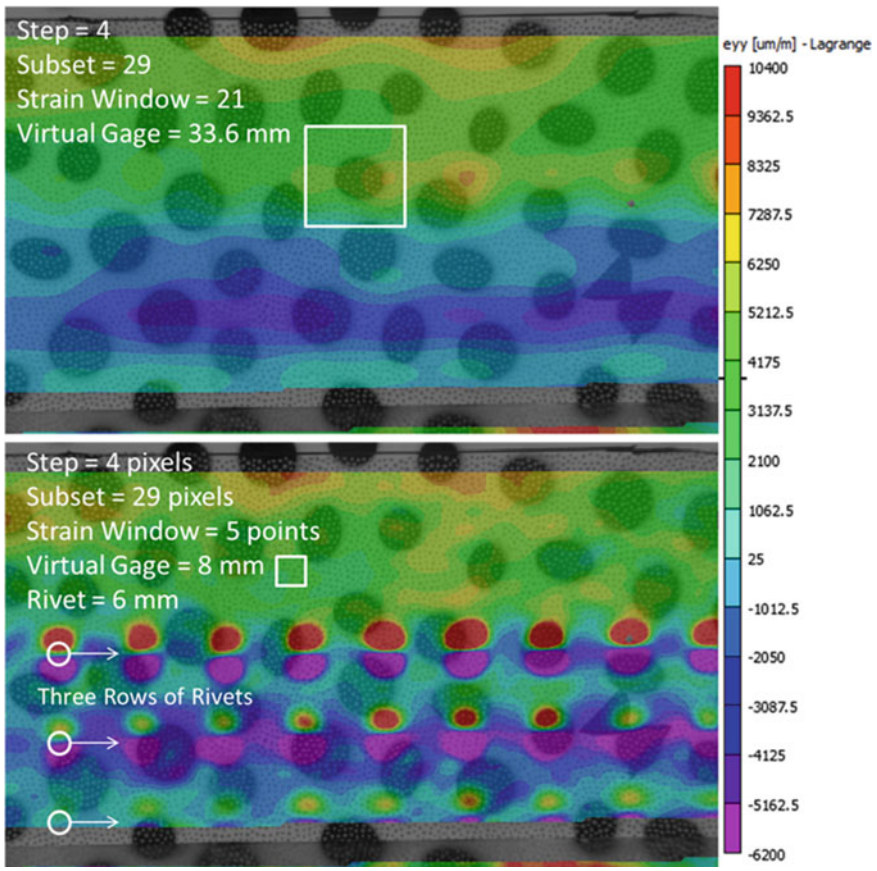

Fig. 14.5 Illustration of virtual gage size on the stain gradients (ε_{yy}) same load step analyzed with different virtual gage sizes and plotted with the same scale

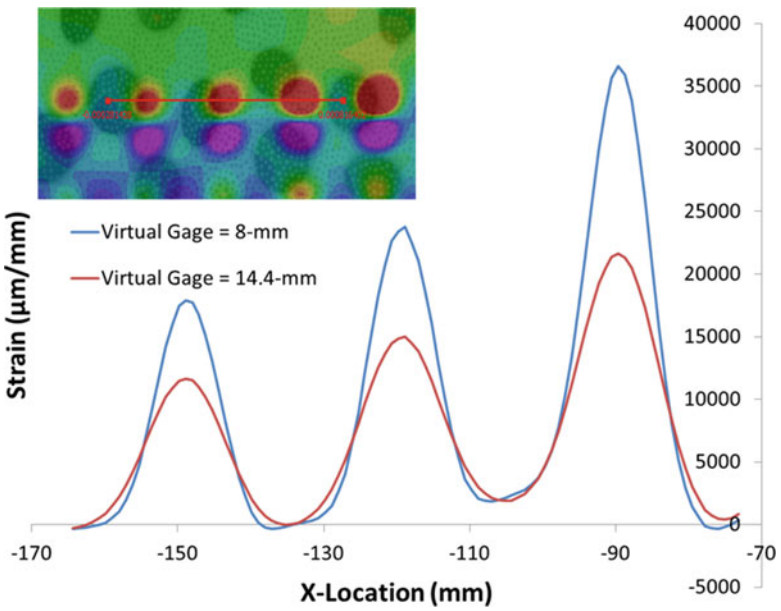

Fig. 14.6 Virtual gage size study. *Red line* is the extracted region plotted

Spatial resolution is even more critical for the strain results, where a region of the DIC displacement results (the virtual gage) is fit before taking a derivative to calculate the strain. The wide view with a strain window of 15 data points would yield a virtual gage size of 180 mm – valid only for giving average strain at best. For the tight FOV, virtual gages of 8 mm are possible and better able to capture the strain gradients around the rivets. Figure 14.6 clearly illustrates the effect of the virtual

gage size on the strain results for two different sizes. Obviously the smaller gage better captures the strain gradients between the rivets, however, to determine where the strain is correct, a “mesh density” type study was done by varying the virtual gage size and is shown in Fig. 14.7. The strain accuracy can be determined by looking for regions where the strain is identical regardless of gage size. Any matching strains are accurate; any non-matching strains are a minimum estimation of the strain.

14.4 Conclusions

A two-tone speckle pattern was used to create overlapping DIC fields-of-view. Due to the tenfold difference in pixel size at the object, the wide view was unable to image the small pattern used for the tight view, yielding data across the entire surface. The tight view was able to image a small enough area that strain was able to be measured around small rivets, which would be completely un-measurable with a single wide FOV. This was illustrated by doing a virtual strain gage size study and looking at the variation in the strain results. An analysis of the influence of Lexan viewports was also completed, showing for this case that the bias errors due to the Lexan would be unacceptably large.

Acknowledgements I would like to thank Michael Bejarano for setting up the DIC experiment and acquiring the images.

Sandia is a multiprogram laboratory operated by Sandia Corporation, a Lockheed Martin Company, for the United States Department of Energy under contract DE-AC04-94AL85000.

Chapter 15
DIC Uncertainty Estimation from Statistical Analysis of Correlation Values

B. Wieneke and R. Prevost

Abstract The uncertainty of a Digital Image Correlation (DIC) displacement field is estimated using a generic post-processing method based on statistical analysis of the intensity patterns. First the second image is dewarped back onto the first one using the computed displacement field which provides two almost perfectly matching images. Differences are analyzed regarding the effect on shifting the minimum of the correlation function. A relationship is derived between the standard deviation of intensity differences over a local region (subset or facet size) and the expected asymmetry of the correlation peak, which is then converted to the uncertainty of the displacement vector. This procedure is tested with synthetic data for various types of noise (random Gaussian noise, photon shot noise, image degradation) and provides accurate estimate of the true error. Finally the technique is applied to experimental data where the true error is estimated independently by other means. The proposed technique provides in many cases a reliable uncertainty estimate for different error sources related to variation in surface pattern as well as illumination and viewing angle changes.

Keywords DIC • DIC error • Uncertainty estimation • Measurement uncertainty • DIC correlation

15.1 Introduction

Various algorithms exist to match two images. The goal is to compute a displacement field dx(x,y) as the best fit between $I_1(\mathrm{x},\mathrm{y})$ and $I_2(\mathrm{x}+\mathrm{dx}(\mathrm{x},\mathrm{y}),\mathrm{y}+\mathrm{dy}(\mathrm{x},\mathrm{y})) = I_2^*(\mathrm{x},\mathrm{y})$. Usually this involves minimizing locally or globally the sum of the L_2-norm or mean squared error $\left(I_1 - I_2^*\right)^2$, sometimes called minimum quadratic difference (MQD) method, least squares matching (LSM) or sum of squared differences (SSD). Alternatively one can maximize the correlation given by the sum of $\left(I_1 I_2^*\right)$. It has been shown that the two methods are mathematically identical provided the intensity I is normalized to $(I(\mathrm{x}) - I_{\mathrm{avg}})/\Sigma(I(\mathrm{x}) - I_{\mathrm{avg}})^2$ [1]. Such normalization is often recommended for DIC experiments compensating variation in illumination intensity.

Image matching algorithms can be further differentiated into a local or global regularization scheme. Global methods like Horn & Schunck [2] or Lukas-Canade-type [3] optical flow iteratively optimize the whole displacement field at once while local methods more common in DIC usually select a small sub-region of the image ('subset') to be matched to the corresponding subset in the second image and repeating the procedure independently for all subsets in the image. Extensive investigations have been done to quantify the accuracy of DIC displacement and strain fields often based on synthetic data varying various image and experimental parameter as well as algorithmic implementation details (see reviews in [4] and [5]).

The focus here is not on a particular DIC algorithm, but to provide a generic uncertainty estimation method for any algorithm as a post-processing step once the displacement field has been calculated. Very little work has been done in this

B. Wieneke (✉)
LaVision GmbH, Göttingen, Germany
e-mail: bwieneke@lavision.de

R. Prevost
LaVision Inc, Ypsilanti, MI, USA

H. Jin et al. (eds.), *Advancement of Optical Methods in Experimental Mechanics, Volume 3*,
Conference Proceedings of the Society for Experimental Mechanics Series,
DOI 10.1007/978-3-319-00768-7_15,

direction with exception of [6] who derive an estimate for the bias and random noise of DIC displacement measurements in the presence of Gaussian noise.

In [6] the simplified 1D variance $\sigma_x{}^2$ of the displacement in x-direction is derived as a function of the Gaussian noise with standard deviation σ_I divided by the sum of the intensity gradients in a given subset:

$$\sigma_x^2 = \frac{2\sigma_I^2}{\sum \nabla I^2} \tag{15.1}$$

This can be explained by a simple argument: In the most ideal case a single pixel at x and at x + 1 can provide sub-pixel shifts with an accuracy of 1 px/|dI| with dI = I(x + 1) − I(x) gray scale levels between I(x) and I(x + 1). Given a noise level σ_I this increases to $\sqrt{2}\,\sigma_I/\mathrm{dI}$. An ensemble of N pixel in a subset will reduce this error by $\sqrt{N}$ down to $\sqrt{2}\,\sigma_I/\sqrt{N}\,\mathrm{var}(\mathrm{d}I)^{1/2}$ which is Eq. 15.1.

The above procedure usually provides a lower-bound uncertainty estimate since it does not account for various error sources present in typical experiments, e.g. the influence of vibration, illumination changes, or pattern degradation. The noise level σ_I was originally taken as the Gaussian camera noise measured e.g. by recording n images at the same condition. This has been extended in [7] to

$$2\sigma_I^2 = \frac{\sum \left(I_2^*(x) - I_1(x)\right)^2}{N} \tag{15.2}$$

with N = number of pixel in the subset. The term I_2^* (x) = I_2 (x + dx) is image 2 warped back by the measured displacement field dx. So ideally I_2^* and I_1 should be identical, differences indicating camera noise and additional error sources, e.g. failure to measure the correct displacement, pattern degradation or illumination changes. The uncertainty estimation according to Eq. 15.2 will be compared to a more general method presented in the next section for various error sources.

15.2 Uncertainty Estimation by Image Matching

A general uncertainty estimation procedure is presented here which takes as input the two images to be matched and the displacement field computed by the DIC algorithm. First image 2 is dewarped back onto image 1 using the displacement field $u(x)$, i.e.

$$I_2^*(x) = I_2(x+u) \tag{15.3}$$

requiring a sufficiently accurate high-order sub-pixel interpolation scheme. Optionally the intensity of image 1 and 2 can be locally normalized such that $\sum I_1^2 = \sum I_2^{*2} = 1$ summed over the size of a subset or, more accurately, over the size L_{sr} of the effective spatial resolution which needs to be determined for any algorithm and the processing parameter used. For the local subset-based SSD-algorithm this may be close but not exactly the size of a subset. For example, when fitting a higher-order polynomial function to the displacement field within each subset, the effective spatial resolution is typically smaller than the subset size.

For simplicity the following equations are given in a 1D notation in x-direction. In the following the sums are evaluated over all N pixels of a subset, in general over a region of $N = L_{sr}^2$ pixel related to the effective spatial resolution. Instead of a square window the sum can be evaluated over a somewhat larger Gaussian weighted subset, where the width of the 2D-Gaussian weighted curve is again L_{sr}. In general one should use the same square or Gaussian subset as the underlying DIC algorithm (Fig. 15.1).

It is assumed that the DIC algorithm has converged sufficiently such that the residual

$$C(u) = \sum \left(I_1(x) - I_2(x+u)\right)^2 = \sum \left(I_1(x) - I_2^*(x)\right)^2 \tag{15.4}$$

is at a minimum with zero slope dC/du. A small distance $\pm\,\Delta x$ away from u the residual $C(u + \Delta x)$ should therefore be equal to $C(u - \Delta x)$:

$$\Delta C = C(u+\Delta x) - C(u-\Delta x) \cong 0 \tag{15.5}$$

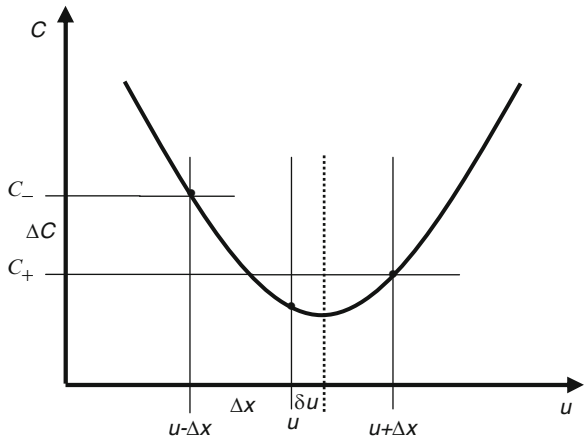

Fig. 15.1 Correlation function $C(u)$

Non-zero ΔC indicates that the algorithm was not able to converge due to some reason, and taking the three points $C(u)$, $C(u-\Delta x)$, and $C(u+\Delta x)$ one could in principle calculate an improved optimal displacement $u + \delta u$ which would be equivalent to an extra iteration step of the DIC algorithm. Fitting a polynomial function of 2nd order through the three points leads to δu given by:

$$\delta u = \frac{\Delta x}{2} \frac{\Delta C}{2C_0 - C_+ - C_-} \tag{15.6}$$

with $C_0 = C(u), C_+ = C(u+\Delta x)$ and $C_- = C(u-\Delta x)$.

Equation 15.5 can be rewritten as:

$$\Delta C = \sum \Delta C_i = \sum \left[(I_1(x) - I_2^*(x+\Delta x))^2 - (I_1(x+\Delta x) - I_2^*(x))^2 \right] \tag{15.7}$$

ignoring small differences from shifting the second term by Δx. Every term ΔC_i is then exactly zero if $I_1 = I_2^*$. When normalizing the intensities and using $\sum I_1^2 = \sum I_2^{*2} = 1$ Eq. 15.7 can be simplified to:

$$\Delta C = \sum \Delta C_i = \sum -2 \left[(I_1(x) I_2^*(x+\Delta x) - I_1(x+\Delta x) I_2^*(x) \right] \tag{15.8}$$

where now every term ΔC_i is zero if $I_1 = aI_2^*$ allowing global intensity changes. Of course, without the factor -2 this is also the correct equation for algorithms maximizing $I_1 I_2^*$.

Due to various error sources I_1 and I_2^* will not match perfectly even for the true displacement u_{true}. Starting at u_{true} the individual ΔC_i would add up in a random walk fashion to a non-zero ΔC which will be optimized away by the DIC algorithm such that ΔC is zero again, leading to an erroneous measured displacement $u_{meas} = u_{true} + \delta u$.

The procedure followed here is that from the given known variability in ΔC_i an estimate of the standard deviation of ΔC is derived which is then related by Eq. 15.6 to an uncertainty estimate of the displacement field. A standard deviation $\sigma_{\Delta C_i}$ of ΔC_i leads according to the standard random walk equation to a standard deviation $\sigma_{\Delta C}$ of:

$$\sigma_{\Delta C} = \sqrt{N}\, \sigma_{\Delta C_i} = \sqrt{N} \left(\frac{\sum \Delta C_i^2}{N} \right)^{\frac{1}{2}} = \left(\sum \Delta C_i^2 \right)^{\frac{1}{2}} \tag{15.9}$$

The requirements are that the ΔC_i have a zero mean ($\sum \Delta C_i = 0$) and are independent random events, which is only true for (camera-)noise sources where the noise of each pixel is independent of its neighbors. It is not required that the ΔC_i conform to a normal distribution, but for accurate statistics many small values of ΔC_i should add up to ΔC.

Using Eq. 15.6 and the fact of a linear relationship between δu and ΔC finally leads to uncertainty estimation of the displacement field of:

$$\sigma_u = \frac{\Delta x}{2} \frac{\sigma_{\Delta C}}{2C_0 - C_+ - C_-} = \frac{\Delta x}{2} \frac{\left(\sum \Delta C_i^2 \right)^{\frac{1}{2}}}{2C_0 - C_+ - C_-} \tag{15.10}$$

There are a number of error sources in DIC where the noise is more related to a spatial scale similar to the typical size of pattern elements of a few pixel. This relates e.g. to different types of pattern degradation due to fatigue or high tension rates, changes in the intensity of each small tilted surface patch (= surface roughness) when viewed from different angles or spray dots not deforming the same way as the underlying surface as discussed by [8]. The relevant spatial scale is the typical speckle pattern size d_p, which can be estimated from the width d_{corr} of the cross-correlation function by a 3-point 1D-Gauss-fit:

$$d_{corr} = \sqrt{2} d_p = 2 \left(2log\left(\sum I_1(x) I_2^*(x) \right) - log\left(\sum I_1(x+1) I_2^*(x) \right) - log\left(\sum I_1(x) I_2^*(x+1) \right) \right)^{-\frac{1}{2}} \tag{15.11}$$

Fortunately Eq. 15.10 can be easily modified to accommodate to a large extent such pattern degradation effects by first convoluting the field ΔC_i with an nxn smoothing filter, where for simplicity a simple top-hat filter is used with n being the closest integer to d_{corr}:

$$\Delta C_i^{'} = S_{nxn} \otimes \Delta C_i \tag{15.12}$$

followed by multiplying Eq. 15.10 by n on the right side:

$$\sigma_u = \frac{\Delta x}{2} \frac{n\ \sigma_{\Delta C}}{2C_0 - C_+ - C_-} = \frac{\Delta x}{2} \frac{n \left(\sum \Delta C_i^{'2} \right)^{\frac{1}{2}}}{2C_0 - C_+ - C_-} \tag{15.13}$$

This effectively reduces the random walk statistics to N/n^2 independent events, which is the number of speckle pattern elements in a subset. This uncertainty estimation is still correct for pixel-independent (camera-)noise, since the smoothing reduces the standard deviation $\sigma_{\Delta C_i}$ by $\sqrt{n \times n}$ which is then compensated by the multiplication with n.

The choice of Δx in Eq. 15.5 and following is guided by the requirement that it should capture well the form of the function to be minimized, where the width around the minimum is close to the typical size of pattern elements. Therefore Δx must be smaller than the pattern size, but well larger than the computed σ_u. So a natural choice is $\Delta x = 1$ pixel which also requires only a single dewarped function $I_2^*(x)$ instead of three.

In summary, the complete procedure to compute the estimated random noise is given by the following steps:

- Image 2 is dewarped back onto I_1 using the displacement field u (Eq. 15.3). It is usually faster to do this once for the complete image than separately for all (overlapping) subsets.

For each subset:

- Compute the summed quantities C_0, C_+ and C_- by Eq. 15.4.
- Compute the typical speckle pattern size n by cross-correlation by Eq. 15.11.
- Compute the field ΔC_i by Eq. 15.7 and smooth it by an nxn top-hat filter.
- Compute the uncertainty estimation σ_u by Eq. 15.13.

It is customary to display the uncertainty estimation as a 95 %-confidence level [9], which corresponds to about $\pm$ 2 σ_u. The above one-dimensional derivation can be done independently for the x-and y-direction. Further error propagation in stereo DIC systems including calibration errors as investigated in [10] or for computing strain values are beyond the scope of this paper. The discussion here is restricted to 2D displacement errors under various error sources.

15.3 Synthetic Data

The procedure has been tested first with synthetically generated images varying various parameter such as noise level, pattern size and density, sub-pixel displacement, strain rate and local intensity change of speckle pattern elements. The image size is 1k $\times$ 1k pixel. If not mentioned otherwise the pattern is generated as overlapping Gaussian blobs of a width of 3 pixel covering densely the complete image and a constant displacement of 0.3 pixel in x and 0.6 pixel in y-direction.

Processing is done by LaVision DaVis 8.1 using the SSD-method with local intensity normalization, bi-spline-6 sub-pixel interpolation and Gaussian weighted subsets of a default size of 15 $\times$ 15 pixel with 8 pixel vector spacing. The true

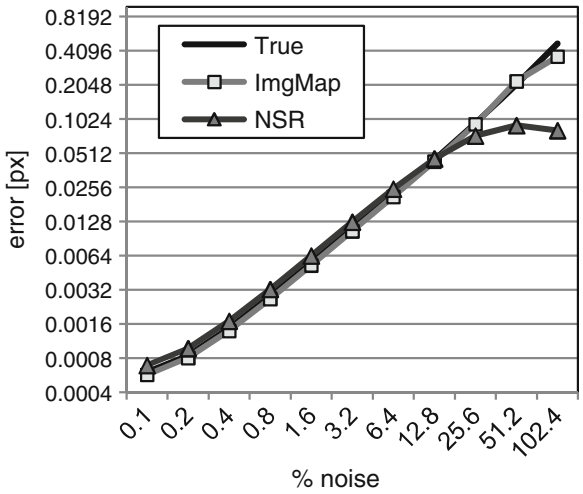

Fig. 15.2 Error as a function of Gaussian pixel noise

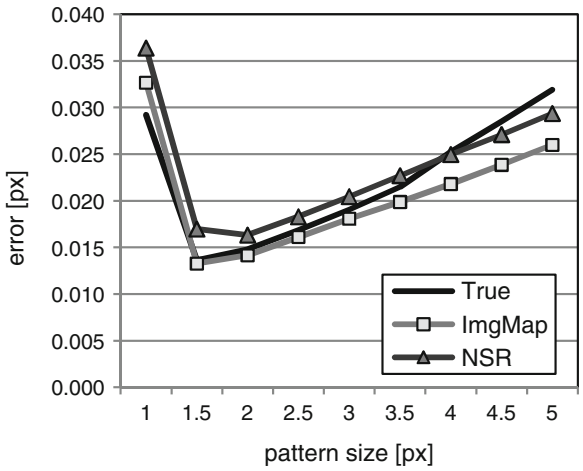

Fig. 15.3 Error as a function of speckle pattern size

displacement error is calculated by subtracting the known true displacement field from the measured one and averaging the total error (bias plus random) over the complete image. The noise-to-signal-ratio uncertainty estimation method from [6, 7] ('NSR') is compared to the new image mapping method ('ImgMap'), both computed on a one-sigma level.

Adding Gaussian noise to each pixel in both images leads to mostly linear relationship between the true error and the noise level as shown in Fig. 15.2, which is well captured by both NSR and ImgMap-method. Only for high noise levels the NSR-method levels off in agreement with Fig. 15.7 in [7]. This is because the sum of gradients in the denominator in Eq. 15.1 then not only contains useful information but is artificially increased by the added noise.

In the following some Gaussian pixel noise is always added to the images simulating real experimental conditions. Camera noise is usually dominated by the background noise level of typ. 5–20 e- together with the photon or shot noise proportional to the sqrt of the number of photon-electrons. 12-bit images are generated with a dynamic range of about 500–1,000 counts assuming a typical camera with a conversion rate of 4 e-/count – relating to a full-well capacity of 16 ke- – together with 16 e-background noise.

Varying the speckle pattern size shows a reasonable agreement between the average true and estimated error for both methods for speckle sizes above about 1.5 pixel (Fig. 15.3). For speckle sizes of <1 pixel the random and bias errors increase drastically ('pixel locking') due to unrecoverable loss of information. Errors for large speckle sizes are slightly underestimated.

Increasing the speckle pattern density increases the information content and therefore decreases the noise level. Both methods accurately capture this behavior as shown for subset sizes of 15 $\times$ 15 and 31 $\times$ 31 pixel (Fig. 15.4). Only for small subset sizes of 15 $\times$ 15 pixel and low pattern density there is a deviation due to subsets not even containing a single speckle pattern and both DIC computation as well as error estimation simply fail.

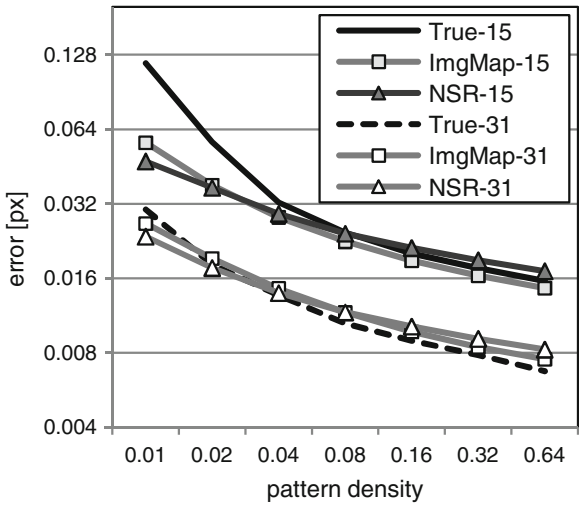

Fig. 15.4 Error as a function of speckle pattern density

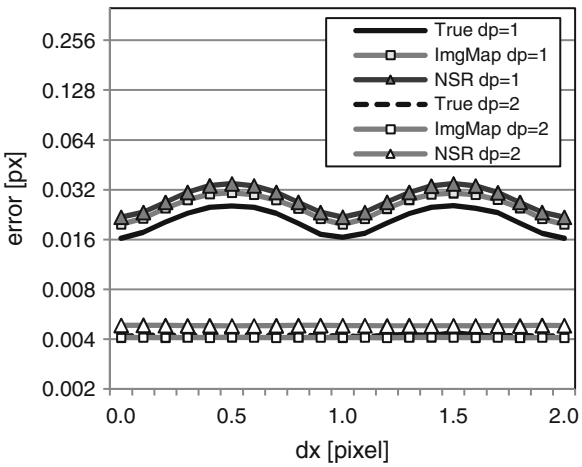

Fig. 15.5 Error as a function of displacement

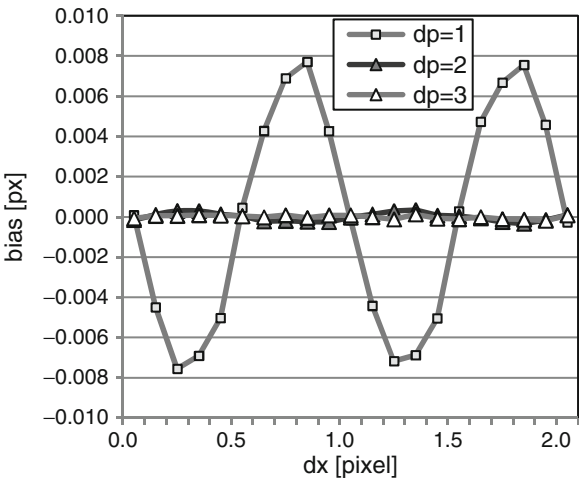

Fig. 15.6 Bias as a function of displacement

Figure 15.5 shows the true error and uncertainty estimation as a function of fractional displacement. For pattern sizes of 2 pixel and larger there is no dependence of the error on the sub-pixel displacement value and virtually no bias (Fig. 15.6). Only for pattern size of 1 pixel (and below) there is, as expected, noticeable bias and random error. Both uncertainty methods provide accurate estimation of the true error.

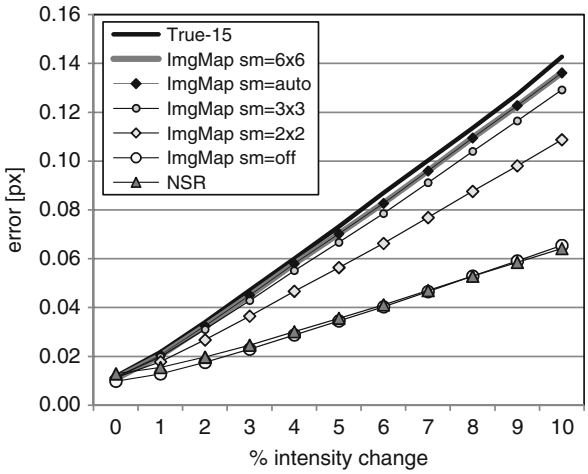

Fig. 15.7 Error as a function of individual random intensity change of speckle pattern elements for 15 × 15 subsets

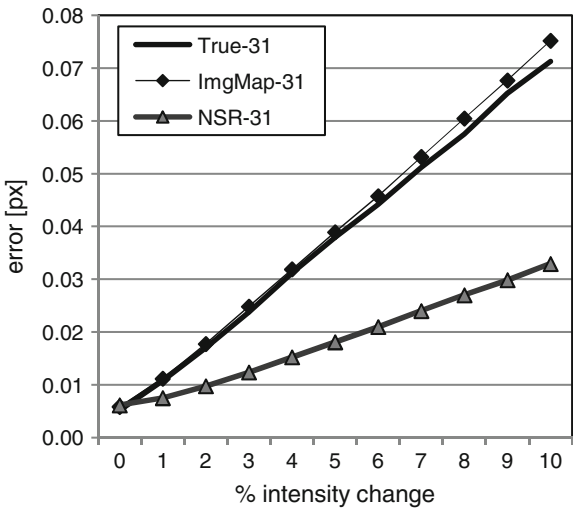

Fig. 15.8 Error as a function of individual random intensity change of speckle pattern elements for 31 × 31 subsets

Next the pattern intensity has been changed randomly on a local scale for each generated Gaussian blob by 0 %–10 %. This pattern degeneration is often encountered experimentally due e.g. to small surface patches changing intensity level e.g. when viewed or illuminated from another angle. In Fig. 15.7 is shown for 15 × 15 pixel subset sizes various curves corresponding to various level of smoothing according to Eqs. 15.12 and 15.13. With smoothing turned off the ImgMap as well as the NSR–method can't capture the true noise level. Increasing the smoothing improves the results until good agreement is reached at 4 × 4 which is the value computed automatically by the ImgMap-method for a pattern size of 3 pixel ($3\sqrt{2} \cong 4$). Further smoothing does not provide any improvement. Figure 15.8 shows the comparison for 31 × 31 subsets where again the NSR method fails to capture the true error. As expected, for 31 × 31 the overall error level is reduced by a factor of 2 due to four times more pixel and information content.

Finally images have been generated with 0–10 % shear in ε_{yx} (Fig. 15.9) where the second image is generated by deforming the first one using a bi-spline-6 sub-pixel interpolator instead of plotting undeformed Gauss blobs. The level of error is well captured by both methods but for higher shear rates the ImgMap-method is slightly low. As experimental data shows a variety of surface pattern changes during shear or tension such synthetic data can only provide limited information about the performance of uncertainty estimators.

Assuming a sufficient convergence of the DIC algorithm the bias error can't be deduced by the ImgMap-method. As done in [6] it can only be estimated for a given pattern size, fractional displacement value and noise level by a-priory Monte-Carlo simulations using a particular sub-pixel interpolation method. For all synthetic data used here the measured bias errors have been much less than the random error components except for very small pattern sizes. Also in all cases the x- and y-components of the random error as calculated by the ImgMap-method are very similar, but further investigation is needed to check for covariance terms.

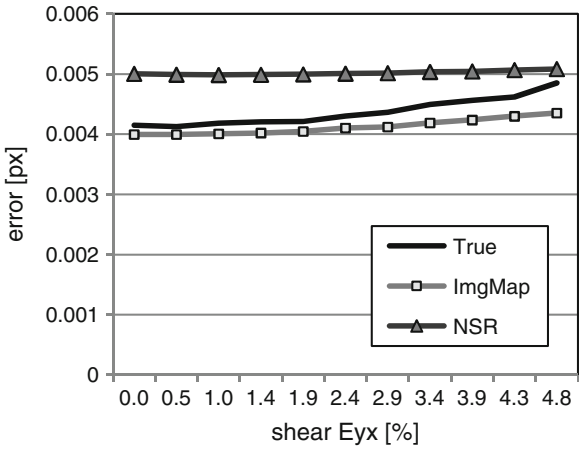

Fig. 15.9 Error as a function of shear rate

15.3.1 Variability of the Uncertainty Estimation

It is important to notice that the uncertainty estimation field will show quite some variability in the order of e.g. 5–20 % even with perfect synthetic data with constant displacement field and same parameters everywhere. This is first of all due to the variability of the random pattern with more or less pattern elements and local contrast in each subset together with more or less random noise. But additionally there is the intrinsic random character of the uncertainty estimation due to the random walk process in Eq. 15.9. It can't be avoided that a computed standard deviation $\sigma_{\Delta C}$ has a one-sigma-variability in the range of $\left(1 \pm 1 \,/\, \sqrt{2N}\right)$ given N independent events, which is e.g. for 10 speckle patterns in a subset already ± 22 %.

15.4 Experimental Data

A few experiments have been performed to validate the uncertainty estimation method in different circumstances. A 12-bit low-noise 2 MPx-camera has been used with a 25 mm focal length objective at F# of 8. Processing is done in the same way as for the synthetic data. Not knowing the true error of the displacement this is estimated by fitting a local 2nd-order polynomial function to e.g. a 9×9 vector neighborhood and subtracting it from the measured data. At first a flat undeformed plate is used, where the displacement field due to perspective distortion is highly smooth such that the residual accurately reflects the random noise components. Bias terms can't be measured and the method fails for strong deformations on a local scale as discussed later. But in many circumstances this polynomial regression method is also a very simple and valuable tool for estimating the measurement uncertainty and, by the way, used to compute smooth strain field.

For smooth displacement fields a large regression kernel is recommended. On the smallest possible scale a 3×3 vector neighborhood can be taken, where a zero-order averaging would be done over the eight neighbors which should be independent to the central vector, i.e. for a 15×15 subset size and vector spacing of 8 pixel the neighbors should be taken at ± 2 vectors away. Subtracting the average from the central vector provides the random noise of the center vector but slightly increased since the average of the eight neighbors still has some noise component. So the central vector needs to be divided by $\sqrt{9/8}$ to provide a realistic estimate of the true error.

In the first experiment pattern degradation due to viewing angle changes has been investigated using a black-on-white spray painted target with optimal pattern size of 2–3 pixel. The target is rotated from 0° to ±40° and opposite images at ±n degrees are correlated which simulates a Stereo DIC system with varying angle between cameras. The cross-correlation between the two cameras is needed at least once to measure the shape of the object and any errors enter directly in subsequent 3D-deformation and strain measurements. Indeed this might be the dominant source of error in many Stereo-DIC experiments. As shown in Fig. 15.10 the noise increases with camera angle due to visual changes in the surface pattern when viewed from different directions. The ImgMap-method agrees well with 9×9 polynomial regression method ('REF') while the NSR-method is slightly higher, all processed with 31×31 subsets.

Processing the same images by correlating images at +n degrees to the image at zero degree simulates some idealized compression of the object in x-direction. This is shown in Fig. 15.11 where again the REF and ImgMap-methods agree well.

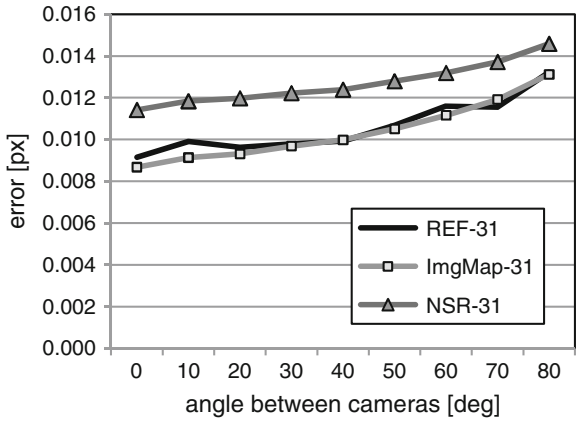

Fig. 15.10 Error as a function of camera angle

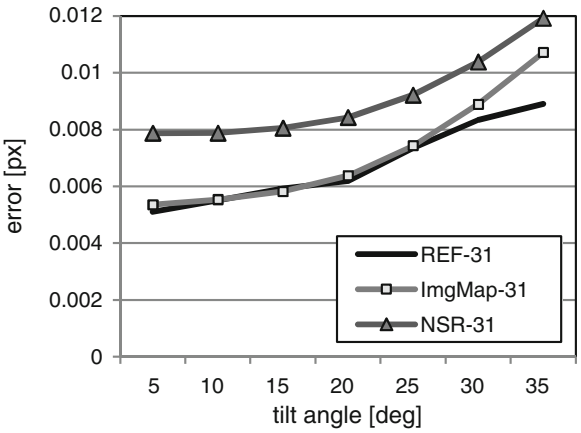

Fig. 15.11 Error as a function of tilt angle

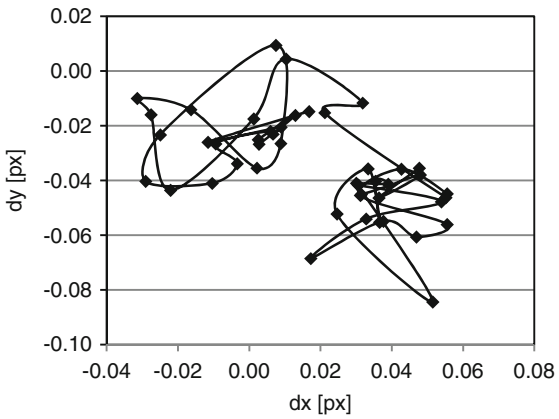

Fig. 15.12 Displacement offset for moving spot light

In the next experiment the plate position has been fixed and is illuminated by a spot light which has been moved around simulating the influence of changing (background) illumination. The effect is quite dramatic with virtual measured plate movements up to ± 0.05 pixel averaged over about 1/3rd of the displacement field in the center of the image (Fig. 15.12). The random error component is of the same order as the bias as shown in Fig. 15.13. The ImgMap-method perfectly agrees with the supposedly true random error measured by polynomial regression, while the NSR-method is up to a factor 2 less.

If the global offset would be constant over the complete image it would not influence any strain values and the strain error would be accurately estimated by the ImgMap method. In the experiment here the displacement field has a gradient of up to

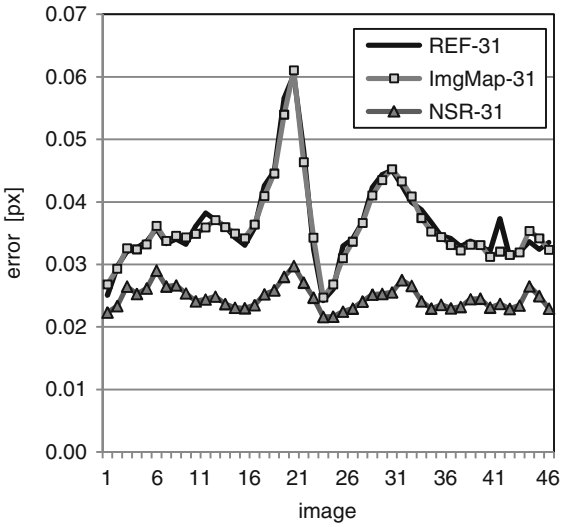

Fig. 15.13 Error for moving spot light

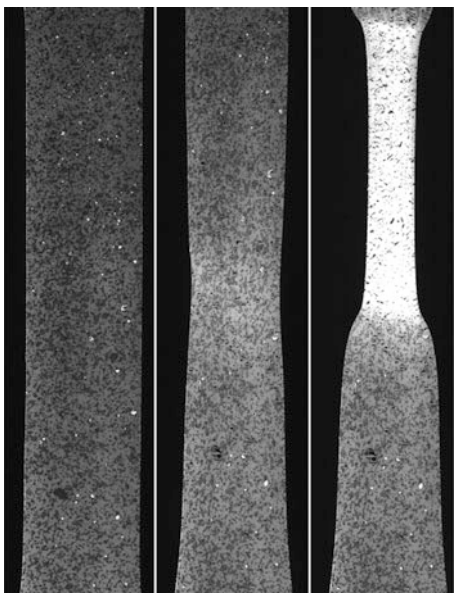

Fig. 15.14 Plastic sample tension test

0.05 px over 500 pixel length which would lead to global strain offsets of up to 100 μS still less than the random strain error which is on the smallest scale about 0.05px/32px = 1,500 μS or when filtered e.g. over a region of 9 × 9 vectors of about 200–400 μS.

In the last experiment a typical tension test of a plastic specimen with strain rates up to 400 % has been performed, where necking occurs at about 80 % strain (middle of Fig. 15.14). It is difficult to determine a ground truth for high strain rates as the surface pattern changes considerably not only due to the underlying deformation field but also due to spray dots disrupting and material brightness changes. In the more homogeneous region indicated in Fig. 15.15 the ImgMap method shows good agreement with the regression filter – considered to be fairly accurate – while the NSR-method differs strongly. In the high-strain region in the necking area there was no consistent comparison possible with deviations by a factor of 2–4 between the methods (Fig. 15.16).

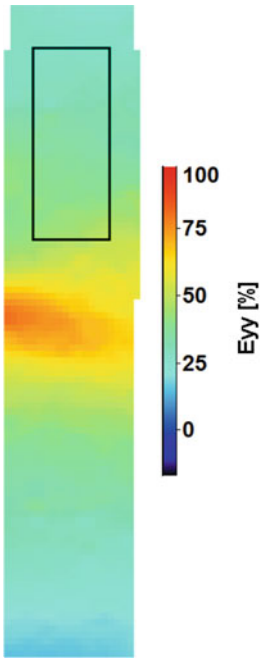

Fig. 15.15 Strain field ε_{yy} at onset of necking

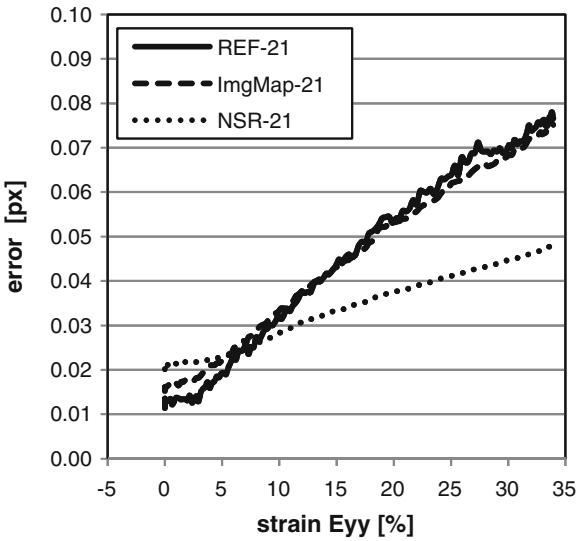

Fig. 15.16 Error versus strain ε_{yy} in the rectangular region defined in Fig. 15.15 up to onset of necking

15.5 Conclusion

The local measurement uncertainty of a DIC displacement field is estimated based on a post-processing of the differences between the two images to be matched. The standard deviation of the pixel-wise contributions of intensity differences to the shape of the correlation function is computed within a local region. This is related to the random uncertainty of the displacement vectors. The size of the local region is given by the spatial resolution of the DIC algorithm, usually close to the subset size. This procedure has been tested with synthetic data varying random Gaussian noise, speckle pattern size and density, fractional displacement, strain rates and local intensity variations. The new method shows very good agreement with the true random error especially for the case of locally varying speckle elements in contrast to a previously suggested estimation method based on a simple noise-to-signal ratio [6] which fails for such type of image degradation. The validity of the new approach is confirmed in experiments varying camera viewing and illumination angles and for the case of strong image degradation due to high tension.

References

1. Medan Y, Yair E, Chazan D (1991) Super resolution pitch determination of speech signals. IEEE Trans Signal Process 39(1):40–48
2. Horn BK, Schunck BG (1981) Determining optical flow. Artif Intell 17:185–203
3. Lucas BD, Kanade T (1987) An iterative image registration technique with an application to stereo vision, image understanding workshop, DARPA, pp 121–130
4. Hild F, Roux S (2006) Digital image correlation: from displacement measurement to identification of elastic properties – a review. Strain 42 (2):69–80
5. Sutton MA, Orteu JJ, Schreier HW (2009) Image correlation for shape, motion and deformation measurements. Springer, New York
6. Wang YQ, Sutton MA, Bruck HA, Schreier HW (2009) Quantitative error assessment in pattern matching: effects of intensity pattern noise, interpolation, strain and image contrast on motion measurements. Strain 45:160–178
7. Ke X-D, Schreier HW, Sutton MA, Wang YQ (2011) Error assessment in stereo-based deformation measurements, part II: experimental validation of uncertainty and bias estimates. Exp Mech 51:423–441
8. Barranger Y, Doumalin P, Dupre JC, Germaneau A (2012) Strain measurement by digital image correlation: influence of two types of speckle patterns made from rigid or deformable marks. Strain 48:357–365
9. Coleman HW, Steele WG (2009) Experimentation, validation, and uncertainty analysis for engineers, 3rd edn. Wiley, Hoboken
10. Wang Y-Q, Sutton MA, Ke X-D, Schreier HW, Reu PL, Miller TJ (2011) On error assessment in stereo-based deformation measurements, part I: theoretical developments for quantitative estimates. Exp Mech 51:405–422

Chapter 16
Indicating DIC Potential Correlation Errors with Optical Modulation Transfer Function

Chi-Hung Hwang, Wei-Chung Wang, Yung-Hsiang Chen, Te-Heng Hung, and Jia-He Chen

Abstract Attempt to indicate the potential correlation errors of DIC method, the modulation transfer function (MTF) test method is proposed in this paper. An Alumnus plate with random pattern on the surface was moved by a linear stage and commercial DIC software was used to calculate the displacement filed while the reference image was taken at focus and the second image set was taken at different field of view. The calculated displacement fields are corrected with a linear function to eliminate unexpected displacement gradient. Meanwhile, the MTF values are also calculated with the same random pattern images. Finally, the MTF values and the slop coefficient of the linear fitting function are related, by this way, once the camera MTFs are known then the possible displacement error can be estimated.

Keywords Digital image correlation • Modulation transfer function • Displacement error

16.1 Introduction

Digital image correlation method (DIC) is an image based optical strain measurement method; in principle, the displacement and strain fields up to sub-pixel level can be calculated by correlating two images captured at different status. DIC has been proposed in early 1980s [1, 2], since that time, the images can be obtained with different "imaging" devices, such as cameras, microscope, SEM, AFM and many others for different object scales [3–7]. Other than measurement scales, DIC method is also known as 2D DIC and 3D DIC methods [8–10]. For 2D DIC method, images obtained from fixed viewing angle, always normal to the object, are used for correlation analysis. For 3D DIC case, images obtained at fixed observation angle cannot use for depth determination. By integrating photogram into DIC method, the applications of DIC are expanded form 2D DIC method into 3D-DIC method and can apply for 3D displacement and strain fields measurement. In recent years many approaches have been developed to enhance the spatial resolution and speed-up the strain computing, such as various sub-pixel registration algorithms and fast DIC method [11, 12]. Not only providing whole field and non-contact strain measurement capabilities, DIC method can be easily implemented at different imaging platform that makes DIC method has been widely used for variety deformation measurements, such as surface strain of amorphous glassy polymer, soft materials and even the deformation of thin plates subject to explosive blast [13, 14].

Considering the DIC method is a potential tool for long term displacement monitoring; however, in this application scenario, tracking displacement path is difficult. While the displacement path is unknown, the cross-correlations might be ill posed because the reference image and the second image set might be obtained from different viewing area. Modulation transfer function (MTF) is an optical performance parameter which can be evaluated with sinusoidal or random patterns [15–18]. Poor images are always happened while the images are taken out-of-focus or around field boundary of the lens. To evaluate the relations between DIC method and images taken from different field of view, a commercial DIC system and associated software are used to construct the displacement error map while the reference image was taken at focus and the

C.-H. Hwang (✉) • Y.-H. Chen
Instrument Technology Research Center, National Atmospheric Research Laboratory, Hsinchu 30073, Taiwan ROC
e-mail: chhwang@itrc.narl.org.tw

W.-C. Wang • T.-H. Hung • J.-H. Chen
Department of Power Mechanical Engineering, National Tsing Hua University, Hsinchu 30013, Taiwan ROC

H. Jin et al. (eds.), *Advancement of Optical Methods in Experimental Mechanics, Volume 3*,
Conference Proceedings of the Society for Experimental Mechanics Series,
DOI 10.1007/978-3-319-00768-7_16,

second image set was taken at three assigned locations. Meanwhile, all the captured images were analysis with Fourier transform to obtain the corresponding MTF. The relation between MTF and DIC analysis errors were determined, by this way, once the camera MTFs are known then the possible displacement error can be estimated.

16.2 Principles

16.2.1 Digital Image Correlation Method

The DIC method utilizes the surface pattern on the objective target; deformation of assigned points can be determined by searching the most-likely sub-image from the corresponding sub-images. As shown in Fig. 16.1, there is a sub-image centered at point $P(X_0, Y_0)$ in the reference image, the matching algorithms is to search the corresponding sub-image of the deformed image which center is point $P'(X'_0, Y'_0)$. Algorithms, such as the predefined cross-correlation and the sum of squared differences criterion, can be used to calculate the similarity between the sub-image in reference image and possible mapping sub-image in the deformed image [19].

16.2.2 Modulation Transfer Function

The modulation transfer function (MTF) is a parameter about the image visibilities of an imaging system can perform with respect to different spatial frequencies, that is, the ability to identify two points separated by different distances. For an optical lens the associated MTF is always called as optical MTF, MTF also can be used to evaluate performance of an imaging system, in such the case, the MTF is called as image MTF. Based on the definition, the maximum MTF value is equal to the diffraction limit of an optical system. In fact, MTF is a spatial frequency, ξ, determined parameter and can be defined as

$$MTF(\xi) = \frac{M_{image}(\xi)}{M_{object}(\xi)}; \tag{16.1}$$

where

$$M(\xi) = \frac{E_{\max} - E_{\min}}{E_{\max} + E_{\min}};$$

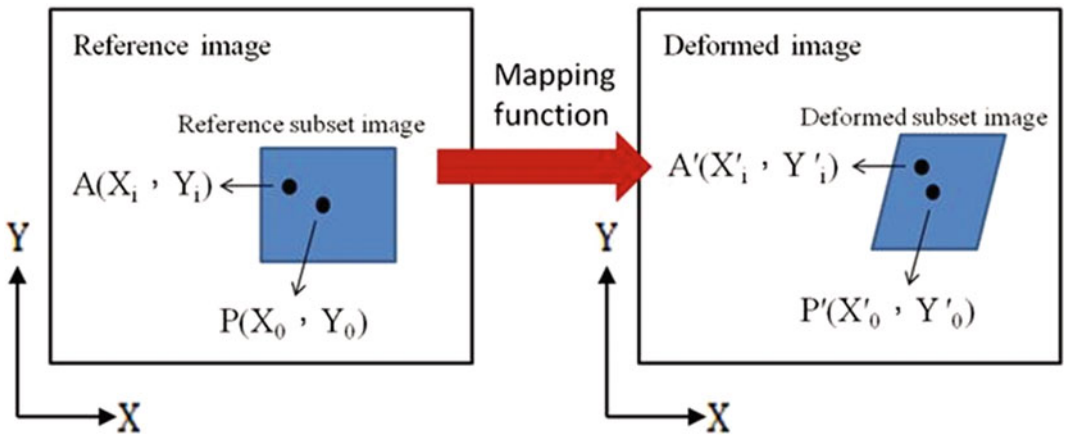

Fig. 16.1 By searching the most-likely sub-image, digital image method can determine the displacement field and the strain filed with two images obtained at different status

E_{max} and E_{min} are the maximum and minimum irradiances respectively. MTF at specified spatial frequency can be determined with a sinusoid repeated pattern target of the same spatial frequency.

16.2.3 Evaluating MTF with Random Speckle Pattern

In practice, MTF is a kind of system transfer function; that means, all the methods used for system identification can be used to evaluate MTF. Similar to system characteristic determination method, MTF can be identified through output/input ratio. For spatial domain, as defined in Eq. 16.1, MTF at spatial frequency, ξ, along a giving axis can be determined with a sinusoid pattern rotated at associated angle. MTF can also be determined with spatial-frequency domain method with the following relations;

$$\left|P_{image}(\xi)\right| = |MTF(\xi)|^2 \left|P_{object}(\xi)\right|; \tag{16.2}$$

where P_{image} and P_{object} is the power spectrum density(PSD) of image and object. Equation 16.2 indicates there patterns can be used for MTF determination; for example, a slit pattern is a one-dimensional plus function which can be determine one-dimensional MTF over wide spatial frequency range; a point pattern which can be treated as a two-dimensional exciting function and can be used for two-dimensional MTF determination. The target with random pattern can be used for two-dimensional MTF measurements over spatial-frequency range limited by the reciprocal of double pixel size. Generally, a typical imaging lens, MTF value along line-of-sight of the lens is always higher than the other field of view and become worse around the edge of the lens.

16.3 Experimental Setup

In this paper, to identify the affection of MTF on DIC measurement results, a 2D-DIC measurement system with single camera is implemented as the test platform, and an alumnus square plate is random patterned on the surface with standard surface preparing process [20]. The camera line of view is aligned perpendicular to the out normal direction of the specimen surface. The specimen derived by computer controlled step-motors to perform in-plan displacements along X-axis. Serial images are then taken at positions, best focus and points 2.5, 5.0 and 7.5 mm right to the best focus, for future analysis. The main parameters of the system are tabulated in Table 16.1 including CCD Camera, lens, linear stage, and DIC software. In this test platform, the CCD pixel size is 4.4 × 4.4 μm and the corresponding Nyquist frequency is about 110 lp/mm; that means, the CCD with a perfect lens is good to image target with 110 line pairs in a millimeter at focus. Besides, to avoid possible lighting problem, a linear light source is fixed on a frame and moved together with the specimen; the images are captured with the same light distribution on the specimen surface (Fig. 16.2).

Table 16.1 System specifications

Specifications	Descriptions
CCD camera	Marlin F-201B CCD camera
	Resolution: ,1,628 × 1,236 pixels. Cell size: 4.4 μm. Max frame rate at full resolution: 12 fps. A/D: 12 bit
Lens	Schneider Kreuznach Xenoplan 1.9/35, 2/3″ 35 mm lens, F#1.9
Linear stage	T-LSM50A – Zaber Technologies Inc.
	Travel Range: 50.8 mm. Accuracy: +/−8 μm. Repeatability: < 1 μm
DIC software	Vic-2D 2007, correlated solutions, Inc
Specimen	Alumnus plate, dimension is 51 × 51 mm

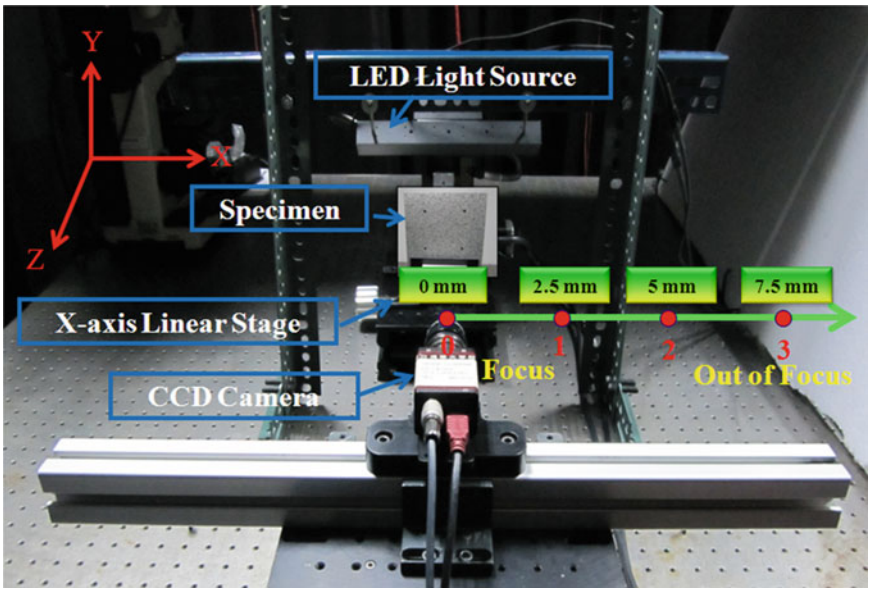

Fig. 16.2 Experimental setup for DIC and associated MTF test

16.4 Results and Discussions

16.4.1 Displacement Measurement Results

In this study, DIC displacement measurement errors are considered to compose by two parts, the first one is the DIC software introduced errors and the image quality introduced errors. To evaluate the software introduced displacement errors, images are taken continuously and then analyzed with Vic-2D. The typical contour image is shown in Fig. 16.3, Fig. 16.3a is the 2D color displacement map and Fig. 16.3b is the associated displacement contours are plot with 100 equal-space sampling points from left to right across the area defined by four marked cross. For future discussion, the specimen coordinate is defined in Fig. 16.3a, the origin is on the left edge of defined area. The measurement repeated 3 times and the numerical result shows the "pseudo-displacement" introduced by the software Vic-2D combined with surface illumination disturbance is about 0.46 μm in this study.

Then specimen is moved to new positions with a linear motor, there are 2.5, 5.0 and 7.5 mm on right side with respect to "focus position" as defined in Fig. 16.2. Series images are then captured and analysis by DIC to calculate the displacements. Figure 16.4 shows all displacement fields calculated by DIC software. Inspecting Fig. 16.4(b-1), (c-1) and (d-1), all the surface plots indicated the calculated displacement fields are not uniform but with displacement gradients. As plotted in Fig. 16.4(b-2), (c-2) and (d-2), all the displacement are increasing from left to right. Figure 16.5 is a typical case which the specimen is moved 2.5 mm. The displacement data are scatted plotted and fitted with a linear function, as shown in Fig. 16.5a. The fitting function is evaluated to be $U = 2.0 \times 10^{-4}x + 2.490$; where U (in millimeter) is displacement calculated by Vic-2D and x (in millimeter) is the specimen coordinate. The displacement field is then corrected with the fitting function, as shown in Fig. 16.5b, the displacement gradient is eliminated. The fitting functions are listed in Table 16.2; in this study, the slop coefficients are increasing as the specimen moved away from $X = 0$. The displacement fields are then corrected with the linear function and the results are listed in Table 16.3. Table 16.3 shows all the averaged displacements are smaller than the nominal displacement controlled and defined by a linear motor. Table 16.3 also indicates the standard derivation can be tremendously improved by eliminating the displacement gradient with fitting function, the standard derivation can reduced from μm to sub-μm level.

16.4.2 Experiments of Modulation Transfer Function

The random pattern images captured for DIC analysis are also used for MTF calculation. The whole process is similar to lens test. While the specimen is placed at $X = 0$ mm which is equivalent to the on-axis MTF test and the maximum MTF is always obtained. While the specimen is moved to 2.5, 5.0, and 7.5 mm on X-axis, those measurements are similar to off-axis

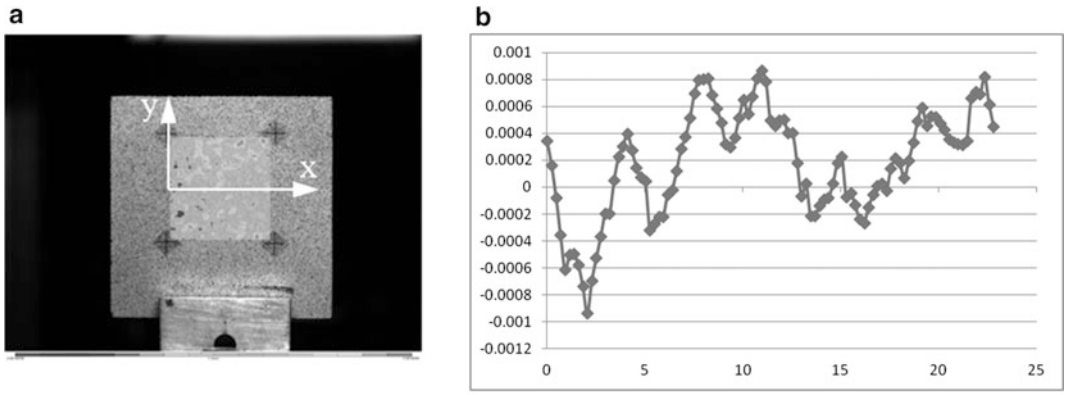

Fig. 16.3 Contour images of DIC measurement results without real displacement at different time (**a**) 2D displacement map with defined specimen coordinate (**b**) Cross-section plot

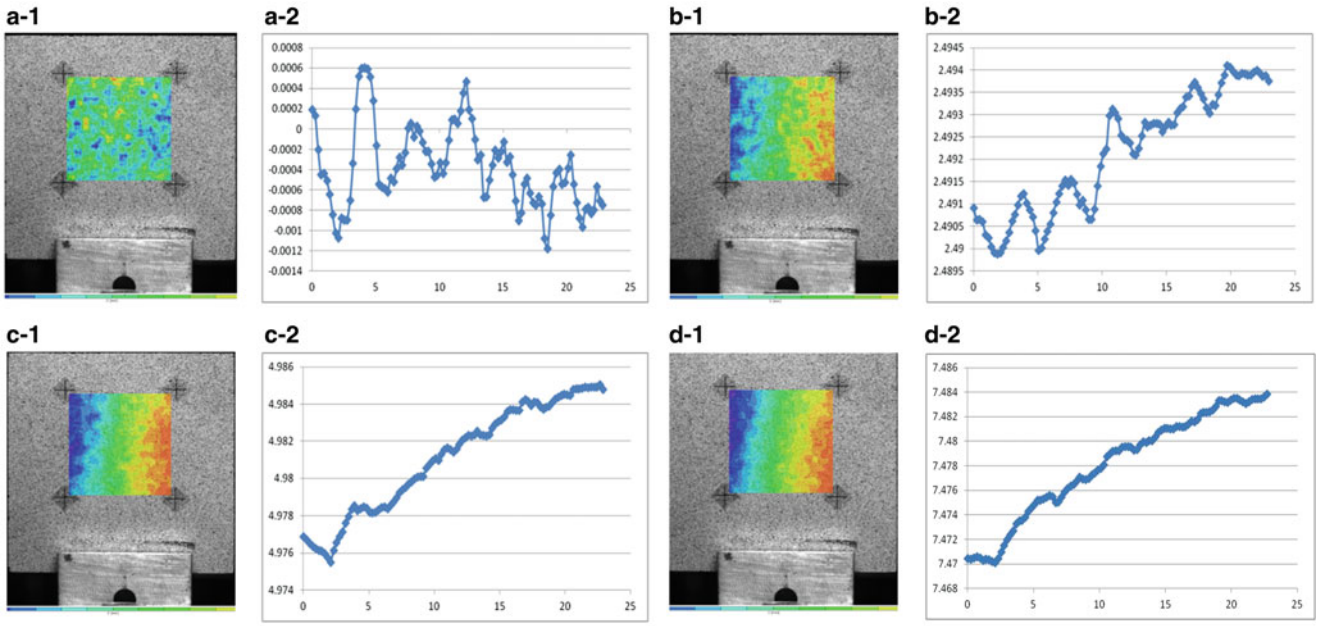

Fig. 16.4 Contour images of DIC displacement error in X axis (**a-1**) Surface plot @ u = 0 mm (**a-2**) Cross-section Plot @ u = 0 mm (**b-1**) Surface plot @u = 2.5 mm (**b-2**) Cross-section Plot @ u = 2.5 mm (**c-1**) Surface plot @ u = 5.0 mm (**c-2**) Cross-section Plot @ u = 0 mm (**d-1**) Surface plot @ u = 7.5 mm (**d-2**) Cross-section Plot @ u = 7.5 mm

(off the optical axis) MTF measurement. In general, off-axis MTFs are always lower than on-axis MTF. As shown in Fig. 16.6, below the Nyquist frequency (or named as cut-off frequency for CCD camera) defined by the pixel size of the CCD chip, the MTF is highest at X = 0 mm and the MTF is degraded as X increase from 0 to 7.5 mm. In previous discussion, the displacement gradients are available in all cases but X = 0. The calculated MTFs at Nyquist frequency (~110 lp/mm, in this study) are plot with respect to the coefficients of slop terms; as shown in Fig. 16.7, as MTF values is decrease the coefficient of slop term is increase. The MTFs-coefficient curve is fitted and parameters can be related by the equation, Coefficient $= 2.27 \times \text{MTF}^2 - 3.79 \times \text{MTF} + 1.58$, in this study.

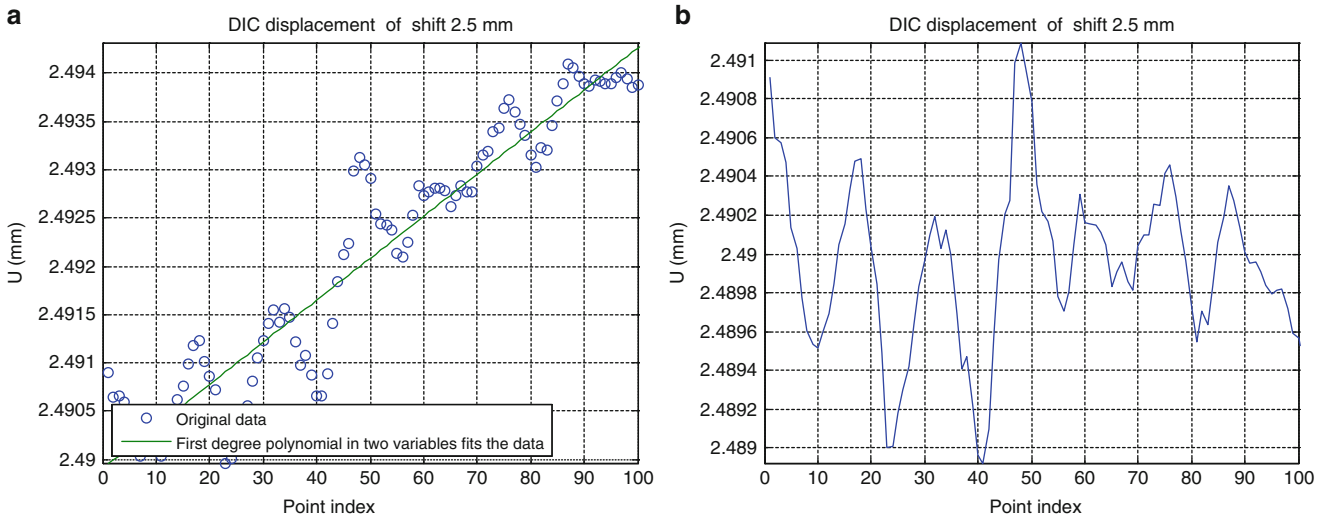

Fig. 16.5 Correcting DIC displacement results with a linear function (**a**) Fitting the scatting displacement data with linear function (**b**)The displacement plot across the specimen corrected

Table 16.2 Fitting function

Displacement (mm)	Fitting function (U, × in mm)	R2
2.5	$U = 2 \times 10^{-4}x + 2.490$	0.8982
5.0	$U = 4 \times 10^{-4}x + 4.976$	0.9674
7.5	$U = 6 \times 10^{-4}x + 7.471$	0.9645

Table 16.3 Displacement measured by 2D-DIC with a signal camera

Displacement		0.0 mm (μm)	2.5 mm	5.0 mm	7.5 mm
Averaged		−0.375	2.490 mm	4.976 mm	7.471 mm
Standard deviation	Before slop correction	0.408	1.346 μm	2.928 μm	4.296 μm
	After slop correction	0.408	0.429 μm	0.529 μm	0.809 μm

16.5 Conclusions

In this paper, DIC method is implemented to calculated displacement field with series images which are taken at position X = 0, 2.5, 5.0 and 7.5 mm. All the averaged displacements are smaller than the nominal displacement controlled and defined by a linear motor. The specimen is moved without external stress, the calculated displacement fields are not uniform that indicates errors are exist. The displacement field is corrected with linear fitting function and the displacement gradient is eliminated successfully and the standard derivation can be tremendously improved by eliminating the displacement gradient with fitting function, the standard derivation can reduced from μm to sub-μm level. Then the MTFs-coefficient curve is fitted and parameters can be related by the equation, $\text{Coefficient} = 2.27 \times \text{MTF}^2 - 3.79 \times \text{MTF} + 1.58$. Employing the developed MTF-Coefficient relation, once the camera MTFs are known the possible displacement error can be estimated and corrected to eliminate the "unexpected" displacement gradient.

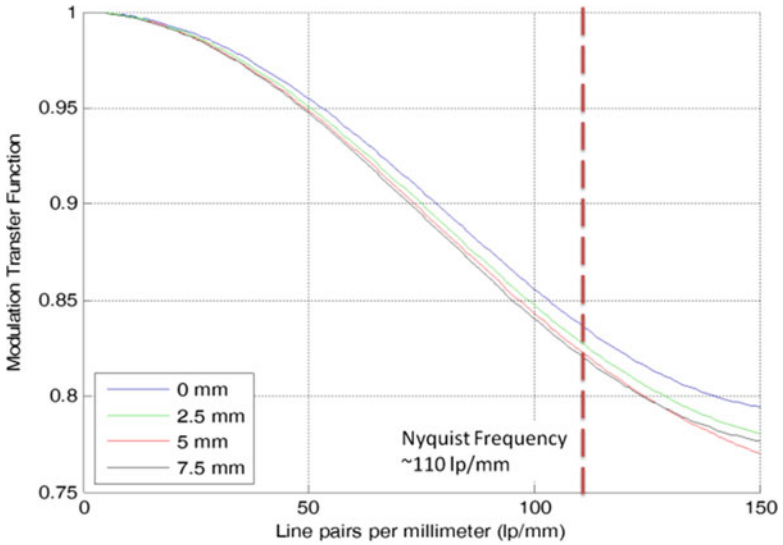

Fig. 16.6 MTF curves along X-axis

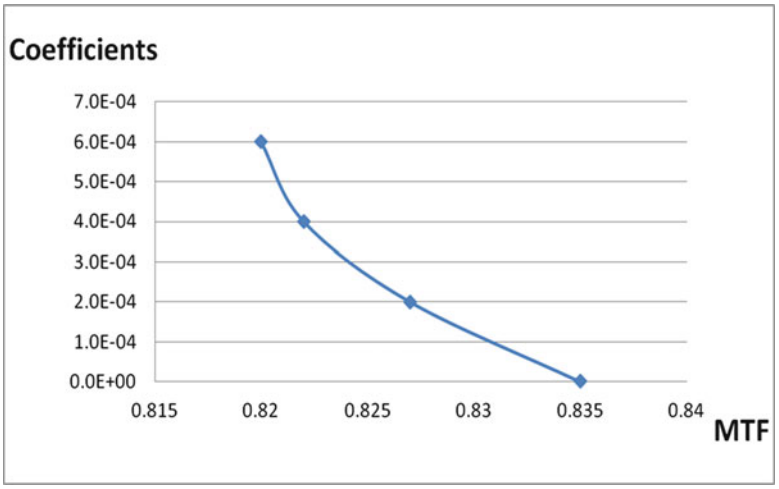

Fig. 16.7 Plot MTF at Nyquist frequency verses slop coefficients of fitting functions

Acknowledgements The study is performed thanks to the financial support provided by the National Science Council of Taiwan, R.O.C. (Grant No. NSC 101-2221-E-492-007) is greatly appreciated.

References

1. Peters W, Ranson W (1982) Digital imaging techniques in experimental stress analysis. Opt Eng 21:427–431
2. Sutton M, Wolters W, Peters W, Ranson W, McNeill S (1983) Determination of displacements using an improved digital correlation method. Image Vision Comput 1(3):133–139
3. Vendroux G, Knauss WG (1998) Submicron deformation field measurements: part 1. Developinga digital scanning tunneling microscope. Exp Mech 38(1):18–23
4. Schreier H, Garcia D, Sutton M (2004) Advances in light microscope stereo vision. Exp Mech 44(3):278–288
5. Doumalin P,Bornert M, Caldemaison D (1999) Microextensometry by image correlation applied to micromechanical studies using the scanning electron microscopy. In: Proceedings of international conference on advanced technology in experimental mechanics, Ube, pp 81–86
6. Gianola DS, Sedlmayr A, Monig R, Volkert CA, Major RC, Cyrankowski E, Asif SAS, Warren OL, Kraft O (2011) In situ nanomechanical testing in focused ion beam and scanning electron microscopes. Rev Sci Instrum 82(6):063–901
7. Zhu T, Sutton MA, Li N, Orteu JJ, Cornille N, Li X, Reynolds AP (2011) Quantitative stereovision in a scanning electron microscope. Exp Mech 51(1):97–109
8. Luo PF, Chao YJ, Sutton MA, Peters WH (1993) Accurate measurement of three-dimensional deformations in deformable and rigid bodies using computer vision. Exp Mech 33(2):123–132

9. Tiwari V, Sutton MA, McNeill SR (2007) Assessment of high speed imaging systems for 2D and 3D deformation measurements: methodology development and validation. Exp Mech 47(4):561–579
10. Sutton MA, Orteu J-J, Schreier HW (2009) Image correlation for shape, motion and deformation measurements–basic concepts, theory and applications. Springer, New York
11. Pan B, Xie HM, Xu BQ, Dai FL (2006) Performance of sub-pixel registration algorithms in digital image correlation. Meas Sci Technol 17(6):1615–1621
12. Pan B, Li K (2011) A fast digital image correlation method for deformation measurement. Opt Lasers Eng 49(7):841–847
13. Miehe C, Göktepe S, Méndez DJ (2009) Finite viscoplasticity of amorphous glassy polymers in the logarithmic strain space. Int J Solid Struct 46(1):181–202
14. Hargather MJ, Settles GS (2009) Laboratory-scale techniques for the measurement of a material response to an explosive blast. Int J Impact Eng 36(7):940–947
15. Daniels A, Boreman GD, Ducharme AD, Sapir E (1993) Random targets for modulation transfer function testing. In: Proceedings of infrared imaging systems: Design, analysis, modeling, and testing IV 1969:184-193, doi:10.1117/12.154714
16. Hong QH, Lettington AH, Macdonald J (1996) Measuring the MTF for focal plane arrays using random noise targets. Meas Sci Technol 7(7):1087
17. Levy E, Peles D, Opher-Lipson M, Lipson SG (1999) Modulation transfer function of a lens measured with a random target method. Appl Opt 38(4):679–683
18. Fernandez-Oliveras A, Pozo AM, Rubino M (2010) Comparison of spectacle-lens optical quality by modulation transfer function measurements based on random-dot patterns. Opt Eng 49(8):083603–083606
19. Pan B, Xie HM, Wang ZY (2010) Equivalence of digital image correlation criteria for pattern matching. Appl Opt 49(28):5501–5509
20. Vic-2D Testing Guide, Correlated Solutions, 2007

Chapter 17
SEM-DIC Based Nanoscale Thermal Deformation Studies of Heterogeneous Material

Siming Guo, Michael Sutton, Xiaodong Li, Ning Li, and Liwei Wang

Abstract Full-field thermal deformation experiments on electronic packaging materials for areas from 50×50 to 10×10 μm^2 and temperatures from RT to ≈200 °C have been successfully performed in a Zeiss Ultraplus Thermal Field Emission SEM using 2D-DIC. First, polishing methods for heterogeneous electronic packages containing silicon, Cu bump, dielectric layer, substrate and FLI (First level interconnect) have been studied to achieve sub-micron surface flatness. Using novel self-assembly techniques, a dense, randomly isotropic high contrast pattern has been successfully applied over the surface of test samples. A high precision Physik Instrumente (PI) Piezo nanopositioning stage has been used to help implement essential drift and spatial distortion correction procedures, which were recently shown to be effective in removing distortions from SEM images. Using thin ceramic films to reduce thermal effects on the FEG SEM source, results indicate that the method is capable of measuring local thermal expansion in selected regions, improving our understanding of these heterogeneous material systems under controlled thermal environmental conditions.

Keywords SEM • DIC • Thermal deformation • Heterogeneous material • Evolution of deformation

17.1 Introduction

Modern electronic packaging and micro-devices are being manufactured with heterogeneities and reduced spatial size. This has resulted in a significant increase in the need for quantitative, full-field deformation data at increasingly smaller scales to improve understanding of the true response of these heterogeneous material systems under controlled thermal, mechanical and hygroscopic environmental conditions.

To obtain quantitative measurements of deformations on such small scale, a combination of Scanning Electron Microscopy (SEM) and Digital Image Correlation (DIC) method has been developed by Sutton [1–3] to obtain full-field, quantitative deformation measurements at reduced length scale. Although there have been some experimental studies and application of SEM-DIC, much of the previous work has focused on mechanical loading, with a limited number of recent studies focusing on thermal effects in nominally homogeneous material systems [4]. Since thermal reliability is a key issue for the development and design of advanced electronics and micron/nano scale packages, which are inherently heterogeneous in nature, the authors applied the SEM-DIC measurement method to quantify the response of small portions of integrated chip (IC) packages (areas from 50×50 μm^2 to 10×10 μm^2) when subjected to thermal loading conditions from RT to ≈200 °C.

S. Guo (✉) • M. Sutton • X. Li • N. Li • L. Wang
Department of Mechanical Engineering, University of South Carolina, 300 South Main Street, Columbia, SC, USA
e-mail: guos@email.sc.edu

H. Jin et al. (eds.), *Advancement of Optical Methods in Experimental Mechanics, Volume 3*,
Conference Proceedings of the Society for Experimental Mechanics Series,
DOI 10.1007/978-3-319-00768-7_17,

17.2 Specimen Preparation and Patterning

The present work is conducted on heterogeneous electronic packages containing silicon, Cu bump, dielectric layer, substrate and/or FLI (First level interconnect). Figure 17.1 shows the cross section surface of one specimen. The regions enclosed by the blue dashed line contain various materials that have different elastic moduli and thermal expansion coefficients. These local regions are the AOIs for this specimen.

All specimens were cut by an IsoMet low speed precision sectioning diamond saw to 5 mm in height to fit a specially designed aluminum holder. The top surface of the specimen (which corresponds to a transverse cross-section of the IC package) initially is mechanically polished with 120–800 grit SiC papers using deionized (DI) water. After completing the initial polish, a refined polish with abrasive powders such as AlO_2 (5 μ, 3 μm) was performed. Finally, an abrasive mixture containing 20 nm colloidal silica (liquid) was used to obtain a reasonably flat surface on the heterogeneous material system.

It is noted that results from AFM scanning of the as-polished chip profile shows the surface roughness is about +/−700 nm, with relatively steep spatial gradients near boundaries where high modulus differences occur (e.g, copper-polymer interfaces) that induced differential surface removal during polishing. These gradients invalidated the use of E-beam lithography for random patterning since the local profile gradients severely affected the quality of the pattern in the interface regions. Figure 17.2 shows a trial E-beam lithography patterning result, where the pattern was not visible at all. Fortunately, Kammers and Daly [6] recently developed a novel self-assembled gold nanoparticle (AuNP) DIC patterning technique that eliminated the need for lithographic methods. By employing their method, the authors have shown that high quality, nanoscale patterns can be deposited on polished heterogeneous material systems such as shown in Fig. 17.1.

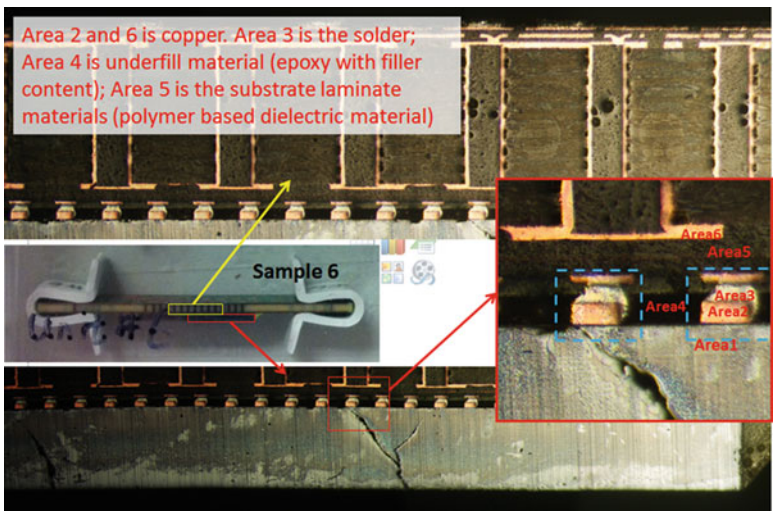

Fig. 17.1 Specimen surface and areas of interest

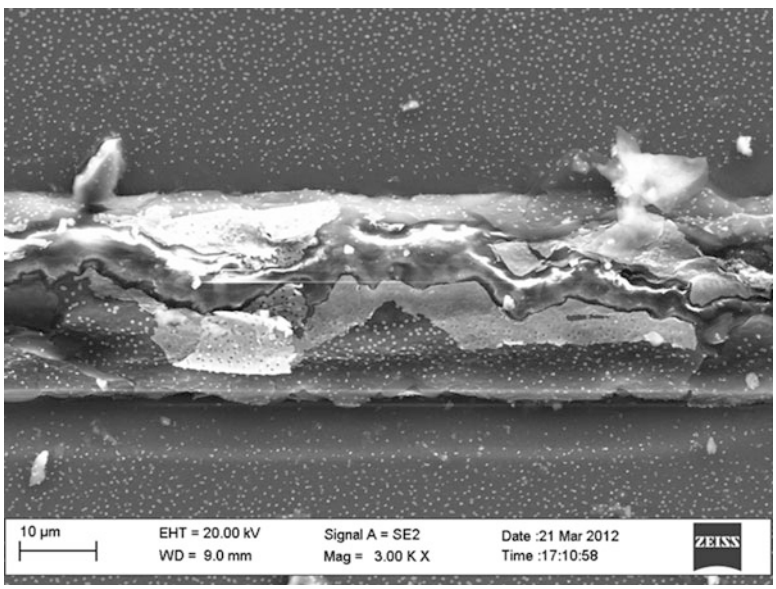

Fig. 17.2 E-beam lithography failed to pattern the area near the material boundary

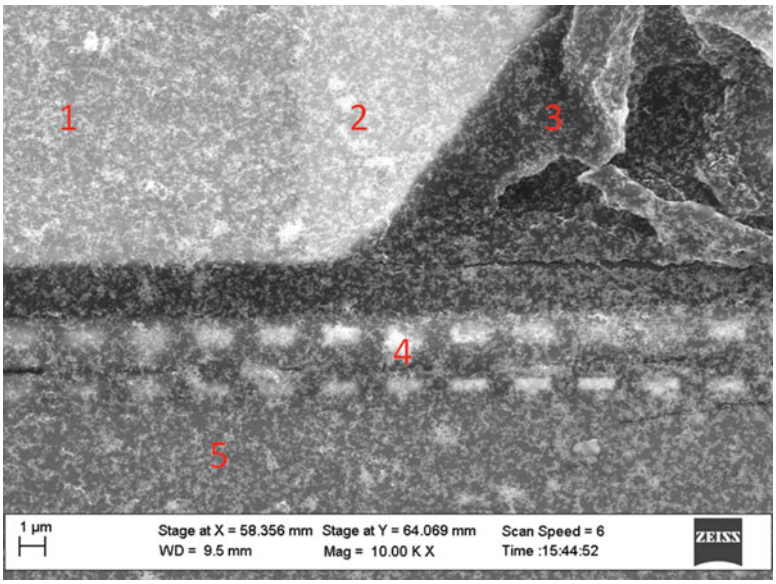

Fig. 17.3 Area 1 is copper, area 2 is solder, area 3 is underfill material (epoxy with filler content), area 4 is copper embedded in silicon, and area 5 is silicon

In their work, Kammers and Daly employed the method for patterning aluminum specimens. As they noted, the gold nanoparticles (AuNPs) are obtained through a reaction between $HAuCl_4$ and Na_3-citrate, with the particle size and distribution density controlled by the proportions in the mixture. Different from the 99.99 % Al substrates used in their studies, the IC package used in our experiments contains multiple materials. Preliminary studies indicated that differential reactions occurred when exposing the surface to the patterning mixture, resulting in a poor spatial distribution of particles as unbounded silane molecules detach from the substrate surface. To overcome this difficulty, the authors coated the surface of the entire specimen (sides and polished surface) with a thin layer of titanium. In this work, results are presented when using a 40 nm titanium layer with a gold pattern obtained using a mixture containing one part of 38.8 mM Na_3-citrate to 20 part of 1 mM $HAuCL_4$. The resulting pattern of AuNPs had the appropriate size and spatial distribution for SEM imaging at the magnifications of interest. It is noted that a side benefit of the coating process was the minimization of "specimen charging", which is induced by the presence of low electrical conductivity materials on the surface of the specimen when scanned by the electron beam during SEM imaging.

Though described in detail in Reference [6], a brief description of the patterning process for this study is presented. First, all surfaces of the specimen were coated with 40 nm of titanium. Then the entire IC chip is immersed in boiling deionized water to hydroxylate the specimen surfaces for pattern application. The substrate surface was silanized by soaking the specimen in vials filled with one part MPMDMS to four parts methanol for 24 h. After removal, the substrate surfaces were immediately immersed in 100 mL methanol, and rinsed for 30 min using a magnetic stirrer. Following the methanol rinse, the specimen was rinsed with deionized water and then placed in a vial for 1 day that contains the mixture 38.8 mM Na_3-citrate to 20 part of 1 mM $HAuCL_4$. Figure 17.3 shows the 10 KX magnification SEM image of the transverse cross-section in Fig. 17.1 after completing the self-assembled gold nanoparticle patterning process. Even though the entire surface is coated by titanium, the underlying heterogeneous nature of the surface is clearly visible. Here, area 1 is copper, area 2 is solder, area 3 is underfill material (epoxy with filler content), area 4 is copper embedded in silicon, and area 5 is silicon. As shown in Fig. 17.3, the entire surface has almost uniform speckle distribution with particle size around 50 ~ 100 nm, which is satisfactory for use of DIC to measure local thermal deformations.

17.3 Experimental Setup

The SEM images in this paper were captured with the secondary electron detector in a Zeiss FEG SEM with a working distance ~10 mm. SEM imaging parameters were selected based on overall quality of the image; (a) If contrast is enough, lower accelerating voltage is preferred to protect the IC chips from undesirable heating; (b) Image size is 1024 × 768 pixels; (c) Line average scanning mode with a Zeiss setting of 6, resulting in a total image scan (frame) time of 15.6 s.

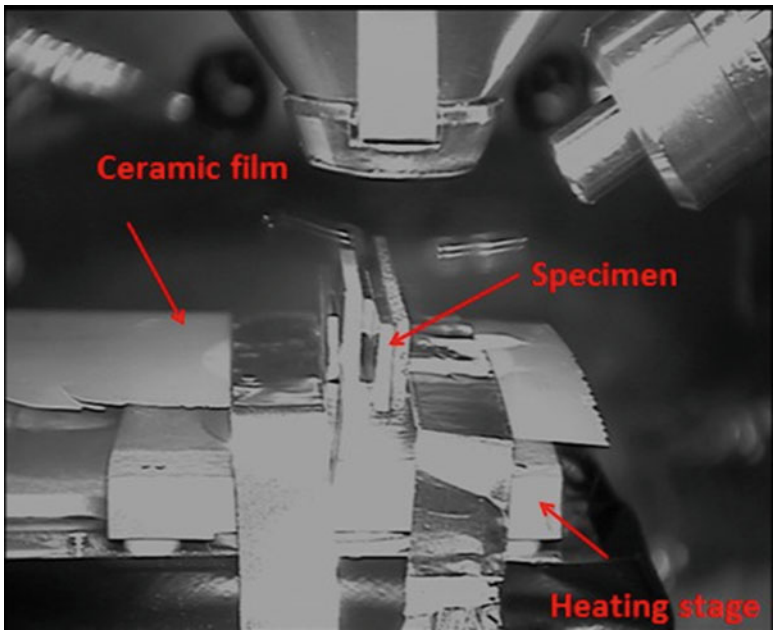

Fig. 17.4 Heating stage in SEM chamber

According to the structure and features of each sample and the gold particle size, a magnification of 5000X was used for the first experiment. In this SEM, 5000X corresponds to ≈56 nm/pixel. Therefore, the regions being imaged are 57 × 43 μm at 5000X. In future experiments, 20000X is preferred which meets oversampling requirements of at least 3 × 3 pixels per gold particle [5] for optimal accuracy.

The heating plate used in these experiments is the INSTEC AHP202. The stage was specially designed for thermal stability over the range 0–200 °C with demonstrated ability to hold temperature within 0.1 °C at 100 °C, while having a slim profile so that it can be used effectively in the Zeiss SEM system. Figure 17.4 shows the heating plate in the SEM chamber. Temperature control was performed using the INSTEC STC200 control system. To perform the control process outside the chamber, all wires from the heating plate are routed out of chamber through a sealed flange.

Results from our studies show that the temperature a few millimeters above the thermal stage can exceed 130 °C in an enclosed environment, which potentially could damage the SEM imaging components. Thin ceramic film was used to reduce the temperature to acceptable levels. We performed experiments to show that the method reduces temperature at 10 mm above the thermal stage to 60 °C using four ceramic film layers, a level that is within working requirements for the Zeiss FEG SEM.

17.4 Preliminary Thermal Test Result

Due to the obvious complexities of high-magnification SEM imaging systems that weaken the normal assumptions for CCD lens systems, the distortions in an SEM cannot be simply corrected by classical parametric distortion models. Sutton et al. [1–3] have developed a new method for accurate measurement of deformations in an SEM at reduced length scale based on their previous work of bundle adjustment method for distortion correction of a general imaging system for use with DIC. Then Li [4] in his work illustrated that higher magnification imaging requires a more robust and accurate translation sequence during calibration to optimize overall accuracy. In this work, a high-precision nanopositioner P-620.2 XY Piezo Stage which has 50 μm travel range, is used to improve the quality of the distortion correction process.

Prior to performing the experiments reported in this study, the specimen underwent several cycles of heating and cooling. As a result of this process, several cracks were initiated on the specimen surface. The DIC results for ε_{xx} and ε_{yy} at 75 °C are shown in Figs. 17.5 and 17.6, respectively. Here, results show that the embedded cracks were gradually closed in the SEM during the heating process, with compression of the crack surfaces clearly evident in the ε_{yy} strain field. In other areas, positive strains are measured due to thermal expansion effects. Consistent with expectations, the top half of specimen, which is mainly copper as mentioned previously, has higher e_{yy} value than the bottom half which is silicon. However, the e_{xx} strain

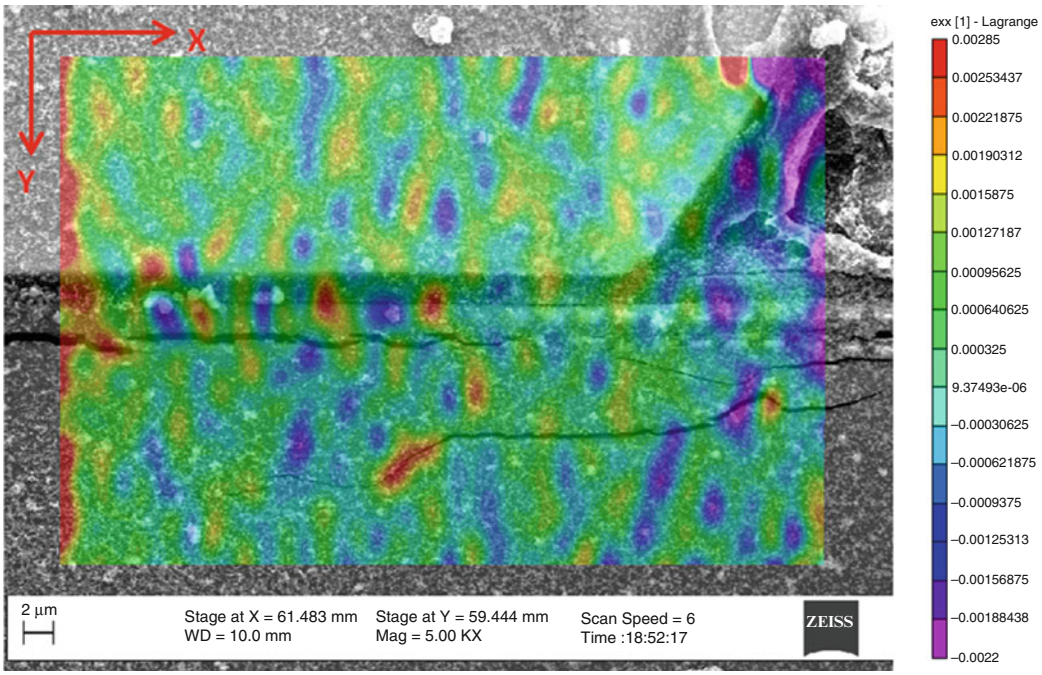

Fig. 17.5 ε_{xx} strain field when temperature equals to 75 °C

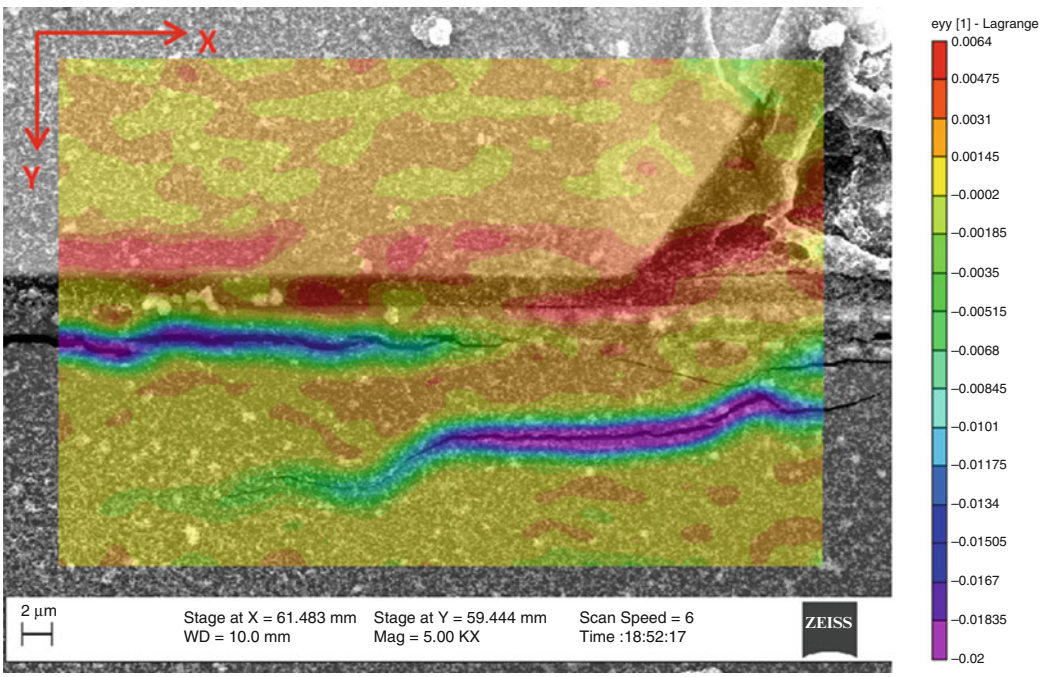

Fig. 17.6 ε_{yy} strain field when temperature equals to 75 °C

field shown in Fig. 17.5 does not have exhibit the same trends, possibly due to constraint effects in this direction. Finally, though not shown, results from thermal loading up to 200 °C have been performed successfully, with trends similar to those shown in Figs. 17.5 and 17.6.

17.5 Conclusions

Using a novel methodology developed by colleagues at the University of Michigan, the entire heterogeneous region on an IC package has been successfully patterned for SEM imaging and digital image correlation successfully performed in an SEM on the microscale. Results clearly show the evolution of deformations around flaws and across the complex material constituents during thermal loading.

Acknowledgement The support of the Intel Corporation and Dr. Liwei Wang via grants # 2011-IN-2171 and financial support provided by the University Of South Carolina College Of Engineering are gratefully acknowledged.

Reference

1. Sutton MA, Li N, Garcia D, Cornille N, Orteu JJ, McNeill SR, Schreier HW, Li X (2006) Metrology in a scanning electron microscope: theoretical developments and experimental validation. Meas Sci Technol 17:2613–2622
2. Sutton MA, Li N, Joy DC, Reynolds AP, Li X (2007) Scanning electron microscopy for quantitative small and large deformation measurements part I: SEM imaging at magnifications from 200 to 10,000. Exp Mech 47:775–787. doi:10.1007/s11340-007- 9042-z
3. Sutton MA, Li N, Garcia D, Cornille N, Orteu JJ, McNeill SR, Schreier HW, Li X, Reynolds AP (2007) Scanning electron microscopy for quantitative small and large deformation measurements part II: experimental validation for magnifications from 200 to 10,000. Exp Mech 47:789–804. doi:10.1007/s11340-007-9041-0
4. Li N, Sutton MA, Li X, Schreier HW (2007) Full-field thermal deformation measurements in a scanning electron microscope by 2D digital image correlation. Exp Mech 48:635–646. doi:10.1007/s11340-007-9107-z
5. Sutton MA, Orteu JJ, Schreier HW (2009) Image correlation for shape, motion and deformation measurements, ISBN 978-0-387-78746-6. Springer, New York
6. Kammers AD, Daly S (2013) Self-assembled nanoparticle surface patterning for improved digital image correlation in a scanning electron microscope. Exp Mech. doi:10.1007/s11340-013-9734-5

Chapter 18
Observation of Thermal Strain on Electronic Packages Using Digital Image Correlation

Yasutaka Tominaga, Shuichi Arikawa, Satoru Yoneyama, Yasuhisa Fujimoto, and Yohei Omoto

Abstract In this study, the thermal expansion of bi-metal specimen is measured by digital image correlation (DIC). A measurement system is developed for the evaluation of complex thermal strain distribution on electronic packages. A heating chamber is designed for applying the thermal load and DIC provides the full-field thermal deformation distribution of the bi-metal specimen due to temperature changes. The in-plane strain distribution measured by DIC is influenced by the out-of-plane displacement. By measuring the thermal expansion of the materials having known thermal expansion coefficient at same time, the effect of the out-of-plane displacement on the in-plane strain measurement is corrected. Experimental Results show that the thermal strain of the bi-metal specimen can be obtained by the measurement system including the out-of-plane displacement correction.

Keywords Digital image correlation • Thermal strain • Bi-metal • Electronic packages • Out-of-plane dispalacement

18.1 Introduction

In recent years, with the needs for miniaturization, weight saving and the improvement of the performance of electronic devices, electronic packages have been miniaturized and highly integrated. Damages such as debonding wires and solder occur by thermal stress caused by the difference of thermal expansions of elements in the packages. Therefore, the improvement of the structural reliability of the packages is required. Thermal strain and stress have been evaluated by the measurement using strain gauges and finite element analysis. However, with the miniaturization and the complication of structures, it is difficult to evaluate the actual thermal deformations. Therefore, in order to ensure the structural reliability of the electronic packages, the development of a quantitative evaluation technique of thermal stress and strain should be used. Considering electronic packages are heterogeneous materials, a full-field and noncontact measurement method is required for the thermal strain measurement. Holography and electronic speckle pattern interferometry (ESPI) are known as such method. However, there are problems that the measurement environment is limited and the process is complex for these methods. On the other hand, digital image correlation (DIC) has low environmental vulnerability and simple measurement process [1–3]. Therefore, it is considered that DIC is effective to measure the thermal deformation.

In this study, the observation method of the thermal strain on electronic packages with DIC is investigated. A heating chamber is designed for applying the thermal load and DIC provides the full-field thermal deformation. A bi-metal specimen is used to measure the inhomogeneous strain distribution. By measuring the thermal expansion of the materials having known thermal expansion coefficient at same time, the effect of out-of-plane displacement which influences in-plane strain distribution measured by DIC is corrected. Thermal strain of the bi-metal specimen can be obtained by the measurement system including the out-of-plane displacement correction.

Y. Tominaga (✉) • S. Arikawa • S. Yoneyama
Department of Mechanical Engineering, Aoyama Gakuin University, 5-10-1 Fuchinobe, Sagamihara 252-5258, Japan
e-mail: c5612096@aoyama.jp

Y. Fujimoto • Y. Omoto
Mitsubishi Electric Corp. Advanced Technology R&D Center, 8-1-1 Tsuhokaguchihonmachi, Amagasaki 661-8661, Japan

H. Jin et al. (eds.), *Advancement of Optical Methods in Experimental Mechanics, Volume 3*,
Conference Proceedings of the Society for Experimental Mechanics Series,
DOI 10.1007/978-3-319-00768-7_18,

18.2 Structure of Heat Chamber

The heat chamber is developed to produce thermal strain on the electronic packages. The structure is shown in Fig. 18.1. The outside frames are made of aluminum alloys. Insulating materials are set inside of the frame. The dimensions of the heating room are the size of 60 × 60 × 10 mm. A heater is inserted under the heat spreader made of copper in the heating room. The temperature is controlled by feedback system including thermocouple attached on the heat spreader and the controller. The controllable temperature range of the chamber is from room temperature to more than 300° which is above the melting point of solder. The sample is set on the heat spreader with thermal transfer grease. A tempered glass plate is used for the upper window of the chamber to take images of the sample surface. The thermal strain is measured by DIC using the images which are captured by CCD camera through the window.

18.3 Basic Principle of DIC

In two-dimensional digital image correlation, displacements are directly detected from digital images of the surface of an object. The plane surface of an object is observed usually by a CCD camera with an imaging lens. The images on the surface of the object, one before and another after deformation, are recorded, digitized and stored in a computer as digital images. These images are compared to detect displacements by searching a matched point from one image to another. Because it is almost impossible to find the matched point using a single pixel, an area with multiple pixel points (such as 20 × 20 pixels) is used to perform the matching process. This area, usually referred as subset, has a unique light intensity (gray level) distribution inside the subset itself. The light intensity distribution basically remains unchanged during deformation. Figure 18.2 shows the part of the digital images before and after deformation. The displacement of the subset on the image before deformation is found in the image after deformation by searching the area of same light intensity distribution with the subset.

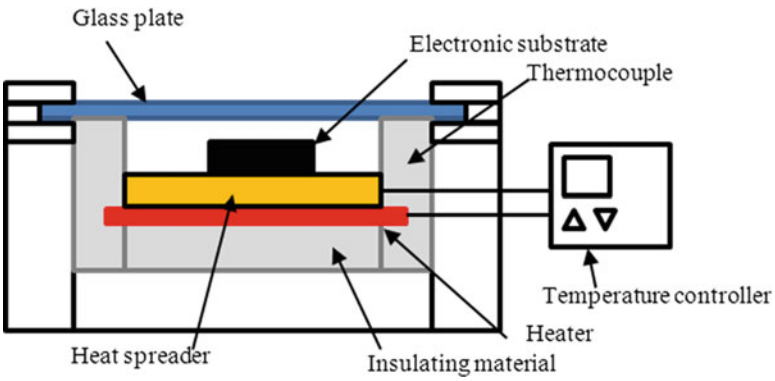

Fig. 18.1 The configuration of heat chamber

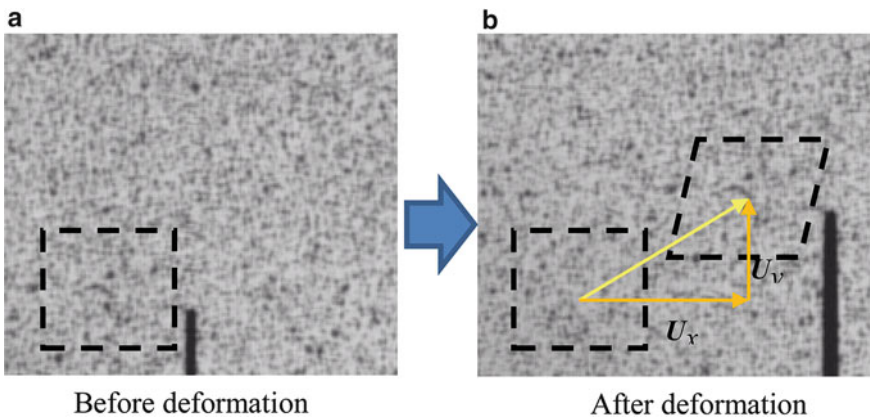

Fig. 18.2 Movement of random pattern (**a**) before deformation (**b**) after deformation

Once the location of this subset in the deformed image is found, the displacement of this subset is determined. Strain distribution is then obtained by differentiating the displacement distribution. In order to perform this process, the surface of the object must have a feature that allows matching the subset. If no feature is observed on the surface of the object, an artificial random pattern must be applied.

18.4 Correction of Apparent Strain Caused by Out-of-Plane Displacement

18.4.1 Correction Method

The heat chamber and the sample have out-of-plane displacement with heating. This phenomenon influence in-plane strain distributions because of the change of the distance between the camera and the sample surface. The out-of-plane displacement before and after deformation is shown in Fig. 18.3. The solid lines in Fig. 18.3 mean a condition before deformation and broken lines mean a condition after deformation. Because the image captured after deformation includes influence of the out-of-plane displacement and the in-plane deformation, the strain measured using DIC represents not actual but apparent strain. Therefore, the additional strain caused by the out-of-plane displacement should be removed. We propose a method for the correction of the additional strain as follows. The apparent strain of a specimen is obtained using DIC. On the other hand, the strain of a reference specimen whose coefficient of thermal expansion (CTE) is known is measured simultaneously. The additional strain caused by the out-of-plane displacement is obtained by subtracting the strain calculated by CTE of the reference specimen from the strain measured by DIC. Then, the actual thermal strain distribution of the sample can be obtained.

18.4.2 Experimental Procedure for Correction

The thermal strains of two specimens which have different CTE are measured by DIC. The specimens are an austenitic stainless steel (JIS SUS304) having CTE of 17.3×10^{-3}/K and an oxygen-free copper (JIS C1020) having CTE of 17.7×10^{-3}/K. The dimension of the specimens is $10 \times 3 \times 0.5$ mm. The surfaces of the specimens are colored with white and black speckle pattern for DIC. The thermal loads are applied with the temperature differences of 50, 100, 150, 200°. The temperature is maintained for 30 min at each step. Then, the images of the samples are captured. Figure 18.4 shows the schematic view of the measurement system. The camera for DIC is Jai CV-M4 + CL. The resolution of the camera is 1380×1030 pixels and 8 bits. The subset size for DIC is set to 51×51 pixels. The strain distributions are calculated from the displacement distributions using local least-squares. The gauge length is set to 200 pixels for the strain calculation.

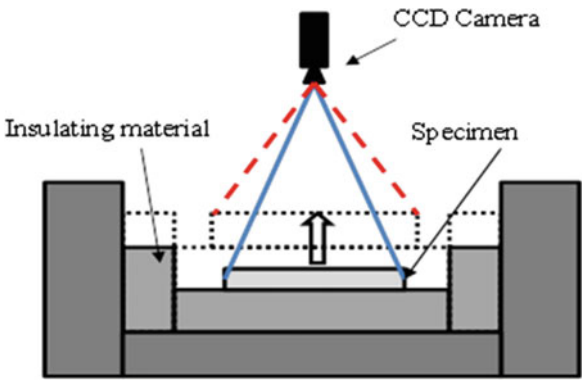

Fig. 18.3 Out-of-plane deformation and increasing strain

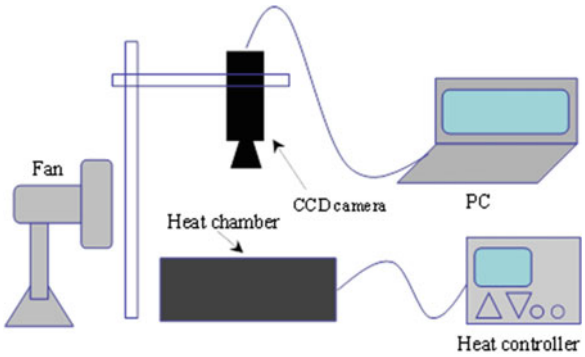

Fig. 18.4 The thermal strain measurement system

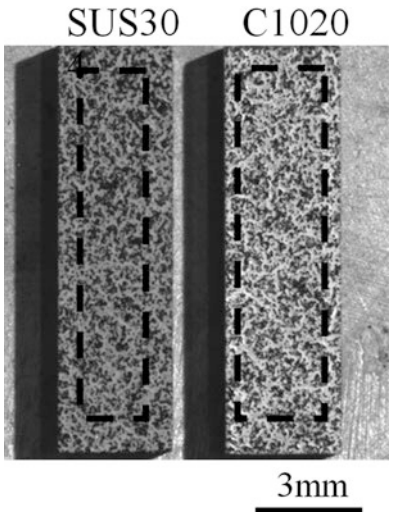

Fig. 18.5 Specimens for calibration

18.4.3 Results and Discussion

The image of two samples is shown in Fig. 18.5. The broken lines on the each sample represent the measurement region. The relation of the measured strains and the temperature is shown in Fig. 18.6. Solid markers show the measured strains which are averaged in the measurement region and open markers show the additional strains that are obtained by subtracting the strain obtained by the CTEs from the measured strains. The lines show the linear approximation of the additional strains. The lines show good agreement. In Table 18.1, the CTEs of materials and the gradients of the approximation lines are shown. The strain values of SUS304 and C1020 are very similar. It is preferred to select copper (C1020) for the correction because the electronic substrate is made of copper.

18.5 Thermal Strain Measurement of Bi-metal Specimen

18.5.1 Experimental Procedure

In electronic packages, the complex thermal stress distribution occurs because the packages consist of the various CTE materials. In order to validate the method of thermal strain measurement, the thermal strain of a bi-metal specimen is measured in this study. Figure 18.7 shows the bi-metal specimen consists of SS400 having CTE of 11.7×10^{-3}/K and C1020 having CTE of 17.7×10^{-3}/K. The dimension of both SS400 and C1020 specimens is $5 \times 10 \times 3$ mm. Figure 18.8

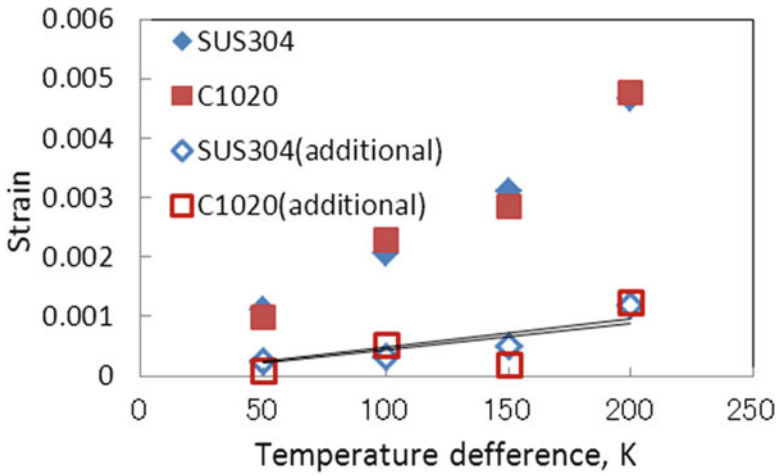

Fig. 18.6 Relationships of strain and temperature

Table 18.1 Rates of changing strain depending on temperature

	SUS304	C1020
CTE[$\times 10^{-6}$/K]	17.3	17.7
Out-of-plane displacement[$\times 10^{-6}$/K]	4.1	4.4

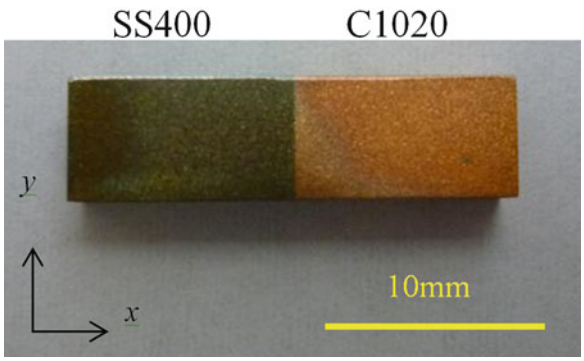

Fig. 18.7 Brazed specimen

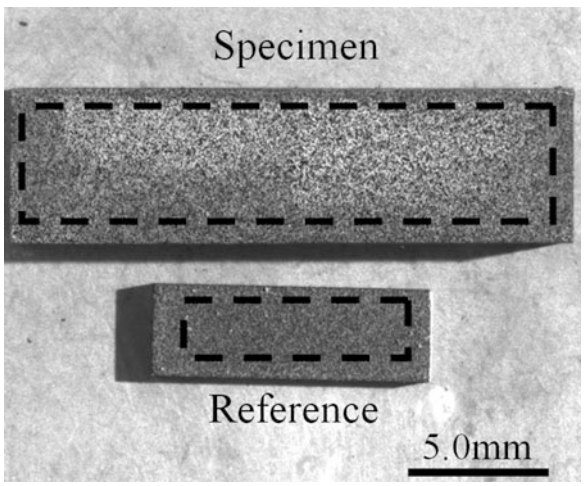

Fig. 18.8 Random patterned specimen

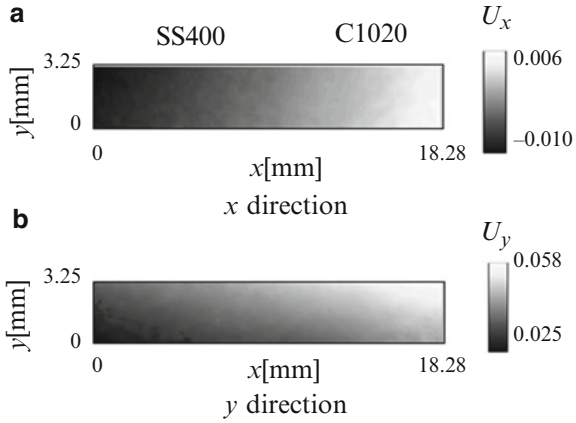

Fig. 18.9 Displacement maps measured by DIC

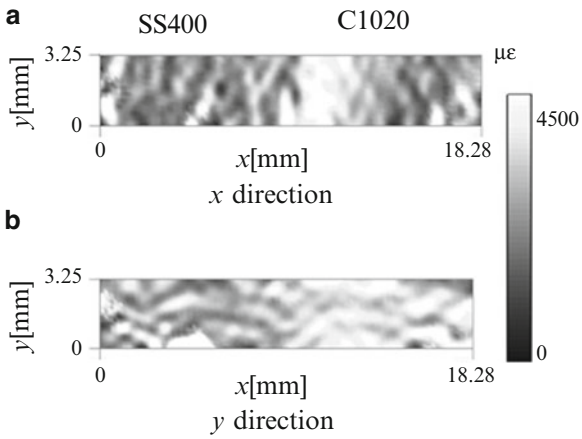

Fig. 18.10 Strain maps measured by DIC

shows the bi-metal specimen and the reference specimen colored in black and white random pattern. The thermal strains of the specimens are measured using the proposed measurement system. The thermal loads are applied with the temperature differences of 50, 100, 150, and 200°. The additional strain caused by the out-of-plane displacement is simultaneously measured and eliminated from the measurement results.

18.5.2 Results and Discussion

Figure 18.9 shows the x and y directional displacement maps of the bi-metal heated from 30° to 230°. The left side of the specimen is SS400 and the right side is C1020. The subset size is set to 31 × 31 pixels and the correlation area does not include the edges of specimen. In the maps of the displacement distribution, it is observed that the thermal expansion occurs. The strain distributions are obtained from the displacement distributions using local least-squares. Figure 18.10 shows the x and y directional normal strain maps. The gauge length of the strain calculation is 60 pixels. The gauge length equals to about 1 mm in this condition. The additional strain caused by the out-of-plane displacement is already corrected. The interface of C1020 and SS400 located at the center of the maps. In the strain maps, the strain values change suddenly around the interface. It suggests that the phenomenon is caused by binding with each other and the CTE difference. In the map of the x directional normal strain, the strains of C1020 and SS400 increase as closing to the interface. On the other hand, in the map of the y directional strain, the strain of C1020 decreases by the binding and the strain of SS400 increases by the tension of C1020 as closing to the interface. In the point away from interface, the strain should close to the value calculated by CTE because the force of the bond decreases. In fact, the thermal strain of C1020 by CTE is calculated as 3.54×10^{-3} and the average value of the measured strain near the edge is 3.55×10^{-3}. These results indicate that the behavior of the thermal strain on bi-metal can be measured.

18.6 Conclusions

The strain distributions of the bi-metal specimen are measured using digital image correlation for the establishment of the measurement system of the thermal strains of the electronic packages. By measuring the strains of the reference specimen simultaneously with the strain of the sample, the effect of the out-of-plane displacement is corrected. Results of the strain measurement of the bi-metal specimen show that the thermal strain of electronic packages can be measured by the proposed method.

References

1. Yoneyama S (2010) Displacement and strain measurement using digital image correlation. J NDI 59(7):306–310
2. Sutton MA (1991) Full-field representation of discretely sampled surface deformation for displacement and strain analysis. J Exp Mech 31(2):168–177
3. Bing P et al (2009) Measurement of coefficient of thermal expansion of films using digital image correlation method. J Polym Test 28(1):75–83

Chapter 19
Observation of the Microstructural Evolution in a Structural Polymeric Foam Using Incremental Digital Volume Correlation

Zhenxing Hu, Huiyang Luo, and Hongbing Lu

Abstract Polymeric structural foams are widely used in many engineering applications due to their exceptional properties including high specific strength and energy absorption. The mechanical properties depend strongly on their microstructures, which also dictate their load-bearing capability under deformation. However, the mechanical behavior of polymer foams in compression is not well understood, due to the complex local deformation and strain characteristics associated with the cellular microstructure. In this paper, unconfined uniaxial compression of a polymeric structural foam was conducted while its microstructure was determined using micro-computed tomography (micro-CT) subjected to large deformations. The detailed local deformations and strains are obtained by using three dimensional digital volume correlations (DVC) method. This incremental DVC allows the use of intermediate bridging images to determine large nonlinear deformations in the foam under compression. The evolution and deformation mechanism of the microstructure are observed during different compression stages using the incremental DVC techniques.

Keywords Cellular material • PMI foam • Digital volume correlation • Cell-walls • Deformation and strain measurement

19.1 Introduction

Polymeric foams have been of particular interest in many applications due to their low thermal conductivity, high specific energy absorption, high specific strength, high acoustic damping, and excellent weight-specific properties. Polymethacrylimide (PMI) foams, commercially known as Rohacell, are closed-cell cellular solids, where the parent polymer of the cell walls has a density about 1.42 g/cm^3, by introducing voids, the foam has very low density, on the order of 0.1 g/cm^3 [1, 2]. It is currently widely used in composite sandwich structures, such as launch rockets, missile shells, military helicopters, and airplane and other energy absorbing packaging applications such as automotive structurals.

Compressive behavior of foams depends heavily on their microstructures, which include a collection of regular or irregular thin-walled cells; its macroscopic compressive behavior is determined by the compressive behavior of individual cells and the collective interactions between neighboring cells [3]. The response of PMI foams is well understood at low strain rates at conventional mechanical testing methods. The macroscopic quasi-static response of Rohacell foams under compression, tension and shear are investigated on different densities [4, 5]. Li and Mines [6] performed uniaxial and hydrostatic compression, tension and shear test on Rohacell 51WF. Later, they conducted a series of uniaxial compression test to measure material parameters for an elastoplastic model and investigated the viscoelastic recovery behavior. Arezoo et al. [7] have focused on the material response at microscopic scales through quasi-static compression, tension, shear and indentation. Most of these experiments were conducted following test standards (e.g. ASTM and ISO). Deformation mechanism was observed using common optical method or scanning electron microscopy. With the development of three dimensional (3D) imaging techniques, such as magnetic resonance imaging (MRI), micro-computed X-ray tomography (micro-CT) and confocal microscopy, cellular materials have been observed for morphology characteristics or microstructure evolution studied during different loading. Micro-CT imaging technique has been applied qualitatively to examine the

Z. Hu • H. Luo • H. Lu (✉)
Department of Mechanical Engineering, The University of Texas at Dallas, 75080 Richardson, TX, USA
e-mail: hongbing.lu@utdallas.edu

H. Jin et al. (eds.), *Advancement of Optical Methods in Experimental Mechanics, Volume 3*,
Conference Proceedings of the Society for Experimental Mechanics Series,
DOI 10.1007/978-3-319-00768-7_19,

gross changes in cellular structures such as cracks [8, 9], void opening [10], buckled cell-walls [2] and other failure patterns [11, 12]. Daphalapurkar et al. [2] used the micro-CT to determine the actual microstructure of PMI foam and input into material point method (MPM) to simulate the deformation. Using this imaging technique, the individual voids, the volume, shape, surface area, as well as the fraction of solid volume as a function of compressive stress can be determined. In this work, an unconfined uniaxial compression experiment on PMI foam was carried out and the microstructure was determined using a micro-CT. The deformed microstructure evolutions of the PMI foam were used as input for incremental digital volume correlation (DVC), and the detailed evolution was evaluated in through DVC to determine the 3D deformation and strain fields.

19.2 Incremental Digital Volume Correlation

DVC as a effective tool for three-dimensional (3D) displacement and strain fields is originally developed by Bak et al [13] in 1999. As a real 3D quantitative technique for internal displacement and strain measuring technique, DVC has attracted increasing attention in the last decades. It has been applied in various investigations on biological tissues [14–17], cellular materials [18–22] with complex loading, such as mechanical fatigue [23, 24]. DVC is a technique which is extended from two-dimensional (2D) digital image correlation (DIC). The basic principle is similar: both are based on digital image processing and numerical analysis. The difference is that DVC uses 3D volume image dataset while DIC uses 2D images. The 3D dataset surrounding the interrogated point in a reference volume image is used as a subvolume dataset to search its corresponding point in the deformed volume image. DVC will determine the deformation that maps the subset in the reference volume image to the deformed image with the best correlation for each correlation point. To determine the deformation $\vec{u}$, DVC will optimize a correlation function to reach the extreme value for the correlation function. Let $f(x)$ be the subvolume for correlation point p in the reference image, $g(x')$ be the same size subvolume in the deformed image, with a point $\boldsymbol{x}$ in the reference subset related to the corresponding point in the deformed subset by the affine transformation defined by a displacement vector u as shown in Fig. 19.1. Similarly to the DIC matching techniques [25], we employed zero-normalized cross-correlation (ZNCC) as the correlation function, giving as,

$$C = \sum_{i=1}^{n} \frac{[f(x_i) - f_m]\left[g\left(x_i'\right) - g_m\right]}{\sqrt{\sum_{i=1}^{n}[f(x_i) - f_m]^2}\sqrt{\sum_{i=1}^{n}\left[g\left(x_i'\right) - g_m\right]^2}} \tag{19.1}$$

where $f(x_i)$ and $g\left(x_i'\right)$ are the values of the subvolume in the reference and deformed subvolumes, respectively; f_m and g_m are the mean intensity values of the reference and deformed subvolume, respectively. Many subvoxel algorithms have also been proposed to improve the sensitivity and accuracy of DVC. However, for a series of volume images obtained during large deformation process, serious decorrlation effect may exist between the first volume image (i.e. the initial reference image) and the large deformed volume images, especially for large deformed structural materials such as polymer foam, which the cellular structure will crash and collapse during the compression loading. Therefore, a reference volume image updating

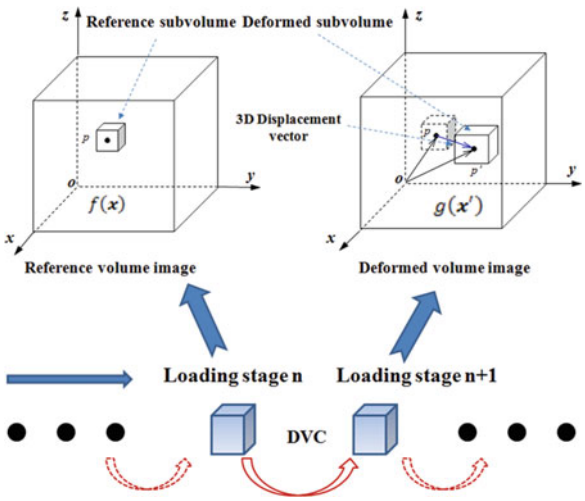

Fig. 19.1 Diagram of incremental DVC for large deformation measurement

scheme, in which the reference volume image in each step is considered as a deformed image in the previous step. For updating the deformed volumes images in the previous step as a reference image in the current step, the interpolation theme is required for updating the grayscale of non-integer grid.

This incremental DVC method is suitable for large deformation measurement with the use of a proper loading step, associated with high accuracy for subvoxel registration, and feasible for linear intensity change case. This DVC technique is verified using a series of rotated 3D volume images, and applied on a compression test of PMI foams without confinement under micro-CT scanning [26]. The new DVC approach helps effectively to resolve the decorrelation issue due to large deformation, making it a suitable technique in the mechanical properties characterization and fracture behavior of the cellular material subjected to large nonlinear deformation.

19.3 Experiments and Analysis

19.3.1 Experiments

A self-made loading assembly using a polycarbonate tube and steel bolt for applying loading was used, for large compressive deformation measurement of PMI foams on the Skyscan 1172 X-ray tomography. The instrument and diagram of the loading stage are shown in Fig. 19.2 left and right, respectively. The testing sample is a cylinder with 6.41 mm in height and 6.35 mm in diameter, fabricated by a hole-die cutter. And several small PVC balls were glued at the bottom lateral area of the sample as fiducially marks for removing the rigid motion. The uniaxial compression test was conducted under the micro-CT at room temperature and ambient pressure.

The compression was loaded by twisting the top screw on the loading cell to a given angle (Fig. 19.2 right). The engineering strains along vertical direction were given as 0 %, 4 %, 7 %, 13 %, 19 %, 23 %, 28 %, 32 %, 37 %, 39 %, 42 %, 45 %, 50 %, 52 %, 55 %, 57 % and 59 %, which were calculated directly from the radiographs at each stage. Thus 17 loading stage volume images were obtained. The small increase in the compression strains makes the incremental DVC program to track the corresponding points through these volume images successfully. At each particular strain, after manually loading on the foam slowly, the sample assembly was placed back to the sample stage for the next scanning at the same location and orientation. Each scanning was to rotate the sample by 0.4 $^{\circ}$ degrees and the radiography was acquired sequentially until 180 $^{\circ}$ of rotation. Each radiographic exposure time was 1 s and three radiographs at one position were captured and averaged for reducing the noise level. The full 3D tomographic imaging took about 50 min for one scanning. After reconstruction, the voxel size was 5.09 μm in all dimensions. The reconstructed cross-section images had a resolution of 2,000 × 2,000 pixels. The initial volume image and the last deformed stages of the PMI are shown in Fig. 19.3a, b, respectively.

Because the current loading fixture was unable to monitor compressive load *in-situ*, additional four compressive tests were conducted on an universal Instron materials testing machine at strain rate of 0.001/s. Two tests were conducted under loading-holding-reloading cycles to simulate the actual process of the compression under micro-CT scanning and the other two were used for single compression loading as a comparison with the loading cycles. Figure 19.4 illustrates the averaged single loading strain–stress curve in black dot line and the loading-holding-reloading strain–stress curve in red line. As the PMI foam was compressed, there was initially a nearly linear elastic stage. The Young's modulus of the PMI foam can be obtained from the initial linear data is 256 ± 18 MPa. During each scanning when the position was held fixed, the

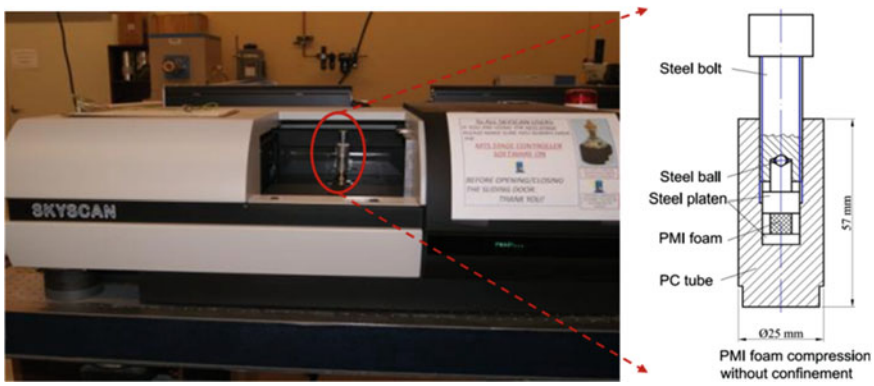

Fig. 19.2 Skyscan 1172 X-ray tomography (*left*) and the custom-made loading cell (*right*)

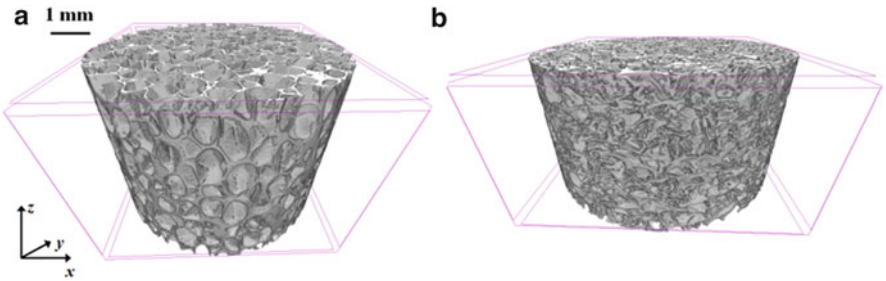

Fig. 19.3 Microstructure of PMI foam, (**a**) the reference stage at strain 0 %; (**b**) the deformed stages at strain 59 %

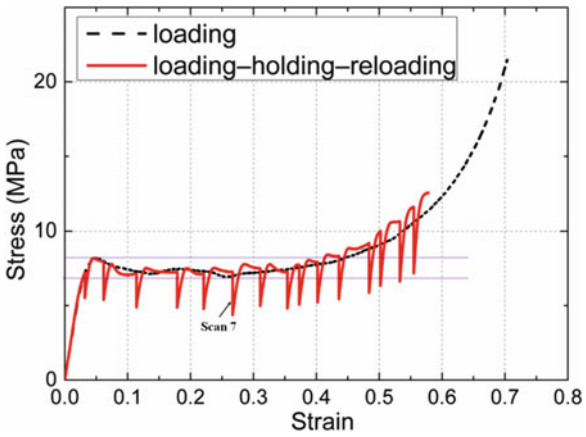

Fig. 19.4 Uniaxial compression of single loading and loading-holding-reloading stress–strain curves

compressive stress was dropping due to relaxation. The strain–stress curve reaches a peak, followed by softening and a plateau. During the plateau regime, the stress reached the lowest at strain 0.26 which was close the scan #7. After the scan #12, the plateau regime ends and large deformation begins. Figure 19.4 also shows two bounds for stress during compaction of the foam.

19.3.2 Volume Image Analysis and DVC

By using image processing techniques, the cross-section images could be smoothed, cropped, segmented and binarization, and the final image size in the X and Y dimensions after cropping was 840 × 840 pixels. Image size in the Z direction corresponds to the compression direction. From each of these 3D volume datasets, the statistical relation to the solid fraction was extracted. Figure 19.5 illustrates the solid fraction versus engineering strain using the middle 45 % images (in the 27 % ~ 72 % height level) for analysis. Due to close pronmity of the X-ray to the fixtures, some X-ray was blocked by the fixtures, making these images unclear, only portions of the cross-section images were used analysis. From Fig. 19.5, it is not intuitive that there are at least four points percent of solid dropped down as the compressive strain increased. That indicates microstructure was changed in these points. As comparing to the previous stages, one explanation of this phenomenon is that these stages indicates the crush of the foam which may happen near the fixture ends at this stage. Another possible error may come from the image processing in smoothing, cropping, segmenting and binarization. Therefore, a three-order polynomial fit curve was plotted on Fig. 19.5, to smooth the individual test data.

The subvolume for DVC calculation was 51 × 51 × 51 pixels. And the interested points were those which had the foam structure. Using parallel computing (c++ code with OpenMPI library [27]), it took about 2.7 h to obtained 18,130 points on 70 CPU cores. Some of the 3D deformations images are illustrated in Fig. 19.6. The color-bar indicates the displacement along Z-direction, which means the displacement between the current stages and the next stage.

Using the incremental calculation DVC, the large deformation of PMI foam was achieved through optimization of the correlation coefficients. In general, a fixed reference volume image was used, which makes it difficult to calculate this large deformation. The decorrelation effect presented in the images with large deformation was effectively overcome by updating the reference volume image. The strain distributions or later analysis on stress distribution were important to investigate the

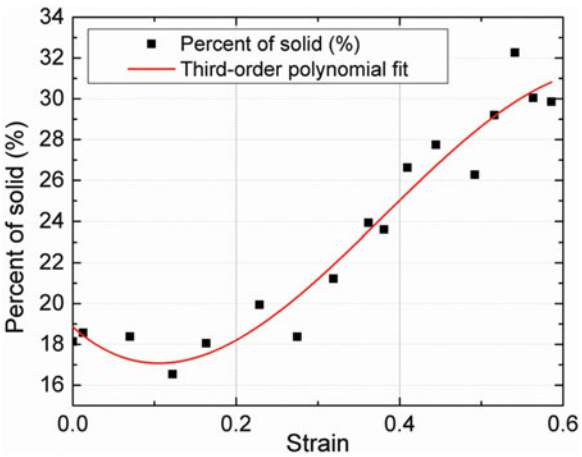

Fig. 19.5 The change in percent solid volume versus compression strain

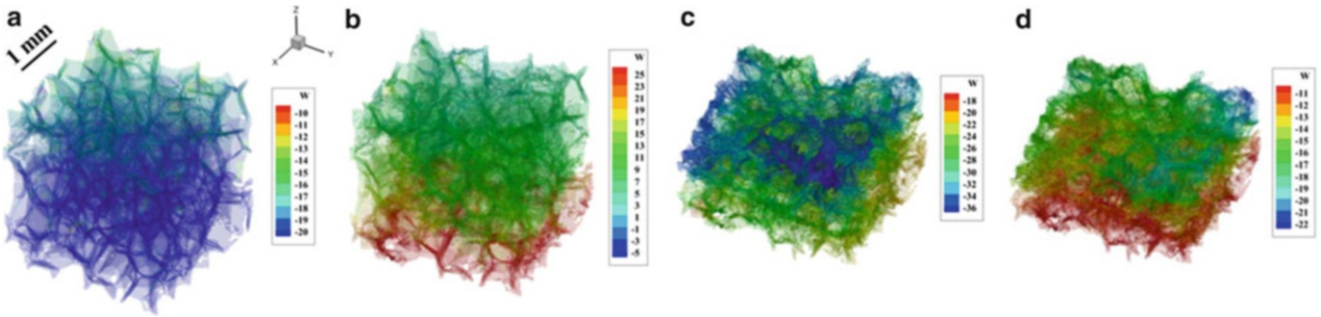

Fig. 19.6 DVC results on the PMI foam compression. (**a**) at strain 0 %; (**b**) at strain 23 %; (**c**) at strain 42 %; (**d**) at strain 57 %

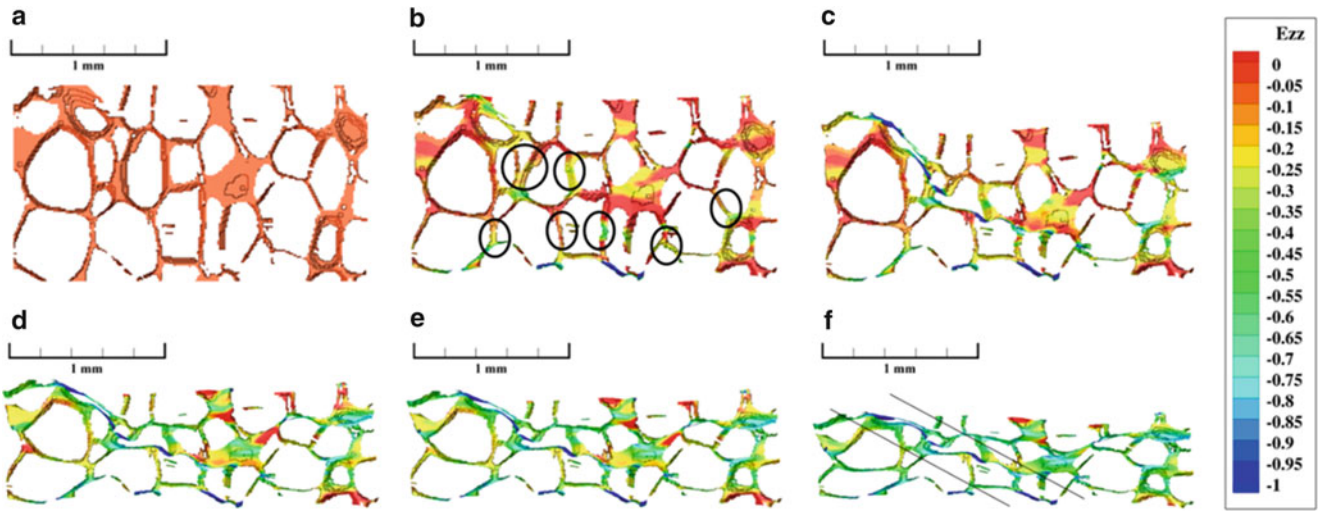

Fig. 19.7 The evolution of the microstructure of y-z section. (**a**) at stage #1; (**b**) at stage #6; (**c**) at stage #7; (**d**) at stage #12; (**e**) at stage #13; (**f**) at stage #17

mechanical properties of cellular structure material subjected to large compressive deformation. Figure 19.7 shows the *Y*-*Z* section of microstructure evolution of the PMI foam during the compression loading obtained from the DVC results. Figure 19.7a–f show 2D sections of the deformed foam structure with the strain distribution in *Z*-direction at stage #1, #6, #7, #12, #13, and #17 respectively. The contour color indicates the strain field in *Z*-directions at the each stage. Figure 19.7a

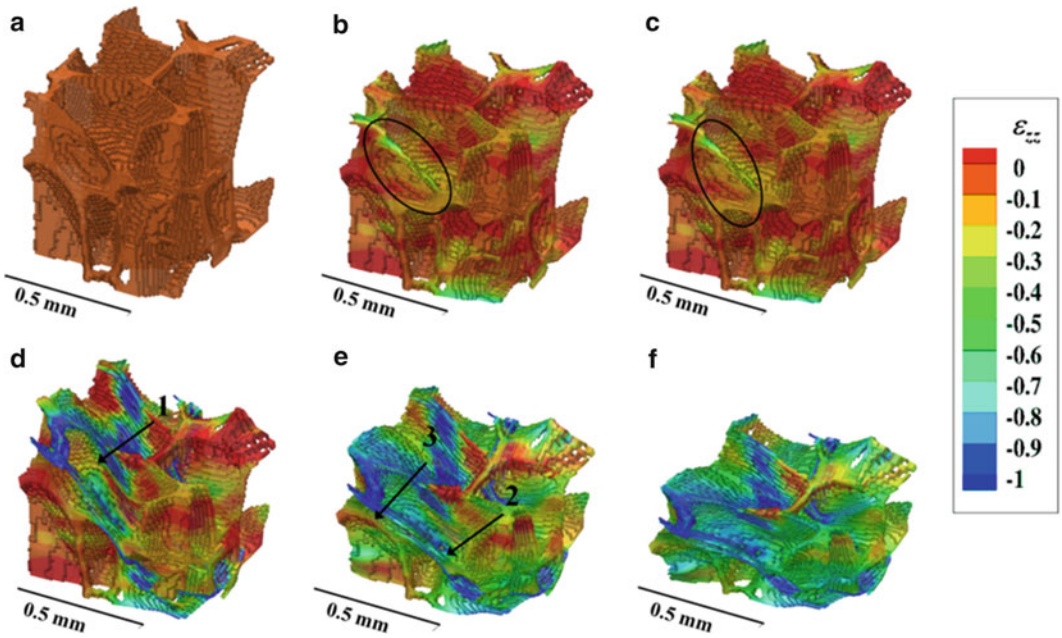

Fig. 19.8 Evolution of the microstructures during the compression. (**a**) at stage #1; (**b**) at stage #6; (**c**) at stage #7; (**d**) at stage #12; (**e**) at stage #13; (**f**) at stage #17

illustrates the undeformed foam microstructure. Comparing Fig. 19.7a with b, the shape of the cells has changed. From stage #1 to stage #6, it was observed that the cell-walls showed a tendency to bend, buckle, and twist to small angles. The cell-buckling phenomena were observed in the vertical section images after the initial stages. The cell-wall marked as circles in Fig. 19.7b reached strain about 0.2. From Fig. 19.4, stages #7 has the lowest stress during softening flowing platen. As comparing with the phenomenon with the Fig. 19.7c, most of the circled cell-walls in Fig. 19.7b are buckled. The buckling of the cell-walls dominates the failure at this stage. The vertical cell-walls buckle reaches its maximum. The general feature of this stage is that the capability of the cell-wall to sustain the compressive force after the cell collapse is smaller than its critical value at which the collapse initiates at the peak stress under 5 % strain (Fig. 19.4). This explains that stage #7 holds the lowest stress in the plateau regime. As the compression continues after stage #7, the buckled sites are observed not only on vertical walls, but also evenly on the more inclined walls which formed an angle as much as 45° with the loading axis as shown in Fig. 19.7d–f. The shear band area has the largest strains in *Z*-direction. Figure 19.7d is the stage #12 approximately corresponding to the end of plateau regime, after this stage the interactions between cell-walls play an important role in the large deformation. The similar evolution of the microstructure was also observed in other section slices along *Z*-direction (axial loading). In this paper, only a few points was noted and mentioned here. Observations were projected to *Y*-*Z* spatial plane in Fig. 19.7. As the deformation increases some material buckles inside and outside of the *Y*-*Z* spatial plane, not visual in these sectioning figures anymore. In addition, although the overall deformation of the sample might be slightly different, a small middle area along *Z*-direction used for analysis is still typical and representative of the behavior for foam deformation.

Several foam microstructures at different location were tracked from DVC results to observe the cell-wall collapse. Figure 19.8 shows the microstructural evolution of the several foam structures in three directions. The initial microstructure is shown in Fig. 19.8a. Figure 19.8b shows the microstructure at stage #6. As soon as the compressive strain reaches a critical value, the cell-walls start to collapse. Cell-wall collapses starts from the cell-wall buckling marked with dark circles in Fig. 19.8b, c. The strain of collapse cell-walls increases dramatically. After the cell-wall labeled as #1 in Fig. 19.8d collapses, the cell-walls labeled as #2 and #3 continue to collapse. This phenomenon due to the cell-wall collapse is localized within the newly collapsed layer of cells until the collapsed cell starts to interact with the neighboring layer when the local higher strain is reached. Further deformation of the collapsed layer of the cells requires increased compressive force, which triggered other layer of the cell-walls to collapse such as #2 and #3 in Fig. 19.8e. After most of the cell-walls collapse initiated, the trend of strain–stress will inverse (at stage #7). The interaction of cell-walls plays an important role till stage #12 at the end of the plateau regime, and then the large deformation regime begin for the compaction.

19.4 Conclusion

A new approach was developed to determine the 3D large deformation fields based on incremental DVC through a series of CT scans of the PMI during compression test for characterization the evolution of microstructure. The mapped displacement field is decomposed with comparison of the neighbor volume images. The cumulative displacement field is obtained. From the tracking field of the microstructure, the cell-walls buckle at the compressive strain in about 0.2. The microstructure evolution is correlated to the macroscopic behavior under compression. Most of the cell-walls buckled at the lowest stress in the plateau regime of this PMI foam. All cell-walls collapse at the end of the plateau regime while the compaction begins. Incremental DVC is shown to be an effective tool to evaluate the microstructures and the macroscopic behavior undergoing large deformations.

Acknowledgements We acknowledge the support of DOE Nuclear Energy University Program (NEUP) grant number 09–416 and ONR Multidisciplinary University Research Initiative program (MURI) BAA 10–026. We also thank NSF CMMI-1031829, CMMI-1121174 and Beercherl Chair for additional support.

References

1. Arezoo S, Tagarielli VL, Siviour CR, Petrinic N (2013) Compressive deformation of rohacell foams: effects of strain rate and temperature. Int J Impact Eng 51:50–57
2. Daphalapurkar N, Hanan J, Phelps N, Bale H, Lu H (2008) Tomography and simulation of microstructure evolution of a closed-cell polymer foam in compression. Mech Adv Mater Struct 15(8):594–611
3. Flores-Johnson EA, Li QM, Mines RAW (2008) Degradation of elastic modulus of progressively crushable foams in uniaxial compression. J Cell Plast 44(5):415–434
4. Zenkert D, Shipsha A, Burman M (2006) Fatigue of closed cell foams. J Sandwich Struct Mater 8(6):517–538
5. Zenkert D, Burman M (2009) Tension, compression and shear fatigue of a closed cell polymer foam. Composites Sci Technol 69(6):785–792
6. Li QM, Mines RAW, Birch RS (2000) The crush behaviour of rohacell-51wf structural foam. Int J Solids Struct 37(43):6321–6341
7. Arezoo S, Tagarielli VL, Petrinic N, Reed JM (2011) The mechanical response of rohacell foams at different length scales. J Mater Sci 46(21):6863–6870
8. Babout L, Ludwig W, Maire E, Buffière JY (2003) Damage assessment in metallic structural materials using high resolution synchrotron X-Ray tomography. Nucl Instrum Methods Phys Res, Sect B 200:303–307
9. Buffiere JY, Ferrie E, Proudhon H, Ludwig W (2006) Three-dimensional visualisation of fatigue cracks in metals using high resolution synchrotron X-Ray micro-tomography. Mater Sci Technol 22(9):1019–1024
10. Dudek MA, Hunter L, Kranz S, Williams JJ, Lau SH, Chawla N (2010) Three-dimensional visualization of reflow porosity and modeling of deformation in Pb-free solder joints. Mater Charact 61(4):433–439
11. Sassov A, Buelens E (2006) Micro-CT for polymers and composite materials. Functional Materials, vol 13. Wiley-VCH Verlag GmbH & Co. KGaA, Berlin, Germany
12. Patterson BM, Henderson K, Smith Z, Zhang D, Giguere P (2012) Applications of micro-CT to in-situ foam compression and numerical modeling. Microsc Anal, pp. S4–S7
13. Bay BK, Smith TS, Fyhrie DP, Saad M (1999) Digital volume correlation: three-dimensional strain mapping using X-Ray tomography. Exp Mech 39(3):217–226
14. Zauel R, Yeni YN, Bay BK, Dong XN, Fyhrie DP (2006) Comparison of the linear finite element prediction of deformation and strain of human cancellous bone to 3D digital volume correlation measurements. J Biomech Eng-T ASME 128(1):1–6
15. Liu L, Morgan EF (2007) Accuracy and precision of digital volume correlation in quantifying displacements and strains in trabecular bone. J Biomech 40(15):3516–3520
16. Jirousek O, Jandejsek I, Vavrik D (2011) Evaluation of strain field in microstructures using micro-CT and digital volume correlation. J Instrum 6, C01039
17. Maskarinec SA, Franck C, Tirrell DA, Ravichandran G (2009) Quantifying cellular traction forces in three dimensions. Proc Natl Acad Sci 106 (52):22108
18. Franck C, Hong S, Maskarinec SA, Tirrell DA, Ravichandran G (2007) Three-dimensional full-field measurements of large deformations in soft materials using confocal microscopy and digital colume correlation. Exp Mech 47(3):427–438
19. Forsberg F, Mooser R, Arnold M, Hack E, Wyss P (2008) 3D micro-scale deformations of wood in bending: synchrotron radiation mu CT data analyzed with digital volume vorrelation. J Struct Biol 164(3):255–262
20. Germaneau A, Doumalin P, Dupre JC (2008) Comparison between X-Ray micro-computed tomography and optical scanning tomography for full 3D strain measurement by digital volume correlation. NDT E Int 41(6):407–415
21. Forsberg F, Siviour CR (2009) 3D deformation and strain analysis in compacted sugar using X-Ray microtomography and digital volume correlation. Meas Sci Technol 20(9):095703
22. Roux S, Hild F, Viot P, Bernard D (2008) Three-dimensional image correlation from X-Ray computed tomography of solid foam. Composites A-Appl Sci Manuf 39(8):1253–1265
23. Rannou J, Limodin N, Réthoré J, Gravouil A, Ludwig W, Baïetto-Dubourg MC, Buffière JY, Combescure A, Hild F, Roux S (2010) Three dimensional experimental and numerical multiscale analysis of a fatigue crack. Comput Methods Appl Mech Eng 199(21–22):1307–1325

24. Carroll J, Efstathiou C, Lambros J, Sehitoglu H, Hauber B, Spottswood S, Chona R (2009) Investigation of fatigue crack closure using multiscale image correlation experiments. Eng Fracture Mech 76(15):2384–2398
25. Giachetti A (2000) Matching techniques to compute image motion. Image Vis Comput 18(3):247–260
26. Hu Z, Luo H, Young W, Lu H (2012) Three-dimensional internal large deformation measurement of PMI foam using incremental digital volume correlation. Int Mech Eng Congress Exposition, Houston, USA
27. Open MPI: Open Source High Performance Computing (2012) http://www.open-mpi.org/

Chapter 20
Strain Measurement at Temperatures Up to 800 °C Utilizing Digital Image Correlation

J.T. Hammer, J.D. Seidt, and A. Gilat

Abstract An experimental technique is introduced to measure full field strains using three dimensional digital image correlation at temperatures up to 800 °C. Challenges include: thermal air gradients, speckle pattern adhesion, image distortion due to viewing window deformation, camera calibration, and infrared light pollution of the camera sensor. Elements of the test setup are designed to address all of these challenges. The technique is used to measure full-field strains on Ti-6Al-4V specimens as they are loaded to failure in tension. The technique provides substantially more data than traditional elevated temperature strain measurement methods.

Keywords High temperature • DIC • Digital image correlation • Ti-6Al-4V • Strain measurement

20.1 Introduction

Engineering components frequently experience elevated operating temperatures, for example, turbine blades and other components in the hot section of a jet engine. It is important to characterize the behavior of these materials at the elevated operating temperatures so that designs may be evaluated using numerical simulations. Therefore, there is a need to conduct mechanical tests on materials at elevated temperatures to determine both their plastic deformation and fracture behavior under these conditions. Specially designed extensometers are commonly used to measure strain directly on the specimen during elevated temperature tension tests. The extensometers measure the strain between two ceramic knife edges attached to the specimen. The actual body of the extensometer typically lies outside of the heated environment and is often times water-cooled. The extensometers work quite well, however, an assumption is made that the strain is uniform between the two knife-edge contact points. This is often not the case, especially for ductile metals that can have dramatic necking localizations at high temperatures. These devices also typically have limited measuring ranges and need to be removed prior to specimen failure.

Digital Image Correlation (DIC) [1] is now widely used to measure component and specimen surface strains in experimental mechanics. This technique is also being employed in more complex test conditions, such as dynamic tests and tests at elevated temperatures. Previous studies [2, 3, 4] have employed the technique to measure the coefficient of thermal expansion (CTE) and elastic deformation of various materials. The authors of these articles outline the following challenges:

- Deformation of furnace windows and variations in the refractive index of the heated air are sources of measurement error.
- Infrared radiation (IR) can pollute the camera sensor and cause measurement error.
- The speckle pattern used on the specimen must survive at elevated temperatures.

This paper presents a method to measure specimen surface strains at temperatures up to 800 °C. 3D DIC is used in conjunction with a servohydraulic load frame and custom furnace designed specifically for this application. Results from tension tests on Ti-6Al-4V are presented. These data are useful for developing temperature dependent models to describe both plastic deformation and failure of materials.

J.T. Hammer • J.D. Seidt (✉) • A. Gilat
Department of and Mechanical and Aerospace Engineering, The Ohio State University, Scott Laboratory,
201 W 19th Ave, Columbus, OH 43210, USA
e-mail: seidt.2@osu.edu

H. Jin et al. (eds.), *Advancement of Optical Methods in Experimental Mechanics, Volume 3*,
Conference Proceedings of the Society for Experimental Mechanics Series,
DOI 10.1007/978-3-319-00768-7_20,

20.2 Experimental

A custom furnace, designed in conjunction with Applied Test Systems, Inc., is employed to heat the test specimen. The furnace has a 38 mm by 102 mm optical grade quartz window, see Fig. 20.1a. The window is free to expand inside a ceramic attachment fixture. This freedom reduces window deformation and lensing of the optical path between the camera sensor and the specimen. The front of the furnace (which contains the window) is mounted to an Instron 1,321 servohydralic load frame to maintain a consistent optical path. The rear of the furnace opens on a hinge granting access to the specimen, see Fig. 20.1c. This design is practical for repeated testing since the camera rig does not need to be moved every time a new specimen is inserted into the furnace. The furnace has an internal Inconel 718 fan that circulates the inside air. The fan is powered by an external electric motor. The circulation ensures uniform specimen heating and reduces lensing from optical distortions due to temperature gradients in the air.

Photron MC2 cameras (CMOS sensors) are mounted vertically, as shown in Fig. 20.1b. The cameras acquire images at 1,000 frames per second at 512 by 512 resolution. Fifty millimeter DG Macro lenses provide a suitable field of view for the specimen. Since CMOS sensors are susceptible to IR radiation, Tiffen hot mirror reflective IR filters are used reflect wavelengths above 700 nm. Fiber optic lamps, Fig. 20.1b, are used to illuminate the specimen. B+W linear polarizer filters are used to reduce image glare.

Axial load is measured by a load cell mounted in series with the upper grip. The grips and pull-rods, see Fig. 20.2, are fabricated from Inconel 718. Water is circulated through cooling collars attached to the pull-rods outside of the furnace to minimize heat transfer to the load cell. Two Omega type K thermocouples are attached to the specimen using Omega CC high temperature cement, see Fig. 20.2. One thermocouple is mounted to the upper portion of the specimen gripping tab, while the second is mounted to the lower. Temperature gradients between the two thermocouples are regularly less than 5 °C. Tests are conducted in stroke control such that the specimen strain rate is roughly 1.0 s^{-1}.

Rustoleum High-Heat paint is used to pattern the specimen. White paint is used for the base coat while black is used to provide contrast, see Fig. 20.3. The paint has a reported operating temperature of 1,093 °C.

Experimental results from selected tension experiments are presented in Figs. 20.3 and 20.4. Figure 20.3 shows the axial strain contours on the surface of Ti-6Al-4V tension specimens just prior to failure at room temperature, 200 °C, 400 °C and

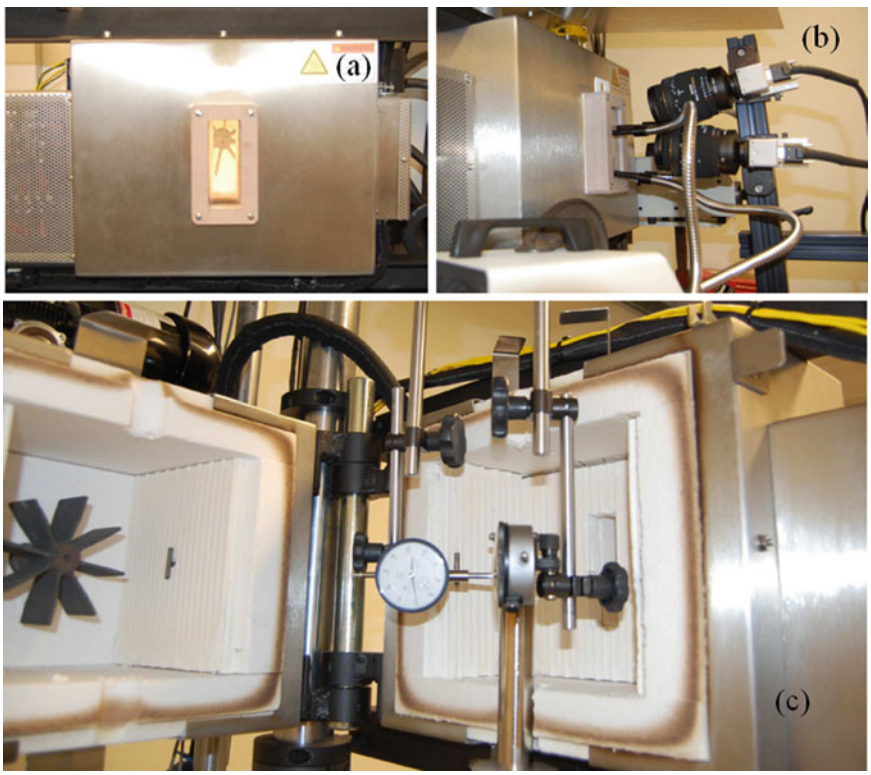

Fig. 20.1 Experimental setup: (**a**) front view of the furnace, (**b**) Photron MC2 cameras and fiber optic light source, (**c**) internal view of the furnace

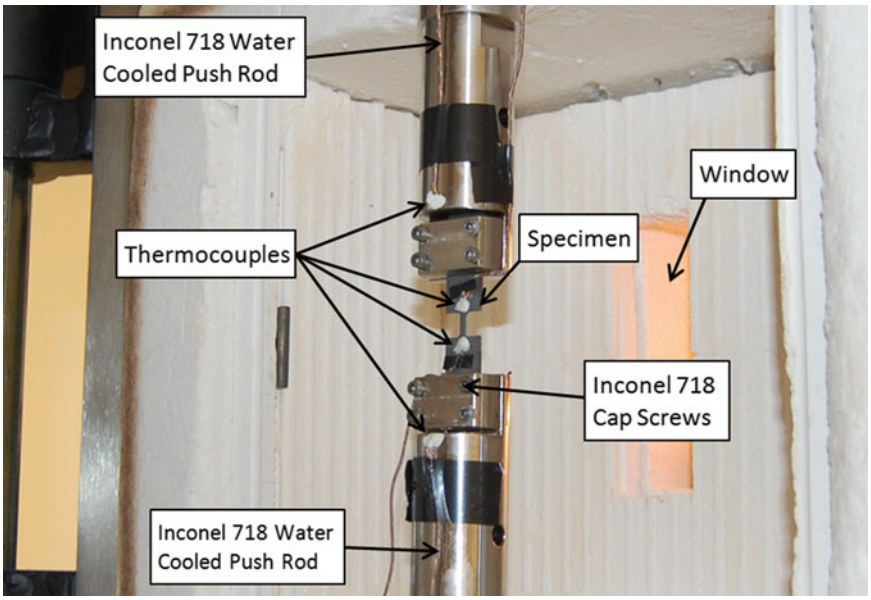

Fig. 20.2 Tension specimen attachment and thermocouple instrumentation

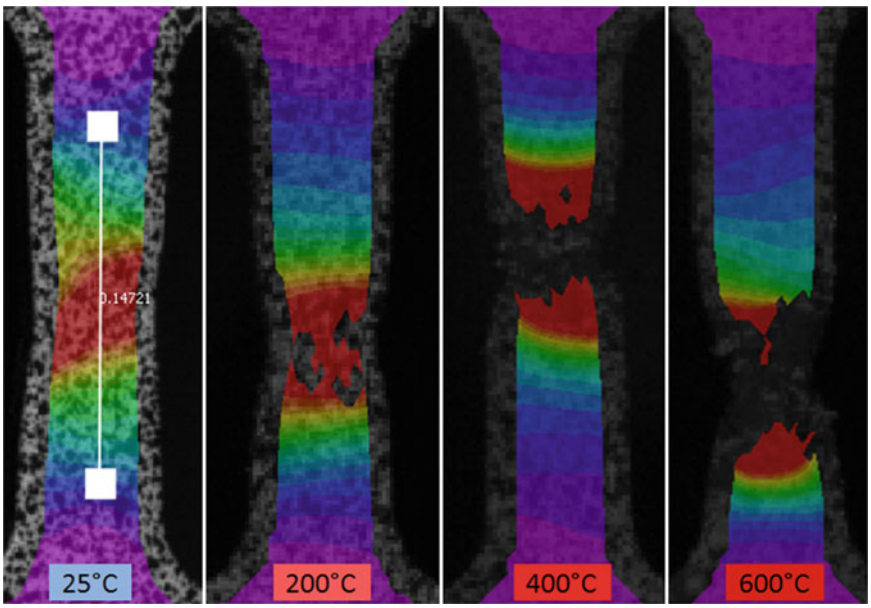

Fig. 20.3 Axial strain contours measured using 3D DIC at temperatures ranging from 25 °C to 600 °C

600 °C. The results show increasing ductility with increasing temperature. As ductility increases, speckle pattern adhesion becomes more challenging. This is clearly evident in the 400 °C and 600 °C data. Figure 20.4 shows engineering stress vs engineering strain of a Ti-6Al-4V specimen at 600 °C. A curve constructed with strain from a 4 mm DIC extensometer is compared to a curve constructed using the stroke from the load frame LVDT. The LVDT curve assumes that the strain is uniformly distributed over the 5.08 mm long smooth section of the specimen. This is clearly not the case, as evident in Fig. 20.3. The DIC curve clearly captures the elastic deformation, yield point and the localization of material more accurately than the LVDT curve.

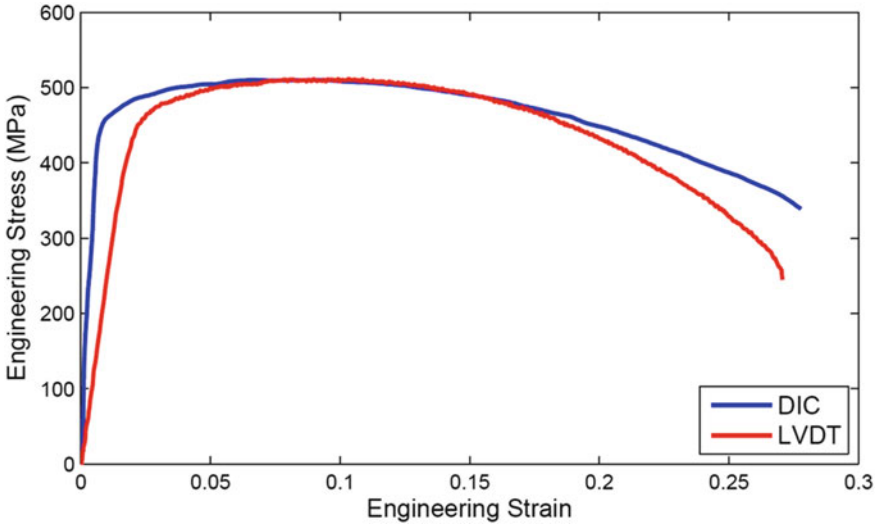

Fig. 20.4 Engineering stress versus engineering strain curves from a tension test on Ti-6Al-4V at 600 °C

20.3 Summary and Conclusions

An experimental technique to measure surface strains of specimens under tensile load at temperatures up to 800 °C is presented. A custom furnace is used in conjunction with a servohydraulic load frame to conduct the experiments. The furnace has a large optical grade quartz window that is free to expand within its ceramic mounting fixture. The front of the furnace (which contains the window) mounts to the load frame to maintain a consistent optical path between the cameras and the specimen. The rear of the furnace opens to allow access to the specimen. The arrangement is convenient for DIC system calibration. An Inconel 718 fan circulates air within the furnace to uniformly heat the specimen and reduce optical distortions due to temperature gradients in the air. The specimen is gripped with water-cooled Inconel 718 fixtures. Temperature on the specimen is monitored with two thermocouples. Tension tests are conducted on Ti-6Al-4V samples until failure at a nominal strain rate of 1.0 s^{-1}. Photron MC2 cameras are used to acquire images as the specimen deforms at 1,000 frames per second. Hot mirror IR and linear polarization filters are used to reduce IR sensor pollution and glare, respectively.

This technique acquires more comprehensive data than those acquired from high temperature extensometers. DIC allows the user to inspect strains from extensometers of any length oriented in any direction. Axial, transverse and shear strains in localization regions of the specimen are also available. These data are valuable for developing and calibrating both plasticity and failure material models.

Acknowledgements The research was supported by the U.S.A. Federal Aviation Administration. The authors would like to thank William Emmerling, Donald Altobelli and Chip Queitzsch of the FAA. The authors also thank Professor Michael Sutton of the University of South Carolina for his noteworthy advice.

References

1. Sutton MA, Orteu J-J, Schreier HW (2009) Image correlation for shape, motion and deformation measurements: basic concepts, theory and applications. New York, Springer
2. Lyons JS, Liu J, Sutton MA (1996) High-temperature deformation measurements using digital-image correlation. Exp Mech 36(1):64–70
3. Grant BM, Stone HJ, Withers PJ, Preuss M (2009) High-temperature strain field measurement using digital image correlation. J Strain Anal Eng Des 44(4):263–271
4. Pan B, Wu D, Wang Z, Xia Y (2011) High-temperature digital image correlation method for full-field deformation measurements at 1200°C. Meas Sci Technol 22(1)

Chapter 21
Novel Thermo-Mechanical Testing Method of Nuclear Fuel Cladding at Elevated Temperature

Luis H. Alva, Xinyu Huang, Michael Sutton, and Li Ning

Abstract Ceramic composites are being developed as the next generation accident tolerant fuel cladding for light water reactors. In this study, we report a novel method to evaluate thermo-mechanical robustness of ceramic nuclear fuel cladding tube under simulated accident conditions. A ceramic surrogate core is used as the "pressurizing media" inside the cladding tube. To mimic accident condition, the surrogate core is electrically heated up to 1,200°C to create a temperature gradient; stress in the cladding tube is generated by the mechanical interference of the surrogate core and the cladding tube. In order to apply digital image correlation (DIC) technique for surface strain measurement, a method to produce temperature-resistance speckle pattern was developed. By using a narrow bandpass filter and a LED source, stable reflective images of speckle pattern was achieved from room temperature up to over 1,000°C. This enabled the first successful full field strain mapping of nuclear fuel cladding at high temperature using 3D DIC technique. The surface strain distribution as well as the temperature data obtained can be used to validate numerical simulation models of nuclear fuel cladding.

Keywords Nuclear fuel cladding • Pellet cladding mechanical interaction • Digital image correlation • Strain measurement • Silicon carbide • High temperature testing

21.1 Introduction

Zircaloy cladding has been successfully used as fuel cladding in light water reactors for many decades. The 2011 accident of the nuclear power plant in Japan (Fukushima Daiichi) highlighted a known weakness of the zircaloy cladding, i.e., low melting temperature and undesirable reactivity of zircaloy with water at high temperature. The metal-water reaction produces hydrogen, an explosion hazard. Alternative accident tolerant fuel claddings are being actively developed. Among them, silicon carbide (SiC) ceramic composite consisting of silicon carbide fiber reinforced silicon carbide matrix [1, 2] is a promising candidate. Nuclear fuel cladding tube is designed to hold the fuel pellets (typically UO_2) in the designed geometry and distribution within the reactor core, allow efficient transfer of heat nuclear fuel pellet (typically UO_2) to the coolant, and prevent the release of radioactive fission products into the coolant loop and outside environment [3]. The thermal mechanical robustness of the cladding tube is of critical importance to ensure that the radioactive fission products are retained during both normal operation and accident conditions, such as the loss of coolant, condition encountered in Fukushima Daiichi plant. As a ceramic material, the toughness of SiC based ceramic cladding under thermo-mechanical loading is of concern.

In this work, a novel testing method is developed to evaluate the thermo-mechanical robustness of the ceramic fuel cladding. The objective is to simulate accident conditions that include the high temperature, high temperature gradient, intense pellet cladding mechanical interaction, and at the same time allow the measurement of full field surface strain distribution on the outer surface of the ceramic cladding tube. Accurate measurement of strain distribution at high

L.H. Alva (✉) • X. Huang
Mechanical Engineering Department, University of South Carolina, 541 Main St., Columbia, SC 29208, USA
e-mail: alvasola@email.sc.edu

M. Sutton • L. Ning
Mechanical Engineering Department, University of South Carolina, 300 Main St., Columbia, SC 29208, USA

H. Jin et al. (eds.), *Advancement of Optical Methods in Experimental Mechanics, Volume 3*,
Conference Proceedings of the Society for Experimental Mechanics Series,
DOI 10.1007/978-3-319-00768-7_21,

temperature is a challenging task. In this study, digital image correlation (DIC) technique was used. High temperature environment presents a number of problems for the application of DIC method. First of all, a surface speckle pattern that can survive the high temperature exposure is needed. Secondly, hot material emits visible light which can change the contrast of the speckle image and confuse the DIC algorithm. Thirdly but not last, the hot air surrounding the sample may potentially distort the image. In this work, we have overcome/avoided these difficulties and achieved, we believe for the first time, a successful surface strain mapping of nuclear fuel cladding under simulated accident conditions. The details of experimental design, implementation, and preliminary data are presented in the following sections.

21.2 Experiment Design

Figure 21.1a shows the experimental scheme. A surrogate tube is placed inside the cladding tube; a ceramic rod heater capable of reaching temperatures of 1,700 °C is placed inside the surrogate tube. To simulate accident condition, the rod heater is electrically heated and maintained at desirable temperature using a variable transformer; a sample chamber (Fig. 21.1b) with quartz windows is used to enclose the hot sample and to control the heat loss rate via regulated air flow through the chamber. A steep temperature gradient can be induced from inside the cladding to outside the cladding. Using this scheme, it was found that the sample outside surface temperature as high as 1,200 °C can be achieved. The expansion of the surrogate tube exert a mechanical stress on the cladding in a manner closely mimic that by the pellet cladding mechanical interaction. Both hoop and axial stress (Fig. 21.1c) can be induced in the cladding tube; it is desirable to capture the deformation process by measuring the surface strain distribution of the cladding sample during the thermo-mechanical "loading" process.

The digital image correlation (DIC) method is adopted here to measure the surface strains. DIC is a non-contact full field strain measurement technique with a broad field of applications [4]. Due to the curved nature of the sample, three-dimensional DIC method enabled by two cameras is used. The arrangement of the optical components for strain measurement is shown in Fig. 21.2d. Two CCD cameras from Point Grey (GRAS-30S5M) are used for image acquisition. The CCD chip in the camera is ICX625AL from Sony. Two 25 mm lenses (NT63-780 from Edmund Optics) are used. The camera is placed at 22 cm away from the sample and the angle between the two optical axes is 10 °.

Following the work of Novak et al. [5], a light filtering scheme is used to overcome the thermal emission problem. The spectral characteristics of the optical instruments are summarized in Fig. 21.2. Two Thorlabs-LIU004 LED lights are used to illuminate the sample behind the fused quartz window which has a transmittance > 0.9 in the range from 280 to 2,000 nm. Two 450 nm bandpass filter from Edmund Optics (BP450) was used in front of each camera to filter the light reaching the camera lenses. Four hundred and fifty nanometer is selected so that the wavelength stays within the sensitive spectra window of the Sony CCD sensor and sufficiently away from thermally emitted light at longer wavelength. This arrangement allows the capture of images with stable surface contrast during the heating process.

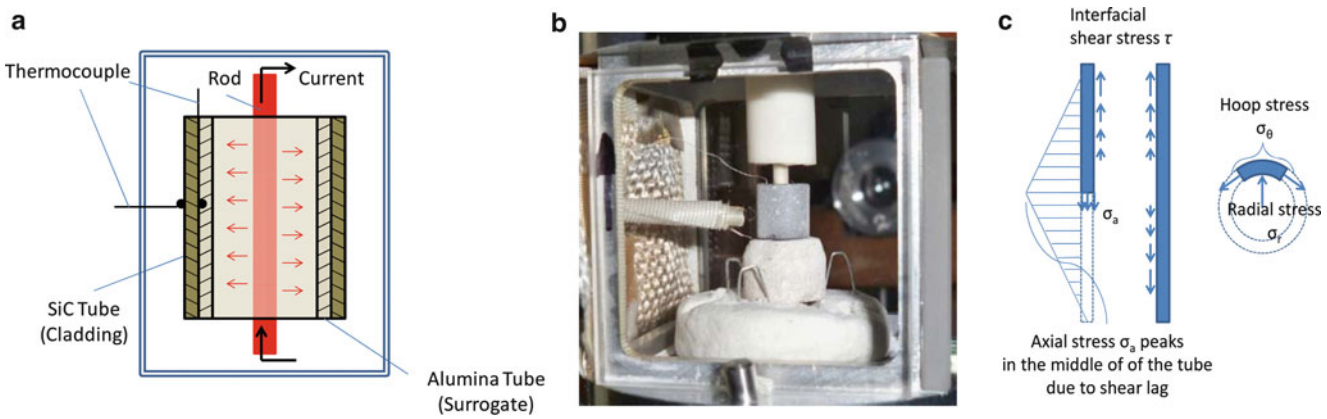

Fig. 21.1 (**a**) Setup schematic, (**b**) picture of sample inside the chamber, and (**c**) stresses acting on the cladding

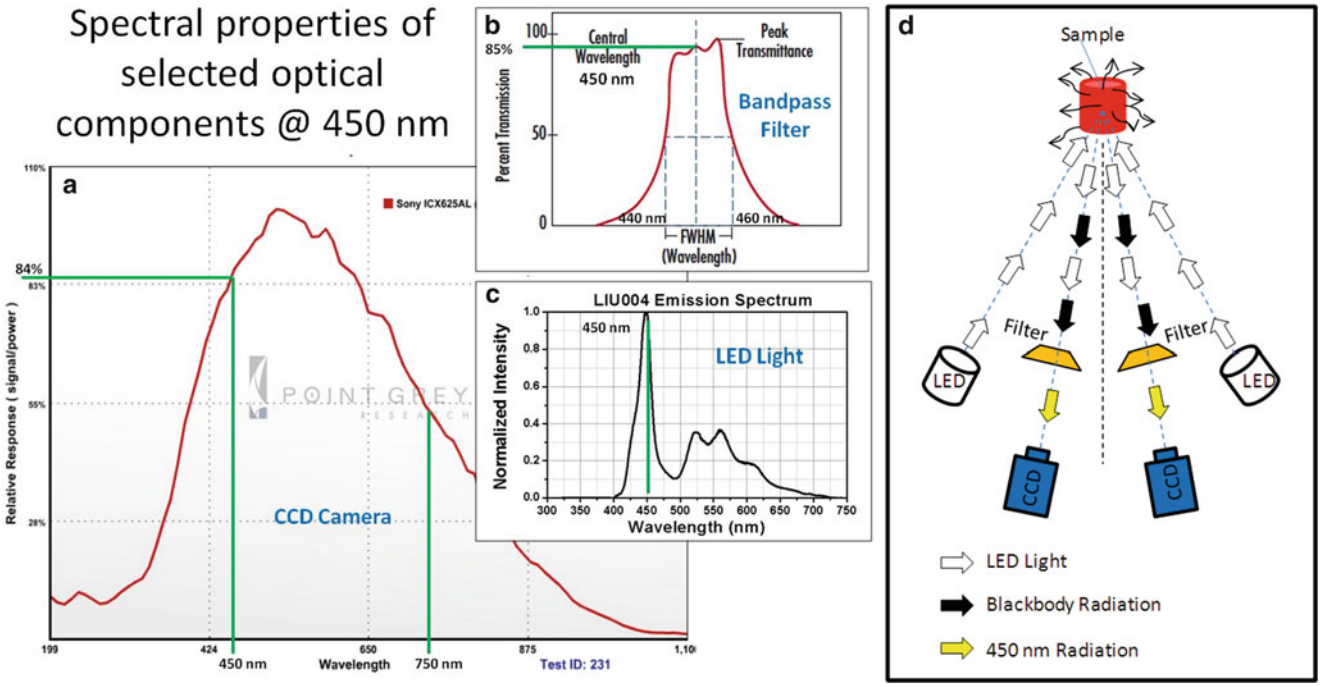

Fig. 21.2 Spectral curves of (**a**) Point grey CCD camera, (**b**) Edmund optics 450 nm bandpass filter, (**c**) Thorlabs LED light, and (**d**) the schematic of the optical setup

21.3 Sample Preparation

A monolithic SiC tube (OD 9.5 mm, ID 6.35 mm) is used to represent SiC nuclear fuel cladding. The heating rod is a partially stabilized ZrO_2 rod (OD 3.48 mm). The surrogate is an Al_2O_3 tube (OD 6.35 mm, ID 4.78 mm). All ceramic tubes/rods were acquired from Ortech Advanced Ceramics (Sacramento, CA). The SiC and alumina tube are first cut into 9.5 mm long segments using a diamond wafering saw and assembled together. A fine wire K-type thermocouple is place at the interface between the surrogate tube and the SiC tube. Suitable surface contrast pattern is critical for DIC measurement. Because the experiment will be conducted at temperature higher than oxidation/decomposition of most regular spray paint, special high temperature paints are used instead. By trial and error, an alumina based high temperature white color spray paint from ZYP coatings was used to paint a pattern of white random spots on the surface of the SiC sample which is dark grey. After painting (Fig. 21.3), the sample was heated in an air furnace to 1,000 °C to test the stability of the contrast pattern. The speckle image contrast before and after heating was observed to be greater than 40 units in the 256-grey scale. This level of contrast is deemed good enough for digital image correlation analysis.

21.4 Experimental Procedure

The assembled surrogate and core sample were placed inside the test chamber. Fine wire thermocouples (R and K type) were installed to measure temperature inside and outside surface of the assembly. The ceramic heating rod was inserted into the center of the assembly. The heater power was adjusted to slowly heat up the sample and stabilize at a series of temperatures when the sample images were acquired using a Vic-Snap program from Correlated Solutions, Inc.

The refractive index of hot air is slightly different than that of cool air. This can potentially cause the distortion of the images acquired. Under steady state during the experiment, we monitored air temperature at half the distance between the rod and the quartz window (inside the chamber), and at 3 mm from the quartz window (outside the chamber) in the direction of the optical axis, a variation of $\pm$ 0.7 °C and $\pm$1.5 °C respectively was observed when the forced air flow is not running. These variations are considered not significant to cause distortion of the images not requiring a fan to mix the air as suggested by Lyons et al. [6].

Fig. 21.3 A-aerosol paint on SiC substrate as speckle pattern

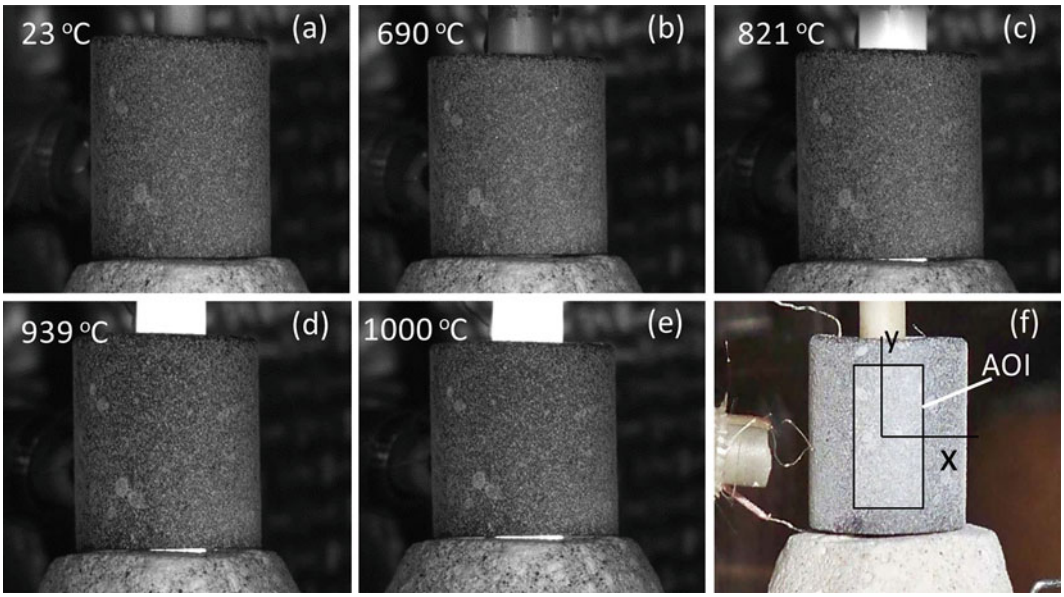

Fig. 21.4 Images of the sample at (**a**) 23 °C, (**b**) 690 °C, (**c**) 821 °C, (**d**) 939 °C, (**e**) 1,000 °C taken using the 450 nm filter, and (**f**) color image of the sample with the AOI and the coordinate system

21.5 Results and Discussion

Our preliminary work has been conducted on SiC tube with shape and size close to real SiC composite cladding. Using this dummy sample, we have identified and solved a number of technical problems associated with full field strain measurement at high temperature, and demonstrated the efficacy of the method. Figure 21.4 shows images acquired at room temperatures, 690 °C, 821 °C, 939 °C, and 1,000 °C respectively as well as a color image of the sample showing the area of interest (AOI) and the coordinate system used for the image correlation. Despite the fact that the sample reached red hot state, no appreciable difference of surface contrast was seen on the image. It is believed the images of SiC surface is formed by reflected light near 450 nm as defined by the bandpass filter. In contrast, the ceramic heating rods (ZrO_2) emits strongly at 450 nm as temperature increases.

The 2010-Vic-3D software from Correlated Solutions, Inc. was used to analyze the collected images and to calculate the strains on the surface of the sample. The correlation algorithm used is based on the normalized square differences criterion which has better tolerance to changes in lighting. The analysis was done using a subset of 29 pixels, and a step of seven pixels. The correlation accuracy obtained is in the order of 0.06 pixels. Based on experience, bad dataset usually has accuracy threshold value greater than 0.1. The plots of strain distribution are shown in Fig. 21.5 below.

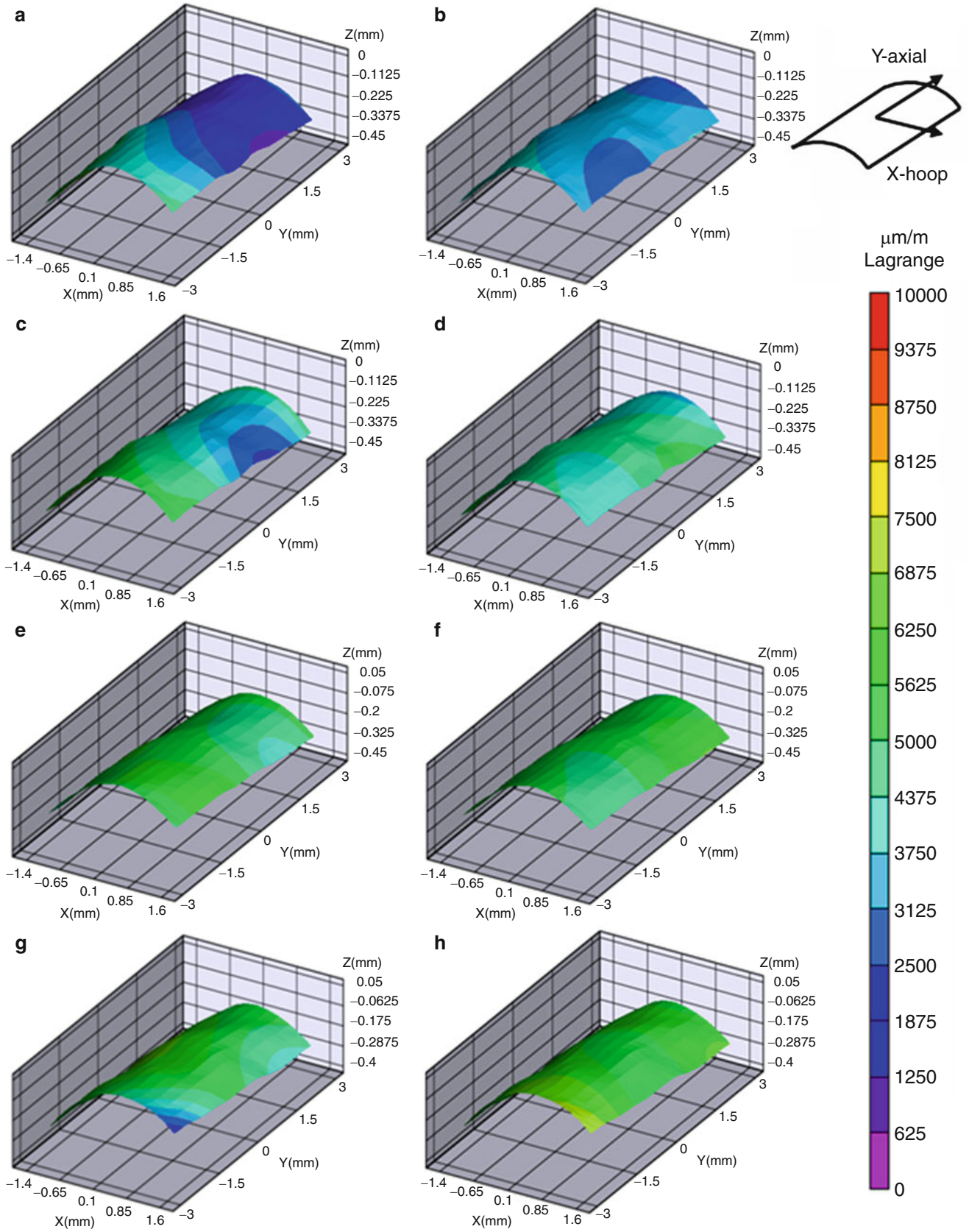

Fig. 21.5 Strains calculated usingVic-3D software, hoop strains (x-direction) (**a**) 690 °C, (**c**) 821 °C, (**e**) 939 °C, (**g**) 1000 °C, and axial strains (y-direction) (**b**) 690 °C, (**d**) 821 °C, (**f**) 939 °C, (**h**) 1000 °C

Table 21.1 Summary of strains

Temperature (°C)	Hoop strain, ε_{xx} (μ strains) Small area at the center	Axial strain, ε_{yy} (μ strains) Small area at the center	Reference: SiC strain (μ strains) No surrogate Calculated using CTE 4 × 10^6 °C^{-1}
690	2,726	3,333	2,668
821	4,134	4,507	3,192
939	5,340	5,209	3,664
1,000	6,211	5,595	3,908

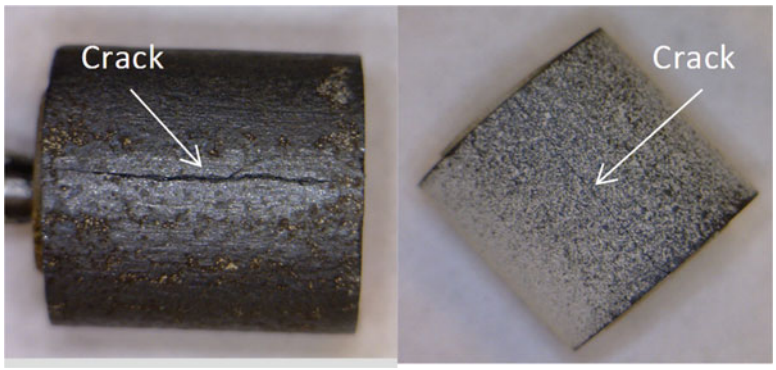

Fig. 21.6 SiC samples with cracks produced by hoop expansion

In Table 21.1 a summary of the average strains corresponding to a small area near the center of the image is presented. As a reference, the free thermal expansion strain for SiC (based on CTE of 4.0 *10^{-6}/°C) is also given at the corresponding temperatures. It is noticed that measured total strain is greater than the free thermal expansion strain of SiC as result of temperature gradient and mechanical interaction between surrogate and the core tube. It is also interesting to notice that significant strain in axial direction is developed during heating, this is likely due to the axial expansion of the surrogate tube and the static friction between cladding and the surrogate. It is believed that such frictional interaction does also occur in the actual pellet cladding interaction.

The results confirmed that the cladding is under a state of biaxial tension, near equal-biaxial tension at lower temperature, and then hoop stress starts to dominate at higher temperature, c.a. 900 °C. As a result, the cladding sample was observed to fail due to hoop stress at high temperature, as shown in Fig. 21.6 where cracks are observed on the outside surface of the cladding. The added mechanical strain at 1,000 °C in the hoop direction is 0.23 % from Table 21.1, this value is very close to the peak strain during failure of 0.202 % for a TREX specimen and 0.224 % for a St. Gobain tubular specimen of monolith SiC reported by Ross et al. [7] when subjected to internal pressurization.

21.6 Conclusions

In summary, we have developed a novel thermo-mechanical testing method for nuclear fuel cladding. The method is particularly suitable to study SiC-based ceramic cladding tubes. The test scheme is relatively simple, safe, and affordable. Strain mapping enabled by 3D digital image correlation was achieved using a spectral filtering technique and a speckle pattern produced by a high temperature paint. The results make qualitative sense. The deformation of the cladding (SiC sample), using a solid surrogate tube as in the method proposed, mimics the deformation of cladding in a nuclear reactor due to pellet clad interacting during accident conditions Frictional loading produced detectable axial strain. The state of strains calculated in this work show qualitatively agreement with the observed failure mode of the SiC cladding.

References

1. Yueh K, Carpenter D, Feinroth H (2010) Clad in clay. Nucl Eng Int 55:14–16
2. Herderick ED, Cooper K, Ames N (2012) New approach to join SiC for accident-tolerant nuclear fuel cladding. Adv Mater Process 170(1):24
3. Azevedo CRF (2011) Selection of fuel cladding material for nuclear fission reactors. Eng Fail Anal 18:1943–1962

4. Sutton MA, Orteu JJ, Schreider HW (2009) Image correlation for shape, motion and deformation measurements. Springer, US
5. Novak MD, Zok FW (2011) High-temperature materials testing with full-field strain measurement: experimental design and practice. Rev Sci Instrum Pract. 82(11):115101
6. Lyons JS, Liu J, Sutton MA (1996) High-temperature deformation measurements using digital-image correlation. Experimental mechanics 36(1):64–70
7. Ross Jr, Denwood F, Hendrich WR (2006) Strength testing of monolithic and duplex silicon carbide cylinders in support of use as nuclear fuel cladding. In: Proceedings of the 30th international conference on advanced ceramics and composites, Cocoa Beach, FL USA

Chapter 22
Stress Analysis of a Metal-Plate-Connection in a Beam Under 3-Point-Bending Using Digital Image Correlation

W.A. Samad and R.E. Rowlands

Abstract Metal-plate-connected wood trusses for roofs and floors have been used in light-frame residential, industrial, and commercial construction for several decades. The behavior of a metal-plate connector (MPC) joint is very complex and is influenced by many variables, including metal-plate properties, joint geometry, and the natural variability of wood. Moreover, boundary conditions of such connectors are not well defined in practice, thus ruling out meaningful analytical or numerical stress analyses. With very little prior research on the state of stress of a MPC, this paper presents a hybrid method for stress analyzing a MPC in a beam subjected to 3-point bending using 3D Digital Image Correlation (DIC). The recorded vertical displacements in the vicinity of one of the holes of the MPC are coupled with an Airy stress function, along with imposed appropriate boundary conditions on the edge of the MPC hole. All stress components are determined from only the vertically recorded displacements. Obtaining reliable experimental data near edges can be challenging, but this is overcame here by filling the MPC holes with extremely compliant clay material and applying the speckle pattern over both materials such that measured displacements are obtained continuously throughout the perforated metal plate.

Keywords Metal-plate connectors • DIC • Hybrid

22.1 Background

Metal plate connectors are popular in construction because they are economical and offer a favorable strength-to-weight ratio [1]. As far back as 1978, annual gross sales of MPCs alone were estimated at well over $100 million [2]. As such, any study that helps better understand the state of stress and ultimately the design of MPCs could provide significant savings. Most of the research in this area has concentrated on determining the overall performance (overall stiffness and failure mode) of different MPC joints and generating analytical models to predict the member forces in wood trusses. The behavior of the MPC itself has received little attention.

This paper determines the state of stress in the vicinity of a single hole in a MPC by synergizing DIC-measured vertical displacement data with an Airy stress function, along with imposing boundary conditions on the edges of the punched MPC hole. The results provided a new insight into the behavior and stress distribution of the complex MPC.

22.2 Experimental Details

Different types of MPC joint configurations and loadings are used in industry, e.g., tensile joints, heel joints, parallel-chord truss joints and web joints [3]. A tensile joint under 3-point bending is analyzed here. As shown in Fig. 22.1, the tensile joint configuration consists of two pieces of wood connected together using a metal plate. The two pieces of (2 by 4) wood

W.A. Samad (✉)
Mechanical Engineering, Rochester Institute of Technology - Dubai, Dubai Silicon Oasis, Dubai, UAE
e-mail: wascad@rit.edu

R.E. Rowlands
Department of Mechanical Engineering, University of Wisconsin, Madison, WI 53706, USA
e-mail: rowlands@engr.wisc.edu

H. Jin et al. (eds.), *Advancement of Optical Methods in Experimental Mechanics, Volume 3*,
Conference Proceedings of the Society for Experimental Mechanics Series,
DOI 10.1007/978-3-319-00768-7_22,

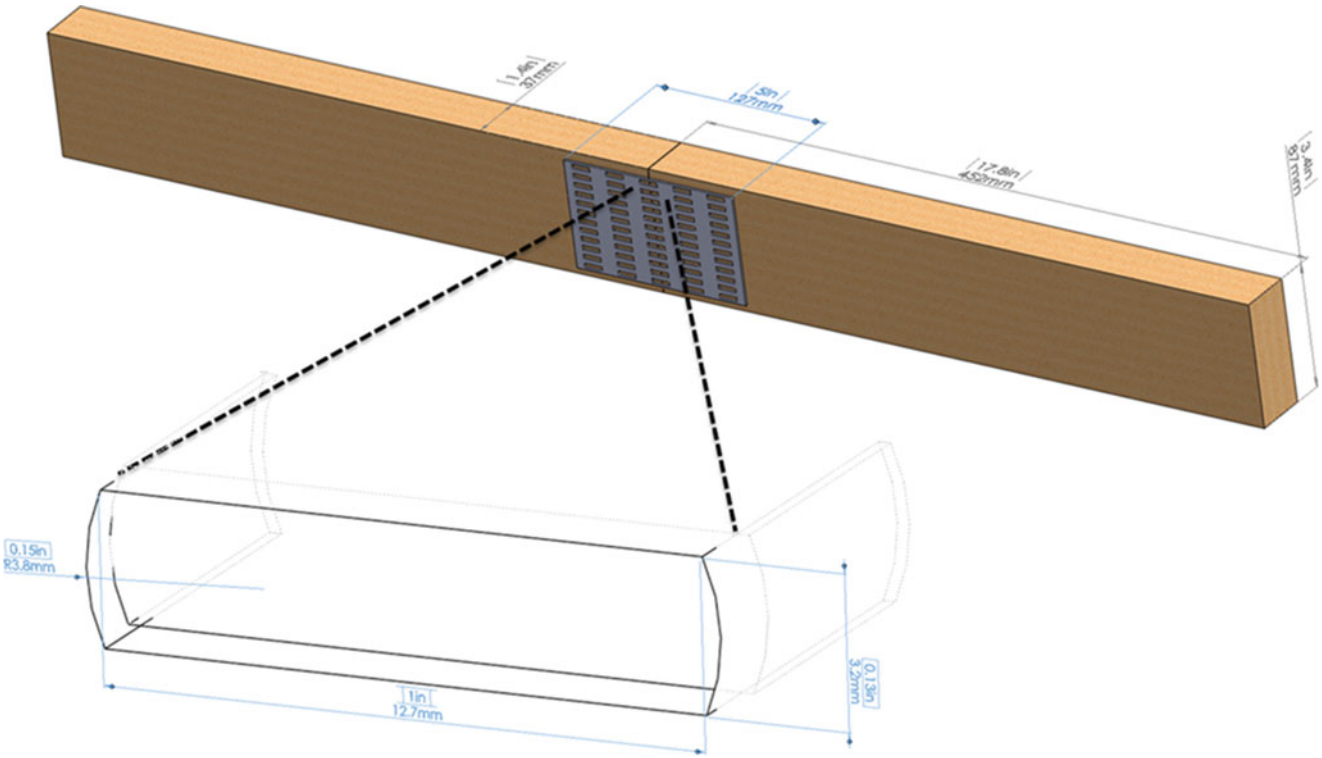

Fig. 22.1 MPC tensile joint 3D CAD model

are 45 cm long, 8.7 cm wide and 3.7 cm thick Southern Pine wood. The MPC (manufactured by Alpine of ITW Building Components Group Inc.) is 12.7 cm long, 7.6 cm wide and 0.16 cm thick ASTM A570 Grade 40 steel with a tooth density of 6.2×10^{-3} teeth per mm^2 (equivalent to four teeth/in^2). The MPC has 60 punched holes with a 0.38 cm spacing in the vertical direction and a 1.27 cm spacing in the horizontal direction, with two teeth stamped per hole, Fig. 22.1. The particular hole analyzed here is the second from the top of the metal plate and at the juncture of the two pieces of wood.

Prior to testing, the MPC holes were filled with highly compliant clay material to enable providing a uniform speckle pattern on the surface as well as to protect the wood underneath the MPC while spray painting. A similar approach has been successfully employed before on structures containing cutouts, [4]. Having filled the holes with clay, the speckle pattern was applied by first spray painting the MPC with Krylon Ultra-Flat white paint to provide a sharp contrast for the subsequently applied black speckle patterns. Only one layer of white paint was applied to avoid changing the shape of the surface or increasing shear effects due to the coating thickness. A black speckle pattern (Krylon Ultra-Flat black paint) was subsequently sprayed onto the white surface, Fig. 22.2. The latter was provided by applying a slight pressure to the trigger of the commercial spray paint container.

The prepared MPC joined beam was loaded in 3-point bending using a 10GL screw-driven MTS machine. A static load of 2,224 N was applied in increments of 222 N while monitoring the overall deflection of the structure as recorded by the MTS crosshead. From the recorded applied load on, and the total deflection of, the joint at the multiple load increments, the stiffness of the joint K was found to be 1,909 kN/m. This is significantly less than the case for a similar joint loaded in pure axial tension [5].

At each load increment, digital images were captured using Point Grey Research CCD Cameras (GRAS-50S5M-C) via the Vic-snap software. The captured images where subsequently analyzed using Correlated Solutions' Vic 3D software. Table 22.1 contains some information regarding the DIC test parameters.

Figure 22.2 below contains an actual photograph of the test setup, with close up images of one MPC hole, the MPC hole filled with clay, the speckle pattern applied and finally the resulting vertical displacements around the MPC hole.

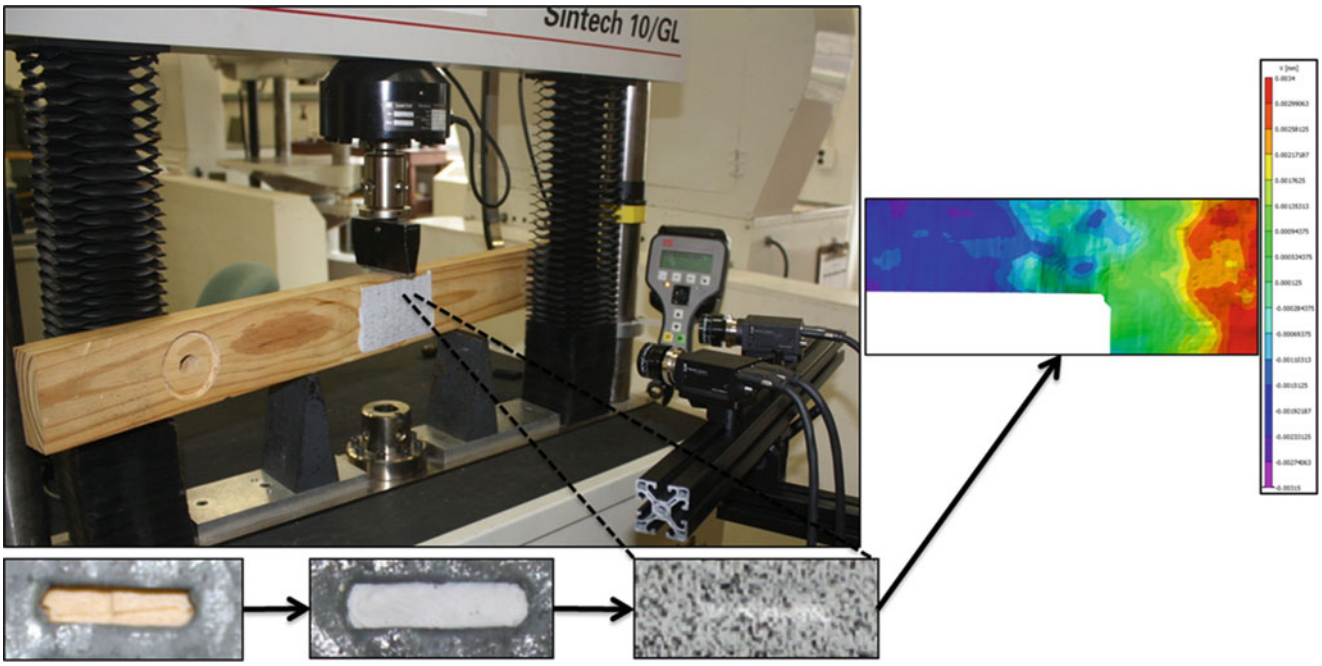

Fig. 22.2 DIC test setup, speckle pattern and vertical displacement, v, data

Table 22.1 DIC test parameters

Lens	17 mm
Aperture	f-4
Sensor resolution	5 MP
External light	Not used
Number of cameras	2 (3D test)
DIC analysis software	Correlated Solutions Vic 3D
Subset size	9
Step size	3

As explained below, the DIC-recorded vertical component of displacements is processed by an Airy stress function to provide the independent components of stress.

22.3 Airy's Stress Function

Assuming a symmetric loading and a state of plane stress when analyzing the central hole, the relevant Airy stress function which satisfies equilibrium and compatibility, i.e., $\nabla^4\phi = 0$, is [6]

$$\phi = a_0 + b_0 \ln r + c_0 r^2 + \sum_{n=2,4,\ldots}^{N} \left\{ \left(a_n r^n + b_n \mathrm{r}^{\mathrm{n}+2} + c_n r^{-n} + d_n \mathrm{r}^{-(\mathrm{n}-2)} \right) \cos n\theta \right\} \tag{22.1}$$

where radius r is measured from the center of the hole and angle θ is measured counterclockwise from the horizontal x-axis, Fig. 22.3. N is the terminating index value of the series and can be any positive even integer.

Upon differentiating Eq. 22.1, the individual polar components of stress become

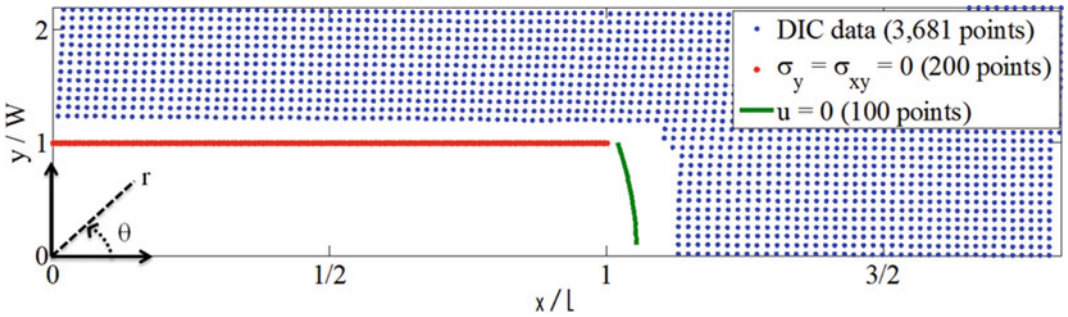

Fig. 22.3 DIC source locations and boundary conditions locations (W = 0.16 cm and L = 0.64 cm)

$$\sigma_r = \frac{1}{r}\frac{\partial \phi}{\partial r} + \frac{1}{r^2}\frac{\partial^2 \phi}{\partial \theta^2} = \begin{array}{l} \frac{1}{r2}b_0 + 2c_0 + \left(\frac{-2c_1}{r^3} + 2rd_1\right)\sin\theta + \left(\frac{-2c'_1}{r^3} + 2rd'_1\right)\cos\theta - \\ \sum_{n=2,3,4,\ldots}^{N}\begin{bmatrix} a_n\ n\ (n-1)\ r^{n-2} + b_n\ (n+1)(n-2)r^n \\ +c_n\ n\ (n+1)\ r^{-(n+2)} + d_n\ (n-1)(n+2)\ r^{-n} \end{bmatrix}\sin(n\theta) \\ -\sum_{n=2,3,4,\ldots}^{N}\begin{bmatrix} a'_n\ n\ (n-1)\ r^{n-2} + b_n'\ (n+1)(n-2)r^n \\ +c'_n n\ (n+1)\ r^{-(n+2)} + d'_n\ (n-1)(n+2)\ r^{-n} \end{bmatrix}\sin(n\theta) \end{array} \tag{22.2}$$

$$\sigma_\theta = \frac{\partial^2 \phi}{\partial r^2} = \begin{array}{l} -\frac{1}{r2}b_0 + 2c_0 + \left(\frac{-2c_1}{r^3} + 6rd_1\right)\sin\theta + \left(\frac{2c'_1}{r^3} + 6rd'_1\right)\cos\theta + \\ \sum_{n=2,3,4,\ldots}^{N}\begin{bmatrix} a_n\ n\ (n-1)\ r^{n-2} + b_n\ (n+1)(n-2)r^n \\ +c_n\ n\ (n+1)\ r^{-(n+2)} + d_n\ (n-2)(n-1)\ r^{-n} \end{bmatrix}\sin(n\theta) \\ +\sum_{n=2,3,4,\ldots}^{N}\begin{bmatrix} a'_n\ n\ (n-1)\ r^{n-2} + b'_n\ (n+1)(n+2)r^n \\ +c'_n n\ (n+1)\ r^{-(n+2)} + d'_n\ (n-2)(n-1)\ r^{-n} \end{bmatrix}\sin(n\theta) \end{array} \tag{22.3}$$

And

$$\sigma_{r\theta} = -\frac{\partial}{\partial r}\left(\frac{1}{r}\frac{\partial \phi}{\partial \phi}\right) = \begin{array}{l} \frac{1}{r2}A_0 + \left(\frac{2c_1}{r^3} + 2rd'_1\right)\cos\theta - \left(\frac{-2c'_1}{r^3} - 2rd_1\right)\sin\theta - \\ \sum_{n=2,3,4,\ldots}^{N}\begin{bmatrix} a_n\ n\ (n-1)\ r^{n-2} + b_n\ n(n+1)r^n \\ -c_n\ n\ (n+1)\ r^{-(n+2)} - d_n\ b(n-1)\ r^{-n} \end{bmatrix}\cos(n\theta) \\ +\sum_{n=2,3,4,\ldots}^{N}\begin{bmatrix} a'_n\ n\ (n-1)\ r^{n-2} + b'_n\ n(n+1)r^n \\ -c'_n n(n+1)\ r^{-(n+2)} + d'_n\ n(n-1)\ r^{-n} \end{bmatrix}\sin(n\theta) \end{array} \tag{22.4}$$

The individual stresses in Cartesian coordinate system can be evaluated from the following transformation equation

$$\begin{Bmatrix} \sigma_x \\ \sigma_y \\ \sigma_{xy} \end{Bmatrix} = \begin{bmatrix} \cos^2\theta & \sin^2\theta & -2\sin\theta\cos\theta \\ \sin^2\theta & \cos^2\theta & 2\sin\theta\cos\theta \\ \sin\theta\cos\theta & -\sin\theta\cos\theta & \cos^2\theta - \sin^2\theta \end{bmatrix} \begin{Bmatrix} \sigma_r \\ \sigma_\theta \\ \sigma_{r\theta} \end{Bmatrix} \tag{22.5}$$

From 2D plane-stress equations and the strain–displacement relationships, the vertical and horizontal displacement can then be expressed as [7]:

$$u = \frac{1}{E}\left[\begin{array}{c} -b_0 \frac{(1+\nu)\cos\theta}{r} + 2c_0(1-\nu)r\cos\theta \\ + \sum_{n=2,4,\ldots}^{N} \left(\begin{array}{c} +a_n r^{n-1} n(1+\nu) \begin{pmatrix} -\cos n\theta \cos\theta \\ -\sin n\theta \sin\theta \end{pmatrix} \\ +b_n r^{n+1} \left(\begin{array}{c} -\begin{pmatrix} (n-2) \\ +\nu(n+2) \end{pmatrix} \cos n\theta \cos\theta \\ -[n(1+\nu)+4] \sin n\theta \sin\theta \end{array} \right) \\ +c_n(1+\nu) r^{-(n+1)} n \begin{pmatrix} \cos n\theta \cos\theta \\ -\sin n\theta \sin\theta \end{pmatrix} \\ +d_n r^{-n+1} \left(\begin{array}{c} \begin{pmatrix} (n+2) \\ +\nu(n-2) \end{pmatrix} \cos n\theta \cos\theta \\ -[n(1+\nu)-4] \sin n\theta \sin\theta \end{array} \right) \end{array} \right) \end{array} \right] \tag{22.6}$$

and

$$v = \frac{1}{E}\left[\begin{array}{c} -b_0 \frac{(1+\nu)}{r} \sin\theta + 2c_0(1-\nu)r\sin\theta \\ + \sum_{n=2,4,\ldots}^{N} \left(\begin{array}{c} +a_n(1+\nu) r^{n-1} n \begin{pmatrix} \sin n\theta \cos\theta \\ -\cos n\theta \sin\theta \end{pmatrix} \\ +b_n r^{n+1} \left(\begin{array}{c} -\begin{pmatrix} (n-2) \\ +\nu(n+2) \end{pmatrix} \cos n\theta \sin\theta \\ +[n(1+\nu)+4] \sin n\theta \cos\theta \end{array} \right) \\ +c_n(1+\nu) r^{-(n+1)} n \begin{pmatrix} \cos n\theta \sin\theta \\ +\sin n\theta \cos\theta \end{pmatrix} \\ +d_n r^{-n+1} \left(\begin{array}{c} -\begin{pmatrix} (n+2) \\ +\nu(n-2) \end{pmatrix} \cos n\theta \sin\theta \\ +[n(1+\nu)-4] \sin n\theta \cos\theta \end{array} \right) \end{array} \right) \end{array} \right] \tag{22.7}$$

where E is the elastic modulus and ν is Poisson's ratio of steel of the MPC.

22.4 Hybrid Methodology

Now that the vertical displacements, v, from DIC and the analytical expression of v, Eq. 22.7, are available, the two are combined together such that the left hand side of Eq. 22.7 contains the measured DIC v displacements and the right hand side would be the evaluated function at the corresponding (r, θ) positions of the DIC data.

Although all the necessary Airy coefficient which occur in the individual components of stress are present in Eq. 22.7, the boundary conditions of the structure are used to provide more side conditions by which to determine the Airy coefficients and thereby improve the quality of results. The local traction-free conditions ($\sigma_y = \sigma_{xy} = 0$) were applied to the top portion of the hole and the horizontal displacement, $u = 0$, imposed at the right portion of the hole where the tooth is punched through the wood structure, i.e.,

$$\begin{cases} \sigma_y = \sigma_{xy} = 0 \ldots \text{at top portion} \\ u = 0 \ldots \text{at right portion} \end{cases} \tag{22.8}$$

The source locations of the measured DIC data, positions where $\sigma_r = \sigma_{r\theta} = 0$ are applied and where $u = 0$ is imposed are identified in Fig. 22.3.

The above information can be assembled in matrix form to determine the Airy coefficients according to following:

$$[A]_{(3681+500)\text{ x }k} \{c\}_{k\text{ x }1} = \{d\}_{(3681+500)\text{ x }1} \tag{22.9}$$

where [A] is the (3,681 + 500) by k Airy matrix composed of 3,681 vertical displacement expressions of the form of Eq. 22.7 in terms of r and θ associated with the selected source locations identified in Fig. 22.3 as well as 500 side conditions of the form of Eq. 22.8, {c} is the set of k unknown Airy coefficients and vector {d} includes the set of 3,681 DIC v measurements

as well as a set of 500 zeros corresponding to the right hand side of Eq. 22.8. An rms (root mean square) analysis was performed to determine the appropriate number of Airy coefficients to use, revealing 22 coefficients to be sufficient. The over-determined system in Eq. 22.9 was solved using the '\' operator in MATLAB and the determined Airy coefficients were subsequently substituted into the stress and displacement analytical expressions of Eqs. 22.2, 22.3, 22.4, 22.5, 22.6 and 22.7.

22.5 Results

Figure 22.4 is a contour plot of the stress in the vertical direction, σ_y, from the hybridized measured DIC vertical displacements. Note that no physical differentiation of the measured displacements was performed in order to determine the stress. This is an advantage over conventional displacement-based experimental methods, especially in the case of small elastic deformations. Moreover, this hybrid method provides smooth contours, free of noise, and most importantly, the of results right at the edges of the MPC are now available, Fig. 22.4.

Figure 22.5 plots the three components of stress in Cartesian coordinates evaluated from $\theta = 0$ to 14 °; spanning the right portion of punched tooth of the MPC.

Results of Figs. 22.4 and 22.5 reveal that the stress distribution across the surface of the MPC is not uniform, with the stresses being concentrated at the location where the cross-sectional area is reduced due to the punched hole.

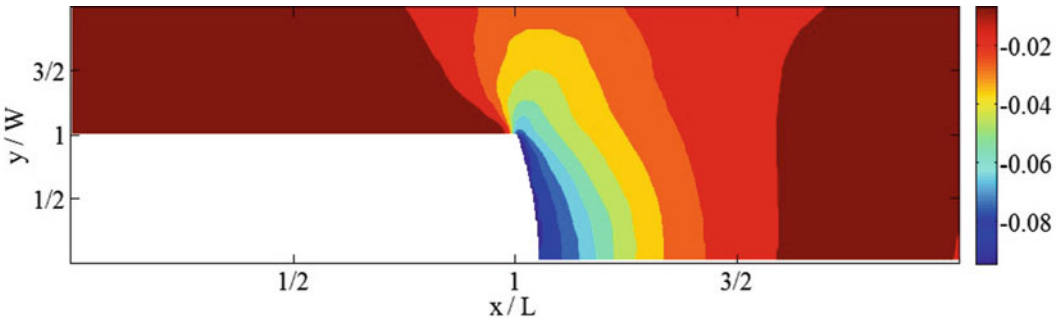

Fig. 22.4 Contour plot of σ_y obtained from hybridized vertical displacements normalized with respect to σ_{yield} = 275 MPa

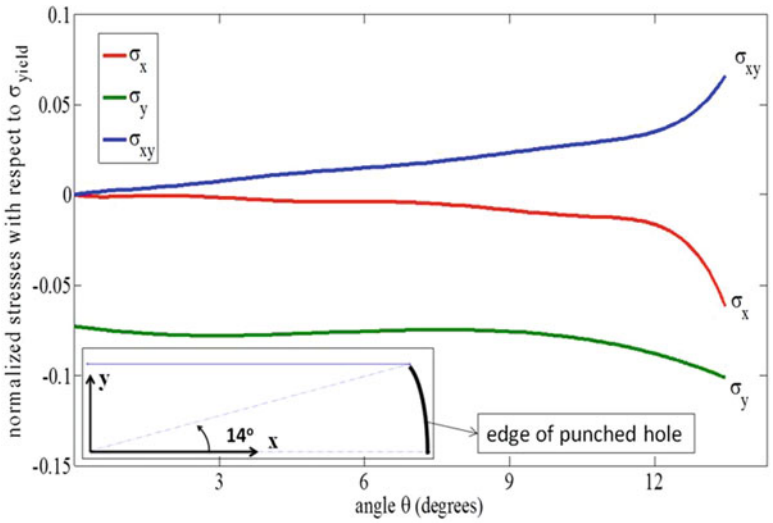

Fig. 22.5 Stress plots of normalized σ_x, σ_y and σ_{xy} along the right edge of the punched hole from hybridized vertical displacements

22.6 Conclusion

The characterization of the stress field around a MPC hole in 3-point bending tensile joint configuration has been performed by hybridizing DIC-measured vertical displacement data. The stresses in both x and y directions at the corner of the punched hole were significantly higher than those in the rest of the MPC structure. A major advantage of the present approach is that measured displacements were not differentiated physically in order to obtain strains or stresses. The non-uniform stress distribution of the stresses on the surface of the metal plate connector illustrates the complexity of such structures and the challenges in determining a set of optimum design parameters for the different types of MPCs and joint configurations. Plane stress is assumed here. However, the zero stress and very small displacements normal to the surface of the metal plate in the region of the end punched tooth suggests that the actual situation there is neither plane stress nor plane strain. The available results indicate more comprehensive investigations, including those with different MPC plates, MPC joint types, punched teeth/holes distribution and loading conditions are warranted to hopefully provide enhanced MPC designs and hence superior connections.

References

1. Cramer SM, Shrestha D, Mtenga PV (1993) Computation of member forces in metal plate connected wood trusses. Struct Eng Rev 5(3):209–217
2. Meeks JE (1979) Industrial profile of the metal plate connected wood truss industry. In: Proceedings of the metal plate wood truss conference, St. Louis, pp 3–5
3. Gupta R, Vatovec M, Miller TH (1996) Metal-plate-connected wood joints: a literature review. Research publication, Forest Research Laboratory Oregon State University
4. Samad WA, Rowlands RE (2012) Nondestructive full-field atress analysis of a finite structure containing an elliptical hole using digital image correlation. Conference paper: international symposium on experimental mechanics ISEM'12, Taipei, 8–11 Nov
5. Gebremedhin PL, Crovella PL (1991) Load distribution in metal plate connectors of tension joints in wood trusses. Struct Environ Div. ASAE 34(1):281–287
6. Soutas-Little RW (1998) Elasticity. Dover Publications, Mineola
7. Samad WA (2013) Hybrid full-field stress analysis of structures containing arbitrarily-shaped cutout geometries. Ph.D thesis, University of Wisconsin-Madison

Chapter 23
Full-Field Displacement Measurement and Crack Mapping on Masonry Walls Using Digital Image Correlation

Rahim Ghorbani, Fabio Matta, and Michael A. Sutton

Abstract Understanding the load resisting mechanisms and failure modes of masonry walls loaded in their plane is key to validate mechanics-based analysis and simulation algorithms. Proof load tests are performed on specimens that are extensively instrumented with transducers (e.g., LVDTs, potentiometers, strain gauges), which are typically mounted on a specimen at specific locations. The resulting measurements are local and cannot describe in detail the complex response of infill and confined masonry systems, which may combine bricks, mortar joints, reinforced concrete (RC), and the associated interfaces. In addition, crack maps are typically marked by hand based on visual inspection, making it likely to overlook cracks especially when they have a relatively small width or close after unloading.

This paper discusses the feasibility of using digital image correlation (DIC) as a non-contact method to measure displacements on large masonry wall specimens and provide faithful crack maps. Feasibility is assessed based on evidence from in-plane reverse-cycle load tests of two full-scale confined masonry walls. The specimens were designed for two different performance levels in terms of in-plane strength and deformability. Deformability was maximized for the case of a wall that was retrofitted using in-plane (horizontal) reinforcement embedded along the bed joints. The DIC measurements were validated vis-à-vis relevant counterparts from linear displacement transducers, including in-plane drift, diagonal deformations, and interface slip between the RC tie columns and the masonry panel. In addition, faithful DIC-based crack maps were obtained where it is easier to recognize cracks compared with hand marked crack maps on the specimens.

Keywords Digital image correlation • Confined masonry • Full-scale test • Full-field measurement • Crack map

23.1 Introduction

The measurement of deformations and mapping of cracks are important tasks when load testing concrete and masonry structures because they help to better understand the load resisting mechanisms, the failure modes and their hierarchy. Measurements are typically performed at discrete locations with sensors that are physically mounted on the structure, such as strain gauges, potentiometers and linear variable differential transformer (LVDT) displacement transducers. Crack maps are usually hand drawn during or at the end of a load test. These local measurements make the comprehensive description of structural response difficult, while the data may be affected by damage or cracks at the sensor location. Also the accepted practice of hand drawing the cracks hardly enables one to faithfully reproduce progressive crack maps at different loading steps.

To overcome some of these limitations, various full-field non-contact optical methods have been developed and used [1]. Digital image correlation (DIC) was developed in the 1980s [2, 3] and is based on a comparative analysis of digital images of the specimen surface captured at different load levels. The specimen surface must have a random distribution of gray levels (i.e., a speckle pattern) that deforms with the specimen surface. The speckle pattern can be the natural texture of the specimen surface or artificially made by black and/or white paint. The region of interest (ROI) on the reference image is divided into a virtual grid of square subsets. In order to calculate the displacements at a point P, a square reference subset

R. Ghorbani, Ph.D. Candidate (✉) • F. Matta • M.A. Sutton
Department of Civil and Environmental Engineering, University of South Carolina, Columbia, SC 29208, USA
e-mail: ghorbanr@email.sc.edu; fmatta@sc.edu; sutton@sc.edu

H. Jin et al. (eds.), *Advancement of Optical Methods in Experimental Mechanics, Volume 3*,
Conference Proceedings of the Society for Experimental Mechanics Series,
DOI 10.1007/978-3-319-00768-7_23,

centered at the point is used to track its corresponding location in the deformed image. More details on the DIC technique for 2D and 3D deformation measurements can be found in Sutton et al. [4]. For 2D measurements, a comprehensive review is provided by Pan et al. [5].

The case studies where DIC measurements are performed on large-scale civil engineering structures are limited. In most studies, the ROI is limited to a small portion of the specimen. Yoneyama et al. [6] and Santini-Bell et al. [7] studied DIC for the non-contact deflection measurement of bridges. The results showed that bridge deflections obtained via DIC measurements were in agreement with those obtained through conventional displacement transducers. In other studies DIC was used to detect cracks [8], investigate the influence of service loads on crack development [9], and study the behavior of a full-scale RC beam with inclined cracks [10]. Tung et al. [11] conducted load tests on a small masonry wall with 45 ° oriented mortar joints and a steel-framed brick wall using DIC to analyze the deformations on the wall surface and detect cracks. The results showed that using the von Mises strain fields and smaller subsets enabled a better definition of the crack locations. Smith et al. [12] tested a scaled hybrid precast concrete wall under in-plane reverse-cycle loading. The results showed that 3D-DIC measurements compared favorably with visual observations and data from conventional sensors.

This paper discusses the feasibility of using 3D-DIC as a non-contact method to measure displacements on large masonry walls loaded in their plane. Feasibility is assessed based on evidence from load tests of two full-scale confined masonry (CM) walls. CM consists of unreinforced masonry walls confined with cast-in-place reinforced concrete (RC) tie columns and beams. The specimens were designed for two different performance levels in terms of strength and deformability, where deformability was improved for the case of a wall that was retrofitted using horizontal reinforcement. The DIC measurements were evaluated vis-à-vis relevant ones from linear displacement transducers, including in-plane drift, diagonal deformations, and interface slip between RC tie columns and masonry. Comparable measurements were obtained. In addition, the DIC maximum principal strain contours were used to visualize and map cracks at different loading steps.

23.2 Experimental Program

23.2.1 Specimen Design

Figure 23.1 shows the geometry and reinforcement layout of the full-scale CM walls. The test results of two walls are presented in this study. One wall was used as a control specimen and is herein referred to as “WU”. The remaining wall, herein referred to as “WR”, was retrofitted using aluminum strips embedded in the horizontal bed joints to enhance in-plane strength and deformability, as illustrated in Fig. 23.2.

The dimensions of the walls reflect typical construction practices [13]. The concrete masonry units (CMU) were laid with a running bond pattern with an average 10 mm thickness for bed and head joints. The thickness (i.e., perpendicular to the plane of the wall) of the RC tie beams, columns and masonry panel was 200 mm. The columns and beams had a cross section depth (i.e., in the plane of the wall) of 200 and 250 mm, respectively. The walls had toothed edges made with quarter blocks at the masonry-RC column interfaces. The horizontal reinforcement in the WR specimen consisted of 6061-T6 aluminum strips with a cross section of 3.2 × 12.7 mm. Grooves having a width of 10 mm and depth of 15 mm were cut along the bed joints with a grinder (Fig. 23.2a) and cleaned. The 90° bent ends were inserted into holes drilled in the tie RC columns (Fig. 23.2b) to maximize anchorage. The strips were inserted in each bed joint alternating from one face to the other face of the wall, and embedded in a conventional cement mortar (Fig. 23.2c, d).

Materials – All the material characterization tests were performed following applicable ASTM standards. CMUs with a net area of 50 %, nominal dimensions of 200 × 200 × 400 mm, and an average net compressive strength of 7.2 MPa were used. The mortar had an average cylinder compressive strength of 8.3 MPa. The average compressive strength of 5.8 MPa of the masonry was estimated by testing two-block prisms. The average cylinder compressive strength of the concrete used in the tie columns and beams cylinders was 12.0 MPa. The average yield strength of the concrete reinforcing bars was 440 MPa. The 6061-T6 aluminum strips used as horizontal reinforcement had an average yield strength of 265 MPa.

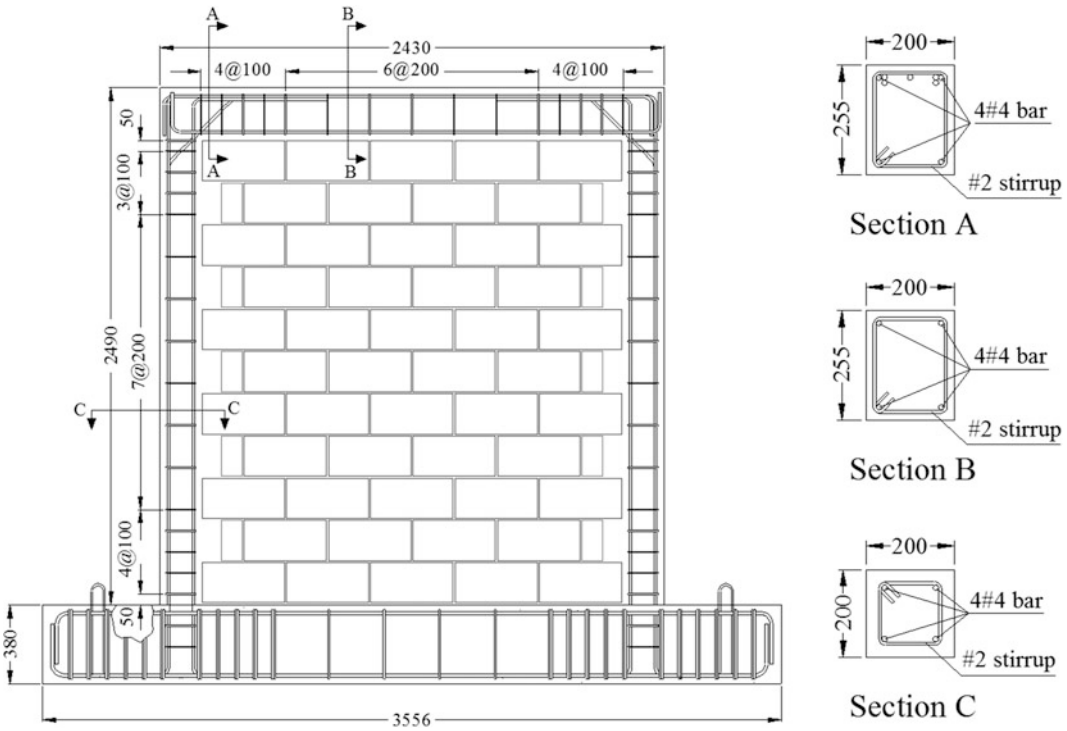

Fig. 23.1 Specimen WU: geometry and RC reinforcement layout (dimention in mm)

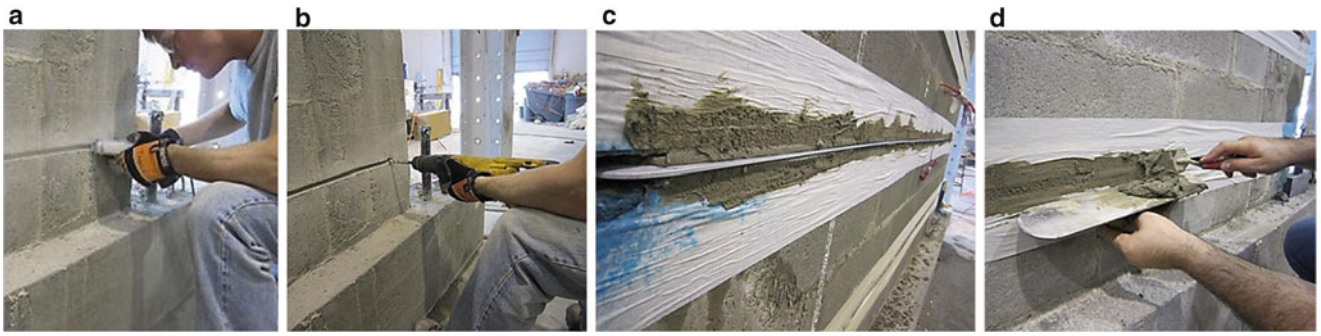

Fig. 23.2 Retrofit of specimen WR: (**a**) cutting grooves along bed joints; (**b**) drilling anchorage holes in tie columns; (**c**) embedding aluminum strips in mortar; and (**d**) filling grooves with mortar

23.2.2 Surface Preparation and Speckle Pattern

Due to the relatively uniform gray color of the CMUs, one surface per wall was painted white as the background of the speckle pattern. In order to make the white layer brittle enough to follow the cracks on the surface of the specimen, a thin white cement grout was used (Fig. 23.3a). Due to large size of the specimens, a stencil with a random hole pattern and a paint spray gun were used to impress the dark speckle pattern on the background (Fig. 23.3b, c). The average diameter of each speckle was 3.175 mm, and the ratio of speckle area to specimen surface area was 33 %.

23.2.3 Test Setup and Loading Protocol

The stereo vision system and the in-plane (lateral) load test setups are illustrated in Fig. 23.4. The load was imparted using a hydraulic actuator with maximum capacity of 500 kN, which was connected to a steel spreader beam that was secured onto the specimen using steel anchors. A constant vertical compressive load of 88.3 kN resulting in a uniformly distributed

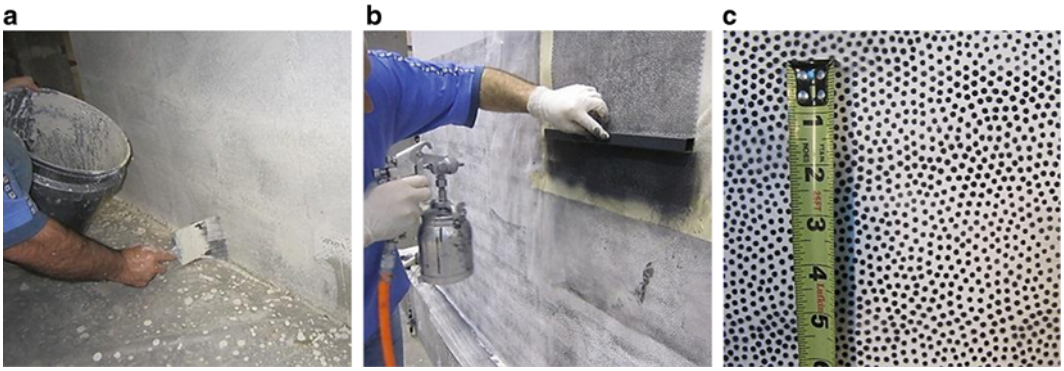

Fig. 23.3 Preparation of speckle pattern: (**a**) background painting; (**b**) spraying dark paint through stencil; (**c**) finished speckle pattern

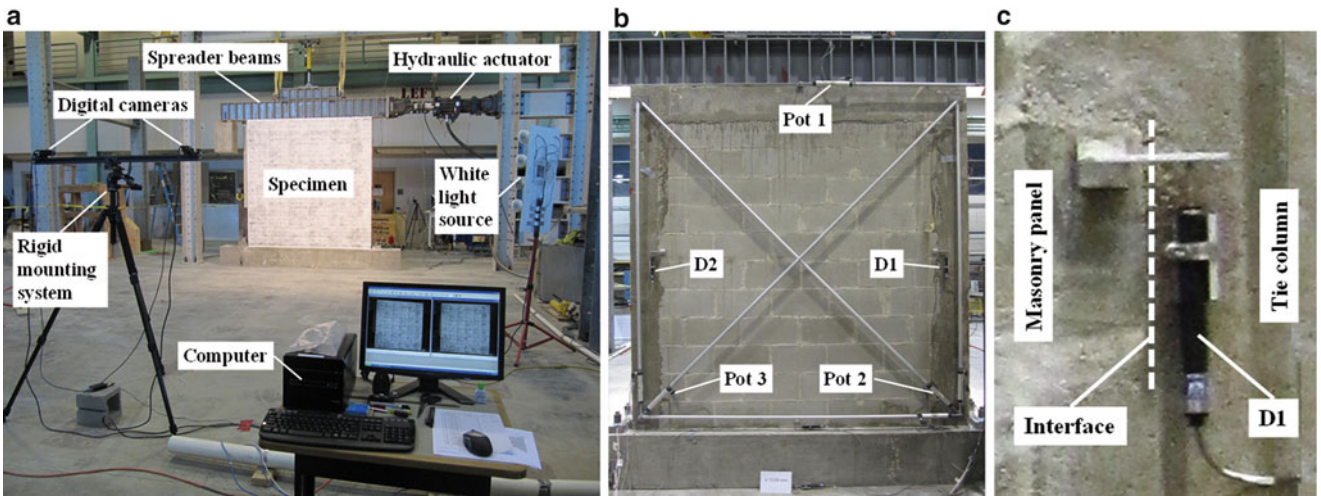

Fig. 23.4 (**a**) Stereo vision system and load test setup; (**b**) layout of contact-based sensors; (**c**) close-up of sensor D1

pressure of 0.2 MPa was applied using a hydraulic jack and two steel spreader beams on top of the wall to simulate the dead load on the first story of a typical two-story CM dwelling. The stereo vision system consisted of two 5.0 MP (2448 × 2048 pixel) CCD cameras that were calibrated to image the entire front face of each specimen. Two sources of low-heat white light were used to illuminate the surface of the specimen. A desktop computer was used to record the images and run the 3D-DIC software Vic-3D [14]. The cameras were spaced 1,110 mm apart and positioned at 6.7 m from the wall face. Based on the field of view of the images (3,330 × 2,790 mm^2) and the resolution of the cameras, each speckle was approximately equal to 2.33 pixels in diameter which lies within the recommended range reported in the literature [15, 16].

Each specimen was extensively instrumented with displacement transducers mounted on the back face of the specimen (without speckle pattern). Figure 23.4b shows the sensor layout, including one potentiometer to measure the in-plane lateral displacement ("Pot 1"), which is typically used to determine the drift ratio to characterize the response to in-plane seismic loads; two potentiometers to measure the diagonal displacement ("Pot 2" and "Pot 3"), which are typically used to estimate shear deformations; and two linear displacement sensors to measure the differential displacement (slip) at the interface between tie columns and masonry panel ("D1" and "D2").

The cyclic load was imparted in displacement control mode following the in-plane lateral displacement ("Pot 1") history in Fig. 23.5a. Three cycles were repeated for each displacement amplitude at a frequency of 0.004 Hz (Fig. 23.5b). The third cycle of each amplitude consisted of two 30 s constant-displacement plateaus, where each served to capture 30 images. The displacement history was intended to accurately characterize the three limit states used to describe the structural response, namely: (1) first crack, when the first significant diagonal crack opens; (2) peak load, when the maximum load is attained; and (3) ultimate, which is associated with the state of specimen at the end of the test (Fig. 23.5c).

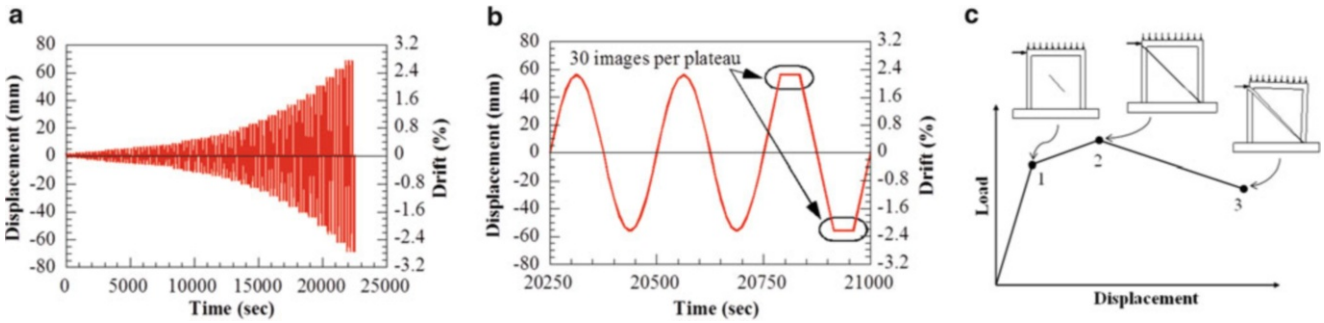

Fig. 23.5 (**a**) loading protocol; (**b**) close-up of imposed lateral displacement history; (**c**) limit states of CM response (first crack, 1; peak load, 2; and ultimate, 3)

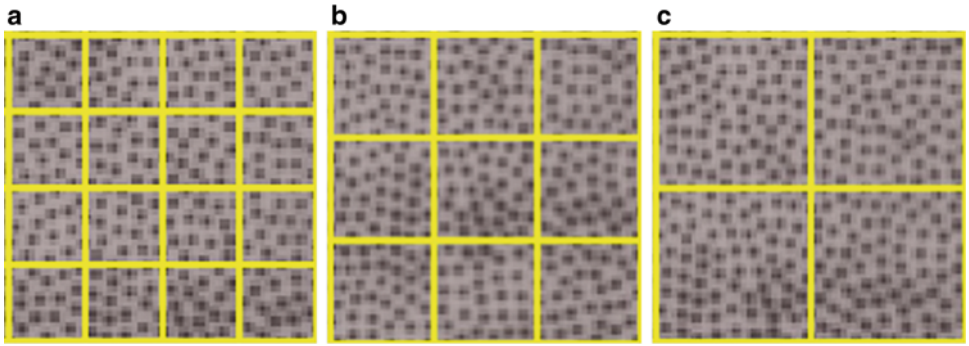

Fig. 23.6 Subset size compared with speckle pattern: (**a**) 15 × 15 pixels; (**b**) 21 × 21 pixels; (**c**) 31 × 31 pixels

23.2.4 Subset Size

A meaningful DIC analysis requires that the size of a subset be large enough so that there is enough distinctive intensity pattern in the subset to distinguish it from the other subsets. Figure 23.6a–c show the comparison between different size subsets and the speckle pattern. It is noted that a 15 × 15 pixel subset contains enough speckles (i.e., enough variation in the gray level) to distinguish it from other subsets. Larger subsets contain more speckles, resulting in a better correlation analysis but with the tradeoff of reduced spatial resolution.

In order to investigate the effect of subset size on the accuracy of the displacements computed via DIC analysis, 30 images were taken on an unloaded specimen. One image was chosen as the reference and for all other images, the mean and standard deviation of horizontal and vertical components of displacement for all data points on the specimen surface were calculated. The average for the mean and standard deviation of the displacement components yields the mean bias error (or systematic error) and standard deviation error (or random error), respectively. Figure 23.7 shows the bias and standard deviation errors estimated using different subset sizes (15 × 15 pixels to 61 × 61 pixels) for the WR specimen. The results show that the bias error does not change with the subset size but the standard deviation error decreases as the subset size increases. As a result, the accuracy improves with a larger subset but a compromise is to be sought between measurement accuracy and spatial resolution.

The DIC maximum principal strain (e1) contours were used for crack detection and crack mapping at different loading steps. The effect of subset size at the same level of load in the WR specimen is illustrated in Fig. 23.8. A smaller subset (e.g., 15 × 15 pixels) offers a better spatial resolution and is suitable for crack detection and mapping. On the other hand, as the width of the cracks increases and a larger subset (e.g., 31 × 31 pixels) is used, the DIC algorithm does not yield meaningful contours, as shown in the marked area in Fig. 23.8c.

Based on these considerations, a 15 × 15 pixel subset was used for crack detection and mapping since it contains a sufficiently distinctive intensity pattern and provides a higher spatial resolution compared to a larger subset. For DIC displacement measurements, a 21 × 21 pixel subset was used since together with a reduced spatial resolution it provides improved accuracy compared with the 15 × 15 pixel subset without problems in the correlation analysis.

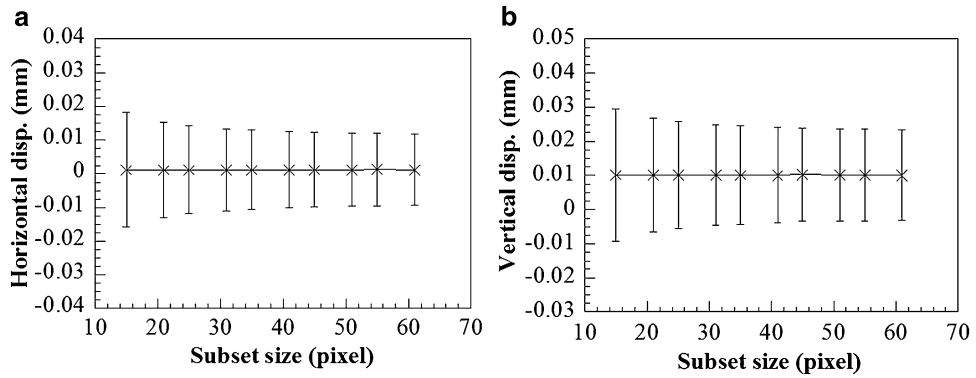

Fig. 23.7 Bias and standard deviation errors at varying subset size at zero load: (**a**) horizontal displacement; (**b**) vertical displacement

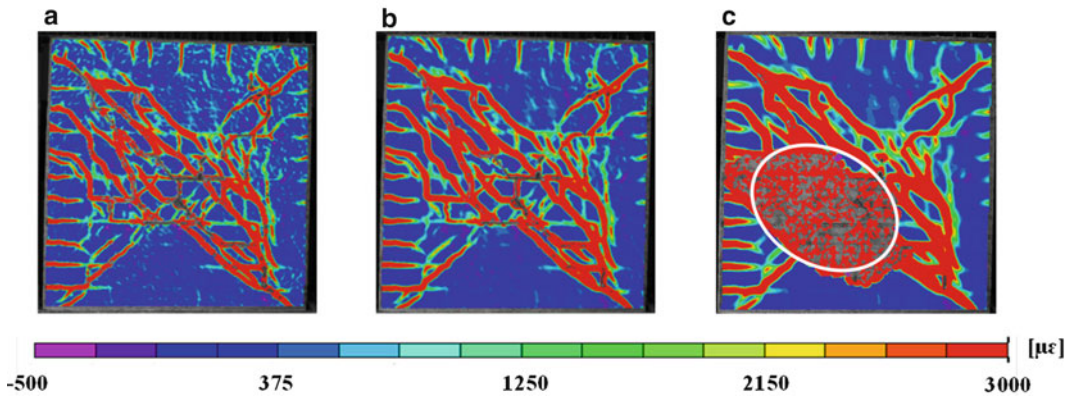

Fig. 23.8 Representative maximum principal strain contour for different subset sizes: (**a**) 15 × 15 pixels; (**b**) 21 × 21 pixels; (**c**) 31 × 31 pixels

23.3 Results and Discussion

23.3.1 Displacement Measurements

In order to compare the DIC measurements with those from the displacement transducers, the positions on the front face (DIC face) that correspond to positions on the back face where the transducers were attached were used. DIC measurements were calculated based on the difference between the distance of two points on the specimen surface at different load s'teps.

In-plane displacements – The sensor "Pot 1" shown in Fig. 23.4b measured the in-plane lateral displacement of the wall. Its measurements are compared with DIC results in Fig. 23.9a, b for the WU and WR specimens, respectively. The percent difference, Δ, between DIC measurements, u_{DIC}, and potentiometer measurements, u_{Pot}, was calculated as follows:

$$\Delta = \frac{u_{DIC} - u_{Pot}}{u_{Pot}} \times 100\% \tag{23.1}$$

The similarity between the load–displacement envelope curves in Fig. 23.9a, b estimated with DIC and the potentiometer shows that DIC measurements are in excellent agreement with those of the potentiometer, with a difference below 5 % after the formation of the first crack, that is, within the range of displacements that is relevant to characterize the load resisting mechanisms and the failure mode. The accuracy of the 3D-DIC was estimated to be 15 μm (~0.01 pixels) for in-plane lateral displacement measurements.

Diagonal deformations – The sensor "Pot 2" was connected to a rigid hollow-core aluminum rod having a length of about 3 m and measured the displacement along one of the diagonals (Fig. 23.4b). This arrangement makes the measurements more susceptible to inaccuracies due to out-of-plane vibrations of the rod. DIC measurements have the potential to be a valid

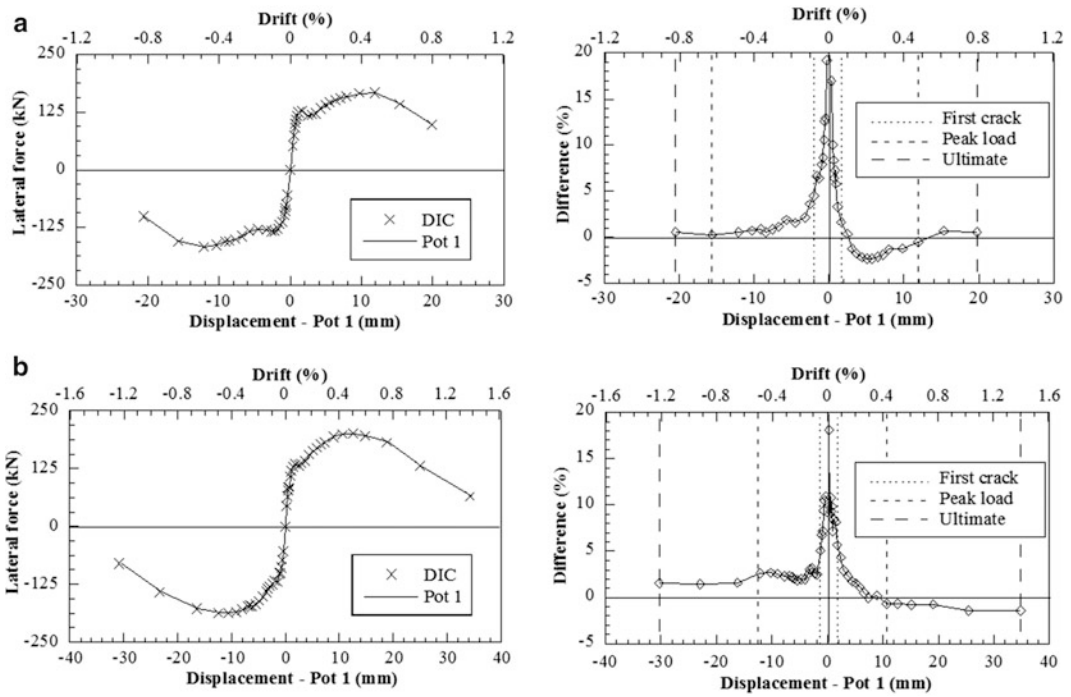

Fig. 23.9 Comparison between displacement measurements through sensor Pot 1 and DIC: (**a**) WU wall; (**b**) WR wall

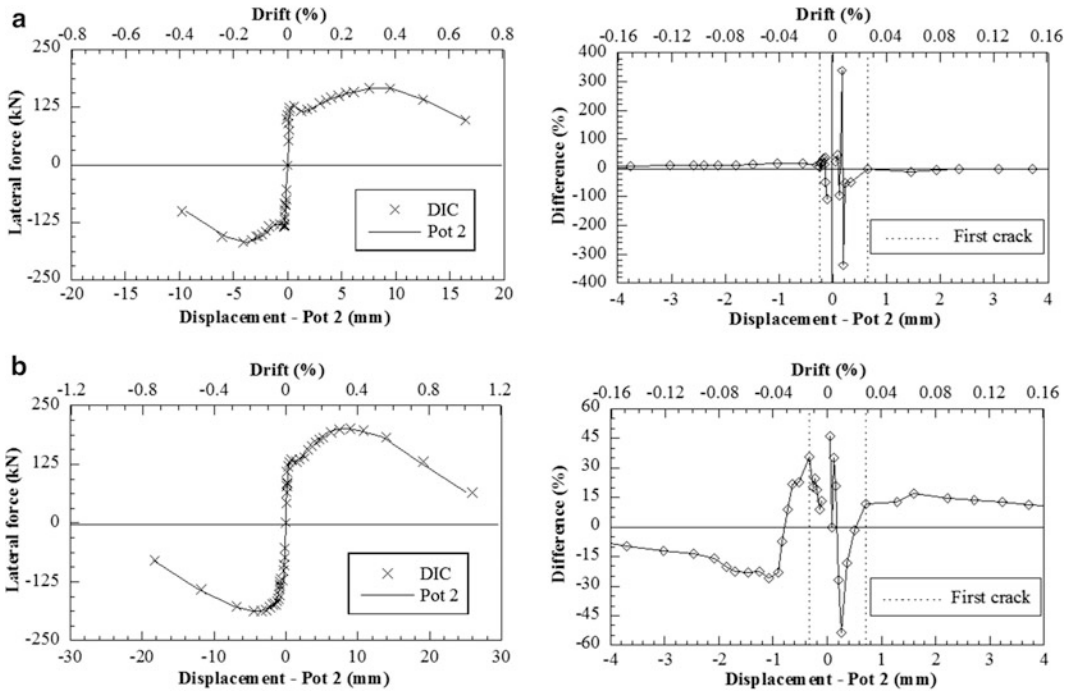

Fig. 23.10 Comparison between Pot 2 and DIC displacement measurements: (**a**) specimen WU; (**b**) specimen WR

alternative based on their comparison with Pot 2's measurements in Fig. 23.10a, b, showing similar results to those obtained for in-plane lateral displacements. The accuracy of the 3D-DIC was estimated to be 45 μm (~0.03 pixels) for diagonal deformation measurements.

Interface slip – The sensor "D1" measures the slip between a tie column and the masonry panel (Fig. 23.4b), which is an important parameter to evaluate the interface compatibility as damage develops at increasing loads and deformations.

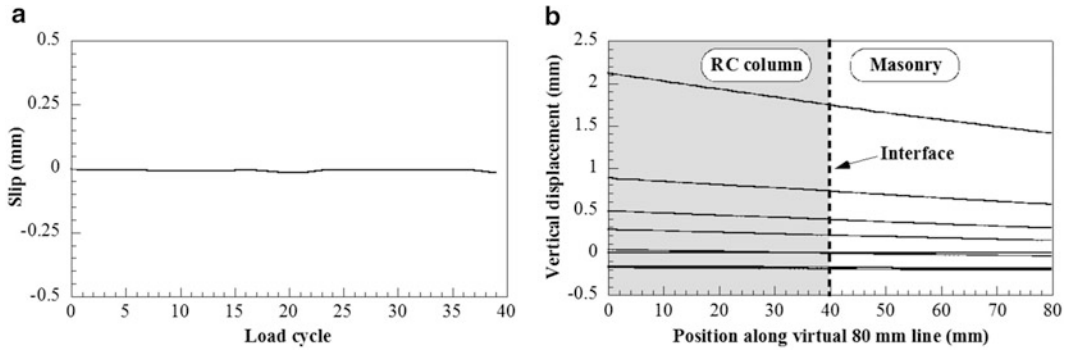

Fig. 23.11 (**a**) Slip measured through sensor D1; (**b**) DIC vertical displacement profile along 80 mm long line perpendicular to RC-masonry interface

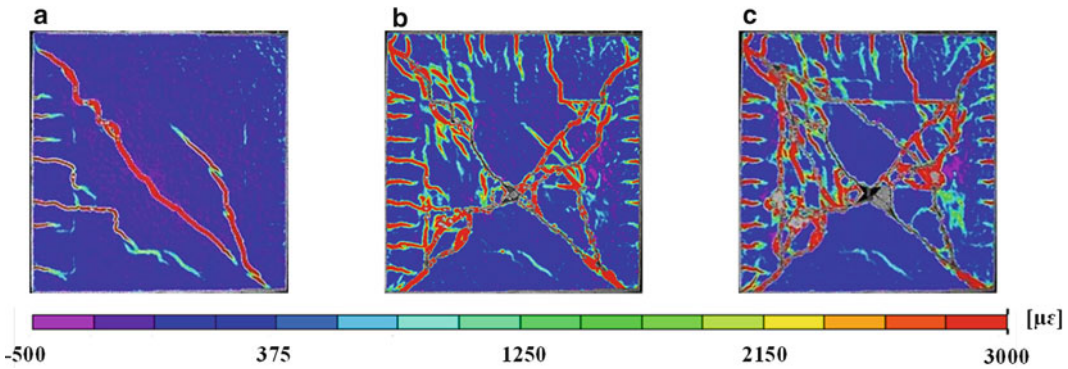

Fig. 23.12 Maximum principal strain contours in specimen WU: (**a**) first (diagonal) crack; (**b**) peak load; (**c**) ultimate

The measurements recorded through D1 during the entire load test are shown in Fig. 23.11a, where a negligible slip is noted. Figure 23.11b shows the vertical displacement profile measured by DIC along a reference 80 mm long horizontal line perpendicular to the interface (Fig. 23.4c). The results show that there are no discontinuities along the displacement profiles irrespective of the load level, which confirms that the interface slip was negligible.

23.3.2 Crack Mapping

Crack detection and mapping are usually done by visual inspection of the specimen's surface. This is an important operation because crack mapping provides empirical evidence to understand the progression of damage, thereby describing load resisting mechanisms and failure modes. However, the detection of hairline cracks and the drawing of faithful progressive (i.e., at increasing loads) crack maps require a close and time consuming inspection at each load step, which is impractical. This problem is exacerbated in the case of full-scale tests on large specimens. DIC is herein shown to be suitable for the accurate detection and mapping of cracks using high resolution images captured at different load steps.

A 15 × 15 pixel subset size was used for crack detection and crack mapping. Figures 23.12 and 23.13 show the crack maps for the WU and WR specimens, respectively, at the three limit states (first crack, peak load, and ultimate) for in-plane loads imparted from left to right. Flexural hairline cracks forming horizontally on the left tie column and propagating inside the masonry panel were detected clearly. The progression of damage in the walls, with the formation and propagation of the typical diagonal cracks produced by in-plane loading, is clearly noticed. In addition, by comparing the strain contours at the peak load and ultimate state of the two specimens, the contribution of the horizontal reinforcement in distributing the cracks more uniformly in the WR specimen, resulting in increased strength and deformability, becomes apparent. Figure 23.14a, b show the photographs of the failed WU and WR specimens, respectively, vis-à-vis the final DIC crack maps. It is noted that faithful DIC-based crack maps were obtained where it is easier to recognize cracks compared with hand marked crack maps on the specimens irrespective of the loading step.

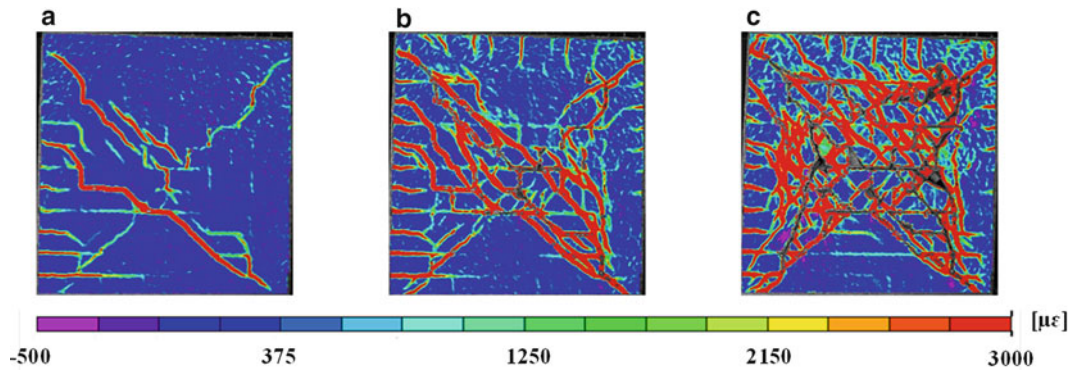

Fig. 23.13 Maximum principal strain contours in specimen WR: (**a**) first (diagonal) crack; (**b**) peak load; (**c**) ultimate

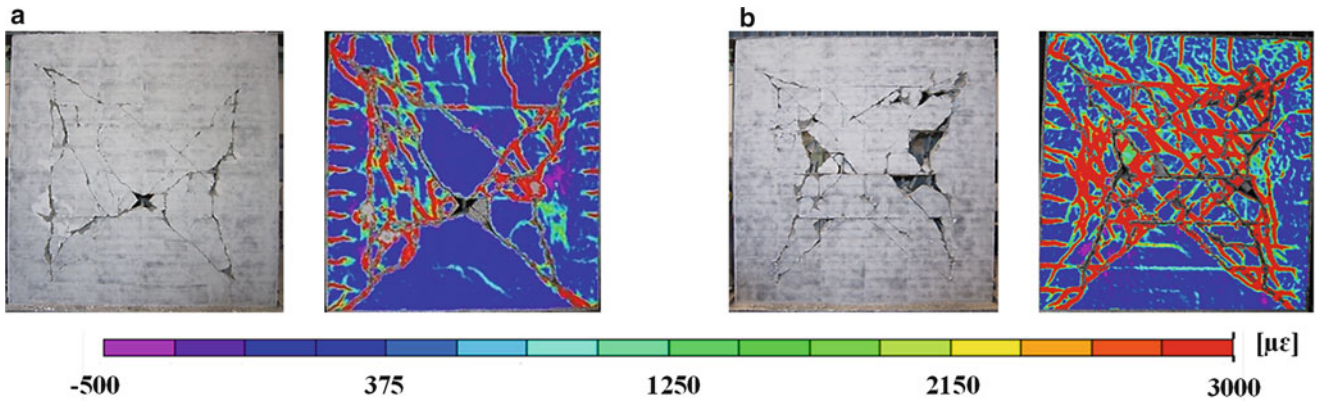

Fig. 23.14 Failed specimen photogtraph and final DIC crack map: (**a**) specimen WU; (**b**) specimen WR

23.4 Conclusions

This paper discusses the feasibility of using a 3D-DIC method to measure displacements on large masonry walls and provide faithful crack maps at different loading steps. Feasibility was assessed based on evidence from in-plane load tests of two full-scale confined masonry walls.

The DIC measurements were compared with relevant ones from linear displacement transducers, including in-plane drift, deformation of the diagonal strut, and interface slip between concrete columns and masonry. A 21 × 21 pixel subset size was used for the DIC analysis, where the accuracy for in-plane lateral displacement and diagonal deformation measurements was estimated to be 15 and 45 μm, respectively. The DIC measurements were in excellent agreement with those of the displacement transducers. The difference between DIC and transducer measurements for the in-plane displacement was at or below 5 % after diagonal cracking.

The DIC maximum principal strain data were used to develop contours to highlight the cracks on the surface of the specimens. A 15 × 15 pixel subset size was used for crack detection and crack mapping since it provides a higher spatial resolution compared to larger subset sizes while containing a sufficiently distinctive intensity pattern for DIC analysis. The DIC method was shown to enable the detection of hairline cracks at early stages of loading and provide faithful crack maps at different loading steps, which would be impractical to obtain by means of traditional visual inspection and marking.

Acknowledgments This material is based upon work partially supported by the National Science Foundation under Grant No. CMMI-1049483. Any opinions, findings, and conclusions or recommendations expressed in this material are those of the authors and do not necessarily reflect the views of the National Science Foundation. The support of the University of South Carolina through the second author's research incentive funds and the Magellan Scholar Program is gratefully acknowledged. Special thanks are extended to Dr. Enrico Garbin (formerly Postdoctoral Fellow), Mr. Siming Guo (Ph.D. student, Mechanical Engineering), Mr. Stephen Jones (Magellan Scholar), and Mr. Bradford DiFranco (NSF-REU student) for their technical assistance.

References

1. Rastogi PK (2000) Photomechanics. Springer, Berlin
2. Sutton MA, Wolters WJ, Peters WH, Ranson WF, McNeill SR (1983) Determination of displacements using an improved digital correlation method. Image Vis Comput 1(3):133–139
3. Sutton MA, Cheng M, Peters WH, Chao YJ, McNeill SR (1986) Application of an optimized digital correlation method to planar deformation analysis. Image Vis Comput 4(3):143–150
4. Sutton MA, Orteu JJ, Schreier HW (2009) Image correlation for shape, motion and deformation Measurements. Springer, US
5. Pan B, Qian K, Xie H, Asundi A (2009) Two-dimensional digital image correlation for in-plane displacement and strain measurement: a review. Meas Sci Technol 20(6):062001
6. Yoneyama S, Kitagawa A, Iwata S, Tani K, Kikuta H (2007) Bridge deflection measurement using digital image correlation. Exp Tech 31(1):34–40
7. Santini-Bell E, Brogan P, Lefebvre P, Peddle J, Brenner B, Sanayei M (2011) Digital imaging for bridge deflection measurement of a steel girder composite bridge. Transportation Research Board 90th annual meeting, Washington DC, Paper no. 11–1633
8. Lacompte D, Vantomme J, Sol H (2006) Crack detection in a concrete beam using two different camera techniques. Struct Health Monit 5(1):59–68
9. Destrebecq JF, Toussaint E, Ferrier E (2011) Analysis of cracks and deformations in a full scale reinforced concrete beam using a digital image correlation technique. Exp Mech 51(6):879–890
10. Küntz M, Jolin M, Bastien J, Perez F, Hild F (2006) Digital image correlation analysis of crack behavior in a reinforced concrete beam during a load test. Can J Civil Eng 33(11):1418–1425
11. Tung SH, Shih MH, Sung WP (2008) Development of digital image correlation method to analyze crack variations of masonry wall. Sadhana 33(6):767–779
12. Smith BJ, Kurama YC, McGinnis MJ (2011) Design and measured behavior of a hybrid precast concrete wall specimen for seismic regions. J Struct Eng 137(10):1052–1062
13. Alcocer SM, Klinger RE (2006) The Tecomán, México earthquake, January 21, 2003: an EERI and SMIS learning from earthquakes reconnaissance report. Earthquake Engineering Research Institute, Oakland
14. http://www.correlatedsolutions.com
15. Sukla A, Dally JW (2010) Experimental solid mechanics. College House Enterprises, LLC, Knoxville
16. Hua T, Xie H, Hu Z, Chen P, Zhang Q (2011) Evaluation of the quality of a speckle pattern in the digital image correlation method by mean subset fluctuation. J Opt Laser Technol 43(1):9–13

Chapter 24
Damage Mechanisms of Chemically Strengthened Glass Bars Due to High-Velocity Ball Impact

Phillip Jannotti and Ghatu Subhash

Abstract Ball impact experiments were conducted on unstrengthened and strengthened glass bars at 261 and 345 m/s, respectively. Damage propagation was recorded using a high-speed camera at frame rates of 281,000 frames per second. Immediately after the ball impact on the unstrengthened glass, the damage front reached a maximum velocity of 1,967 m/s before falling to zero within a short distance. However, the longitudinal wave created due to the impact continued down the bar towards the rear-end. Upon reflection from the rear-end of the bar, a secondary damage front was initiated at 3,192 m/s, which eventually arrested. On the other hand, the damage front in the strengthened glass reached a maximum of 2,275 m/s immediately after impact, and then stabilized at 1,921 m/s until the bar was consumed. It was determined that the stored elastic energy in the strengthened glass fueled the self-sustained damage and allowed it to propagate at a near constant rate. For both glasses, high-speed imaging allowed for observation of energy dissipation modes such as fracture propagation (fracture surface area), radial bar dilation, and high velocity jetting of fine glass particles at the impact site. In addition to the triangular dilation observed in the unstrengthened glass at the impact site, the strengthening process also led to uniform dilation of the entire rod.

Keywords Strengthened glass • Ion armor • Dynamic fracture • Ball impact • Residual stress

24.1 Introduction

Strengthened glasses are prime candidates for a range of civilian, military and homeland security applications ranging from screen covers for cell phones, pharmaceutical autoinjector (epipen®) cartiriges, hurricane- and earthquake-resistant architectural windows, to bullet- and blast-resistant windows for armored vehicles [1].

Surface modification by ion exchange has been shown to result in reduced surface flaw sensitivity, increased fracture strength and improved mechanical properties [1]. However, the applicability of strengthened glasses for dynamic applications, where high velocity impact is expected, requires that the high rate impact response be well-understood. Thus, to examine the impact performance of chemically strengthened glass, ball impact experiments have been identified as a means of observing and quantifying the dynamic fracture characteristics. The results of a study to understand the influence of chemical strengthening on the damage morphology and damage propagation characteristics are presented.

24.2 Experimental

Two types of lithium aluminosilicate glass bars of approximate dimensions 10 × 7.6 × 100 mm were used in the current study. Glass bars prior to chemical treatment are referred to as "unstrengthened". The glass bars were strengthened by Saxon Glass Technologies, Inc., Alfred, NY, using a patented ion exchange process. The glass bars are immersed in a mixed molten

P. Jannotti • G. Subhash (✉)
Mechanical and Aerospace Engineering, University of Florida, Gainesville, FL 32611, USA
e-mail: subhash@ufl.edu

H. Jin et al. (eds.), *Advancement of Optical Methods in Experimental Mechanics, Volume 3*,
Conference Proceedings of the Society for Experimental Mechanics Series,
DOI 10.1007/978-3-319-00768-7_24,

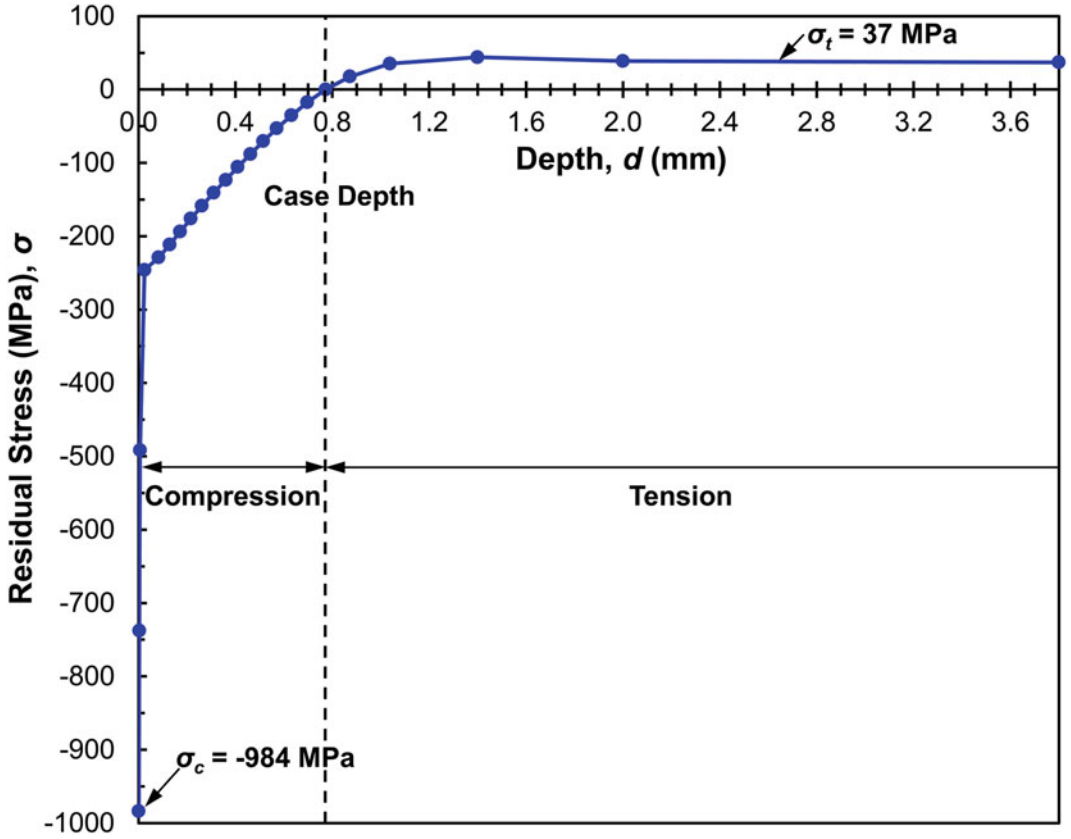

Fig. 24.1 Residual stress profile for Ion Armor™ glass by Jannotti et al. [3] determined by photoelasticity

salt bath containing sodium-nitrate and potassium-nitrate salts for up to 24 hours. This allowed lithium ions from the glass to exchange with salt ions which resulted in the development of residual surface compression (in the exchange zones) and balancing interior tension (equilibrium). The resulting glass bars, trade-named Ion Armor ™, are referred to as "strengthened". The exchange between lithium and sodium results in a thick surface layer (~0.8 mm) of moderate residual compression, while the exchange between sodium and potassium results in a thin layer (~25 μm) of large near-surface residual compression [2].

A typical residual stress profile for the strengthened glass is shown in Fig. 24.1, which illustrates the evolution of residual stress from the surface of the glass into the glass interior [3]. In the outer layers of the glass a severe stress gradient was present, where the compressive stresses rapidly fell from −984 MPa near the surface to around −250 MPa within 25 μm depth. The stress state then became tensile at around ~0.8 mm from the surface and reached a near constant tensile stress value of 37 MPa.

In order to examine the suitability of the strengthened glasses for dynamic applications, ball impact experiments were performed on unstrengthened and strengthened glass bars. A schematic of the experimental setup is shown in Fig. 24.2. Damage patterns were captured using high-speed imaging (Vision Research® Phantom v710®) at frame rates of 281,000 frame per second.

24.3 Results and Discussion

Figure 24.3 represents the typical damage front evolution and propagation for ball impacts on unstrengthened and strengthened glass bars at 261 and 345 m/s, respectively. Upon impact, the unstrengthened glass experienced radial dilation, with maximum dilatational velocity at the impact plane and decreasing velocity (linearly) away from the impact site (triangular shaped) (Fig. 24.3a inset). Additionally, high velocity jetting of fine particles (ejecta) was observed at the impact-

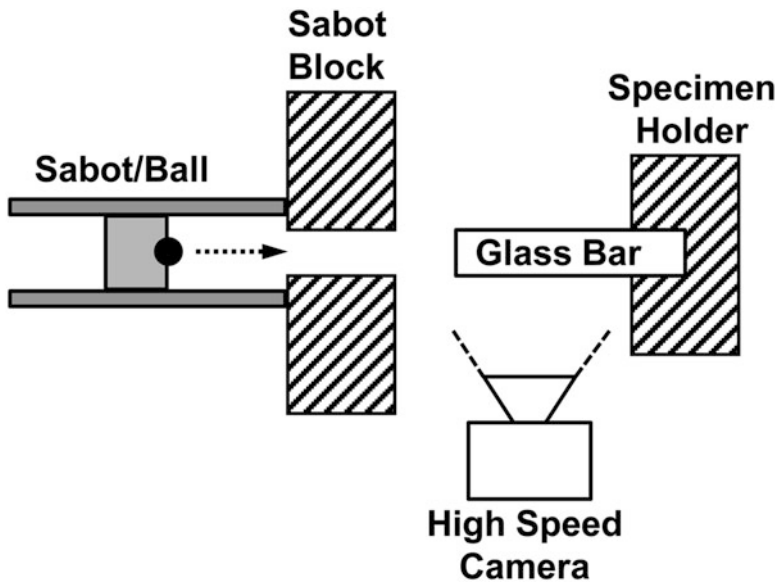

Fig. 24.2 Schematic of the test setup for ball impact experiments

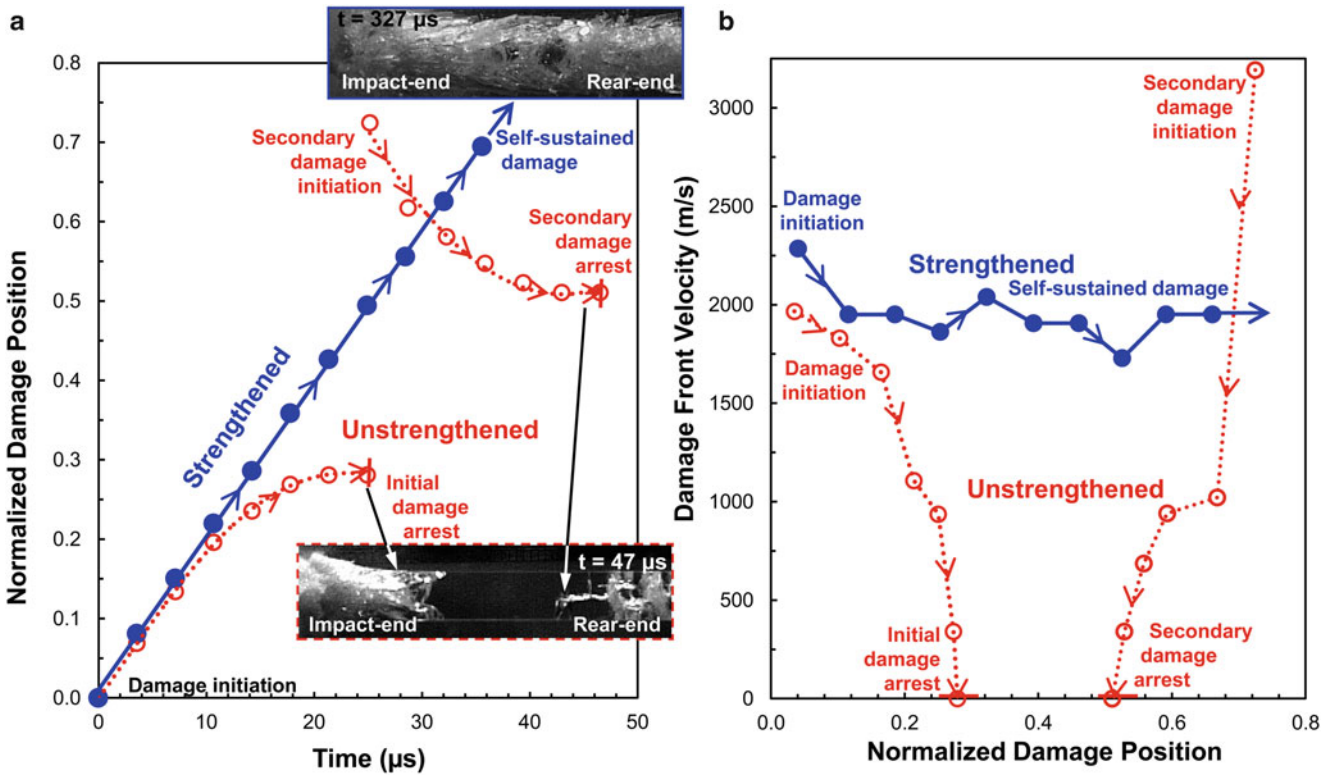

Fig. 24.3 (**a**) Plot of the normalized distance travelled by the damage front as a function of time with insets of damage patterns in each type of glass. Also shown is (**b**) a plot of the damage front velocity as a function of normalized distance travelled by the damage front. Note that the impact velocity on the unstrengthened and strengthened glass was 261 and 345 m/s, respectively. Additionally, distance has been normalized by bar length (i.e., 100 mm)

end. In Fig. 24.3a, it was seen that the damage propagated at a near linear rate for ~10 μs and then decayed over the next 15 μs as the propagation became non-linear. The total span of the initial damage propagation was 28 mm. In terms of velocity, the maximum value of 1,967 m/s (52 % of the shear wave velocity) was observed immediately after impact before decaying to zero (Fig. 24.3b). The longitudinal wave induced due to impact (compressive in nature) travels the length of the bar and reflects from the rear-end of the bar as tension and initiates a secondary damage front. Unlike at the impact-end, the bar does

not experience dilation. The secondary damage front propagated at a peak velocity of 3,192 m/s (86 % of the shear wave velocity) before rapidly decaying to zero over a length of 21 mm, leaving a central section of the glass bar intact and undamaged (confined between the initial and secondary damage).

For the strengthened glass, similar modes of damage as in the unstrengthened glass, i.e., (triangular) radial expansion of the bar and high velocity ejecta, were observed (Fig. 24.3a inset). The damage front propagation was observed to be approximately linear during the entire duration of damage propagation (see Fig. 24.3a). In terms of velocity, the damage front reached a maximum velocity of 2,275 m/s (or 60 % of the shear wave velocity) immediately after impact, and then propagated at approximately 1,921 m/s (51 % of the shear wave velocity) for the remaining duration (Fig. 24.3b). Recall that the development of residual stresses in the strengthened glass bar also leads to the generation of stored elastic energy. It is this stored elastic energy that allows for sustained damage growth and propagation. Once the damage has reached the interior tensile region of the glass, small volumes of stored elastic energy were progressively released just ahead of the damage front. Thus, a self-sustained damage front was generated and the entire bar was consumed by damage. As noted, in addition to the impact-end of the rod "peeling open" (triangular dilation), the entire rod was observed to exhibit uniform radial dilation about the rod axis as the damage propagated along the bar. This uniform dilation took place at a visibly slower rate compared to the triangular dilation at the impact-end and is the result of the unloading process, whereby high levels of in-plane compression are reversed to tensile (expansive) forces.

24.4 Conclusions

Ball impact experiments at 261 and 345 m/s were performed on unstrengthened and strengthened glass bars, respectively. The presence of stored elastic energy due to chemical strengthening led to self-sustained damage front propagation and extensive fragmentation in the strengthened glass. Although yielding similar damage front velocities, the damage in the strengthened glass maintained a near constant propagation velocity until the entire bar was consumed. Also, the unloading of the (initially) compressive outer layers of glass led to an additional form of energy dissipation in the form of uniform bar dilation.

Acknowledgements The authors are thankful to Dr. Arun Varshneya of Saxon Glass Technologies, Inc., for supplying the glass specimens used in this study. Financial support from the National Defense Science and Engineering Graduate Fellowship program for Phillip Jannotti is also sincerely acknowledged.

References

1. Varshneya AK, Spinelli IM (2009) High-strength, large case-depth chemically strengthened lithium aluminosilicate glass. Am Ceram Soc Bull 88(5):213–220
2. Jannotti P, Subhash G, Ifju P, Kreski PK, Varshneya AK (2011) Photoelastic measurement of high stress profiles in ion-exchanged glass. Int J Appl Glass Sci 2(4):275–281
3. Jannotti P, Subhash G, Ifju P, Kreski PK, Varshneya AK (2012) Influence of ultra-high residual compressive stress on the static and dynamic indentation response of a chemically strengthened glass. J Eur Ceram Soc 32(8):1551–1559

Chapter 25
Stereo X-Ray System Calibration for Three-Dimensional Measurements

Timothy J. Miller and Enrico C. Quintana

Abstract Advances in multiple view computer vision techniques have made it possible to make highly accurate three-dimensional (3D) measurements using calibrated stereo image systems. Recent experiments conducted at Sandia National Laboratories have demonstrated the feasibility of applying these techniques on an X-Ray system. Acquiring measurements from stereo image systems, be it visible or x-ray, require the estimation of the system's intrinsic and extrinsic parameters via a calibration process. There are several calibration methods depending on the system's configuration and its intended use. In most cases, one or more image pairs of a calibration artifact such as a 3D object of known dimension or a 2D target board are processed to estimate the system's calibration parameters. For this paper, methods based on both types of calibration artifacts will be discussed along with experimental results.

Keywords X-ray • High-speed stereo X-ray • Stereo camera calibration • Three dimensional imaging • Computer vision • Computed tomography

25.1 Introduction

Advances in computed tomography (CT) have revolutionized the ability to visualize the internal volume of objects in three-dimensions (3D). However, acquiring CT datasets can take anywhere from minutes to hours depending on material composition and complexity and while acquiring a CT scan, the test object needs to remain completely still. The resulting data is a volumetric stack of images that provide the ability to measure the exact location of features within an object. Sandia National Laboratories endeavors to develop a new measurement tool that will allow quantitative characterization of the displacement/movement of internal features during dynamic experiments. It is not possible to acquire a CT dataset without a significant investment, due to the motion constraints of the technique, within the time it takes to execute the types of dynamic experiments required. Consequently, a stereo x-ray approach is being developed using multiple view computer vision techniques.

Stereo x-ray is not a new concept in radiography. Traditional stereo x-ray was typically used to empirically visualize 3D information using stereoscope techniques, where a pair of ray images were acquired using a single x-ray machine repositioned for each view [1]. The angle between the images was set to correspond to the human visual system. However, this technique while providing a qualitative intuition in 3D does not provide quantitative information suitable for subsequent analysis of dynamic experiments.

This paper explores some of the initial work accomplished towards a high-speed stereo x-ray system by applying multiple view computer vision techniques.

T.J. Miller (✉) • E.C. Quintana
Sandia National Laboratories, PO Box 5800, Albuquerque, NM 87185, USA
e-mail: tjmille@sandia.gov

H. Jin et al. (eds.), *Advancement of Optical Methods in Experimental Mechanics, Volume 3*,
Conference Proceedings of the Society for Experimental Mechanics Series,
DOI 10.1007/978-3-319-00768-7_25,

25.2 Background

The primary aim in any computer vision system is to relate real world information in such a way that it can be processed and understood by a computer. As one can imagine, there are many steps involved. The number of steps and level of complexity of the system and its analysis software depends on the information required and any a priori information regarding the imaging system and the real world. In most cases, the imaging system and the world scene(s) are constrained to simplify analysis.

The ubiquitous pinhole camera model is one of the most common methods of relating the world to a digital image. The pinhole camera model simplifies the equations that relate the known positions of objects in the real world to their respective projections onto the camera's imaging plane (i.e., sensor). The parameters derived from these equations are commonly referred to as the camera's intrinsic parameters and are composed of the camera's focal length (f), optical center (O.C.), and sensor skew (θ). Figure 25.1 shows the basic pinhole camera model. In practice, the focal length and optical center parameters are broken into their respective X and Y-components relative to pixel size. This is to account for the fact that sensor may have non-square pixels.

Another simplification for stereo (or multi-camera) systems implies that images from different views are acquired from non-moving synchronized cameras and that the scene being imaged can be assumed to be static. This is typically accomplished using fast camera shutters such that any movement can be considered negligible. This simplification provides the basis for determining how the imaging systems from each view relate to one another. The parameters used to describe the relative positions and orientations of each imaging system are called the extrinsic parameters. Extrinsic parameters can be composed in several ways. One common form, especially for a stereo system, is to provide the translation vector and rotation matrix of one camera relative the other, where one camera is assumed to be coincident with the world coordinate frame. Another (and more general) form is to provide the translation and rotation of each camera relative to a world coordinate system.

Once the intrinsic and extrinsic parameters for the entire imaging system are known, quantitative 3D information can be estimated. Finding the intrinsic and extrinsic parameters for each camera in a multiple view computer vision system is known as the camera calibration. There exists a plethora of literature[1] on camera calibration and multi-view computer vision techniques.

One of the most common methods for camera calibration employs a calibration artifact having known non-planar dimensions from which the camera parameters are estimated from a single pair of images (Method-1). Another common method builds up 3D information in the scene by capturing multiple image pairs of a planar target board, thus providing a rich set of 3D points to estimate the calibration parameters from (Method-2). There are (of course) advantages and disadvantages to each approach. The primary advantage of Method-1 is that a system can be calibrated from a single pair of images. This is important for flash x-ray systems where only a few calibration image frames can be captured.

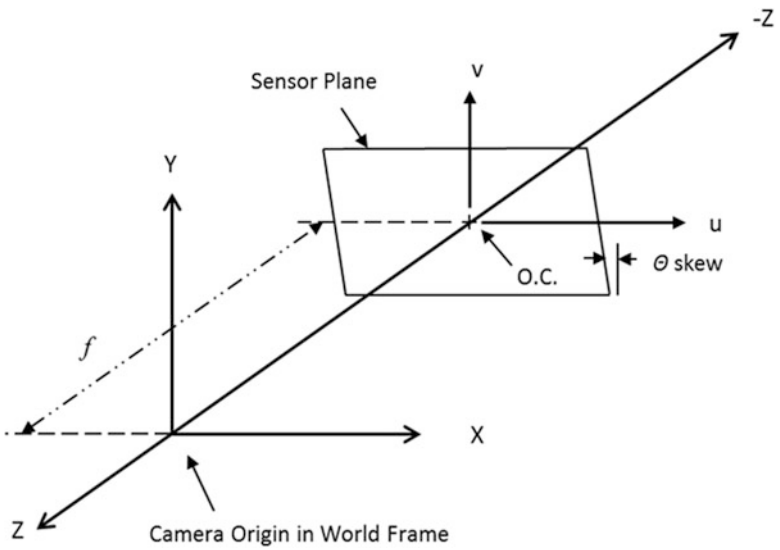

Fig. 25.1 Pinhole camera model

[1] See [2, 3] for a few helpful references on multiple view computer vision techniques.

A disadvantage for Method-1 is that there are not as many 3D points from which to estimate the calibration parameters which can adversely affect accuracy. On the other hand, calibrations using Method-2 using a planar calibration board being imaged while it is moved through the volume of interest provide more 3D points for calibration and often yield more accurate results. For the case of flash x-ray, the Method-1 is required. For high-speed and quasistatic x-ray imaging, Method-2 would be the best choice. The results presented in this paper are the first attempt to evaluate the quality of both calibration methods in a basic stereo x-ray system.

This paper presents results obtained using both calibration methods discussed above. For Method-1 utilizing a single pair of images obtained of a non-planar calibration artifact, the algorithm presented in the *"Camera Parameters from the Projection Matrix"* section (pp 132–136) of Turcco and Verri's book [2] was applied. For Method-2, based on multiple stereo views of a planar calibration board, a commercial 3D Digital Image Correlation (DIC) application was utilized to provide the system calibration.[2]

25.3 Experimental Setup

25.3.1 Stereo X-Ray System

The experimental setup consists of two x-ray machines and two detectors. The detectors utilized for the bench-top test are composed of reconfigurable enclosures containing an x-ray scintillator, a 45° degree turning mirror, and a scientific grade cooled CMOS camera with a lens focused on the back of the scintillator via the turning mirror (See Fig. 25.2). The scintillator converts the x-ray photons into visible light photons. The 45° turning mirror is used to direct these photons towards the camera, while keeping the camera out of the direct x-ray beam.

It should be noted that this system is not intended to be the final high-speed system. However, it was constructed for both experimental purposes and to aid in the development of algorithms to be used by future systems containing high-speed cameras and scintillators.

The left and right images processed by the stereo camera calibration algorithms correspond to the images created by the left and right x-ray machines, respectively. The reason for this is that the geometry of an x-ray machine mimics the geometry of the pinhole camera model from which the calibration algorithms are based on. In other words, the pinhole camera model is based on light rays emanating from visible objects in the scene, which are focused on the origin of the camera by the lens. In a similar (but reversed) manner, x-rays emanate from the x-ray source and are attenuated from hitting the scintillator with the same energy the non-blocked rays do thus creating an "x-ray shadow" having less intensity on the scintillator, which are subsequently imaged by a camera. The "reversal" comes from the fact that the x-ray source is the origin of photon energy whereas with the pinhole camera the photon source are the visible objects themselves radiating reflected light.

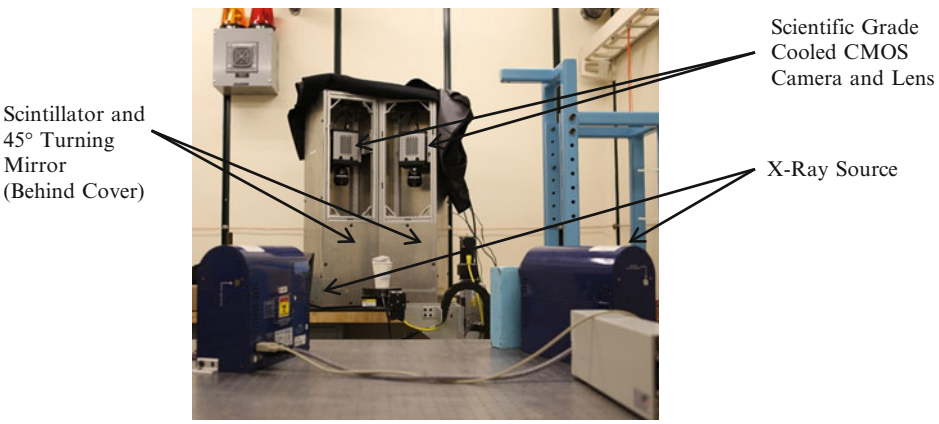

Fig. 25.2 Stereo X-Ray system

[2] See [4] for a good reference on 3D Digital Image Correlation.

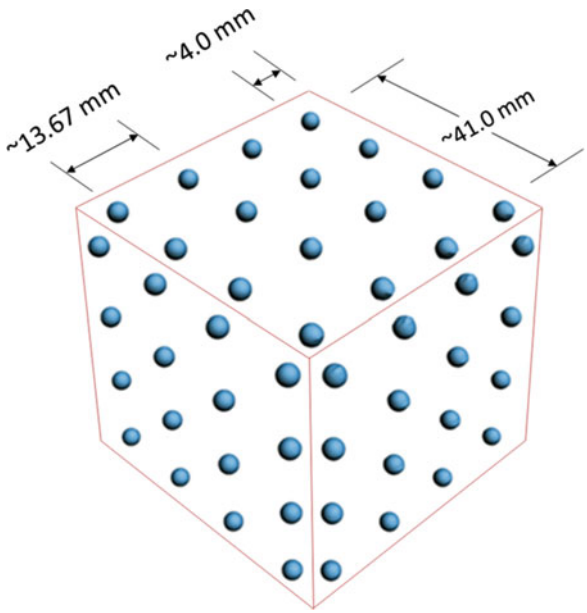

Fig. 25.3 Three-dimensional rendering of CT scanned data of calibration block (dimensions are for a sense of scale only)

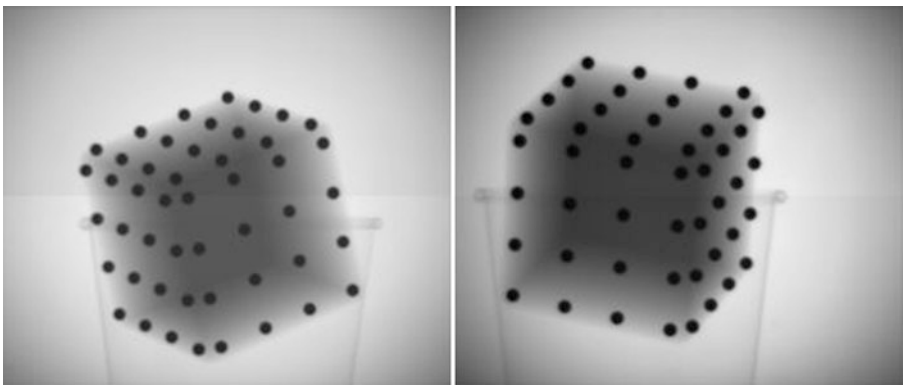

Fig. 25.4 Left and right x-ray images of calibration block acquired with stereo x-ray system

25.3.2 System Calibration

For both calibration methods, a priori knowledge of the calibration object and corresponding pixel locations of its features from the left and right x-ray images are required. The non-planar calibration artifact developed to test Method-1 was constructed by hand using a small cube with 16 ball bearings evenly spaced on three of the six cube faces. The accuracy of Method-1 is highly dependent on the known positions of the ball bearings on the calibration cube. For this reason, the calibration cube was measured using computed tomography in order to acquire the precise locations of the center of each ball bearing rather than using the assumed positions of the handmade cube. The surface of each ball bearing from the CT dataset is shown in Fig. 25.3. The CT surface data from each ball bearing was fit to a sphere so that the computed centroid of the sphere can be used for the precise location of each bearing. The relative positions of the ball bearing centroids form the basis for the camera calibration coordinate system and are used to estimate both the intrinsic and extrinsic calibration parameters of the stereo x-ray system via Method-1 (the non-planar camera calibration algorithm). Left and right x-ray images of the calibration cube are shown in Fig. 25.4.

One of the primary reasons for using ball bearings on the faces of the calibration cube is that the centroids of the bearings in the calibration images directly correspond to the 3D centroids locations from the CT scan. In addition, there are well known algorithms for calculating the sub-pixel locations for each ball bearing in image coordinates.

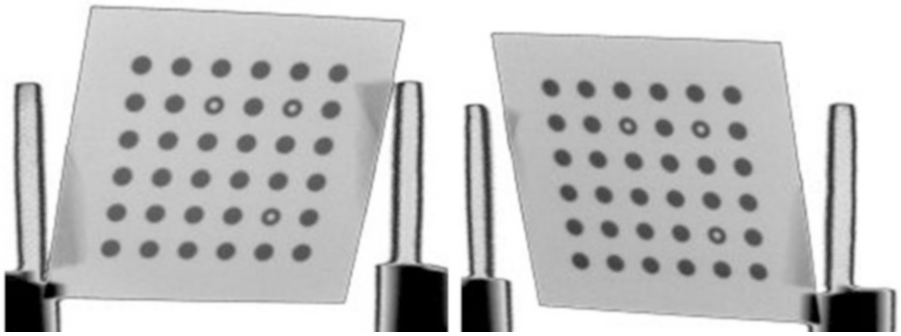

Fig. 25.5 Left and right x-ray images of the 2D calibration target constructed from printed circuit board material

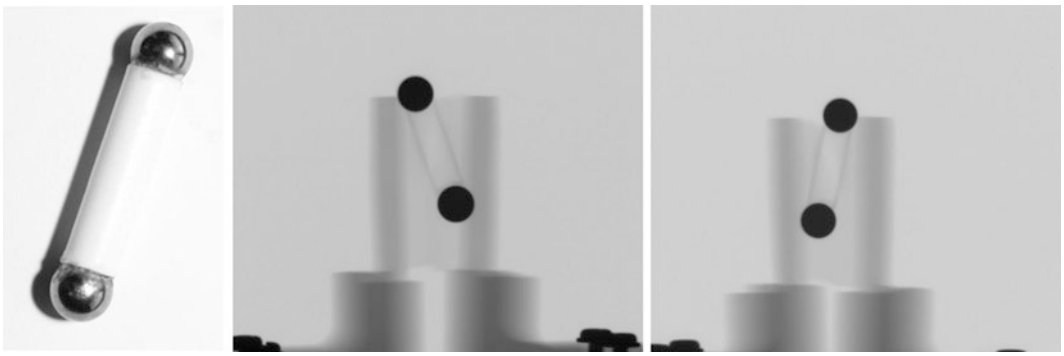

Fig. 25.6 Optical image of ball bearing target (*left*), ant the left and right x-ray images, respectively

Both the 3D world locations of the bearing centroids and the 2D pixel locations from the left and right calibration images are processed by the camera calibration algorithm,[3, 4] to estimate the intrinsic and extrinsic parameters of each x-ray system. Once this is done the calibration parameters from the left and right system are combined to form the calibration for the stereo x-ray system.

For Method-2, a planar calibration target was constructed to be consistent with the 2D calibration boards used by the commercial DIC application with the modification that the calibration target needs to be imaged by x-rays rather than optically. To accomplish this, the 2D target pattern was constructed as a printed circuit board where gold was used as the high-z material to be imaged. Left and right x-ray images of a printed circuit board designed to imitate a 2D calibration target used by a commercial DIC application are shown in Fig. 25.5.

25.4 Data Collection and Processing

For the initial test, a simple plastic rod with a ball bearing on either side was constructed. The test item was placed on a four axes staging system (three translational, one rotational). The dataset was acquired with the test item set at a slight angle and was rotated through 360 ° while acquiring stereo x-ray images[5] every 15°. An image of the test item along with example left and right x-ray images are shown in Fig. 25.6. As expected; there is no concept of depth or location of for each ball bearing in the x-ray images.

[3] The algorithm used for the Method1 is present in the "*Camera Parameters from the Projection Matrix*" section (pp 132–136) of Turcco and Verri's book [2], which was as adapted from a paper by Tsai [5].

[4] A MATLAB implementation by Siddhant Ahuja can be found at: http://siddhantahuja.wordpress.com/2010/02/20/570/

[5] Note: Due to a mistake during the image acquisition, the 315° and 330° image pairs are duplicates of the 300° degree image pair. This is clearly visible in the 3D results shown in Fig. 25.7.

Each image pair was processed to extract the left and right sub-pixel centroid locations of each ball on the test item. The sub-pixel locations along with the calibration parameters found using Method-1 were processed by a non-optimum triangulation process to produce a set of 3D measurements corresponding to the 3D-locations of each bearing for each pair of images. Likewise, the same sub-pixel locations along with the calibration parameters found by the commercial 3D DIC application (Method-2) were triangulated using the same non-optimum triangulation process used for Method-1.

25.5 Results

Both methods produced similar 3D data. However, the 3D coordinate systems used by each method are unique to the calibration parameters and calibration method. In other words, the coordinate system for Method-1 is based on the non-planar calibration artifact's coordinate system. The coordinate system for Method-2 is set between the two x-ray systems. Consequently, the two 3D datasets differ by a coordinate transformation. In order to simplify the comparison between the two datasets and ignore errors caused by attempting to align them, it was decided to compare the relative distanced between each bearing on the test item. This allows comparison between the two datasets as well as comparisons within each dataset between the individual 15° steps for each pair of images.

Figure 25.7 shows a plot of the relative 3D locations of the top and bottom bearings of the test item as it is rotated through 360°. To aid in visualizing the top and bottom ball bearings corresponding to a pair of x-ray images, a line was drawn connecting the ball bearings of every other image pair. The red 'x' points in Fig. 25.7 are the data from Method-1. To visualize how close the two methods are when aligned, the data from Method-2 was aligned to Method-1 and plotted as 'o' in Fig. 25.7, also.

Figure 25.8 shows a plot of the measured distance between the ball bearings as processed by the both methods. The overall rod length was measure with a caliper several times as was the diameter of the ball bearing. The average of both was taken and the diameter of the ball bearing was subtracted from the overall rod length to provide the distance the between the ball bearing centers. The caliper accuracy is 0.01 mm.

The plot in Fig. 25.8 shows a small bias difference between each system, which may be due to scale differences between the two calibration methods. The bias between the true rod length and Method-1 is 0.110 mm compared to 0.040 mm for Method-2.

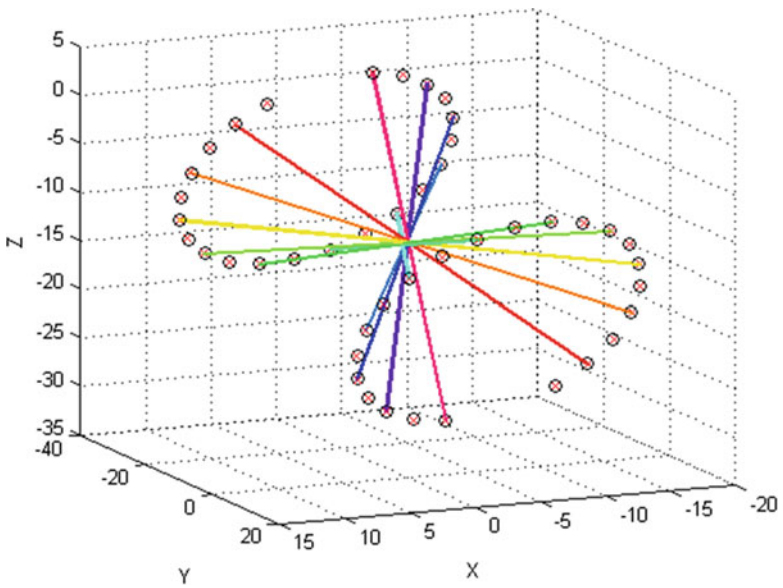

Fig. 25.7 Plot showing the relative locations of the top and bottom bearings on the test item rotated through 360° (Note: For every other image pair, lines are drawn between the top and bottom ball bearings)

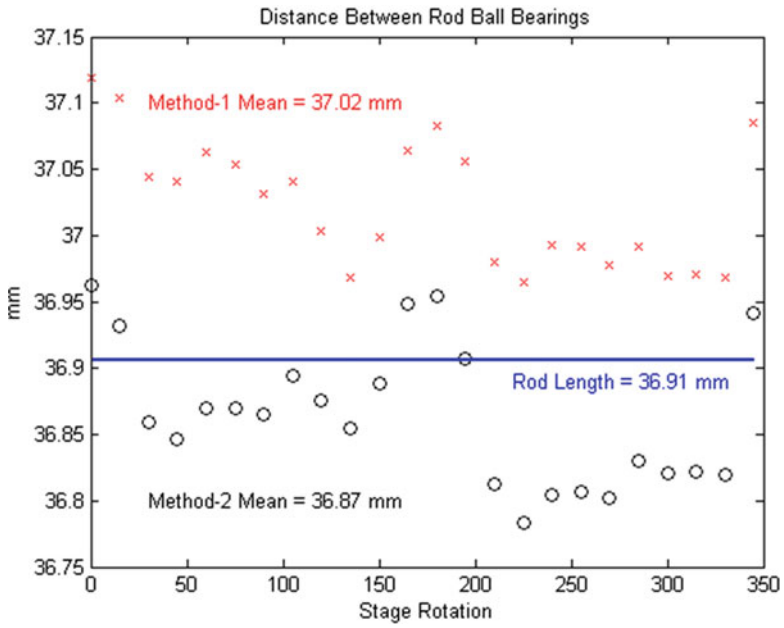

Fig. 25.8 Plot showing rod distances for Method-1 (x), Method-2 (o), and rod length

25.6 Conclusions

We demonstrated two Methods of calibrating a stereo x-ray system. Method-1 uses a single non-planar target, and Method-2 uses a planar target. The calculated calibration parameters for both methods were then used to measure a test item in 3D space. The comparison showed that Method-2 yielded lower measurement uncertainty (better calibration) most likely due to the larger number of calibration points used. Method-1 still gave usable results, and is more applicable in flash x-ray systems where only one calibration pair can be acquired.

While this system still has limited applications and is very specialized, it has the potential to provide unprecedented data during dynamic experiments when scaled up to high-speed. The success of this diagnostic relies on the ability to track unique objects (uniquely identifiable using x-ray imaging) in consecutive x-ray images. This project still leaves the correspondence problem between the two images of a test object unsolved. The example test item was greatly simplified to aid correspondence beyond what would be needed for a practical stereo x-ray system. Building correspondence between object features in visible stereo images can be a challenging problem. This problem is compounded in x-ray images in that the full volume of the scene is "visible" complicating the correspondence problem. Consequently, new methods will need to be developed to find matches.

Acknowledgements Sandia National Laboratories is a multi-program laboratory managed and operated by Sandia Corporation, a wholly owned subsidiary of Lockheed Martin Corporation, for the U.S. Department of Energy's National Nuclear Security Administration under contract DE-AC04-94AL85000.

References

1. Mcintire P, Bryant L (eds) (1985) Nondestructive testing handbook volume three radiography and radiation testing, 2nd edn. American Society for Nondestructive Testing, Columbus. ISBN 0-931403-00-6
2. Trucco E, Verri A (1998) Introductory techniques for 3-D computer vision. Prentice Hall, Upper Saddle River. ISBN 0132611082
3. Hartley R, Zisserman A (2004) Multiple view geometry in computer vision, 2nd edn. Cambridge University Press, Cambridge. ISBN 0521540518
4. Sutton Michael A, Orteu J-J, Schreier H (2009) Image correlation for shape, motion and deformation measurements: basic concepts, theory and applications. Springer, New York. ISBN 9780387787466
5. Tsai RY (1987) A versatile camera calibration technique for high-accuracy 3D machine vision metrology using off-the-shelf tv cameras and lenses. IEEE J Robot Automat RA-3(4):323–344

Chapter 26
Performing DVC at the Voxel Scale

F. Hild, H. Leclerc, and S. Roux

Abstract To analyze the displacement field in volumes imaged by X-ray tomography at several deformation states, a new approach is proposed whereby the displacement is measured down to the voxel scale and determined from a mechanically regularized system using the equilibrium gap method and additional boundary regularizations. It is then possible to compute a displacement vector for each voxel, inducing lower residuals (in terms of experimental data). As representative reconstructed volumes lead to large numbers of degrees of freedom, a dedicated GPU computational strategy has been developed and implemented. A set of volumes of size $100 \times 170 \times 256$ voxels (i.e., more than 13 million kinematic unknowns), which corresponds to a part of a sample made of nodular graphite cast iron and tested in tension, is analyzed.

Keywords Digital volume correlation • GPU • In situ test • Regularization • X-ray tomography

26.1 Introduction

When displacement fields are measured, one key aspect is to get local fluctuations in the material to understand, for instance, how they can be correlated to the underlying microstructure. This requires the measurements to be as accurate as possible on the smallest possible scale. When dealing with volumes obtained via X-ray tomography, a voxel-scale analysis seems to be one of the ultimate scales of description. The aim of the present paper is to show that this goal can be reached via an adapted digital volume correlation (DVC) technique. Because the number of degrees of freedom increases substantially with such an approach, numerical issues need also to be addressed to meet the challenge of analyzing very large amount of data.

In the early developments of digital volume correlation, local approaches were implemented in which a volume of interest (i.e. a small part of the reconstructed volume) is chosen in the reference configuration and registered with a volume in the deformed configuration [1–3]. An alternative approach is to resort to global analyses in which the whole region of interest is analyzed by using, say, 8-noded cube elements to form a mesh (i.e. so called C8-DVC [4]). In this approach, a spatial regularization is enforced, namely, the displacement field is assumed a priori to be continuous. One way to achieve even smaller spatial resolutions is to regularize with mechanical requirements (e.g. static equilibrium [5]). It was shown that calculations could be performed at the voxel scale when coupling DVC with an elastic calculation. This result means that the spatial resolution was enhanced by at least one order of magnitude when compared to standard global and local approaches.

To be applicable to analyze real data (i.e. reconstructed volumes whose size can easily reach Gbytes), voxel-scale calculations are computationally very demanding. In the present paper, graphics processing units (GPUs) are used to perform these large scale calculations. With the development of GPUs, there are potential gains to be expected in terms of computation time and memory requirements when processing a series of pictures or volumes. Digital Image Correlation (DIC) has benefitted from the use of GPUs (e.g., FFT-DIC [6] and global DIC [7–9]). This is also the case for local and global DVC [5, 10, 11].

F. Hild (✉) • H. Leclerc • S. Roux
LMT-Cachan, ENS Cachan/CNRS/Université Paris 6/PRES UniverSud Paris, 61 avenue du Président Wilson,
F-94235 Cachan Cedex, France
e-mail: hild@lmt.ens-cachan.fr

H. Jin et al. (eds.), *Advancement of Optical Methods in Experimental Mechanics, Volume 3*,
Conference Proceedings of the Society for Experimental Mechanics Series,
DOI 10.1007/978-3-319-00768-7_26,

26.2 Voxel-Scale Digital Volume Correlation (V-DVC)

Let us consider f the volume in the reference configuration, and g the volume in the deformed configuration. Those two volumes capture the random texture that is passively advected during the experiment. The gray level conservation at any voxel location $\mathbf{x}$ then reads

$$f(\mathbf{x}) = g(\mathbf{x} + \mathbf{u}(\mathbf{x})) \tag{26.1}$$

where $\mathbf{u}$ is the displacement vector. Because the conservation law is never strictly satisfied due to acquisition noise, reconstruction artifacts and the number of unknowns exceeds the number of equations, it is not possible to determine the displacement vector $\mathbf{u}$ from the *sole* knowledge of f and g. The correlation procedure is generally written on a given domain that contains more than 1 voxel. Thus it aims, for instance, at minimizing the sum of squared differences

$$T_{DVC} = \int_{\Omega} (f(\mathbf{x}) - g[\mathbf{x} + \mathbf{u}(\mathbf{x})])^2 \mathrm{d}\mathbf{x} \tag{26.2}$$

over the considered region of interest Ω in which the displacement field is interpolated as

$$\mathbf{u}(\mathbf{x}) = \Sigma_n u_n \Psi_n(\mathbf{x}) \tag{26.3}$$

where $\mathbf{\Psi}_n$ are (chosen) vector fields, and u_n the associated degrees of freedom gathered in a global vector $\{\mathbf{u}\}$. The measurement problem then consists in minimizing T_{DVC} with respect to the unknown vector $\{\mathbf{u}\}$.

If a voxel-scale determination of the displacement field is sought, additional information is needed to regularize the previous measurement problem. This is achieved by using, say, the equilibrium gap method [12]. To enforce mechanical admissibility in an FE sense, the equilibrium gap is first introduced. If linear elasticity applies, the equilibrium equations read

$$[\mathbf{K}]\{\mathbf{u}\} = \{\mathbf{f}\} \tag{26.4}$$

where $[\mathbf{K}]$ is the stiffness matrix, and $\{\mathbf{f}\}$ the vector of nodal forces. When the displacement vector $\{\mathbf{u}\}$ is prescribed and if the (unknown) stiffness matrix is not the true one, load residuals $\{\mathbf{f}_r\}$ will arise

$$\{\mathbf{f}_r\} = [\mathbf{K}]\{\mathbf{u}\} - \{\mathbf{f}\} \tag{26.5}$$

In the absence of body forces, interior nodes of Ω are free from any external load. Consequently, the minimization of the equilibrium gap consists in minimizing the following quantity

$$T_{EG} = \{\mathbf{u}\}^t [\bar{\mathbf{K}}]^t [\bar{\mathbf{K}}]\{\mathbf{u}\} \tag{26.6}$$

where t is the transposition operator, $[\bar{\mathbf{K}}]$ the rectangular stiffness matrix associated with the inner nodes and those belonging to traction-free boundaries. Similarly, boundary regularization can be considered when the ROI boundary is not a free edge, and an ad hoc functional is considered T_{BR} [13]. Because this functional should be invariant under a rigid body motion, it has to be based on a homogeneous differential operator (or its discrete form) of second order whose quadratic norm is to be minimized. Therefore, in terms of scaling properties, the boundary regularization behaves in a comparable way to the bulk equilibrium gap term. Yet, these three functionals are not of the same dimensional nature. Consequently, normalized quantities are constructed by normalizing by $T_{DVC}(\mathbf{v})$, $T_{EG}(\mathbf{v})$ and $T_{BR}(\mathbf{v})$, where $\mathbf{v}$ is a chosen trial displacement field (for which mechanical admissibility is not mandatory). One possible choice, among many, is a plane wave $\mathbf{v} = \mathbf{v_0} \exp(2\pi i \mathbf{n} \cdot \mathbf{x}/\lambda)$, whose wavevector is aligned with $\mathbf{n}$ and where λ is the wave length whose value should be much smaller than the size of the ROI (i.e. the cubic root of the ROI volume) and yet much larger than the voxel size. The total functional T to be minimized then reads

$$T(1 + w_e + w_b) = \tilde{T}_{DVC} + w_e \tilde{T}_{\mathrm{EG}} + w_b \tilde{T}_{\mathrm{BR}} \quad \text{with} \quad \tilde{T}_\bullet = \frac{T_\bullet(\mathbf{u})}{T_\bullet(\mathbf{v})} \tag{26.7}$$

where the weights w_e and w_b are related to the regularization lengths ℓ_e and ℓ_b

$$w_e = \left(\frac{\ell_e}{\lambda}\right)^4 \text{ and } w_b = \left(\frac{\ell_b}{\lambda}\right)^4 \tag{26.8}$$

Note that the scaling of the weights with respect to the wave length λ (exponent 4) results from the fact that the regularization kernels are the squares ($\times$ 2) of second order ($\times$ 2) differential operators. The larger the weights, the more the constraints defined by functionals T_{EG} and T_{BR} are enforced. This setting can be viewed as a filtering that enforces mechanical admissibility below a cut-off size equal to ℓ_e or ℓ_b. These length scales can be adjusted with the weight levels w_e and w_b.

Let us also emphasize that the minimization of T leads to a linear system for which a Green function (i.e. displacement field solution for a second member is equal to unity on a single voxel) can be defined in a mean-field sense. The latter has an algebraic (power-law) decay away from the point source and vanishes exponentially above a characteristic scale of order ℓ_e. The key property is that the solution to the linear regularized problem has a complexity that can be compared to that of an elastic problem up to size ℓ_e. As it is expected to seek mode values of this length scale (say of the order of 10 voxels at most), convergence is not anticipated to be an issue (unless complicated crack geometries are considered). This guides towards an implementation scheme where the challenge is the efficient handling of memory, but not really the efficient convergence. The nature of the problem and hence the implementation strategy would be different if large ℓ_e were to be used.

26.3 Implementation

The mechanical regularization gives access to local and detailed kinematic features since a voxel-scale DVC (or V-DVC) is considered. Consequently, it leads to costly systems (e.g. about 2×10^8 DOFs for a 400^3-voxel volume). Fortunately, the long-range coupling between these degrees of freedom is essentially controlled by the correlation kernel, whereas the mechanical regularization only controls short range couplings (at distances smaller than ℓ_e). Thus, a conjugate gradient with a block Jacobi preconditioner is expected to give a sufficient convergence rate to compete against direct or iterative solvers with more complex preconditioners. Jacobi preconditioners generally lead to poor convergence properties but can be highly parallelized, which permits to take full advantage of the current GPU hardware with an SIMD or SIMT programming model. However, if avoiding the need for synchronization is one of the first prerequisite to get correct execution speeds, memory access has also to be aligned within thread blocks as much as possible. Furthermore, and more specifically for GPUs, one has to take into account the fact that the cache memory is currently very small, even on recent models.

To solve these issues, a specific storage scheme has been developed for the considered volumes. Data are stored as tiny blocks (usually $4 \times 4 \times 4$ voxels in each block) that are assembled by chunks of size greater than the maximum warp size for the involved kernels (i.e. usually 256). Each block is then associated with a 'thread,' meaning than within a block, offsets are typically equal to $\{0 \times 256, 1 \times 256, \ldots, 4^3 \times 256\}$. Thus, for a tiny block of size n^d, memory access to the neighboring data, which is mandatory for the mechanical operators, are aligned in $100\ n^d/(n+1)^d$ percent of the cases (≈ 0.51 for 4^3 blocks, ≈ 0.64 for 4^2 blocks for the two dimensional case). However, the main point is that unrolling loops for the processing of a block enables for the use of static aligned offsets, besides the possibility to use registers and to let the compiler find a way to make static and explicit caching of data.

26.4 Analysis of Tensile Test

A nodular graphite cast iron specimen is loaded in situ in a testing machine installed in ID 19 beam-line at the European Synchrotron Radiation Facility (ESRF) in Grenoble (France) [14]. Two reconstructed volumes are analyzed, namely, one in the reference configuration (applied load: 22 N), and a second for a 273-N tensile load. For each load level, a set of 600 radiographs was recorded during a 180 ° rotation on a charge coupled device (CCD) camera. This device was coupled with a fluorescent screen via optical lenses. The white beam coming from the synchrotron ring was rendered monochromatic by a multilayered monochromator. The energy of the beam was set to 60 keV. Reconstruction of the tomographic data was performed with a filtered back-projection algorithm developed at ESRF that provided 8-bit gray-scale 3D images with an isotropic voxel size of 5.1 μm. The gauge volume is parallelepipedic, 1.6×0.8 mm^2 in cross-section and 10 mm in length. As can be seen in Fig. 26.1a, the graphite nodules are well dispersed in the matrix and with a rather high volume fraction (14 %). They provide a very good texture for DVC. The characteristic diameter of nodules is of the order of 50 μm

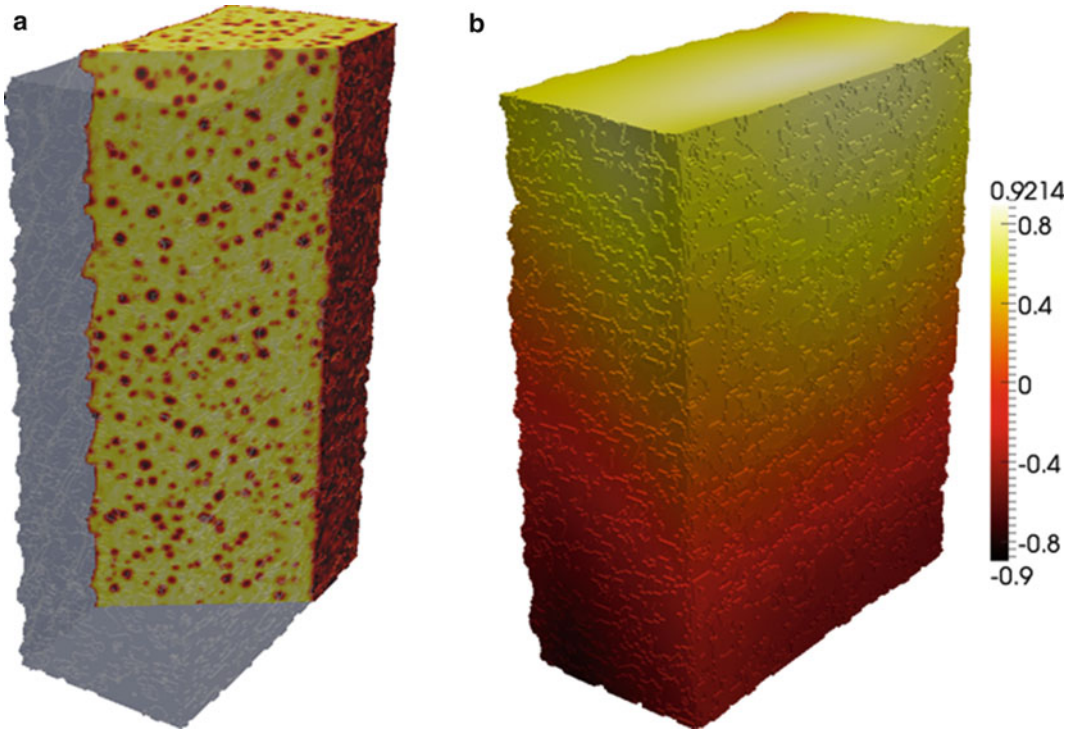

Fig. 26.1 (**a**) Region of interest in the reference configuration. Its size is 100 × 170 × 256 voxels. (**b**) Transverse displacement along the longer edge direction expressed in voxels when $\ell_e = 32$ voxels. Warp factor is equal to 10. The ROI contains the outer (lateral) boundaries. The physical size of one voxel is equal to 5.1 µm

and the mean distance between them is 50 µm, or 10 voxels. Furthermore, the X-ray attenuation is very different for graphite (nodules) and iron (ferritic matrix) so that a very good contrast is observed between the graphite nodules and the ferritic matrix.

Figure 26.1b shows the displacement field obtained with the V-DVC algorithm when the parallelepipedic region of interest includes four free (lateral) faces. Note that the steps visible over the lateral faces corresponds to the voxel-scale discretization of the actual sample roughness (it was as cast with no surface finish). The estimated displacement field is smooth, while staying close with the experimental data (as will be shown in the following).

The mesh used in the previous calculations is shown in Fig. 26.2. Since the size of the analyzed volume is 100 × 170 × 256 voxels, more than four million elements are used, and therefore about 13 million degrees of freedom are needed to express the measured displacement field. The use of GPUs makes this type of calculation still tractable.

An illustration of typical convergence rates is shown in Fig. 26.3. For instance, volumes of size 100 × 170 × 128 voxels are processed in approximately 10 min. It is far greater than that needed for a standard C8 global analysis (≈ 0.2 s when 16^3-voxel elements are chosen for the same considered volume) but it is worth remembering that each voxel has 3 degrees of freedom, leading in this case to about 6,528,000 unknowns!

Figure 26.4 shows the change of the mean dimensionless correlation residual for the tensile test when convergence is reached. The proposed approach (V-DVC) leads to very low residuals, especially for small regularization lengths for which the displacement fluctuations are better captured. All these trends are confirmed when the present results are compared with a global DVC approach with 8-noded cubes (of edge size ℓ), i.e. C8-DVC. For large ℓ_e values, comparable residuals are observed because in the studied case as the displacement field is mostly affine, and hence no systematic error is made because of the space in which displacements are sought. However, in the general case, the mechanical regularization only removes the non-admissible part of the mechanical displacements below a chosen length scale, while other representations operate also as a high-frequency filter but introduce a somewhat *arbitrary* small scale smoothness that does not do justice to the mechanical behavior. Because the mechanical regularization is more faithful to the very nature of the measured field, the cut-off frequency of the filter can be pushed much higher than for other approaches, and hence the spatial resolution reaches unprecedented levels.

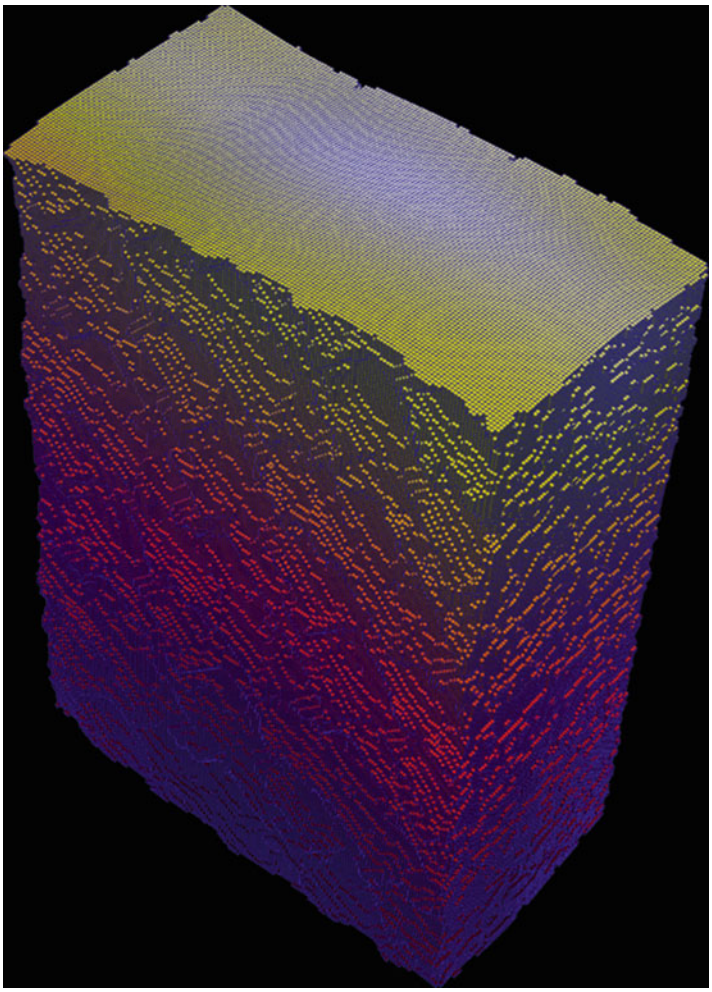

Fig. 26.2 Mesh of region of interest in the reference configuration composed of more than four million C8 elements. The colors correspond to the same displacement component as in Fig. 26.1b

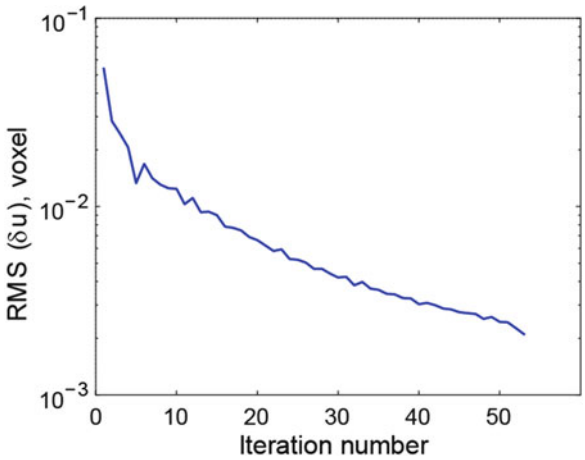

Fig. 26.3 Root mean square of the displacement corrections per voxel versus iteration with a chosen $\ell_e = 64$ voxels, and without any multiscale procedure. The analyzed volume contains $100 \times 170 \times 128$ voxels

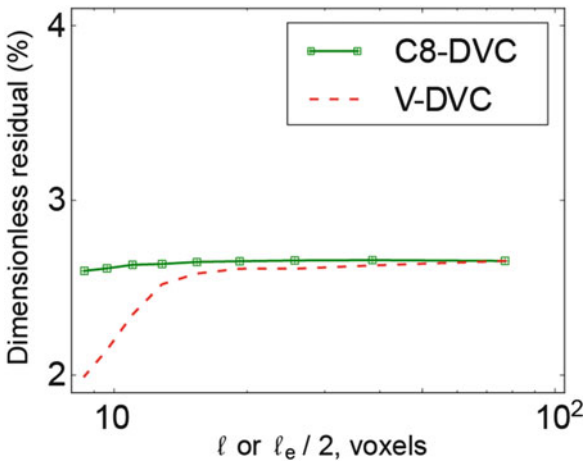

Fig. 26.4 Dimensionless correlation residual versus regularization length ℓ_e (in voxels) for V-DVC (*red* dashed curve) or element size ℓ for C8-DVC (plain *green* line with square symbols)

26.5 Conclusion

The presented mechanical regularization allows us to perform measurements at the voxel scale with digital volume correlation. The described GPU implementation (in Cuda language) enabled representative volumes with more than six million degrees of freedom to be analyzed in less than 10 min on a GPU for a voxel-scale volume correlation. Further optimizations for this type of GPU implementation can still be achieved and will be investigated in the future. Let us also stress that key advantage of the voxel scale discretization is that the description of the geometry (domain boundary, but also inner porosities or cracks) can be described without interference with the mesh geometry as sub-voxel details are not expected to be relevant. In fact, a boundary is not described as such, namely, the voxels that do not belong to the specimen are simply attributed vanishing elastic constants (Figs. 26.1b and 26.2).

It is to be emphasized that the lower scale discretization (here at the voxel scale) tend not to play any role when the actual displacement field is smooth. The voxel scale was chosen here because it allows for a generic implementation irrespective of the material, its rich or poor texture, and specimen geometry. Thus it enables for efficient implementations. However, the very same strategy can be used with a coarser kinematic discretization if no rapid variations are expected. In that case, regularization is no longer a computationally demanding procedure but it may constitute a very efficient tool to deal with very poor material textures without being too harmful to the description of kinematic fields.

Last, such an approach opens the way of using the mechanical regularization as a tool to identify mechanical parameters, or analyzing cracked samples with complex geometries. By identification, one may imagine elastic properties, either globally or by phase (referenced by their gray levels), or shapes or boundaries (say crack surface) to be precisely defined, or parameters of non-linear constitutive laws.

Acknowledgments The support of the French Agence Nationale de la Recherche through 'RUPXCUBE' project (ANR-09-BLAN-0009-01) is acknowledged. The tomographic images were obtained at ESRF through a grant for the experiment MA-501 on beamline ID 19. The scans used herein were obtained with the help of Drs. J.-Y. Buffière, A. Gravouil, N. Limodin, W. Ludwig, and J. Rannou.

References

1. Bay BK, Smith TS, Fyhrie DP, Saad M (1999) Digital volume correlation: three-dimensional strain mapping using X-ray tomography. Exp Mech 39:217–226
2. Bornert M, Chaix J-M, Doumalin P, Dupré J-C, Fournel T, Jeulin D, Maire E, Moreaud M, Moulinec H (2004) Mesure tridimensionnelle de champs cinématiques par imagerie volumique pour l'analyse des matériaux et des structures. Instrum Mes Métrologie 4:43–88
3. Verhulp E, van Rietbergen B, Huiskes R (2004) A three-dimensional digital image correlation technique for strain measurements in microstructures. J Biomech 37:1313–1320
4. Roux S, Hild F, Viot P, Bernard D (2008) Three dimensional image correlation from X-Ray computed tomography of solid foam. Compos Part A 39:1253–1265
5. Leclerc H, Périé J-N, Roux S, Hild F (2011) Voxel-scale digital volume correlation. Exp Mech 51:479–490
6. Asmara RA, Hariadi M (2009) Accelerating phase based motion estimation with hierarchical search technique using parallel threading in graphical processing unit (GPU). Int J Comput Sci Netw Secur 9:140–146

7. Leclerc H, Périé J-N, Roux S, Hild F (2009) Integrated digital image correlation for the identification of mechanical properties. In: Gagalowicz A, Philips W (eds) Mirage. Springer, Berlin, pp 161–171
8. Marzat J, Dumortier Y, Ducrot A (2009) Real-time dense and accurate parallel optical flow using CUDA. In: Proceedings WSCG 2009, University of West Bohemia, Plzeň, Czech Republic, pp 105–111
9. Mitzel D, Pock T, Schoenemann T, Cremers D (2009) Video super resolution using duality based TV-L1 optical flow. Lect Notes Comput Sci 5748:432–441
10. Gates M, Lambros J, Heath M (2012) High-performance digital volume correlation for experimental mechanics applications. In: Proceedings SEM XII, Costa Mesa
11. Leclerc H, Périé J-N, Hild F, Roux S (2012) Digital volume correlation: what are the limits to the spatial resolution? Mech Indust 13(6): 361–371
12. Claire D, Hild F, Roux S (2004) A finite element formulation to identify damage fields: the equilibrium gap method. Int J Numer Meth Eng 61:189–208
13. Tomičević Z, Hild F, Roux S (2013) Mechanics-aided digital image correlation. J Strain Anal (in press). doi: 10.1177/0309324713482457
14. Réthoré J, Limodin N, Buffière J-Y, Hild F, Ludwig W, Roux S (2011) Digital volume correlation analyses of synchrotron tomographic images. J Strain Anal 46:683–695

Chapter 27
Interior Deformation Measurements Using X-Ray Tomography and Digital Volume Correlation

Ning Li and Michael Sutton

Abstract Volumetric Digital Image Correlation (VDIC) or Digital Volumetric Correlation (DVC) is becoming more widely used in biological research, micro-structural studies in materials, geological sciences and other fields. With DVC, volumetric image sets obtained by X-Ray tomography, magnetic resonance imaging or confocal microscopy can be analyzed to obtain volumetric deformation measurements throughout the interior of a specimen, provided that there is sufficient contrast (local changes in contrast) within the interior region of interest. Using software developed by the authors [1], results from a series of experimental studies on a small circular disk specimen are presented that demonstrate the accuracy of the method when adequate contrast exists.

Keywords Volumetric images • Digital volumetric correlation (DVC) • Internal deformation measurements • Displacement map • Strain map

27.1 Introduction

The recent development of efficient 3D imaging tools such as X-Ray Computed Micro-Tomography, combined with the extension of image correlation methods to DVC, opens a wide range of applications for intensive study, including new composite materials. DVC imports volumetric images of the specimen in reference and deformed states and calculate the full 3D displacement and strain map. It is a powerful non-intrusive technique for the identification of sub-surface material deformation and is capable of identifying defects, discontinuities or other material characteristics.

In this study, which follows the work of Bay et al. [2, 3], the correlation computation optimizes the merit function given as:

$$\chi = \sum_{n=1}^{N} \left\{ I_{def}[a(R_n)] - I_{ref}[R_n] \right\}^2$$

where N is the total number of voxels in a sub-volume, I is the intensity at a voxel position $\boldsymbol{R}(X,Y,Z)$ in reference (ref) or deformed (def) image set, and $\boldsymbol{a}$ is the shape function. In this study, the shape function is an affine transformation that includes translation, rotation and deformation. It is noted that the effects of rotation are especially important when the sampling frequency is not uniform in all directions; typically image resolution along one direction (e.g., Z) is lower than it is in the other two (e.g., X and Y in an image slice). Strain components at the center of a given sub-volume are obtained by fitting a quadratic polynomial by displacements of all surrounding sub-volumes.

N. Li (✉) • M. Sutton
Department of Mechanical Engineering, University of South Carolina, 300 Main Street, Columbia, SC 29208, USA
e-mail: lini@cec.sc.edu

H. Jin et al. (eds.), *Advancement of Optical Methods in Experimental Mechanics, Volume 3*,
Conference Proceedings of the Society for Experimental Mechanics Series,
DOI 10.1007/978-3-319-00768-7_27,

27.2 Results

Figure 27.1a shows a typical horizontal slice through the puck specimen. The 150 × 150 × 150 mm field of view was constructed using 1,000 × 1,000 × 1,000 voxels, resulting in an average voxel size of 0.15 mm in each direction. The cylindrical specimen is 20 mm thick, 75 mm in outer diameter, with a central 25 mm diameter interior hole. The puck is made of rubber that has been seeded with silica particles that range from 0.3 to 0.6 mm in size. The reference image set is acquired before compression is applied along its diametral direction. Figure 27.1b shows the deformed image slice acquired when the vertical diameter is compressed from 75 to 56.25 mm.

Figure 27.2 shows the deformed cross-section that is defined by the dashed line in Fig. 27.1. As shown in Fig. 27.2, the puck cross-section has a trapezoidal shape due to the stress state in the central region of the puck specimen.

Using a 23 × 23 × 23 sub-volume size for DVC throughout the interior of the specimen, Fig. 27.3 shows a vector plot of the computed displacement field on the mid-thickness plane of the puck, with W being the displacement in the vertical (Z) direction and U being the displacement in horizontal (X) direction. It is consistent with the result of FE analysis.

Figures 27.4, 27.5 and 27.6 show the measured strain fields ε_{xx}, ε_{xy} and ε_{yy}, respectively, on the diametric cross-section shown in Fig. 27.2.

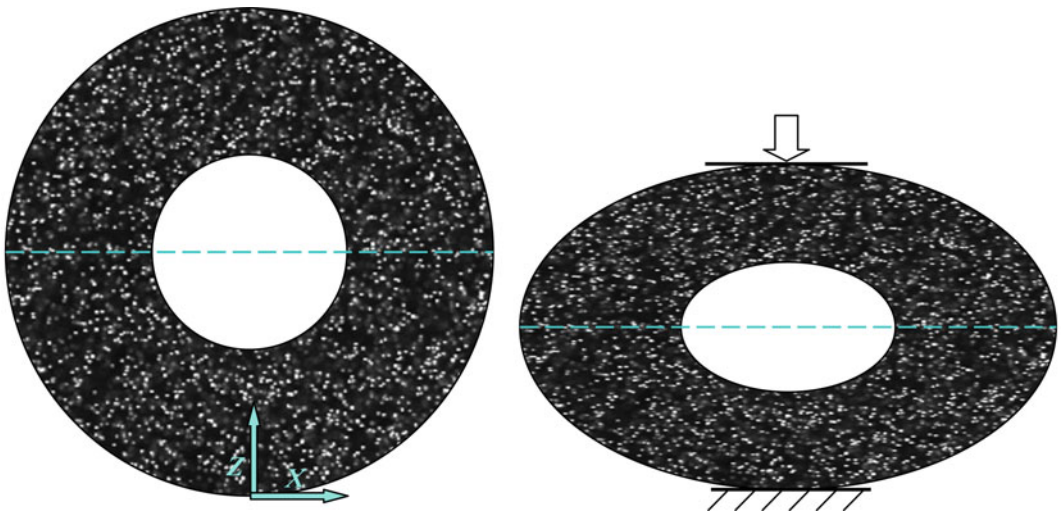

Fig. 27.1 (**a**) Specimen in un-deformed state, (**b**) specimen undergoing vertical compression

Fig. 27.2 Centerline cross-section of deformed specimen after applying compressive loading

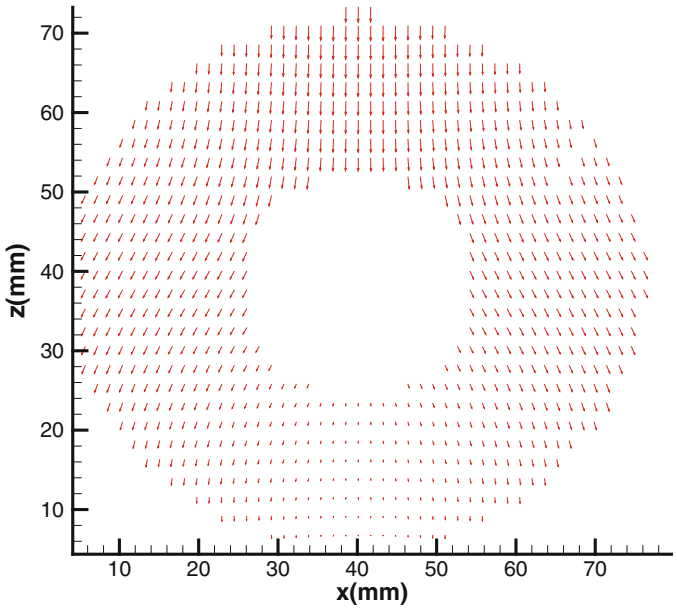

Fig. 27.3 Measured displacement fields, U and W, at mid-thickness of specimen ($y = 10$ mm)

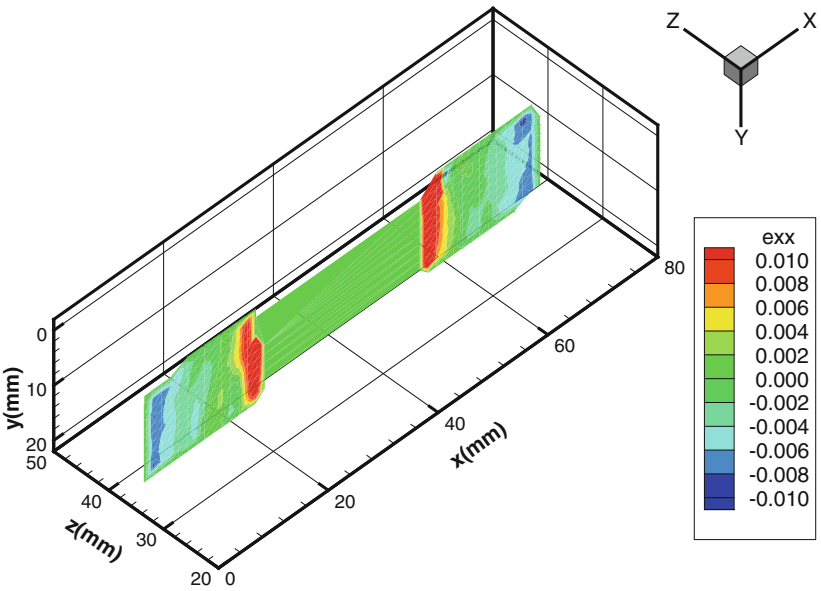

Fig. 27.4 Strain ε_{xx} on the diametric cross-section shown in Fig. 27.2

27.3 Discussion

Though not shown, finite element results are in very good agreement with the measurements throughout the puck interior, providing a measure of validation for the DVC-based measurements. Additional developments are underway to allow for point-wise particle tracking so that rosette-type interior measurements can be obtained without requiring a dense set of interior markers that may alter the response of the material due to density differences in the materials.

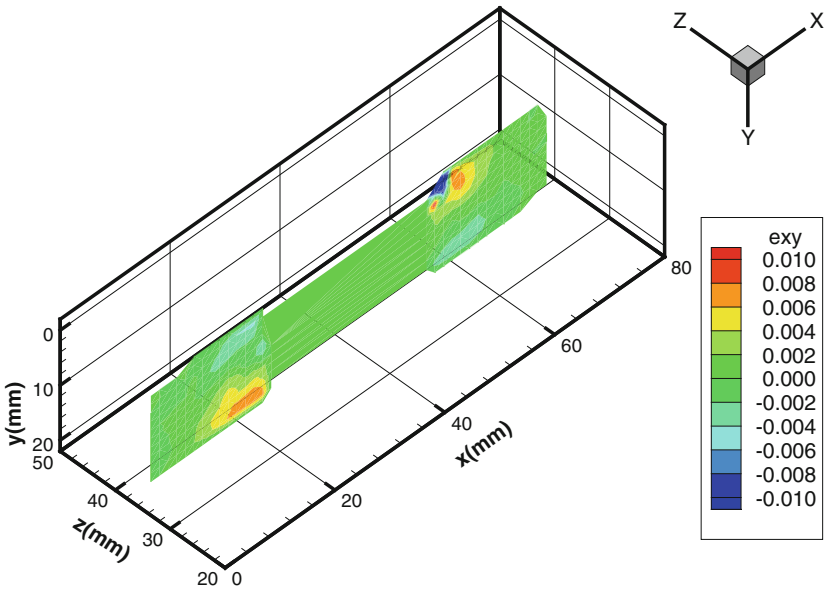

Fig. 27.5 Strain ε_{xy} on the diametric cross-section shown in Fig. 27.2

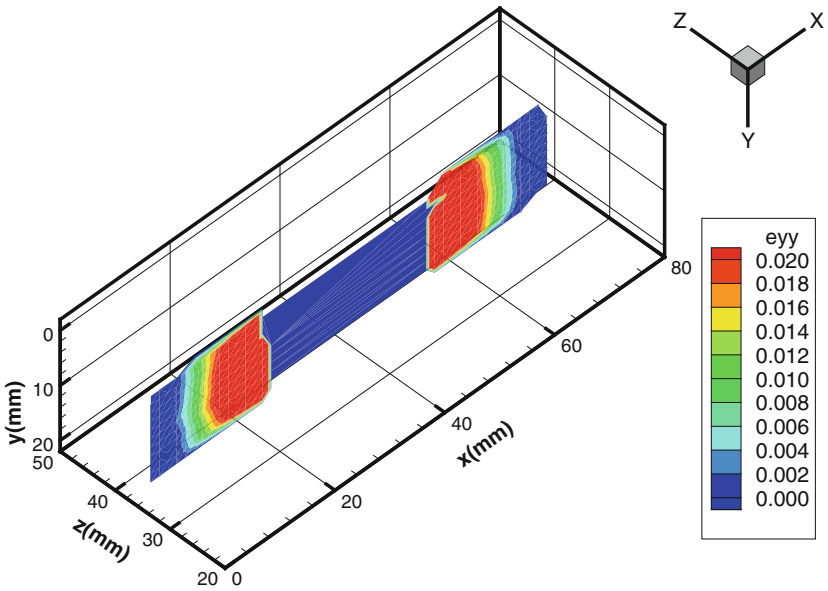

Fig. 27.6 Strain ε_{yy} on the diametric cross-section shown in Fig. 27.2

References

1. Sutton MA, Orteu JJ, Schreier H (2009) Image correlation for shape, motion and deformation measurements. doi: 10.1007/978-0-387-78747-3, Springer
2. Smith TS, Bay BK, Rashid MM (2002) Digital volume correlation including rotational degrees of freedom during minimization. Exp Mech 42(3):272–278
3. Bay BK, Smith TS, Fyhrie DP, Saad M (1999) Digital volume correlation: three-dimensional strain mapping using X-Ray tomography. Exp Mech 33(3):217–226

Chapter 28
Measurement of Surface Topography of Transparent Objects by Using Digital Phase-Shifting Shadow Moiré Method Without Painting

Wei-Chung Wang and Wen-Yi Kang

Abstract Light guide plate (LGP) is one of the essential components of a back light module (BLM). Warpage may be produced during the manufacturing process due to the lower structural strength of the LGP in a thinner thin film transistor liquid crystal display (TFT-LCD) as required by the market. Basically, the fringe pattern produced by the digital phase-shifting shadow moiré (DPSSM) method is generated from interference between the reference grating and its projected grating on the test surface. For a transparent object such as a LGP, reflective painting is generally sprayed on the object's surface to make the projected grating sufficiently visible. However, the LGP may no longer be re-used or may be damaged during the process of painting or de-painting. To investigate the feasibility of obtaining the surface topography of a transparent object by employing the DPSSM method without painting, fringe patterns generated from different capture angles with the same incident angle were examined. With the help of the image correction program, it was found that skewed images obtained from different capture angles can be successfully recovered. The surface topography of a LGP can then be correctly determined.

Keywords Light guide plate • Transparent object • Surface topography • Shadow moiré method • No painting • Image correction

28.1 Introduction

In recent years, lighter and thinner structure of the liquid crystal display (LCD) has become a trend. Correspondingly, the optical components in the back light module (BLM) have become much thinner. Thus, the structural strength of the optical components may be reduced. Light guide plate (LGP) is one of the essential components of a BLM. The major functions of a LGP are for increasing luminous flux and enhancing the brightness of the LCD. However, with the thinner optical components, the lower structural strength of the LGP may lead to warpage during the manufacturing process. Optical characteristics of the LGP may also be affected. Therefore, effective quality inspection of surface topography of the LGP is crucial.

The shadow moiré method (SMM) [1] is a simple and convenient optical technique for the measurement of surface topography and out-of-plane displacement [2–5], the state of stress [6, 7], material properties [8] and delamination [9]. However, the LGP is a transparent object with high transmissivity. Based on the principle of the SMM, it's required to spray the reflective paint on the LGP's surface to make the interference fringe pattern (IFP) sufficiently visible [1]. Thus, LGP may no longer be re-used or may be damaged during the process of painting or de-painting. Moreover, the requirement of the use of the painting has prevented the application of SMM from the on-line real-time inspection of LGP and other transparent materials.

Therefore, in this paper, the well-developed digital phase-shifting shadow moiré (DPSSM) method [10, 11] was used to measure the LGP's surface topography without painting. High intensity of reflective light was achieved by employing different capture angles in the DPSSM setup to make the IFP sufficiently visible. Besides, with the help of the image correction program, the skewed IFP can be successfully recovered to the image as if the image acquisition equipment is placed normal to the test surface. The LGP's surface topography can then be correctly determined.

W.-C. Wang (✉) • W.-Y. Kang
Department of Power Mechanical Engineering, National Tsing Hua University, Hsinchu, Taiwan 30013, Republic of China
e-mail: wcwang@pme.nthu.edu.tw

H. Jin et al. (eds.), *Advancement of Optical Methods in Experimental Mechanics, Volume 3*,
Conference Proceedings of the Society for Experimental Mechanics Series,
DOI 10.1007/978-3-319-00768-7_28,

28.2 Theory

28.2.1 Shadow Moiré Method

As depicted in Fig. 28.1, a collimated light passes through the reference grating and be reflected by the test surface. Based on the geometrical relationship of the triangle BCD in Fig. 28.1, an equation for calculation of the out-of-displacement can be determined as follow

$$W(x,y) = N(x,y)\left(\frac{P}{\tan\alpha + \tan\beta}\right) \tag{28.1}$$

where W is the out-of-plane displacement of the test surface;P is the pitch of the reference grating;α is the incidence angle of the light source;β is the capture angle of an image acquisition equipment (e.g. the CCD camera used in this paper);N is the fringe order. To simplify the experimental setup and subsequent calculation, $\beta = 0°$ is generally selected, i.e. the image acquisition equipment is normal to the test surface.

By analyzing the fringe pattern generated from interference between the reference grating and its projected grating on the test surface, the topography of the object can be obtained.

28.2.2 Image Correction

In order to obtain IFPs with high contrast, changing the capture angle of the image acquisition equipment from normal to oblique position was attempted. However, the obtained IFP was found become skewed at the same time. Therefore, with the use of MATLAB [12], an image correction program was developed to recover the skewed IFP so that the surface topography of an object can be correctly determined.

To implement the image correction procedure, the IFP taken at $\beta = 0°$ was used as the reference image. Four corner points of the LGP were chosen as characteristic points so that the relationship between coordinate systems of the reference image and skewed IFP can be established. By using the coordinate transformation performed by the correction program, the skewed IFP can be successfully recovered into the IFP as obtained when the CCD camera is normal to the test surface. The IFPs before and after image correction at $\beta = 50°$ are shown in Fig. 28.2.

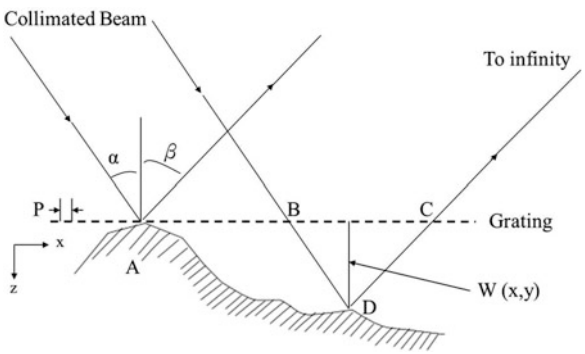

Fig. 28.1 Schematic diagram of the principle of shadow moiré method [1]

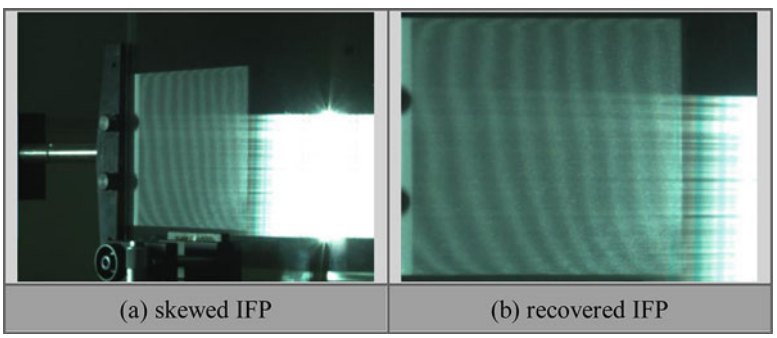

Fig. 28.2 The IFPs obtained before and after image correction $\beta = 50°$ (**a**) skewed IFP, (**b**) recovered IFP

28.3 Experimental Setup

The experimental setup of the DPSSM method is shown in Fig. 28.3. The setup is mainly composed of a light source, a reference grating, a stepping motor with its controller and a CCD camera. The light source used in this paper is a 150 W Xenon light bulb. The major purpose of the experiments performed in this paper is to investigate the feasibility of obtaining the surface topography of a transparent LGP by employing the DPSSM method without painting. Therefore, the fringe patterns generated from different capture angles with the same incident angle were examined.

The incidence angle of the light source is fixed at 40°. To change the capture angle, the CCD camera is placed on a linear guide. Seven different capture angles were selected, i.e. $\beta = 30°, 35°, 40°, 45°, 50°, 55°$ and 60°. The reference grating is made of glass with pitch 120 μm. The grating is clamped on the stepping motor so that the distance between the LGP and the grating can be adjusted to perform the phase shift.

As shown in Fig. 28.4, the LGP used in this paper was produced by the etching process. The LGP is transparent with microstructure on the top surface. The material of the LGP is polymethyl methacrylate (PMMA) with dimensions 138 mm (length) × 106 mm (width). The thickness linearly increases from 1 to 2.5 mm along the width. When the LGP is clamped on the holder, the bottom surface of the LGP faces toward the light source and the CCD camera.

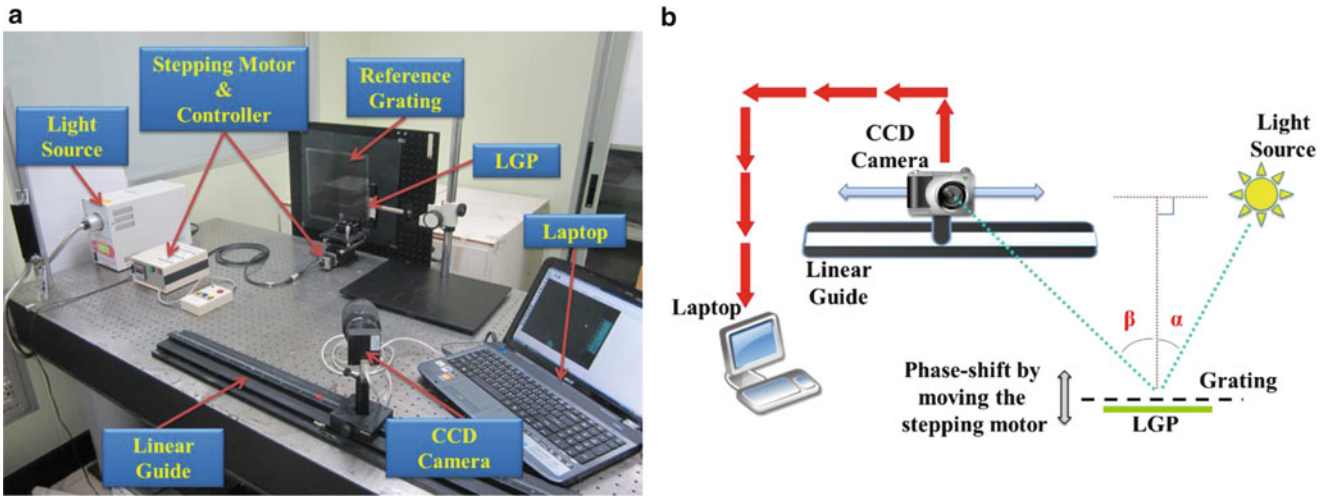

Fig. 28.3 The experimental setup of the DPSSM method (**a**) Photograph, (**b**) Schematic diagram

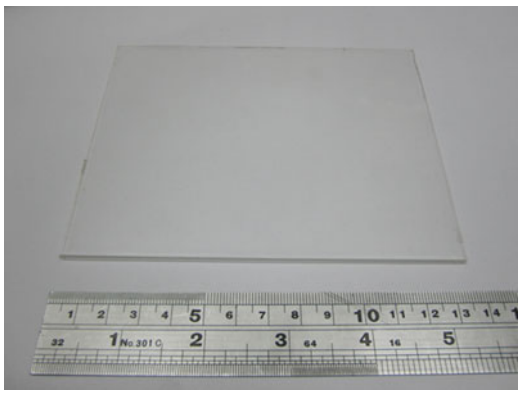

Fig. 28.4 The photograph of a LGP produced from the etching process

28.4 Results and Discussions

The obtained IFPs, wrapped and unwrapped phase (WUP) results at $\beta = 30°$, 35°, 40°, 45°, 50°, 55° and 60° are shown in Figs. 28.5, 28.6, 28.7, 28.8, 28.9, 28.10 and 28.11, respectively.

At $\beta = 30°$, a small region of overexposure appears at the left end of the IFP while low contrast IFP appears at the opposing end. Based on the law of reflection, the intensity of the reflection light is higher when the capture angle is closer to the incidence angle and hence the induced overexposure in the image. As depicted in Figs. 28.6 and 28.7, when $\beta = 35°$ and 40°, the degree of overexposure is so significant that the IFP and WUP results are scarcely appeared in the region of overexposure. At the same time, high contrast IFP still exists in the non-overexposure region. Therefore, with sufficient high intensity of reflection light and appropriate chosen capture angle, high contrast IFP can be obtained by employing the DPSSM method on a transparent object such as a LGP without painting.

At $\beta = 45°$, similar to the IFP at $\beta = 30°$, the phenomenon of the overexposure occurs in a small region on the right part of IFP. At the same time, low contrast IFP appears on the left end. From $\beta = 50° \sim 60°$, overexposure effect is totally disappeared, however, the visibility of the IFP is decreased with the increasing angle. In fact, the contrast of IFPs at $\beta = 55°$ and 60° is significantly lower than that at $\beta = 45°$ and 50°. Possible errors may be induced from the low contrast during the wrapping and unwrapping phase processes. As shown in Figs. 28.9c, 28.10c and 28.11c, the error regions of the unwrapped phase are increased with the increasing angle. Since there is less overexposure in the IFP and the contrast of the IFP is better for $\beta = 45°$ and 50°, the best choice of the capture angle for the DPSSM setup used in this paper is $\beta = 45° \sim 50°$.

At this stage, it is important to check whether the skewed image can be correctly recovered by the image correction program. With the same DPSSM setup, experiments were performed for a LGP with painting at $\beta = 0°$, 25° and 50°. Again, the IFP taken at $\beta = 0°$ was used as the reference image. The IFPs taken at $\beta = 25°$ and 50° were corrected by the image correction program. The IFPs captured at $\beta = 0°$, 25° and 50° before and after image correction are shown in Fig. 28.12. For both $\beta = 25°$ and 50°, it is very obvious that IFPs obtained before and after image correction matched well to each other.

It is also crucial to check whether the LGP's surface topography obtained from different capture angles are the same or not. The results of wrapped phase and surface topography obtained at $\beta = 0°$, 25° and 50° after image correction are shown in Fig. 28.13. The magnitude of surface topography was calculated by substituting the unwrapped phase data into Eq. 28.1 and plotted by Origin [13]. It is interesting to note that even the wrapped phase results at $\beta = 0°$, 25° and 50° are not quite the same, the obtained surface topography of the LGP of those three capture angles are almost the same.

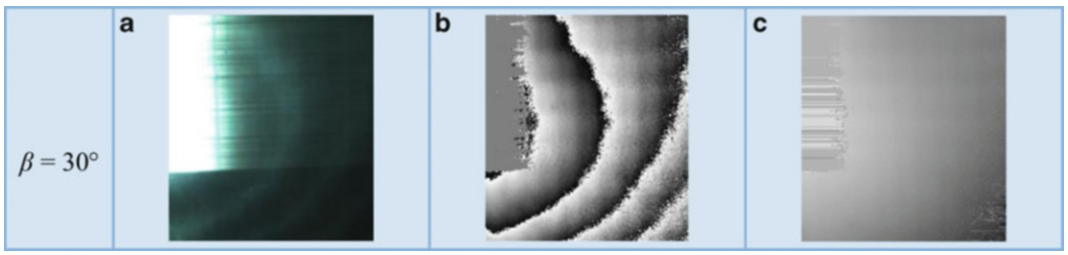

Fig. 28.5 The IFP and WUP results at $\beta = 30°$ (**a**) IFP. (**b**) Wrapped phase. (**c**) Unwrapped phase

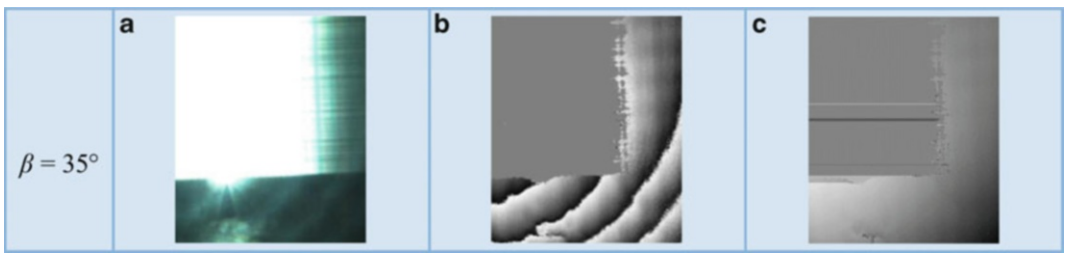

Fig. 28.6 The IFP and WUP results at $\beta = 35°$ (**a**) IFP. (**b**) Wrapped phase. (**c**) Unwrapped phase

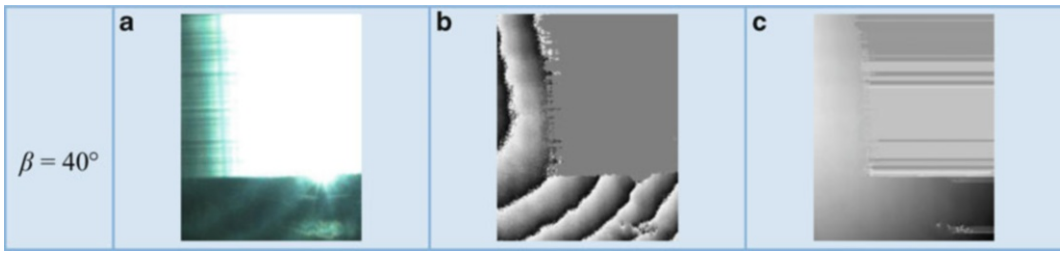

Fig. 28.7 The IFP and WUP results at $\beta = 40°$ (**a**) IFP. (**b**) Wrapped phase. (**c**) Unwrapped phase

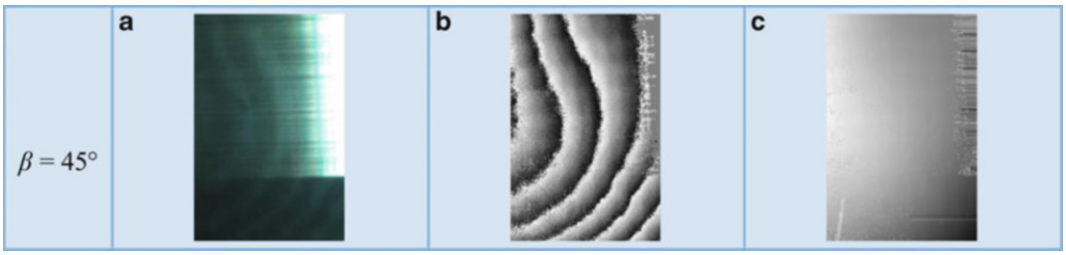

Fig. 28.8 The IFP and WUP results at $\beta = 45°$ (**a**) IFP. (**b**) Wrapped phase. (**c**) Unwrapped phase

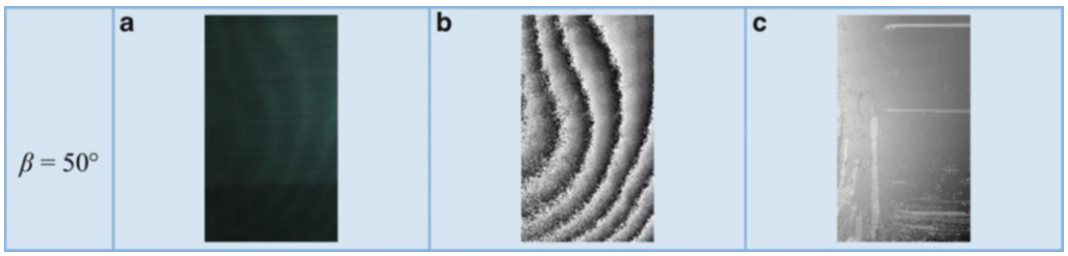

Fig. 28.9 The IFP and WUP results at $\beta = 50°$ (**a**) IFP. (**b**) Wrapped phase. (**c**) Unwrapped phase

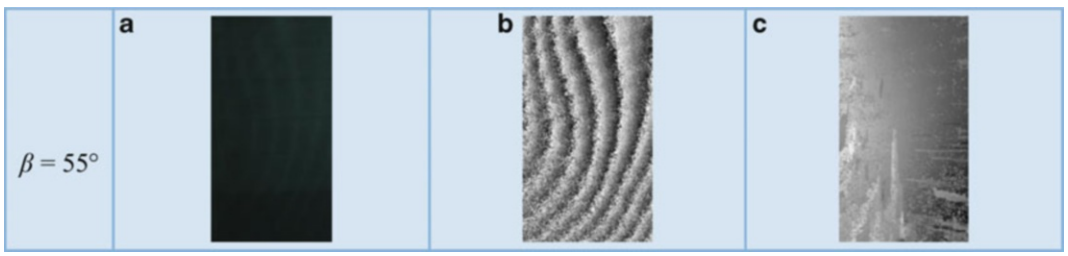

Fig. 28.10 The IFP and WUP results at $\beta = 55°$ (**a**) IFP. (**b**) Wrapped phase. (**c**) Unwrapped phase

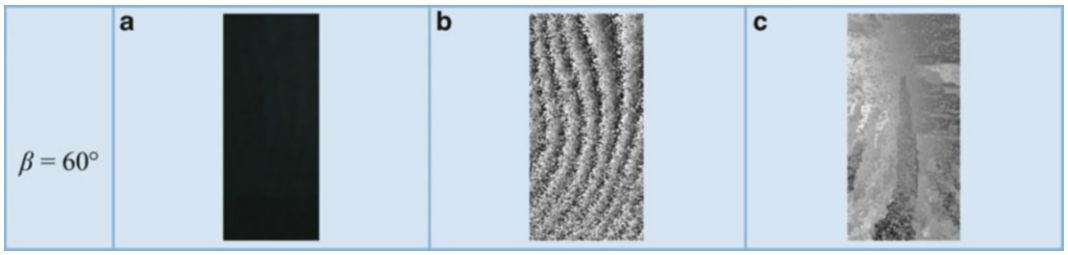

Fig. 28.11 The IFP and WUP results at $\beta = 60°$ (**a**) IFP. (**b**) Wrapped phase. (**c**) Unwrapped phase

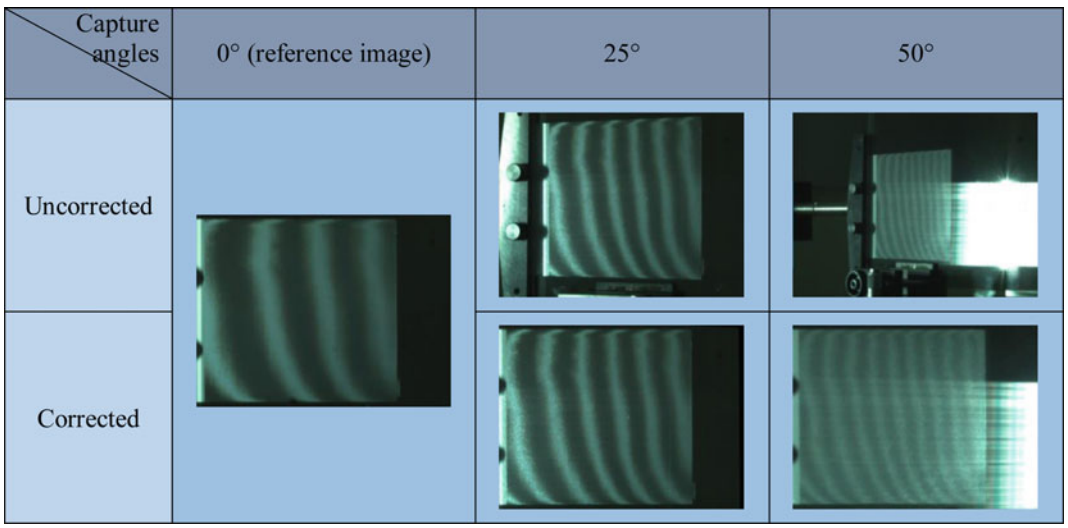

Fig. 28.12 The IFPs captured at different capture angles before and after image correction

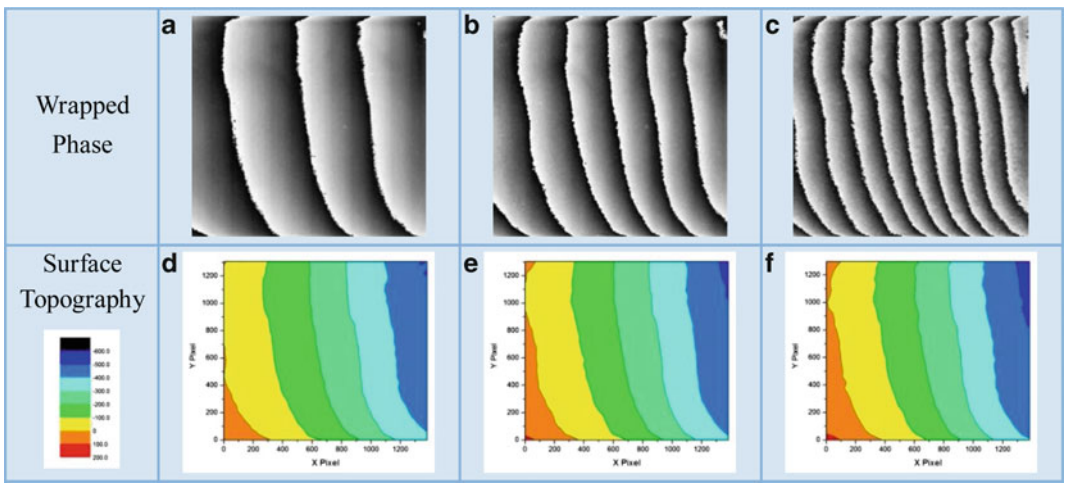

Fig. 28.13 The results of wrapped phase and surface topography obtained from different capture angles after image correction (**a**) $\beta = 0°$, (**b**) $\beta = 25°$, (**c**) $\beta = 50°$, (**d**) $\beta = 0°$, (**e**) $\beta = 25°$, (**f**) $\beta = 50°$

28.5 Conclusions

By selecting several different image capture angles, the DPSSM method was used in this paper to directly obtain high contrast IFP from the transparent LGP without painting. The LGP's surface topography was successfully obtained by the phase-shift analysis. Moreover, even for a transparent object without painting, as long as the overexposure effect can be avoided and the reflective light intensity is sufficiently high, high contrast image can be obtained when the capture angle is not too close to the incident angle of the light source. With the help of the image correction program, the skewed images obtained from oblique capture angles can be successfully recovered. Furthermore, the LGP's surface topographies obtained from different capture angles are almost the same. As a result, the surface topography of a LGP can be correctly determined. Based on the experimental findings of this paper, the DPSSM method is full of potential for the on-line real-time inspection system of the LGP.

Acknowledgments This paper was supported in part by the National Science Council of the Republic of China (grant no. NSC 98-2221-E007-012-MY3).

References

1. Sirohi RS, Chau FS (1999) Optical methods of measurement. Marcel Dekker, New York
2. Takasaki H (1970) Moiré topography. Appl Opt 9:1467–1472
3. Sullivan JL (1991) Phase-stepped fractional moiré. Exp Mech 31:373–381
4. Stiteler MR, Ume C (1997) System for real time measurement of thermally induced PWB/PWA warpage. J Electron Pack 119:1–7
5. Dang AXH, Ume IC, Bhattacharya SK (2000) A study on warpage of flexible SS substrates for large area MCM-D packaging. J Electron Pack 122:86–91
6. Chen KS, Chen TYF, Chuang CC, Lin IK (2004) Full-field wafer level thin film stress measurement by phase-stepping shadow moiré. IEEE Trans Compon Pack Technol 27:594–601
7. Lee KS, Tang CJ, Chen HC, Lee CC (2008) Measurement of stress in aluminum film coated on a flexible substrate by the shadow moiré method. Appl Opt 47:C315–C318
8. Lim JH, Ratnam MM, Khalil HPSA (2003) An experimental and finite element analysis of the static deformation of natural fiber-reinforced composite beam. Polym Test 22:169–177
9. Seif MA, Khashaba UA, Rojas-Oviedo R (2007) Measuring delamination in carbon/epoxy composites using a shadow moiré laser based imaging technique. Compos Struct 79:113–118
10. Wang WC, Hsu HH, Chang YH (2008) Experimental and numerical analysis of hygrothermal deformation of backlight modules, In: International conference on experimental mechanics 2008, Nanjing proceedings of SPIE, vol 7375, pp 73753F-1-15
11. Wang WC, Lin YS (2011) Investigation of warpage of light guide plates under different hygrothermal loads, (in Chinese). In: Proceedings of 28th National conference of mechanical engineering, chinese society of mechanical engineers, Taichung paper no C06-001, pp 1–6
12. "MATLAB", Version R (2009a) MathWorks, Inc., Natick
13. "Origin", Version 7.0 (2002) OriginLab Corporation, Northampton

Chapter 29
Micro-Polarizer Array Based Instantaneous Phase-Stepping Interferometry for Observing Dynamic Phenomena

S. Yoneyama and S. Arikawa

Abstract We propose a method for determining phase distribution of interference fringes utilizing a CCD camera equipped with a micro-polarizer array. An optical setup of polarization interferometry using a Mach-Zehnder Interferometer with two polarizers is constructed to analyze the distribution of the thickness change of the transparent sample. Light emerging from the interferometer is recorded using a CCD camera that has a micro-polarizer array on a CCD plane. This micro-retarder array has four different principal directions. The four images separated from the image recorded by the CCD camera are reconstructed using gray level interpolation. Subsequently, the distributions of the Stokes parameters that represent the state of polarization are calculated from the four images. The phase distribution of the interference fringe pattern produced by the Mach-Zehnder interferometer is then obtained from these Stokes parameters. This method is applicable to dynamic phenomena because multiple exposures are unnecessary for sufficient data acquisition for phase analysis of fringes.

Keywords Instantaneous phase-stepping method, interferometry • Micro-polarizer array • Polarization • Fringe

29.1 Introduction

The phase-stepping method is one of the most important and widely accepted techniques for the analysis of fringe pattern in the field of optical measurement. However, it is known that a temporal phase-stepping method has the disadvantage of a time lag during phase stepping and acquisition between phase steps. Therefore, it is difficult for the conventional temporal phase-stepping method to apply time-variant phenomena. An approach to real-time measurement or instantaneous recording of phase-stepped images is a spatial phase-stepping method. The spatial phase-stepping method generates simultaneous phase-stepped interferograms using polarization optics or diffraction grating [1]. Several researchers have developed an instantaneous spatial phase-stepping method that uses multiple cameras for the acquisition of phase-stepped interferograms [2–6]. The major drawback of this technique is the high complexity of the experimental setup, which requires perfect alignment and calibration of the pixels of multiple cameras. On the other hand, Novak et al. [7] proposed a method for recording multiple phase-stepped images using a camera with micro-polarizers. Similarly, one author [8, 9] proposed instantaneous phase-stepping interferometry and photoelasticity using a camera equipped with a micro-retarder array. Recently, on the other hand, a high-speed camera that is equipped with a micro-polarizer array on the sensor plane is available [10–12]. Whereas this camera has been developed for the measurement of birefringence, it is considered that the instantaneous recording of phase-stepped interference fringes is possible using this camera, similar to the Novak's method [7].

In this paper we propose an instantaneous phase-stepping method for determining phase distribution of interference fringes utilizing a camera equipped with a micro-polarizer array on the sensor plane. An optical setup of polarization interferometry using a Mach-Zehnder Interferometer with two polarizers is constructed to analyze the distribution of the thickness change of the transparent sample, i.e., the sum of principal stresses in the case of the plane stress state. Light emerging from the interferometer is recorded using a camera that has a micro-polarizer array on a sensor plane. This micro-polarizer array has four different optical axes. That is, an image obtained by the camera contains four types of information corresponding to four different optical axes of the polarizer. The four images separated from the image recorded by the

S. Yoneyama (✉) • S. Arikawa
Department of Mechanical Engineering, Aoyama Gakuin University, 5-10-1 Fuchinobe, Sagamihara, Kanagawa 252-5258, Japan
e-mail: yoneyama@me.aoyama.ac.jp

H. Jin et al. (eds.), *Advancement of Optical Methods in Experimental Mechanics, Volume 3*,
Conference Proceedings of the Society for Experimental Mechanics Series,
DOI 10.1007/978-3-319-00768-7_29,

camera are reconstructed using gray level interpolation. Subsequently, the distributions of the Stokes parameters that represent the state of polarization are obtained from the four images. The phase distribution of the interference fringe pattern produced by the Mach-Zehnder interferometer is then obtained from these Stokes parameters. It is emphasized that this method is applicable to time-variant phenomena because multiple exposures are unnecessary for sufficient data acquisition in the completion of the phase analysis.

29.2 Instantaneous Phase Stepping Interferometry

Figure 29.1 portrays the outline of the camera equipped with the micro-polarizer array on the sensor plane. As shown in this figure, many sets of four (2 × 2) micro-polarizers whose optical axes subtend four different angles, 0, π/4, π/2, 3π/4 rad, form the large array the sensor. The size of a single micro-polarizer is equivalent to a single pixel of the sensor. The micro-polarizer position is aligned with the sensor. A single sensor detects the intensity of a light that passes through a single polarizer with a specific angle of the optical axis. Then, the four light intensity distributions corresponding to the four optical axes are obtained as a single image. Spatial resolution of each light intensity distribution is reduced to one-fourth of the CCD's resolution. In addition, the spatial positions of the four light intensity distributions do not mutually correspond. Therefore, light intensities other than the angle of the polarizer at the point are determined from light intensities at the neighboring points using interpolation such as bilinear or bicubic interpolation methods. Then, the four light intensity distributions whose respective sizes are equivalent to the original image are obtained by a single exposure. The four light intensity distributions are therefore phase-stepped images, similar to those obtained in other phase-stepping methods.

The interferometer used in this study is shown in Fig. 29.2. This interferometer consists of a Mach-Zehnder interferometer, two polarizers, and a quarter-wave plate. Light emitted from a point light source is collimated using a collimator lens. Then, a beam splitter divides the light. The light beam reflected by the beam splitter passes through a polarizer whose optical axis is vertical and a transparent specimen. On the other hand, the light that passes through the beam splitter passes a polarizer whose optical axis is horizontal. In the case of an ordinary Mach-Zehnder interferometer, the two light beams interfere at the beam splitter. Then, the interference fringe pattern is observed. On the other hand, no interference fringe pattern is observed for the interferometer shown in Fig. 29.2 because polarization directions of the two light beams cross at the right angles. The Stokes vector of the light emerging from the beam splitter is expressed as

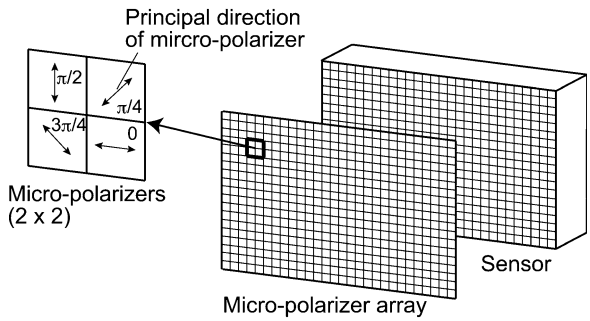

Fig. 29.1 Configuration of the micro-polarizer array on the sensor plane

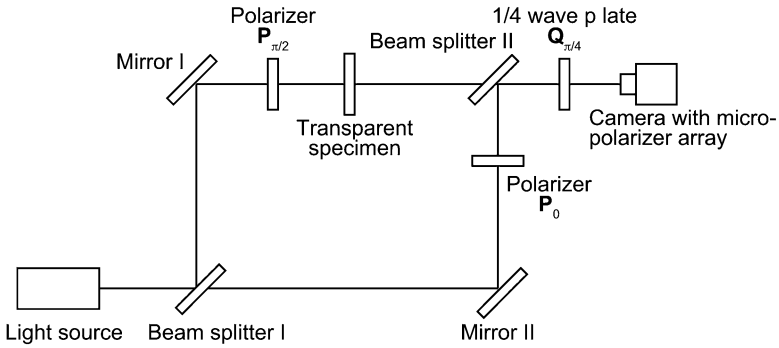

Fig. 29.2 Optical setup of Mach-Zehnder interferometry with polarizers and quarter-wave plate

$$\mathbf{s} = \begin{Bmatrix} s_0 \\ s_1 \\ s_2 \\ s_3 \end{Bmatrix} = \begin{Bmatrix} A_x^2 + A_y^2 \\ A_x^2 - A_y^2 \\ 2A_xA_y\cos\delta \\ 2A_xA_y\sin\delta \end{Bmatrix}, \tag{29.1}$$

where s_0, s_1, s_2, and s_3 are the Stokes parameters, A_x and A_y are the amplitude components, δ represents the phase difference. The light beam passes through a quarter-wave plate and the polarizer attached on the sensor plane whose optical axis is θ. The Stokes vector **s'** of the light beam at the sensor plane is expressed as

$$\mathbf{s}' = \mathbf{P}_\theta \mathbf{Q}_{\pi/4}\mathbf{s} = \begin{bmatrix} \frac{1}{2} & 0 & \cos\theta\sin\theta & -\frac{1}{2}\cos 2\theta \\ \frac{1}{2}\cos 2\theta & 0 & \frac{1}{4}\sin 4\theta & -\frac{1}{2}\cos^2 2\theta \\ \cos\theta\sin\theta & 0 & \cos^2\theta\sin^2\theta & -\frac{1}{4}\sin 4\theta \\ 0 & 0 & 0 & 0 \end{bmatrix} \begin{Bmatrix} s_0 \\ s_1 \\ s_2 \\ s_3 \end{Bmatrix}. \tag{29.2}$$

Therefore, the four light intensities, I_0, I_1, I_2, I_3, corresponding to the four different angles of the polarizers, θ = 0, π/4, π/2, 3π/4 rad are obtained as

$$\begin{Bmatrix} I_0 \\ I_1 \\ I_3 \\ I_4 \end{Bmatrix} = \begin{bmatrix} \frac{1}{2} & 0 & 0 & -\frac{1}{2} \\ \frac{1}{2} & 0 & \frac{1}{2} & 0 \\ \frac{1}{2} & 0 & 0 & \frac{1}{2} \\ \frac{1}{2} & 0 & -\frac{1}{2} & 0 \end{bmatrix} \begin{Bmatrix} s_0 \\ s_1 \\ s_2 \\ s_3 \end{Bmatrix}. \tag{29.3}$$

Then, the Stokes parameters s_2 and s_3 of the light emerging from the interferometer are obtainable as

$$\begin{aligned} s_2 &= I_1 - I_3 \\ s_3 &= I_2 - I_0. \end{aligned} \tag{29.4}$$

Therefore, the phase value of the interference fringe is obtained as

$$\tan\delta = \frac{s_3}{s_2}. \tag{29.5}$$

Using the above interferometer and the camera, the wrapped phase map is obtainable from an image obtained by a single exposure. A phase unwrapping procedure can be introduced to obtain the unwrapped phase map. It is noted that this method can be applied to other interferometers than the Mach-Zehnder interferometer with the similar principle.

29.3 Observation of Dynamic Phenomena

The phase analyses of the time-variant interference fringes are performed by the proposed method. The outline of the specimen and the loading device is schematically shown in Fig. 29.3 A transparent specimen made of polymethylmethactylate (PMMA) is used. The modulus of elasticity E and the Poisson's ratio ν of the material are measured as E = 3.0 GPa and ν = 0.3, respectively. The specimen adopted is a strip plate with 80 mm in width, 20 mm in height and 3 mm in thickness, having a notch of the 2 mm in length. The notch is introduced by a razor. The specimen is placed on a four-point bending device. Then, a weight is dropped onto the upper loading device. The specimen is subjected to the impact

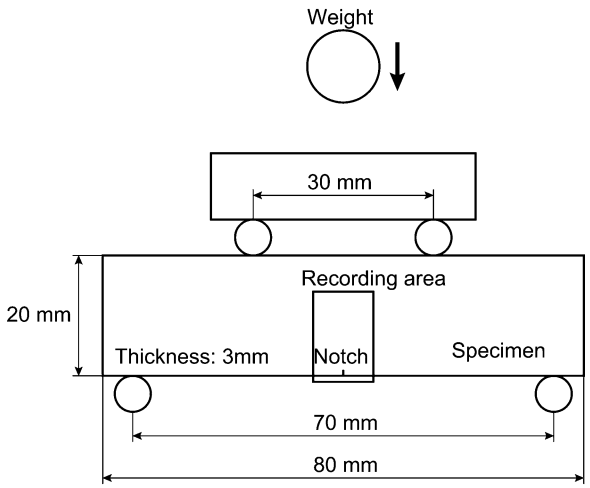

Fig. 29.3 Specimen and loading configuration for dynamic test

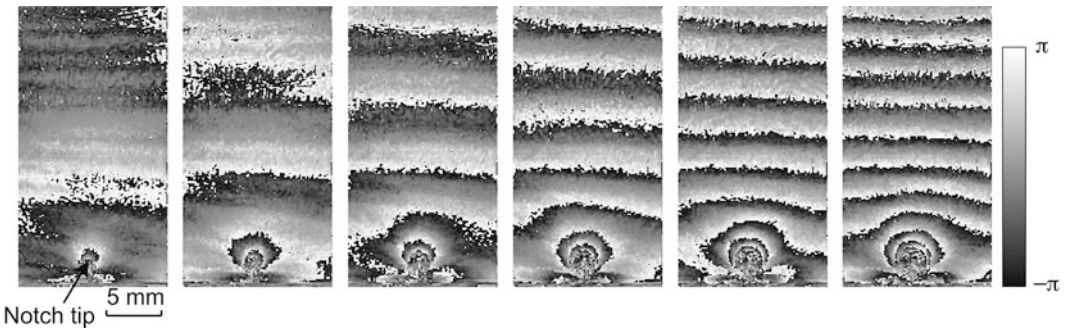

Fig. 29.4 Series of six consecutive phase maps of Mach-Zehnder fringes around a notch: camera speed↓150,000 frames per sec

load by the dropped weight. The time-variant interference fringes around the notch are then recorded by the camera with the micro-polarizer array (Photron FASTCAM SA5P) at the frame rate of 150,000 fps. The image size is set to 128 × 240 pixels. The light source is a YAG laser with the wavelength of 532 nm. A quarter-wave plate for the wavelength of 514.5 nm is used for the interferometer because a quarter-wave plate for 532 nm is not available in the present stage.

Figure 29.4 shows the consecutive phase maps of the Mach-Zehnder fringes obtained by the proposed method. There phase maps are obtained by subtracting the phase at the static state before the load from the phase after the load. That is, the phase maps in Fig. 29.4 represent the phase difference between the images before and after the load. It is observed that the number of the interference fringes increase with time and the fringes concentrate at the notch tip. It is noteworthy that, as shown in this figure, the phase values of the time-variant interference fringes are obtainable using the instantaneous phase-stepping method based on the micro-polarizer array.

29.4 Conclusions

In this paper we propose an instantaneous phase-stepping method for determining phase distribution of interference fringes utilizing a camera equipped with a micro-polarizer array on the sensor plane. Light emerging from the interferometer is recorded using a camera that has a micro-polarizer array on a sensor plane. An image obtained by the camera contains four types of information corresponding to four different optical axes of the micro-polarizer. Subsequently, the distributions of the Stokes parameters that represent the state of polarization are evaluated from the four images. The phase distribution of the interference fringe pattern produced by the Mach-Zehnder interferometer is then obtained from these Stokes parameters. It is emphasized that this method is applicable to time-variant phenomena because multiple exposures are unnecessary for sufficient data acquisition in the completion of the phase analysis.

Acknowledgements The authors express their thanks to Messrs. A. Mihara, T. Sasaki, and T. Onuma of Photron Limited for kindly providing the high-speed camera equipped with the micro-polarizer array. Our thanks are extended to Mr. Y. Furuichi for his help in the experiments.

References

1. Huntley JM (1997) Automated fringe pattern analysis in experimental mechanics: a review. J Strain Anal Eng Des 33:105–125
2. Smythe R, Moore R (1984) Instantaneous phase measuring interferometry. Opt Eng 23:361–364
3. Koliopoulos CL (1991) Simultaneous phase shift interferometer. Proc SPIE 1531:119–127
4. Van Haasteren AJP, Frankena HJ (1994) Real-time displacement measurement using a multicamera phase-stepping speckle interferometer. Appl Opt 33:4137–4142
5. Ngoi BKA, Venkatakrishnan K, Sivakumar NR, Bo T (2001) Instantaneous phase shifting arrangement for microsurface profiling of flat surfaces. Opt Commun 190:109–116
6. Sivakumar NR, Hui W, Venkatakrishnan K, Ngoi BKA (2003) Large surface profile measurement with instantaneous phase-shifting interferometry. Opt Eng 42:367–372
7. Novak M, Millerd J, Brock N, North-Morris M, Hayes J, Wyant J (2005) Analysis of a micropolarizer array-based simultaneous phase-shifting interferometer. Appl Opt 44:6861–6868
8. Yoneyama S, Kikuta H, Moriwaki K (2005) Instantaneous phase-stepping interferometry using polarization imaging with a micro-retarder array. Exp Mech 45:451–456
9. Yoneyama S, Sakaue K, Kikuta H, Takashi M (2008) Observation of stress field around an oscillating crack tip in a quenched thin glass plate. Exp Mech 48:367–374
10. Murata W, Umezaki E, Onuma T, Mihara A (2010) Phase-shifting photoelasticity using polarization high-speed camera. In: 5th international symposium on advanced science and technology in experimental mechanics, Kyoto, Nov 2010
11. Onuma T, Otani Y (2012) Real-time measurement method for birefringence distribution by dynamic stokes polarimeter. In: International symposium on optomechatronic technologies, Hong Kong, Nov 2012
12. Kakue T, Yonesaka R, Tahara T, Awatsuji Y, Nishio K, Ura S, Kubota T, Matoba O (2011) High-speed phase imaging by parallel phase-shifting digital holography. Opt Lett 36:4131–4133

Chapter 30
Automated Surface Profile Measurement of Printed Circuit Boards by Phase-Shifted Shadow Moiré

T.Y. Chen and J. Lin

Abstract Phass-shifted shadow Moire has gained more applications in electronic industry. However, printed circuit boards (PCB) may contain many cavities or specular materials on the surface that make the phase-unwrapping of Moire fringe patterns more difficult or fail. In this paper, a method is proposed to overcome this difficulty to process the phase-shifted fringe patterns effectively and automatically for surface profile measurement. Firstly the intensity values of the original four phase-shifted fringe patterns are averaged and differentiated to enhance the erroneous spots. Then the median grey-level value of the enhanced image is used as the threshold to binarize the enhanced image to find the erroneous bright and black spots. According to the largest size of erroneous spot, the size of a structuring element is determined for morphology filtering. Thereafter the phase can be calculated and unwrapped correctly. Test of the method on a PCB is demonstrated and discussed.

Keywords Surface profile • Printed circuit board • Phase-shifted shadow Moiré • Morphology • Phase unwrapping

30.1 Introduction

Current trend in the electronic industry is making the printed circuit boards (PCB) smaller, thinner and more densely populated, which may result in a serious reliability problem due to warpage. A slight twist or bend in a board during manufacturing can also make adding components devices difficult, or may cause previously mounted electronics to break off.

Surface warpage is calculated based on the surface profile. Thus it is very important to measure the surface profile accurately. Classical interferometry [1] using visible light is not applicable to the PCB because the surface is not specular. Other interferometric techniques such as speckle interferometry[2] and holographic interferometry[3] can measure profile of non-specular surfaces with sensitivity of a fraction of a micron, which is usually too high for typical surface encountered in PCB. Moire methods have emerged as real-time, non-contact, full-field techniques with high resolutions in packaging applications. Shadow Moiré measurement can be improved by adjusting the line width of gratings, and has been used for electronic packaging studies [4–6].

Phase-shifted shadow moiré method can be employed to measure the surface profile of PCB. However, the impinging light that reflected directly to the CCD or blocked by some holes cause erroneous bright or black spots on the phase-shifted images. Further unwrapping of the calculated phase map may be difficult or fail. To solve this problem, Chen [7] proposed a method by setting several thresholds from the grey-level addition and/or difference among the four phase-shifted images to identify the erroneous spots. After filtering the spots, the phase map could be unwrapped successfully. Since the thresholds were determined manually, it is not robust. In this study, a robust method by using differential filtering and mathematical morphology is proposed to automatically filtering the erroneous spots and to unwrap the phase map correctly. Test of the proposed method on a real specimen is shown.

T.Y. Chen (✉)
Department of Mechanical Engineering, National Cheng-Kung University, Tainan 70101, ROC, Taiwan

Center for Micro/Nano Science and Technology, National Cheng-Kung University, Tainan 70101, ROC, Taiwan
e-mail: ctyf@mail.ncku.edu.tw

J. Lin
Department of Mechanical Engineering, National Cheng-Kung University, Tainan 70101, ROC, Taiwan

H. Jin et al. (eds.), *Advancement of Optical Methods in Experimental Mechanics, Volume 3*,
Conference Proceedings of the Society for Experimental Mechanics Series,
DOI 10.1007/978-3-319-00768-7_30,

30.2 Phase-Shifted Shadow Moire Measurement

Moiré technique is an important optical sensing technique used for detecting movement or deformation of objects. It usually utilizes two gratings to generate fringes for the general displacement measurement. For out of plane displacement measurement, the shadow Moiré technique is usually used. Figure 30.1 illustrates a schematic of shadow moiré technique. As shown in Fig. 30.1, a reference grating is placed above the object to be measured. A diffused light source provides the necessary illumination. If the gap between the object and the grating is sufficiently small, shadow of the grating will be generated on the surface of the objects. The interference between the reference and the shadow gratings results in fringing pattern and can be observed by the CCD camera. The light transmits through the transparent part of the reference grating and forms bright zone on location A, C, E, and so on. Location B and D are dark since the incident light cannot penetrate the opaque part of the reference grating. The specimen contacts the reference grating at point A, where the fringe order is assigned as zero. Since the next bright zone will appear at C and then E, and so on, we therefore call its fringe order one, two, and so on. In general, we use N to represent the fringe order for subsequent analysis. The relationship between N and the gap between body surface and grating can be calculated by geometry shown in Fig. 30.2 as [8]

$$Ng = W \tan \alpha + W \tan \beta \tag{30.1}$$

where N, g and W is the fringe order, pitch of grating, and the distance between the object and the grating, respectively. α and β are the incident and observation angles and both of them are position dependent. From Eq. 30.1, W can be obtained as

$$W = Ng \,/\, (\tan \alpha + \tan \beta) \tag{30.2}$$

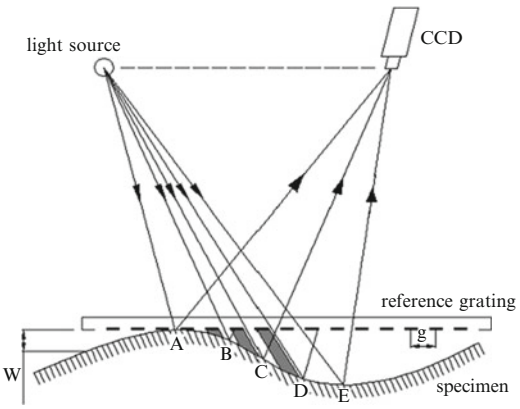

Fig. 30.1 Schematic setup and the illustration of fringe patterns

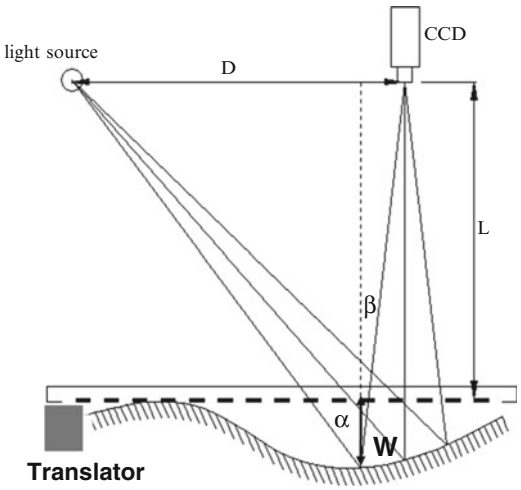

Fig. 30.2 Schematic of the phase shifting shadow Moiré system generated by shadow Moiré

By Eq. 30.2, it is possible to calculate W by the measured N. However, Eq. 30.2 is valid only when the distance between the light source and the reference grating is much greater than W. In addition, since both α and β are variables along the x-axis, as a result, W in Eq. 30.2 is not proportional to N. Nevertheless, as shown in Fig. 30.2, it can be shown that

$$\tan\ \alpha + \tan\beta = D/L = K \tag{30.3}$$

Thus Eq. 30.2 can be simplified as

$$W = Ng/K \tag{30.4}$$

where the surface altitude W can be calculated from the fringe order N easily.

By using Eq. 30.2, it assumes that the location to be measured is exactly on the center of a particular fringe. However, if the point of interest is not located at the center of a particular fringe, the accuracy in most cases is not acceptable due to the limitation of the grating resolution. As a result, a special procedure called phase shifting can be employed to provide a better resolution than that of simple interpretation. Among the phase shifting scheme, the four-step phase shifting is the most frequently used procedure. By adjusting the position of the reference grating by g/4, a net phase shift of π/2 can be obtained. The intensity of these four phase-shifted images can be expressed as

$$\begin{aligned} I_1 &= I_0 + A\cos\phi \\ I_2 &= I_0 + A\cos\left(\phi - \frac{\pi}{2}\right) \\ I_3 &= I_0 + A\cos(\phi - \pi) \\ I_4 &= I_0 + A\cos\left(\phi - \frac{3\pi}{2}\right) \end{aligned} \tag{30.5}$$

where I_0, A and ϕ is the intensity of the background, amplitude, and phase of a particular location, respectively. It is also important to point out that all four quantities depend on the position of the reference grating. By solving Eq. 30.5, the phase can be found as

$$\phi = \tan^{-1}\left(\frac{I_2 - I_4}{I_1 - I_3}\right) \tag{30.6}$$

Hence, by Eq. 30.6, it is possible to precisely determine the out of plane position of any locations between fringes. However, the phase obtained by Eq. 30.6 has wrapped phase values between $-\pi/2$ and $+\pi/2$, and discontinuities exist from period to period (i.e., pitch to pitch). As a result, the procedure proposed by Macy [9] can be applied to obtain a continuous phase distribution.

30.3 Methods for Automated Finding Bright and Dark Spots

When the surface of an PCB is measured using the phase-shifted shadow moire method, the phase map of PCB has to be calculated first from the four-phase shifted fringe patterns and unwrapped correctly. Figure 30.3 shows four phase-shifted shadow Moire fringe patterns of an PCB. It can be observed that erroneous bright and dark spots of various sizes exist on the image due to light reflected or blocked by bright surface and the holes. In order to unwrap the phase successfully, these erroneous spots must be found and eliminated from the phase map.

30.3.1 Image Enhancement

Since the erroneous spots may exist in most or all four phase-shifted fringe patterns. Theoretically, averaging the four phase fringe patterns represented by Eq. 30.5 results in a constant I_0. Therefore the erroneous spots in the fringe pattern can be

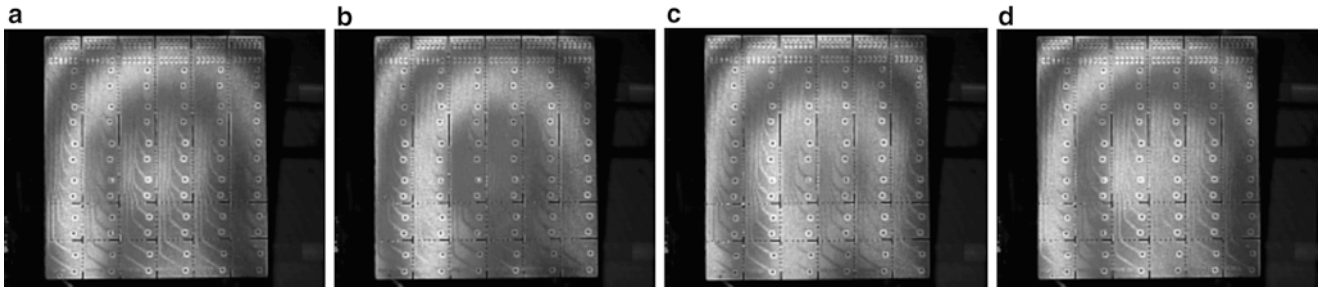

Fig. 30.3 Phase-shifted fringe patterns of an ECB with phase (**a**) 0, (**b**) π/2, (**c**) π, and (**d**) 3π/2

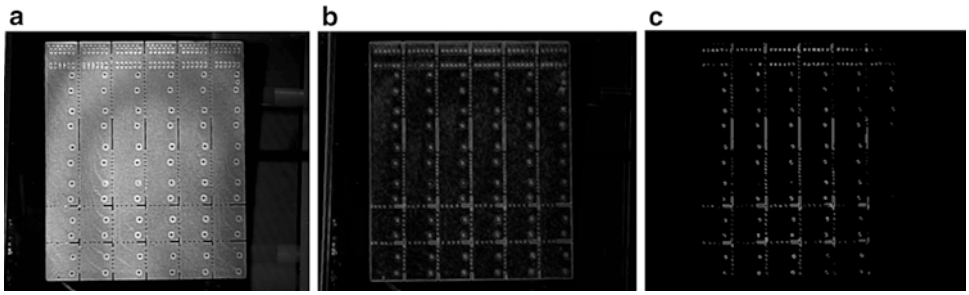

Fig. 30.4 (**a**) Averaged image of the four fringe patterns shown in Fig. 30.1, (**b**) after being differential filtered, and (**c**) after binarized

enhanced. For better recognition of the erroneous spots, a differential filter can be applied to highlight those spots. Considering a 2x2 structure element, the differential filter adopted for point P(i, j) can be expressed as follows:

$$p_{(i,j)} = \max\left[\left|p_{(i-1,j)} - p_{(i,j)}\right|, \left|p_{(i-1,j-1)} - p_{(i,j)}\right|, \left|p_{(i,j-1)} - p_{(i,j)}\right|\right] \tag{30.7}$$

The filtering process produces continuous contours by highlighting each pixel where an intensity variation occurs between itself and its three upper-left neighbors. Figure 30.4a shows the averaged image from the four fringe patterns in Fig. 30.3. The enhancement of the erroneous spots can be easily observed. After being filtered, the image is shown in Fig. 30.4b. It can be seen that the erroneous spots are highlighted, and the median gray-level value of the image is chosen automatically as the threshold to binarize the filtered image as shown in Fig. 30.4c.

30.3.2 Morphology Filtering

Morphology operations change the structure of objects of an image. Some common approaches are dilatation, erosion, opening, closing . . . etc. [10]. Its main principle is using a structuring element to remove or increase the area of the object, in order to achieve the results we want. Different structuring elements for processing, the resulting shape is not the same. Most common structuring elements are eight neighboring elements or four neighboring elements. Bigger structuring elements such as 5×5 and 7×7 are also possible.

Erosion is a function that basically removes pixels from the border of objects. B set is eroded by S denoted $B \Theta S$ and defined as the following expression:

$$B \Theta S = \left\{z | ((S)_Z \in B\right\} \tag{30.8}$$

The expression Eq. 30.2 means that after B set is eroded z size of pixel by S, then all subsets are contained in B. The z size is related by structuring element. A dilation adds pixels to the border of objects, denoted $B \oplus S$ and defined as shown in the following expression.

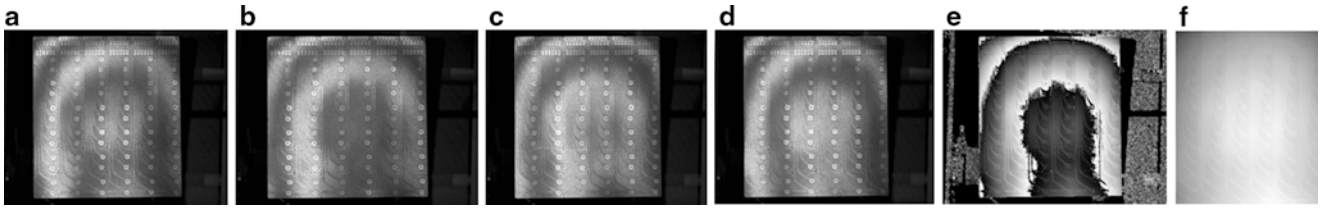

Fig. 30.5 Fringe patterns in Fig.30.1 after being (**a**–**d**) morphology processed, (**e**) calculated phase map, and (**f**) unwrapped phase of (**e**)

$$B \oplus S = \left\{ z | [(S)_Z \cup B] \in B \right\} \tag{30.9}$$

Opening and closing are functions that combine erosion and dilation functions. The opening function is defined as an erosion followed by a dilation using the same structuring element. B set is opened by S that denoted $B \circ S$ and the definition is shown in the following expression

$$B \circ S = (B \ominus S) \oplus B \tag{30.10}$$

Usually objects of the original image are not significantly changed by opening (O); however, small objects are removed. The closing(C) function is defined as a dilation followed by an erosion using the same structuring element as

$$B \cdot S = (B \oplus S) \ominus B \tag{30.11}$$

Again, objects of the original image are not significantly changed, and small holes in objects can be closed. Proper opening can remove bright pixels isolated in dark regions and smooth the boundaries of bright regions. The formula is shown as

$$\text{proper} - \text{opening}(B) = \min(B, \text{OCO}(B)) \tag{30.12}$$

Proper-opening extracts the minimum value of each pixel between the source image B and its transformed image obtained after an opening, followed by a closing and followed by another opening. Conversely, Proper closing can removes dark pixels isolated in bright regions and smooth the boundaries of dark regions. The formula is shown in the following expression

$$\text{proper-closing}(B) = \max(B, \ \text{OCO}(B)) \tag{30.13}$$

The proper-closing extracts the maximum value of each pixel between the source image B and its transformed image obtained after an opening, followed by a closing and followed by another closing.

After the pixel area of the largest erroneous spot is calculated, and the size of a square structure element having pixel area larger than the largest erroneous spot can be determined for morphology processing. In the present case, 45 pixels were found in the largest erroneous spot, and the structure element used is 7×7. Figure 30.5a–d shows the fringe patterns after the morphology processing. The calculated phase map is given in Fig. 30.5e, and a successfully unwrapped phase by Macy is shown in Fig. 30.5f.

30.4 Summary

In this study, a method is proposed to process the phase-shifted fringe patterns effectively and automatically for surface profile measurement. Averaging the intensity values of the original four phase-shifted fringe patterns and differentiated enhance the erroneous spots. The used of median grey-level value of the enhanced image the threshold to binarize the enhanced image can effectively find the erroneous bright and black spots. According to the largest size of erroneous spot, the size of structuring element determined for replacing those erroneous spots in the original images by morphology processing is shown. The phase calculated can be unwrapped correctly. Test of the method on a PCB is demonstrated.

Acknowledgments This work is supported by National Science Council, Republic of China under the contract no. NSC-101-2221-E-006-101.

References

1. Malacara D (1992) Twyman-green interferometer. In: Malacara D (ed) Optical shop testing. Wiley, New York, ch. 2
2. Moore AJ, Tyrer JR (1990) An electronic speckle pattern interferometry for complete in-plane displacement measurement. Meas Sci Technol 1:1024–1030
3. Butters JN, Leendertz JA (1971) Holographic and video techniques applied to engineering measurement. J Meas Control 4:349–354
4. Zheng T, Danyluk S (2000) Nondestructive measurement of in-plane residual stress in silicon strips. Proc Mater Res Soc Symp 591:283–287
5. Vrinceanu ID, Danyluk S (2002) Measurement of residual stress in single crystal silicon wafers. In: Proceeding 8th international symposium advanced package materials, Stone Mountain, GA, USA, pp 297–301
6. Wang Y, Hassell P (1998) On-line measurement of thermally induced warpage of BGA's with high sensitivity shadow Moiré. Proc Int J Microcircuit Electron Packag 23:191–196
7. Chen T Y, Chen JS (2011) Warpage measurement of printed circuit board by using phase-shifted shadow moiré 2011 International conference on Advanced Technology. In: Experimental mechanics, Kobe, Japan
8. Post D, Han B, Ifju P (1994) High sensitivity Moiré. Springer, New York, pp 85–133
9. Macy WW (1983) Two-dimensional fringe-pattern analysis. Appl Opt 22(23):3898–3901
10. Kinger T (2003) Image processing with LabVIEW and IMAQ Vision. Prentice Hall, Upper Saddle River

Chapter 31
Phase Retrieval and Phase Derivative Determination in Digital Holography

C. Quan, D. Balakrishnan, W. Chen, and C.J. Tay

Abstract With the advent of CCD camera and the rapid development of computer technology, digital holographic technique has recently attracted much attention from various research fields. This paper presents spatial phase retrieval techniques in digital holography. In the spatial domain, a novel method using the concept of complex phasor is proposed to determine the phase difference map in digital holography. A simple method based on finite difference is also proposed to compute high quality phase derivatives. Based on a deformation phase map obtained by the complex phasor method, slope, curvature and twist maps can be determined. Unwrapped derivative maps can be determined directly from a wrapped phase map without any phase unwrapping process. Simulation and experimental results demonstrate that the proposed method has high measurement accuracy and can effectively determine high resolution phase derivative with less computational effort. It is shown that the proposed techniques can effectively and accurately overcome theoretical and application problems in digital holography.

Keywords Digital holographic interferometry • Phase retrieval • Phase derivative determination • Numerical reconstruction • Numerical differentiation

31.1 Introduction

In recent years, digital holographic technique [1, 2] has been successfully applied in various areas. Digital holography records whole field information of an object using an electronic device, and the reconstruction of an object wave is carried out numerically. Several algorithms [3–5] such as convolution method and pure Fourier transform have been proposed for reconstructing an object wave. Recording and reconstruction are integrated into one system, and processing of holograms can be realized digitally without any intermediate photographic recording. In digital holographic interferometry, phase difference can be determined by digital phase subtraction [2] between the initial and second states, and fringe pattern evaluation is not required. In digital holography, spatial frequency is limited by the electronic devices [1, 2]. However, with the development of electronic devices, this limitation would be negligible.

In digital holography interferometry (DHI), the determination of derivatives of displacement map, slope, curvature and twist are important since they are proportional to the strain, flexural moment and torsional moment. In the last decade, different methods have been proposed for determination of these derivative maps in DHI. Complex phasor method of determining the phase derivatives was suggested. In this method, the product of complex conjugate of phase map and virtually sheared phase map provide the phase derivatives. Since the output in that method would be noisy, sin-cos filtering and short time Fourier transform (STFT) filtering, also known as window Fourier transform (WFT), were used for filtering [6, 7]. This method required more computation and the derivatives calculated were wrapped maps so a separate phase unwrapping process is required. A different approach of modeling the DHI reconstructed interference field as a piecewise polynomial phase was developed. The derivative maps were determined by computing polynomial coefficients of different segments of the interference field using high order instantaneous moments of the signal [8, 9]. This method was more suitable for determining the first order derivative than determining the higher order derivatives hence the complex lag moment method for the determination of high quality higher order derivatives was proposed [10, 11]. Cross derivative map such as torsional

C. Quan (✉) • D. Balakrishnan • W. Chen • C.J. Tay
Department of Mechanical Engineering, National University of Singapore, 9 Engineering Drive 1, 117576 Singapore, Singapore
e-mail: mpeqcg@nus.edu.sg

H. Jin et al. (eds.), *Advancement of Optical Methods in Experimental Mechanics, Volume 3*,
Conference Proceedings of the Society for Experimental Mechanics Series,
DOI 10.1007/978-3-319-00768-7_31,

derivatives cannot be obtained using this method because this method is only useful for the determination of any nth order derivative in a given direction. This method required N times of Fourier transform for determining each derivative map, where N is the row or column size of the reconstructed hologram. In this paper, the spatial phase in DHI is retrieved by using complex phasor and a simple method is proposed for the determination of derivatives using numerical differentiation. The proposed method does not require phase unwrapping. The unwrapped slope, twist and curvature maps can be determined directly from wrapped displacement map. A lesser computational effort is required for this method compared to the complex lag moment method. Simulation and experiment were conducted for evaluating and comparing the proposed method with the existing techniques.

31.2 Principle of Method

With the reconstructed complex amplitude, both intensity and phase distributions of the test specimen can be directly determined. If pure Fourier transform reconstruction method is applied, the reconstruction can be described by

$$\Gamma(m,n) = \mathrm{C} \quad \exp\left[j\pi\lambda d\left(\frac{m^2}{M^2\Delta x^2}+\frac{n^2}{N^2\Delta y^2}\right)\right] \times \sum_{k=0}^{M-1}\sum_{l=0}^{N-1} H(k\Delta x, l\Delta y)\exp\left[j\left(\frac{2\pi mk}{M}+\frac{2\pi nl}{N}\right)\right] \tag{31.1}$$

where $\Gamma(m,n)$ is a matrix of M X N points, C denotes a complex constant, d denotes the reconstruction distance, λ is the wavelength, and $\triangle x$ and $\triangle y$ denote pixel sizes at the hologram (or CCD) plane. For simplicity, the pixel in the reconstruction plane is denoted as (m,n). Hence, phase map $\phi(m,n)$ and intensity distribution $I(m,n)$ can be directly extracted from the reconstructed complex amplitude $\Gamma(m,n)$.

$$\varphi(m,n) = \arctan\frac{\mathrm{Im}[\Gamma(m,n)]}{\mathrm{Re}[\Gamma(m,n)]} \tag{31.2}$$

$$I(m,n) = |\Gamma(m,n)|^2 \tag{31.3}$$

where Im and Re denote the imaginary and real parts of the reconstructed complex amplitude, respectively. In the conventional calculation of a phase difference map, digital phase subtraction method is commonly used. Since the extracted wrapped phase map is highly contaminated by speckle noise, the subsequent phase unwrapping operation may not succeed. One strategy to overcome this problem is that a filter algorithm is employed to process the original wrapped phase map before phase unwrapping. However, in many practical applications, direct filtering of the wrapped phase map will not succeed due to reasons, such as dense fringes and high-level noise. It is well known that phase itself is not a signal but rather a property of the signal [12]. Hence, it is necessary to develop a new method which can effectively avoid the direct filtering of the wrapped phase map. In this paper, a new method based on the concept of complex phasor is proposed. Since the result by using a reconstruction algorithm can be considered as a complex value, the reconstructed result calculated by Eq. (31.1) can be described as a complex exponential signal. A complex phasor $A(m,n)$ is calculated by multiplying $\Gamma(m,n,2)$ at the second (or deformed) state by the conjugate of $\Gamma(m,n,1)$ at the initial state. Without a loss of generality, only a given pixel (m, n) is considered.

$$\begin{aligned} A(m,n) &= \Gamma(m,n,2)\Gamma^*(m,n,1) \\ &= a(m,n,2)\ a(m,n,1)\exp\{j[\varphi(m,n,2)-\varphi(m,n,1)]\} \\ &= a'(m,n)\exp\{j\ [\Delta\varphi(m,n)]\} \end{aligned} \tag{31.4}$$

where * denotes the complex conjugate, the amplitude $a'(m,n) = a(m,n,2)a(m,n,1)$, and the phase difference map $\triangle\phi(m,n) = \phi(m,n,2)\text{-}\phi(m,n,1)$. As the complex phasor method is used, a filtering algorithm can be used to filter the imaginary and real parts of the complex phasor [12, 13]. In the presence of noise, the filtered result highly relies on the point whose amplitude is higher. It means that the phase value is much more reliable if the amplitude is high. Another distinctive advantage of the proposed method is that phase manipulation is effectively avoided, so better results can be expected. If an average filter is employed, the wrapped phase map in Eq. (31.4) can be expressed by

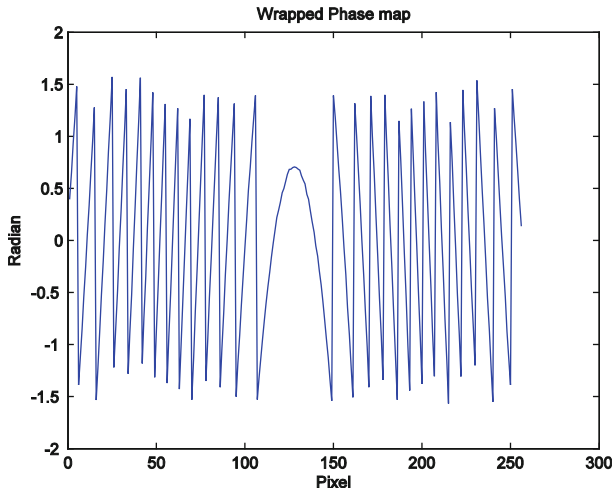

Fig. 31.1 Wrapped phase signal

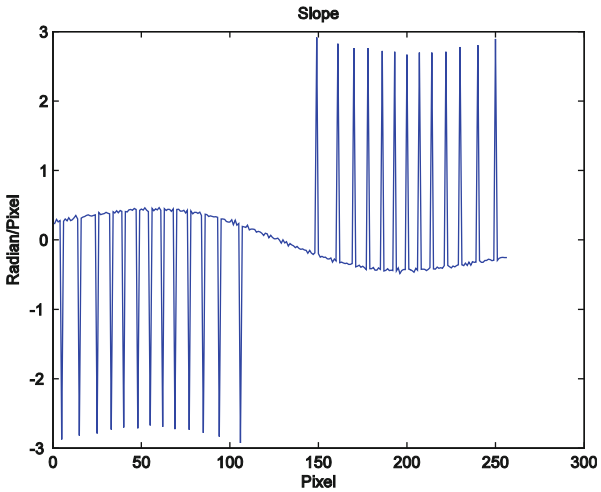

Fig. 31.2 Derivative of the wrapped phase signal

$$\Delta\varphi(m,n) = \arctan\frac{\sum \mathrm{Im}[\Gamma(m,n,2)\Gamma^*(m,n,1)]/9}{\sum \mathrm{Re}[\Gamma(m,n,2)\Gamma^*(m,n,1)]/9} \tag{31.5}$$

The derivatives of the phase difference can be determined by numerical differentiation. The numerical differentiation is the method for estimating the derivative of mathematical function only with the help of values of the function rather than knowing the complete definition of the function. The simplest method in numerical differentiation is finite difference formula.

$$f'(x) = \lim_{h\to 0}\frac{f(x+h)-f(x)}{h} \tag{31.6}$$

where h is a nonzero value. Choosing a big value for h will result in more estimation error so the value of h should be small enough to overcome the estimation error. At the same time, it should be large enough to prevent rounding error due to floating point calculation. Since the finite difference formula is ill-conditioned, it will always provide some amount of error, which varies based on the chosen value of h. In this paper, the finite difference method is applied in the wrapped phase map for finding the derivatives. Since the phase map is calculated using DHI, the smallest possible h value is a pixel distance in the CCD sensor. It is also important to note that the value of h can be increased with the resolution of single pixel distance. Since the value for h can be chosen with the constraint of CCD pixel size, it is inevitable to have errors in the derivative estimation. The error due to this causes some noises in the derivative maps along with the speckle noise which is present in the displacement map. Either a mean or a Fourier transform filter should be used to remove the noises (Fig. 31.1).

The displacement map calculated by the complex phasor method from Eq. (31.6) is a wrapped phase map. If a finite difference formula is applied over a wrapped phase map, the derivative estimated will have spikes due to phase jumps. Figure 31.2 shows the spikes due to phase jump in the wrapped phase signals shown in Fig. 31.1. Once the spikes in the

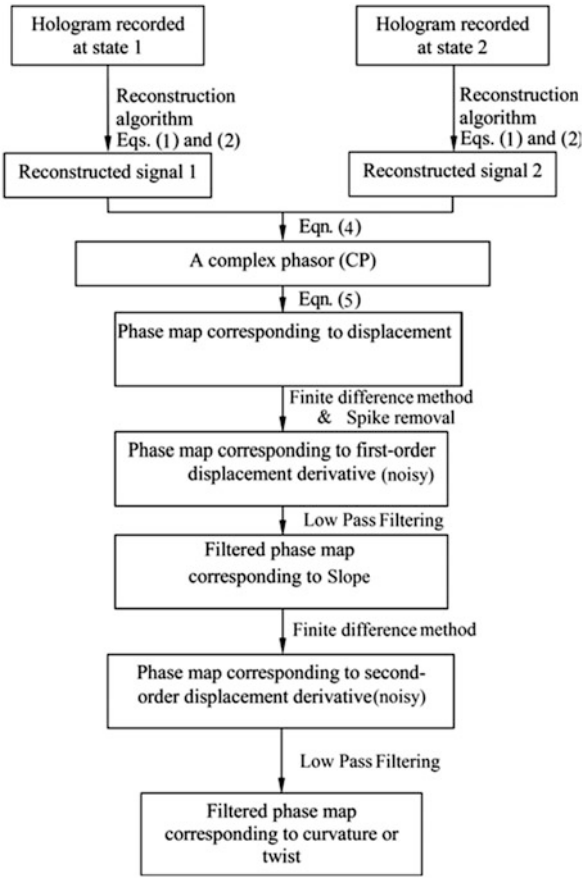

Fig. 31.3 Flow Chart of phase retrieval and measurement of slope, curvature and twist using the proposed method

derivative map are removed, the resultant map will be similar to that of an unwrapped map. In this way, unwrapped derivative map could be obtained from the wrapped phase map without the phase unwrapping process (Fig. 31.3).

Steps for calculating phase difference and its derivatives slope, curvature and twist:

1. A phase map is computed using a complex phasor method after numerical reconstruction.
2. A finite difference method is applied over the phase map with a h value equal to one pixel to find the first order derivative i.e. the pixel value is subtracted from the next adjacent pixel in the direction of the derivative.
3. Spikes in the derivative map are removed, i.e. the value at any instance deviates more than $\pi/2$ from its adjacent position are corrected by applying mean filter with the 1×3 window 0.5|0|0.5 in that instance.
4. Either a mean or a frequency filter (low pass) is applied throughout the map to remove noise due to estimation error and speckle.
5. A finite difference and filtering are applied over the derivatives obtained to determine the second order derivatives.
6. A finite difference method and filtering are applied over the first derivative in the y direction (perpendicular) to determine the twist.

31.3 Experimental Work

An experiment is conducted to evaluate the validity of proposed method. Figure 31.4 shows a schematic experimental arrangement for recording a digital hologram in spatial-domain analysis. A fiber optic coupler separates a He-Ne laser beam (wavelength of 632.8 nm and the power of 30 mw) into two beams of intensity ratio 90:10, i.e., object and reference waves. A polarizer is placed in the reference wave path to regulate the intensity. A beam splitter cube is placed in front of a CCD camera to recombine the object and reference waves, and a digital hologram is recorded by the CCD camera of resolution

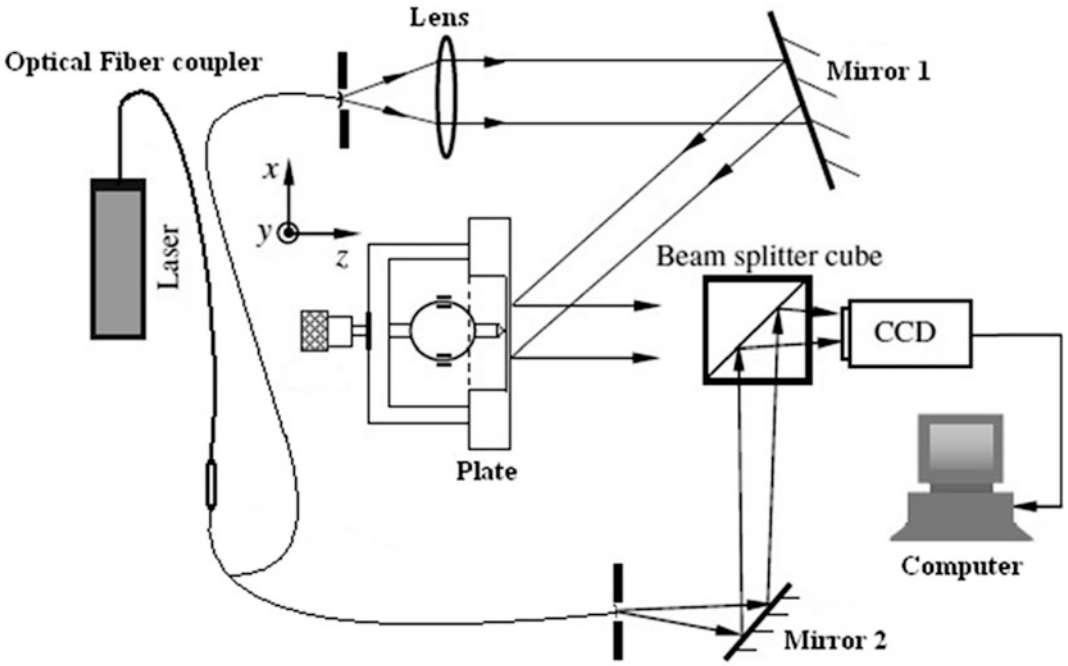

Fig. 31.4 A schematic experimental setup for recording digital holograms

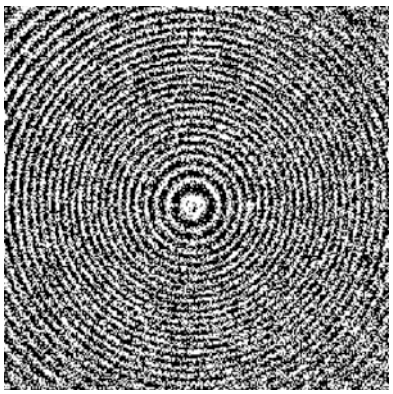

Fig. 31.5 An unfiltered wrapped phase map

1024 × 1024 with pixel size of 4.65 μm. A circular aluminum plate with center point load is chosen as a specimen for the experiment. The plate is 1.5 mm thick loaded at center and 50 mm in diameter. The distance between the specimen and the CCD is 93 cm.

Figure 31.5 shows an unfiltered wrapped phase map between the initial and deformed states. As can be seen, the wrapped phase map is quite noisy. Figure 31.6 shows a wrapped phase map obtained by the proposed complex phasor method with a median filter. Figure 31.7 shows a wrapped phase map obtained by the proposed complex phasor method with an average filter. It can be seen that the phase map extracted by complex phasor method is much smoother, and complex phasor method with an average filter performs better than complex phasor method with a median filter. Figures 31.8, 31.9 and 31.10 shows the slope, curvature and twist maps determined from the experimental data using the proposed finite difference method.

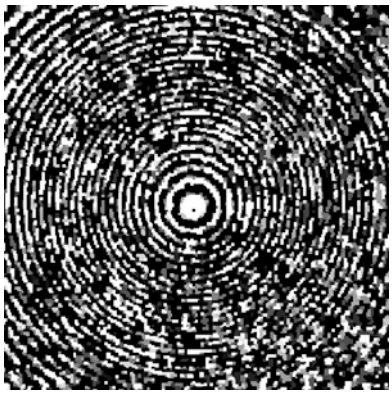

Fig. 31.6 Filtered wrapped phase (Median)

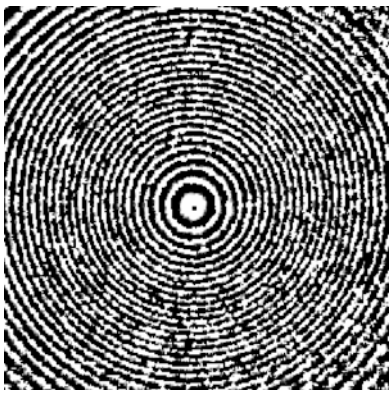

Fig. 31.7 Filtered wrapped phase (Mean)

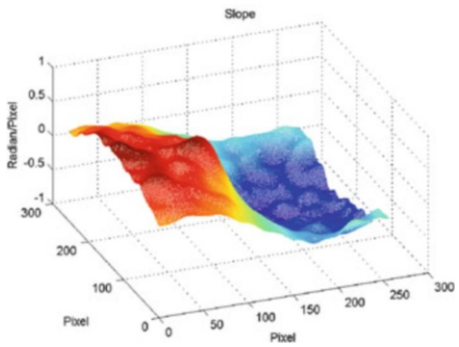

Fig. 31.8 First order phase derivative

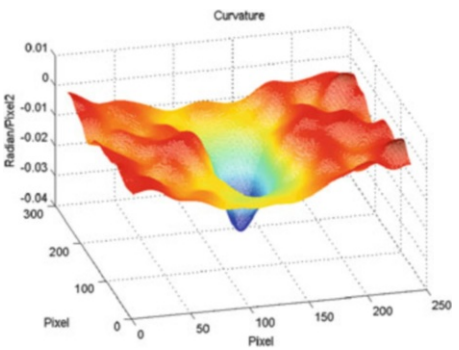

Fig. 31.9 Second order phase derivative

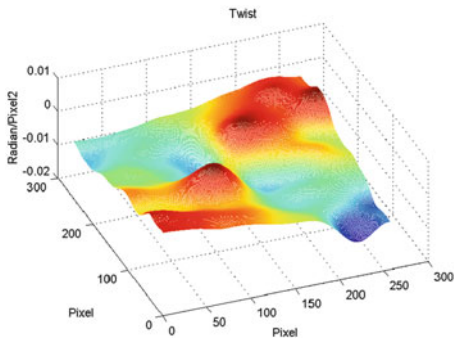

Fig. 31.10 Cross second order derivative

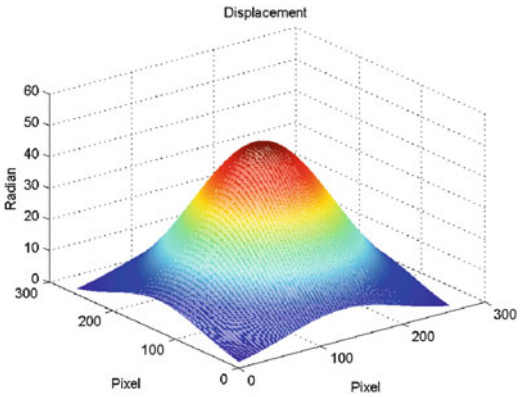

Fig. 31.11 Simulated displacement map

31.4 Results and Discussion

To evaluate the accuracy of the proposed method and to compare this method with existing methods, 256 × 256 displacement map is simulated in MatLab and Gaussian noise of 25 SNR is applied using 'awgn ()' function in the MatLab. The proposed method is applied in the simulated map and found that 20 iterations of mean filter, with the window size of3 × 3, are required to obtained high quality derivative map. The window size can be increased to reduce the number of iterations. The boundaries of the derivative map are smeared due to high number of iterations. The extrapolation method for calculating the boundary values is applied to resolve this problem. It is found that the computation for the mean filter increases with the increase in both the window size and number of iterations. The output map smoothness increases with the increase in the number of iterations till 35 iterations, after which, the value of the derivatives starts deviating from the desired value. The root mean square error (RMSE) of the output starts increasing drastically after 35 iterations Figs. 31.11, 31.12, 31.13, 31.14, 31.15, 31.16, 31.17 and 31.18.

The Fourier transform filtering (FTF) and window Fourier transform filtering (WFTF) were applied instead of the mean filtering. The computation used for FTF is equal to that of 20 iterations of mean filter with 3 × 3 window size and the noise reduction is proportional to the threshold chosen for the FTF filtering. WFTF took more computation time than other filters and noise reduction is similar to that of FTF. Since the local values in the derivative maps are not significant exploiting local values in WFTF is not necessary. The proposed method with three different filters is compared against the complex lag moment method as shown in Table 31.1.

The first derivative slope determined by the proposed method with a mean filter of 6 iterations shows a RMSE value 0.0025 (radian/pixel). The twist and curvature determined with a mean filter of 35 iterations shows RMSE values $1.14 \times 10^{-4}$and 3.8×10^{-3} (radian/pixel^2). The pixels at the border region were not considered in the analysis. As mentioned in Ref. [5], the RMSE values of complex lag moment method shows that the proposed method provides a more accurate first order derivative map than the complex lag moment method. Even though the complex lag moment method providing better second derivative map, it requires more than 100 s of CPU time to determine the first and second order derivative maps. The proposed method provides all the three derivative maps in less than 2 s of CPU time. It gives accuracy on par with that of the complex lag moment method but the computation efficiency is much better than the complex lag moment method.

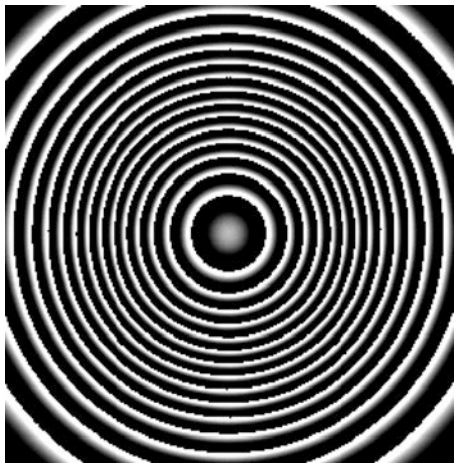

Fig. 31.12 Fringe pattern simulated

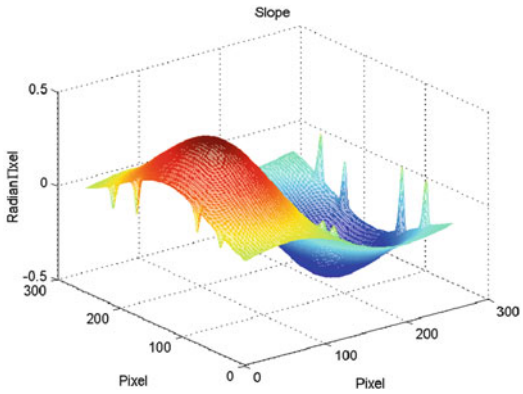

Fig. 31.13 First order derivative determined

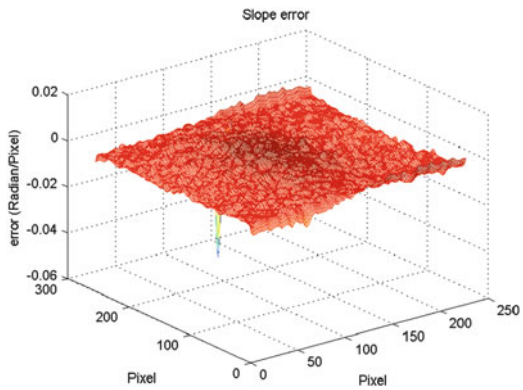

Fig. 31.14 Estimation error of slope

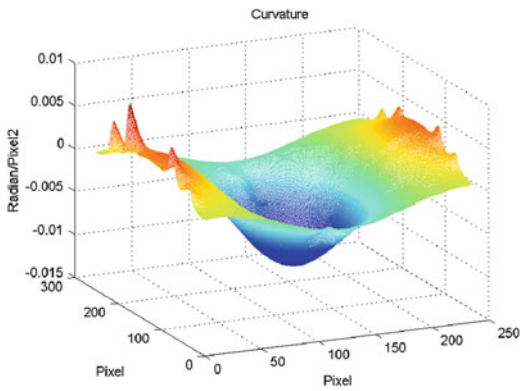

Fig. 31.15 Second order derivative determined

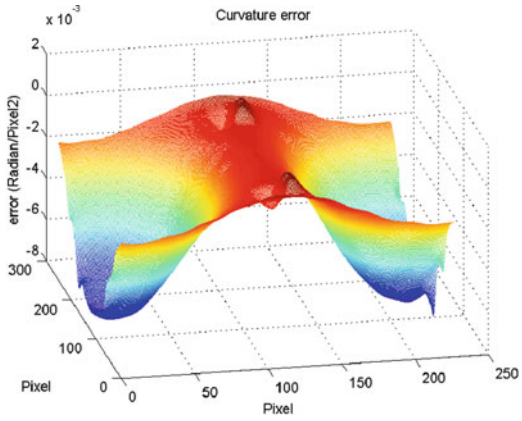

Fig. 31.16 Estimation error of curvature

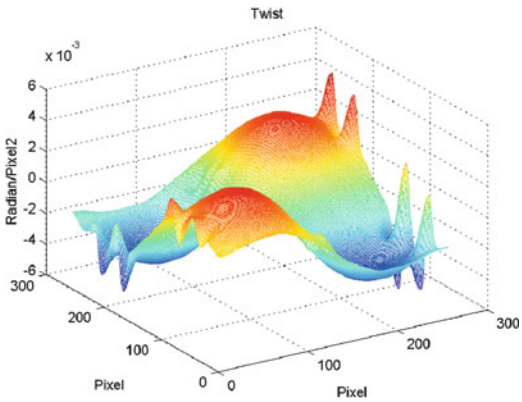

Fig. 31.17 Cross second order derivative determined

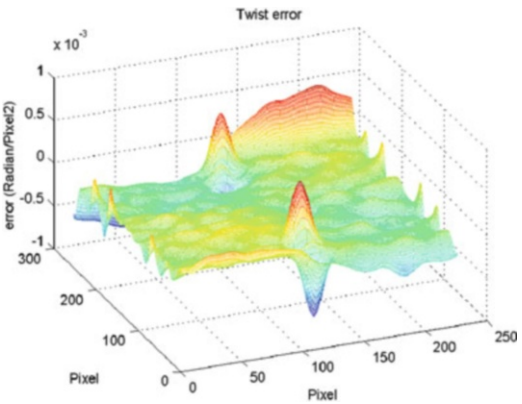

Fig. 31.18 Estimation error of twist

Table 31.1 Comparison of proposed method with different filters against complex lag moment method

	Computation time (second)	RMSE slope (radian/pixel)	RMSE twist (radian/pixel^2)	RMSE curvature (radian/pixel^2)
Mean filter	1	0.0025	1.14×10^{-4}	3.8×10^{-3}
FTF	1	0.0450	1.2×10^{-3}	5.3×10^{-3}
WFTF	10	0.0165	3.46×10^{-4}	4.4×10^{-3}
Complex lag moment method	>100	0.008	NA	2.19×10^{-4}

31.5 Conclusion

In this paper, a new algorithm using complex phasor is proposed to extract a wrapped phase map. Since the wrapped map obtained is noisy, a filtering algorithm is embedded to reduce the noise. In addition, a simple method for determining phase derivative is proposed. The proposed method is easy to implement and it is possible to determine cross derivative map (twist). It has taken less computational effort than the existing methods. As mentioned our method does not require any phase unwrapping for the determination of a derivative map. Even though the results produced are of high quality, there is still scope for improvement by calculating the value of h precisely for achieving least estimation error. This will further reduce the computation effort for filtering and also provide better quality.

References

1. Kreis T (2005) Handbook of holographic interferometry: optical and digital methods. Wiley-VCH, Weinheim
2. Schnars U, Juptner WPO (1994) Direct recording of holograms by a CCD target and numerical reconstruction. Appl Opt 33(2):4373
3. Wagner C, Seebacher S, Osten W, Juptner W (1999) Digital recording and numerical reconstruction of lensless Fourier holograms in optical metrology. Appl Opt 38(22):4812–4820
4. Cuche E, Marquet P, Depeursinge C (1999) Simultaneous amplitude-contrast and quantitative phase-contrast microscopy by numerical reconstruction of Fresnel off-axis holograms. Appl Opt 38(34):6994–7001
5. Grilli S, Ferraro P, Nicola SD, Finizio A, Pierattini G, Meucci R (2001) Whole optical wavefields reconstruction by digital holography. Opt Express 9(6):294–302
6. Chen W, Quan C, Tay CJ (2008) Measurement of curvature and twist of a deformed object using digital holography. Appl Opt 47 (15):2874–2881
7. Quan C, Tay CJ, Chen W (2009) Determination of displacement derivative in digital holographic interferometry. Opt Commun 282 (5):809–815
8. Gorthi SS, Rastogi P (2009) Piecewise polynomial phase approximation approach for the analysis of reconstructed interference fields in digital holographic interferometry. J Opt A Pur Appl Opt 11(6):1–6
9. Gorthi SS, Rastogi P (2009) Simultaneous measurement of displacement, strain and curvature in digital holographic interferometry using high-order instantaneous moments. Opt Express 17(20):17784–17791
10. Rajshekhar G, Rastogi P (2011) Application of complex-lag distributions for estimation of arbitrary order phase derivatives in digital holographic interferometry. Opt Lett 36(19):3738–3740
11. Cornu C, Stanković S, Ioana C, Quinquis A, Stanković L (2007) Generalized representation of phase derivatives for regular signals. IEEE Trans Signal Process 55(10):4831
12. Ghiglia DC, Pritt MD (1998) Two dimensional phase unwrapping: theory, algorithm, and software. Wiley, New York
13. Ströbel B (1996) Processing of interferometric phase maps as complex-valued phasor images. Appl Opt 35(13):2192–2198

Chapter 32
Speckle Interferometry Analysis of Deformation Behavior of Crystal Grains in Polycrystal

Ryosuke Ogasawara, Shuichi Arikawa, and Satoru Yoneyama

Abstract The deformation behavior of crystal grains of polycrystal aluminum is observed using speckle interferometry. Coarse grained pure aluminum specimens with grains about 5 mm in diameter are fabricated to observe the deformation behavior easily. The specimens are plastically deformed by a tensile and a compression test. Then, the bidirectional in-plaine deformation distributions of the specimen surfaces containing multiple crystal grains are measured. The measurement results show that the various deformation behaviors in each grain are observed. Additionally, the longitudinal, transverse and shearing strains in each crystal grain are analyzed from the measurement results. In the strain maps, the complex deformations and slip bands are observed.

Keywords Speckle interferometry • Deformation behavior • Strain analysis • Crystal grain • Anisotropy

32.1 Introduction

In late years, the miniaturization of electrical and mechanical devices is ongoing. With the advancing miniaturization, elements in devices are manufactured with the size of sub-micro or micro-nano scale in such as micro electro-mechanical systems (MEMS). Because metal materials are frequently used for the elements, the understanding of the characteristics of the materials is important to improve the performance and the reliability of the devices. In metallic materials having polycrystalline structure, the mechanical characteristics are usually considered as homogeneous and isotropic in macro scale. However, in micro scale, these materials have heterogeneous and anisotropic properties because each crystal grain constituting the material has heterogeneous and anisotropic properties and the number of the grains is too small to equalize the properties. Therefore, the understanding of the mechanical interaction of adjacent grains is important.

Simulation approaches for the study about the deformation of polycrystal have been performed, such as the crystal plasticity finite element method [1] and the molecular dynamics method [2, 3]. To some extent, the interaction of adjacent grains can be analyzed by such method. To improve the validity of the analysis, experimental verification is required. However, experimental approaches for the study have not been sufficiently performed because the observation of the deformation behavior of the crystal grains in polycrystal is difficult. Recently, plastic strain distributions can be analyzed by analysis of crystal orientation using electron backscatter diffraction (EBSD) [4], whereas it is still difficult to measure the actual deformation of crystal grains.

On the other hand, laser interferometric techniques can measure displacements with micro-nano scale. Above all, speckle interferometry [5, 6], also called ESPI (Electronic speckle pattern interferometry), is available to measure deformation distribution of object surface. Therefore, it is expected that such deformation behavior of polycrystal can be measured by this technique. However, applying ESPI to the observations in microscopic scale is not easy. Accordingly, it can be available for the observation by coarsening the crystal grains.

In this study, the deformation behavior of crystal grains of polycrystal material is observed using ESPI. Coarse grained pure aluminum specimens with the grains about 5 mm in diameter are obtained by a strain-annealing method. The specimens

R. Ogasawara (✉) • S. Arikawa • S. Yoneyama
Department of Mechanical Engineering, Aoyama Gakuin University,
5-10-1 Fuchinobe, Chuo-ku, 252-5258 Sagamihara-shi, Kanagawa, Japan
e-mail: c5612083@aoyama.jp

H. Jin et al. (eds.), *Advancement of Optical Methods in Experimental Mechanics, Volume 3*,
Conference Proceedings of the Society for Experimental Mechanics Series,
DOI 10.1007/978-3-319-00768-7_32,

containing coarse grains are plastically deformed by a tensile and compression test. The bidirectional in-plane deformation distributions of the specimen surfaces containing multiple crystal grains are measured. As the result, various deformation behaviors in each crystal grain are observed. In the strain maps, the complex deformation and the slip bands are observed. The results show that the ESPI analysis is effective for the study about the deformation of polycrystal.

32.2 Experimental

32.2.1 ESPI Set Up

The speckle interferometer for the bidirectional in-plane deformation measurement is a dual-beam interferometer arranged to horizontal (x axis) and vertical (y axis) displacement sensitivities. A schematic diagram of the top view of the setup is shown in Fig. 32.1. The laser beam from the light source is separated into four beams by half mirrors, then two beams enter the object from horizontal directions and the other two beams enter it from vertical directions as shown in Fig. 32.2. Each beam is expanded through lenses attached on the path and illuminates the observation region. Each incident angle is set to 45° from perpendicular line to the surface. A 5 mW stablized He-Ne laser with the wavelength of 632.8 nm (MELLES RIOT, model 05 STP 905) is used as the light source. Speckle images are acquired by a CCD camera (SONY, model XCD-X710) with the resolution of 1024 × 768 pixels and cell size of 4.65 × 4.65 μm. The F-number of the camera lens is set to 8. Phase stepping images are obtained by shifting the wedge prism attached on the beam path.

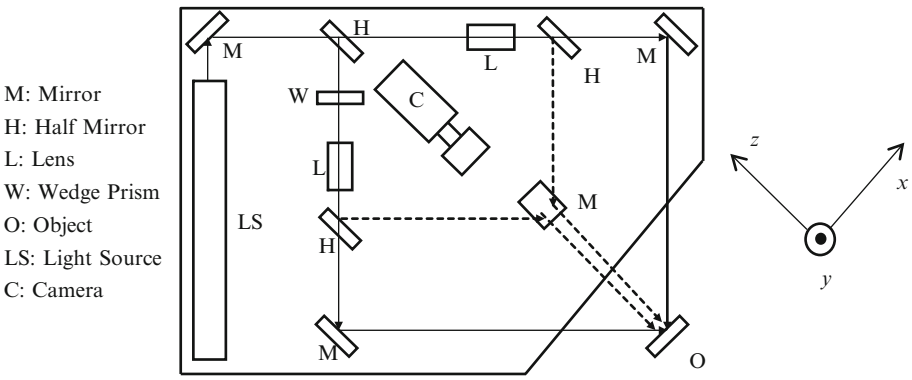

Fig. 32.1 Schematic figure of the ESPI set up

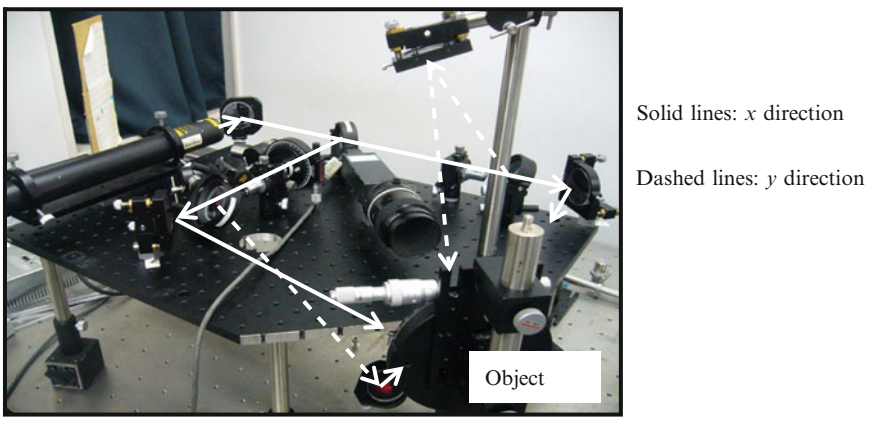

Fig. 32.2 Route of laser beam of x and y direction

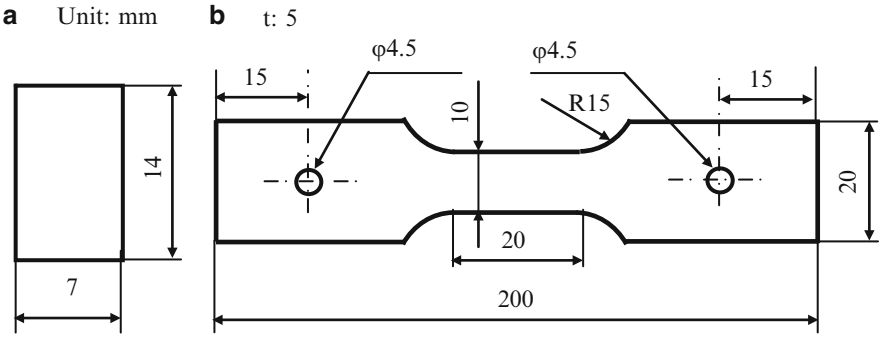

Fig. 32.3 Specimens configuration (**a**) For compression. (**b**) For tensile

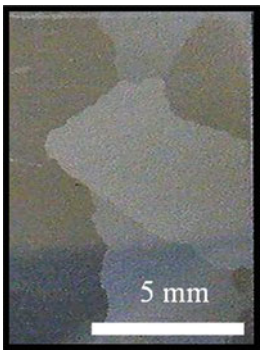

Fig. 32.4 Coarsen grained specimen

32.2.2 Specimen

Polycrystalline specimens are made of a cold-rolling aluminum (JIS A1050) plate with the thickness of 5 mm. The grain size is grown up by a strain-annealing method. Firstly, an aluminum plate is annealed at about 530°. Secondly, the plate is plastically deformed until the strain of 3 % by tensile loading. Finally, it is annealed again at about 630° for 24 h. By this process, the coarse grained aluminum with the grain size of about 3 ~ 5 mm is obtained. The final shapes of the tensile and the compression specimens are shown in Fig. 32.3. These specimens are polished and etched by the sodium hydroxide solution for the visualization of the grain boundaries. The photograph of the specimen surface is shown in Fig. 32.4. Coarse crystal grains can be observed on the specimen. Here, the etching makes the sufficient roughness for the ESPI measurement.

32.2.3 Experimental Procedure

The tensile and compression tests are performed to observe the deformation behavior of the crystal grains. The experimental setup is shown in Fig. 32.5. The specimens are subjected to the load by driving a screw of a micrometer head. Then, the speckle images of the specimen surface are captured by the CCD camera in the interferometer attached in front of the specimen. For the phase analysis, the four phase stepped images at the initial and deformed states for each direction. In this study, a random phase stepping method [7] is applied for the analysis. For the strain analysis and the noise reduction, a local least-squares is applied to the analyzed phase maps. Additionally, the deformation behavior of a fine grained aluminum specimen having average grain size of about 50 ~ 60 μm is observed for comparison.

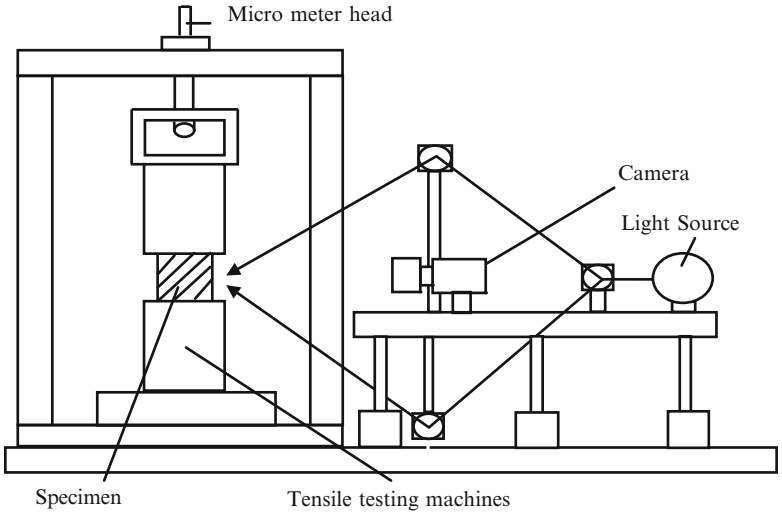

Fig. 32.5 Schematic view of the experimental device

32.3 Results

32.3.1 Measurement Results of Fine Grained Specimen

Captured speckle images at each state for each direction are shown in Fig. 32.6a. The specimen is subjected to the tensile load and the applied displacement is 20 μm. Figure 32.6b shows the phase maps obtained by the phase-stepping method. This result shows a comparatively good result in ESPI measurement. The fringe pattern for the x directional displacement shows the compression deformation and the pattern of the y direction shows the tensile deformation. The fringe patterns on each direction are parallel to each direction. It means the rotation and the bending do not occur in the deformation. The strain component distributions, ε_x, ε_y, and γ_{xy}, obtained from the phase maps are shown in Fig. 32.7a–c respectively. The low level fine fluctuations in the strain values are observed on the strain distributions. Such low level noise is usually obtained in ESPI measurement results, thus these results show the uniform deformations.

32.3.2 Measurement Results of Coarse Grained Specimen

Figure 32.8 shows the phase maps of the deformation behavior of the coarse grained specimen. White curves show the grain boundaries obtained from the photograph shown in Fig. 32.4. The specimen is subjected to the tensile load and the given displacement is 20 μm. The complex phase maps compared with those of the fine grained specimen are observed. The strain components, ε_x, ε_y, and γ_{xy}, obtained from the phase maps are shown in Fig. 32.9a–c respectively. As shown in this figure, the strain values much higher than the low level noise in Fig. 32.7 are observed. The nonuniform strain distributions in the grains are observed.

The phase maps and the strain distributions for the compression test are shown in Figs. 32.10 and 32.11. The applied displacement of the compression loading is 50 μm. The complex phase maps are obtained as shown Fig. 32.10. From the phase maps, the strain components are obtained as shown Fig. 32.11a–c. Also, the nonuniform strain distributions can be observed. In the ε_y map, the errors in the strain value are observed near the upper right corner.

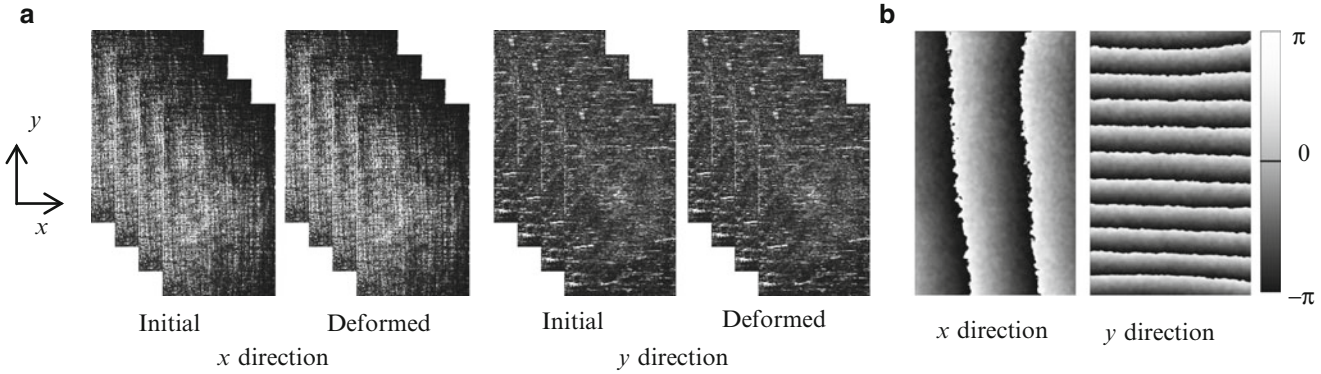

Fig. 32.6 Speckle images and phase difference images using fine grained specimen (**a**) Speckle image. (**b**) Phase difference image

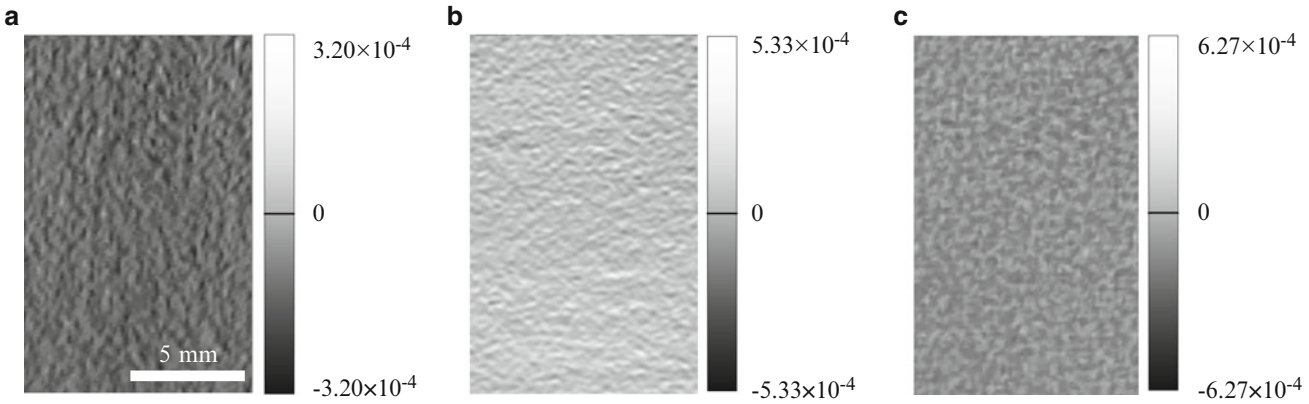

Fig. 32.7 Strain distribution with tensile test using fine grained specimen (**a**) ε_x, (**b**) ε_y, (**c**) γ_{xy}

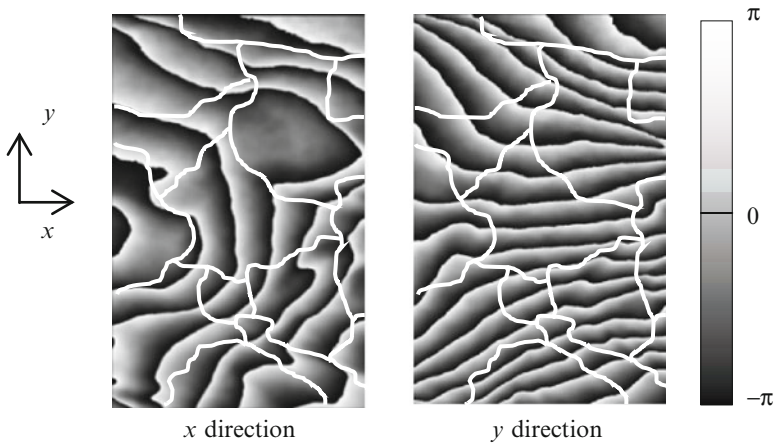

Fig. 32.8 Phase difference image with tensile test using coarsen grained specimen

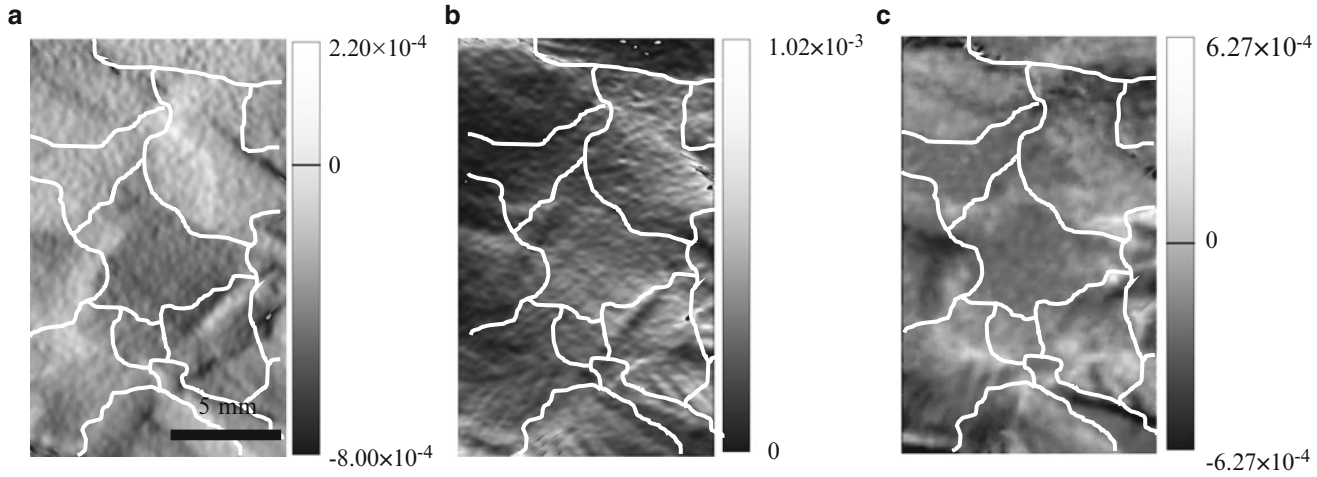

Fig. 32.9 Strain distribution with tensile test using coarsen grained specimen (**a**) ε_x, (**b**) ε_y, (**c**) γ_{xy}

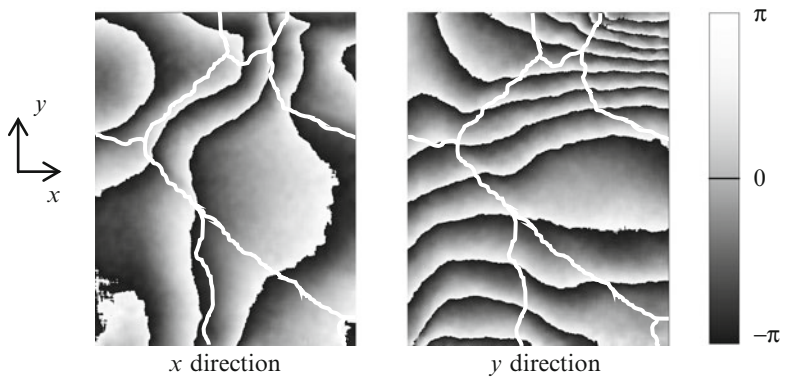

Fig. 32.10 Phase difference image with compression test using coarsen grained specimen

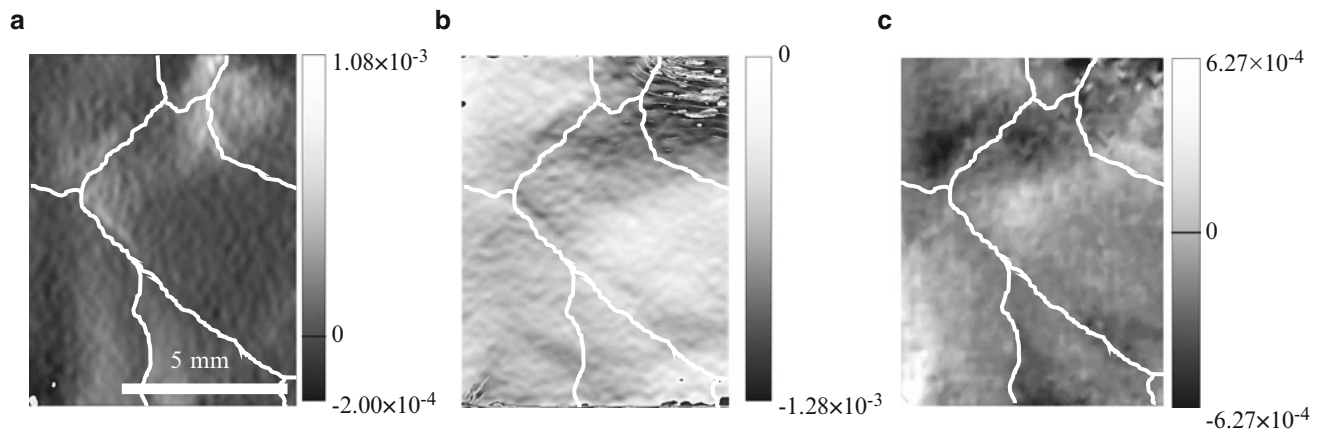

Fig. 32.11 Strain distribution with compression test using coarsen grained specimen (**a**) ε_x, (**b**) ε_y, (**c**) γ_{xy}

32.4 Discussion

32.4.1 Measurement Resolution

The length of one pixel corresponds to 15.7 μm on the specimen surface. The region for the local least-squares for calculating strains is 15 × 15 pixels. Therefore, the spatial resolution of the strain maps is about 300 μm. On the other hand, the grain size of the fine grained specimen is about 50 ~ 60 μm. The grain size is smaller than the resolution; hence the deformations in the crystal grains of the fine grained specimen cannot be captured. The grain size is enough smaller than the specimen, thus the homogeneous deformation is obtained. There is still a possibility that inhomogeneous deformations caused by the interactions of the multiple grains are slightly contained in the spatial noises. The spatial frequency of the fringe pattern increase with increasing the absolute strain of the object. However, it seems that decreasing the error is possible by improving the analysis process.

32.4.2 Deformation in Crystal Grains

In the results of the deformation measurement of the coarse grained specimen, the grain size of about 5 mm is enough larger than the spatial resolution of the measurement to obtain the deformation data in the crystal grains. The inhomogeneous deformation behaviors in Figs. 32.9 and 32.11 suggest that the deformation behavior by the interaction of the adjacent grains can be measured. The slantwise line-like strain distributions in Fig. 32.9 suggest that behaviors of the crystal slips are obtained. These deformations of the crystals are the three-dimensional in general. To obtain the detailed information of the deformation, the out-of-plane deformation measurement is also required. If the deformation information is combined with the information of the crystal orientation, the detailed analysis of the deformation behavior by the interaction of the adjacent grains is possible. Therefore, the ESPI analysis is effective for the study about the deformation of polycrystal.

32.5 Conclusion

In order to observe the deformation behaviors of crystal grains of a polycrystal aluminum specimen with ESPI, the specimens with the grain size of about 5 mm are obtained by the strain-annealing method. The tensile and compression tests are carried out with those specimens. The deformation behavior by the interaction of the adjacent grains is measured using ESPI. In the strain maps, the complex deformations and the crystal slips are observed. The use of ESPI is effective for the study on the deformation of polycrystal.

Acknowledgements The authors thank Japan Aluminum Association for supporting this study.

References

1. Albers A, Metz D (2005) Influence of the microstructure on the strain of micro components. Microsyst Technol 12:685–690
2. Shimokata T, Nakatani A, Kitagawa H (2002) Molecular dynamics study of structure and mechanical properties of grain boundaries nanocrystalline materials. Trans Jpn Soc Mech Eng Series A 68(670):858–865
3. Shimokata T, Kinari T, Shintaku S, Nakatani A, Kitagawa H (2005) Deformation and localized necking mechanism of nanocrystalline materials by molecular dynamics simulation. J Soc Mater Sci (Jpn) 54(4):399–406
4. Kamiya M, Wilkinson AJJ, Tichmarsh M (2005) Measurement of plastic strain of polycrystalline material by electron backscatter diffraction. Nucl Eng Des 235:713–725
5. Chiang FP (1989) Speckle metrology, Nondestructive Evaluation and Quality Control (ASM International), ASM handbook 17:432–437
6. Sirohi RS (2002) Speckle interferometry. Contemp Phys 43:161–180
7. Zhaoyang W (2004) Advanced iterative algorithm for phase extraction of randomly phase-shifted interferograms. Opt Soc Am 29:1671–1673

Chapter 33
Optical Interferometry for Evaluation of Adhesion Strength of Thin-Film Systems

David Didie, Daniel Didie, Bishwas Ghimire, Konrad Kabza, Sushovit Adhikari, Sanichiro Yoshida, Chiaki Miyasaka, and Ik-Keun Park

Abstract Optical interferometry and contact angle goniometry are applied to evaluate the adhesion strength of nano-scale thin-film systems. The optical interferoemtry is used to characterize the harmonic response of the film-substrate interface, and the contact angle goniometry is used to measure the surface energy of the substrate. The thin-film specimen is configured as one of the end-mirrors of a Michelson interferometer and driven from the rear with an acoustic transducer at audible frequencies. The resultant film's displacement is detected as interferometric fringe patterns behind the beam splitter. A mathematical procedure is developed to estimate the film's displacement from the Fourier spectrum of the fringe pattern. Specimens of a titanium-film coated on a silicon substrate, a gold-film coated on a titanium pre-coated silicon substrate, and a platinum-film coated on a titanium pre-coated silicon substrate are tested. In all these specimens, the titanium film is coated either on the silicon substrate whose surface is treated with plasma bombardment (the surface-treated specimens), or directly on the silicon substrate without pre-coating treatment (the untreated specimens). The surface treatment is known to enhance the adhesion. The surface energy measurement by contact angle goniometry indicates that the surface treatment substantially alters the surface energy of the silicon substrate. Interestingly, however, the harmonic response of the film surface measured by the interferometer indicates that in a certain frequency range the surface-treated specimen shows greater oscillation amplitude than the non-surface treated cases.

Keywords Thin-film systems • Adhesion strength • Michelson interferometer • Nondestructive evaluation • Contact angle goniometry

33.1 Introduction

Thin film systems are used in various fields. An emerging field of application is coating on implanted artificial knee joints. To make the contact surface strong, titanium is widely used as the material to coat the surface. While this makes the joint robust, it causes a problem of delamination, which has become the most severe form of damage to be encountered in total knee replacements. In a study of 33 PCA (Porous-coated anatomic) inserts, the group noted that 53 % PCA's showed severe delamination within 4 years of use [1]. To strengthen the adhesion at the substrate-film interface, the substrate surface is treated prior to the coating. For this purpose, the oxygen plasma bombardment technique is widely used to treat silicon substrates. It is believed that the oxygen plasma knocks off hydro-carbons and thereby strengthens the silicon-titanium adhesion (Horn M, Jin Y, Private communication, 2012). However, detail mechanism of the adhesion enhancement is not known. For further studies of the enhancement mechanism, proper techniques to evaluate the adhesion are necessary. Ultrasonic techniques [2] are available to test adhesion strength. In these techniques, a sound wave is excited inside the thin-film specimen and resultant film surface motion is detected. To excite sound wave in the specimen, typically an acoustic

D. Didie • D. Didie • B. Ghimire • K. Kabza • S. Adhikari • S. Yoshida (✉)
Southeastern Louisiana University, Department of Chemistry and Physics, SLU 10878, Hammond, LA 70402, USA
e-mail: syoshida@selu.edu

C. Miyasaka
Pennsylvania State University, Department of Engineering Science and Mechanics, University Park, PA 16802, USA

I.-K. Park
Seoul National University of Science and Technology, Seoul, Republic of Korea

H. Jin et al. (eds.), *Advancement of Optical Methods in Experimental Mechanics, Volume 3*,
Conference Proceedings of the Society for Experimental Mechanics Series,
DOI 10.1007/978-3-319-00768-7_33,

frequency of 100 MHz or higher is required. The use of such high frequency causes issues. First, the film displacement at this frequency range is small. Consequently, signal amplification such as lock-in amplification is necessary, making the evaluation process time-consuming and expensive. Second, this frequency range is many orders of magnitude higher than the dominant frequency of typical knee motion. As an example, the peak-frequency of knee vertical-acceleration caused by side step is typically 20 Hz or lower [3].

To solve this problem, we devised an opto-acoustic technique [4]. In this technique, the specimen is oscillated with an acoustic transducer from the rear surface of the substrate and the resultant out-of-plane displacement of the film surface is read out with the use of optical interferometry. The basic idea behind this technique is as follows. To the first order approximation, the force that binds a thin-film to the substrate can be considered as spring force. Moreover, the stiffness (the spring constant) associated with this force at the film-substrate interface is considered to be lower than those of the substrate or the film material. Consequently, if the specimen is oscillated at a certain frequency, which is low enough not to excite an acoustic wave in the bulk and high enough to make the film surface displacement large, the differential motion of the film surface can be enhanced. If the driving frequency is swept in a range that contains a resonance frequency of the interface, the amplitude of this differential motion is expected to be prominent in the frequency domain. Previously, we tested this method using gold-coated silicon specimens prepared with and without the oxygen-plasma surface treatment, and were able to differentiate the film surface displacement of the untreated specimen from that of the treated specimens [4]. In this experiment, we observed resonance-like behavior in a frequency range of 10–50 kHz. This raised a question. Does the titanium-silicon adhesion possibly have resonance in the frequency range of typical knee motions? Generally speaking, deformation leads to fracture most easily when the object is disturbed near resonant frequency.

This situation has led us to apply the opto-acoustic technique to a lower frequency range, independently investigate the effect of the surface treatment, and further investigate the resonance-like behavior observed in the previous study [4]. Thus, we have modified the previous interferometer so that it has sensitivity as low as 2 kHz. To evaluate the surface treatment, we have assembled a contact angle goniometer and estimated the surface energy of the treated and untreated silicon substrates. To examine if the spectral peaks observed in the previous study are due to resonance of the interface, we have varied the mass of the film and seen if the peak frequency shifts inversely proportional to the square root of the mass. The aim of this paper is to report these recent progresses and discuss the results.

33.2 Experimental

33.2.1 Specimens

Three different types of specimens are used. All three types are coated on oxygen-plasma treated and untreated silicon substrates. They are originally fabricated as a disk of 75 mm in diameter and cut into specimens of an approximately 5 mm × 5 mm square. Table 33.1 lists the three types of specimens with the thickness of the film materials. On the first type, labeled Ti, a 75 nm-thick film of titanium is coated on the treated/untreated silicon substrates. On the second and third types, labeled Ti-Au and Ti-Pt, a 10 nm thick film of titanium is first coated on the treated/untreated silicon substrates, and a 100 nm thick gold or platinum film is coated over the titanium film.

The resonance frequency of a simple spring-mass system is proportional to the square root of the ratio of the stiffness to the mass, $\sqrt{k/m}$. This indicates that the resonance frequency of the silicon-film interface varies inversely proportional to the square root of the film mass. The third row of Table 33.1 indicates the square root of the ratio of the film mass of the Ti-Au and Ti-Pt specimens to that of the Ti specimen. If the observed peak is due to resonance of the same spring constant of the interface, the frequency should shift in proportion to this factor.

Table 33.1 Three specimens used in this study and the film thickness

	Ti	Ti-Au	Ti-Pt
Thickness (nm)	75	10/100	10/100
Density (g/cc)	4.51	19.30/4.51	21.45/4.51
sqrt(mass ratio)	1	2.4	2.5

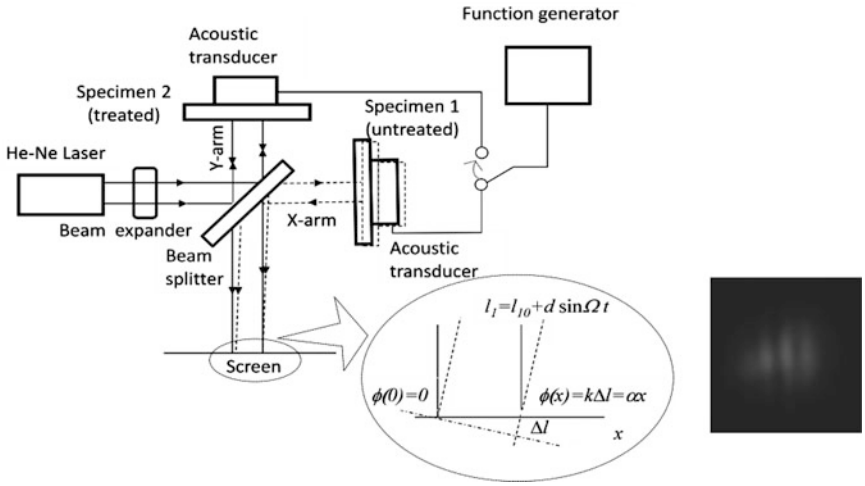

Fig. 33.1 Experimental setup

33.2.2 Principle of Measurement

33.2.2.1 Optical Interferometry

Figure 33.1 illustrates the interferometric setup used in this study. Details about the optical interferometer and the principle of operation are described elsewhere [4]. In short, the specimen is configured as one of the end-mirrors of a Michelson interferometer with the coated surface facing inward to the beam splitter. The specimen is driven with an acoustic transducer attached to the rear surface of the silicon substrate. The driving frequency of the transducer is less than 30 kHz so that a sound wave is not excited within the bulk of the Si substrate or the film. The interference from the two arms is observed on the screen placed behind the beam splitter with a CCD (Charge Coupled device) camera. The end-mirror of the X-arm is slightly tilted so that the optical path difference between the two arms varies in proportion to the transverse distance from the optical axis on the screen forming a fringe pattern consisting of dark stripes (Fig. 33.1).

When the film surface oscillates at a frequency much higher than the frame rate of the CCD camera (30 frame per second), the dark stripes captured by the CCD camera becomes blurry. The intensity of the image is given as a function of the transverse distance along the optical axis on the screen as follows.

$$I(x,t) = 2I_0(1+\cos\Delta\phi) = 2I_0\{1+\cos(\alpha x + kd\sin\Omega t)\} \tag{33.1}$$

Here $\Delta\phi$ is the phase difference between the two arms, x is the horizontal spatial coordinate on the screen, α is a constant that represents the x-dependence of ϕ, k is the wave number of the light, d is the oscillation amplitude of the film surface, and Ω is the oscillation frequency. With the use of Bessel functions, Eq. 33.1 can be put in the following form.

$$I(x,t) = 2I_0[1+\cos(\alpha x)\{J_0(\delta)+2J_2(\delta)\cos(2\Omega t)+\cdots\cdots\} - \sin(\alpha x)\{2J_1(\delta)\sin(\Omega t)+2J_3(\delta)\sin(3\Omega t)+\cdots\cdots\}] \tag{33.2}$$

Here

$$\delta = kd \tag{33.3}$$

The signal detected by the CCD camera, $S(T)$, is the time integral of $I(x,t)$expressed by Eq. 33.2, where T is the exposure time of the camera. So it can be expressed as follows.

$$S(T) \propto \int_0^T \{1 + \cos(\alpha x) J_0(\delta)\} dt + 2\cos(\alpha x) \left\{ J_2(\delta) \int_0^T \cos(2\Omega t) dt + J_4(\delta) \int_0^T \cos(4\Omega t) dt + \cdots \right\} - 2\sin(\alpha x) \left\{ J_1(\delta) \int_0^T \sin(\Omega t) dt + J_3(\delta) \int_0^T \sin(3\Omega t) dt + \cdots \right\} \quad (33.4)$$

Of the terms on the right-hand side of Eq. 33.2 the first two terms are independent of time, and the rest oscillate as a function of time. Consequently, when the frame rate is substantially lower than the oscillation frequency, hence the limit of integration T is much greater than the oscillation period, all the terms on the right-hand side of Eq. 33.4 oscillates but the first two terms increase in proportion to T. This means that the dc term and the first peak of the Fourier spectrum of the signal $S(T)$are much higher than the rest when the frame rate is lower than the oscillation frequency. The first term of the right-hand side of Eq. 33.4 indicates that the height of the first peak reduces in proportion to the oscillation amplitude via $J_0(\delta)$term. It is thus possible to estimate the oscillation amplitude from the height of the first peak and Eq. 33.3.

In the frequency domain, the spectrum is the product of the oscillation amplitude of the transducer's active surface, the transfer functions of the substrate, the interface and the film. Since the driving frequency is too low to excite a sound wave in the bulk of the substrate or film, they oscillate as rigid bodies. Thus, their transfer functions can be assumed to be unity (no frequency dependence). Consequently, the observed spectrum represents the transfer function of the interface. The height of the first peak can be used to indicate the transfer function; the lower the peak, the greater the oscillation amplitude.

33.2.3 Contact Angle Measurement

Generally speaking, the bonding at the interface of different materials is stronger when their surface energy is closer to each other. From the viewpoint of strengthening the adhesion of a thin-film to its substrate, it is therefore favorable to make the substrate's surface energy closer to that of the film's material. The surface energy of a material can be measured by the technique known as contact angle goniometry [5] and Zisman's plot [6]. This technique basically utilizes the fact that a liquid drop placed on a solid surface completely spreads out when its surface tension is the same or less than the surface energy of the solid, and rounds more tightly as the surface tension becomes greater than the surface energy. The surface tension of a drop of a solution varies with the concentration of judiciously chosen solute, and the value of surface tension is known as a function of the concentrations. Therefore, by measuring the contact angle of a drop varying the solution's concentration, it is possible to plot the contact angle as a function of the surface tension and estimate the surface energy by extrapolating the plot towards the contact angle corresponding to the situation where the drop completely spreads out (the critical contact angle). Figure 33.2 shows a sample contact angle observed in this study, and Fig. 33.3 is the Zisman's plot resulting from this study. By estimating the surface energy of the substrate with various pre-coating treatment, it is thus possible to find the condition that makes the surface energy of the substrate closest to that of the coated material.

33.3 Results and Discussion

33.3.1 Surface Energy Measurement

Figure 33.3 is the Zisman plot we made for our untreated silicon surface, oxygen-treated silicon and argon treated silicon as a reference. It is seen that the estimated surface energy of the plasma-treated surfaces is considerably higher than that of the untreated surface. This information is insufficient to make quantitative arguments on the silicon-titanium adhesion, but indicates that the plasma treatment can drastically change the dynamic behavior of the silicon-titanium interface.

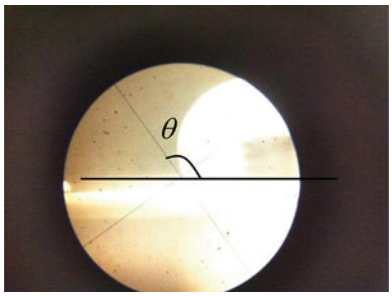

Fig. 33.2 Contact angle (θ)

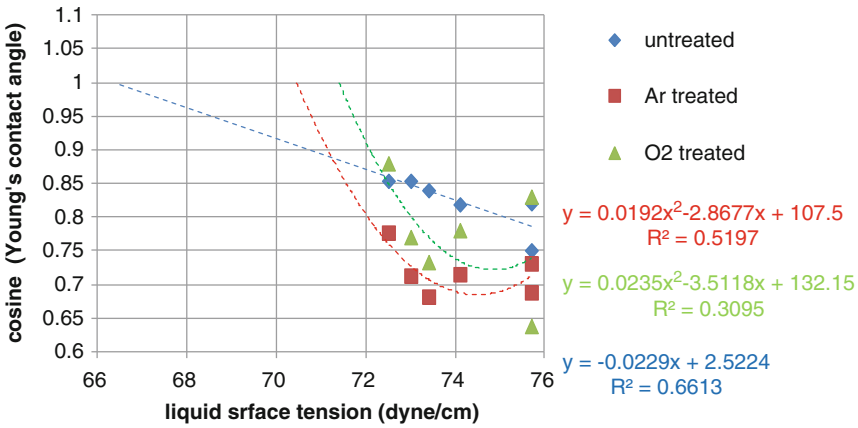

Fig. 33.3 Sizman plot

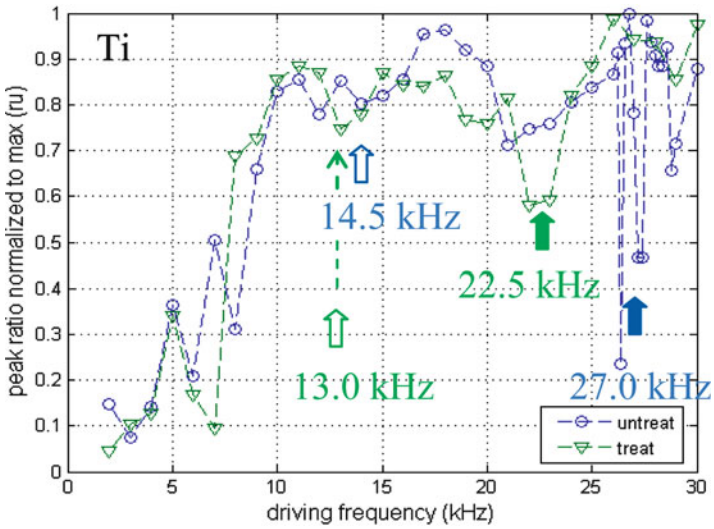

Fig. 33.4 Relative first peak (Ti only)

33.3.2 Resonance Peaks

Based on Eq. 33.4 and the argument that relates the oscillation amplitude of the film surface to the first peak value of the Fourier spectrum of the fringe pattern via $J_0(\delta)$, the harmonic response of the titanium-silicon interface can be discussed quantitatively. Figures 33.4, 33.5 and 33.6 are the height of the first peak of the Fourier spectrum of the fringe patterns obtained for the three types of the specimens as a function of the driving frequency. Here the spectrum is obtained from Fast Fourier transform of the spatial variation of the pixel intensity along an axis perpendicular to the fringes [4]. The data are normalized to the highest value observed in the driving frequency range tested. Since the lower spectrum peak corresponds

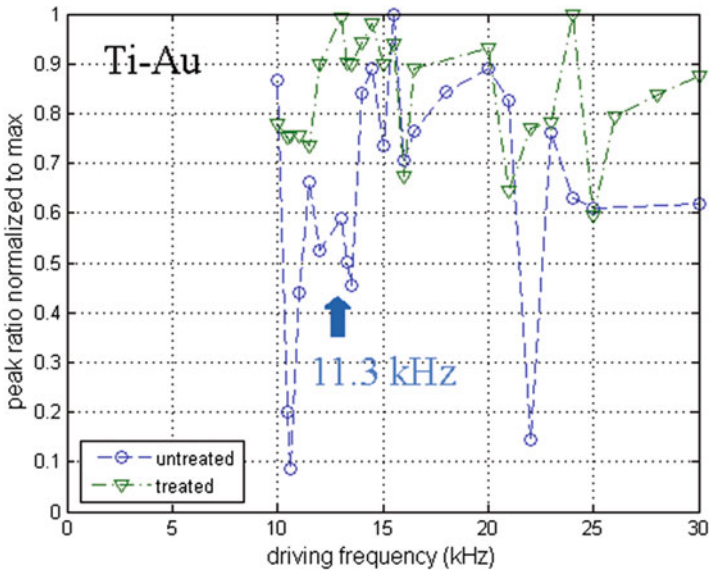

Fig. 33.5 Relative first peak (Ti-Au)

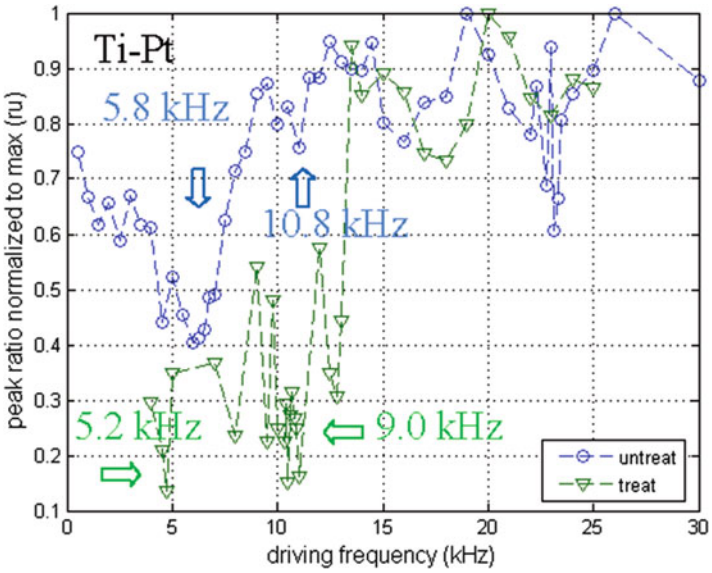

Fig. 33.6 Relative first peak (Ti-Pt)

to the higher oscillation amplitude, we call the valleys peak frequencies. In Fig. 33.4, the plot of Ti specimen coated on the untreated and treated substrates respectively show prominent peaks at 27.0 and 22.5 kHz. According to the mass ratio factor shown in Table 33.1, these peaks correspond to 27/2.4 = 11.3 and 22.5/2.4 = 9.4 kHz in the Ti-Au specimens and 27/2.5 = 10.8 and 22.5/2.5 = 9.0 kHz in the Ti-Pt specimens. Figures 33.5 and 33.6 show the peaks corresponding to 27 kHz. Figure 33.6 shows the peak corresponding to 22.5 kHz as well. Figure 33.5 does not have data lower than 10 kHz because the instrument did not have sensitivity below 10 kHz when the data for the Ti-Au specimens were taken. Figure 33.6 indicates that the untreated and treated Ti-Pt specimens have prominent peaks at 5.8 and 5.2 kHz, respectively. Figure 33.4 indicates that the Ti specimens have peaks at the corresponding frequencies, though they are not as prominent as Figure 33.6. These corresponding peak frequencies are listed in Table 33.2.

The low frequency peaks (<10 kHz) observed in the untreated and treated Ti-only specimens are on top of each other. This indicates that the resonance is not caused by the treatment. However, the peaks observed in the same low frequency range in the Ti-Pt specimens show clear difference between the untreated and treated cases. This observation supports the above argument that these low frequency peaks observed in the Ti-Pt specimens are down-converted from the corresponding peaks in the Ti-only specimens. Figure 33.7 compares the 5.8 kHz peak observed in the present study for the untreated Ti-Pt specimen with the peak observed for an identical Ti-Pt specimen in an independent study conducted with the use of the same

Table 33.2 Peak frequencies observed in Ti-only specimens and expected frequencies in Ti-Au and Ti-Pt specimens based on mass ratio. (Unit: kHz)

	Ti	Ti-Au	Ti-Pt	
Untreated	14.5	(6.0)	5.8	⇧
Untreated	27.0	11.3	10.8	⬆
Treated	13.0	(5.4)	5.2	⇧
Treated	22.5	(9.4)	9.0	⬆

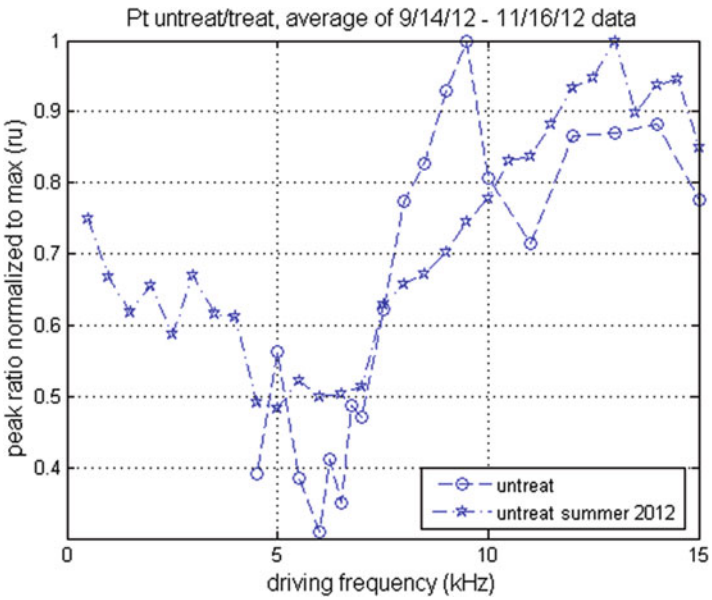

Fig. 33.7 Low frequency peaks observed in untreated Ti-Pt specimens with different experimental setups

concept but a different experimental setup[1]; the optical mounts, laser source, and acoustic transducer are all different from the present study. Reasonable agreement between the two data sets indicates that this peak at 5.8 kHz is indeed due to the specimen, not the experimental setup.

33.4 Conclusions

The present study supports the previous proposition that peaks observed in the frequency dependence of the film surface oscillation represent resonance behavior of the film-substrate interface. The contact angle goniometry confirms that the plasma-bombardment treatment alters the surface energy of the silicon substrate. However, the observation that the surface treated specimens also show the same type of resonance-like behaviors indicates the necessity of further investigation on the effectiveness of the plasma bombardment treatment for better adhesion. The fact that the resonance-like peaks are found on the low frequency end of the diving frequency indicates the necessity of experimentation in further lower frequency range as well as identification of the dynamics underlying the resonance-like behavior.

Acknowledgement The authors are grateful to Mark Horn and Yao Jin of the Pennsylvania State University for provision of specimens and helpful discussions regarding the science of thin-film coating. This study has been supported in part by the National Science Foundation International Research Experience for Student Grant (IRES-0927033) awarded to Southeastern Louisiana University, the Tokyo Denki University internal research grant and the National Research Foundation of Korea (grant No. 2011-001790).

[1] The experiment was conducted by L. Winstead, A. Nakagawa and S. Yoshida as part of the 2013 summer program supported by the National Science Foundation, IRES (International Research Experience for Student) grant.

References

1. McTighe T, Clarke I (2009) Failure mechanisms on total knee arthroplasty. Joint Implant Surgery & Research Foundation, Chagrin Falls, Ohio, USA
2. Telschow KL, Deason VA, Cottle DL, Larson JD III (2003) Full-field imaging of gigahertz film bulk acoustic resonator motion. IEEE Trans Ultrason 50:1279–1285
3. McLean SG, Su A, van den Bogert AJ (2003) Trans ASME 125:864–874
4. Yoshida S, Adhikari S, Gomi K, Shrestha R, Huggett D, Miyasaka C,Park I (2012) Opto-acoustic technique to evaluate adhesion strength of thin-film systems. AIP Adv 2(2):022126-1–022126-7
5. Förch R, Schönherr H, Jenkins ATA (2009) Appendix C: contact angle goniometry. In: Surface design: applications in bioscience and nanotechnology. Wiley, Weinheim, Published online
6. Kabza, KG, Gestwicki JE, McGrath JL Contact angle goniometry as a tool for surface tension measurements of solids, Using Zisman plot method, Phys Chem Experiment, J Chem Ed 77(1):63–65

Chapter 34
Low Cost Digital Shearography Prototype

Dirk Findeis, Oliver Hobson, and Jasson Gryzagoridis

Abstract Digital Shearography is an optical non-contacting non- destructive testing technique. The inspection method has found many applications and is particularly suited for amongst others, in-situ inspection of composite components for defects such as low velocity impact damage and delaminations. Due to advancing technologies smaller and more cost effective components are readily available for integration into such an inspection system.

This paper presents the latest portable prototype developed at the University of Cape Town. The technique and it's application is described in detail. The layout and design of the prototype including camera, laser and optical configuration is outlined and presented. Using the system, initial results from inspections of a known defect sample is presented in an attempt to evaluate the performance of the prototype. The paper is concluded with a discussion of the results obtained and possible recommendations for refinements and improvements.

Keywords Shearography • Optical interference techniques • Flaw detection • NDT • Composites

34.1 Introduction

Non-Destructive Testing and Evaluation (NDT/E) techniques have been used for many years to inspect components either after manufacture or during maintenance inspections for flaws and defects that could compromise the performance of the component and cause it to fail in service. Due to the ever increasing use of composite materials in high load, high performance critical applications, a need arose for fast and effective non-destructive inspection method that could evaluate the integrity of components in-situ [1]. Research projects have determined that one of these techniques called Digital Shearography which was developed in the early 1980s and is an optical NDT method, is one such suitable technique. As key working components reduced in cost and computing power increased, the cost of the inspection system decreased and the rate of inspection increased.

Shearography is a full field, non-contacting, optical NDT method. Amongst others, it has the ability to detect flaws in composite structures by detecting out-of-plane surface deformations in the form of surface displacement derivatives which are observed in the produced image. The types of flaws that have been detected include: delamination, impact damage, foreign objects, cracks, porosity, wrinkles, core disbonds, and leakage detection [2]. Digital Shearography also has other uses such as strain measurement, leakage detection, residual stress measurement and measurement of vibrations [3]. Currently the method is used in several industries including the aerospace, space, renewable energy and automotive sectors as well as materials research activities.

D. Findeis (✉) • O. Hobson • J. Gryzagoridis
Department of Mechanical Engineering, University of Cape Town, Private Bag, Rondebosch 7700, South Africa
e-mail: dirk.findeis@uct.ac.za

H. Jin et al. (eds.), *Advancement of Optical Methods in Experimental Mechanics, Volume 3*,
Conference Proceedings of the Society for Experimental Mechanics Series,
DOI 10.1007/978-3-319-00768-7_34,

34.2 Theory

A highly coherent, monochromatic laser beam is used to illuminate the object to be inspected. The reason for using this source of illumination is that shearography relies on the interference of light waves [4]. The constructive and destructive interference of these reflections produces unique speckle patterns, which can be processed to reveal the test sample's response to an applied force. The process can be described with the aid of the illustration in Fig. 34.1a, b below. A laser beam is expanded via a beam expander and used to illuminate the component under inspection. The light reflecting off the object surface (ideally a diffuse surface) travels in various directions. These reflecting light rays interfere with each other and when viewed, produce a unique pattern consisting of bright and dark speckles or commonly referred to as the salt and pepper effect. A camera connected to a computer is focused on the object. The camera however is set up to view the object through a shearing device, typically a Michelson type interferometer. The purpose of the interferometer is to split the incoming light wave of the object into two distinct images with the aid of a beam splitter, as seen in Fig. 34.1b. The first of the two split images strikes a tilt mirror. This mirror is tilted at a small angle with respect to the normal of the incident angle of the light wave. The light reflecting off this mirror thus does not return along the same incident axis, but instead at a small offset angle, depending on the amount of mirror tilt. The second image is directed onto the second mirror (shift mirror) which is normal to the incident beam. This mirror has the ability to be shifted along its normal axis via a PZT which will be elaborated later. The image is thus reflected back along the incident axis onto the beam splitter. However as the reflection of the first image has been tilted, the two reflections do not realign with each other and are offset, or sheared. The beam splitter is both a transmitter and reflector and thus part of the first reflected image is transmitted and part of the reflected image two is reflected causing the two images to combine and interfere with each other to produce yet another unique speckle pattern. This final image is then captured by the camera and stored in the computer.

Should the object undergo a deformation which produces a relative displacement of the object surface, the interference speckle pattern will change. These object surface deformations are typically produced when the object is stressed. The techniques used to stress an object include pressurisation, partial vacuum stressing, thermal stressing, vibrational excitation, microwave excitation, impact stressing and other mechanical loading methods. Very often the shape of the object or material used to manufacture the object will dictate which stressing technique is best suited. Once stressed, the modified speckle pattern is also captured in the PC and compared with the original speckle pattern for areas of correlation. The result of this comparison process is mapped into a grey scale image to produce a fringe pattern. Mathematically the fringes can be represented as follows [5]:

$$\Delta\phi = \frac{4\pi}{\lambda}\left(\frac{\partial d}{\partial x}\right)S \tag{34.1}$$

where: $\partial\phi$ = correlation phase,
$\partial d/\partial x$ = rate of displacement,
S = magnitude of shear,
λ = wavelength of the laser light,

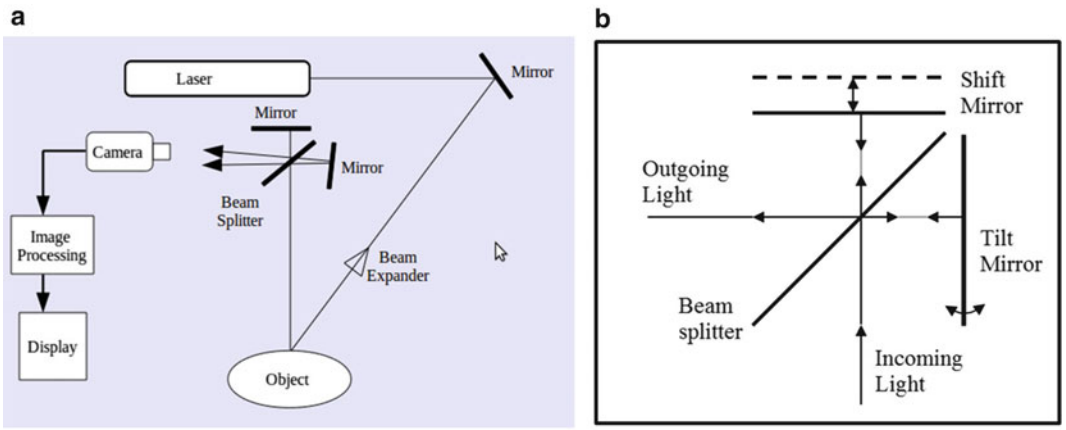

Fig. 34.1 (**a**) Typical shearography set-up, and (**b**) Detailed interferometer

Equation 34.1 indicated that the displacement gradient along each correlation fringe in the fringe pattern is a constant. In order to calculate the magnitude of the displacement gradient the following equation can be used [6]:

$$\frac{\partial p}{\partial x} = \frac{\lambda N}{2S} \tag{34.2}$$

where $\partial p/\partial x$ = displacement gradient in the x (or y) direction,
λ = wavelength of the laser light
N = number of fringes counted,
S = shear magnitude

Equation 34.2 also indicates that for each successive fringe the displacement gradient magnitude increases by a set amount.

In order to determine the direction of displacement, the modulation of the laser phase due to the object displacement needs to be determined. This is achieved via a phase stepping technique. In this approach, the shift mirror in Fig. 34.1b is stepped through a discreet distance between each successive speckle image capture. With a suitable amount of image processing the arc tan of the phase modulation of the laser beam can be obtained in the form of a fringe pattern. The fringes are generated as a saw tooth profile. Mathematically this can be represented as follows:

$$I_i(x,y) = I_B(x,y) + I_{MP}(x,y)\cos(\theta(x,y) + i \cdot \pi/2) \tag{34.3}$$

$$\phi(x,y) = \arctan\left(\frac{I_3(x,y) - I_1(x,y)}{I_4(x,y) - I_2(x,y)}\right) \tag{34.4}$$

$$\beta(x,y) = \phi_a(x,y) - \phi_b(x,y) \tag{34.5}$$

where i = 1,2,3,4
$\phi_a(x,y)$ = phase distribution after stressing,
$\phi_b(x,y)$ = phase distribution before stressing.

The presence of a defect in a component generally weakens the structure in the vicinity of the defect. The defect region of the structure will therefore, when stressed, deform in a different manner than the immediate surroundings of the defect region. As Digital Shearography detects the rate of displacement of an object in response to an applied stress these displacement anomalies present themselves in the final fringe pattern produced. As a summary of the process described above the key images are depicted in Fig. 34.2 below.

At the University of Cape Town's NDT Laboratory which is housed in the Department of Mechanical Engineering research into optical NDT techniques has been conducted for a number of years. The work has produced a number of prototypes. The two recent units, the DS03 and the DS04 are depicted in Figs. 34.3a, b below [7, 8]. Both images depict the Shearography head unit with all the optics and lasers integrated into a sealed enclosure. These units are connected to a portable industrial PC which contains the purpose written software to control the camera, image acquisition and processing routines, and the phase stepping routines, not to mentions all the image management options. The DS03 is based on a Cameralink camera and dedicated PC based image acquisition card, PC board level phase stepping functionality and standalone laser illumination. Integrated into the software are licensed proprietary image processing routines. The casing

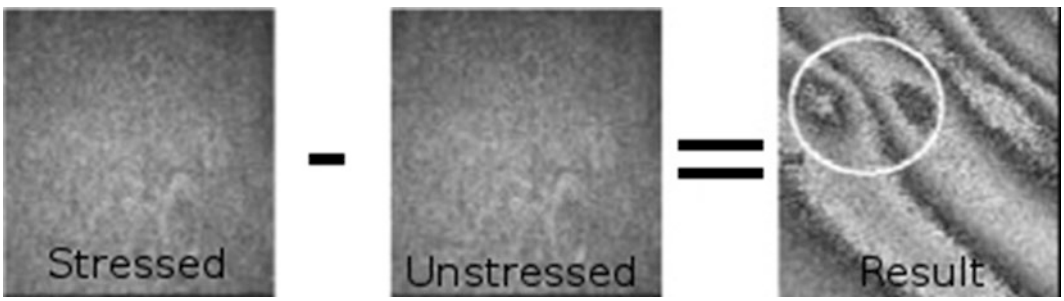

Fig. 34.2 Phase images of stressed and unstressed component and the resultant phase stepped fringe pattern

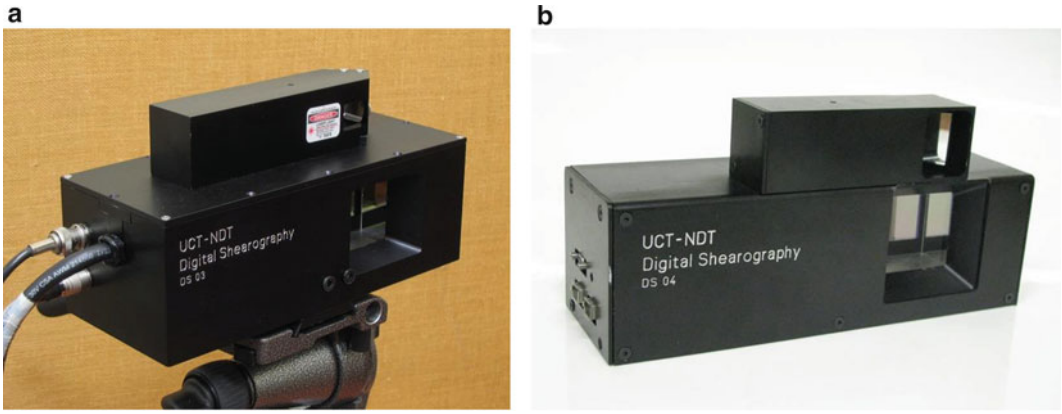

Fig. 34.3 (**a**) DS03 Digital Shearography prototype (**b**) DS04 Digital Shearography prototype

is manufactured from a single block of aluminium which makes for a very sturdy assembly and stable optical configuration. The DS04 on the other hand consists of an OEM firewire based camera, on-board laser illumination and on-board phase stepping functionality. The software is also written in C++ but does not make use of proprietary image processing libraries. Instead the camera manufacturer's SDK has been used for the image processing routines. The unit makes use of a purpose designed phase stepper driver unit. Also this unit's framework differs in that it is made of a base sheet and sheet metal enclosure.

34.3 Final Solution

The aim of the work reported in this paper was to review the current Digital Shearography system, reduce its cost and further refine and extend the unit's functionality in the form of a new prototype.

The phase stepper unit is an important component and is required to have a fast response time and accurate and repeatable functionality. The DS03 employed a purpose designed amplifier circuitry to drive the PZT based mirror shifting unit. The voltage range used to shift the mirror by ½ a laser wavelength was from 5 to 50 V. The DS 04 on the other hand has an on-board phase stepper voltage circuitry which is only capable of delivering a maximum of 5 V. As a result, an oversized, large capacitance actuator had to be used. As PZTs are designed to operate across a large voltage range and 0–5 V only covers 3.5 % of its usable range, a marginal amount of drift was noticed when the unit was operated over extended periods. This is due to the influence of noise in the narrow voltage operating bandwidth. It thus was decided to source an off the shelf PZT controller in a small form factor so that it could be fitted on-board into the Digital Shearography head unit. A 40 μF, low current PZT with a maximum stroke of 4.5 μm was matched to the controller and amplifier.

The camera selection process considered the camera solutions currently employed. The Cameralink interface was seen as too costly in that it required a separate framegrabber card to acquire the images. For a laptop configuration this would mean a breakout box and dedicated interface card to house the PC based acquisition card. The firewire based camera was considered a viable solution, but closer analysis of current laptops revealed that almost all of them had discontinued the firewire interface. USB3 was considered but due to lack of available hardware options was discarded. The final solution utilised a Gig-E Vision interface monochrome camera with a resolution of 1.44 MP. This camera was chosen since it had two data interfaces, one for image data transfer to a PC and then a RS-232 data interface for additional peripheral devices. The supplier was also able to provide an OEM board level version with the possibility to provide future support for power over Ethernet. The camera was fitted with a fixed focal length lens. Stepper motors and worm gears were added to control the aperture and focus settings remotely from the PC application.

The optics employed were fixed to purpose made mounts and bases. To reduce costs, a plate beamsplitter was used in conjunction with two first surface coated mirrors for the two images in the shearing assembly. The tilt mirror was fixed on a custom designed mount that used stepper motors to change the shearing angle in the horizontal and vertical directions via the PC application. The unpackaged PZT responsible for the shift functionality of the second mirror was fitted into a secure bracket and mechanism which preloaded the piezo stack to ensure that it returned to the zero position when the voltage potential was removed.

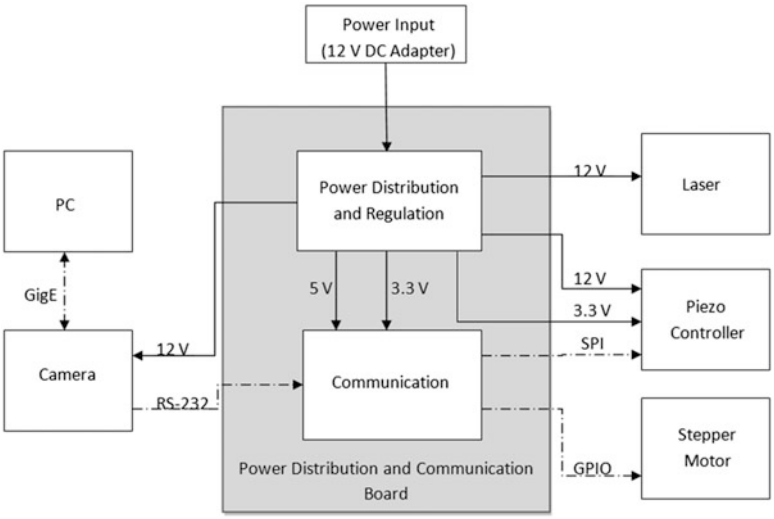

Fig. 34.4 Schematic of the pcb layout to interface the Digital Shearography head unit components

Fig. 34.5 Final low cost prototype with one laser module

To illuminate the component under inspection, a new laser module was designed utilising a 660 nm, 100 mW laser diode, with an integrated third party temperature controller and thermoelectric cooler to ensure a steady laser light output The entire unit was packaged into an enclosure mounted onto a ball swivel connection, thereby allowing the laser illumination to be directed onto the inspection area.

To allow all of the above components to operate collectively, care was taken in ensuring that all interfaces between them were compatible with each other. To this end the design of the printed circuit board needed to facilitate the required voltages and data interfaces is shown in Fig. 34.4 above. As can be seen, the entire head unit is powered via a 12 V DC external power source. The control of the head unit components via the PC is achieved through the secondary RS232 port on the camera. The existing version of the Digital Shearography Inspection software was updated to include the control of the camera lens and the shearing optics and shift mirror. Similarly the software was updated to accept the camera SDK commands and perform the required image processing routines.

From the experience gained using the DS03 and the DS04 it wa apparent that the box machined from a solid block of aluminium was the more solid design solution. Careful consideration had to be given to the optical layout in order to ensure that all items could be inserted into the Digital Shearography head unit from above and the box then closed securely with a screw down lid.

With the above approach the material and licensing costs of this prototype were reduced by approximated 25 % when compared with the firewire based Digital Shearography system. The cost reduction when compared with the Cameralink system is far greater due to the large software licensing cost associated with this system. The final assembly with one of the possible four laser modules connected is shown in Fig. 34.5 above.

34.4 Testing

The final prototype was tested on a helicopter rotor blade section consisting of honeycomb core which was covered with a carbon fibre skin and protected with a shaped stainless steel sheet along the leading edge of the blade. This blade then had nine artificial flaws of varying depth and 38 mm diameter introduced into it, as can be seen in Fig. 34.6a. The testing was carried out on a vibration isolating table using a Helium-Neon laser so that the performance of the new prototype could be verified independently from the new laser module. The table is shown in Fig. 34.6b with the test specimen, existing Digital Shearography unit, the new Digital Shearography head and laser appropriately positioned.

The test specimen was thermally stressed using an infra-red heating lamp, with the defect free surface facing the Shearography units. The results from the testing are shown in Fig. 34.7 with all image processing centred around flaw 3. In the figure the presence and location is clearly indicated by the characteristic double bulls-eye fringe pattern. The fringe pattern can be clearly seen especially once the image has been filtered, as shown in Fig. 34.8. The processing if this image to generate the phase unwrapped intensity distribution is shown in Fig. 34.9 with the corresponding 3D gradient map shown in Fig. 34.10. The next step was to test the laser module for temperature stability through the use of thermocouples attached

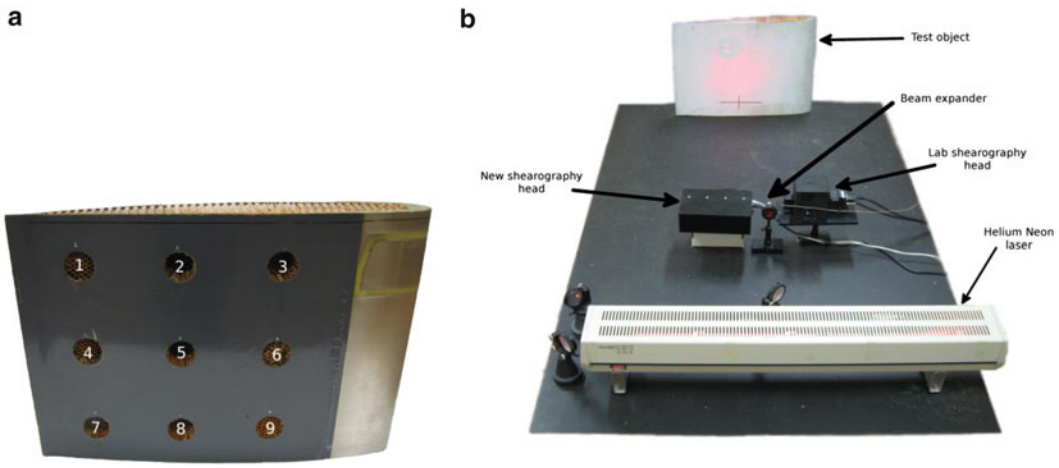

Fig. 34.6 (**a**) Helicopter blade section (**b**) Inspection test set-up with both Digital Shearography head units

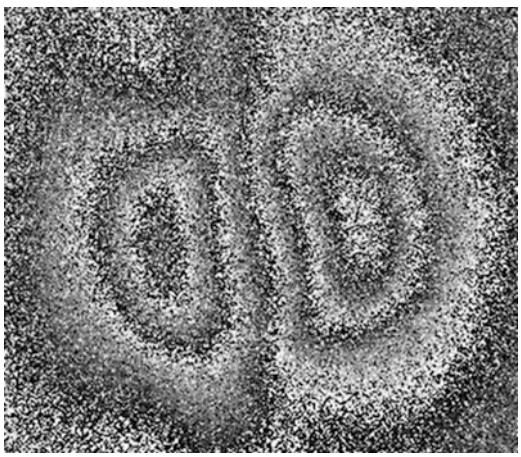

Fig. 34.7 Phase stepped fringe pattern

Fig. 34.8 Filtered equivalent of Fig. 34.7

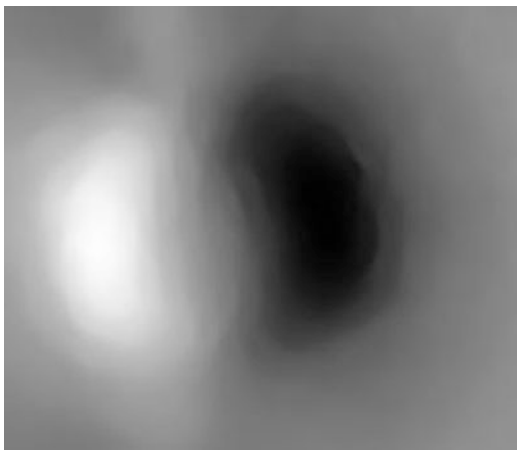

Fig. 34.9 Phase unwrapped result

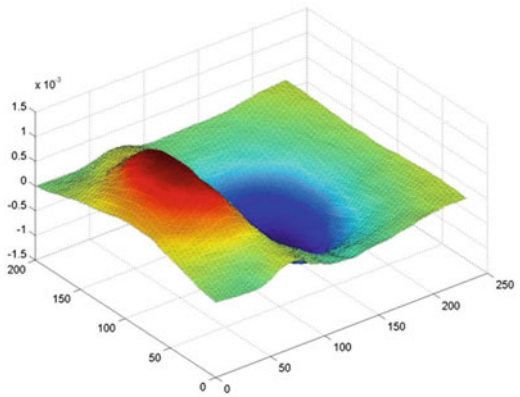

Fig. 34.10 Gradient plot of phase unwrapped result

near the laser diode, on the rear surface of the TEC and another one to measure the ambient temperature. The unit was tested for an extended duration of 70 min. The data revealed that a 0.25 °C operating temperature variation had occurred over the duration of the test. To verify the wavelength stability of the laser, the laboratory software setup was used. Since Digital Shearography reveals differences in wave fronts, this ability was used to test the laser for wavelength stability. The software was therefore set up for real-time inspection without any stresses being applied to the test panel. Instead the quality of the

final image was observed. During the running of this test, a light fringe, randomly appearing and moving across the display was observed and attributed to a gradual shift in the output wavelength of the laser module. The new laser module thus exhibited a level of wavelength drift.

34.5 Conclusion and Recommendations

The test results reveal that a low cost Digital Shearography prototype has been developed and is able to inspect components for defects. When comparing the unit with the existing laboratory unit the quality of the fringes are on par. In addition, the updated software is able to generate the fringe patterns, unwrap the results obtained and generate gradient plots of the test sample in response to the applied stress.

The laser module is of a sufficient power to illuminate the object to be tested. Additional laser modules can be utilised, should the inspection surface exhibit poor reflectivity characteristics. Unfortunately the laser did exhibit a level of wavelength drift which introduces unwanted fringes in the final fringe pattern. This aspect will have to be investigated further to determine if this is an operational warming up phenomenon, or whether the influence of the reference ambient temperature causes the laser operating temperature to drift. It is however anticipated that this aspect can be resolved.

References

1. Gryzagoridis J, Findeis D (2008) Benchmarking shearographic NDT for composites, Insight Non-Destructive Testing and Condition Monitoring 50(5):249–252
2. Hung Y (1996) Shearography for non-destructive evaluation of composite structures. Opt Lasers Eng 24(2-3 Spec ISS):161–182
3. Hung Y, Ho H (2005) Shearography: an optical measurement technique, Materials science and engineering: R: Reports, vol 49. http://www.sciencedirect.com/science/journal/0927796X
4. Hariharan P (1985) Optical interferometry. Orlando Academic Press, Sydney
5. Findeis D, Gryzagoridis J (2006) Simultaneous shearographic and thermographic NDT of aerospace materials. Insight 48(5):294–297
6. Maas A, Somers P (1997) Two-dimensional deconvolution applied to phase-stepped shearography. Opt Lasers Eng 26:351–360
7. Findeis D, Gryzagoridis J, Xaba E, Reid-Rowland D (2000) Aircraft tire inspection using portable shearography and electronic speckle pattern interferometry. Non-Destructive Testing Laboratory, University of Cape Town
8. Andhee A (2005) A novel compact shearographic NDT system, Master's thesis, University of Cape Town

Chapter 35
Local Stiffness Identification of Beams Using Shearography and Inverse Methods

F. Zastavnik, L. Pyl, J. Gu, H. Sol, M. Kersemans, and W. Van Paepegem

Abstract Shearography is an interferometric method that produces full-field displacement gradients of the inspected surface. In high-technology industry it is often used qualitatively to detect material defects, but quantitative applications are still rare. The reasons for that are the complicated calibration procedure as well as the denoising, unwrapping, the local sensitivity vector estimation and the local shearing angle estimation needed to get quantitative gradient-maps. To validate the technique and its calibration, results obtained from shearography are compared to results obtained from scanning laser vibrometry. Beams are acoustically excited to vibrate at their first resonant frequency and the mode shape is recorded using both shearography and scanning laser vibrometry. Outputs are compared and their properties discussed. Separate inverse method algorithms are developed to process the data for each method. They use the recorded mode shape information to identify the beam's local stiffness distribution. The beam's stiffness is also estimated analytically from the local geometry. The local stiffness distributions computed using these methods are compared and the results discussed.

Keywords Shearography • Inverse methods • Scanning laser vibrometry • Local stiffness identification • Euler-Bernoulli beams

35.1 Introduction

Many methods have already been proposed for the identification of uniform material properties in beam-like or plate-like specimens, based on a limited amount of observations [1]. However, if the material properties in the specimens vary from point to point, more measured observation information is needed. There are several possible experimental techniques that can be used to measure the vibrational mode shapes, and to identify the local bending stiffness distribution in test beams. Our group already proposed a technique involving data obtained from scanning laser vibrometry (SLV) [2]. In these experiments the test beams were freely suspended and the mode shapes excited acoustically. Another option for data acquisition is using shearography.

Shearography is an imaging technique based on interfering principles of coherent (laser) light. The laser scanning vibrometry produces the out-of-plane deformation as the output of the experiments. Shearography produces the gradient of the out-of-plane deformation. The used *isi-sys SE3 shearography system* [3] is intended mainly for qualitative examination, such as finding delaminations and internal defects of materials. A setup using shearography is assembled in order to identify the local bending stiffness, *EI*, of thin aluminium beams. In the measurements we conducted the shearography system is calibrated and used quantitatively. The experiment design, procedures as well as the result processing algorithm is described and discussed in the following sections.

F. Zastavnik (✉) • L. Pyl • J. Gu • H. Sol
Department Mechanics of Materials and Constructions (MeMC), Vrije Universiteit Brussel (VUB), Pleinlaan 2, 1050 Brussels, Belgium
e-mail: filip.zastavnik@vub.ac.be

M. Kersemans • W. Van Paepegem
Department Materials Science and Engineering, Universiteit Gent (UGent), Technologiepark-Zwijnaarde 903, 9052 Zwijnaarde, Belgium

H. Jin et al. (eds.), *Advancement of Optical Methods in Experimental Mechanics, Volume 3*,
Conference Proceedings of the Society for Experimental Mechanics Series,
DOI 10.1007/978-3-319-00768-7_35,

35.2 Basic Principles of Shearography

The schematic of the shearography procedure that calculates the gradient of deformation is presented in Fig. 35.1. The surface of the observed object consisting of points A, B and C is illuminated by coherent laser light. The light from two points – A_1 and C_1 – on the surface of the inspected object is guided by the shearing device onto the same point (pixel at $\{i, j\}$) of the CCD sensor. The two points A_1 and C_1 are separated by a shear distance in the x direction, δx. In the state 1, which represents the undeformed state, the two light waves coming from A_1 and C_1 are in phase. The light waves will constructively interfere and will register as a maximum intensity on the CCD. The intensity captured by the CCD camera can be evaluated back into phase difference. For the undeformed state, as illustrated in Fig. 35.1, the phase difference will be evaluated back to $\phi_1 = 0$ (in radians). When the surface is deformed – state 2 – two points A_2 and C_2 are out of phase and the CCD at that pixel will register a smaller intensity. The phase difference between A_2 and C_2 is ϕ_2. The relative phase change (in radians) is defined as $\Delta = \phi_2 - \phi_1$ and it encodes the gradient of deformation.

The gradient of deformation is calculated from relative displacements of points A and C and is valid for the point B. In the case presented in Fig. 35.1, where w is the displacement in the z direction, the displacement gradient $\partial w / \partial x$ of a point on the surface at $\{x\}$ will be encoded by the relative phase change of its neighbouring points $\{x + \delta x/2\}$ and $\{x - \delta x/2\}$. The whole surface of the inspected object is registered as a Δ-image with each point at pixel $\{i, j\}$ encoding the local gradient of deformation. In order for the point to have its gradient of deformation properly captured, it needs to have points $\{x + \delta x/2\}$ and $\{x - \delta x/2\}$ on the same surface. The edges of the scanned surface in the region $[0, \delta x/2\rangle$ do not satisfy this condition, so in the Δ-image they are not captured. The edge regions of the surface need to be estimated – linear extrapolation of the deformation is used.

The shearing distance, δx, is variable and can be set to a desired value. As the shearing distance δx is increased, keeping the deformation constant, Δ is increased, effectively increasing the sensitivity to deformations. The values of Δ are relative to the wavelength of the used light, so the value of the displacement difference will be $\lambda\ \Delta$. The gradient of deformation can be calculated as [4]

$$\frac{\partial w}{\partial x} = \frac{\lambda\, \Delta}{4\pi\, k_z\, \delta x}, \tag{35.1}$$

where k_z is the sensitivity vector, dependent on the position of the light source. The equation is valid for small δx.

To acquire deformation gradient from harmonically vibrating objects stroboscopic illumination is used. When the light pulses are synchronised with the excitation signal only the vibrations at a fixed vibration phase are observed. This effectively freezes the vibration and enables mode shape acquisition for the beams vibrating at the resonant frequency used in this paper.

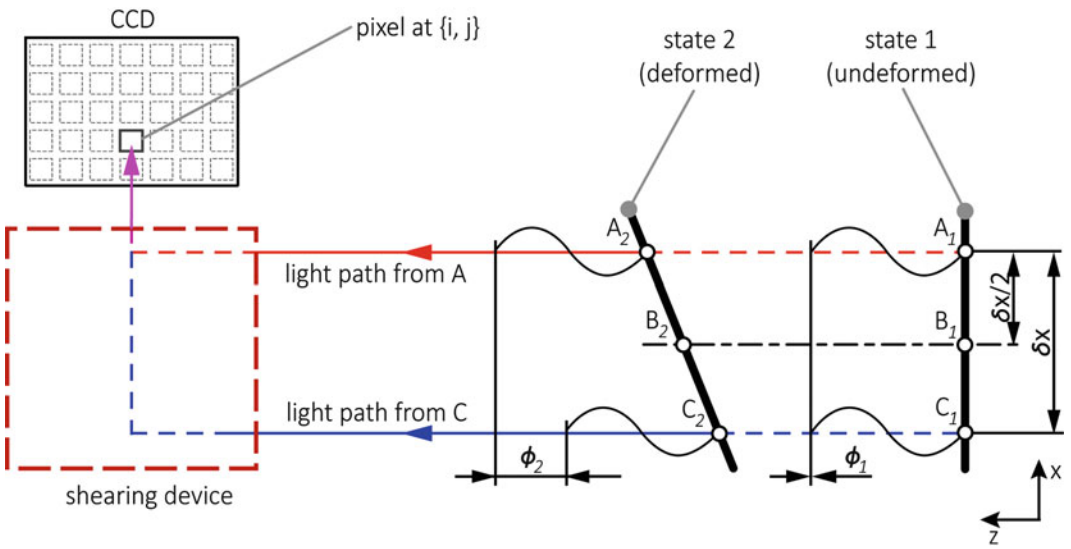

Fig. 35.1 Deformation of the observed specimen creates a phase difference

The images shearography is producing have a high amount of noise, so *image filtering* is required in post-processing. As with other interferometric optical techniques, the produced images are *wrapped* to one wave-length of the light – deformations of $w + n\,\lambda$ appear to have the same value, w. This results in the characteristic appearance of "fringes". *Unwrapping* algorithms [5] are used to remove the fringes, thus expand the maximum range of deformation the system can register. Unwrapping is the second step in the post-processing routine.

35.3 Local Stiffness Identification

The local stiffness is identified assuming the thin beam Euler-Bernoulli (EB) behaviour using both the resonance frequency and the mode shape information. The mode shapes need not to be mass normalised. The modal identification can be carried out based on the responses only. The case where the modal parameters are identified without knowing the loads exciting the system is called the modal identification of output-only systems. The method is a linear, model based, inverse method and aims the determination of the location and quantification of the beam stiffness. The use of the information contents of the first bending mode shape is adequate enough for the identification of a complete stiffness pattern.

The time independent normal differential equation of the equilibrium in an arbitrary point in the domain of a beam vibrating in resonance at a circular frequency ω neglecting damping is:

$$\frac{\mathrm{d}^2}{\mathrm{d}x^2}\left[EI(x)\frac{\mathrm{d}^2 W(x)}{\mathrm{d}x^2}\right] - \rho A(x)\,\omega^2 W(x) = 0 \tag{35.2}$$

where $W(x)$ is the arbitrary scaled modal deformation term of the associated mode shape, ρ is the density and A is the area of the beam's cross section. The product ρA is the mass per unit length of the beam and can be an arbitrary function of the independent variable x. Equation (35.2) can be seen as the differential equation of an EB-beam (see text books about strength of materials and constructions, Seed [6]) loaded statically with a distributed pressure $p(x) = \rho\ A\ \omega^2\ W(x)$. The product EI (with E being the Young's modulus and I the moment of inertia of the beam's cross section) is called the flexural beam rigidity or "stiffness" and its value can be an arbitrary function of the independent variable x. So the stiffness can be identified locally in an arbitrary small sub-domain and is therefore called "sub-domain identification". The – a priori unknown – distributed beam stiffness values EI are the parameters in a finite element model of the beam. The modal amplitudes of the first bending mode shape of the freely suspended composite test beam are the measured output values. The beam stiffness value in a small sub-domain of the test beam is iteratively tuned in such a way that the computed modal amplitudes in the sub-domain match the measured modal amplitudes. This principle comparing measured output values from an experiment on a test specimen with the computed output values of a numerical model of the same specimen loaded with the same boundary and initial values is the basic idea of an inverse method [7, 8]. The boundary conditions of a virtually isolated sub-domain must be such that they represent the action of the remaining parts of the considered domain on the boundaries of the selected sub-domain. The sub-domain can be hence isolated without changing the stress state conditions in arbitrary points of the sub-domain. The beam stiffness will be identified or *scanned* in an arbitrary number of beam sub-domains which are sufficiently small to assume constant flexural rigidity EI and constant mass per unit length ρA. The beam sub-domain is in each of the two boundary points x_k and x_l subjected to prescribed transversal displacements $\overline{W}_k$ and $\overline{W}_l$ as Dirichlet boundary conditions and prescribed bending moments $\overline{M}_k$ and $\overline{M}_l$ as Von Neumann boundary conditions.

Equation (35.2) can be transformed into an equivalent integral formulation having the same solution for the dependent variable $W(x)$. By using the weighted residual method with a virtual displacement field $\delta V\,(x)$ as weighting function for the differential equation, and V_k and V_l as arbitrary weighting scalars for the Von Neumann boundary conditions, the integral formulation over the sub domain (x_k, x_l) is:

$$EI\int_{x_k}^{x_l}\frac{\mathrm{d}^2 W}{\mathrm{d}x^2}\frac{\mathrm{d}^2\delta V}{\mathrm{d}x^2}\,\mathrm{d}x = \rho A\,\omega^2\int_{x_k}^{x_l} W\,\delta V\,\mathrm{d}x + \overline{M}_k\frac{\mathrm{d}^2\delta V}{\mathrm{d}x^2}(x_k) - \overline{M}_l\frac{\mathrm{d}^2\delta V}{\mathrm{d}x^2}(x_l) \tag{35.3}$$

The transversal displacement amplitude $W(x)$ of the modal deformation of the first mode shape is expressed in a finite element approximation as a linear combination of Lagrange shape functions $N_i(x)$ multiplied with W_i, the value of $W(x)$ in the node i. The latter is one of the M nodal points of a regular grid in which the beam sub-domain (x_k, x_l) is divided into.

Only the transversal displacement amplitude $W(x)$ is taken as a degree of freedom in the finite element formulation. This is possible because, unlike in traditional beam finite element formulations, slope continuity is not required as the beam sub-domains are not assembled and thus the derivative of $W(x)$ is redundant.

Using the same interpolation functions N_i to express the virtual field δV and replacing the Cartesian coordinate x by a local homogenized coordinate ξ, having values in the range $(-1, +1)$ in the considered sub-domain, an expression can be obtained which allows to evaluate the stiffness EI as a function of W_i, boundary conditions and known beam parameters:

$$EI = \frac{\rho A \omega^2 L^{e4} B_{ij} W_i W_j + 4L^{e2}\overline{M}_1 W_i \frac{\mathrm{d}N_i}{\mathrm{d}\xi}(-1) - 4L^{e2}\overline{M}_M W_i \frac{\mathrm{d}N_i}{\mathrm{d}\xi}(1)}{16 A_{ij} W_i W_j} \tag{35.4}$$

with

$$A_{ij} = \int_{-1}^{1} \frac{\mathrm{d}^2 N_i}{\mathrm{d}\xi^2} \frac{\mathrm{d}^2 N_i}{\mathrm{d}\xi^2} \, \mathrm{d}\xi,$$

$$B_{ij} = \int_{-1}^{1} N_i N_j \, \mathrm{d}\xi \, ,$$

$$i = 2, 3 \ldots M - 1,$$

$$j = 1, 2 \ldots M$$

and L_e being the length of the considered beam sub domain.

The transversal displacement amplitude W_i is assumed to be measured in all the interior points $i = \{2, M-1\}$ of the selected beam sub domain. Thus the evaluation of equation (35.4) requires in addition the values $\overline{M}_1$ and $\overline{M}_M$ and W_1 and W_M at the boundaries of the sub-domain. The reduction elements $Q(x)$, the transverse shear force at position x, and $M(x)$, the bending moment at position x, can be derived starting from the knowledge of the resonance frequency and the associated mode shape $W(x)$. In case of a free-free beam with length L, the transverse shear force and the bending moment value are zero at the beam boundaries $x = 0$ and $x = L$. Physically this means that a beam element is considered with known boundary conditions W and M and that the value EI in the finite element is tuned such that the computed interior values of W match the measured values. The measurement techniques are discussed in the next paragraph.

35.4 Experimental Setup

Aluminium beams are selected for experiments. The tested beams are flat beams with constant thickness of 4 mm, 220 mm long and 25 mm wide. The aluminium used has a Young's modulus $E = 69$ GPa, making the first resonant frequency of the beams $f_1 = 427.5$ Hz.

In order to obtain good results from shearography, the observed surface needs to be diffusely reflective. Diffusely reflective (optically rough) surfaces scatter light upon reflection while specularly reflective surfaces (e.g. polished metals and mirrors) reflect light in a single direction. Tested aluminium beams are sprayed with a thin coating of white powder due to their specularly reflective surface. The thickness of the coating is 20–30 μm and it is adhering well to the surface – it will not affect the stiffness of the beam nor will it mass-load it.

The bending stiffness of the test beam is calculated from the observations of the mode shape of its first resonant mode. In order to induce the mode shape the beams are excited acoustically. During the experiment a beam is suspended from a stiff frame, by two fine cotton threads at the nodal points – this approaches a free-free boundary condition. Beams were noticed to be swaying back-and-forth during experiments which was disturbing the shearographic image acquisition. The tested beam is thus additionally rested against two pins at the nodal points, stopping the beam swaying (Fig. 35.2). Resting of the beam does not interfere with the free-free boundary condition.

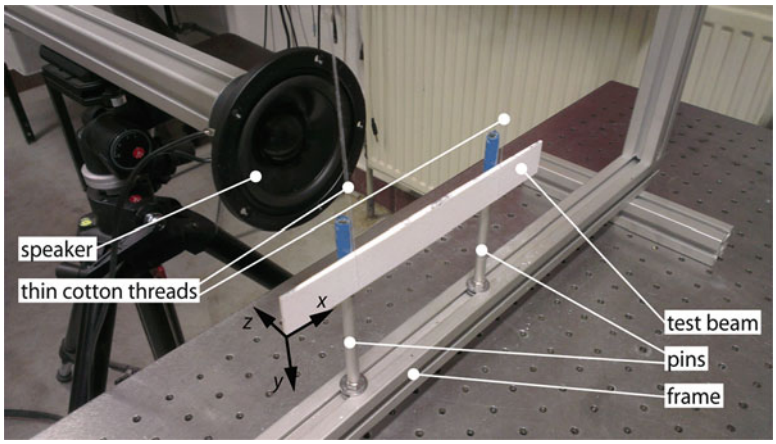

Fig. 35.2 Close-up on the beam hanging at nodal points

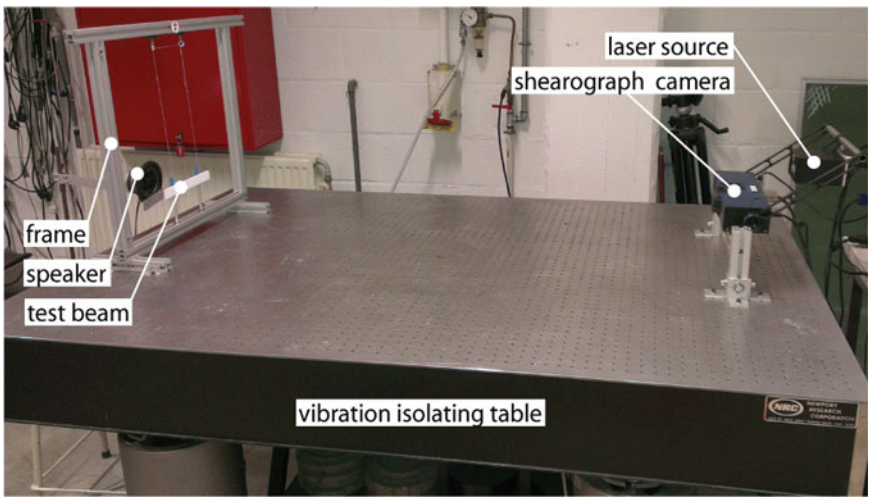

Fig. 35.3 Frame and shearography camera are mounted on a vibration-isolating table

The coordinate system defines x as the horizontal direction in the shearography images, and the beams are precisely placed so that it also aligns to the beam's direction of length. y is the image's vertical direction, and the beam's width direction. z is defined as the out-of-plane direction, in the direction of the camera. Displacements of the surface are defined as u, v and w – in the x, y and z direction respectively (Fig. 35.2).

Since shearography is developed to operate on μm scale deformations, outside influences, such as vibrations and air-flow, can disturb the imaging and produce deterioration of the quality of the images. Keeping the setup on a vibration-isolating table dramatically improves the signal-to-noise ratio in the images. The vibration-isolating table is pneumatically actuated – it is connected to a source of compressed air, damps any environmental vibrations and keeps the table's surface level, Fig. 35.3. The acoustic excitation device is placed outside of the table in order not to induce unwanted vibrations.

The resulting data is produced in the form of an image (Fig. 35.4a) which values are proportional to the gradient of out-of-plane deformation of the surface, $\partial w / \partial x$. The shearography camera is placed at 1,420 mm distance from the AL beams in order to be able to capture the whole beam's length within its field-of-view. The camera is able to capture images with a resolution of 1, 392 $\times$1, 040 pixels.

35.5 Results and Comparison to the Scanning Laser Vibrometry

Shearography is compared to scanning laser vibrometry (SLV). A Polytec Scanning Vibrometer is using a laser beam to measure the response of the beam to the excitation signal. The SLV is a full-field system for automated vibration measurement, mapping, visualization and analysis. It measures the modal amplitudes point by point in a scanning mode. The Polytec Scanning Vibrometer software version 8.7.3.0 is used to analyse the signal.

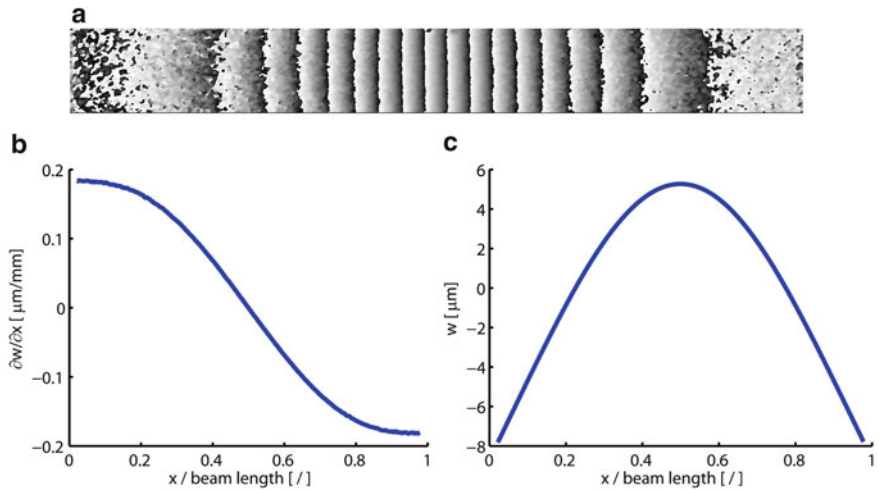

Fig. 35.4 The Δ-image of the vibrating beam (**a**) is filtered and unwrapped. Using Eq. (35.1) the gradient of deformation (**b**) is calculated. Mode shape (**c**) is integrated from the gradient

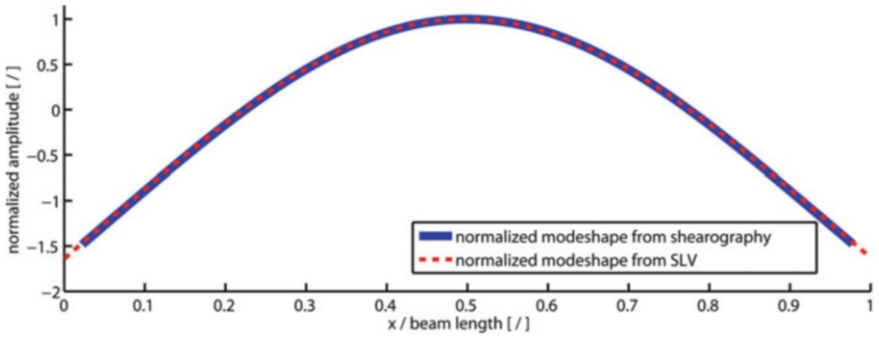

Fig. 35.5 The mode shape amplitudes from shearography and SLV overlap completely

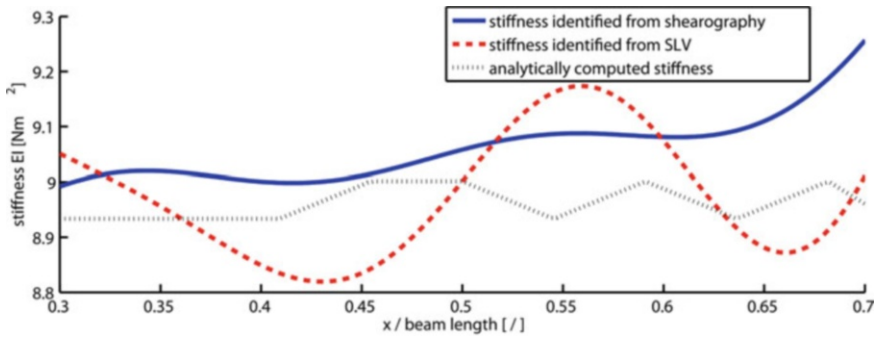

Fig. 35.6 Identified stiffness has a relative error compared to the analytical value up to 3. 3 % for shearography and up to 2. 5 % for SLV, in the range (0. 3, 0. 7) of beam's length

The mode shape acquired from shearography and the SLV are compared in the Fig. 35.5. The mode shapes show nearly identical values. For the purpose described here, the main difference between the two acquisition methods is in the time needed for a single scan. A scan with the SLV takes approximately 6 min, while a shearography image is acquired in 2–3 s. The scan with SLV was done at 360 points on the length of the beam while the shearography has data point at every pixel of the sensor – in the case presented here 1,200 points. For larger beams and for plate specimens long scanning with SLV can become an issue, since it scales with number of scan points. The shearography scan takes the same time no matter the size of the specimen. The shearography image however, does not include the region of the edges of the object of $\delta x/2$, typically in the range 2–5 mm. The data for this edge region can be extrapolated since there is nearly no curvature at the extreme ends and thus this region does not carry useful information for the identification.

From the mode shapes acquired from shearography and the SLV (Fig. 35.5), the stiffness EI is identified using the described inverse algorithm. The edges of the beam have a low curvature, $\partial^2 w/\partial x^2$, so they carry insufficient information for accurate identification. In the region (0. 3, 0. 7) of the beam's length, the identification gives best results so this region is presented in Fig. 35.6. The stiffness is compared to the analytical stiffness EI, computed from the known longitudinal

stiffness E and by accurately measuring the beam's thickness, thereby computing the moment of inertia of the beam's cross section I. The analytical EI cannot be considered completely accurate, since the surface roughness doesn't allow for an accurate measurement of the thickness.

All the methods presented here to identify the local beam stiffness, the inverse identification from the shearography and the SLV scans, and the analytical computation, show very good agreement. In the region of interest, the range (0. 3, 0. 7) of beam's length, the maximal relative error is 3. 3 % for sherography and 2. 5 % for SLV.

35.6 Conclusion

The mode shapes of aluminium beams have been successfully scanned with both shearography and the scanning laser vibrometry (SLV). The mode shapes scanned with both methods show very low noise levels at μm-scale vibrations. The shearography acquires the mode shape in higher resolution then the SLV, and a single scan is done faster.

It is shown that using high-resolution scans of mode shapes, stiffness EI can be identified accurately. Both methods used for scanning, shearography and SLV, show comparably accurate results. In the future the identification will be expanded to more complex geometries of beams and to plate-like structures.

Acknowledgements Part of this research has been sponsored by FWO – the Fund for scientific research of Flanders, Belgium.

References

1. Sol H, Guillaume P (2002) Damage scanning of beams using mode shape information. Technical report
2. Pyl L, Sol H, Zastavnik F, Gu J, Paepegem WV, Kersemans M (2012) Damage identification of prepreg composites subject to accelerated fatigue tests. In: 10th international conference on durability of composites systems (DURACOSYS), Brussels, no i, pp 1–10
3. Maeckel P (2010) Non destructive testing by shearography/Vibrography on wind turbine blade structures. Technical report 49(1):1–32
4. Steinchen W, Yang L (2003) Digital shearography: theory and application of digital speckle pattern shearing interferometry. SPIE, Bellingham
5. Ghiglia DC, Pritt MD (1998) Two-dimensional phase unwrapping: theory, algorithms, and software. Wiley-Interscience, New York
6. Seed G (2000) Strength of materials. Saxe Coburg Publications, Edinburgh
7. Sol H, Oomens C (1997) Material identification using mixed numerical experimental methods. In: Proceedings of the Euromech colloquium, Kerkrade
8. Friswell M, Mottershead J (1999) Finite element updating in structural dynamics. Kluwer, Dordrecht

Chapter 36
Long-Term Effects of Cyclic Environmental Conditions on Paintings in Museum Exhibition by Laser Shearography

Morteza Khaleghi, Ivo Dobrev, Ellery Harrington, Philip Klausmeyer, Matthew Cushman, and Cosme Furlong

Abstract To better evaluate current condition standards commonly used for the exhibition of canvas paintings, it is necessary to have a quantitative technique capable of measuring degradation components induced by changes in temperature and relative humidity, as well as the effects of ambient vibration and the thermomechanical effects of museum lighting. This paper presents advances in our development of a customized laser shearography system for temporal characterization of in-plane displacements of canvas paintings when subjected to changes in exhibition conditions. The shearography system performs concomitant measurements of gradients of displacement along two orthogonal shearing directions and is synchronized with a thermal IR camera to provide thermal maps of the area being analyzed. Recent innovations incorporated into the system include a real-time temporal phase unwrapping algorithm, and high-resolution Fast Fourier Transform (FFT) methods to calibrate applied shearing levels that allow a wide range of measuring resolutions. Examples will be presented that illustrate the system's capabilities to detect cracks in the paint surface and measure and map associated strain vectors as a function of changes in condition parameters. Included are representative results of continuous 30 h recordings on American nineteenth century oil on canvas painting. Multi-domain data has been combined and correlated using the shearography and IR data from our system, temperature and humidity data from the museum's climate control system, as well as activity log from museum's security system.

Keywords Shearography • Gradients of displacement • Temporal phase unwrapping • Mapping cracks in painting

36.1 Introduction

On exposure to light, pigments of paintings can fade, or, in certain cases, darken. Light has an effect on the paint binding medium, particularly for oil paints which will darken, and on surface varnishes, which also discolor over time. Temperature changes and high and low temperatures are generally less damaging than changes in relative humidity or increases in light level [1]. However, artificially-induced temperature changes without accompanying humidification or dehumidification result in a shift of relative humidity in the air of an exhibition room, and should therefore be avoided. For a better understanding of these phenomena and in order to visualize and quantify how changes in temperature and humidity effect on painting, quantitative techniques are needed to characterize long-term thermomechanical effects of cyclic environmental conditions of the museum. This paper presents advances in the development of a real-time shearography-based defect detection system to quantify the effects of light and humidity on canvas paintings. Some unique characteristics of the shearography system include being portable, making concomitant measurements of temperature variations, and measuring the gradient of displacements in two orthogonal axes as well as presenting measurement results in real-time [2].

M. Khaleghi (✉) • I. Dobrev • E. Harrington • C. Furlong
Center for Holographic Studies and Laser micro-mechaTronics (CHSLT), Worcester Polytechnic Institute, Worcester, USA

Mechanical Engineering Department, Worcester Polytechnic Institute, Worcester, MA 01609, USA
e-mail: mkm@wpi.edu

P. Klausmeyer • M. Cushman
Worcester Art Museum, Worcester, MA 01609, USA

H. Jin et al. (eds.), *Advancement of Optical Methods in Experimental Mechanics, Volume 3*,
Conference Proceedings of the Society for Experimental Mechanics Series,
DOI 10.1007/978-3-319-00768-7_36,

36.2 Methods

36.2.1 Theoretical Background of Shearography

In shearography, an optically rough surface is illuminated by an expanded laser beam forming a speckle pattern [3]. This speckle pattern is optically mixed with an identical but displaced, or sheared, speckle pattern to form a speckle interferogram, which can be recorded by a CCD camera. The image shearing may be achieved by using, for example, a Michelson interferometer with one tilted mirror, as shown in Fig. 36.1. Shearography is sensitive to displacement gradients that are determined by the sensitivity vector, which is the bisector of the illumination and viewing direction vectors, and the direction and magnitude of applied shear. The measuring sensitivity is adjustable by changing the magnitude of shear applied by the shearing element in the interferometer.

If surface of interest undergoes deformation, the optical pathlength of the incident light changes and optical phase difference due to this deformation is characterized by fringe-locus function, $\Omega(x, y)$ [4]. For near parallel illumination-observation conditions, out-of-plane gradient of displacement along horizontal and vertical axes are calculated by Eqs. 36.1 and 36.2, respectively [2].

$$\frac{\delta w}{\delta x} = \frac{\lambda \Omega}{4\pi \Delta x}, \tag{36.1}$$

$$\frac{\delta w}{\delta y} = \frac{\lambda \Omega}{4\pi \Delta y}, \tag{36.2}$$

where Ω is the fringe-locus function, λ is the laser wavelength, and Δx and Δy are the magnitude of the shear in horizontal and vertical axes, respectively. These two gradients of displacement are part of the strain tensor S, shown in Eq. 36.3, which is composed of nine components: six surface strain displacement gradient components and three bulk strain components. Shearography is able to measure all the surface strain components but is not able to measure the bulk strain components, $\frac{\delta u}{\delta x}$, $\frac{\delta v}{\delta y}$ and $\frac{\delta w}{\delta z}$ [5]. Our shearography setup can measure the out-of-plane gradients of displacement $\frac{\delta w}{\delta x}$ and $\frac{\delta w}{\delta y}$, by using Eqs. 36.1 and 36.2.

$$S = \begin{bmatrix} \frac{\delta u}{\delta x} & \frac{1}{2}\left(\frac{\delta u}{\delta y} + \frac{\delta v}{\delta x}\right) & \frac{1}{2}\left(\frac{\delta u}{\delta z} + \frac{\delta w}{\delta x}\right) \\ \frac{1}{2}\left(\frac{\delta u}{\delta y} + \frac{\delta v}{\delta x}\right) & \frac{\delta v}{\delta y} & \frac{1}{2}\left(\frac{\delta v}{\delta z} + \frac{\delta w}{\delta y}\right) \\ \frac{1}{2}\left(\frac{\delta u}{\delta z} + \frac{\delta w}{\delta x}\right) & \frac{1}{2}\left(\frac{\delta v}{\delta z} + \frac{\delta w}{\delta y}\right) & \frac{\delta w}{\delta z} \end{bmatrix}. \tag{36.3}$$

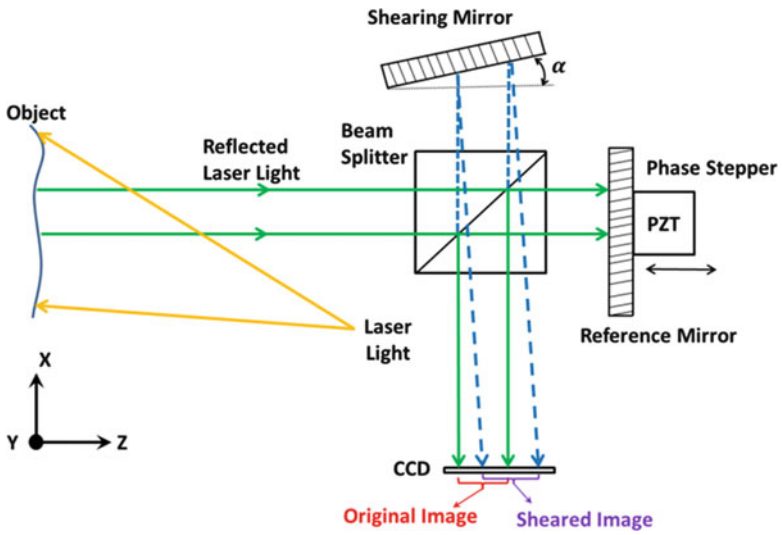

Fig. 36.1 Schematic of the optical configuration of one of the shearography systems under development [2, 4]

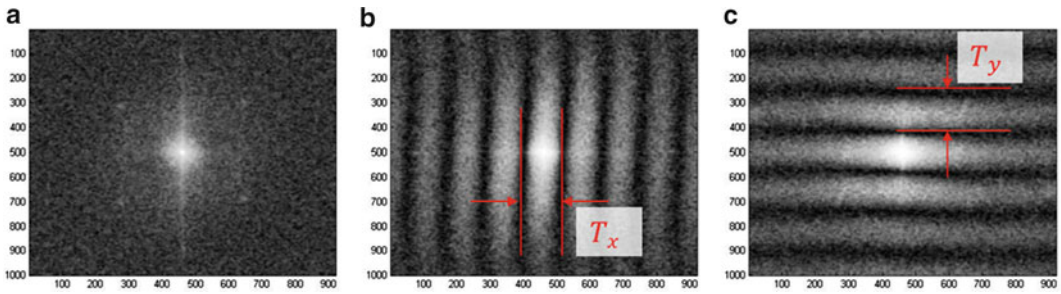

Fig. 36.2 Application of FFT algorithm to measure the amount of shear: (**a**) FFT power spectrum of the image of the painting without shear; (**b**) FFT power spectrum of the image of the painting with shear in horizontal direction; and (**c**) FFT power spectrum of the image of the painting with shear in vertical

36.2.2 Shear Estimation by FFT Algorithm

The sensitivity of the system is highly affected by the amount of shear. In order to determine the amount of shear, an FFT-based algorithm [2] is developed which is based on shift theorem of Fourier Transform (FT). If the FFT of the original image,$a(x, y)$, is defined by$A(\xi, \eta)$, therefore, based on the shift theorem, the FFT of the sheared image, $b(x, y) = a(x - \Delta x, y - \Delta y)$, is calculated by

$$B(\xi, \eta) = e^{-i2\pi(\xi\Delta x + \eta\Delta y)} A(\xi, \eta). \tag{36.4}$$

Also, the FFT of the superposed image, $c(x, y) = a(x, y) + a(x - \Delta x, y - \Delta y)$, is calculated by

$$C(\xi, \eta) = \left[1 + e^{-i2\pi(\xi\Delta x + \eta\Delta y)}\right] A(\xi, \eta). \tag{36.5}$$

Magnitudes of shear along horizontal and vertical directions are approximated by Eqs. 36.6 and 36.7, respectively.

$$\Delta x \approx p_x m_0, \tag{36.6}$$

$$\Delta y \approx p_y n_0, \tag{36.7}$$

where p_x and p_y are the width and height of each pixel of the CCD sensor and m_0 and $n_0$are the equivalent amount of shear in pixel number. In our measurements, p_x and $p_y$are equal. By discretization of the obtained spectra in the frequency domain, Eq. 36.5 can be rewritten as

$$C(k, l) = \left[1 + e^{-i2\pi\left(k\frac{m_0}{M} + l\frac{n_0}{N}\right)}\right] A(k, l), \tag{36.8}$$

where M and N are the spatial resolution of the CCD sensor, $\xi = \frac{k}{Mp_x}$ and $\eta = \frac{l}{Np_y}$ are discretized units in frequency domain, and k and l are the corresponding discrete variables. The spatial frequency of the spectrogram of Eq. 36.8 is

$$f_x = \frac{m_0}{M}. \tag{36.9}$$

Therefore, by combining Eqs. 36.6 and 36.9, the amount of shear is calculated by Eq. 36.10

$$\Delta x \approx p_x \frac{M}{T_x}. \tag{36.10}$$

The same solution is applicable to calculate amount of shear along y-axis. T_x and T_y are calculated with a custom algorithm that detects the period of the modulated pattern of the spectrogram as shown in Fig. 36.2.

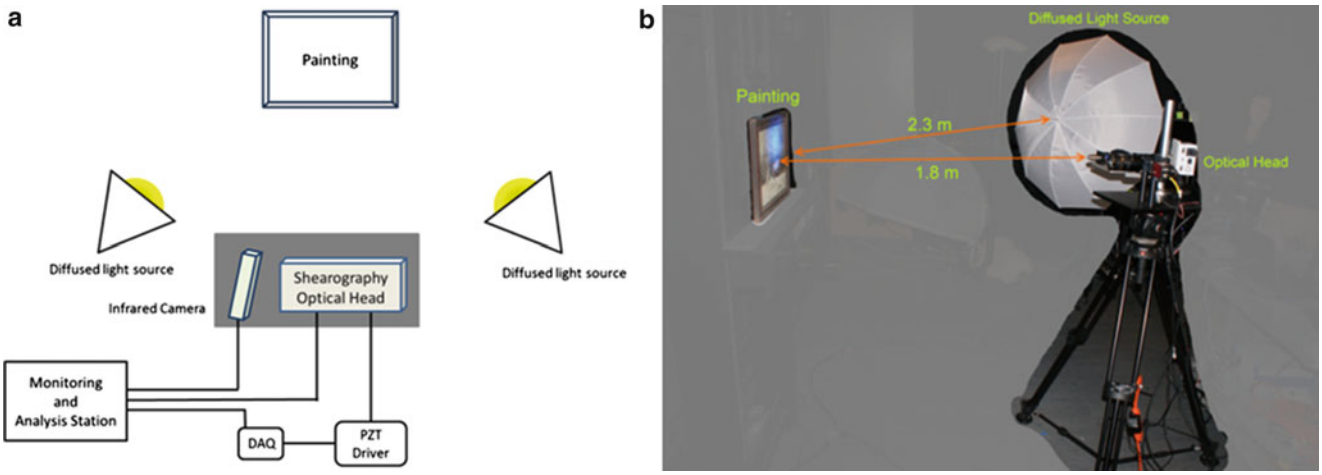

Fig. 36.3 Overall view of the shearography system: (**a**) schematic of the entire arrangement; and (**b**) system deployed in the conservation department of the Worcester Art Museum [6]

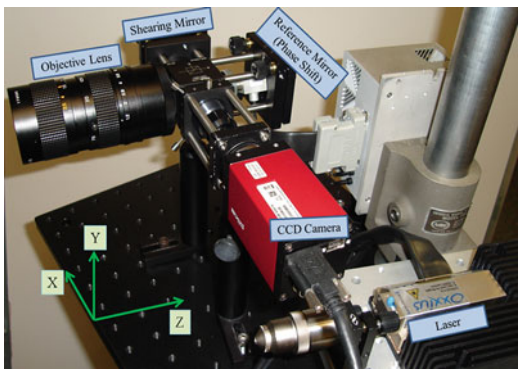

Fig. 36.4 Detailed view of the optical head including a solid-state laser, and a Michelson interferometer

36.2.3 Experimental Investigations

Schematic view of our shearography system is shown in Fig. 36.3. As shown in Fig. 36.3a, the system consists of a shearography optical head, a piezo driver for phase shifting, data acquisition (DAQ), an infrared camera to monitor the temperature variations during the experiments, a computer to monitor, analyze, and implement the amount of shear, thermal loads, and the object under investigation. Figure 36.3b illustrates the use of the shearography system as set up in the conservation department of the Worcester Art Museum [6]. Thermal loading was induced by means of two diffused light sources, each at 2.3 m away and 45° to the surface of the painting. The optical head was located at a working distance of 1.8 m from the painting. The conditions resemble those that occur during a typical photographic documentation setup.

Figure 36.4 illustrates a detailed view of the optical head that utilizes a continuous solid-state laser with the wavelength of 473 nm and power of 50 mW to illuminate the object of interest. Beam splitter with a ratio of 50:50 is used in a Michelson interferometer.

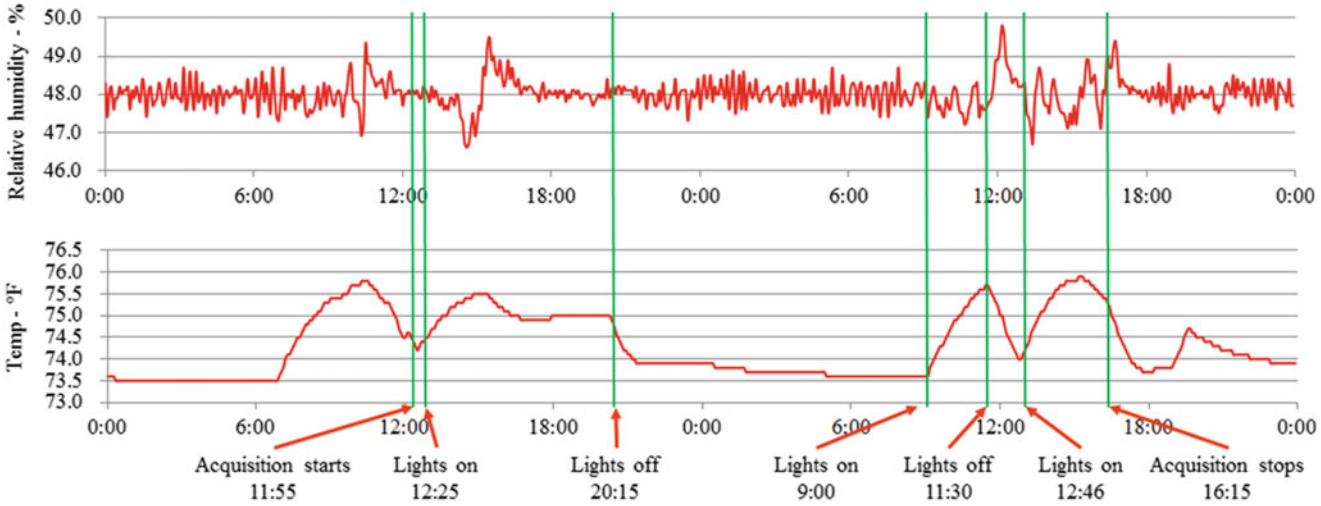

Fig. 36.5 Graphs of the temporal variation of the relative humidity and temperature over a span of 48 h. Based on the museum's security log significant events and their time of occurrence are marked by vertical lines

36.3 Results

Measurements were continuously performed for 30 h on an American nineteenth century oil on canvas painting. In order to isolate random vibrations, padding materials were placed behind the painting to stabilize the painting. During the experiments and every 5 min, museum temperature and humidity percentage were recorded, and the data showed a temperature variations of 2.4 °F (73.5–75.9 °F), while the humidity variations was 3.2 % (46.6–49.8 %). Figure 36.5 shows temperature and humidity variations for 48 h.

Figure 36.6 shows some representative results of the post-processed data. The system is set to capture and record an interferogram every 10 s. All the data are analyzed and compared with respect to the first interferogram in which all the lights were off. An interesting phenomenon is represented in Fig. 36.6d that corresponds to the data that were captured in the second day, just before the museum lights came on. As shown in Fig. 36.6d, there are some activities at this interferogram, in particular at the left side of the image, that indicate relative change in other environmental conditions of the museum.

36.4 Conclusions

In this paper, we presented a shearography system currently under development and its application in quantifying light-induced strain on canvas paintings. To control the sensitivity of the measuring system, we have developed an FFT-based shear estimation algorithm to evaluate and implement suitable amount of shear in real-time. The preliminary results show that paintings are suffering thermal cyclic loading by turning the museum's environmental conditions on an off, every day, at the starting and finishing time of the museum working hours. These cyclic loading may expedite thermomechanical fatigue on the surface of the painting. Therefore, the lighting and environmental conditions of the museum should be accurately selected.

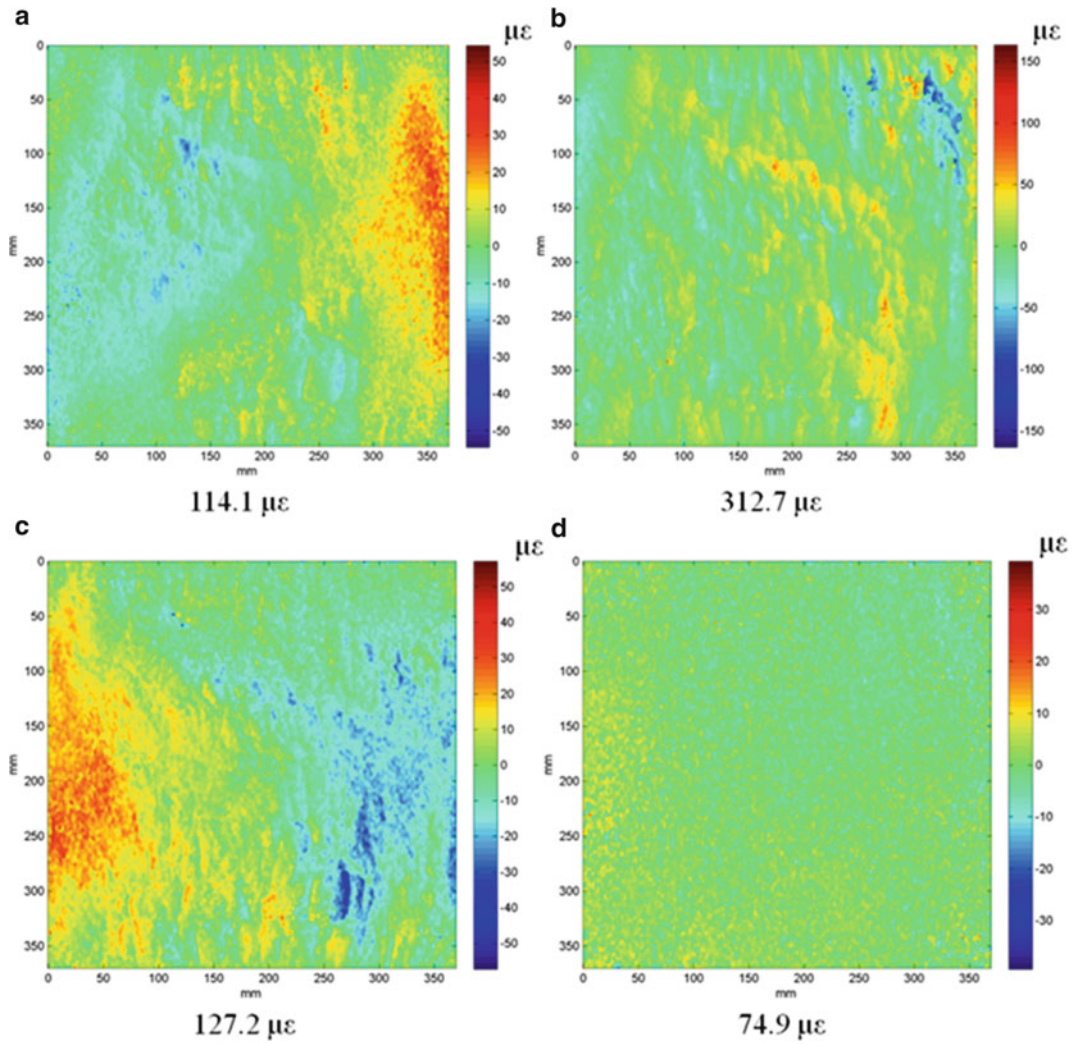

Fig. 36.6 Gradients of displacement at different times of the 30 h shearographic data: (**a**) 10 s after lights have been turned on at 12:25 on day 1 of the experiment; (**b**) 30 s after lights have been turned on at 12:25 on day 1; (**c**) 10 s after lights have been turned off at 20:15 on day1; (**d**) 10 s before lights are turned on at 9:00 on day 2

References

1. National Gallery of London (2013) website http://www.nationalgallery.org.uk/paintings/caring-for-the-paintings/paintings-and-their-environment/*/viewPage/4
2. Meybodi MK, Dobrev I, Klausmeyer P, Harrington E, Furlong C (2012) Investigation of thermomechanical effects of lighting conditions on canvas paintings by laser shearography. In: Proceeding SPIE, vol 8494, Interferometry XVI: Applications, 84940A. doi:10.1117/12.958089
3. Kreis T (2005) Handbook of holographic interferometry: optical and digital methods. Wiley, Weinheim, pp 243–255
4. Pryputniewicz RJ (1992) Electronic shearography and electronic holography working side by side. Proc SPIE 1821:27–37
5. Groves RM, James WS, Tatam RP (2004) Shape and slope measurement by source displacement in shearography. Opt Lasers Eng 41:621–634
6. Worcester Art Museum (2013) Worcester. http://www.worcesterart.org

Chapter 37
First Application of a New Optical Rosette for Strain Measurements

Liang Wang, Keyu Li, and Salahaddin Sanusei

Abstract Interferometric strain/slope rosette technique is an optical technique based on laser interferometric. It has advantages such as short gage length, non-contacting, thermal resistant, measuring both in-plane strains and out-of-plane deformations' slopes simultaneously. Six-faced delta rosette has been always utilized. In this paper, a new type of rosette, the eight-faced rectangular rosette was first applied. Besides the advantages described above, the new rosette has the advantage for measuring strains/slopes directly in two orthogonal directions. This avoids the strain transformation process which was generally required by the delta rosette. Also, since the rectangular rosette measures strains directly along the two objective directions instead of measuring in the direction with an angle, higher sensitivity will be achieved. Two preliminary tests using the new rosette were presented in this paper. First, it was adapt to measure strains in a compression test of an aluminum block at each loading step. Resistance strain gage rosette was also applied for evaluating the result. Second, the new rosette was introduced for measuring the real time strain during an arc welding process. Strain history during the welding process was successfully obtained and compared well with results using delta rosettes.

Keywords Laser interference • Optical rosette • Strain • Strain transformation • Welding strain

37.1 Introduction

Strain, by its definition in engineering, is the deformation of a body in a given direction divided by the original length in that direction, usually due to the application of external forces [1]. Researchers have worked for centuries in the attempt to measure strain accurately. From the measurement principal perspective, strain measurement techniques can be divided into four categories such as mechanical, electrical, optical and acoustical methods.

Interferometric Strain/Slope Rosette (ISSR) technique is one laser based optical method for measuring in-plane strains and out-of-plane displacements' slopes simultaneously. The precursor of the ISSR technique, the Interferometric Strain Gage (ISG), was first introduced by Sharpe in 1968 [2, 3], which measures in-plane strains by measuring the optical fringe pattern motion. The fringe pattern was produced by the interference of laser beams reflected from two grooves on a polished specimen surface. By introducing the fringe pattern from illuminating the six-faced shallow indentations by a laser beam, the ISG was further developed to the ISSR technique [4–6]. Following same idea of resistance strain rosette (RSR), three pairs of indentations have been used to form the delta interferometric strain rosette for measuring strains in three directions. In addition, multiple indentations (more than three) were applied to form certain multi-ISSR rosettes for measuring strains, slopes and rigid body motions [7]. Compared with the conventional RSR method, both the ISG and ISSR techniques show the advantages such as short gage length (~ 100 μm), non-contacting, high sensitivity and resolution and applicable at high temperature.

The idea of both the delta and rectangular rosettes was proposed in [4]. However, only delta rosette formed by three six-faced indentations has been introduced for measuring strains. No tests have been done using the rectangular rosette, which requires three eight-faced indentations. In this paper, the first application of the rectangular ISSR is presented.

L. Wang (✉) • K. Li • S. Sanusei
Department of Mechanical Engineering, Oakland University, Rochester, MI 49309, USA
e-mail: Lwang@oakland.edu

H. Jin et al. (eds.), *Advancement of Optical Methods in Experimental Mechanics, Volume 3*,
Conference Proceedings of the Society for Experimental Mechanics Series,
DOI 10.1007/978-3-319-00768-7_37,

To make it work, modifications of the delta rosette ISSR system have been accomplished such as introduction of eight-faced indentations, test set up, and data acquisition software. For verifying the new optical rosette, both the RSR and rectangular ISSR were installed in a compression test to measure two orthogonal strains versus loading step. After that, the rectangular ISSR was introduced for measuring the real time strains during an arc welding process.

37.2 Principal of Eight-Faced Rectangular ISSR

For a single indentation illuminated under an incident laser, each facet on the indentation will reflect and diffract the laser beam. However, no interfernce will occur unless there are two laser beams meet each other in the same direction. This leads to the invention of the ISG method, whose principle is to relate the strain to the shift of the interfenence pattern created by two grooves. In order to measure three in-plane strains, three indentations formed into rosettes as shown in Fig. 37.1a, b were invented and named as delta and rectangular ISSR, respectively. For both rosettes, each pair of indentations acts like a two-point source generating a pair of Young's interference fringe pattern when illuminated under an incident laser. Therefore, for the rectangular rosette, there will be three linear interference patterens, as shown in Fig. 37.2, introduced by three pairs of parallel facets. When the three patterns are captured by the optical sensor, they overlay together forming the bright-dark fringe pattern shown in Fig. 37.3. For the rectangualr rosette, the three indentations form three gages, which measure the in-plane strains along 0°, 90°, and 45° gage directions. In the 135° direction, although there will be also three interference patterns. However, because there is no pair of facets are in the same line along the 135° direction, no gage is built to correlate fringe shift to the distance change between the facets.

When the material is deformed, the distance between each indentation will change which leads to the shift of the interference fringe pattern. Assuming the original distance between two indentations shown in Fig. 37.1a is d_1 known as the gage length, and the incremental distance change between the two indentations is Δd, the incremental strain is then calculated as

$$\Delta\varepsilon = \frac{\Delta d}{d_1}. \tag{37.1}$$

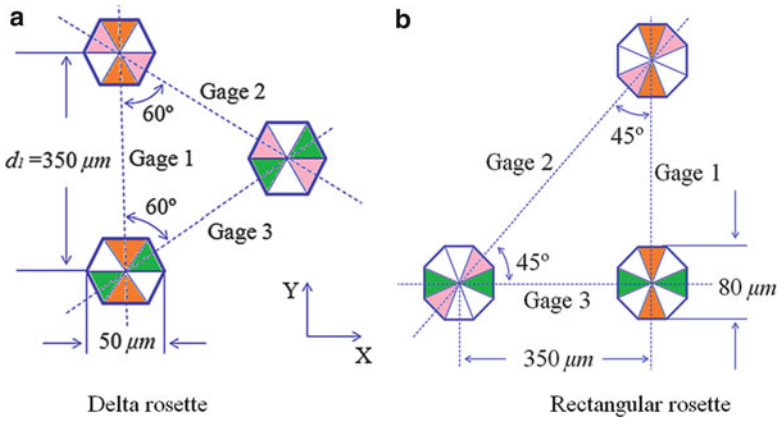

Fig. 37.1 Schematic of delta rosette and rectangular rosette (gages were formed by facets in same color)

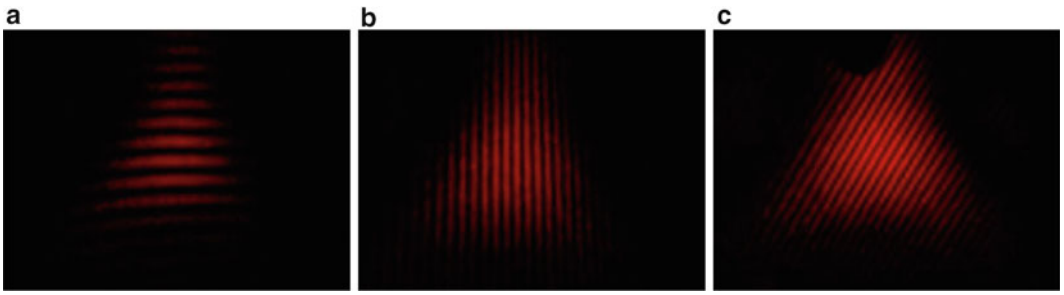

Fig. 37.2 Linear interference fringes formed by faces (**a**) in 0°direction (**b**) 90° direction (**c**) 45° direction

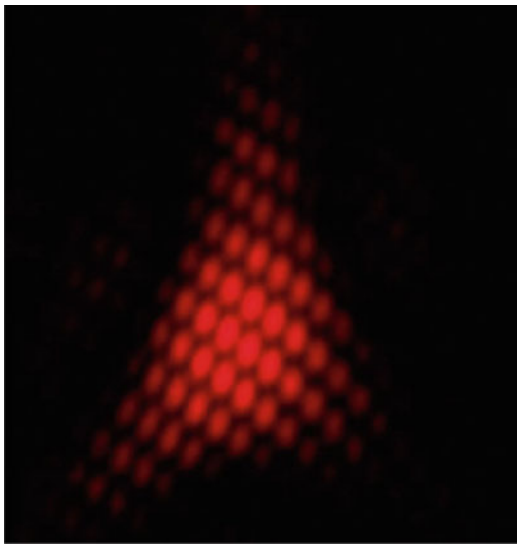

Fig. 37.3 The overlaped fringe captured at the optical sensor

From the optical perspective, the distance change Δd between the two indentations leads to the path difference change between the two laser beams, which relates to the fringe shift by [2]

$$\Delta PD = \Delta F \times \lambda. \tag{37.2}$$

Where ΔPD is the optical path difference between the two laser beams from the two indentation facets, ΔF is the fringe shift and λ is the wavelength of the laser. During the experiments, the fringe shift of each interference pattern is captured by linear photodiode. The path difference, which can be determined by sketching the optical transmitting path, is derived relating to the Δd and out-of-plane displacement Δw [6]:

$$\Delta PD = \Delta d \sin\theta + \Delta w(1 + \cos\theta). \tag{37.3}$$

Where θ is twice the inclination angle of the facet and it is approximately 42° for indentations used in this paper. There are two unknowns, Δd and Δw, in Eq. 37.3, two equations are needed to solve for the solutions. Therefore, two fringe pattern shifts from two opposite facets in each gage direction as shown in same color in Fig. 37.1 are used. Assuming the inclination angle for one facet is θ, the angle for the opposite facet should be $-\theta$. Thus,

$$\Delta PD' = \Delta d \sin(-\theta) + \Delta w(1 + \cos(-\theta)). \tag{37.4}$$

Because the photodiodes capturing the two interference patterns are mounted at opposite direction, the amount of fringe shifts ΔF are also in opposite sign for the two fringes. Taking this into consideration and combing Eqs. 37.1, 37.2, 37.3, and 37.4 gives the relationship between the fringe shift and the incremental strain as [6]

$$\Delta\varepsilon = \frac{\lambda}{2d\sin\theta}(\Delta m_1 + \Delta m_2). \tag{37.5}$$

Where Δm_1 and Δm_2 denote the amount of fringe shifts in the two opposite facet's directions, d is the gage length which is 350 μm for 0° and 90° directions and 495 μm for the 45° direction. Applying Eq. 37.5 three times in the three gage directions, three in-plane incremental strains can be easily obtained by measuring the fringe shifts in the gage directions. The cumulative strain is then determined by summing all the incremental strains.

The challenging part for the above process is how to determine the fringe shifts before and after deformation. As mentioned previously, six linear photodiodes are used to capturing the interference fringe pattern. On each photodiode, there are 512 pixels, each of which sensors the intensity of the interference pattern. Optical data acquisition system and data translation are used converting the analog fringe intensity to the digital voltage information. Connecting the corresponding voltage at each pixel, the digital interference patterns measured at six photodiodes are obtained shown in Fig. 37.4. These curves look like sine wave, which represents the change of fringe intensity from bright to dark.

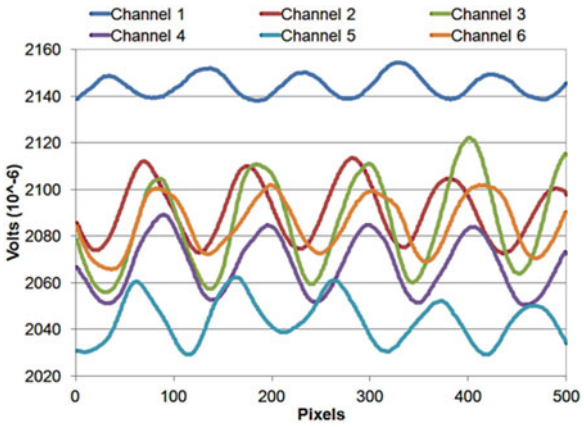

Fig. 37.4 Six inference patterns captured by linear photodiodes (only 1–500 pixels are recorded)

When material deforms, the interference fringe pattern shifts. To determine the amount of shift at each channel, tracking the intensity at one pixel before and after deformation will work. For convenience, the pixel is selected as the one with local minimum intensity (a valley shown in Fig. 37.4). Because the intensity of the first valley and last valley in a channel is relatively lower than those in the middle, which may induce some error, fringe shift at middle valley is preferred. Also, to obtain a more accurate fringe shift and also compromise the shift differences between valleys, an average shift from the three middle valleys are used.

Three steps are conducted in the data process program to find the valley locations for each channel. First of all, a routine is programmed to find the transition regions where the intensity changes from descending order to ascending order. The routine searches the local minimum values in small section of data points from beginning of the curve to the end of the curve. The width of the section depends on the period of the intensity curve. For fringe curves shown in Fig. 37.4, the first forty (40) data points are selected to find the minimum valley. If a minimum valley is observed among the 40 data, the routine will check the next 40 data point sets. However, when no valley is found in the first 40 data points, the program will scan a new data set which is defined by moving the previous data set to the right with one data point increment (2nd to the 41th, 3rd to the 42th etc) till a valley is observed. The algorithm for the first routine is to determine the differential for the 40 data points by subtracting a data by its adjacent next data. The result which is defined as a vector includes the information that a positive number indicates a descending order and a negative number means an ascending order. The small section (40 data points) is further equally divided into two parts, the left and right parts. For data in each of the two parts, the total count of positive number and negative number are saved, and two new variables which will be used for determine the overall order are defined as:

$$\begin{aligned} R_{check} &= R_{negative} - R_{positive} \\ L_{check} &= L_{positive} - L_{negative} \end{aligned} \tag{37.6}$$

Where R_{check} and L_{check} are the two variables, $R_{negative}$ and $R_{positive}$ are the two counts of negative and positive values on the right part of the vector, $L_{positive}$ and $L_{negative}$ are the two counts of positive and negative results on the left. Data in different orders such as ascending, descending, ascending and descending, and descending and ascending would have varied R_{check} and L_{check} signs and values. Only when the R_{check} is greater than 2 and also the L_{check} is greater than -2, there is chance that a valley exists among the data set. After the data section which contains the local minimum is determined, the next step is to find where the valley locates among the data section, and a descending ordering method is used to locate the approximate valley position. This method original defines the first data as the minimum, and compare it with the second data. If the second data is higher than the minimum, the third data is going to be compared and so on. When a new data is found that it is lower than the minimum, this new data is set to be the new minimum and compare with next data point till last data. After comparing all the data point in the section, the minimum value among the data set will be obtained, which is the approximated valley location.

However, due to the fluctuation of the raw data, the approximated valley locations obtained from step 2 is not accurate and repeatable. Therefore, the third step of the program is to curve fit the adjacent 20 data points around the approximated valley location, and find the exact minimum location of the fitted curve. Least square parabola method is used to curve fit the 21 data points [8]. Defining a best fitted parabola curve $f(x)$ in the following format

$$f(x) = a_0 + a_1 x + a_2 x^2. \tag{37.7}$$

Also, the 21 data points are listed as (x_1,y_1), (x_2,y_2),. . .(x_{21},y_{21}) where x_i is the X axes in pixel, and y_i is the Y axes in micro volts. The best fitted curve *f(x)* has the least square error for the 21 data points, therefore

$$R = \sum_{i=1}^{21} (f(x_i) - y_i)^2 = \min \tag{37.8}$$

Because R is a minimum value, the first derivative of R respect to the three unknown coefficients would equal to zero. Thus,

$$\begin{aligned} \frac{\partial R}{\partial a_0} &= 2\sum_{i=1}^{21} [(a_0 + a_1 x_i + a_2 {x_i}^2) - y_i] = 0 \\ \frac{\partial R}{\partial a_1} &= 2\sum_{i=1}^{21} x_i[(a_0 + a_1 x_i + a_2 {x_i}^2) - y_i] = 0 \\ \frac{\partial R}{\partial a_2} &= 2\sum_{i=1}^{21} {x_i}^2[(a_0 + a_1 x_i + a_2 {x_i}^2) - y_i] = 0 \end{aligned} \tag{37.9}$$

Eq. 37.9, which can be reorganized in matrix format as shown in Eq. 37.10, yields to three equations for determining the three unknowns.

$$\begin{pmatrix} \sum_{i=1}^{21} {x_i}^0 & \sum_{i=1}^{21} {x_i}^1 & \sum_{i=1}^{21} {x_i}^2 \\ \sum_{i=1}^{21} {x_i}^1 & \sum_{i=1}^{21} {x_i}^2 & \sum_{i=1}^{21} {x_i}^3 \\ \sum_{i=1}^{21} {x_i}^2 & \sum_{i=1}^{21} {x_i}^3 & \sum_{i=1}^{21} {x_i}^4 \end{pmatrix} \begin{pmatrix} a_0 \\ a_1 \\ a_2 \end{pmatrix} = \begin{pmatrix} \sum_{i=1}^{21} y_i {x_i}^0 \\ \sum_{i=1}^{21} y_i {x_i}^1 \\ \sum_{i=1}^{21} y_i {x_i}^2 \end{pmatrix} \tag{37.10}$$

Inputting all the raw data in Eq. 37.10, the coefficients of the least square fitted curve are obtained. Then, the minimum valley location can be easily determined by $-a_1/2a_2$.

Encoding previously described algorithms, a FORTRAN data acquisition and control software was programmed. After the program gets the starting command, the program sends a triggering signal to the optical data acquisition system which starts scanning the intensities at each photodiode. After the analog intensity signals are converted by the data translation card, the digital voltage information is processed to find and save the corresponding minimum valley locations. When this process is done, the program will automatically scan the fringes and calculate the strain and slope based on minimum valley location at current step and previous step. Based on the current data acquisition hardware and software, the strain/slope sampling rate is 0.17 data per second, which is good enough for dynamic strain measurement applications. Also, the program has option for static loading application which calculates the incremental strain after each loading step.

37.3 Experiments

Strain measurements using six-facet delta ISSR have been applied for measuring real time strain in tension test and welding strain applications. Conjunct with hole-drilling method and ring-core cutting method, the delta ISSR was also applied for estimating residual stresses by measuring the released strains. Although the idea of rectangular rosette has been proposed, no application was accomplished. Compared with the delta rosette, the rectangular ISSR can directly measure strains in two orthogonal directions such as sample's XY directions, while for delta ISSR a strain transformation have to be applied. When the delta ISSR was installed on the sample surface, it is hard to control and measure the angle between the gage direction and sample's XY coordinate, which is required by the strain transformation process, the transformed strains for delta ISSR may contain errors. Also, for measuring the orthogonal strains, the rectangular ISSR can be installed so that two gauges are along the orthogonal directions, which gives the highest sensitivity. However, for delta rosette, only one gage can be applied along one of the orthogonal directions with higher sensitivity.

37.3.1 Compression Test

Because it is first to apply the rectangular ISSR for strain measurements, both ISSR and RSR were installed on a thin aluminum plate to measure the strains in a compression test for validation purpose. The schematic drawing of ISSR and RSR locations and test set up is shown in Fig. 37.5. Two perpendicular strain gages in a commonly used strain rosette (EA-13-031RE120) were installed on both the upper and lower surface of the aluminum sample. The ISSR was installed only on the upper surface symmetric to the RSR referring to the central dash line in X axis. During the compression test, resistance strain gages are connected to a strain indicator to measure the cumulative strains on each gage. Among the four channels connecting the strain gages, channels 1 and 3 measured the strains on the upper and lower surface along sample's Y axes, and channels 2 and 4 measured the strains on the upper and lower surface along sample's X axes, respectively. For the ISSR, gage 1 measured the incremental strains along Y axes, and gage 3 measured the strains along X axes. Compared with the gage length of 0.79 mm of resistance strain gage, the gage length of the ISSR is one time shorter which is only 350 um. Also, the matrix size of the RSR (7.4*7.4 mm^2 for gage used in this paper) is much bigger than ISSR.

Incremental torques is applied by hand to the middle of the clamp step by step so that the aluminum plate is compressed gradually and smoothly. When it is difficult for the hand to apply the torque required to compress the plate, release torques are applied also step by step to unload the plate. Figure 37.6 shows the cumulative strains measured by both RSR and ISSR.

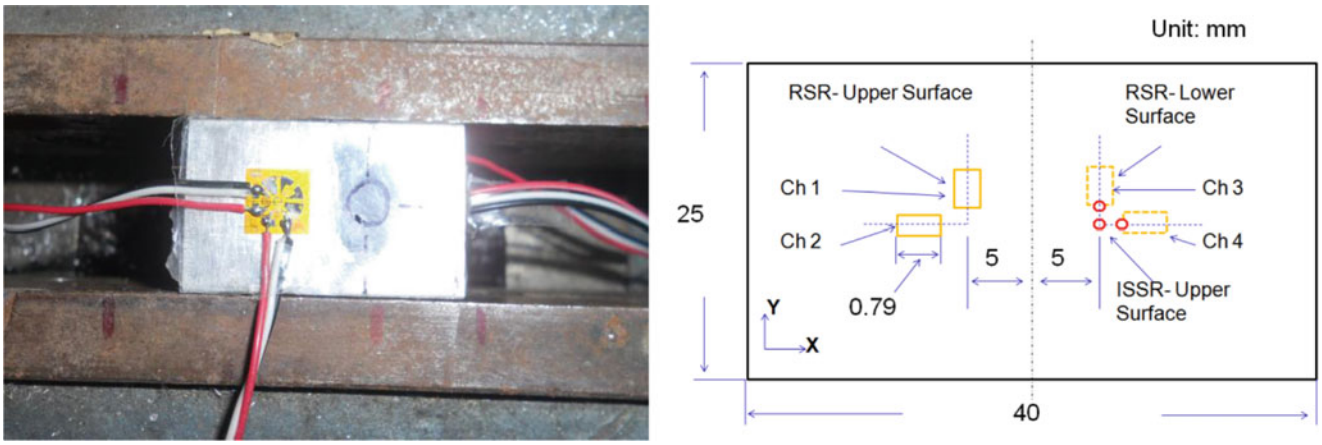

Fig. 37.5 Photo of test specimen with RSR and ISSR installed and schematic drawing their locations and orientations, load is applied by closing the clamp step by step

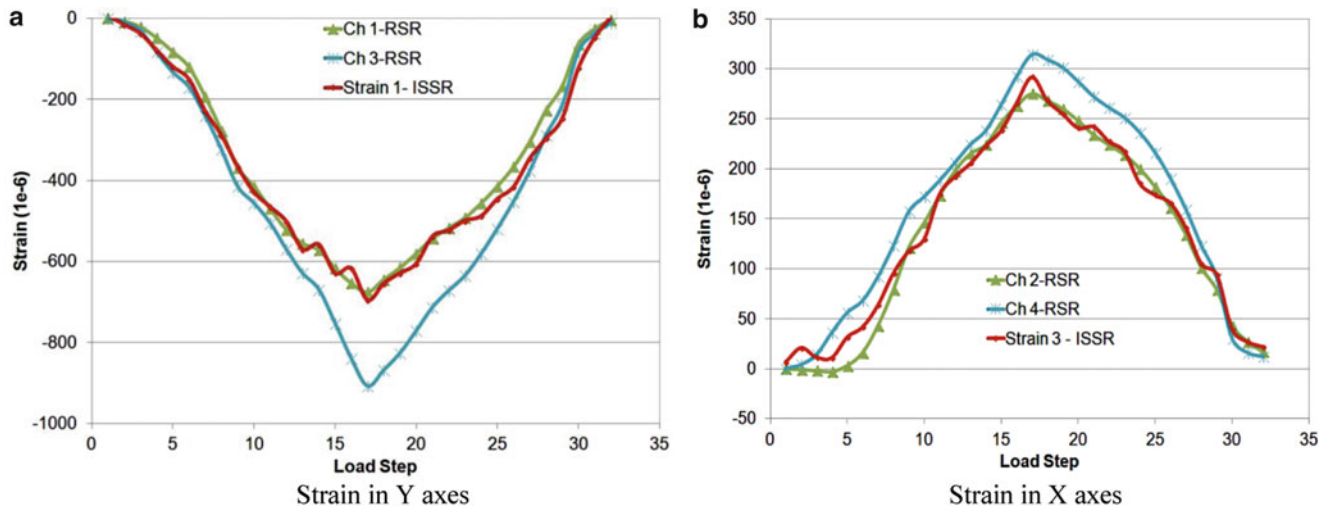

Fig. 37.6 Comparisons of cumulative strains measured by RSR and ISSR

Compressive strains are measured during the loading stage along the Y axes, and tensile strains are measured along the X axes. For the strain magnitudes, they increase with loading during the loading stage. During the unloading stage, strain magnitudes in both X and Y directions decrease. The average ratio of the transverse strains to the longitudinal strains, which is Poisson's ratio, is calculated as 0.37 for the material used. It is very close to the general Poisson's ratio of aluminum material, which is 0.33.

Comparing the strain results measured by RSR and ISSR, strains measured by ISSR agree very well with strains measured by RSR on upper surface of the plate for both X and Y directions. Strains on the lower surface are generally higher in magnitude than strains on the upper surface measured by both ISSR and RSR, because loads are applied much closer to the lower surface.

37.3.2 Real Time Welding Strain Application

Besides the static loading case as shown in previous section, the rectangular ISSR was also applied to measure the real time strains during the welding process. Measuring the dynamic strains during welding is a challenging problem for conventional strain measurement techniques such as RSR, holography, Shearography and moiré due to higher temperature, strong welding light intensity and steep strain gradient near welding. Because of the short gage length and non-contacting nature, ISSR can be used for measuring high temperature and steep strain gradient applications. However, the strong welding light intensity incapacitates the capturing of the laser interference pattern by the photodiodes. To overcome this problem, laser filters which will only allow light with certain band of wavelength pass were installed in front of the photodiodes. Also, special shield structure was designed and applied during the welding to block the dusts and portion of light occurred. Both these improvements capacitate the ISSR technique for measuring real time strain during welding process.

The schematic drawing of the testing is shown in Fig. 37.7. Welding was applied on a 1,018 carbon steel plate along X direction from left to right. MIG arc welding was applied using a wire feed welder. The 0.89 mm diameter wire was used during the test with welding speed of 6 mm/s. A rectangular ISSR with 350 um gage length in gage 1 and gage 3 was pre-installed on the steel surface before the welding test. The two orthogonal gages measure the dynamic incremental strains during welding along and transverse to the welding direction.

Welding strains are results of the transient welding temperature change. Therefore, two K type thermocouples were installed on the two sides of the rectangular ISSR, as shown in Fig. 37.7, to measuring the real time temperature during welding and cooling process. Figure 37.8 show the temperatures measured during the tests. As shown, temperature increases to a peak value when welding was applying and decreases to room temperature from weld stops. The peak temperature for the test in this paper is 128 °C.

Once welding starts, the rectangular rosette starts to measure the incremental strains. The total duration of the welding process is 16 s. After weld stops, the ISSR continues to record the transient strains during the cooling process till temperature at ISSR is close to room temperature. The cumulative real time strains measured by the rectangular rosette are shown in Fig. 37.9. As shown, strain changes rapidly during the welding process. Much more fluctuation is observed along welding direction. Much higher peak strain magnitudes are measured transverse to the welding direction. Based on the yield strain calculation, the measured peak strain Y is higher than yield strain. This indicates that ISSR technique can be used for high strain measurement such as after yielding.

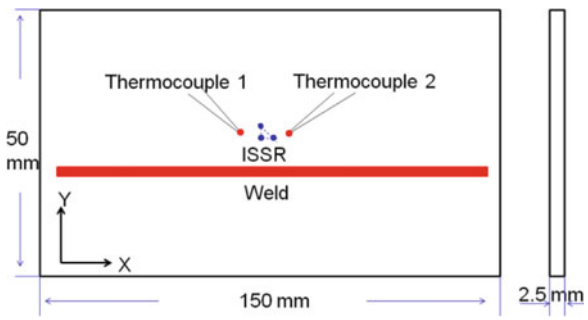

Fig. 37.7 The schematic drawing of the test set up

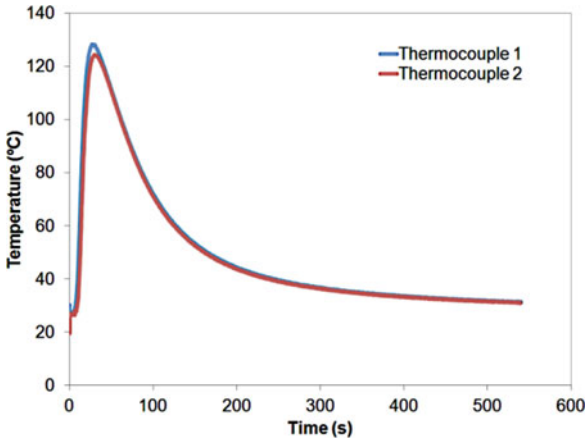

Fig. 37.8 Temperature results measured during the welding and cooling process

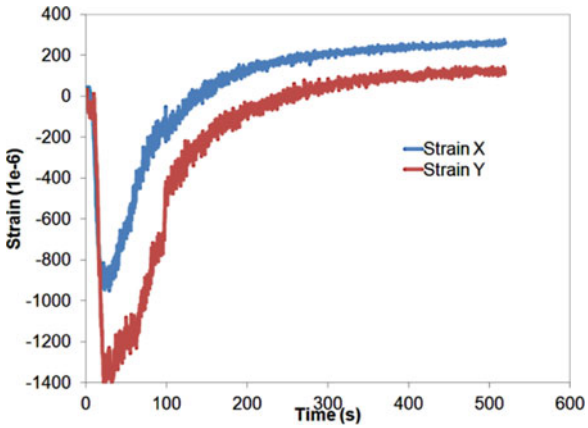

Fig. 37.9 The cumulative strains during the welding and cooling process

Two obvious sections of strain are observed for strain transverse to welding direction. As temperature increases, compressive strains are measured. However, as temperature decreases to room temperature, material at ISSR experience tension. When the temperature reaches room temperature, no more strain is measured. And the final strain values at room temperature are defined as the residual strains stored in the material. As shown, tensile residual strains are measured in both along and transverse to welding directions. Thus, tensile residual stresses X and Y are expected at test location at ISSR.

37.4 Conclusions

The first application of a rectangular ISSR is presented in this paper. By measuring the fringe shifts of the laser interferences patterns, the rectangular ISSR measures two orthogonal strains directly. In order to determine the shift, the discrete digital fringe intensity signals were processed following three steps such as differential method to find the transition from descending to ascending, descending ordering algorithm to find the approximated valley locations and least square analysis to obtain the accurate local valleys. Encoding these data process methods, both static and dynamic data acquisition and control software was programmed. Compression test was conducted to validate the application of the new rosette and results from ISSR compared very well with results from RSR. Rectangular ISSR was further successfully applied for measuring the real time strains during an arc welding process to measure the strains along and transverse to the welding direction. Strain history during the welding and cooling process was measured and tensile residual strains were measured.

References

1. Perry CC, Lissner HR (1962) The strain gage primer. McGraw Hill, New York
2. Sharpe WN (1968) The interferometric strain gage. Exp Mech 8(4):164–170
3. Sharpe WN (1982) Applications of the interferometric strain/displacement gage. Opt Eng 21(3):483–488
4. Li K (1995) Interferometric 45 and 60 strain rosettes. Appl Opt 34(28):6376–6379
5. Li K (1996) The interferometric strain rosette technique. Exp Mech 36(3):199–203
6. Li K (1997) Interferometric strain/slope rosette for static and dynamic measurements. Exp Mech 37(2):111–118
7. Tjhung T (2007) Applications and developments of the interferometric strain/slope rosette. Ph.D. dissertation, Oakland University
8. Bjorck A (1996) Numerical methods for least squares problems. SIAM, Philadelphia

Chapter 38
High-Speed Shape Measurements by Fringe Projection Method: SOPRA 3D

Chaoyang Ti, Xiaoran Chen, John Tyson, Ellery Harrington, Ivo Dobrev, Babak S. Aghazadeh, and Cosme Furlong

Abstract Accurate and high-speed three-dimensional (3D) shape measurements are becoming increasingly important in many industries. Recent advances in the development of high-resolution detectors, light sources, MEMS, and computational power are enabling the availability of noncontact and noninvasive optical methods, which can be applied to new and challenging applications requiring 3D and high-speed measurements.

In this paper, we describe our recent advances in the development of a fringe projection-based system for high-speed 3D shape measurements, as part of the Surface Optical Profilometry Roadway Analysis (SOPRA) system for evaluation of the public road quality within the urban infrastructure. The system is mounted on a vehicle moving at speeds of up to 100 km per hour and it consists of a custom built structured light projector and a recording and analysis sub-system. Fast-Fourier Transform (FFT) and discrete wavelet transform (DWT) single frame methods as well as optimized spatial phase unwrapping methods have been developed as part of the analysis sub-system. We have also developed innovative Graphics Processing Unit (GPU) accelerated algorithms to improve the analysis and post-processing speeds to run live phase retrieval at up 40 fps. Automatic road curvature and crack detection algorithms quantify the road quality index. The system has been field tested for real-time road measurements in daylight conditions.

Keywords Crack detection • Fringe projection • GPU • Road analysis • 3D shape measurements

38.1 Introduction

This paper focuses on recent advancements in our development of a system based on fringe-projection for 3D shape measurements. The measuring system is designed for high-speed applications, using the Fast Fourier Transform (FFT) in single frame method, as well as Discrete Wavelet Transform (DWT), which are being applied to measure road indices (RI) at driving speeds. Its goal is to map the surface of roads in 3D in near-real-time at highway driving speeds, in order to subjectively rate road quality. This projection system is developed for SOPRA 3D (Surface Optical Profilometry Roadway Analysis), part of VOTERS (Versatile Onboard Traffic Embedded Roaming Sensors), a project funded by NIST [1].

C. Ti (✉) • X. Chen • E. Harrington • I. Dobrev • B.S. Aghazadeh • C. Furlong
Center for Holographic Studies and Laser micro-mechaTronics-CHSLT, Mechanical Engineering Department, Worcester Polytechnic Institute, Worcester, MA 01609, USA
e-mail: chaoyang@wpi.edu

J. Tyson
Trilion Quality Systems, Plymouth Meeting, PA 19462, USA

H. Jin et al. (eds.), *Advancement of Optical Methods in Experimental Mechanics, Volume 3*,
Conference Proceedings of the Society for Experimental Mechanics Series,
DOI 10.1007/978-3-319-00768-7_38,

38.2 System Setup and Acquisition

38.2.1 Design Requirements

As shown in Fig. 38.1, the single frame fringe projection system consists of three major components: an illumination system, an optical imaging device, and a Charged-Couple Device (CCD) camera. The illumination system contains a strobe light that is triggered with each integration of the camera. The strobe light system, with a frequency of 50Hz provides 1 J electrical input to a Xenon strobe light with a typical corresponding light energy output of 0.1 J per pulse. This results in an average power of 10 kW during the pulse, i.e., well beyond sunlight for the visible range. Camera's exposure time is longer than the flash duration and it is kept as short as possible. Because of the advantages of strobe light, such short flash duration can allow us to measure at up to around 720 km/h driving speed with 5 mm image smear during exposure. The CCD camera has a 1936 $\times$ 1456 resolution and with a 12 mm focal length objective, we can capture images with a field-of-view (FOV) of size 1.5 $\times$ 1.5 m^2. Based on the FOV and the effective size of images that can be analyzed (1 $\times$ 1 m^2), the maximum frame rate of the camera (40Hz), and the requirement of no less than 40 % overlap between two consecutive frames, the maximum potential driving speed is in the order of 86.4 km/h.

38.2.2 System Configuration

The fringe projection system is in a crossed-optical-axes configuration, which means that the optical axes of the camera and projector cross on the reference plane, as is shown in Fig. 38.1. This orientation is preferred over the parallel axis setup because it allows the grating to be in line with the optical axis of the projector, thus making the system more compact. Also, the system sensitivity increases with larger triangulation angles, but on the other hand, the system becomes more susceptible to irresolvable areas caused by shadowing [2–4].

38.3 Phase Retrieval

Due to the speed of the van, temporal phase sampling is not applicable and in order to overcome this constrain, we have implemented single frame techniques based on spatial phase shifting and Fourier and wavelet profilometry.

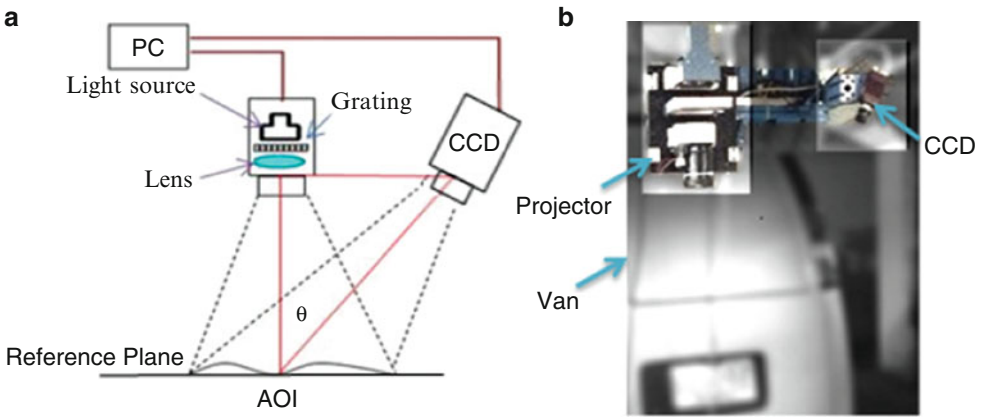

Fig. 38.1 Developed fringe projection setup: (**a**) a schematic of the system showing the light source, grating, projection lens, and the CCD camera separated by triangulation angle, θ; and (**b**) realization of our system mounted on a van.

38.3.1 Fourier Transform Profilometry (FTP)

For high-speed applications, the FTP process uses the Fast Fourier transform (FFT) method to obtain the optical phase from a single image [5]. In this method, the recorded intensity distribution, I, is

$$I(x,y) = a(x,y) + c(x,y) + c^*(x,y), \tag{38.1}$$

with

$$c(x,y) = \frac{1}{2} b(x,y) e^{i\Omega(x,y)}, \tag{38.2}$$

where $c^*(x,y)$ is the corresponding complex conjugate of $c(x,y)$. The fringe-locus function, $\Omega(x,y)$, containing shape information is recovered by applying a 2D FFT to the intensity distribution and filtering one of the two complex conjugated terms as well as the DC component [5].

By shifting the spectrograph back to its origin and taking an inverse FFT function, the spectrograph is transformed back to its spatial domain. The phase map can be calculated using an inverse tangent function with

$$\Omega(x,y) = \arctan\left\{\frac{imag[c(x,y)]}{real[c(x,y)]}\right\}. \tag{38.3}$$

38.3.2 Wavelet Transform Profilometry (WTP)

Wavelet transform profilometry (WTP), another method of fringe analysis, is an alternative approach to FTP [6]. Similar to FTP, WTP is capable of extracting the wrapped phase from a single frame. The one-dimensional wavelet transform (WT) is the inner product of a signal,f, with translations, b, and dilations, a, of a compactly supported mother wavelet (ψ). Unlike the FTP, which utilizes sinusoidal functions to extract phase information, WTP has the flexibility in choosing a "Mother Wavelet", for any application, which improves the overall accuracy of results. Generally, the most suitable mother wavelet for phase evaluation applications is the complex Morlet [6]. This is because it provides improved localization in both spatial and frequency domains. Also, the Gaussian window function used in the Morlet wavelet is the optimal window shape [7], which is defined as

$$\Psi(x) = \frac{1}{\sqrt[4]{\sigma^2\pi}} \exp(i\omega_0 t) \exp\left(\frac{-t^2}{2\sigma^2}\right), \tag{38.4}$$

where ω_0, and σ are a fixed spatial frequency, and a bandwidth parameter, respectively. The Morlet wavelet must satisfy $\omega_0 \geq \pi\sqrt{2/\log(2)}$. The values of 6 and 2π are common choices for ω_0. Also, often $\sigma = 1$ is chosen, in which case there are five significant oscillations under the Gaussian envelope. However, it is shown that the performance of Morlet wavelets in fringe analysis is improved by setting $\sigma = 0.5$ [7]. In our work, ω_0 and σ are set to be 2π and 0.5, respectively. The wavelet transform $W(a,b)$ of one row of a fringe pattern, $I(x)$, is a two-dimensional complex array and can be computed as

$$W(a,b) = \frac{1}{\sqrt{a}} \int_{-\infty}^{\infty} I(x) \Psi^*\left(\frac{x-b}{a}\right) dx, \tag{38.5}$$

where * denotes complex conjugate and the phase can be computed with

$$\phi(a,b) = \tan^{-1}\left\{\frac{\mathrm{Im}[W(a,b)]}{\mathrm{Re}[W(a,b)]}\right\}, \tag{38.6}$$

where $\mathrm{Im}\{W(a,b)\}$and $\mathrm{Re}\{W(a,b)\}$are the imaginary and real parts of the WT, respectively. Once a row of a fringe pattern image is processed, the phase of the row is obtained by the direct maximum ridge extraction algorithm [6, 7]. In this method, the maximum value of each column in the modulus array is determined and its corresponding phase is chosen from the phase array. This process is repeated on the fringe pattern image for all the rows to obtain the final wrapped phase map.

38.4 Results

38.4.1 Wrapped Phase Extraction Using FTP and WTP Methods

A sample image containing a manhole cover and several cracks is shown in Fig. 38.2a. The corresponding wrapped phase maps obtained using FTP and WTP are shown in Figs. 38.2b, c, respectively. For a qualitative comparison, the difference between the results of those two methods is not substantial. However, for a quantitative comparison, cross-sections of processed images are shown in Figs. 38.2d, e. As it is observed, the main advantage of WTP over FTP is that the results are more accurate in terms of the detection of sharp height variations. Additionally, discontinuous fringes can be detected and processed more reliably using WTP. The main disadvantage of WTP is that it is computationally more expensive compared to FTP. The processing speed of WT of a full-resolution image in our system is 6.49 s, which is beyond the requirement of analysis in near-real-time. In contrast, the corresponding time of FFT processing is 0.82 s with the same computing power and image resolution. Based on the requirement that the measuring system needs a relatively high-speed processing time, we chose the FFT algorithm and further accelerated it using GPU to achieve more than 20 fps of processed 3D images.

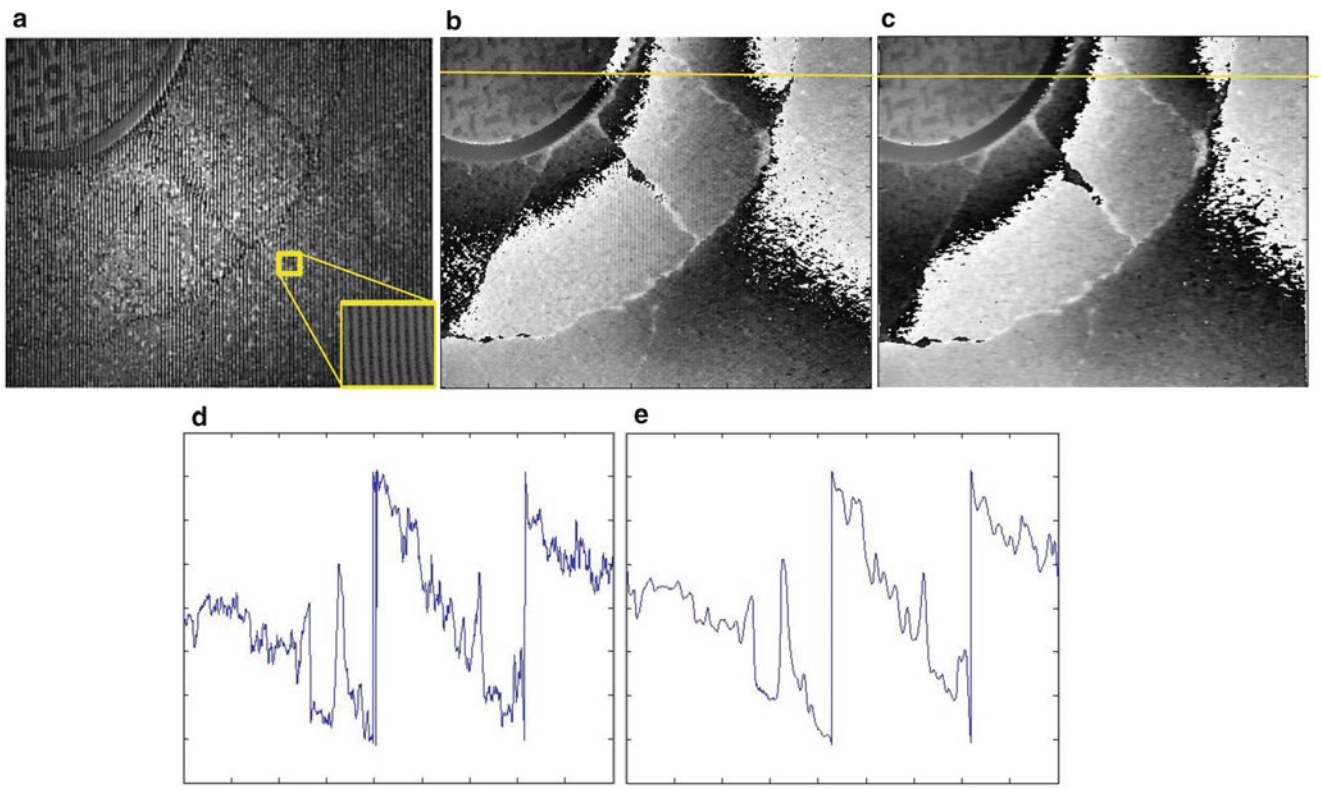

Fig. 38.2 The comparison between wrapped phase obtained using FFT and WT: (**a**) live image of a manhole cover and cracks with projected fringes, see inset for details; (**b**) corresponding wrapped phase analyzed by FFT method; (**c**) corresponding wrapped phase analyzed by WT method; (**d**) and (**e**) are representative cross sections of (**b**) and (**c**), respectively

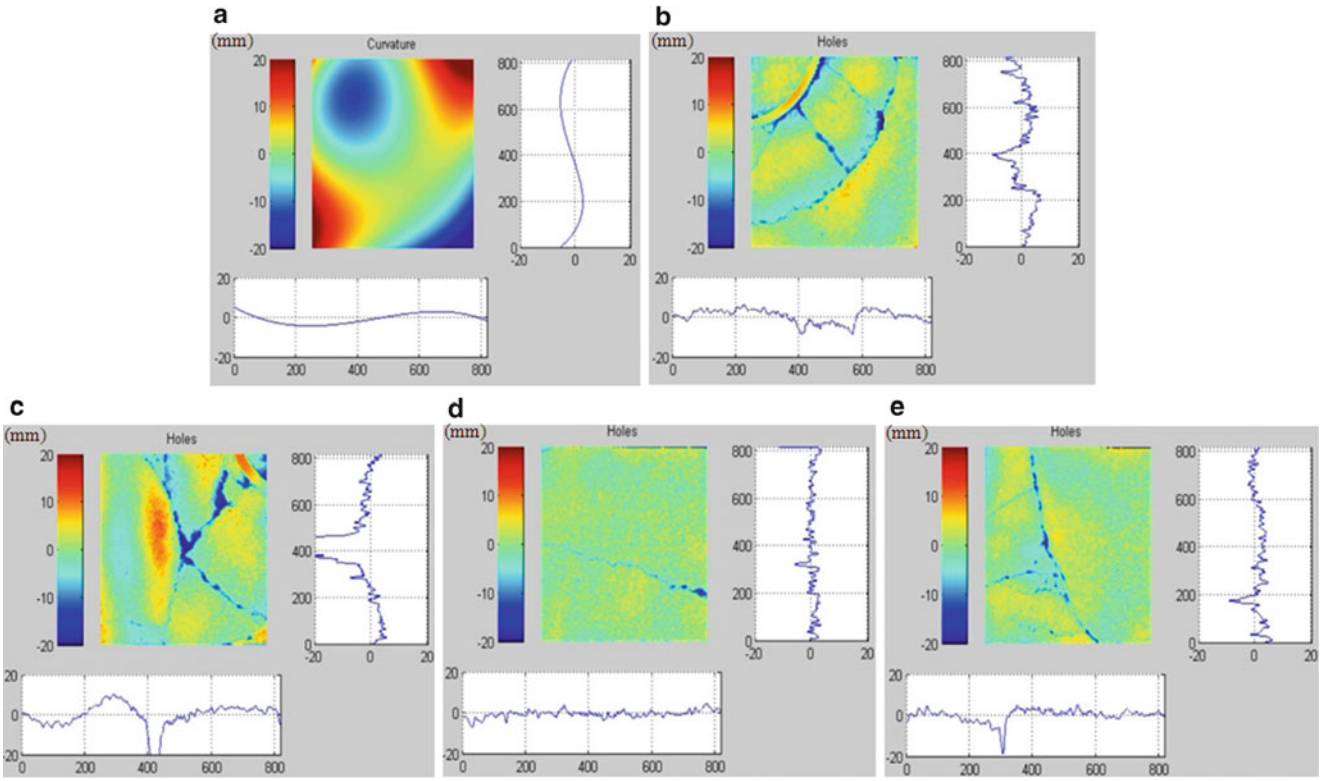

Fig. 38.3 3D rendering of a manhole cover and cracks: (**a**) corresponding curvature of road surface and center cross section in horizontal and vertical directions; (**b**) crack details of a manhole cover with subtracted road curvature from 3D road information; (**c**), (**d**), (**e**) obtained after removing road curvature components from 3D road shape information

38.4.2 Curvature, Shape, and Crack Results

The wrapped phase is unwrapped with a spatial unwrapping algorithm [8]. This unwrapping algorithm is optimized and designed specifically for use with the road measurement system. The unwrapped phase in radians is then converted into millimeters in the z-axis using the geometry of the system, and the pixels are assigned x and y coordinates in millimeters based on the field of view and camera calibration. The 3D data can be saved in various formats and the road curvature is extracted from 3D unwrapped images using a low-pass filter with spatial frequency less than 5 lp/m being cut off, and cracks are subtracted by high pass filter with spatial frequency more than 10 lp/m being remained, as shown in Fig. 38.3.

38.4.3 Crack Detection

We are currently developing algorithms to analyze 3D road shape measurements in order to extract crack boundaries, as well as areas and volumes that define cracks. This enables improved methods to identify, characterize, and classify road conditions. Figure 38.4 shows representative results highlighting capabilities to determine crack locations and corresponding geometrical features.

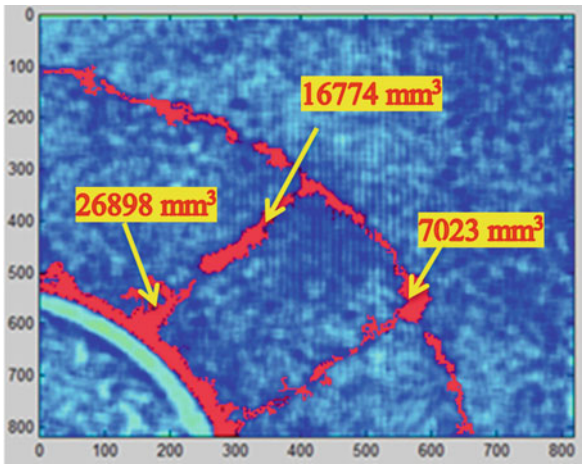

Fig. 38.4 Analysis of 3D road shape data to determine crack volumes

38.5 Conclusion and Future Work

We have shown representative results highlighting our efforts toward the development of high-speed, single frame, 3D shape measurements of road surfaces by fringe projection. Measuring system is capable to operate during day light conditions by the incorporation of a high-energy strobe light source. Image analyses are performed by Fourier and wavelet transformation methods that enable 3D road measurements at nearly 20 fps and at driving speeds in the order of 40 km/h.

Our future developments are focused on the analysis and extraction of 3D shape features to obtain accurate characterization of road conditions. Also, the opto-mechanical design of the measuring system will be made more rugged and robust.

Acknowledgements The authors gratefully acknowledge the support provided by NIST program at Worcester Polytechnic Institute. We would also like to thank our colleagues at the CHSLT labs and at Trilion Quality Systems.

References

1. VOTERS Sensor Systems (2013) Northeastern University. http://www.northeastern.edu/voters/research
2. Bothe T, Osten W, Gesierich A, Juptner W (2002) Compact 3D-camera. Proc SPIE 4778:48–59
3. Chen X, Xi J, Tao J, Ye J (2008) Research and development of an accurate 3D shape measurement system based on fringe projection: model analysis and performance evaluation. Proc Eng 32:215–221
4. Furlong C, Dobrev I, Harrington E, Hefti P, Khaleghi M (2012) Miniaturization as a key factor to the development and application of advanced metrology systems. Proc SPIE Speckle 2012:84130T–84130T
5. Takeda M, Ina H, Kobayashi S (1982) Fourier-transform method of fringe-pattern analysis for computer-based topography and interferometry. J Opt Soc Am 72(1):156–160
6. Zhong J, Weng J (2004) Spatial carrier-fringe pattern analysis by means of wavelet transform: wavelet transform profilometry. App Opt 43:4993–4998
7. Abid AZ, Gdeisat MA, Burton DR, Lalor MJ, Abdul-Rahman HS, Lilley F (2008) Fringe pattern analysis using a one-dimensional modified Morlet continuous wavelet transform. SPIE 7000:1–6
8. Harrington E, Furlong C, Rosowski JJ, Cheng JT (2011) Automatic acquisition and processing of large sets of holographic measurements in medical research. Proc SPIE Opt Meas, Model Metrol 5:219–228

Chapter 39
High-Resolution Shape Measurements by Fringe Projection and Reflectance Transformation Imaging

Chaoyang Ti, Philip Klausmeyer, Matthew Cushman, John Tyson, and Cosme Furlong

Abstract In this paper, we consider the advantages and limitations of two existing techniques: structured light fringe projection (FP) and reflectance transformation imaging (RTI), and we propose a new hybrid shape measurement approach that combines their advantages. FP allows direct full field-of-view measurements of shape; however, due to the nature of the technique, the high frequency shape details of the object may not be captured. RTI is a recently developed technique that allows high resolution measurements of surface normal vectors, which are related to high frequency details of shape of the object; however, extracting the object shape from RTI data requires numerical integration, which leads to cumulative low frequency bias errors. We present representative results that demonstrate the ability of our approach to perform high resolution shape measurements and non-destructive testing of structures.

Keywords Fringe projection • High-resolution measurements • Optical metrology • Reflectance transformation imaging • 3D shape measurements

39.1 Introduction

As technological developments progress, components having more complex geometries and shapes are required. In addition, new manufacturing methods to produce these components as well as corresponding metrology tools to guarantee their dimensional specifications are needed. Also, 3D shape measurements of such components become critical in terms of investigating their geometry as well as for rapid prototyping of similar objects in future applications. Shape measurements using optical techniques have become popular because of their non-contact and non-invasive nature.

In this work, a new hybrid high-resolution optical shape measurement method that combines structured-light fringe projection (FP) and reflectance transformation imaging (RTI) is developed. FP allows direct full-field-of-view measurements of shape. However, in this technique, the spatial details defining the shape of the object under investigation may not be captured at a sufficient resolution. RTI is a recently developed technique that allows high-resolution measurements of surface normal vectors, which can be related to the spatial details defining the shape of the object under investigation. To extract shape information from RTI measurements, numerical integration is required. However, numerical integration is prone to errors, which prevent the use of RTI to perform direct shape measurements. Our hybrid shape measurement method exploits the advantages of FP and RTI.

We present representative results of the approaches, which demonstrate the ability of our hybrid method to perform high-resolution shape measurements.

C. Ti (✉) • C. Furlong
Center for Holographic Studies and Laser micro-mechaTronics – CHSLT, Mechanical Engineering Department, Worcester Polytechnic Institute, Worcester, MA 01609, USA
e-mail: chaoyang@wpi.edu

P. Klausmeyer • M. Cushman
Worcester Art Museum, Worcester, MA 01609, USA

J. Tyson
Trilion Quality Systems, Plymouth Meeting, PA 19462, USA

H. Jin et al. (eds.), *Advancement of Optical Methods in Experimental Mechanics, Volume 3*,
Conference Proceedings of the Society for Experimental Mechanics Series,
DOI 10.1007/978-3-319-00768-7_39,

39.2 Fringe Projection System (FP)

Our phase-shifting FP system consists of two major components: a spatial light modulator (SLM) and a digital charged-couple device (CCD) camera, shown in Fig. 39.1. The SLM is a digital light processing (DLP) unit containing a Digital Micro-mirror Device (DMD) with a 1,920 × 1,080 pixel resolution [1]. Each of the independent 10.8 × 10.8 μm^2 micro-mirrors, or pixel, is controlled by a duty cycle representing a percentage of time each mirror is in the on-state; thus, the SLM has intensity modulation control, which enables the projection of sinusoidal fringe patterns. The second component of the system is a CCD camera with 1,000 × 1,000 chip resolution, 7.4 × 7.4 μm^2 pixel size, a maximum frame rate of 60 frames per second at full resolution, and a maximum bit-depth of 14-bits. Depending on the application and required field-of-view (FOV), a different camera may be used.

The optical imaging system projects a structured light pattern onto an object that is recorded by a camera separated by an angle via the method of triangulation. System sensitivity increases with larger triangulation angles, but is more susceptible to irresolvable areas caused by shadowing [1–3].

39.3 Reflectance Transformation Imaging (RTI)

RTI is a new photographic method that captures an object's shape and color and enables the interactive re-lighting of the object from any direction by the application of computational methods that combine multiply images obtained by changing the direction of illumination between recordings [4]. Figure 39.2 shows schematic representation of RTI geometry.

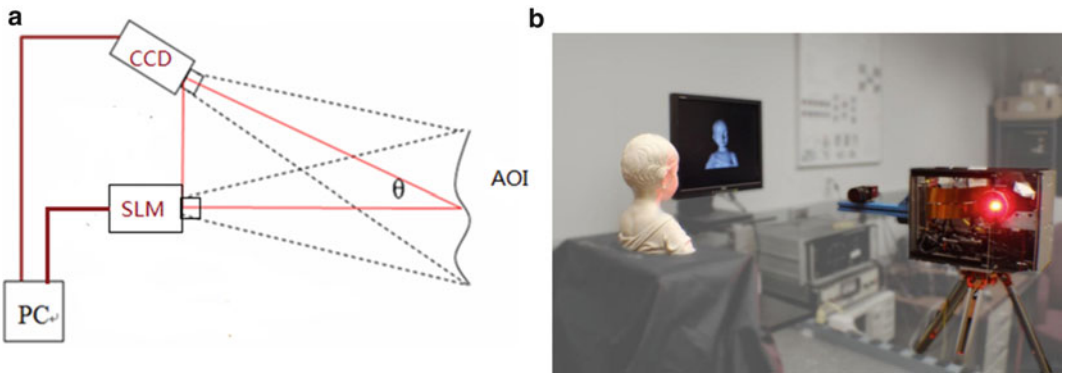

Fig. 39.1 (**a**) Schematic of the FP geometry showing the triangulation angle defined by the locations of CCD camera and the spatial light modulator [1]; and (**b**) FP system setup

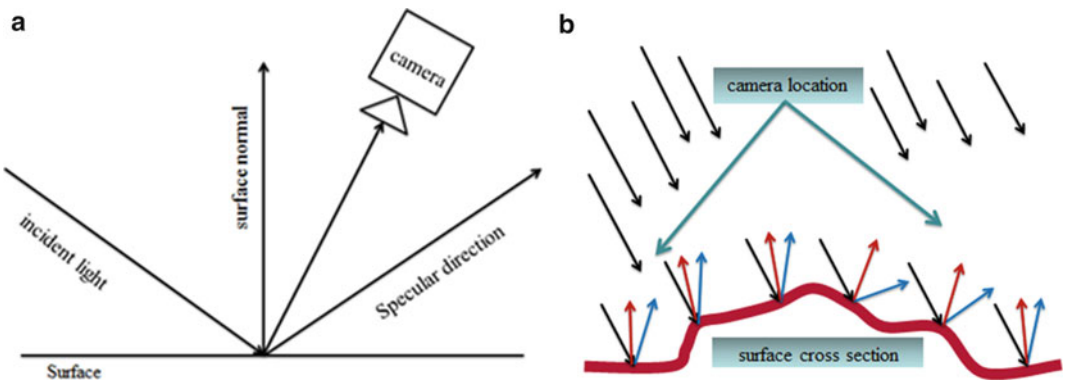

Fig. 39.2 Schematic of the reflectance transformation imaging geometry: (**a**) normal vectors defined by the direction of the incident light; (**b**) normal vectors are used by reflectance models to numerically compute the interaction of light rays with an illuminated surface. Models enable the computation of surface reflectivity at any angle of illumination

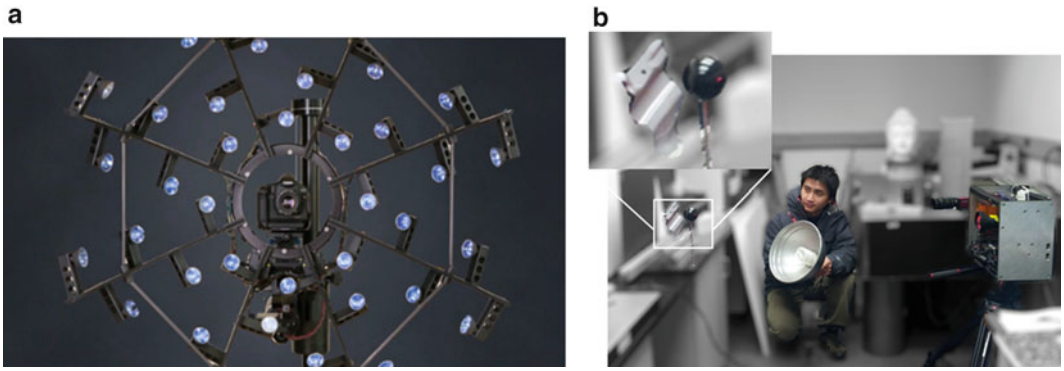

Fig. 39.3 (**a**) Typical RTI system, and (**b**) a typical highlight-RTI setup. Setup in (**b**) consists of object of interest, reference sphere, handheld light, and camera

RTI models are based on bidirectional texture functions (BTF), wherefore the constant surface reflection angle orientated towards the observation direction, can be modeled with biquadratic functions [4]:

$$L(u,\, v; I_u, I_v) = a_0(u,\, v)I_u^2 + a_1(u,\, v)I_v^2 + a_2(u,\, v)I_u I_v + a_3(u,\, v)I_u + a_4(u,\, v)I_v + a_5(u,\, v) \tag{39.1}$$

where (I_u, I_v) are projections of the normalized light vector into the local texture coordinate system(u, v) and L is the resultant surface luminance. The local coordinate system is defined per vertex, based on the normal and tangent to the surface with the binormal derived from the local texture coordinates. A separate set of coefficients $(a_0 - a_5)$ is fitted to an image data set at each pixel and stored as a spatial map, which is referred to as a Polynomial Texture Map (PTM). An essential step in producing a 3D representation is to calculate the surface normals at each position of the image. The normals are readily extracted from the RTI representation because the six coefficients stored for each pixel already contain the directional luminance information. An estimate of the normal at each pixel can be extracted from the RTI by setting $\frac{\partial L}{\partial u} = \frac{\partial L}{\partial v} = 0$ to solve for the maximum of the biquadratic function represented by Eq. 39.1.

A RTI system includes a hemisphere illumination frame, which typically contains 40 flash lights that are arranged in five tiers, and a high resolution camera mounted on the North Pole above an object placed on the horizontal baseboard in the equatorial plane, Fig. 39.3. A typical highlight-RTI setup uses a camera, a highly reflective sphere mounted on a long screw bar positioned near the object, one light source, and a string, which is used to keep a constant distance between the light source and the object [4, 5].

39.4 Representative Results

To obtain the shape information of an object, the FP system shown in Sect. 39.2 is used. Sinusoidal fringes are generated through the DMD, and the resulting fringe patterns at eight densities are projected by the LED projector onto the object. For the phase quantification, the four-step phase shifting method is implemented. Therefore, four sinusoidal fringe patterns with a phase shift of $\pi/2$ are sequentially projected onto the object. This is repeated for all eight fringe densities to allow for temporal phase unwarping [1].

Based on a particular application, FP and RTI can be combined in three different approaches: the first is by importing the FP results to RTI and generate a simulated RTI; the second is by integrating the corrected surface normal vectors based on the data gathered by FP and RTI; and the third is by optimizing the shape by minimizing the errors between FP and RTI measurements. In this work, we implement the first approach.

39.4.1 Cracked Statue

A work of art has been tested using FP and RTI. The representative FP results are shown in Fig. 39.4 for a characteristic dimension of 400 mm. Measurements contain in the order of 250,000 measurement points and have a measurement resolution in the x and y axes of 300 µm, and in the z-axis of 100 µm, respectively.

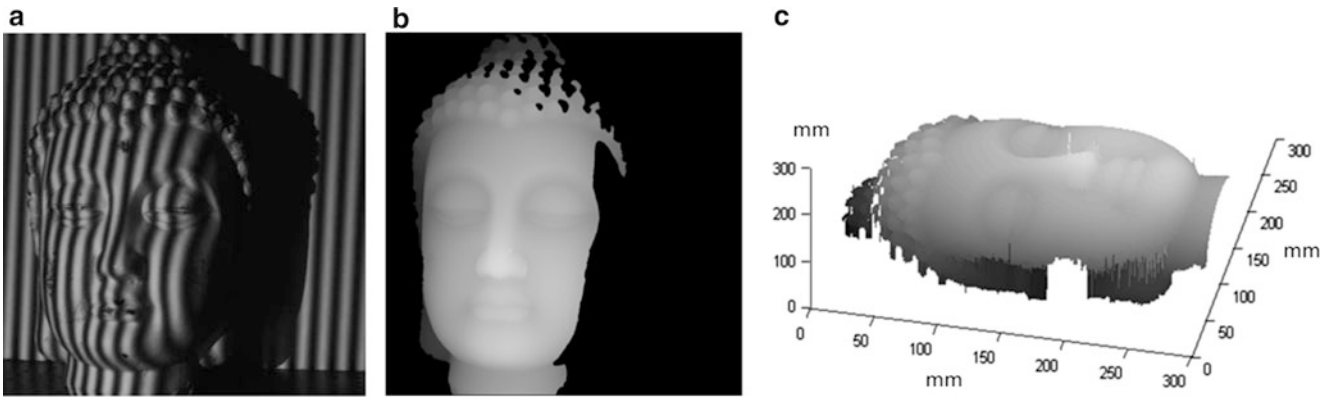

Fig. 39.4 Representative shape measurement results of a piece of art obtained by FP: (**a**) fringes projected on the object; (**b**) unwrapped optical phase of the object; and (**c**) 3D rendering of the object's shape

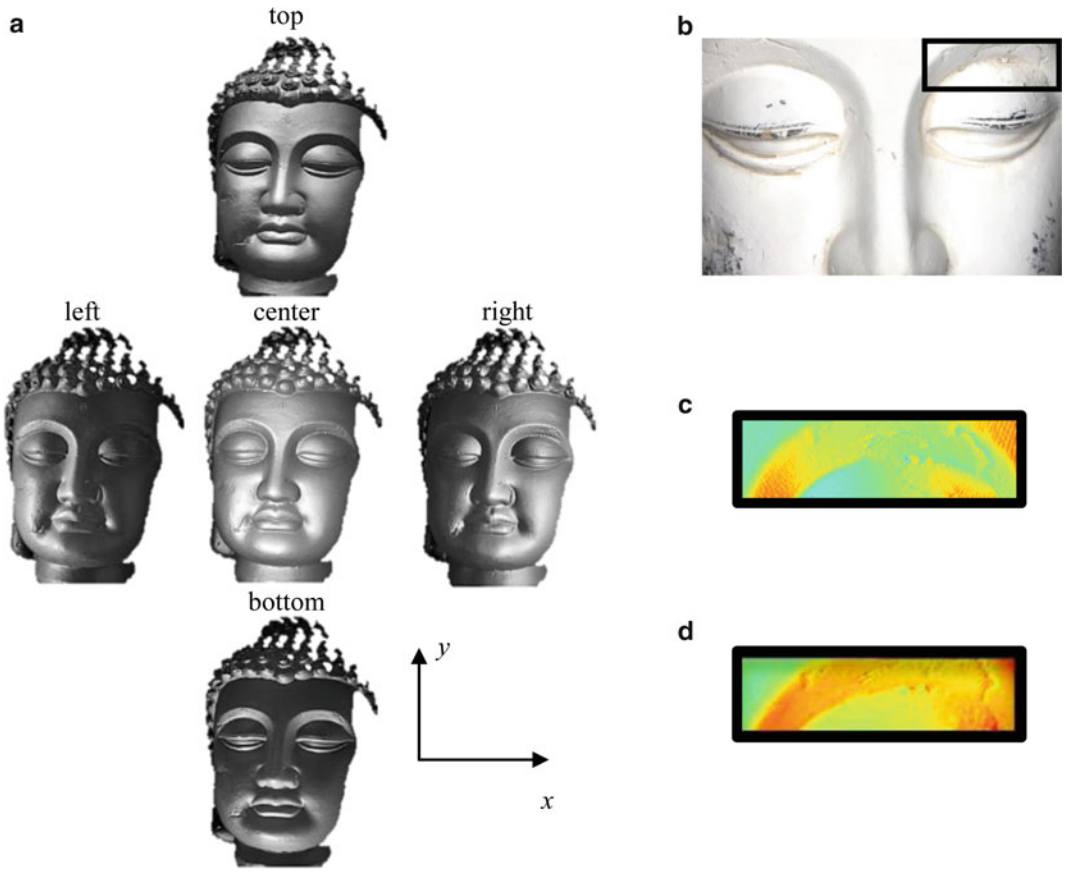

Fig. 39.5 Representative results of combining of FP and RTI from the shape measurements shown in Fig. 39.4: (**a**) RTI method applied to FP data with five predetermined positions and orientations of the reconstructing light source; area of interest (**b**) to compute normal vectors along the *x*-axis from simulated RTI (**c**); and (**d**) normal vectors along the *x*-axis from real RTI of the same area

To use FP data to generate simulated RTI, we imported predetermined positions and orientations of light source to be used in simulations. With our software, based on the shape measurements from FP data, we simulated a RTI measurement. Representative results are shown in Fig. 39.5 for a characteristic dimension of 400 mm. From Figs 39.5c, d, we observe that FP and RTI preserve low spatial frequency data (0.2 lp/mm); however, the real RTI, Fig. 39.5d, also preserves high spatial frequency information (2 lp/mm).

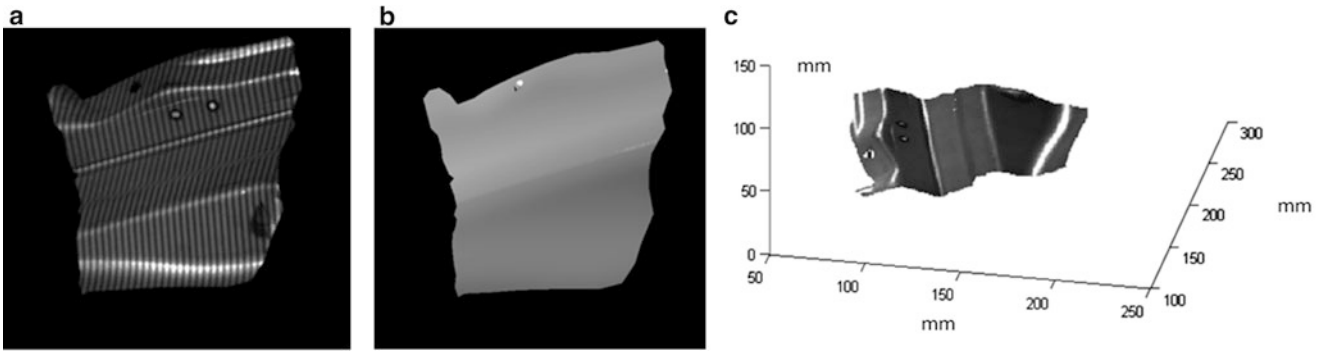

Fig. 39.6 Representative shape measurement results of a cracked aluminum component obtained by FP: (**a**) fringes projected on the object; (**b**) unwrapped optical phase of the object; and (**c**) 3D rendering of the object's shape

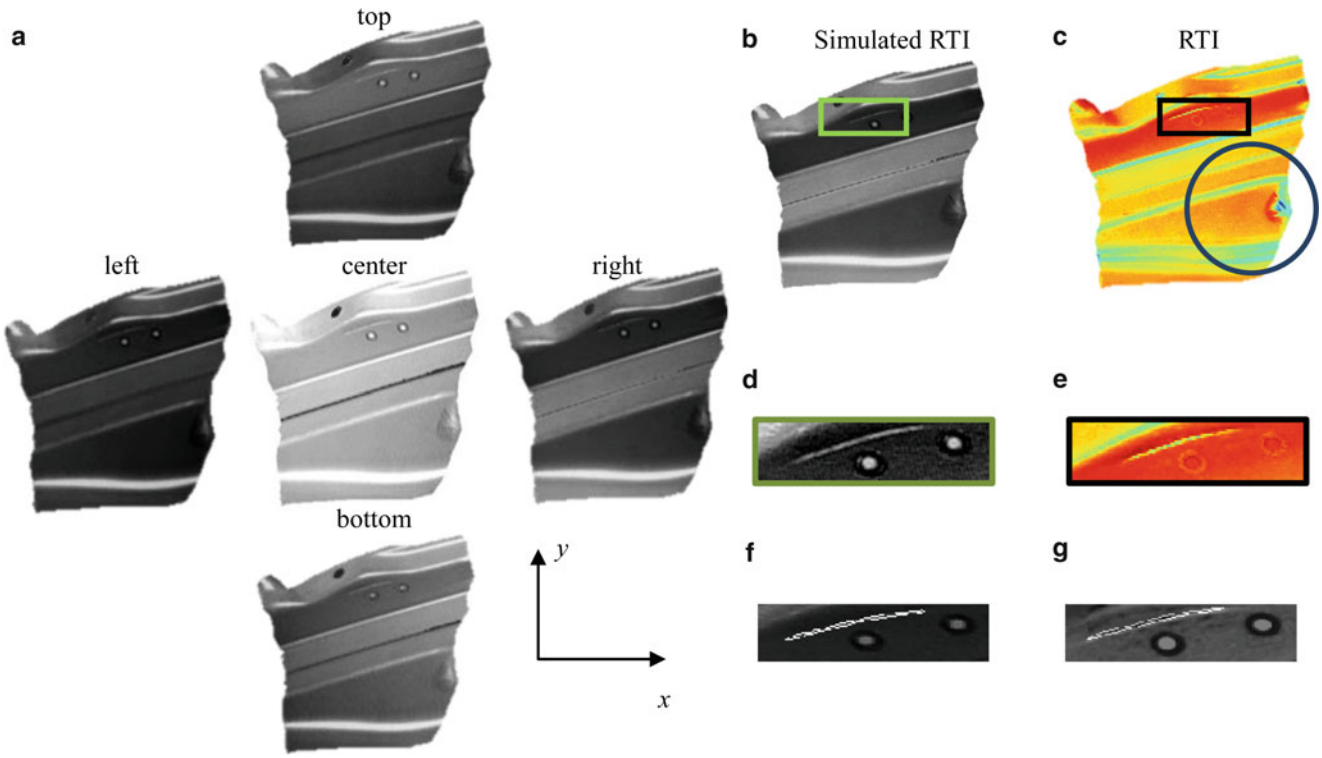

Fig. 39.7 Representative results of combining FP and RTI: (**a**) RTI method applied to FP data with five predetermined positions and orientations of light source; (**b**) simulated RTI; (**c**) normal vectors along x-axis from real RTI; (**d**) the crack is detected from (**b**); (**e**) the crack is detected from (**c**); (**f**) the crack is overlaid with its boundary from simulated RTI; (**g**) the crack is overlaid with its boundary from real RTI. The crack areas in (**f**) and (**g**) are 1.9 and 2.1 mm^2, respectively

39.4.2 Cracked Aluminum Component

A cracked component from an automobile manufacturer has also been tested using FP and RTI. The representative FP results are presented in Fig. 39.6 for a characteristic dimension of 150 mm. Measurements contain in the order of 100,000 measurement points, with a measurement resolution in the x and y axes of 300 µm, and in the z-axis of 100 µm, respectively.

The surface of the sample shown in Fig. 39.4 is uniform, matte, convex, and smooth; it has continuous first and second partial derivatives. However, the cracked aluminum component of Fig. 39.6 has a surface that modifies the angle of reflection and also has a varying degree of gloss that produces a specular component of reflection. These introduce noise into the computation of surface normal vectors from RTI images. With our developed methods, we can obtain quantitative results to characterize cracks, which include detecting the boundaries and measuring the areas and volumes that defining cracks. Figure 39.7 shows representative results that highlight our capabilities to determine crack dimensions and corresponding locations.

39.5 Conclusion and Future Work

Representative results show that our new hybrid, fringe projection (FP) and reflectance transformation imaging (RTI), approach enables new and versatile means to perform of high-resolution shape measurements. Future work will focus on integrating the corrected surface normal vectors based on data gathered by FP and RTI and optimizing the shape by minimizing the errors between FP and RTI measurements.

Acknowledgements The authors gratefully acknowledge the support of the Worcester Art Museum, Trilion Quality Systems, and the Worcester Polytechnic Institute, Mechanical Engineering Department.

Reference

1. Furlong C, Dobrev I, Harrington E, Hefti P, Khaleghi M (2012) Miniaturization as a key factor to the development and application of advanced metrology systems. Proc SPIE Speckle 2012 8413:84130T–84130T
2. Chen X, Xi J, Tao J, Ye J (2008) Research and development of an accurate 3D shape measurement system based on fringe projection: model analysis and performance evaluation. Prec Engg 32:215–221
3. Bothe T, Osten W, Gesierich A, Juptner W (2002) Compact 3D-camera. Proc SPIE 4778:48–59
4. Malzbender T, Gelb D, Wolters H (2001) Polynomial texture maps. In: Proceedings of ACM SIGGRAPH'01, New York, pp 519–528
5. MacDonald L, Robson S (2010) Polynomial texture mapping and 3D representations. In: International archives of photogrammetry, remote sensing and spatial information sciences, Commission V Symposium, Newcastle upon Tyne, vol XXXVIII, Part 5

Chapter 40
Strain Measurements Using DIC, Strain Gages and Reflection Photoelasticity

Leonardo Dantas Rodrigues, José Luiz de França Freire, and Ronaldo Domingues Vieira

Abstract This investigation applied, simultaneously, two or three experimental strain measurement techniques to different structural models in order to highlight their specific advantages and fields of application. The applied techniques were the digital image correlation method (DIC), the electrical resistance strain gage method (SG), and the reflection photoelasticity method (RP). The DIC, SG and RP results for strains measured at the same points or at similar points of the tested models proved to be satisfactorily close.

Keywords Photoelasticity • Strain gages • Digital image correlation • U-notch • Hole

40.1 Introduction

Although just recently developed, if compared with the electrical resistance strain gage (SG) [1] and reflection photoelasticity (RP) [1] techniques, digital image correlation (DIC) [1, 2] is a global field technique that has proven to be a sound choice for measuring finite elastic and plastic surface strains. The SG and RP techniques are complementary and very well proven strain measurement techniques. The structural models used in this investigation were: (1) bar under tensile load; (2) simple short-beam shear (SBS) three-point bend specimens, which are well-suited for measuring multiple constitutive elastic properties of composite materials [3]; (3) single U-notched bars under bending loads; and (4) a single bar with a circular hole under tensile load [4]. The Vic-3D Test System and Software provided by Correlated Solutions Inc. was used in all the DIC experiments presented in this paper.

40.2 Bar Under Tensile Load

In order to determine the fringe order value of a piece of PS-1 photoelastic material (Vishay Measurements Group) used in two of the experiments reported on in this paper, a long bar specimen with a thickness of 1.95 mm and a width of 26 mm was loaded with tension. An electrical resistance strain gage with a length of 5 mm and a width of 1.4 mm was bonded with cyanoacrylate adhesive to one of the sides of the specimen. The other side of the specimen received three layers of paint. A layer of silver-colored paint was first applied to make possible a reflection of circular polarized light emitted by the white light source from a reflection polariscope. A second, white paint layer and then a third, black speckled spray paint layer were

L.D. Rodrigues
PRIMA-7S – Structural Integrity, Rio de Janeiro, Brazil
e-mail: leodr@prima7s.com

J.L.F. Freire (✉)
Pontifical Catholic University of Rio de Janeiro, Rio de Janeiro, Brazil
e-mail: jlfreire@puc-rio.br

R.D. Vieira
StrainLab- Experimental Stress Analysis
e-mail: ronaldovieira@strainlab.com.br

H. Jin et al. (eds.), *Advancement of Optical Methods in Experimental Mechanics, Volume 3*,
Conference Proceedings of the Society for Experimental Mechanics Series,
DOI 10.1007/978-3-319-00768-7_40,

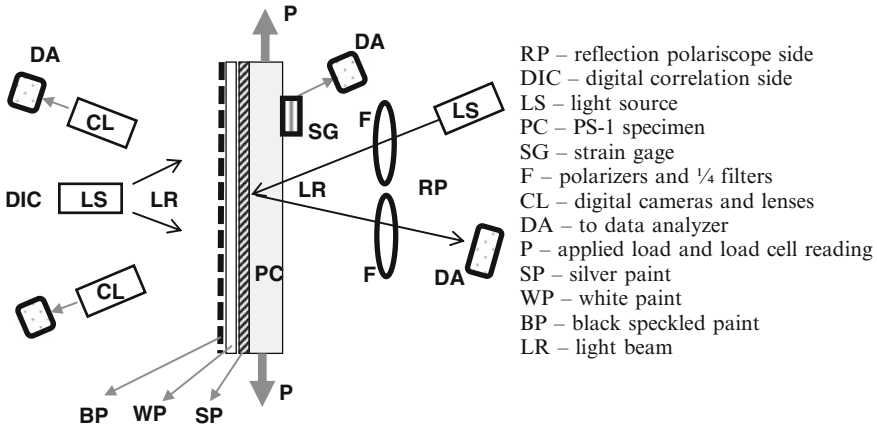

Fig. 40.1 Sketch of experimental arrangement of bar under tensile load for simultaneous strain gage, DIC and reflection photoelasticity measurements

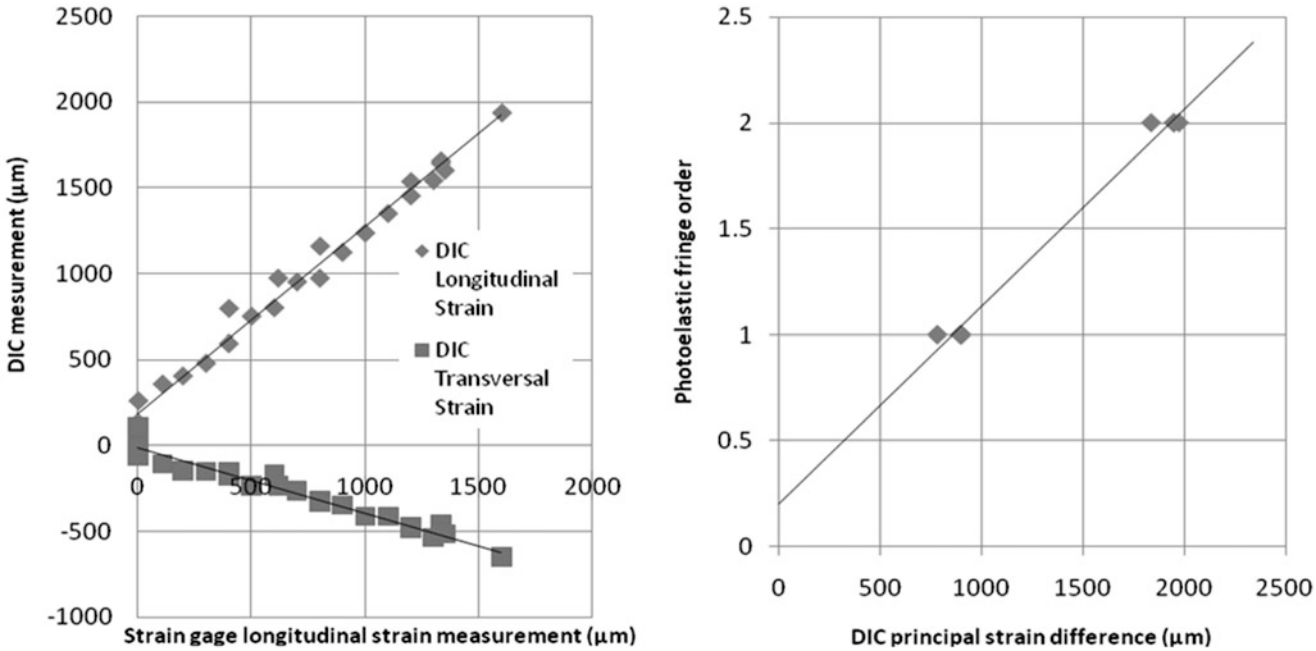

Fig. 40.2 Strain gage, simultaneous DIC and reflection photoelasticity measurements of a PS-1 bar under tensile load

applied over the silver paint to allow for digital correlation image strain measurements while the tensile load was being applied. Figure 40.1 shows a sketch of the experiment.

The data collected from this experiment is presented in Fig. 40.2, showing an excellent agreement between SG and DIC strain measurements and DIC strain and RP fringe order measurements. DIC strain data was determined over a rectangular investigation area with a longitudinal side equal to 30 mm and a transversal side equal to 15 mm. About 2,000–4,000 points inside this area were investigated with 39-pixel sub-sets and 21-pixel steps. A statistics tool of the Vic-3D software was used to extract the average and standard deviation of the strain measurements inside the selected area. The values determined for the standard deviation of the strain measurements inside the pre-designed uniform strain field varied from 80 με (at zero load) to 60 με (at maximum load or maximum strain equal to 1,600 με), resulting in a maximum coefficient of variation equal to 5 % related to the maximum applied strain. From the DIC strain data obtained in both the longitudinal and transversal direction, it was possible to determine the Poisson coefficient of the photoelastic material equal to $\mu = 0.348$. The Young Modulus determined by using the DIC data and the tensile load P measured by a load cell was equal to $E = 2.18$ MPa. The strain fringe value determined by using the DIC principal strain differences and the white light response of the polariscope was equal to 4,063 με.mm/fringe.

40.3 Bar Subjected to Three Point Bending

The American Society for Testing and Materials (ASTM) Standard D2344/D 2344M [5] describes the conditions for using short-beam shear (SBS) tests to determine the strength of polymer matrix composite materials and their laminates. The SBS specimens can be relatively small and short and their use was extended in reference [3] to determine elastic properties of the composite laminates. Due to the high-gradient strain distributions in the SBS specimens, the use of even small strain gages is not recommended. In this case, the use of full-field non-invasive deformation measurement techniques – for example, the DIC method – is appropriate.

In this section, the use of DIC is presented to determine the linear strain distribution along a particular section (halfway between the concentrated applied load and one of the two short beam supports). The same PS-1 specimen used in the previous section (bar under uniform tension) was reloaded using three point-bending, as depicted in Fig. 40.3. Concentrated load P was measured using a load cell, and simultaneous measurements of reflection photoelastic fringe orders and DIC displacement data were made for purposes of comparison and also for determining the Young modulus (E) of the photoelastic material used in the test.

The DIC strain distribution presented in Fig. 40.4 for measurements made along section AB located in one fourth of the beam span is seen to be linear when plotted against position along the Y vertical coordinate axis. Linear extrapolation of the strain distribution to determine the extreme strain values occurring at boundary points A and B led to – 1,270 and 1,330 με, respectively, under a concentrated load of 40 N. Photoelastic fringe orders of 1.6 and 1.8, respectively,

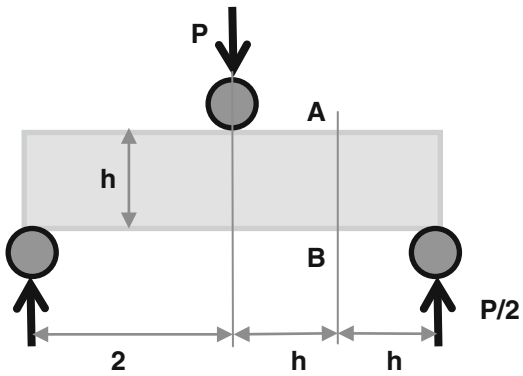

Fig. 40.3 The short-beam tested using bending (width h = 26 mm, thickness t = 1.95 mm)

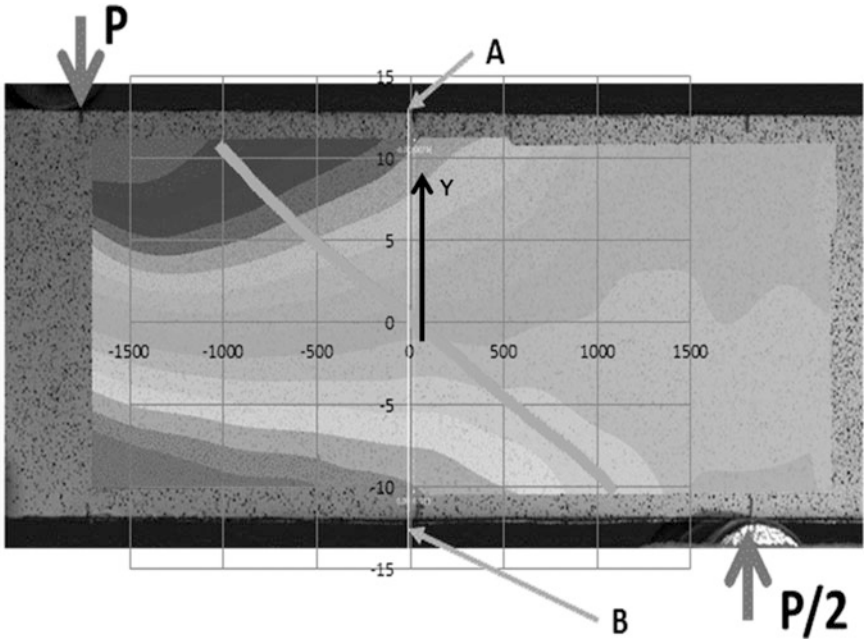

Fig. 40.4 DIC strain distribution (με) along position (mm) in the vertical axis of section AB

measured for these points yielded uniaxial strains of −1,236 and 1,391 με. By applying to this AB cross-section a Euler-Bernoulli classic theory approach and the average DIC extreme strain of 1,300 με, the value of the E modulus comes to 1.8 GPa, which is lower than the PS-1 value of 2.48 GPa as given in [1] and the value of 2.18 GPa determined in the earlier section of this paper.

40.4 Single U-Notch Bars Subject to Pure Bending

Simultaneous applications of the DIC and RP techniques were used to analyze the strain distribution in the neighborhood of small, deep U-notches on bars loaded using pure bending. Figure 40.5 shows the response of both techniques applied for determining the strain difference variation along the symmetry axis, which runs through the midpoint of the deep U-notch. The bar was made of polycarbonate and one of its sides was painted with silver paint (for RP analysis), white paint and pulverized black speckles to allow for the DIC data collection (similar procedure illustrated in Fig. 40.1). The dimensions of the bar and U-notch were: bar width D = 51 mm, bar thickness t = 3.0 mm, U-notch depth d = 21.4 mm, U-notch radius ρ = 1.05 mm. Pure bending was applied by means of four-point bending with loads varying from 500 to 4,000 N.mm.

In the present case, the steep strain gradients prohibited accurate data collection for the application of both techniques. Although macro field lenses were used, the strain gradients could not be accurately detected in the near field (inside the distance of 1 mm from the notch radius). As can be seen in the DIC strain image plot and the RP fringe image plot in Fig. 40.5, strain and fringe resolutions were not even reasonable inside the distance of about ρ/2 = 0.525 mm from the notch's root. Problems like this can be solved in two ways. The first way entails using hybrid methods, where, for example, Westergaard, in connection with the Paris-Creager elastic stress-field equations [6], can be used to numerically fit the field data and hence determine parameters of the stress distributions such as the stress intensity and the stress concentration factors. The second way entails enhancing the experimental apparatus by using a microscope for larger field magnification and much smaller black speckles, in the case of the DIC technique, or using the microscope coupled to much thinner bars, in the case of the RP technique. Figure 40.6 illustrates the response of the strain plot when DIC analysis is carried out using a stereo-microscope.

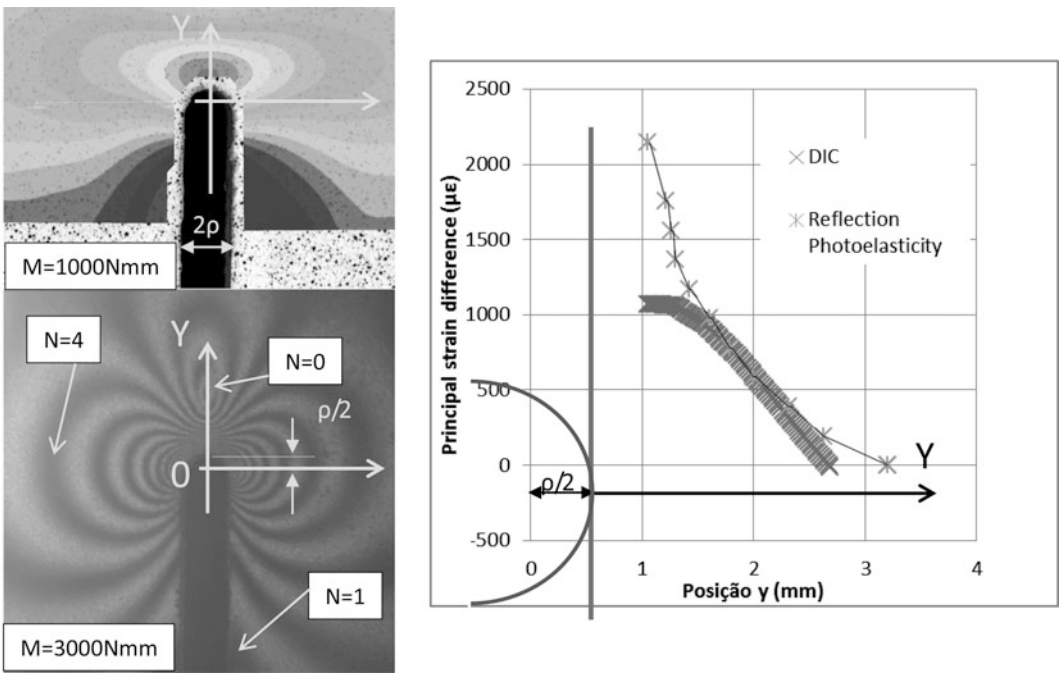

Fig. 40.5 Strain distribution along the symmetry axis of the U-notch bar under pure bending determined using DIC and Reflection Photoelasticity. Notch radius ρ = 1.05 mm, notch depth d = 21.4 mm, bar width D = 51 mm. The variation of the plotted strain difference was normalized for pure bending moment equal to 1,000 Nmm. Photoelastic fringe orders are marked in the figure

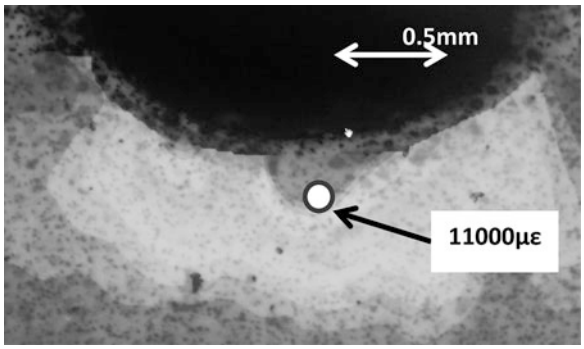

Fig. 40.6 Strain distribution around the boundary of a U-notch with radius $\rho = 1.05$ mm in bar subjected to bending

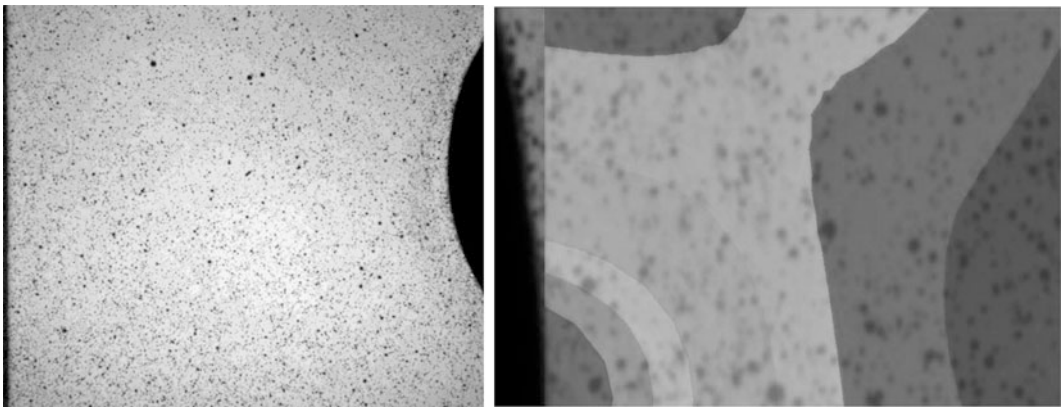

Fig. 40.7 Random pattern of speckles painted near the edge of the hole and example of ε_{yy} strain distribution determined from the DIC analysis

40.5 Bar with a Central Hole Subject to Tensile Load

The experimental specimen was a normalized SAE 1020 steel plate (width $D = 131.4$ mm and thickness $t = 4.70$ mm) with a relatively large central hole (diameter $d = 42.2$ mm). The measured yield strength of the steel plate was equal to $S_y = 275$ MPa. The analysis area of the plate was near the edge of the hole and was first painted with a white paint and sprayed with a black paint to create the random dot distribution that forms the speckle pattern appropriate for the DIC system [4]. Three electrical resistance strain gages (gage length and width equal to 5 and 1.4 mm, respectively) were bonded to the opposite side of the specimen and close to the hole (distances of 1.5, 10.7, and 21.7 mm from the center of the strain gages to the edge of the hole).

The tensile loads were applied in a 100 kN servo-hydraulic Instron machine, under load control. The plate was initially submitted to incremental loads of 10 kN, until reaching 40 kN. This incremental load step was then gradually reduced until reaching 1 kN from 52 kN (near the initial plasticization of the notch tip) up to the final 90 kN load used for the analysis.

A detailed plane stress finite element model of the tested plate was built using the Abaqus FE software. The geometry, representing 1/2 of symmetry, was discretized with CPS4R and CPS3 elements from the Abaqus library, having 4 and 3-node linear elements, respectively.

Figure 40.7 shows the aspect of the maximum strain ε_{yy} (y is parallel to the vertical direction in the figure) field close to the notch's root field measured by the DIC equipment under elastic–plastic conditions.

In Fig. 40.8, the ε_{yy} profiles predicted by the finite element, and measured by the DIC system and by the strain gages placed in the plate's residual ligament are compared for several load levels. It can be concluded from these results that a very good agreement is achieved among the results determined by using the two experimental techniques and the numerical method.

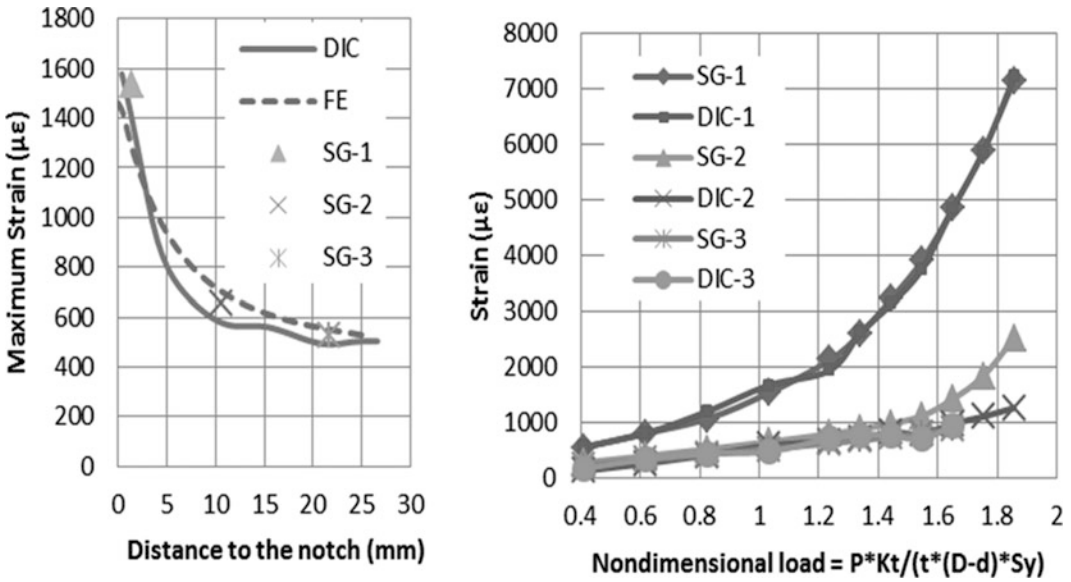

Fig. 40.8 Strain distribution along the horizontal X axis (initiated at the edge of the hole). The results determined by the DIC and SG techniques and by the finite element analysis are plotted in the figure on the left for the tensile load equal to 50 kN (beginning plasticity at the edge of the hole, equivalent to the non-dimensional load defined in the plot on the right equal to 1) and hole diameter equal to 42.2 mm. The figure on the *right* shows how DIC and strain gage results coincide satisfactorily during elastic (up to non-dimensional load equal to1) and elasto-plastic loading. The non-dimensional load was calculated using the stress concentration factor $K_t = 2.31$

References

1. Shukla A, Dally JW (2010) Experimental solid mechanics. College House Enterprises, Knoxville
2. Sutton MA, Orteu JJ, Schreier HW (2009) Image correlation for shape, motion and deformation measurements. Springer Science+Business Media, New York
3. Makeev A, He Y, Carpentier P, Shonkwiler B (2012) A method for measurements of multiple constitutive properties for composite materials. Compos Part A 43:2199–2210
4. Góes RCO, Rodrigues LDR, Castro Neto J, Castro JTP, Freire JLF, Martha LF (2011) Measurement of elastic–plastic strains around notches using DIC techniques. In: Proceedings of the Brazilian conference of mechanical engineering – COBEM 2011, Natal, published (CD) by Brazilian Society for Mechanical Engineering and Mechanical Sciences – ABCM, 2011
5. ASTM Standard D 2344/D 2344M (2006) Standard test method for short-beam strength of polymer matrix composite materials and their laminates. ASTM International, West Conshohocken
6. Freire JLF, Carvalho EA, Cavaco MAM (1993) Determination of stress concentration factors for shallow and sharp V-notches using a hybrid method. Applied Mechanics Reviews 46(11):129–135

Chapter 41
Spatial-Temporal Hybrid Retrievals of Photoelastic Phase Map

M.J. Huang, F.Y. Lao, and S.C. Liu

Abstract A spatial-temporal hybrid approach for retrieving the isoclinic and isochromatic phase messages of practical photoelastic problems is proposed. With the aid of the proposed method, the undefined problem caused by the null term of denominator in the phase map calculation as well as the ambiguity zone problem during temporal phase unwrapping can be respectively solved. Four plane polariscope phase stepping frames are utilized first to correctly restore the isoclinic data of the test sample, of which a white lighting source with full color CCD is used for the colored photoelastic interferograms recording to circumvent the undefined problem. Then after, the retrieved isoclinic is further substituted into the isochromatic formulation to decouple its isoclinic dependence and get a decoupled isochromatic phase map for the following spatial phase unwrapping without much difficulty. In addition, a temporal retrieving of isochromatic phase map is also implemented too; a different wavelength approach is applied to check the performance of the proposed algorithm. It is proved that the robustness and effectiveness of the proposed method are both acceptable.

Keywords Photoelasticity • Temporal phase unwrapping • Spatial phase unwrapping • Isoclinic • Isochromatic

41.1 Introduction

Temporal phase unwrapping is an effective way of phase retrieving method, like load stepping method [1] and different wavelength method [2, 3]. Later, temporal unwrapping technique is also applied both on isoclinic as well as on isochromatic wrapped phase retrieving. Baldi et al. in 2007 proposed the temporal phase unwrapping method [4] to retrieve wrapped data. This algorithm works under certain limitation – the differential phase values of the comparison pair should be within the range of π, which is the essential constrain for firmly applying temporal retrieval upon photoelastic phase map. However, lots of area on general tested samples violate this limitation and thus leave data of those exceptional areas undetermined.

This article proposes that, from spatial point of view, it is necessary to further check the temporal isoclinic unwrapping results to see whether there exist discontinuities or not among neighbored data. If any, marks all the discontinuity individuals by regions. Then, unwraps them alternatively into a continuous distribution and the correct isoclinic retrievals can be achieved. Either different loadings or alternative wavelengths can be applicable. Simulations and experimental works are both conducted to verify the effectiveness of the proposed algorithm.

41.2 Phase Stepping Photoelasticity

A general optical arrangement of a plane polariscope and a circular polariscope are shown in Figs. 41.1 and 41.2, respectively. White light is used as the light source and a general digital camera with RGB filters is used as the fringes recorder. Table 41.1 summarizes the used phase stepping parameters and their corresponding intensity results. The isoclinic φ_w and isochromatic δ_w parameters can be obtained as follows [5].

M.J. Huang (✉) • F.Y. Lao • S.C. Liu
Mechanical Engineering, National Chung Hsing University, 250, Kuo-Kuang Road, Taichung 40227, Taiwan R.O.C.
e-mail: mjhuang8421@gmail.com

H. Jin et al. (eds.), *Advancement of Optical Methods in Experimental Mechanics, Volume 3*,
Conference Proceedings of the Society for Experimental Mechanics Series,
DOI 10.1007/978-3-319-00768-7_41,

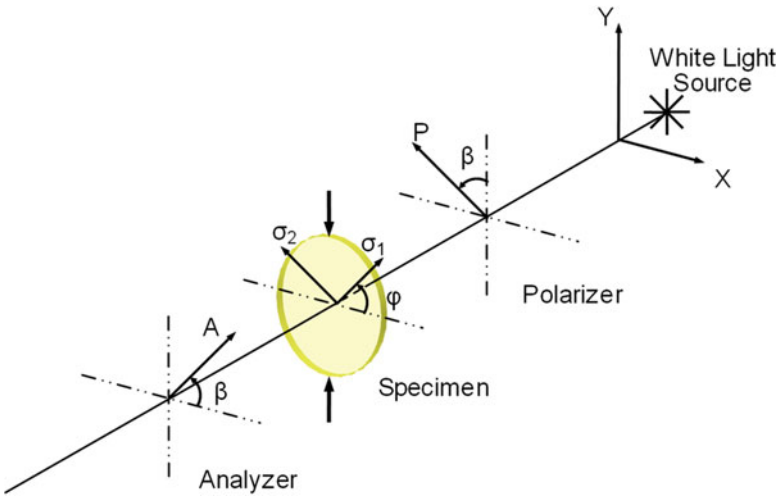

Fig. 41.1 The optical arrangement of plane polariscope

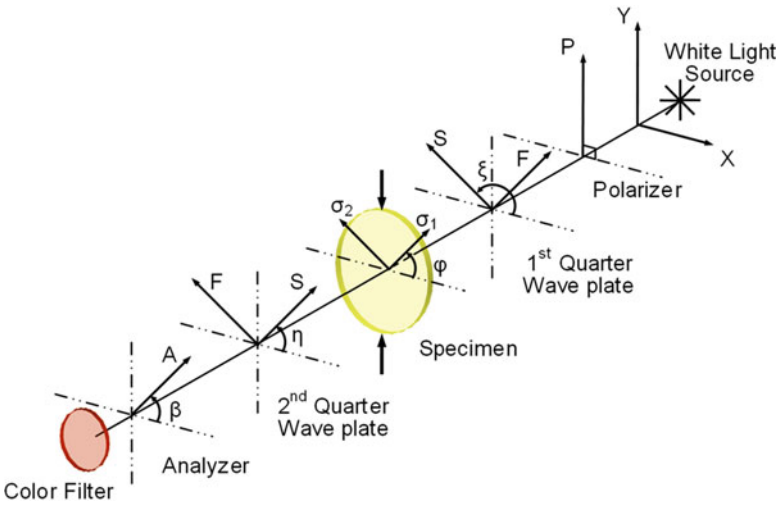

Fig. 41.2 The optical arrangement of circular polariscope

Table 41.1 Polariscope arrangement and the intensity results for phase stepping algorithm

ξ	η	β	Intensity equation
–	–	0	$I_{1,i} = I_{B,i} + \frac{1}{2} I_{A,i} \sin^2 \frac{1}{2} \delta_i (1 - \cos 4\alpha)$
–	–	$\pi/8$	$I_{2,i} = I_{B,i} + \frac{1}{2} I_{A,i} \sin^2 \frac{1}{2} \delta_i (1 - \sin 4\alpha)$
–	–	$\pi/4$	$I_{3,i} = I_{B,i} + \frac{1}{2} I_{A,i} \sin^2 \frac{1}{2} \delta_i (1 + \cos 4\alpha)$
–	–	$3\pi/8$	$I_{4,i} = I_{B,i} + \frac{1}{2} I_{A,i} \sin^2 \frac{1}{2} \delta_i (1 + \sin 4\alpha)$
$3\pi/4$	$\pi/4$	$\pi/2$	$I_5 = I_b + \frac{1}{2} I_a (1 + \cos \delta)$
$3\pi/4$	$\pi/4$	0	$I_6 = I_b + \frac{1}{2} I_a (1 - \cos \delta)$
$3\pi/4$	0	0	$I_7 = I_b + \frac{1}{2} I_a (1 - \sin 2\phi \sin \delta)$
$3\pi/4$	$\pi/4$	$\pi/4$	$I_8 = I_b + \frac{1}{2} I_a (1 + \cos 2\phi \sin \delta)$
$\pi/4$	0	0	$I_9 = I_b + \frac{1}{2} I_a (1 + \sin 2\phi \sin \delta)$
$\pi/4$	$3\pi/4$	$\pi/4$	$I_{10} = I_b + \frac{1}{2} I_a (1 - \cos 2\phi \sin \delta)$

$$\begin{aligned}\phi_w &= \frac{1}{4}\tan^{-1}\left\{\frac{n\langle I_4^s - I_0\rangle - n\langle I_2^s - I_0\rangle}{n\langle I_3^s - I_0\rangle - n\langle I_1^s - I_0\rangle}\right\} \\ &= \frac{1}{4}\tan^{-1}\left\{\frac{\sin\phi}{\cos\phi}\right\},\end{aligned} \tag{41.1}$$

$$\phi = W^{-1}\{\phi_w\}, \tag{41.2}$$

$$\begin{aligned}\delta_w &= \tan^{-1}\left\{\frac{(I_9 - I_7)\sin 2\phi + (I_8 - I_{10})\cos 2\phi}{I_5 - I_6}\right\} \\ &= \tan^{-1}\left\{\frac{I_a \sin\delta}{I_a \cos\delta}\right\},\end{aligned} \tag{41.3}$$

where

$$I_0 = \frac{1}{4}\left(I_1^s + I_2^s + I_3^s + I_4^s\right), \tag{41.4}$$

$$I_j^s = \frac{1}{3}\left(I_{j,R} + I_{j,G} + I_{j,B}\right) \quad \text{for } j = 1, \ldots, 4, \tag{41.5}$$

$W^{-1}\{\}$ represents the unwrapping operator, and $n\langle\rangle$ means normalization operator to eliminate any effect caused by isochromatic parameter. $\tan^{-1}\{\}$ of Eqs. 41.1 and 41.3 is arctan2 function with their results ranging between $-\pi/4 \sim \pi/4$ and $-\pi \sim \pi$, respectively. Since the isochromatic data is dependent on the isoclinic data, the isoclinic data should be correctly unwrapped and ranged in the range of $-\pi/2 \sim \pi/2$ before substituting into Eq. 41.3. Provided the substituted isoclinic data are correct, the isochomatic calculation is ambiguity free and that makes the following retrieval work of the isochromatic data extremely easy.

41.3 Earlier Temporal Phase Unwrapping Algorithm and Its Limitation

A load stepping case is utilized herein to depict the problem encountered. For any non-zero-isochromatic-value sample loading point, the true phase value of the bigger loading one should be larger than that of the smaller loading one. However, their wrapped phases don't obey this rule. It is because that the value of wrapped isochromatic depends, according to phase stepping digital photoelasticity, not only on the principal stress value itself but also on its principal stress direction. To simplify the dependence relationship between them, Baldi et al. [4] proposed that provided that the true isochromatic is constrained in the $(0, \pi)$ interval, the aforementioned relation violation results only from the wrapped isoclinic substitution instead of the true isoclinic substitution. Therefore, its wrapped isoclinics should be added by $\pi/2$ to yield its true one. Therefore, the $(0, \pi)$ constrain becomes the limitation of this rule. The isochromatics around sample loading points easily go beyond this constrain interval and the rule fails there.

41.4 The Proposed Algorithm

Physically, the principal stress differences of a loaded sample should be continuously distributed. However, since the wrapped isochromatics is calculated from the six-field grabbed phase-stepping interferograms [6] and the wrapped isoclinic, which is also calculated from the grabbed phase-stepping interferograms, the correctness of the calculated isochromatics depend strongly upon the correctness of the substituting elements. Either a wrong substitution of the wrapped isoclinic or the wrapped isochromatics itself with respect to those of its neighbored points can yield a discontinuous isochromatic distribution.

Based on the continuity requirement of the unwrapped isochromatics, the proposed algorithm says that no discontinuity can exist in the retrieved isochromatics. If there exists any, find them and unwrap them spatially. Most data of isoclinic and isochromatic parameter unwrap through earlier temporal method would succeed except those under vitiated area. A diametric compression disk sample along vertical direction is used for demonstration. Figure 41.3 is a hybrid result, with

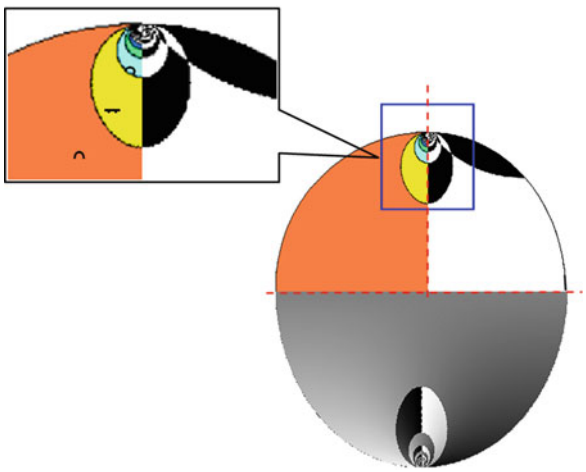

Fig. 41.3 Isoclinic unwrapped result by earlier temporal phase unwrapping algorithm

Table 41.2 Ambiguity check and correction rules for wrapped isoclinic and isochromatic data

Wrapped difference	Ambiguity zone	Correct or not
$(-2\pi, -\pi)$	No	No
$(-\pi, 0)$	Yes	Yes
$(0, \pi)$	No	No
$(\pi, 2\pi)$	Yes	Yes

the first quadrant the ambiguity zone, the second quadrant the true isochromatic partition, the third quadrant the unwrapped isochromatic, and the fourth quadrant the areas needed to be spatially unwrapped. As shown in Fig. 41.3, the upper left part of the diagram displays the true isochromatic partition, each represents one π interval partition. Only for the $(0, \pi)$ interval – the largest one, its correctness of the temporal unwrapped results are guaranteed by the algorithm. It is obvious that around the loading point lots of other area, whose true isochromatic value are not within the $(0, \pi)$ interval. Whatever if the same temporal unwrapping algorithm is applied for retrieval, the correctness of its result would be no longer guaranteed. Looking at the second quadrant, those black areas are set as ambiguity zones by the algorithm and their isoclinic data should be add $\pm \pi/2$ (depending on the sign of its wrapped data). After that, the tuned isochromatic data is shown as the third quadrant of the hybrid plot. Clearly, there exists discontinuity phenomenon after temporal phase unwrapping. Those parts which are needed to be further corrected are found first. Then, set the biggest area as the reference. The area nearest to this referenced area has to be unwrapped once while the next area need not and so on, and the way to unwrap the area is to add $\pm\pi/2$.

The steps to complete the full field unwrapping is summarized as follows. First, calculate the differences between every neighboring point. Second, find the locations where values of difference are bigger than the threshold, which is set as $\pi/4$. Third, use the location we found to segment the area. Fourth, set the largest part as the reference. Fifth, use the period phenomenon to find out the area needed to be corrected by adding $\pm\pi/2$. After these procedures, the phase unwrapping is completed.

Supposed that the 2π-module wrapped isochromatic value is in the 2π interval with values ranging between $(-\pi, \pi)$ and thus the difference of the wrapped data of load-stepping pair will be ranged in the $(-2\pi, 2\pi)$ interval, which is further divided into four equal segments with π interval each. Table 41.2 summarizes the ambiguity check rule for the wrapped isoclinics. It is shown that the first and the third interval ranges are of non-ambiguity zone and no correction is needed. However, the second and fourth interval ranges are of ambiguity zone and their isoclinic and isochromatic data needed to be tuned. The correction rule is that its isoclinic data should be added by $\pm\pi/2$ (plus for negative and minus for positive wrapped isoclinics) and its isochromatic data should be changed by its sign.

41.5 Experimental Results

Diametric compression stress-frozen circular disk sample under white light illumination combined with four-stepping digital photoelasticity is applied to get the four frames polarization stepping interferograms (see Fig. 41.4a–d), from which the wrapped isoclinic is calculated and shown as Fig. 41.4e. Besides of the isoclinic data, two-wavelength (red and green) filters is used to get the six phase stepping interferograms for isochromatic calculations.

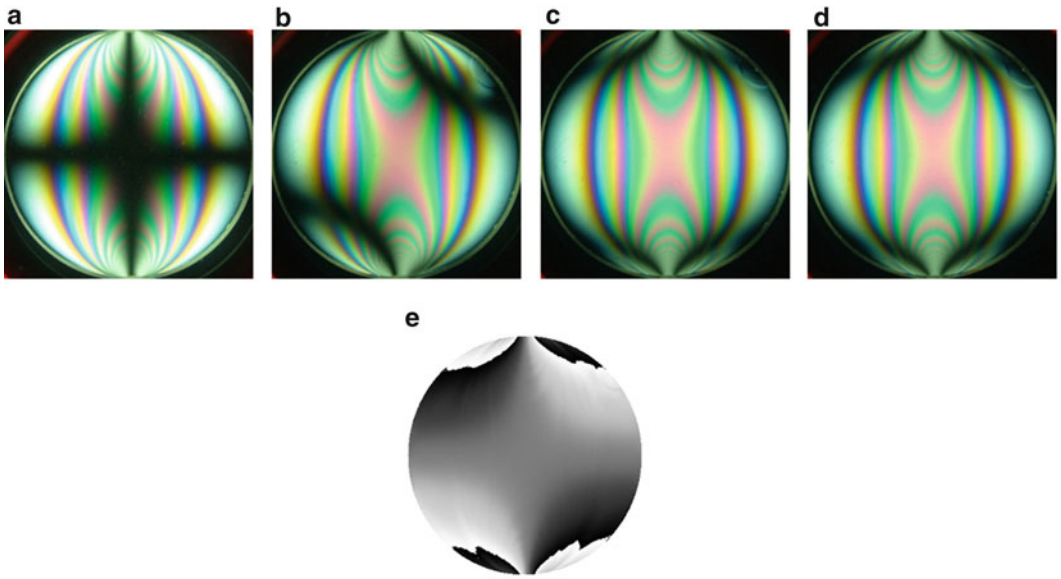

Fig. 41.4 The four (*white light* illuminating) polarization stepping interferograms for isoclinic calculation are shown as (**a–d**) and their calculated isoclinic wrapped map is shown as (**e**)

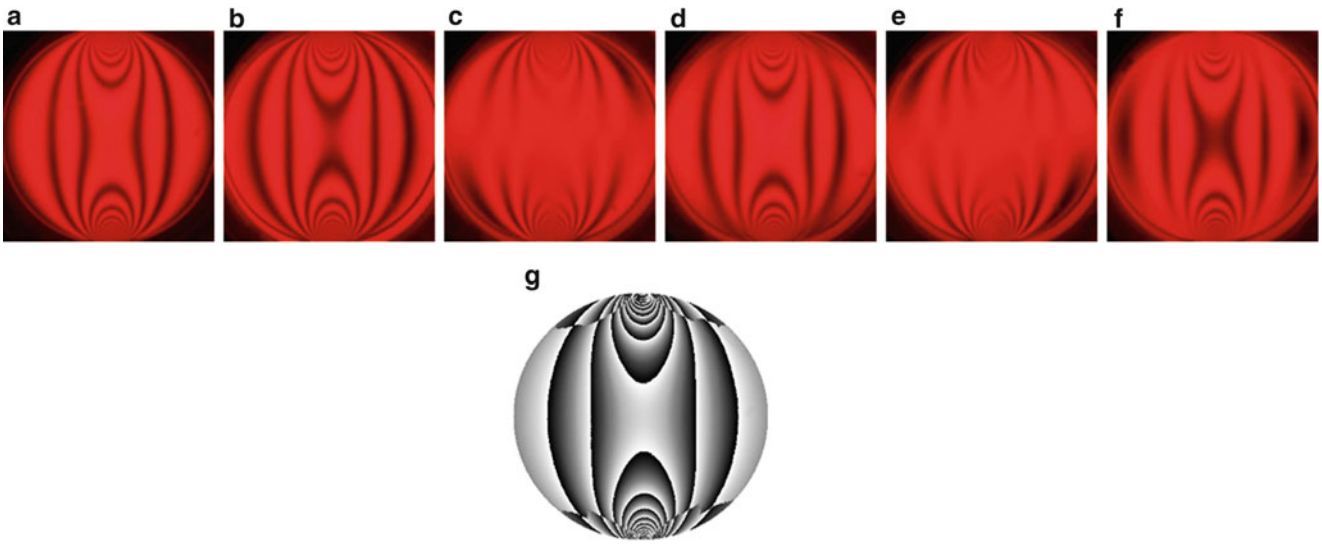

Fig. 41.5 The six polarization stepping interferograms for isochromatic calculation of *red light* are shown as (**a–f**) and their isochromatic wrapped map is shown as (**g**)

Figure 41.5 shows the six-frame phase stepping interferograms (see a–f) of red light, which together with the isoclinic wrapped data (Fig. 41.5e) are fed into the isochromatic formulation to yield the isochromatic wrapped map of Fig. 41.5g. A different wavelength is needed to provide another six-frame phase stepping interferograms. A green filter is used and the six grabbed interferograms are shown as Fig. 41.6a–f. Similarly, they are substituted with isoclinic data into the isochromatic formulation to get the isochromatic wrapped map of green light shown as Fig. 41.6g. Since the wavelength of the green light is smaller that that of the red light, therefore the true isochromatic phase of the green light should be bigger than that of the red light. Their wrapped phase differences are checked according to the rules of Table 41.2 and the original isoclinic wrapped map Fig. 41.4e is corrected and its result is shown as Fig. 41.7a. It is shown that in the central top and button regions, where their true isochromatic data are bigger than π and thus violate the necessary constrain for the temporal phase unwrapping working well. The errors happen in the $(\pi, 2\pi)$, $(3\pi, 4\pi)$, $(5\pi, 6\pi)$,. . .. . . It is also shown that there also exist region errors near the circular boundary and it is because where the isochromatic values are low also the signal to noise ratio

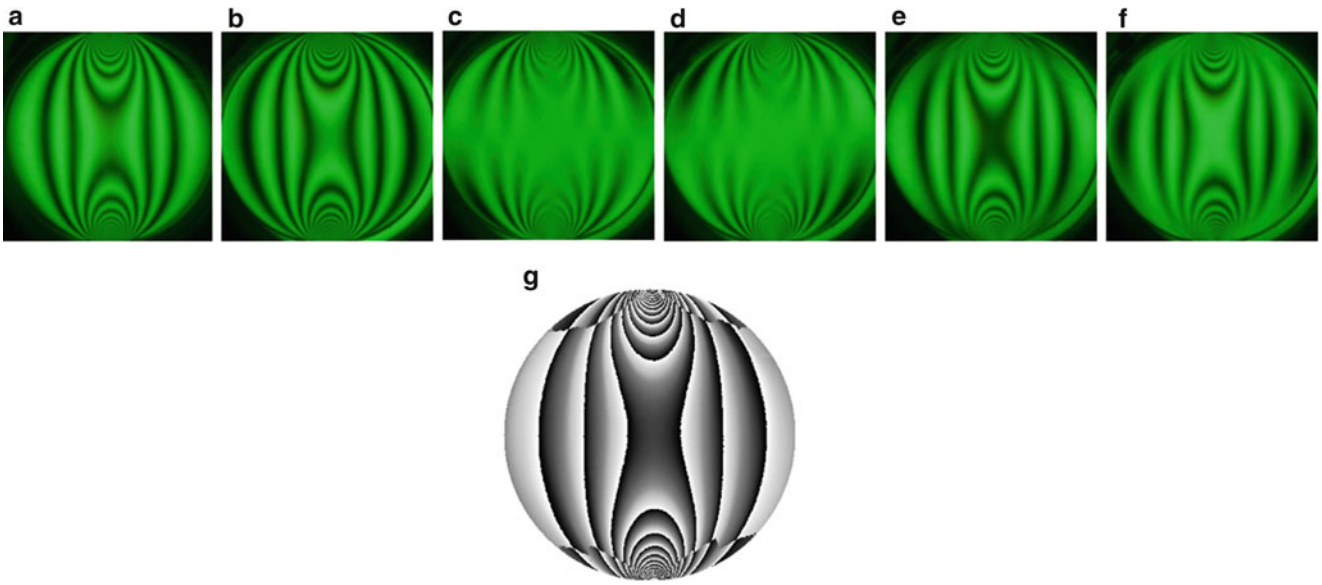

Fig. 41.6 The six polarization stepping interferograms for isochromatic calculation of *green light* are shown as (**a**–**f**) and their isochromatic wrapped map is shown as (**g**)

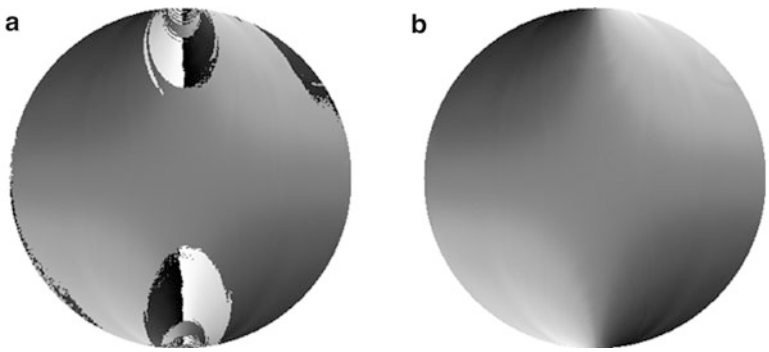

Fig. 41.7 The unwrapped isoclinics, where (**a**) is retrieved by the temporal phase unwrapping but ignores the (0, π) isochromatic limitation and (**b**) is the correction result of (**a**) by spatially unwrapping all the spatial discontinuities

are bad too. Not surprised that errors are easily to be conducted there. From Fig. 41.7a, the clear discontinuities can be detected by naked eyes and signal processing rules. Eliminating the discontinuities yield the continuous isoclinics shown as Fig. 41.7b.

41.6 Discussions and Conclusions

The earlier temporal phase unwrapping algorithm is valid only under the limitation condition of the value of its true isochromatic should be in the range of (0, π). However, this condition is easily violated for any general loading sample like points on which loadings apply. Ignoring this limitation of the temporal phase unwrapping rule and applying this rule on the tested sample lead to error isoclinic and isochromatic results. Since the error is due to constrain of rule applicable range and a periodic pattern of the wrapped isoclinic difference exists, clear discontinuities exist along the integer multiple of π of the true isochromatic phase values. Find the discontinuities and spatially unwrap the discontinuous individuals lead to a perfect isoclinic retrieving result.

Load-stepping experiment can't apply on the stress frozen sample. Alternatively, two wavelengths of red and green are used in the experiment for a diametric compression circular disk stress frozen sample. The shorter wavelength of green light imitates the bigger loading of the load-stepping case and the longer wavelength of red light simulates the smaller loading one. In photoelasticity, isoclinic and isochromatic data are the two most important parameters, from which the principal stress directions and principal stress differences of the tested sample can be found. According to the results, designers and engineers can estimate and judge the working condition of the sample. To decide the isoclinic value the exact incremental difference of the two load-stepping loads is not really necessary but it is definitely needed to be ensured to inversely retrieve the true isochromatics. However, the quarter waveplate under two different wavelengths can induce certain degree of error and cause the error of the unwrapped isochromatic.

It is shown that the proposed algorithm can fully extend the applicable range to the full span including the cases around the sample loading points where the isochromatic data is much bigger than the limitation constrain of the earlier temporal phase unwrapping rule.

Acknowledgments The authors would like to thank the National Science Council of the Republic of China for financially supporting this research under contract Number NSC100-2221-E-005-019.

References

1. Nurse AD (2002) Load-stepping photoelasticity. Optic Laser Eng 38:57–70
2. Ramesh K, Deshmukh SS (1996) Three fringe photoelasticity – use of color image processing hardware to automate ordering of isochromatics. Strain 32:79–86
3. Chen TY (1997) Digital determination of photoelastic birefringence using two wavelengths. Exp Mech 37:232–236
4. Baldi A, Bertolino F, Ginesu F (2007) A temporal phase unwrapping algorithm for photoelastic stress analysis. Optic Laser Eng 45:612–617
5. Huang MJ, Song PC (2010) Regional phase unwrapping algorithm for photoelastic phase map. Optics Express 18:1419–1429
6. Prasad VS, Madhu KR, Ramesh K (2004) Toward effective phase unwrapping in digital photoelasticity. Optic Laser Eng 42–44:421–436

Chapter 42
Linear Birefringence and Dichroism in Fe_3O_4 Magnetic Nanoparticles

Jing-Fung Lin and Meng-Zhe Lee

Abstract We adopt an improved co-precipitation method to prepare the Fe_3O_4 magnetic nanoparticles (MNPs). Influence factors such as surfactant amount, stirring speed, dispersion mode, and Fe^{3+}/Fe^{2+} molar ratio are considered. Using the TEM and XRD, we characterize the dispersibility and size of the products. The appropriate values of experimental parameters are determined, such as stirring speed is 1,000 rpm in titration, simultaneous ultrasonic vibration and mechanical stirring in titration and surface coating, and surfactant amount of oleic acid is 1.2 ml for Fe^{3+}/Fe^{2+} molar ratios including 1.7, 1.8, and 1.9. The average diameters of these Fe_3O_4 MNPs are determined around 11 nm by XRD analysis. In addition, the saturation magnetization for the MNP produced by Fe^{3+}/Fe^{2+} molar ratio as 1.7 is 50.17 emu/g with near paramagnetism. Above all, the linear birefringence and dichroism of the kerosene-based ferrofluids are investigated by a developed Stokes polarimerter. Finally, compared to the results with those for a commercial product and the influences of particle size distribution and magnetization are discussed.

Keywords Birefringence • Co-precipitation • Dichroism • Ferrofluid • Nanoparticle

42.1 Introduction

Fe_3O_4 magnetic fluid or ferrofluid (MF, FF) is a colloidal suspension consisting of magnetite nanoparticles with a typical dimension around 10 nm and carrier liquid like water or hydrocarbons [1]. Due to the high ratio of surface to volume and magnetization, Fe_3O_4 nanoparticles are prone to aggregate. To enhance the compatibility between the Fe_3O_4 magnetic nanoparticles (MNPs) and water or oil, and to control and/or tailor of the surface properties of the nanoparticles, the surface modification for Fe_3O_4 magnetic nanoparticles is a necessity. In the research of Fe_3O_4 magnetic fluids, it is important to prepare magnetic nanoparticles and ensure the stable suspension of Fe_3O_4 magnetic fluids [2]. The preparation methods of magnetite powders mainly include co-precipitation, oxidation of $Fe(OH)_2$ by H_2O_2, microemulsion, and thermal decomposition of $Fe(CO)_5$ [2–4]. The chemical co-precipitation method is frequently used because of its advantages of low cost, simple equipment, usual raw materials, easy control of the size and shape of the nanoparticles, and precise control of the property and chemical composition of the product.

Further, as for the linear birefringence and linear dichroism measurements in magnetic fluids, Taketomi [5] proposed a simple experimental setup for the study of birefringence in a magnetic fluid thin film. To substitute four parameters' values including the two absorption coefficients of magnetic fluids with respect to the ordinary ray and extraordinary ray and the maximum and minimum transmitted intensities when rotating the analyzer, the birefringence (the difference between the refractive indices for extraordinary and ordinary light, respectively) can be easily obtained by this experimental setup and method. Afterwards, Di et al. [6] discussed the particle agglomeration in magnetic fluids using the structure proposed in [5] and Pu et al. [7] discussed the influence of ambient temperature on the magnetic-field-induced birefringence of the magnetic fluids.

J.-F. Lin (✉) • M.-Z. Lee
Graduate School of Computer Application Engineering, Far East University, No.49, Zhonghua Rd., Xinshi Dist., Tainan City 74448, Taiwan ROC
e-mail: jacklin@cc.feu.edu.tw

H. Jin et al. (eds.), *Advancement of Optical Methods in Experimental Mechanics, Volume 3*,
Conference Proceedings of the Society for Experimental Mechanics Series,
DOI 10.1007/978-3-319-00768-7_42,

Kooij et al. demonstrated the versatility of spectroscopic ellipsometry in transmission mode for simultaneously measuring the linear magneto-optical quantities with high accuracy in 2006 [8]. The relations between the ellipsometric quantities Ψ and Δ on one hand and the birefringence and dichroism on the other hand, are derived. Further, Pu et al. developed a simple optical configuration based on a polarizer and derived the analytical expression of the transmitted elliptically polarized light [9]. From the rotation angle of the principal axis of the ellipse and the degree of polarization of the elliptically polarized light after magnetic fluids, the magnetic-field-induced linear birefringence and dichroism are investigated by numerical simulation. The results indicate it is usually improper to ignore the linear dichroism for some applications. In our previous study [10], an optical scheme based on Stokes-Mueller formalism and rotating-wave-plate Stokes polarimeter was successfully developed for obtaining concurrent measurements of the linear birefringence and dichroism, and three probed lights, linearly polarized orientated at 0°, 45°, and circularly polarized are utilized.

In the present investigation, Fe_3O_4 MNPs were prepared by an improved co-precipitation, using NH_4OH as the precipitating agent to adjust the pH value. The effects of surfactant amount, stirring speed, and molar ratio of Fe^{3+}/Fe^{2+} salts in dispersibility and size of MNPs are studied. Mechanical stirring with appropriate speed and ultrasonic vibration are adopted in the titration and surface coating processes. Afterwards, the Fe_3O_4 MNPs were used as the precursor of oil-based FFs. We used oleic acid as surfactant and kerosene as solvent. Characterization of dispersibility, size, particle size distribution, and magnetization in MNPs involved using transmission electronic microscope (TEM), X-ray diffractometry (XRD), dynamic light scattering (DLS), and superconducting quantum interference device (SQUID). Finally, the linear birefringence and dichroism measurements of FF samples are executed for different molar ratios of Fe^{3+}/Fe^{2+} salts by our previously developed Stokes polarimeter with a feasible algorithm. The influences of particle size distribution and magnetization in the birefringence and dichroism measurements of FFs are discussed.

42.2 Experiment

42.2.1 Synthesis of MNPs

To synthesize Fe_3O_4 MNPs, in a typical experiment, a solution with 25 ml of $FeCl_3$ (2 mol/l) and 25 ml of $FeSO_4/7H_2O$ (1 mol/l), respectively, mixed with a molar ratio of 2:1 (ideal ratio) was prepared in a three-necked flask without N_2 protection, and was ultrasonically vibrated for 30 min. In a room temperature of 20 °C, ammonia aqueous solution (25 %) of 20 ml was then charged into the mixed solution at a rate of 0.15 ml/s with vigorously mechanical stirring of 1,000 rpm and ultrasonic vibration, until the pH value of solution reached nine. Thereafter, the temperature was raised to 70 °C and the solution was kept on stirring for additional 30 min. The resulted black precipitate was collected and washed three times with deionized water and ethyl alcohol interactively until the pH value of mixture was around seven. Then the deionized water of 100 ml was added to the mixture. Mechanical stirring of 900 rpm and ultrasonic vibration were done for 30 min. While the mechanical stirring is still on, the temperature was raised to 80 °C, the oleic acid is dropped into the solution by four times, total volume of 0.8, 1.2, 1.6, and 2 ml were used, respectively. Finally, the reaction was done and then dried under vacuum at 60 °C for 12 h. The ground powder of nanoparticles with 1,000 mg was added to the kerosene of 20 ml, ultrasonic vibration is done for 30 min, and the FFs were obtained.

42.2.2 Effects of the Amount of Surfactant

We fix the molar ratio between Fe^{3+} and Fe^{2+} salts as an ideal value of 2:1, the stirring speed is set as 800 rpm in titration, the operating temperature is set as 70 °C, the reaction temperature in surface coating is set as 80 °C, and only change the amount of surfactant as oleic acid from 0.8 to 2 ml in increments of 0.4 ml. It is noted that the dispersion mode is chosen as only ultrasonic vibration when surface coating is done. The effect of the amount of surfactant is studied through performing TEM (JEOL, JEM-1400, Japan) and XRD (Shimadzu, XRD-6000, Japan) analysis. From the comparisons of TEM micrographs, as shown in Fig. 42.1a–d, the dispersibility for the amount of oleic acid with 1.2 ml in Fig. 42.1b is best and fewer agglomerations are found in 100 nm scale.

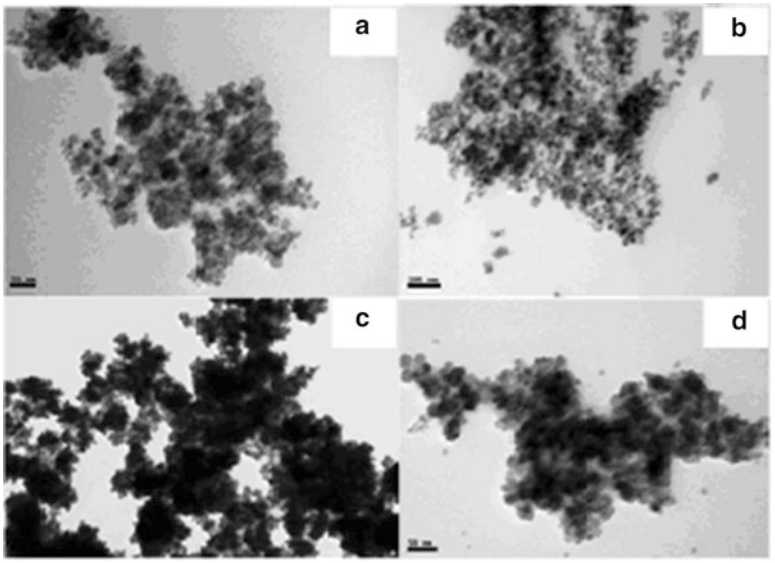

Fig. 42.1 TEM morphology of magnetite under different amounts of oleic acid with 0.8, 1.2, 1.6, 2.0 ml, respectively

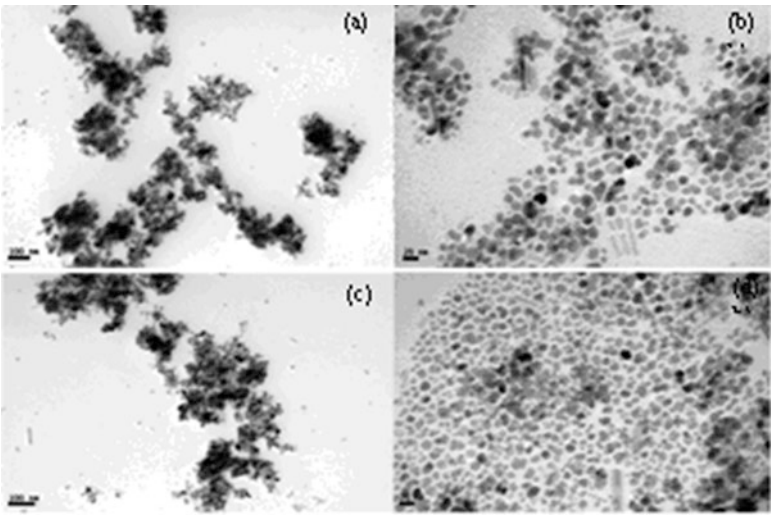

Fig. 42.2 TEM morphology of magnetite under different stirring speeds in titration but with simultaneous ultrasonic vibration and mechanical stirring of 900 rpm when surface coating, (**a**) 700, (**b**) 800, (**c**) 900, (**d**) 1,000 rpm

42.2.3 Effects of the Stirring Speed in Titration

In this part, the molar ratio between Fe^{3+} and Fe^{2+} salts is fixed as 2:1 and the amount of oleic acid is 1.2 ml, the dispersion mode is changed as simultaneous ultrasonic vibration and mechanical stirring of 900 rpm for 30 min when surface coating is done, and the stirring speed in titration is changed from 800 rpm in Sect. 42.2.2 to other speeds ranging from 700 to 1,000 rpm. The other experimental parameters are the same as those in Sect. 42.2.2. One reason for considering higher stirring speed in titration is the higher speed can help the full contact between the reaction solutions and avoid the uneven mixing and the induced higher partial concentration, thus the crystal core can produce and grow well and the diameter is synthesized to be small scale [11]. It is known that the mechanical stirring is suitable for mixing evenly and opening the larger agglomeration and the ultrasonic vibration is suitable for the dispersion of smaller agglomeration. Its dispersion is based on the high frequency vibration and cavitations' effect to produce strong injection and local shocking wave, thus to destroy and refine the particles.

From the TEM micrographs, as shown in Fig. 42.2, it is found that when the stirring speed is 1,000 rpm in titration and simultaneous ultrasonic vibration and mechanical stirring in surface coating are done, excellent dispersibility (with clear boundary and few agglomerations) is obtained, as shown in Fig. 42.2d in 20 nm scale. Most of the particle's diameter in Fig. 42.2d is below 20 nm and with near-spherical shape. In addition, when the stirring speed in titration is 800 rpm,

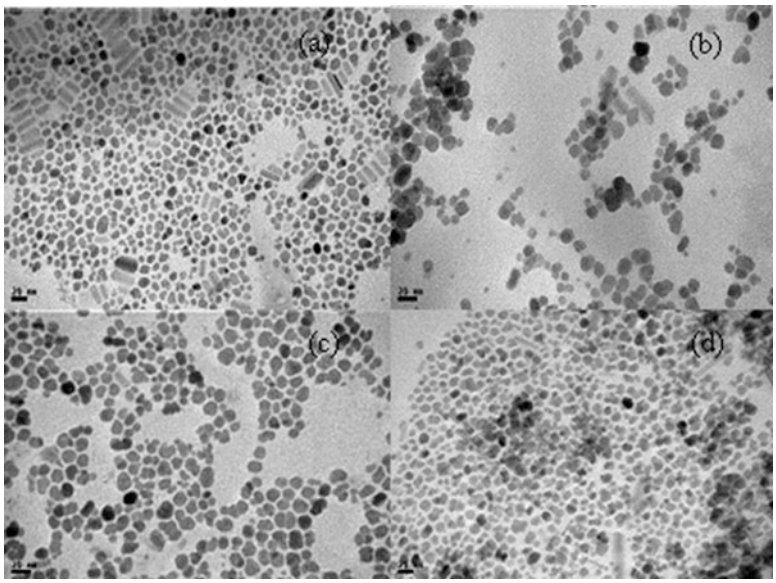

Fig. 42.3 TEM morphology of magnetite under the stirring speed of 1,000 rpm in titration, the simultaneous dispersion mode when surface coating, and for different molar ratios of Fe^{3+}/Fe^{2+} salts as (**a**)1.7:1, (**b**) 1.8:1, (**c**) 1.9:1, and (**d**) 2:1

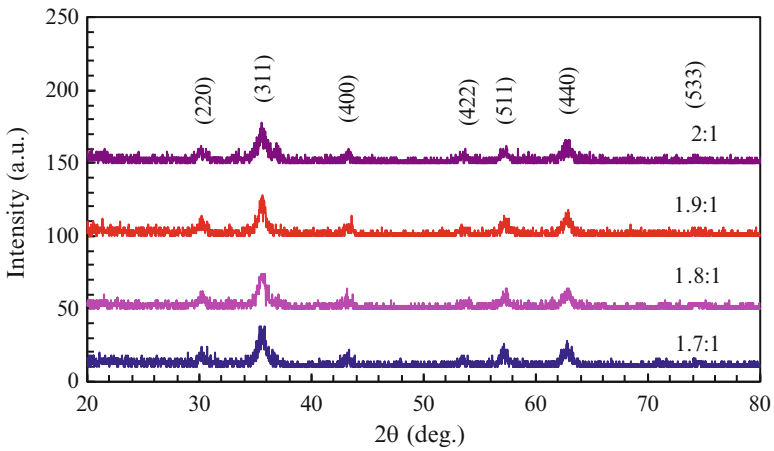

Fig. 42.4 XRD patterns of Fe_3O_4 nanoparticles synthesized under different molar ratios of Fe^{3+}/Fe^{2+} salts as 1.7:1, 1.8:1, 1.9:1, and 2:1, respectively

as shown in Fig. 42.2b in 20 nm scale, good dispersibility (few agglomerations) is found. Compared to Fig. 42.1b in 100 nm scale with only ultrasonic vibration when surface coating is done, the dispersibility is improved obviously. Therefore, the dispersion mode by simultaneous ultrasonic vibration and mechanical stirring in surface coating is helpful.

42.2.4 Effects of the Molar Ratio of Fe^{3+}/Fe^{2+} Salts

We fix the amount of oleic acid to be 1.2 ml, the string speed of 1,000 rpm in titration, and the dispersion mode is chosen as ultrasonic vibration and mechanical stirring of 900 rpm simultaneously for 30 min in surface coating. It is noted that we perform experiments without the protection of nitrogen and the Fe^{2+} is easily oxygenated to be Fe^{3+} in reaction process and cause the amount of Fe^{2+} to be insufficient. In addition, the amount of Fe^{3+} salts is excess to generate Fe_2O_3 and have an influence in the purity of Fe_3O_4. Hence we choose lower molar ratios of Fe^{3+}/Fe^{2+} salts as 1.7:1, 1.8:1, and 1.9:1 (close to 2:1) to avoid the problems described above. From the TEM micrographs, shown as in Fig. 42.5 in 20 nm scale, the better dispersibility is obtained for the molar ratios of 1.7:1 and 1.9:1 (Fig. 42.3a, c). Most of the particle's diameter is below 15 nm with spherical shape, and fewer agglomerations exist.

Figure 42.4 shows XRD patterns of Fe_3O_4 MNPs, synthesized under different molar ratios of Fe^{3+}/Fe^{2+} salts, it was found that all the different peaks at $2\theta = 30.1$, 35.4, 43.1, 53.4, 56.9, 62.6, and 73.9° could be well indexed to the inverse cubic spinel structure of Fe_3O_4. The average crystallite sizes of Fe_3O_4 MNPs obtained under different molar ratios of Fe^{3+}/Fe^{2+}

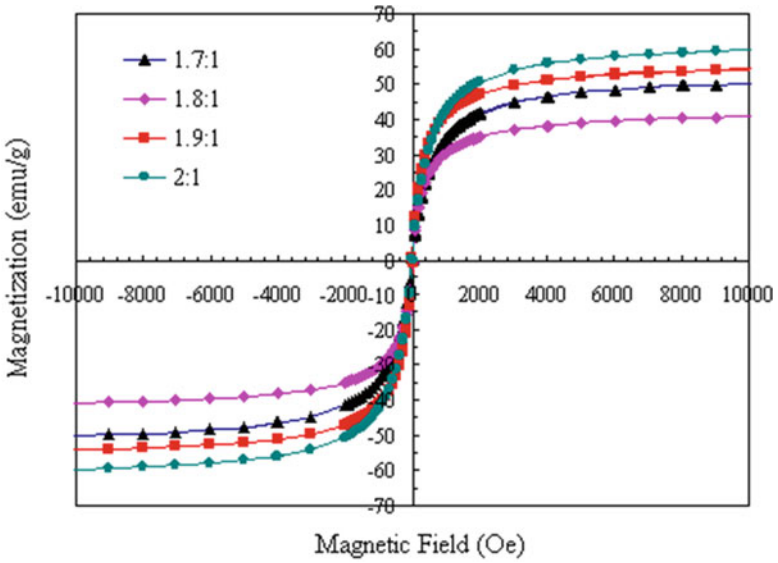

Fig. 42.5 Magnetization curves of magnetic nanoparticles synthesized at different Fe^{3+}/Fe^{2+} ratios

salts (1.7:1, 1.8:1, 1.9:1, and 2:1) were determined to be 10.8, 10.9, 10.5, and 9.8 nm, respectively. The sizes of these MNPs, respectively, are below the critical size of 15 nm, the superparamagnetic iron oxides are therefore obtained under the above experimental conditions.

Via SQUID (Quantum Design, MPMS-XL7, USA) measurements at room temperature and magnetic field intensity between −10,000 and 10,000 Oe, the saturation magnetization of Fe_3O_4 powder for Fe^{3+}/Fe^{2+} ratio equal to 2:1 was about 59.74 emu/g, and those are about 50.17, 40.91, 54.27 emu/g for the other powders of Fe^{3+}/Fe^{2+} ratio equal to 1.7:1, 1.8:1, and 1.9:1, respectively, as shown in Fig. 42.5. The ratios of saturation magnetization for these MNPs to that of the bulk magnetite (92 emu/g) range from 45 % to 65 %. These Fe_3O_4 MNPs could be said to have supermagnetization for their remanent magnetization close to zero and low coercivity. The reason why these MNPs are close to superparamagnetic is the size for some parts of these MNPs are larger than 15 nm.

42.2.5 Measurement of the Linear Birefringence and Dihroism in Ferrofluids

After producing Fe_3O_4 MNPs, we used the previously developed Stokes polarimeter for measuring the linear birefringence and dichroism in FFs. The individual ferrofluid samples in Sect. 42.2.4 were injected in to a liquid cell with a thickness of 12 μm and were then introduced into the measurement system. Figures 42.6 and 42.7 present the results obtained for the birefringence and dichroism of the FF samples under external magnetic field (0–1 A in increments of 0.1 A, i.e. from 0 T to 64.5 mT). The propagation direction of the light is normal to the applied transverse magnetic field. Magnetic field is generated by a magnetic generator (U-shaped core, GMBH, Germany).

From inspection, as shown in Fig. 42.6, the experimental results show the magnitude of retardance increases with the increasing magnetic fields. And it is observed that the retardance of the FF sample with a molar ratio of Fe^{+3}/Fe^{+2} salts as 1.9:1 under magnetic field ranging from 0 T to 64.5 mT, respectively, is smaller than those of the FF samples with molar ratios of Fe^{3+}/Fe^{2+} salts as 1.7:1 and 1.8:1, respectively (with calibration of empty cell). The retardance is 1.20° when the FF sample with a molar ratio of Fe^{3+}/Fe^{2+} salts as 1.7:1 under magnetic field of 64.5 mT, which is lower than that of 12.13° for a commercial FF product as EMG 905 (Ferrotech Inc., US) with a concentration of 2 % [10].

From inspection, as shown in Fig. 42.7, the magnitude of dichroism increases with the increasing magnetic fields. And it is shown that the FF sample with a molar ratio of Fe^{3+}/Fe^{2+} salts as 1.9:1 results in lower absorption (with a value of 0.021 under 64.5 mT) than the other FF samples with molar ratios of Fe^{3+}/Fe^{2+} salts as 1.7:1 and 1.8:1, and is lower than that of 0.048 for EMG 905 with a concentration of 2 % [10]. It is known that the dichroism value of the FF sample with a molar ratio of Fe^{3+}/Fe^{2+} salts as 1.7:1 is little larger than that of FF sample with a molar ratio of Fe^{3+}/Fe^{2+} salts as 1.8:1. As for the retardance and dichroism values of the FF sample with a molar ratio of Fe^{3+}/Fe^{2+} salts as 2:1, those values are the lowest, as shown in Figs. 42.6 and 42.7.

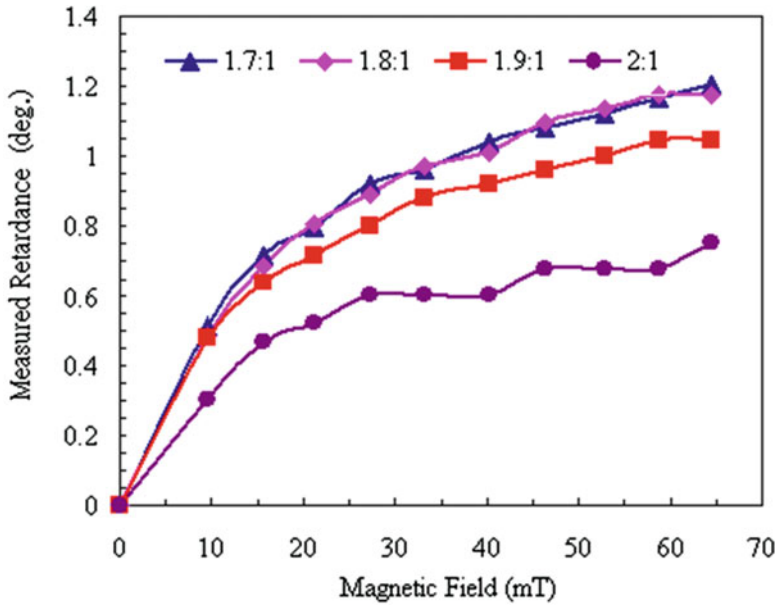

Fig. 42.6 Experimental results of retardance in ferrofluid samples with molar ratios of Fe^{3+}/Fe^{2+}salts from 1.7:1 to 2:1

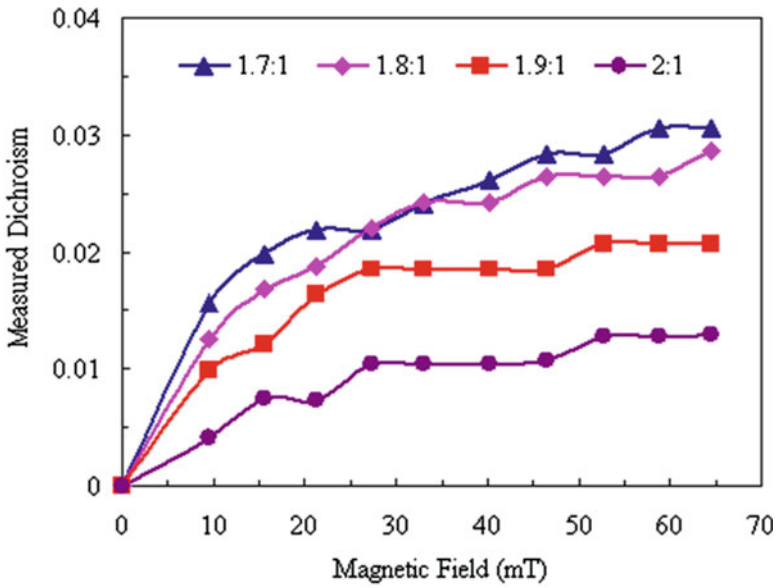

Fig. 42.7 Experimental results of dichroism in ferrofluid samples with molar ratios of Fe^{3+}/Fe^{2+}salts from 1.7:1 to 2:1

It is known that the birefringence (retardance) are sensitive to particle size (shape), mono- or poly- disperse distribution, and in terms of the second order Langevin function, which is function of the magnetic field strength, the particle physical diameter, and the temperature [12, 13]. It is noted that when the system is a polydisperse suspension, calculating the birefringence (refractive index difference between ordinary and extraordinary rays), the particle size distribution is needed to be taken into account. The measurement results of DLS (Malvern, 3000-HAS, UK) for FF samples with molar ratios of Fe^{3+}/Fe^{2+} salts as 1.7:1 and 1.8:1 are as shown in Figs. 42.8 and 42.9 (for a molar ratio of 2:1 is not measured for its smaller retardance).

For the FF samples with molar ratios of Fe^{3+}/Fe^{2+} salts as 1.7:1 and 1.8:1, as shown in Figs. 42.8 and 42.9, are considered as bi- and poly- disperse suspensions, respectively. Further, for the FF sample with a molar ratio of Fe^{3+}/Fe^{2+} salts as 1.7:1, the particle size distribution is concentrated around 2.8 and 7.5 nm (bidisperse suspension), while for the FF sample with a molar ratio of Fe^{3+}/Fe^{2+}salts as 1.8:1, the particle size distribution is concentrated around 10.6 nm and distributed widely. In addition, form the TEM analysis, as shown in Fig. 42.3a, b, indicating the MNPs for a molar ratio of Fe^{+3}/Fe^{+2} salts as 1.7:1 is smaller and more disperse than those of MNPs for Fe^{3+}/Fe^{2+} salts as 1.8:1. Thus, the saturated magnetization of the MNPs

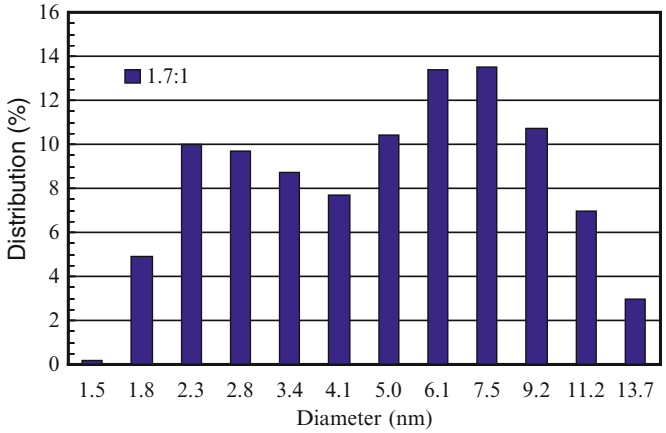

Fig. 42.8 Experimental results of particle size distribution in ferrofluid with a molar ratio of Fe^{3+}/Fe^{2+} salts as 1.7:1

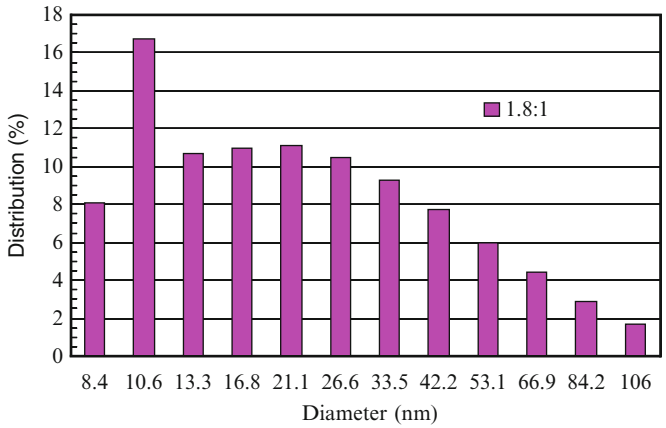

Fig. 42.9 Experimental results of particle size distribution in ferrofluid with a molar ratio of Fe^{3+}/Fe^{2+} salts as 1.8:1

for a molar ratio of Fe^{+3}/Fe^{+2} salts as 1.7:1 is larger than that of MNPs for Fe^{3+}/Fe^{2+} salts as 1.8:1. The small size, high dispersion, and high saturated magnetization (magnetic response) may dominate the magnetic-field induced birefringence behavior of FFs. Additionally, it is indicated that the FF sample with a molar ratio of Fe^{3+}/Fe^{2+} salts as 1.7:1 (bidisperse suspension with a narrower particle range and higher magnetization) has a little higher retardance and dichroism than those of FF sample with a molar ratio of Fe^{3+}/Fe^{2+} salts as 1.8:1.

42.3 Conclusions

Via the TEM and XRD analysis, we found the appropriate parameters of an improved co-precipitation method in preparing the Fe_3O_4 MNPs without the protection of nitrogen. The results showed that important factors include the amount of surfactant, the stirring speed in titration, the dispersion mode by simultaneous ultrasonic vibration and mechanical stirring, and the molar ratios of Fe^{3+}/Fe^{2+} salts, which decide the dispersibility and size of the Fe_3O_4 MNPs. The best conditions for the preparation of Fe_3O_4 MNPs are included those as the amount of oleic acid is 1.2 ml, the stirring speed in titration is 1,000 rpm, and the simultaneous dispersion is adopted in the titration and surface coating processes. Via the XRD analysis, the average diameters of these Fe_3O_4 MNPs are 11 nm for molar ratios of Fe^{3+}/Fe^{2+} salts ranging from 1.7:1 to 1.9:1.

The linear birefringence and dichroism measurements of these kerosene-based FF samples for molar ratios of Fe^{3+}/Fe^{2+} salts ranging from 1.7:1 to 1.9:1, which result in lower retardance and absorption than those of the commercial FF as EMG 905 with a concentration of 2 %. Further, according to the results of TEM, DLS, and SQUID measurements of these MNPs, it is indicated that the FF with a molar ratio of Fe^{3+}/Fe^{2+} salts as 1.7:1 (bidisperse suspension with a narrower particle range

and higher magnetization as 50.17 emu/g) has a little higher retardance and dichroism than those of FF with a molar ratio of Fe^{3+}/Fe^{2+} salts as 1.8:1 (polydisperse suspension with a wider particle range and lower magnetization as 40.91 emu/g). The influences of particle size distribution and magnetization in the birefringence and dichroism measurements of FFs are discussed.

Acknowledgments The financial support provided to this study by the National Science Council of Taiwan under Grant NSC-100-2622-E-269-016-CC3 is gratefully acknowledged.

References

1. Wang YM, Cao X, Liu GH, Hong RY, Chen YM, Chen XF, Li HZ, Xue B, Wei DG (2011) Synthesis of Fe_3O_4 magnetic fluid used for magnetic resonance imaging and hyperthermia. J Magn Magn Mater 323:2953–2959
2. Hong RY, Pan TT, Han YP, Li HZ, Ding J, Han S (2007) Magnetic field synthesis of Fe_3O_4 nanoparticles used as a precursor of ferrofluids. J Magn Magn Mater 310:37–47
3. Wei Y, Han B, Hu X, Lin Y, Wang X, Deng X (2012) Synthesis of Fe_3O_4 nanoparticles and their magnetic properties. Procedia Eng 27:632–637
4. Liang X, Shi H, Jia X, Yang Y, Liu X (2012) Dispersibility, shape and magnetic properties of nano-Fe_3O_4 particles. Mater Sci Appl 2:1644–1653
5. Taketomi S (1983) Magnetic fluid's anomalous pseudo-Cotton Mouton effects about 10^7 times larger than that of nitrobenzene. Jap J Appl Phys 22:1137–1143
6. Di Z, Chen XF, Pu SL, Hu X, Xia Y (2006) Magnetic-field-induced birefringence and particle agglomeration in magnetic fluids. Appl Phys Lett 89:211106
7. Pu SL, Liu M, Sun GQ (2010) Influence of ambient temperature on the magnetic-field-induced birefringence of the nanostructured magnetic fluids. Acta Photon Sin 39:1742–1746
8. Kooij ES, Gâlcă AC, Poelsema B (2006) Versatile transmission ellipsometry to study linear ferrofluid magneto-optics. J Colloid Interface Sci 304:261–270
9. Pu S, Dai M, Sun G, Liu M (2009) Linear birefringence and linear dichroism coupled optical anisotropy of magnetic fluids by external magnetic fields. In: Proceedings of IEEE SOPO, Wuhan, pp 1–6
10. Lin JF, Lee MZ (2012) Concurrent measurement of linear birefringence and dichroism in ferrofluids using rotating-wave-plate Stokes polarimeter. Opt Commun 285:1669–1674
11. Chen TR. Sun J (2009) Study on preparation of magnetic Fe_3O_4 nano-particles with liquid-state co-precipitation method. Master Dissertation, Qingdao University, p 22
12. Koralewski M, Pochylski M, Mitróová Z, Timko M, Kopcanský P, Melníková L (2011) Magnetic birefringence of natural and synthetic ferritin. J Magn Magn Mater 323:2413–2417
13. Socoliuc V (1999) Investigation of concentration and surface quality influence on magnetic particle agglomeration in ferrofluids from static linear dichroism experiments. J Magn Magn Mater 207:146–157

Chapter 43
Shape Measurement Using CAD-Based Stereo-DIC

J.-E. Dufour, B. Beaubier, F. Hild, S. Roux, and S. Leclercq

Abstract The aim of this study is to measure the (complex) shape of an object by using a priori information given by its CAD representation in a 3D-DIC framework. In order to follow a 3D object during its deformation and to determine 3D surface displacement fields, a first measurement of the object shape is necessary. The main goal of the present method is to obtain a CAD representation of this measurement by updating the CAD reference via a global approach to 3D-DIC. Although in the majority of the shape measurement methods a cloud of points is obtained and subsequently interpolated to create a continuous description of the surface, CAD-based stereoDIC is devised to directly measure a 3D shape described by NURBS. This approach allows a direct link to be established between the theoretical CAD model and its true geometry thereby yielding the metrology of the measured surface in the CAD language.

Keywords Stereo-correlation • Global approach • Shape measurement • DIC • NURBS

43.1 Introduction

Many techniques are presently used to extract the shape of an object. Most of them (e.g. laser speckle interferometry, CMM, DIC [1–4]) consist in evaluating the position of some points on the surface and then interpolating this cloud to obtain a continuous representation of the surface. These techniques have many degrees of freedom during the point cloud evaluation which is subsequently reduced by interpolation. The present approach consists in adding as much 'a priori' information as possible to find the real surface. In the case of industrial parts, a CAD model of the theoretical surface is generally available and can be used as a first estimation. By resorting to a global approach to stereo-DIC, this surface can be deformed to fit as best as possible (from a DIC point of view) the real shape.

Shape reconstruction via StereoDIC consists in finding the 3D coordinates of a point using its 2D coordinates in two (or more) pictures taken by different cameras [1]. This assumes that a calibration of the stereovision system has already been performed by any technique [1, 5–7]. Classical (local) approach performs this operation on many particular points to extract a cloud of 3D points from the 2D pictures. The method developed herein does not reconstruct point to point surfaces but uses NURBS to measure their shape as a mathematical representation without any interpolation step.

The outline of the paper is as follows. First, the main equations of the global DIC problem will be detailed, and then the principle of the reconstruction method will be explained. Finally, an example on an industrial part with a complex shape will be developed.

J.-E. Dufour (✉) • F. Hild • S. Roux
LMT Cachan, ENS Cachan/CNRS UMR 8535/Univ. Paris 6/PRES UniverSud Paris, 61 Avenue du Président Wilson, 94235 Cachan Cedex, France
e-mail: dufour@lmt.ens-cachan.fr

B. Beaubier
LMT Cachan, ENS Cachan/CNRS UMR 8535/Univ. Paris 6/PRES UniverSud Paris, 61 Avenue du Président Wilson, 94235 Cachan Cedex, France

PSA Peugeot Citroën, Centre Technique de Vélizy B Zone aéronautique Louis Bréguet, Velizy Villacoublay 78140, France

S. Leclercq
Messier-Bugatti-Dowty, Inovel Parc Sud, Velizy Villacoublay 78140, France

H. Jin et al. (eds.), *Advancement of Optical Methods in Experimental Mechanics, Volume 3*,
Conference Proceedings of the Society for Experimental Mechanics Series,
DOI 10.1007/978-3-319-00768-7_43,

43.2 CAD-based Stereo-DIC Formulation

The DIC problem can be formulated as the minimization of a functional η evaluated over a region of Interest

$$\eta^2 = \int\int_{ROI} [r(x^r + u^r(x^r)) - l(x^l + u^l(x^l)]^2 \mathrm{d}v\mathrm{d}w \tag{43.1}$$

where v and w are parameters defining the observed surface. A Taylor expansion of this functional leads to

$$\eta^2 = \int\int_{ROI} \left(r(x^r) + \nabla r(x^r) \cdot u^r(x^r) - l\left(x^l\right) - \nabla l\left(x^l\right) \cdot u^l\left(x^l\right)\right)^2 \mathrm{d}v\mathrm{d}w \tag{43.2}$$

The 'pseudo' displacement $u(x)$ is written in terms of sensitivity fields associated with the parameters of the surface to be measured

$$u^{r,l}\left(x^{r,l}\right) = \frac{\partial u^{r,l}}{\partial X} \cdot \frac{\partial X}{\partial P_i} \cdot dP_i \tag{43.3}$$

with $\dfrac{\partial u^{r,l}}{\partial X} = F(M^{r,l})$ depending on the transformation matrices evaluated during the calibration process, and $\dfrac{\partial X}{\partial P_i} = N$ the shape function matrix of the NURBS surface [8]. Minimizing η^2 leads to a series of linear problems

$$\mathbf{C} \cdot \mathrm{d}P = B \tag{43.4}$$

with

$$C_{ij} = \int\int_{ROI} \left(\frac{\partial u^r}{\partial X} \cdot \frac{\partial X}{\partial P_i} \cdot \nabla r(x^r) - \frac{\partial u^l}{\partial X} \cdot \frac{\partial X}{\partial P_i} \cdot \nabla l\left(x^l\right)\right) \otimes \left(\frac{\partial u^r}{\partial X} \cdot \frac{\partial X}{\partial P_i} \cdot \nabla r(x^r) - \frac{\partial u^l}{\partial X} \cdot \frac{\partial X}{\partial P_i} \cdot \nabla l\left(x^l\right)\right) \mathrm{d}v\mathrm{d}w$$

and

$$B_i = \int\int_{ROI} \left(\frac{\partial u^r}{\partial X} \cdot \frac{\partial X}{\partial P_i} \cdot \nabla r(x^r) - \frac{\partial u^l}{\partial X} \cdot \frac{\partial X}{\partial P_i} \cdot \nabla l\left(x^l\right)\right) \cdot \left[l\left(x^l\right) - r(x^r)\right] \mathrm{d}v\mathrm{d}w$$

A regularized form of this equation can be constructed using a Levenberg-Marquard algorithm [9]

$$(\mathbf{C} - \lambda \mathbf{I})\mathrm{d}P = B + \lambda\left(P - P^0\right) \tag{43.5}$$

where $\boldsymbol{P}$ is the current estimation of the control point coordinates, $\boldsymbol{P}^0$ is the first guess of the control point coordinates, and λ is a parameter (to be chosen). It can be noticed that a lack of information in a given area will lead the system to remain close to the $\boldsymbol{P}^0$ value of this area. This procedure allows the system to be solved to remain well-conditioned at the beginning of the iterations. This is important when studying complex shapes. By solving this system iteratively with a decreasing λ (e.g. λ starts close to the maximum eigenvalue of $\mathbf{C}$ and decreases to reach levels at least two orders of magnitude lower than the minimum eigenvalue). An estimation of the real observed surface is obtained without being perturbed by uncertainties coming from the high degree NURBS shape estimation.

43.3 Principle of the Reconstruction

The first guess of the shape (e.g. the virtual surface) is first projected onto the 2D space using the calibration matrices generating two grids. Right and left pictures are interpolated through these grids to create two sub-pictures in the parametric space. An integrated approach to DIC [10] is performed between these two sub-figures using the sensitivity fields introduced above. This leads to an estimation of the increment of control point position $\mathrm{d}P$ that can be added to the previous coordinates (Fig. 43.1). A new iteration with the new guess of the shape is then performed.

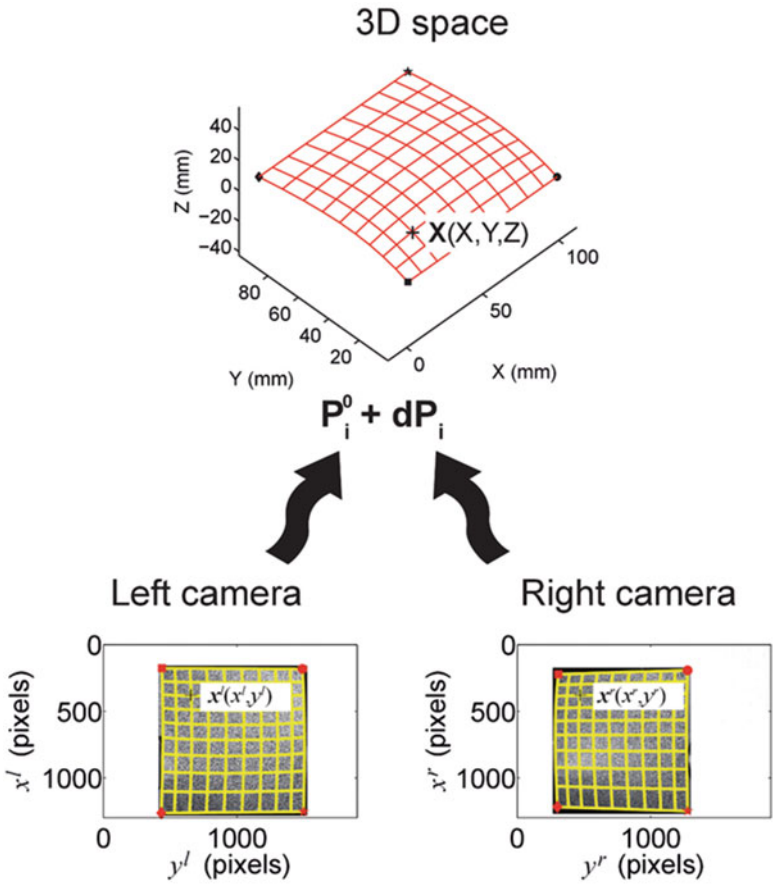

Fig. 43.1 CAD-Based StereoDIC principle for the registration of the observed surface

43.4 Example on an Industrial Part

This method has been tested on an industrial part with a complex shape. It consists of a cylinder and eight ribs parallel to its axis (shown in Fig. 43.2). The theoretical shape used in this case is quite distant from the real one and the rib is very smooth compared to the observed one (Fig. 43.4).

The calibration of the stereosystem is performed using a self-calibration method [4]. Figure 43.3 shows the theoretical shape used as a first guess during the calibration step. The colors correspond to the residual map of the calibration operation. As expected, the rib is very distant from the real one so that very high residuals are observed in its immediate vicinity.

In order to perform an accurate reconstruction of the rib, the surface contains more control points on this specific area than in the cylindrical part (Fig. 43.4). One example of the correlation residuals obtained during the registration process is shown in Fig. 43.5.

Due to the Levenberg-Marquardt regularization and relaxation, the algorithm currently needs a lot of iterations (i.e. 78 in the present case) to reach convergence. Once the control point displacements are less than 10^{-5} mm, the shape of the reconstructed surface is obtained directly in a NURBS formulation (Fig. 43.6).

The rib on the reconstructed surface has been sharpened (Fig. 43.7). It fits well the real shape on one side. The other side cannot be reconstructed as accurately because it is not properly visible by one of the cameras. Thanks to the proposed approach, it does not lead to an area with no information at all.

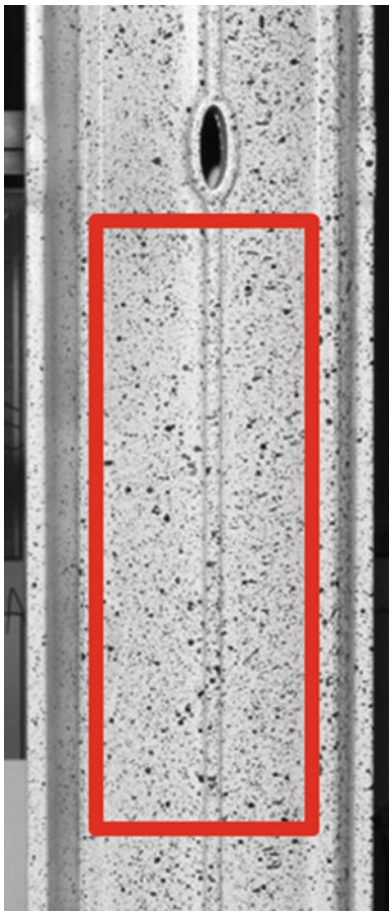

Fig. 43.2 Industrial part uses in this study. The reconstructed zone is shown in the *red box*

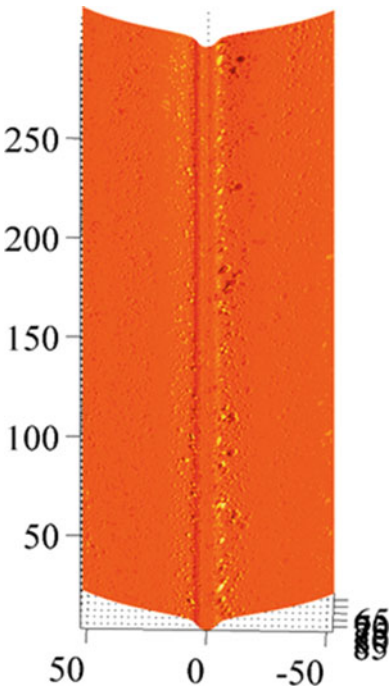

Fig. 43.3 Theoretical shape used as first guess (dimensions in mm). Colormap indicates correlation residuals for the calibration procedure

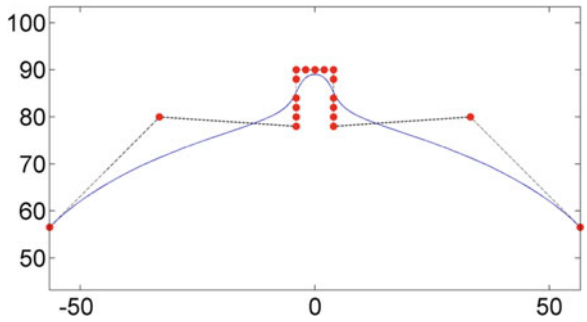

Fig. 43.4 In *blue*, the theoretical shape profile used herein (the numbers are expressed in mm). The *solid circles* are control points

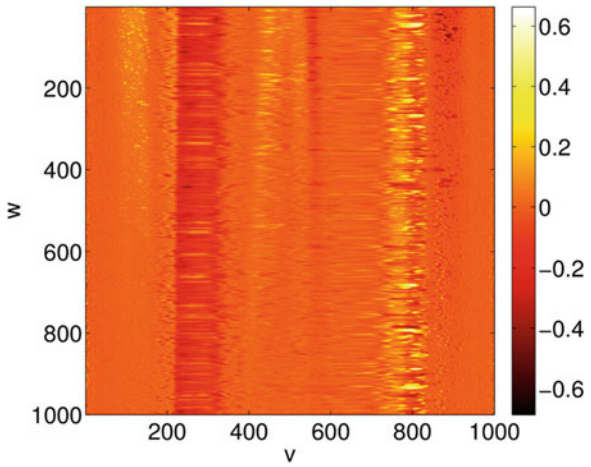

Fig. 43.5 Map of the final correlation residuals expressed in a ratio to the dynamic range of the analyzed pictures (RMS value of $\eta = 7.42\,\%$) and shown in the parametric space. The residuals are blurred because of the large amount of data points on the rib as compared to other areas

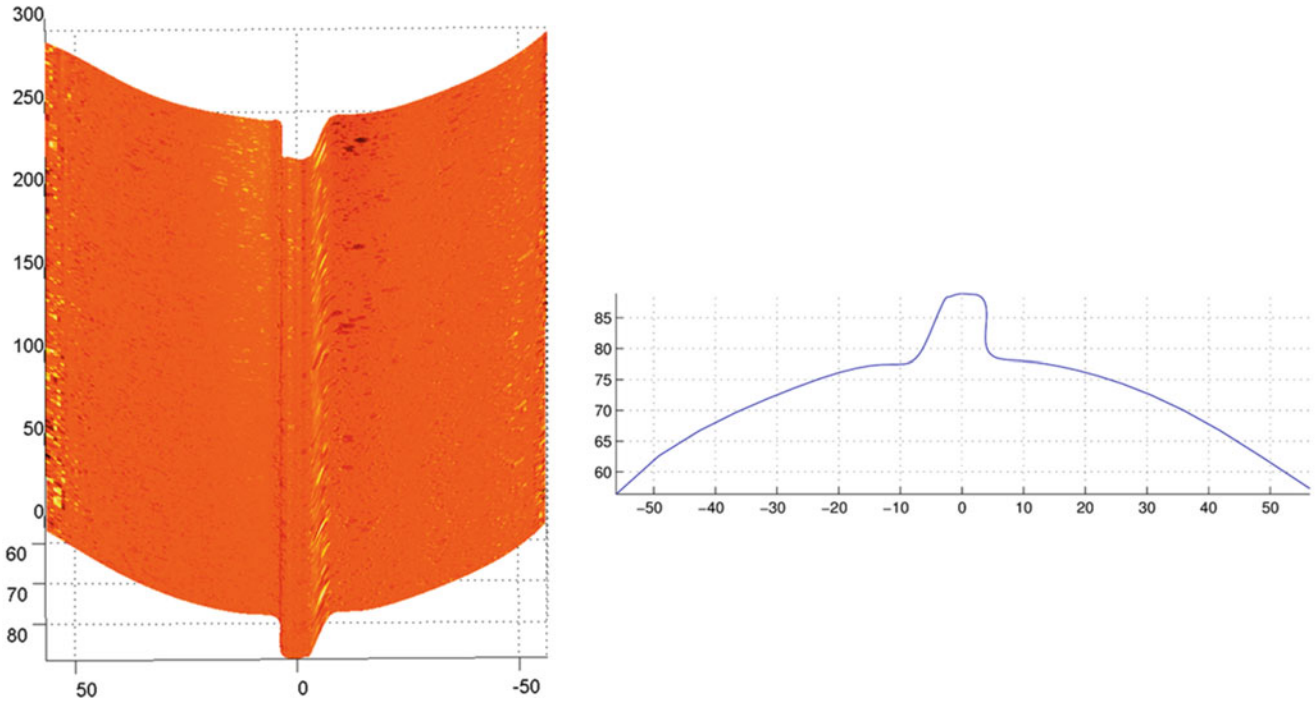

Fig. 43.6 Final shape obtained after 78 iterations (dimensions in mm) and corresponding cut at the *top* of the final shape (the control points are too distant to be represented at the scale of the picture)

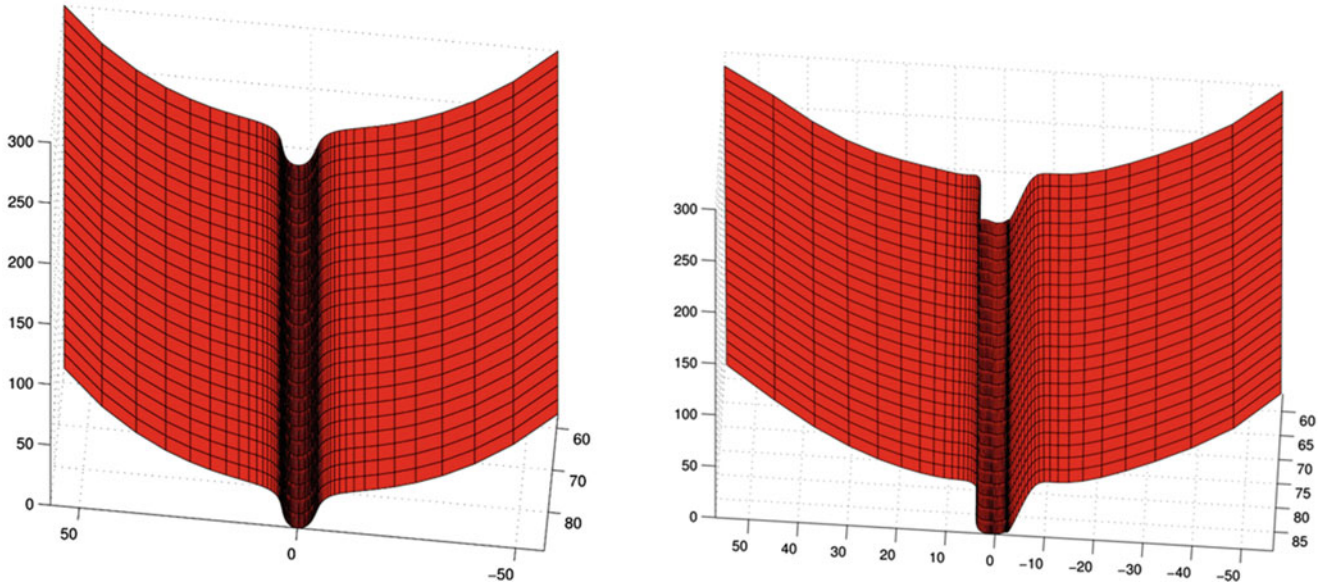

Fig. 43.7 Theoretical and reconstructed shapes. The rib profile has been sharpened on one side. The other side is not visible by one of the camera and thus cannot be reconstructed without the a priori knowledge

43.5 Conclusions

A complex shape containing a rib on a cylinder has been reconstructed thanks to a global approach to stereoDIC. This reconstruction considers a NURBS formulation during the whole registration process and thus can be used as such without any subsequent interpolation stage. This new procedure can also be utilized as a second step in the calibration method proposed by Beaubier et al. [7], or as a shape measurement method if the stereo jig is already calibrated. This method can be applied to shapes of any complexity degree as far as a NURBS formulation is available and a regularization procedure used when the number of unknowns becomes too large to avoid spurious shape fluctuations.

References

1. Sutton MA, Orteu JJ, Schreier HW (2009) Image correlation for shape, motion and deformation measurements: basic concepts, theory and applications. Springer, New York
2. Garcia D, Orteu JJ, Penazzi L (2002) A combined temporal tracking and stereo-correlation technique for accurate measurement of 3D displacements: application to sheet metal forming. J Mater Process Technol 125–126:736–742
3. Besnard G, Lagrange JM, Hild F, Roux S, Voltz C (2010) Characterization of necking phenomena in high speed experiments by using a single camera. EURASIP J Image Video Proces, 2010(21595):15p
4. Chen F, Brown GM, Song M (2000) Overview of three-dimensional shape measurement using optical methods. Opt Eng 39:10–22
5. Fusiello A (2000) Uncalibrated Euclidean reconstruction: a review. Image Vision Comput 18:555–563
6. Salvi J, Armague X, Battle J (2002) A comparative review of camera calibrating methods with accuracy evaluation. Pattern Recogn 35:1617–1635
7. Beaubier B, Lavernhe-Taillard K, Besnard G, Lavernhe S, Hild F, Roux S (2012) CAD-based calibration of a 3D-DIC system. In: Proceedings of SEM XII international congress and exposition on experimental and applied mechanics, Costa Mesa, CA
8. Piegl LA, Tiller W (1995) The NURBS book. Springer-Verlag, New York, NY
9. Marquardt D (1963) An algorithm for least-squares estimation of nonlinear parameters. SIAM J Appl Math 11:431–441
10. Roux S, Hild F (2006) Stress intensity factor measurements from digital image correlation: post-processing and integrated approaches. Int J Fract 142:51–67

Chapter 44
Image Based Local Strain Measurement of Wood

C.S. Moilanen, P. Saarenrinne, B.A. Engberg, and T. Björkqvist

Abstract A new method for local strain measurement of soft materials like wood is proposed. Norway spruce samples were subjected to radial compression in an encapsulated split-Hopkinson device (ESHD). High speed photography was used at two magnifications for image based analysis. The strain estimation was made from high magnification images showing compression on local, fiber level for 1–2 growth rings and from low magnification images showing compression on sample level, for 5–8 growth rings. Strain gauges on the ESHD bars give stress and average strain for comparison. Image analysis based on PIV technique gives local and average strain propagation as a function of time. Wood is an inhomogeneous material and thus, local strain is a more proper measure of the response of the material. The high magnification captures differences between earlywood and latewood while the low magnification gives the strain distribution over the whole sample. Both magnifications are important in order to understand the response of the wood material to the sudden compression. A way to estimate the stress field was developed. The results showed similarity to the strain gauge measurement results.

Keywords Image based measurement • Wood • Split-Hopkinson bar • Local strain • Mechanical pulping

44.1 Introduction

The wood fiber structure varies slightly depending on the season due to growth rate variations. In spring, the wood grows fast and the tree needs good water transportation. This leads to fibers with thinner cell walls and large lumen, called earlywood. Later on, the growth slows down and fibers with thicker cell walls and smaller lumen, that support the steam, are formed. This part of the growth ring is called latewood. The purpose of mechanical pulping is to separate fibers from the wood matrix in a form suitable for papermaking. Wood compression behavior is of great significance in mechanical pulping. *Norway spruce* (*Picea abies*) is the most common raw material used in the Nordic countries. A drawback with Norway spruce is distinct differences in the mechanical properties of fibers on growth ring level. Due to these differences, local compression behavior is more important than overall compression behavior. Previous research in the field has shown that strain rate, temperature and moisture content has major impact on overall wood compression behavior [1, 2]. It is therefore essential to make measurements at conditions as close to the ones in mechanical pulping as possible. To achieve the compression circumstances of a refiner the strain rate should be of the order several thousands. In this strain rate range, the Split-Hopkinson Bar (SHB) is commonly used [3].

The Hopkinson Bar is reviewed in detail by Gama et al. [3]. The fundamentals of the method were described by Davies [4] and Kolsky [5] already at the end of the forties. The use of the device together with strain gauges is a well-known material testing method, giving deformation, strain, strain rate and stress information. The method applied on wood samples is

C.S. Moilanen (✉) • P. Saarenrinne
Department of Engineering Design, Tampere University of Technology, P.O. Box 589, FI-33101 Tampere, Finland
e-mail: carolina.moilanen@tut.fi

B.A. Engberg
Department of Natural Sciences, Engineering and Mathematics, Mid Sweden University, Holmgatan 10, SE-85170 Sundsvall, Sweden

T. Björkqvist
Department of Automation Science and Engineering, Tampere University of Technology, P.O. Box 692, FI-33101 Tampere, Finland

H. Jin et al. (eds.), *Advancement of Optical Methods in Experimental Mechanics, Volume 3*,
Conference Proceedings of the Society for Experimental Mechanics Series,
DOI 10.1007/978-3-319-00768-7_44,

presented for example in Widehammar [6]. Recently the SHB is combined with image based displacement measurements Siviour [7], Gilat et al. [8] and Saari et al. [9]. This combination provides the possibility to measure the local displacement field of the sample directly and derive strain rate and stress fields independently.

Digital Image Correlation (DIC) is used for displacement field measurement in material testing also for heterogeneous elastoplastic materials [10]. The method is described in detail by Sutton et al. [11]. DIC applies best to strain measurements in planar surfaces where the tracked surface texture stays visible all the time and the deformation is modest. An iterative digital image correlation algorithm with subsets is typically used, which can easily cope with complex deformation fields. Usually, some optimization criterion is used to yield accurate results. The squared sum of differences (SSD), however, is just one of many optimization criteria that can be used for template matching, and indeed, the digital image correlation method owes its name to the use of the normalized cross-correlation criterion by incorporating subset shape functions into the matching algorithm. The algorithm is therefore the preferred choice for deformation measurements and stereo matching.

The suitability of DIC technique to test wood samples was evaluated by Zink et al.[12]. They found the method applicable for the study of properties of wood. They concluded that the DIC strain measurement results were in close agreement with independent measurement results. Utilizing DIC to full field strain distributions through an increasing load series revealed progressive failure development in the wood specimens, the eventual failure mode, and a shift in strain concentrations during load application. Vessby et al. [13] used DIC to evaluate strain distribution in a wood Fiber Reinforced Polymer (FRP) lap joint. The experimental, analytical and numerical results were shown to be in close agreement with respect to the strength and the strain distribution obtained. Saari et al. [9] measured strain distribution in annual rings under compression by high speed photography and DIC for displacement measurement in an Encapsulated Split-Hopkins Device. They were able to measure instantaneous strain fields for wet wood samples inside annual rings during a sudden high strain rate pulse. They showed the applicability of the method in order to evaluate the behavior of the wood under compression during a refining process.

Valla et al. [14] used Electronic Speckle Pattern Interferometry (ESPI) and Digital Image Correlation (DIC) for the measurement of two-dimensional strain distribution on mechanically stressed wood specimens. The results of a model experiment with plywood showed that the results delivered by both methods are very similar. ESPI provides reasonably fast experimental set-up and data acquisition, and fast, straightforward post-processing. Compared with ESPI, DIC is a more versatile method demanding skilled sample preparation and post processing is often more time consuming. Thuvander et al. [15] used electronic speckle photography to study crack tip strain fields in the scale of growth ring in a wood sample.

In the analysis of the soft materials like wood new aspects arise. The sample deformation is large and fracture of cells during the test is possible. Also the moisture (water in structure) can spread out during the compression. This makes big changes to the surface patterns and part of the sample can be shadowed by water droplets. In these circumstances it is useful to apply a correlation calculation method used in Particle Image Velocimetry (PIV) (Raffel et al. [16]). The method is widely used in measurements in fluid mechanics. The method is to a great extent analogous to the DIC, but the correlation function estimation is based on the most probable displacement for the texture on a subset. This gives the possibility that part of the texture disappears between the images and an estimate for the displacement is still achieved.

The measurement setup is first presented. The data analysis part of the paper is divided in two parts. The first part describes the image based local strain analysis and the second the image based stress analysis. The image based method is compared to a strain gauge based reference method in the end of the image based stress section. The method has been developed based on a measurement series of eight samples with growth ring magnification and two samples with fiber magnification. The method is here presented using one growth ring sample and one fiber sample as example.

44.2 Measurements

The samples were carefully cut from fresh wood and frozen to keep the moisture content high as it is naturally. Details of the samples are presented in Fig. 44.1 together with registered example images. Measurements were made on $12 \times 12 \times 6\,\text{mm}^3$ samples of Norway spruce. The measurements were conducted at room temperature and the moisture content of the samples was approximately 30 %. The moisture content was calculated by comparing the sample mass to the mass of a dried sample from the same piece of wood. The samples were cut with a microtome before the measurement in order to get as clear fiber ends for the imaging as possible. The surfaces of the growth ring magnification level samples were spray painted with white and black paint to achieve suitable texture for the PIV. The measurements were conducted in an encapsulated split-Hopkinson device (ESHD) presented by Holmgren et al. [17] at high strain rate (around 2,400 s^{-1}) with possibility to control temperature and pressure.

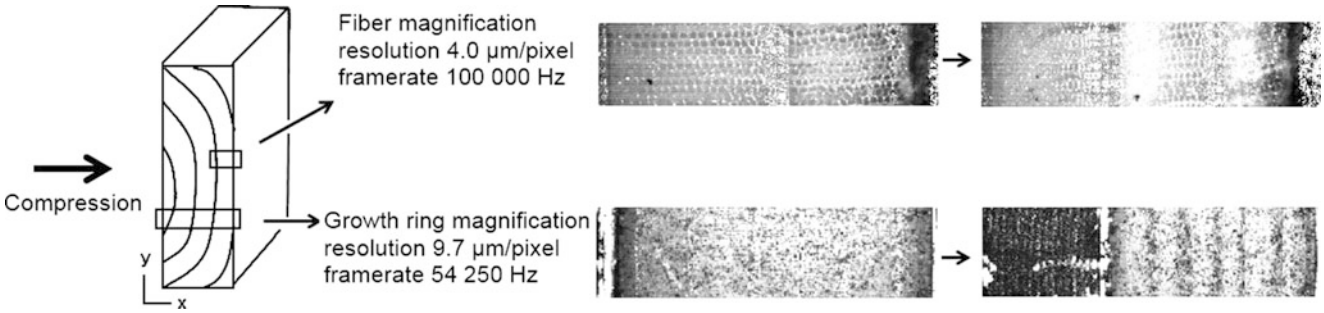

Fig. 44.1 A sketch showing the measurement setup, image parameters and examples of registered images, the images were always from the middle of the sample in y direction

During the compression a Photron SA5 high speed camera captured images at 100,000 Hz in fiber magnification and at 54,250 Hz in growth ring magnification. An Infinity K2 long distance microscope with one converter was used in the measurements with a CF2 front lens for the growth ring magnification and a CF4 front lens for fiber level magnification. A Cavilux HF pulsed diode laser (500 W, 808 nm) was used for illumination. During the compression, approximately 40 frames were captured at fiber level and 20 at growth ring level with these frame rates. A digital oscilloscope captured data from strain gauges connected to the incident and transmitter bars of the split-Hopkinson device. The stress and average strain were calculated from the strain gauge data using appropriate time shifts and numerical integration. These results were used as reference when evaluating the image based method.

44.3 Image Based Strain

The local displacements are calculated by standard PIV technique [18]. The frame is divided into interrogation areas and the displacement between two sequential frames is calculated by correlation technique. The advantage of PIV technique is that it gives the result for all the marker texture inside an interrogation area. The displacement is then the most probable value for this pattern. This gives the possibility to that part of the texture can disappear between images. The more frequently used DIC method traces fixed texture pattern. More information on PIV techniques can be found in [16].

The displacement data achieved this way was used to calculate the local movement of fixed points of the sample during the compression. In the first frame, the points are situated regularly as can be seen in Fig. 44.2a. In the next frame, the position of a point is updated according to the measured displacement between previous and current frame. The displacement is then added to the closest grid point. The grid points are presented in Fig. 44.2b at maximum compression.

The distances between grid points were used to calculate local strain, in this case local compression, according to Eq. 44.1,

$$\varepsilon(\mathbf{t}) = \frac{l(t) - l_0}{l_0} \tag{44.1}$$

where $l(t)$ is the distance between points in x direction at time t and l_0 is the distance between points in the first frame. The local strain calculated for the wood sample is presented as strain maps, where the strain is plotted according to the points in the first frame, see Fig. 44.3.

Erroneous outliers of the displacement data are removed, causing holes in the strain map. Blank areas also appear on the edge where the material is pushed out of the image. This can be seen both Fig. 44.2 showing the points moving out of the image and the resulting blank area in Fig. 44.3.

Changes in the displacement calculation parameters affect the final strain map significantly. The needed frame rate determines image size, the magnification determines the spatial resolution of the images and the interrogation area size determines the uncertainty of the displacement. More detail can be seen in the strain map when the interrogation area size is reduced or the overlap is increased. The optimal value for overlap was sought. The overlap was 50 % in Fig. 44.3 and 75 % in Fig. 44.4. The best results were achieved when the interrogation area was 64 × 64 pixels for the first pass and 16x16 pixels for the second pass with 50 % overlap.

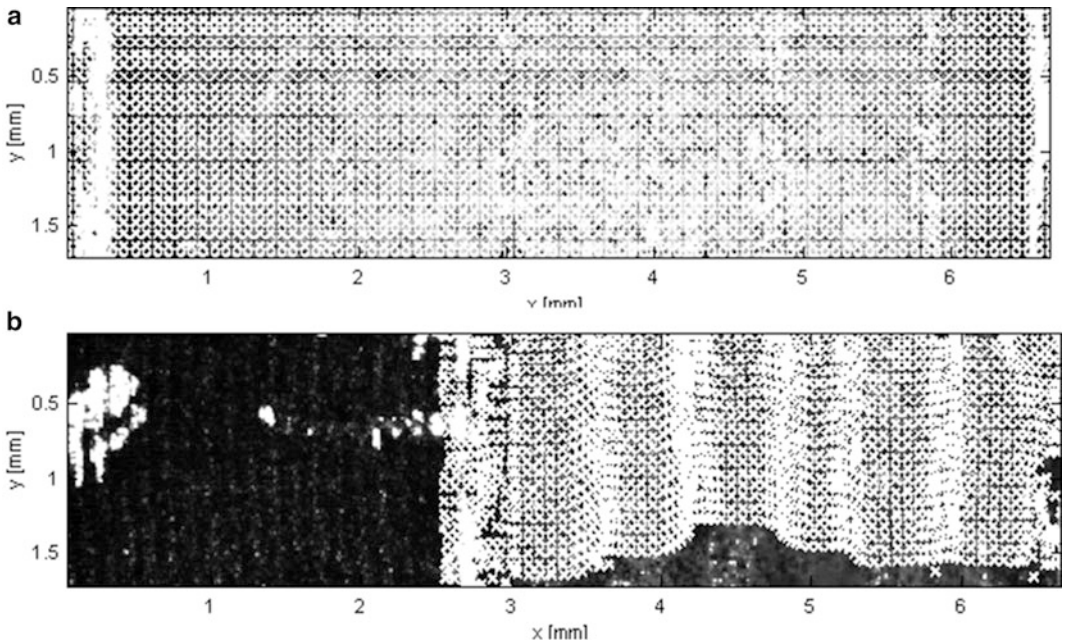

Fig. 44.2 Location of grid points used for strain calculations of a growth ring magnification sample (**a**) before compression and (**b**) at maximum compression

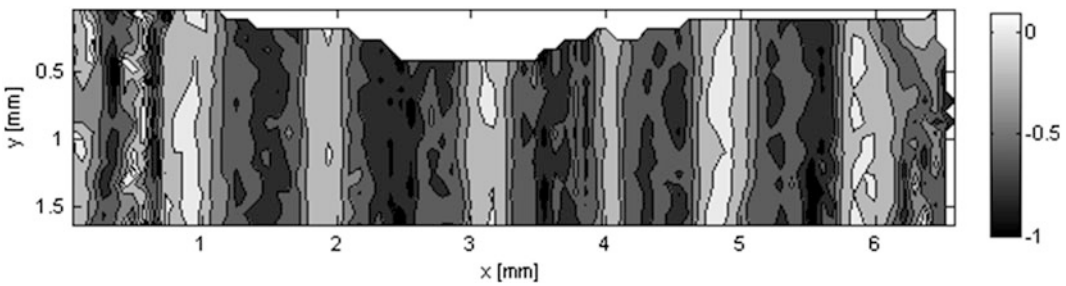

Fig. 44.3 Strain map according to Eq. 44.1 for a growth ring magnification wood sample with 50 % interrogation area overlap

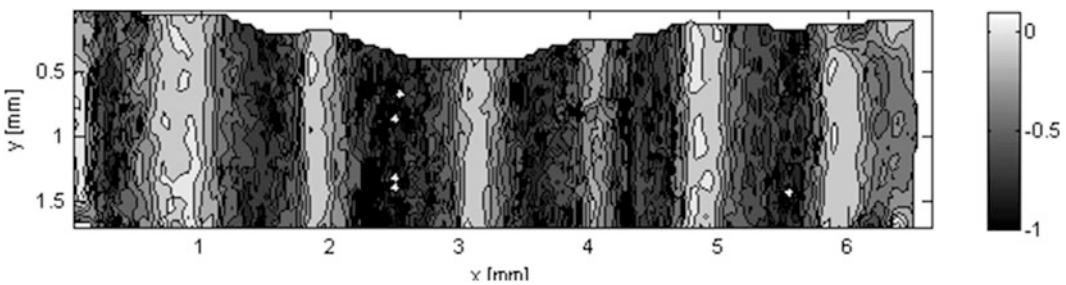

Fig. 44.4 Strain map according to Eq. 44.1 for a growth ring magnification wood sample with 75 % interrogation area overlap

In some samples, the latewood parts of the sample are so thin that compression behavior cannot be detected. In some cases, reduction of the interrogation area to 8 × 8 pixels for the second pass showed the latewood compression but the amount of erroneous points in the middle of the latewood area increases which indicates larger error. The fiber level magnification measurements enable more detailed comparison of the compression of earlywood and latewood. As can be seen in Fig. 44.5, the latewood is not significantly compressed. The strain presented in Fig. 44.5 is calculated as an average over 3 points for the latewood and the average over 15 points for earlywood at y = 0.3 mm. This is approximately in the middle of the fiber level magnification image.

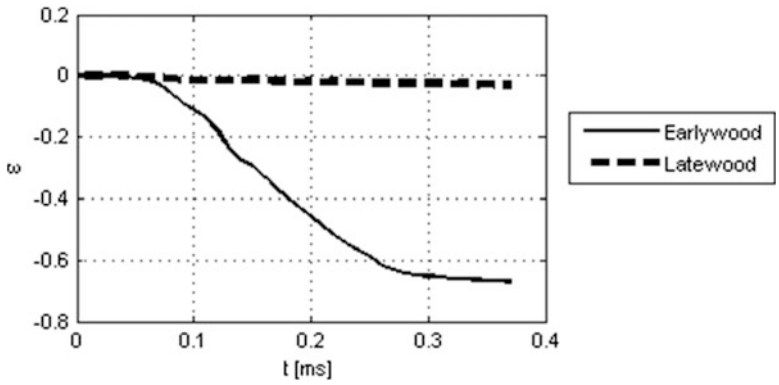

Fig. 44.5 Strain in earlywood and latewood as a function of time for a higher magnification case

44.4 Image Based Stress

The reference method for stress calculation is based on strain gauge measurements. The strain gauge measurement method is presented in references [6, 17]. The strain gauge measurement based stress pulse for one specific sample is presented in Fig. 44.6 and this same sample is further explored in this section with an image based method. The incident bar end velocity measured from the images was used to estimate the stress. The image based method is based on the theory presented by Davies [4].

Davies [4] presented that the stress could be calculated from the displacement of the end of the bar according to Eq. 44.2

$$\sigma(\mathrm{t}) = -\frac{1}{2}\rho c u_T(\mathrm{t}) \tag{44.2}$$

where ρ is the density of the aluminum alloy, c is the wave propagation velocity in the aluminum and u_T is the velocity of the incident bar end. The wave propagation velocity can be calculated from Eq. 44.3 below

$$c = \sqrt{\frac{E}{\rho}} \tag{44.3}$$

where E is the Young's modulus of the aluminum alloy (73 GPa) and ρ the density (2,770 kg/m^3). The incident bar end velocity is calculated from the average displacement. The wave propagation velocity can be calculated by Eq. 44.3. The incident stress calculated by Eq. 44.2 is presented in Fig. 44.7.

If the characteristic impedance of the bar is close enough to that of the sample, only a small part of the incident pulse is reflected. In the case of wood as a soft material, only a small part of the incident pulse propagates through the sample. Siviour [7] presented an equation for the stress transmission coefficient, Eq. 44.4,

$$T_{B-S} = \frac{2\rho_S c_S A_B}{\rho_B c_B A_B + \rho_S c_S A_S} \tag{44.4}$$

where ρ is the density, c the wave propagation velocity and A the area. The index b refers to the bar and the index s to the sample. The cross-section of the split-Hopkinson bars was 12 × 12 mm^2. The wood density was calculated separately for each sample from the mass and dimensions registered before the split-Hokinson measurement. The sample dimensions were also used for a more exact sample cross-sectional area. The wood Young's modulus was assumed to be 1,160 MPa [19]. The stress that propagates through the sample is the incident pulse multiplied by the transmission coefficient. For the sample presented here, the transmission coefficient was 0.1074. Kolsky presented a similar equation, the only difference that Kolsky did not take the different cross-section areas of the bar and the sample into account [20].

Material behavior is often described by stress–strain curves. This is a good way to compare the image based method to the strain gauge based reference method, see Fig. 44.8.

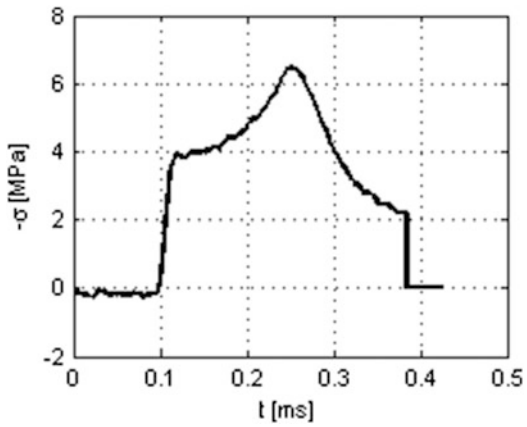

Fig. 44.6 Strain gauge measurement based stress as a function of time

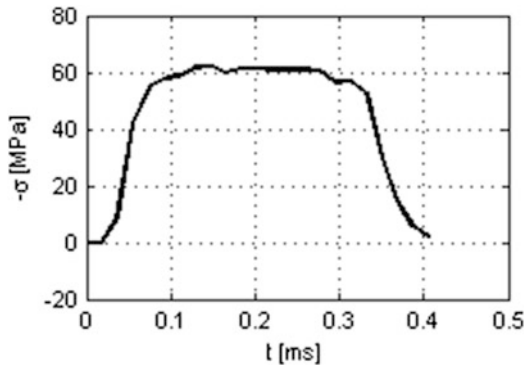

Fig. 44.7 Stress as a function of time according to Eq. 44.2 [4]

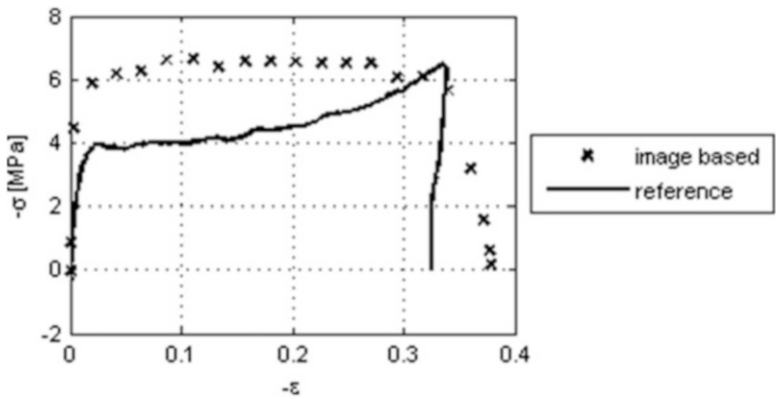

Fig. 44.8 Stress–strain curves for a wood sample

The different shape of the stress pulses, seen in Figs. 44.6 and 44.7, leads to different shapes of the stress–strain curves. It can be seen in Fig. 44.8 that the yielding is achieved with both the strain gauge method and the image based method. The yield limit is different for the two methods but that could be due to error in the transmission coefficient. The transmission coefficient is dependent on the wood density and Young's modulus. The density is determined separately for each sample but the Young's modulus was assumed to be the same as Keunecke presented [19]. The density measured for the samples measured here was higher than the densities reported by Keunecke and since the Young's modulus is dependent on the density this means that the Young's modulus should be lower and thus should the transmission coefficient also be lower. The strain hardening that can be seen from the strain gauge measurement is not seen with the image based method.

44.5 Conclusions

The split-Hopkins device is used to measure sample strain with high strain rate. The strain is measured with strain gauges assembled on the bars. This measurement gives overall values for the strain of the sample. If local strain values inside a sample are needed, the image based method should be used. If sample material is soft, like wood, where the yield limit can be achieved during the test, the image based measurement is a necessity. The from PIV analysis known cross-correlation technique is applicable in this situation. This method allows the texture disappearance between the images. The usual DIC method assumes stable surface texture.

The strain maps are a good way to visualize the strain distribution in a wood sample. The local strain values can be used to explore the strain inside a non-homogeneous sample like wood. The results show that the material differences in a sample can be explored. In a wood sample the different earlywood and the latewood behavior could be detected. The measured strain fields were in line with strain gauge measurement results.

A method where the incident bar end velocity is used for stress estimation is here presented. The advantage of this is that we can use the known material properties of the aluminum for stress estimation. The estimate was based on the use transmission coefficient. The achieved results are encouraging; the stress–strain curves are of the same order of magnitude and have similar shape.

References

1. Uhmeier A, Salmén L (1996) Influence of strain rate and temperature on the radial compression behavior of wet spruce. J Eng Mater Technol Trans ASME 118(3):289–294
2. Widehammar S (2004) Stress–strain relationships for spruce wood: influence of strain rate, moisture content and loading direction. Exp Mech 44(1):44–48
3. Gama BA (2004) Hopkinson bar experimental technique: a critical review. Appl Mech Rev 57(4):223–250
4. Davies RM (1948) A critical study of the Hopkinson pressure bar. Philos Trans R Soc Lond Sect B 240(821):375–457
5. Kolsky H (1949) An investigation of the mechanical properties of materials at very high rates of loading. Proc Phys Soc Lond Sect B 62(II-B):676–700
6. Widehammar S (2002) A method for dispersive split Hopkinson pressure bar analysis applied to high strain rate testing of spruce wood. Dissertation, Department of Materials Science, Uppsala University
7. Siviour CR (2009) A measurement of wave propagation in the split Hopkinson pressure bar. Meas Sci Technol 20(6):065702
8. Gilat A, Schmidt T, Walker A (2009) Full field strain measurement in compression and tensile split Hopkinson bar experiments. Exp Mech 49:291–302
9. Saari V, Björkqvist T, Engberg BA, Saarenrinne P (2009) Strain distribution in annual rings under compression by high speed photography. In: Proceedings of international mechanical pulping conference, 31st May–4th June 2009, Mid-Sweden University, Sunsvall
10. Allais L, Bornert M, Bretheau T, Caldemaison D (1994) Experimental characterization of the local strain field in a heterogeneous elastoplastic material. Acta Metallurgica Et Materialia 42(11):3865–3880
11. Sutton M, Orteau J, Schreier H (2009) Image correlation for shape, motion and deformation measurements. Springer, New York
12. Zink A, Davidson R, Hanna R (1995) Strain measurement in wood using a digital image correlation technique. Wood Fibre Sci 27:346–359
13. Vessby J, Serrano E, Enquist B (2010) Contact-free measurement and numerical and analytical evaluation of the strain distribution in a wood-FRP lap-joint. Mater Struct 43:1085–1095
14. Valla A, Konnerth D, Keunecke D, Niemz P, Muller U, Gindl W (2011) Comparison of two optical methods for contactless, full field and highly sensitive in-plane deformation measurements using the example of plywood. Wood Sci Technol 45:755–765
15. Thuvander F, Sjödahl M, Berglund L (2000) Measurement of crack tip strain field in wood using a digital image correlation technique. J Mater Sci 35:755–765
16. Raffel M, Willert CE, Wereley ST, Kompenhans J (2007) Particle image velocimetry, a practical guide, 2nd edn. Springer, Heidelberg/New York
17. Holmgren S-E, Svensson BA, Grandin PA, Lundberg B (2008) An encapsulated split Hopkinson pressure bar for testing of wood at elevated strain rate, temperature, and pressure. Exp Tech 32(5):44–50
18. Product-manual for Davis 8.0. LaVision GmbH, Göttingren, Germany (2012)
19. Keunecke D, Sonderegger W, Pereteanu K, Lüthi T, Niemz P (2007) Determination of Young's shear moduli of common yew and Norway spruce by means of ultrasonic waves. Wood Sci Technol 41:309–327
20. Kolsky H (1963) Stress waves in solids. Dover Publications, New York

Chapter 45
Thermographic Identification of Defects in Adhesively Bonded Joints

Rachael C. Waugh, Janice M. Dulieu-Barton, and Simon Quinn

Abstract The potential use of pulse phase thermography (PPT) and thermoelastic stress analysis (TSA) to identify artificial defects in CFRP single lap joints has been studied. PPT was able to identify defects in adhesive bonds where there was a contrast between defect and non-defect thermal properties. Where a lack of thermal contrast occurred it was found that the application of a small load was sufficient to reveal a previously unidentified defect. TSA was able to reveal defects where there was a change in stress distribution caused by the defect; however it did not identify inclusions that had very little effect on stress distributions. It may be argued that such an inclusion is not a defect. It is necessary to clarify this as false identification of defects may lead to unnecessary repair work.

Keywords Pulse phase thermography • Thermoelastic stress analysis • Non-destructive evaluation • Bonded joints • Defects

45.1 Introduction

The use of adhesive joints allow the weight saving associated with the use of composites to be maximised and the stress concentrations associated with mechanical fastenings to be removed [1]. Adhesives also offer good corrosion resistance [2]. If the use of adhesive joints is to become more wide-spread, especially in primary structure locations, the reliability of the joints must be assured [3]. There must be a good understanding of the likelihood and type of defects occurring that may affect the joint efficiency. Reliable non-destructive evaluation (NDE) procedures must be developed that are able to accurately identify these defects.

The ability of two non-destructive thermography based approaches to identify defects in adhesive bonds are compared. A study has been carried out to assess the differences in detectability of two types of defect using thermoelastic stress analysis (TSA) and pulse phase thermography (PPT). The effect of static loading on the detectability of defects using PPT was also investigated. Single lap joint specimens were constructed out of carbon fibre reinforced plastic (CFRP) and epoxy adhesive with the defect taking the form of either the addition of silicon grease contamination or a PTFE insert, see Fig. 45.1.

45.2 Methodology

In PPT [4] a pulse of heat is applied to the surface of a component. The subsequent temperature of that surface is monitored using an infrared detector as the heat front propagates through the component. If the material below the surface is uniform across the component then the surface temperature will decay uniformly, however, if there is a region of differing thermal properties this will cause a perturbation in the surface temperature data. The thermal decay across the surface may be used to identify subsurface defects. Direct analysis of the thermal data is called pulsed thermography (PT); in PPT this thermal

R.C. Waugh (✉) • J.M. Dulieu-Barton • S. Quinn
University of Southampton, Southampton, UK
e-mail: rcw1n09@soton.ac.uk

H. Jin et al. (eds.), *Advancement of Optical Methods in Experimental Mechanics, Volume 3*,
Conference Proceedings of the Society for Experimental Mechanics Series,
DOI 10.1007/978-3-319-00768-7_45,

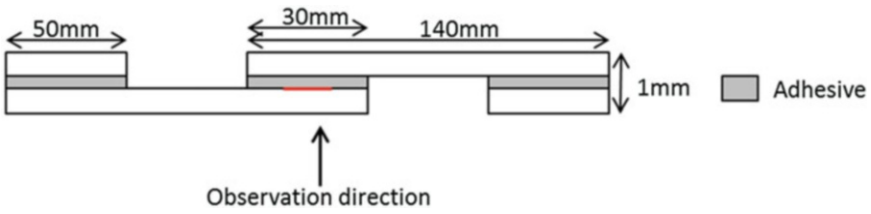

Fig. 45.1 Schematic of CFRP lap joint samples with artificial defects included between the adhesive and the front CFRP lap

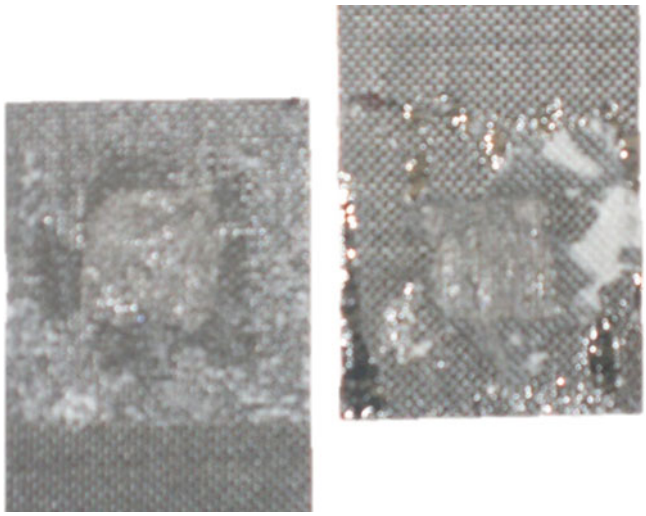

Fig. 45.2 Silicon grease contaminated lap joint tensile loaded to failure to inspect contamination location and find loading conditions for TSA

decay is then processed using a fast Fourier transform (FFT) and phase values are produced with reference to the start point of the FFT. The extraction of the phase data enables deeper probing than possible using PT, as well as minimising the identification of false defects caused by optical surface effects, such as uneven heating.

In TSA a cyclic load is applied to a sample to induce a thermoelastic response in the form of a small temperature change, which is related to changes in the sum of the principal stresses in the material [5]. One of the assumptions of the general formula used in TSA is that temperature changes occur adiabatically. Phase values are uniform across the sample where adiabatic conditions are present. Where adiabatic conditions are not present phase values begin to vary. This has been reported to be the case at crack tips [6].

The current paper reports on work undertaken to study the difference between the detectability of defects in a CFRP lap joint using the phase values from TSA, which show non-adiabatic conditions, and the phase values of PPT, which highlight areas of subsurface variation of thermal conduction properties. Whereas in TSA a cyclic load is applied, in PPT a stationary load of the mean of the cyclic load is applied for comparison of the two approaches. PPT data from an unloaded specimen is also collected.

Tensile tests to failure were carried out on silicon contaminated lap joints to confirm that the contaminant added to the bond line was remained where it had been added during the manufacture of the joint. Figure 45.2 shows that the silicon grease has remained where applied with minimal smearing during joint manufacture. Such tensile tests were also used to establish loading conditions for TSA to ensure elastic loading was applied. A series of loading conditions were carried out on each sample but the data presented in the current paper is for the loading conditions of 3 ± 1 kN at 5 Hz.

45.3 Results and Discussion

The TSA change in temperature (ΔT), TSA phase data, unloaded PPT and PPT statically loaded at 3 kN is presented for the CFRP lap joint containing PTFE, Fig. 45.3, and silicon grease, Fig. 45.4. A marker box has been added to the images where the defects are not visible as an indicator of defect size and location of defects in each lap joint. Markers have not been added to images where defects are visible to avoid masking the data.

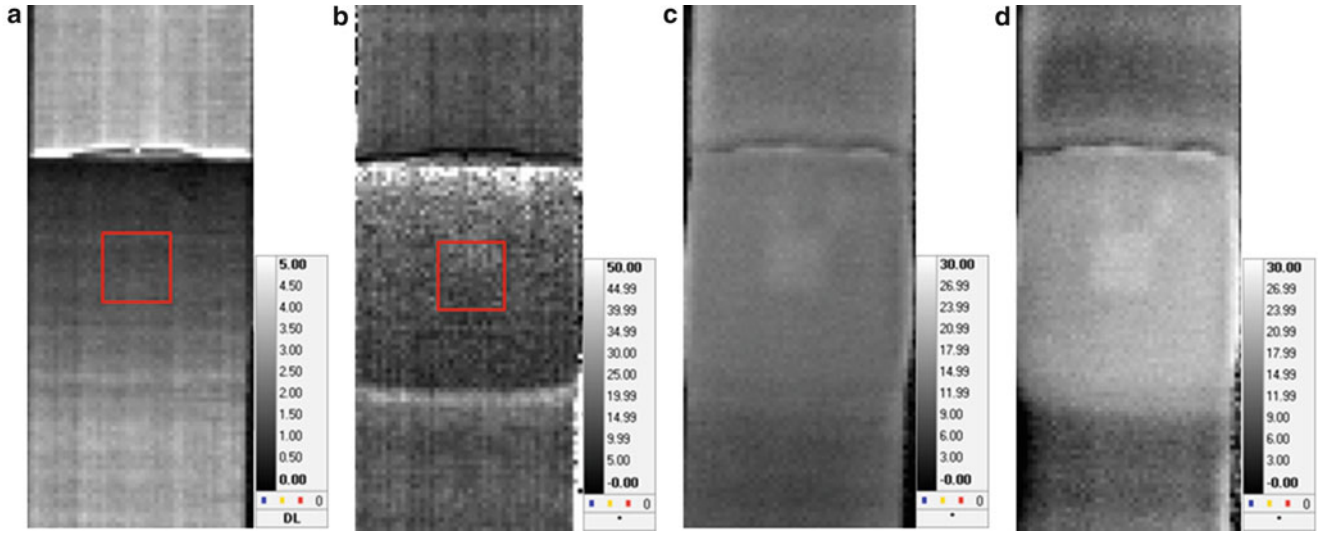

Fig. 45.3 PTFE insert results (**a**) TSA ΔT (3±1 kN), (**b**) TSA phase data, (**c**) PPT phase data (0 kN) and (**d**) PPT phase data (3 kN)

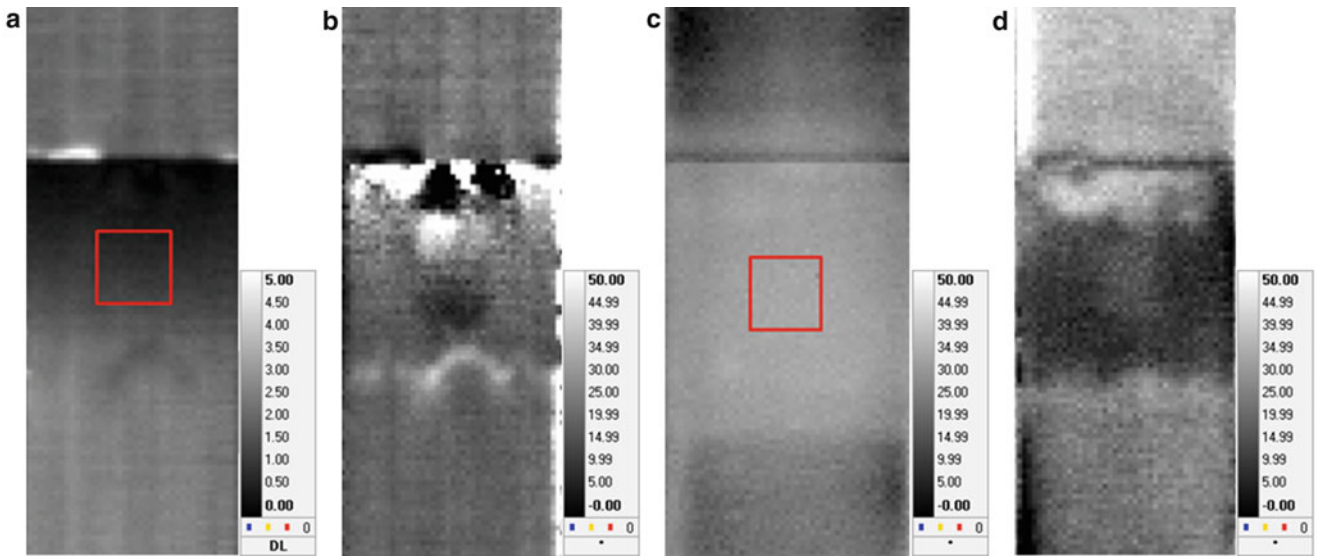

Fig. 45.4 Silicon grease contamination results (**a**) TSA ΔT (3 ± 1 kN), (**b**) TSA phase data, (**c**) PPT phase data (0 kN) and (**d**) PPT phase data (3 kN)

There is no sign of any stress redistribution caused by the PTFE insert in the TSA ΔT data however the gradient of TSA phase values across the lapped area in Fig. 45.3b illustrates the bending of the joint which is confirmed in the ΔT image by the stress concentrations at the upper and lower edges of the joint, see Fig. 45.3a. The free edge of the joint nearest to the IR detector is the upper edge of the lap in the images shown. The stress concentration is greatest at the free edge where peel stresses are high. The stress concentration at the lower edge of the lap is a localised compressive stress, which was caused by bending. The PTFE insert is not affecting the stress distribution in the joint and so, for the purposes of this study, may not be classed as a defect. As the PTFE is a loose insert it may have become encapsulated in the adhesive and thus is not causing a defect in the joint.

The PPT is able to identify the PTFE insert due to its contrasting heat transfer properties to the surrounding material, see Fig. 45.3c. The loaded and unloaded PPT data reveal the same information about the PTFE insert in terms of defect size and phase contrast, see Fig. 45.5a. Defect size has been calculated using a full width at half maximum (FWHM) approach [7] and found to be 6.8 ± 0.7 mm. This supports the TSA data in that no significant change is found between the two PPT data sets.

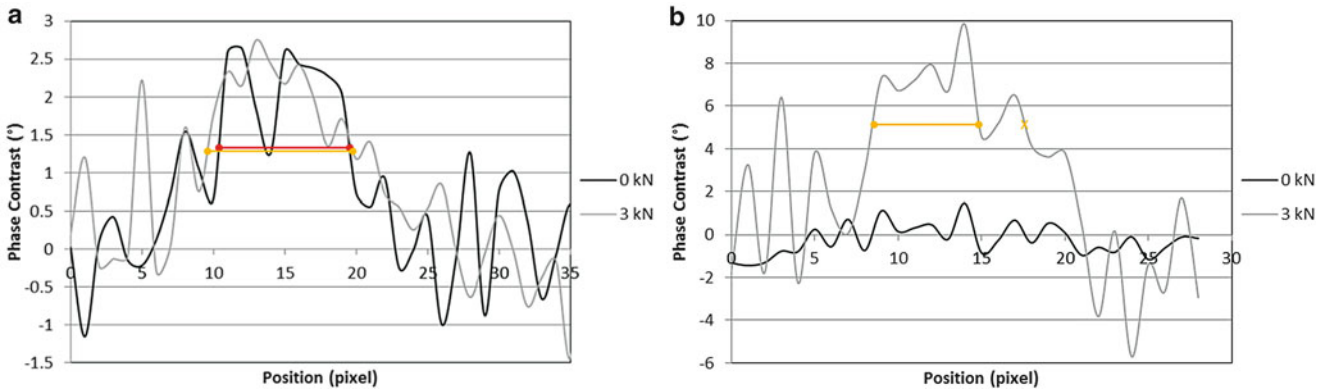

Fig. 45.5 Profile plots of phase contrast across centre of defects inspected via PPT (0 kN) and PPT with an applied load (3 kN) for both (**a**) PTFE insert and (**b**) Silicon grease contamination. FWHM positions have been highlighted using *red* for unloaded sample and *orange* for loaded samples

The TSA ΔT data identifies some stress concentrations in the silicon grease contaminated lap joint, see Fig. 45.4a. Whilst these effects are small they demonstrate that the addition of the silicon grease is having an effect on the stress distribution in the joint. The TSA phase data shows that the lap joint is beginning to fail at the upper and lower edges of the lap, caused by previous loading. A redistribution of stress in the joint has taken place, creating stress concentrations above and below the defect where new areas of tension (above) and compression (below) are created, see Fig. 45.4b.

PPT without loading was unable to identify the silicon grease contamination due to the low thermal contrast, see Fig. 45.4c. When the joint is loaded to 3 kN, PPT was able to identify peeling at the upper edge of the joint, due to bending, see Fig. 45.4d. Bending of the joint enhances thermal contrast of defects as it results in the defects being opened and thin air gaps being created. The silicon grease defect was also identified in this way with an introduced air gap creating a stronger thermal contrast. The width of the silicon defect, measured using the FWHM approach, was found to be 4.29 ± 0.7 mm, see Fig. 45.5b. The defect size in this case is underestimated as the FWHM approach takes the first time the line crosses half of the peak contrast, however it is shown in Fig. 45.5b that it may be more appropriate to take the reading from the second time the half maximum value is crosses on the right side of the defect with a negative gradient, marked with an orange x, as when considering the data of the full width this region appears to still be within the defect. This amended defect size would be 6.4 ± 0.7 mm.

The FWHM approach tends to underestimate the size of the defects as it assumes a steep decline in phase contrast between defect and defect free regions. However, the effects of lateral conduction around the defect are greatest at the edges of the defects and so reduce the thermal contrast in that region. This reduced thermal contrast will in turn lead to a reduction in phase contrast and to a gentler phase contrast gradient at the edges of the defect, thus causing an underestimation in defect size.

45.4 Conclusions

TSA phase data was unable to positively identify the PTFE inclusion in the lap joint. This result suggests that the PTFE inclusion may not be a defect as there has been not change to the stress distribution through the joint. TSA has shown that the addition of silicon grease to the lap joint has an effect on the stress distribution within the joint leading to stress concentrations above and below the defect. However, it is possible that the identification of this type of defect may be dependent on the geometry of the defect. Further investigation must be carried out to ascertain whether such identification is geometry dependent. Unloaded PPT is only able to identify defects when there is reasonable contrast between the defect and bulk material thermal characteristics but not identify if the feature identified is causing a real defect. It was found that while there was sufficient variation in thermal properties between the PTFE and the surrounding materials the thin layer of silicon grease contamination was insufficient to provide such contrast and was unidentified. Application of a load to the lap joints enabled defects to be opened and defect detectability was enhanced. While tensile loading in a test machine increased the detectability of the silicon defect in this study, a more practical method of load application must be developed for out of lab applications.

References

1. Flom Y, Arsenault RJ (1986) Interfacial bond strength in an aluminium alloy 6061 – SiC composite. Mater Sci Eng 77:191–197
2. da Costa Mattos HS, Sampaio EM, Monteiro AH (2011) Static failure analysis of adhesive single lap joints. Int J Adhes Adhes 31:446–454
3. Ehrhart B, Valeske B, Muller C-D, Bockenheimer C (2010) Methods for the quality assessment of adhesive bonded CFRP structures – a resume. In: Proceedings of 2nd international symposium on NDT in aeronspace 2010, Hamburg
4. Maldague X (2001) Theory and practice of infrared technology for nondestructive testing, Wiley series in microwave and optical engineering, K. Chang. Wiley, Chichester
5. Emery TR, Dulieu-Barton JM, Earl JS, Cunningham PR (2008) A generalised approach to the calibration of orthotropic materials for thermoelastic stress analysis. Compos Sci Tech 68(3–4):743–752
6. Dulieu-Barton JM, Fulton MC, Stanley P (1999) The analysis of thermoelastic isopachic data from crack tip stress fields. Fatigue Fract Eng Mater Struct 23(4):301–313
7. Avdelidis NP, Ibarra-Castanedo C, Maldague X, Marioli-Riga NP, Almond DP (2004) A thermographic comparison study for the assessment of composite patches. Infrared Phys Tech 45:291–299

Chapter 46
Mechanical Conjectures Explaining Cold Nuclear Fusion

A. Carpinteri, O. Borla, A. Goi, A. Manuello, and D. Veneziano

Abstract Several evidences of anomalous nuclear reactions occurring in condensed matter have been observed during electrolysis, solid fracture and liquid cavitation. Despite the great amount of experimental results coming from the so-called *Cold Nuclear Fusion* and Low Energy Nuclear Reaction research fields, the comprehension of these phenomena still remains unanswered. On the other hand, as reported by most articles devoted to *Cold Nuclear Fusion*, one of the principal features is the appearance of micro-cracks on the electrode surfaces after the experiments. In the present paper, a mechanical explanation is proposed considering a new kind of anomalous nuclear reactions, the piezonuclear fissions, which are a consequence of *hydrogen embrittlement* of the electrodes during electrolysis. Energy emissions in the form of neutrons and alpha particles were measured during the experiments, where the electrolysis is obtained using Ni-Fe and Cr-Co electrodes in an aqueous solution. The electrode compositions were analyzed both before and after the experiments recognizing the effects of piezonuclear fissions occurring in the host lattices.

Keywords Cold nuclear fusion • Piezonuclear fissions • Hydrogen embrittlement • Electrolysis

46.1 Introduction

During the last 20 years several evidences of anomalous nuclear reactions occurring in condensed matter have been observed. These tests were characterized by significant neutron and alpha emissions as well as by extra heat generations, together with appreciable variations in the chemical composition of the solution during electrolysis, solid fracture and fatigue, and liquids cavitation [1–9, 11–17, 19–21, 23–42].

Most representative works on the so-called *Cold Nuclear Fusion* described experimental activities conducted on electrolytic cells powered by direct current and filled with heavy water solutions. In particular, in 1989, Fleischmann and Pons reported the first method involving electrolysis to obtain anomalous nuclear fusion [13]. They asserted that the Pd metallic electrode reacted with the deuterium coming from the solution [13]. Later works reported that Pt and Ti electrodes had also been electrolyzed with D_2O to produce extra energy and nuclear products with the appearance of chemical elements before absent [36, 41]. Extra energy has been also produced from electrolysis with Ni cathodes and H_2O-based electrolyte [4, 20]. Furthermore, it has been demonstrated that a voltage sufficient to induce plasma generated a large variety of anomalous nuclear reactions when Pd, W or C cathodes were adopted [19, 23, 30, 31, 35, 38].

In many of these experiments, the generated power was calculated to be several times the input one and the neutron emissions rate, during electrolysis, was measured to be about three times the natural background level [13]. In 1998, Mizuno presented the results of the measurements conducted by means of neutron emission detectors and compositional analysis techniques and related to different electrolytic experiments [23]. A strong heat generation was observed when the cell was supplied with high electric power, with an excess energy of 2.6 times the input one. Remarkable neutron emissions were revealed during these tests, as well as a considerable amount of new elements, i.e. Pb, Fe, Ni, Cr and C, was produced and the isotopic distribution of Pb deviated greatly from the natural isotopic abundance [23]. These results suggested that some nuclear transmutation reactions took place in the Pd during the electrolysis process [23]. Later on, in 2002 Kanarev and

A. Carpinteri (✉) • O. Borla • A. Goi • A. Manuello • D. Veneziano
Politecnico di Torino, Department of Structural, Geotechnical and Building Engineering, Corso Duca degli Abruzzi 24, Torino 10129, Italy
e-mail: alberto.carpinteri@polito.it

H. Jin et al. (eds.), *Advancement of Optical Methods in Experimental Mechanics, Volume 3*,
Conference Proceedings of the Society for Experimental Mechanics Series,
DOI 10.1007/978-3-319-00768-7_46,

Mizuno reported the results obtained from the surface composition analysis of Fe electrodes (99.90 % of Fe) immersed in KOH and NaOH solutions [17]. After the experiments, EDX measures revealed the appearance of several chemical elements before absent. Concentrations of Si, K, Cr and Cu were found on the surfaces of the operating cathode immersed in KOH. Analogously, concentrations of Al, Cl and Ca were noticed on Fe electrode surfaces operating in NaOH. These findings are evidence of compositional changes occurring during plasma formation in electrolysis of water [17]. Furthermore, in 2008, Mosier-Boss et al. [27, 28] obtained important proofs of anomalous measurements in experiments conducted by electrolytic co-deposition cells. In particular, anomalous effects observed in the Pd/D system include heat and helium-4 generation, energetic charged particles, tritium, neutrons, gamma/X-ray emissions and transmutations [2, 20, 27, 28].

As reported by Storms and Preparata, despite the great amount of experimental results observed by a large number of scientists, a unified interpretation and theory of these phenomena has not been accepted and their comprehension of these phenomena still remains unsolved [2, 13, 33, 34, 36, 37]. On the other hand, as shown by most articles devoted to *Cold Nuclear Fusion*, one of the principal features is the appearance of micro-cracks on electrode surfaces after the tests [36, 37]. Such evidence might be directly correlated to the *hydrogen embrittlement* of the material composing the host metal electrodes (Pd, Ni, Fe, Ti). This phenomenon, well-known in metallurgy and Fracture Mechanics, characterizes metals during forming or finishing operations [22]. During the gas loading, performed with deuterium (or hydrogen), the host matrix (for example Pd) is subjected to mechanical damaging and fracturing due to atoms penetration. In Fracture Mechanics, hydrogen effects are largely studied especially in metals, where the presence of H free atoms in the material matrix causes the metal to become more brittle and less resistant to crack propagation. In particular, high pressure hydrogen generates an internal stress that lowers the apparent fracture stress of the metal and brittle crack growth can occur under a hydrogen partial pressure below 1 atm. [18, 22].

Furthermore, some experimental evidence demonstrated that neutron emissions are strictly correlated to fracture of radioactive or inert materials. From this point of view, anomalous nuclear emissions and heat generation had been verified during fracture in fissile materials [12, 16, 42] and in deuterated solids [11, 15, 33]. The experiments recently proposed by Carpinteri et al. [5, 7–9] represent the first evidence of neutron emissions and anomalous fissions from inert, stable, and non-radioactive solids under compression, as well as from non-radioactive liquids during ultrasound cavitation [5]. In the present paper, we analyze energy emissions during tests conducted on an electrolytic cell, where the electrolysis is obtained using Ni-Fe and Cr-Co electrodes in aqueous solution. Voltage, current intensity, solution's conductivity, temperature, alpha and neutron emissions were monitored. The compositions of the electrodes were analyzed both before and after the tests. These evidences suggested that the so-called *Cold Nuclear Fusion*, interpreted under the light of *hydrogen embrittlement*, may be explained by anomalous fission reactions (piezonuclear reactions) occurring in the host metal instead of the fusion of H isotopes dissolved in the lattice. These new kind of fission reactions have been recently observed from the laboratory to the Earth's crust scale, when particular conditions of stress produce fracture or fatigue phenomena or in correspondence of an impending earthquake [5–10].

46.2 Experimental Set Up and Measurement Equipments

46.2.1 The Electrolytic Cell and the Power Circuit

Over the last ten years specific experiments have been conducted on an electrolytic reactor (owner: Mr. A. Goi et al.). The aim was to investigate whether anomalous energy emissions, heat generation, and compositional variations on the electrodes may be correlated to new type nuclear reactions during electrolysis phenomena. The reactor was built in order to be appropriately filled with a salt solution of water and Potassium Carbonate (K_2CO_3). The electrolytic phenomenon was obtained using two metal electrodes immersed in the aqueous solution. The liquid's container, named also reaction chamber in the following, was a cylinder-shaped element of 100 mm diameter, with 150 mm of height and 5 mm of thickness. For the reaction chamber, two different materials were used during the experiments: Pyrex glass and Inox AISI 316 L steel. The two metallic electrodes were connected to a source of direct current: Ni-Fe based electrode as positive pole (anode) and Cr-Co based one as negative (cathode) (see Fig. 46.1).

After approximately 10 operating hours, the generation of cracks was observed on the glass container, which forced the authors to adopt a more resistant reaction chamber made of steel. Teflon lids are sealed to the upper and the lower openings of the chamber respectively. The reaction chamber base has a ceramic plate preventing the direct contact between liquid solution and Teflon lid (see Fig. 46.1a). Two threaded holes host the electrodes, which were screwed to the bottom of the chamber successively filled with the solution. A valve at the top of the cell allows the vapor to escape from the reactor

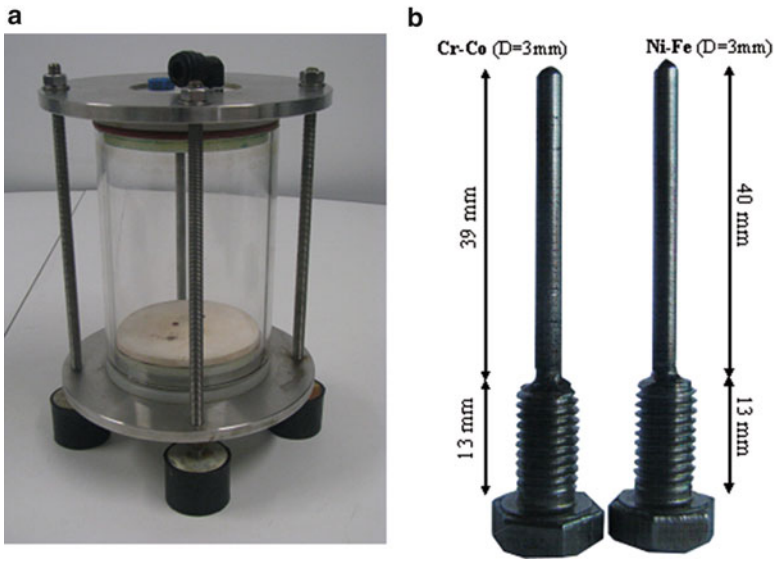

Fig. 46.1 The reaction chamber was a cylinder-shaped element of 100 mm diameter, with 150 mm of height and 5 mm of thickness (**a**). The two electrodes presented an eight of about 40 mm of the operating part and a diameter of about 3 mm. The threaded portions and the base are 13 and 5 mm length respectively (**b**)

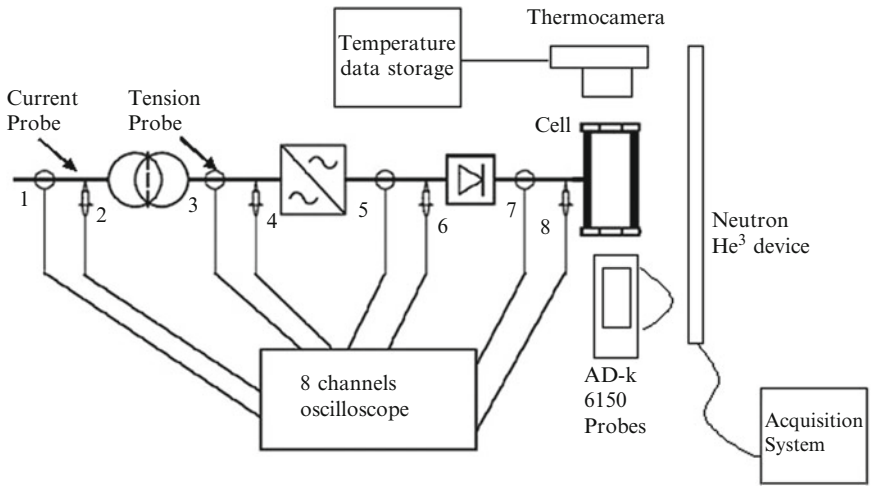

Fig. 46.2 Scheme of the experimental set up adopted and disposition of the measurement equipments employed during the tests

chamber and condense in an external collector. Externally, two circular Inox steel flanges, fastened by means of four threaded bars, hold the Teflon layers. The inferior steel flange of the reactor is connected to four supports isolated from the ground by means of rubber based material. As mentioned before, a direct current passes through the anode and the cathode electrodes, provided by a power circuit connected to the power grid through an electric socket. The components of the circuit are an isolating transformer, an electronic variable transformer (Variac), and a diode bridge linked in series (Fig. 46.2).

46.2.2 Measurement Equipment and Devices

Different physical quantities were measured during the experiments, such as voltage, current, temperature, neutron and alpha particle emissions. First of all, a thermal camera was adopted to monitor the temperature trend on specific regions of interest of the operating cell. Secondly, current and voltage probes were positioned in different parts of the circuit as reported in Fig. 46.2. The voltage measurements were performed by a differential voltage probe of 100 MHz with a maximum rated voltage of 1,400 V, the current was measured by a Fluke I 310S probe with a maximum rated current of 30 A. Particular attention was given to the data obtained from the current and voltage probes positioned at the entrance of the reaction chamber (probes 7 and 8 in Fig. 46.2) in order to evaluate the power absorbed by the cell.

Regarding the neutron emission measurements, since neutrons are electrically neutral particles, they cannot directly produce ionization in a detector, and therefore cannot be directly detected. This means that neutron detectors must rely upon a conversion process accounting the interaction between an incident neutron and a nucleus, which produces a secondary charged particle. Such charged particle is then detected and the neutron's presence is revealed from it. For an accurate neutron evaluation a He^3 proportional counter was employed. The detector used in the tests is a He^3 type (Xeram, France) with pre-amplification, amplification, and discrimination electronics directly connected to the detector tube. The detector is supplied with a high voltage power (about 1.3 kV) via NIM (Nuclear Instrument Module). The logic output producing the TTL (transistor–transistor logic) pulses is connected to a NIM counter. The logic output of the detector is enabled for analog signals exceeding 300 mV. This discrimination threshold is a consequence of the sensitivity of the He^3 detector to the gamma rays ensuing neutron emission in ordinary nuclear processes. This value has been determined by measuring the analog signal of the detector by means of a Co-60 gamma source. The detector is also calibrated at the factory for the measurement of thermal neutrons; its sensitivity is 65 cps/$n_{thermal}$ ($\pm$10 % declared by the factory), i.e., the flux of thermal neutrons was one thermal neutron/s cm^2, corresponding to a count rate of 65 cps.

For the alpha particle emission, a 6150 AD-k probe a sealed proportional counter was used, which does not require refilling or flushing from external gas reservoirs. The probe is sensitive to alpha, beta, and gamma radiation. An electronic switch allows for the operating mode "alpha" to detect alpha radiation only, such that in this mode the radiation recognition is very sensitive because the background level is much lower. A removable discriminator plate (stainless steel, 1 mm) distinguishes between beta and gamma radiation detection. An adjustable handle can be locked to the most convenient orientation. During the experiments the 6150 AD-k probe was used in the operating mode alpha to monitor the background level before and after the switching on of the cell.

Finally, before and after the experiments Energy Dispersive X-ray spectroscopy has been performed in order to recognise possible direct evidence of piezonuclear reactions that can take place during the electrolysis. The elemental analyses were performed by a ZEISS Auriga field emission scanning electron microscope (FESEM) equipped with an Oxford INCA energy-dispersive X-ray detector (EDX) with a resolution of 124 eV @ MnKa. The energy used for the analyses was 18 KeV.

46.3 Experimental Results

46.3.1 General Remarks and Preliminary Stage

The operating cell showed interesting effects of phenomena uneasy to interpret. After switching on the cell power, an initial phase was observed: the container temperature kept increasing up to approximately 100 °C during a time interval of about 1 h, after which the liquid started to boil. After the increase in the temperature, a steady state regime was observed until the switch off. The steady temperature phase was characterized by the presence of an "irregular vibrating light" in correspondence of one of the two electrodes (see Fig. 46.3a). A simple ampere-meter was applied at the input line of the cell, and the electric current absorbed seemed to decrease when the temperature reached a steady value. In this phase, part of the produced vapour gas started to condense in the external collector and emissions of H, O and He could be observed.

From the observation conducted during the experiments, the phenomenon of the electrolysis is accompanied by different types of energy exchange. The thermal energy exchange is the most evident in terms of liquid boiling and vapour gas production. A smaller portion of energy is emitted in the external environment by heat conduction between the reactor surface and the surrounding air.

In Fig. 46.3b, the two electrodes used for the tests are shown. The initial measurement phase implied the use of the Energy Dispersive X-ray spectroscopy (EDS) technique to obtain measurements useful to evaluate the chemical composition of the two electrodes before the experiments. In particular, a series of measures were repeated in three different regions of interest for each electrode in order to obtain a sufficient amount of reliable data. Such regions of interest are the upper, the intermediate and the lower part of the single electrode, as reported in Fig. 46.3b.

In Fig. 46.4a, b the average element concentrations of the electrodes used for the electrolysis are shown. In the initial condition the Ni-Fe electrode (anode) is composed by approximately 44 % in Ni, 30 % in Fe, and 23 % in O. The remaining 3 % includes contents of Si, Mn, Ca, Al, K, Na, Mg, Cl, and S, appeared only in traces (Fig. 46.4a). On the other hand, the Cr-Co cathode is composed by approximately of 44 % in Co, 18 % in Cr, 4 % in Fe, 25 % in O, and traces of other elements such as Si, Al, Mg, Na, W, Cu, and S (Fig. 46.4b). Table 46.1 summarizes the results for the compositional analysis conducted on the K_2CO_3 the salt used for the aqueous solution (K_2CO_3 + H_2O), where the solute to solvent ratio was approximately 40 g/l.

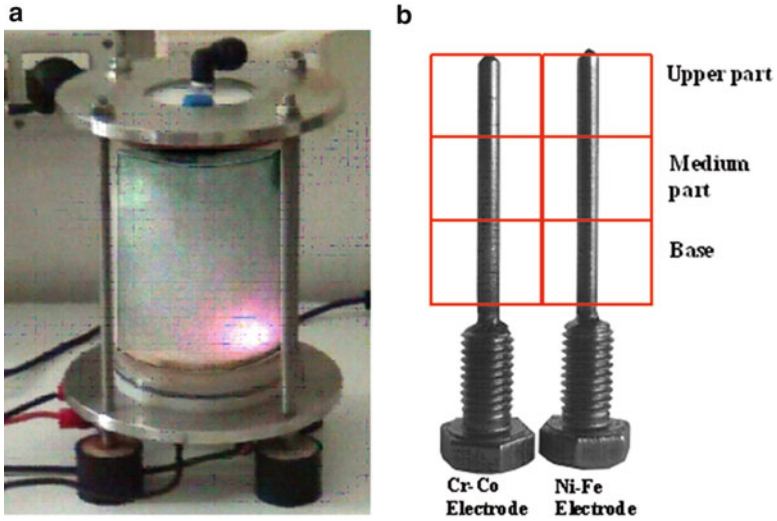

Fig. 46.3 Reaction chamber during the experiment (**a**). The presence of an "irregular vibrating light" in correspondence to one of the two electrodes has been observed together with a significant heat flux from the chamber surface (**a**). A series of EDS measures were repeated in three different regions of interest for each electrode in order to obtain a sufficient amount of reliable data (**b**)

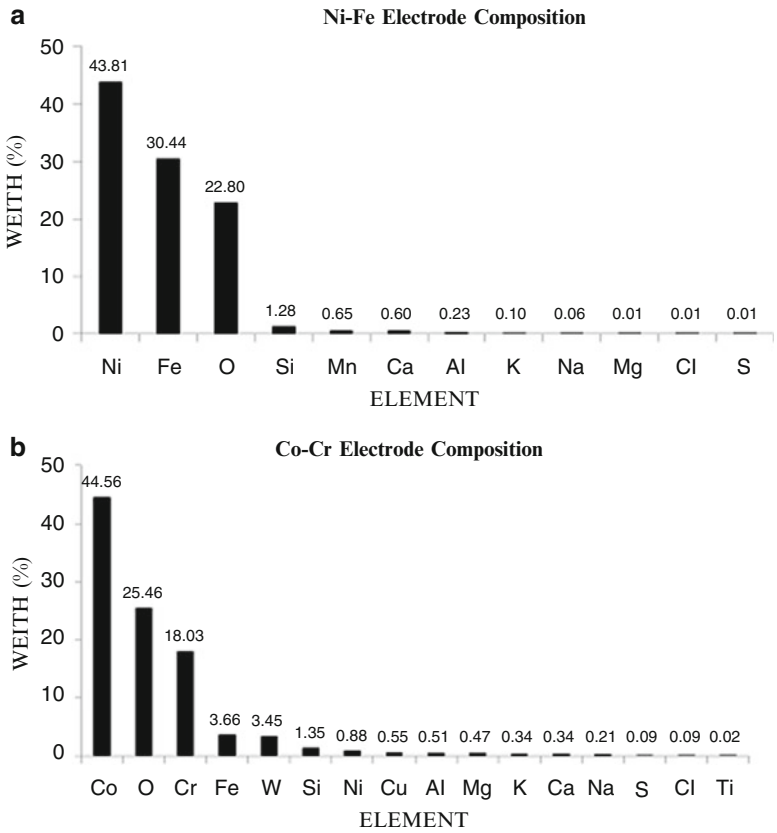

Fig. 46.4 Mean element concentrations of the two electrodes used for the electrolysis

Table 46.1 EDS of the K_2CO_3 salt used for the aqueous solution

Element	Weight%	Atomic%	Compd%	Formula
C	13.02	22.05	47.72	CO_2
K	43.40	22.57	52.28	K_2O
O	43.58	55.38		
Totals	100.00			

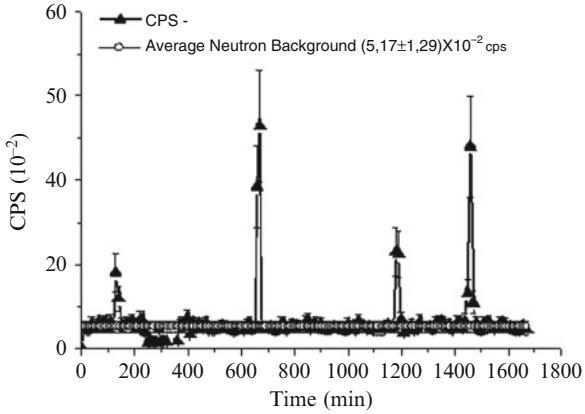

Fig. 46.5 Neutron emission measurements. Emissions between 4 times and 10 times the background level have been observed during the experiments

46.3.2 Energy Emissions: Neutron and Alpha Detection During the Experiment

Neutron emission measurements performed during the experimental activity are represented in Fig. 46.5. The measurements performed by the He^3 detector were conducted for a total time of about 26 h. The background level was measured for different time intervals before and after switching on the reaction chamber. These measurements reported an average neutron background of about $5.17 \pm 1.29 \times 10^{-2}$ cps. Furthermore, when the reaction chamber is active, it is possible to observe that after a time interval of about 3 h (200 min) neutron emissions of about 4 times the background level may be recognized. After 11 h (650 min) from the beginning of the measurements, it is possible to observe a neutron emission level of about one order of magnitude greater than the background level. Similar results were observed after 20 h (1,200 min) and 25 h (1,500 min) when neutron emissions of about 5 times and 10 times the background were measured respectively.

In Fig. 46.6a, b, the alpha particle emissions are reported. The data are related to an alpha emission level monitored by means of the 6150 AD-k probe set to the operating mode "alpha". The measurements shown in Fig. 46.6a are referred to the data acquired for a time interval equal to 60 min when the reaction chamber was operating (cell on). The data in Fig. 46.6b represent the alpha particle emissions corresponding to the background level and are obtained by measurements acquired, also in this case, for a time interval of 60 s (cell off). From this first evidence, it can be assumed that the number of count per second acquired by the probe increased considerably when the reaction chamber was operating (cell on) (Fig. 46.6). In addition, the mean value of the two alpha emission time series during the working time and for the background have been computed. In the first case, when the cell is switched on, the mean value of the alpha emission is about 0.03, whereas in the second case, when the cell is switched off, only the background of the laboratory is detected with a mean value of about 0.01 Cs^{-1}. From this evidence, an alpha particle emission up to three times the background may be considered during the electrolysis. These results, together with the evidence of neutron emissions reported in Fig. 46.5 are particularly interesting when considering the compositional variation that is reported in the following and will be useful to corroborate the hypothesis of piezonuclear fission for the chemical elements constituting the electrodes. In Fig. 46.6c, the cumulative curves for the alpha emission counts are reported. It is evident that the total counts value, monitored when the cell was operating (Cell On), is approximately twice the value measured for the background level (Cell Off).

46.3.3 Compositional Analysis of the Electrodes

As reported in the previous section, Energy Dispersive X ray spectroscopy has been performed in order to recognise possible direct evidence of piezonuclear reactions that can take place during the electrolysis. Fig. 46.7a shows the Ni-Fe electrode during the analysis, whereas the middle part of the Co-Cr electrode is reported in Fig. 46.7b. In Fig. 46.7c, d two images of the electrode surface before the experiment and after 32 h of work are reported. It is shown that the electrode after many operating hours presented cracks and micro-cracks visible on its external surfaces (see Fig. 46.7d).

The experimental activity was developed in four different phases in order to investigate possible compositional variations on the electrode surfaces. The first phase is devoted to evaluate the composition of the electrodes at the beginning of the

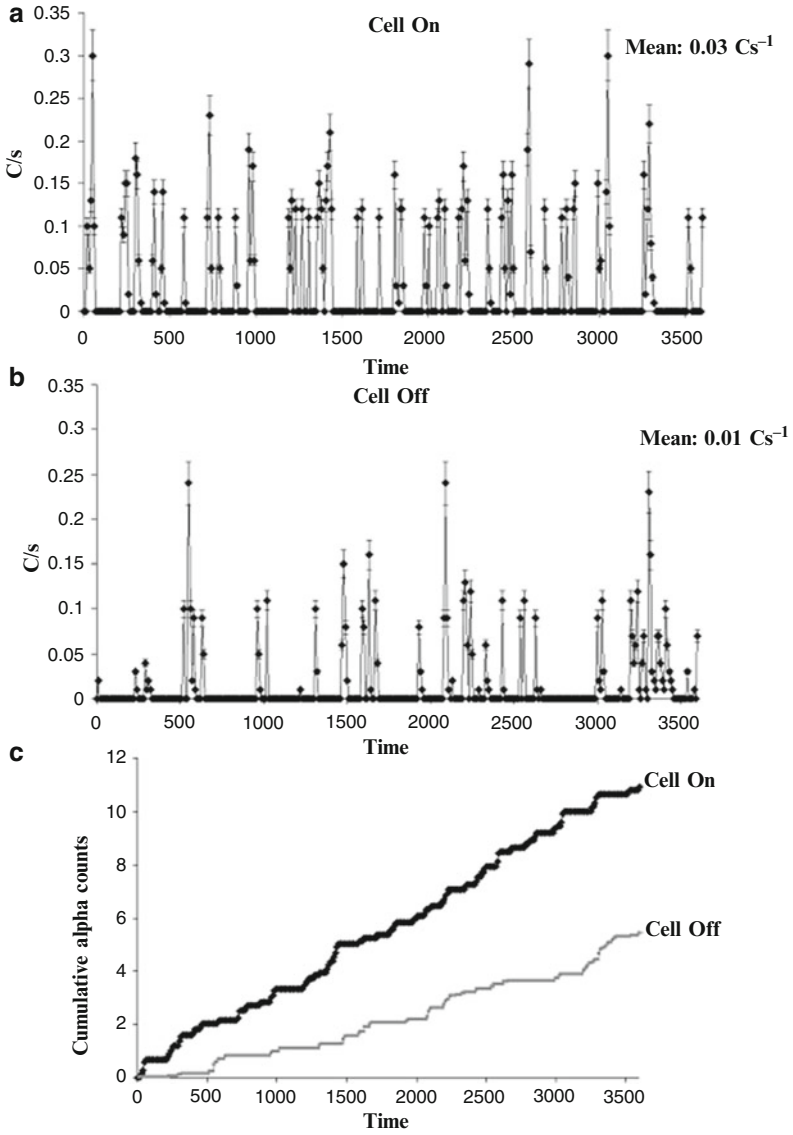

Fig. 46.6 The measurements shown are referred to the data acquired for a time interval equal to 60 min when the reaction chamber was operating (**a**). The alpha particle emissions corresponding to the background level for a time interval of 60 min (**b**). Cumulative curves for the alpha emissions (**c**)

experiment (0 h), and it corresponds to the compositional analysis before the reaction chamber activation (see Table 46.2). The second stage corresponds to an initial operating time of the electrolytic cell of about 4 h (see Table 46.2). After this step, a third and a fourth phases were considered. In these two steps, the cell was operating for 28 and 6 h, with a cumulative working time of the reaction chamber of 32 and 38 h respectively (see Table 46.2). In the case of the Ni-Fe electrode, the resulting mean concentrations of Ni, Si, Mg, Fe and Cr are reported for each step in Table 46.2.

For the Ni-Fe electrode, compositional changes may be observed after 32 h in the concentrations of Ni, Si, Mg, Fe and Cr as reported in Table 46.2 and in Figs. 46.8, 46.9, 46.10, 46.11, and 46.12. In these figures the EDS measurements for each element are reported considering the four phases previously mentioned (Figs. 46.8a, 46.9a, 46.10a, 46.11a, and 46.12a). At the same time, the evolutions of the mean value of each time series, corresponding to 0, 4, 32 and 38 h, are reported by histograms (Figs. 46.8b, 46.9b, 46.10b, 46.11b, and 46.12b). After 38 h further variations were observed for the elements previously mentioned and the appearance of Cr, before absent, was detected as reported in Table 46.2 and in Fig. 46.12a. In particular, the Ni concentration showed a total average decrease of 8.6 % from 43.9 % to 35.3 % after 38 h (see Table. 46.2 and Fig. 46.8a, b). This Ni depletion is one fourth the initial Ni concentration. A mean increment in Si concentration after 32 h of about 3.9 % and an average increment in Mg concentration, starting from a concentration of 0.1 % up to 4.8 %, can be

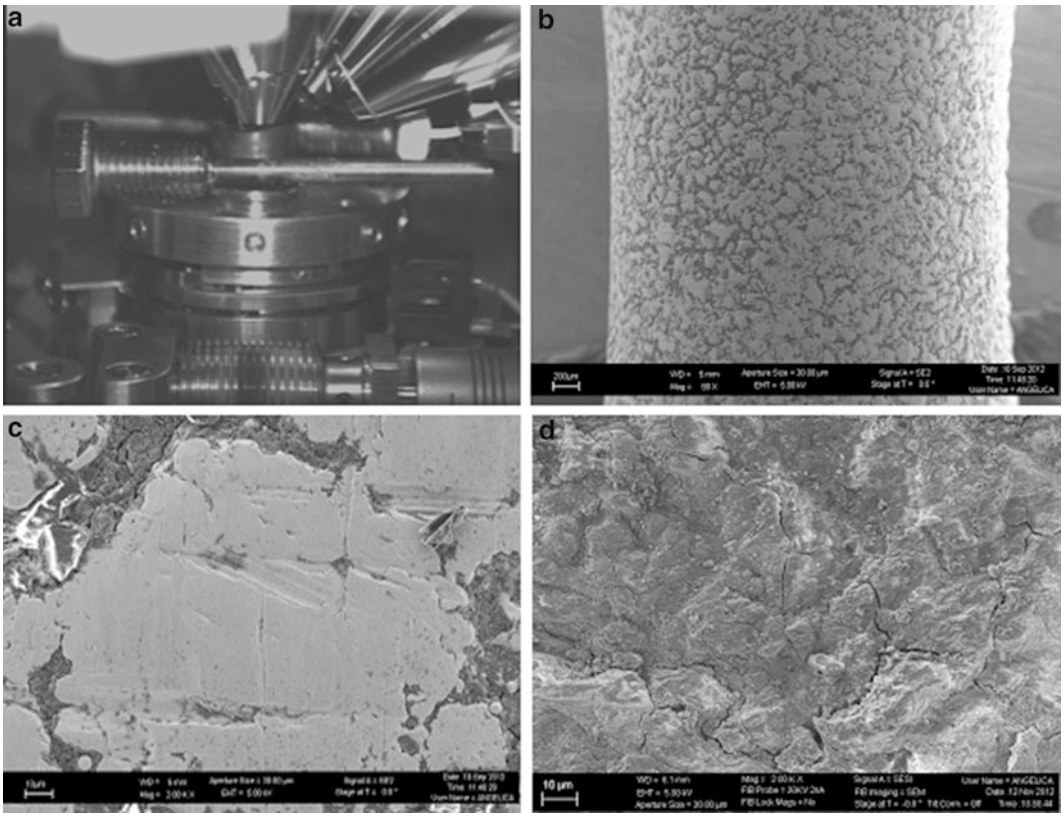

Fig. 46.7 (**a**) The FESEM characterization of the Cr-Co electrode middle part is reported (**b**). Image of the electrode surface before the experiment (**c**). The electrode after many operating hours presented cracks and micro-cracks visible on the external surfaces (**d**)

Table 46.2 Ni-Fe electrode, element concentration before the experiment, after 4, 32 and 38 h of the test

	Ni (%)	Si (%)	Mg (%)	Fe (%)	Cr (%)
Before the experiment	43.9	1.1	0.1	30.5	–
After 4 h	43.6	0.5	0.4	30.7	–
After 32 h	35.2	5.0	0.2	27.9	–
After 38 h	35.3	1.5	4.8	27.3	3.0

The values reported for the mass % of each element are referred as the mean value of all the effectuated measurements

observed from the data reported in Table 46.2, Figs. 46.9 and 46.10. Similar considerations may be done also for Fe and Cr concentrations. The mean Fe content decreased by about 3 % changing from 30.5 % to 27.3 % at the end of the experiment (see Table 46.2 and Fig. 46.11). On the contrary, average Cr concentration appeared to be different from the last phase with an appreciable increase of about 3 % (see Table 46.2 and Fig. 46.12). These decreases in Ni and Fe seem to be almost perfectly counterbalanced by the increases in the other elements: Si, Mg, and Cr. In particular, considering the following balance: Ni (−8.6 %) = Si (+3.9 %) + Mg (+4.7 %), it may be explained by the following piezonuclear fissions:

$$\mathrm{Ni}_{28}^{58} \rightarrow \ 2\mathrm{Si}_{14}^{28} + 2 \text{ neutrons}, \tag{46.1}$$

$$\mathrm{Ni}_{28}^{58} \rightarrow \ 2\mathrm{Mg}_{12}^{24} + 2\mathrm{He}_{2}^{4} + 2 \text{ neutrons}. \tag{46.2}$$

At the same time, the balance considering Fe and Cr, Fe (−3.2 %) ≅ Cr (+3.0 %), may be used to introduce another reaction:

$$\mathrm{Fe}_{26}^{56} \rightarrow \ \mathrm{Cr}_{24}^{52} + \mathrm{He}_{2}^{4} \ . \tag{46.3}$$

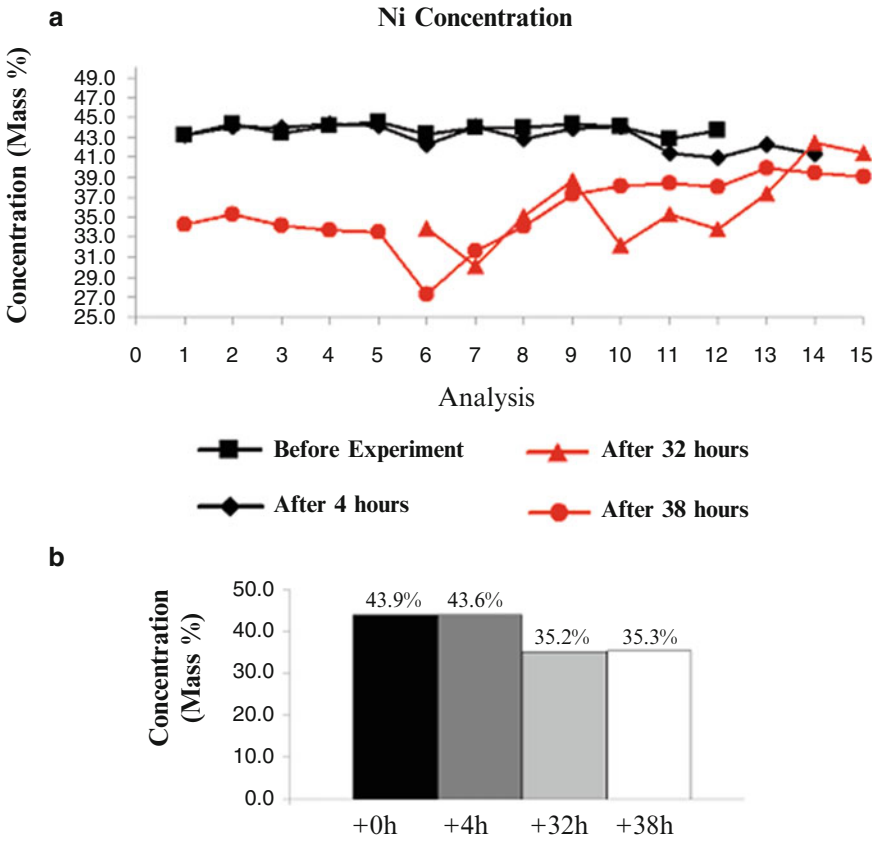

Fig. 46.8 Ni concentration before the experiment, after 4 h, after 32 and 38 h (**a**). The average values of Ni concentration change from a mass percentage of 43.9 % at the beginning of the experiment to 35.2 % and 35.3 % after 32 and 38 h respectively (**b**)

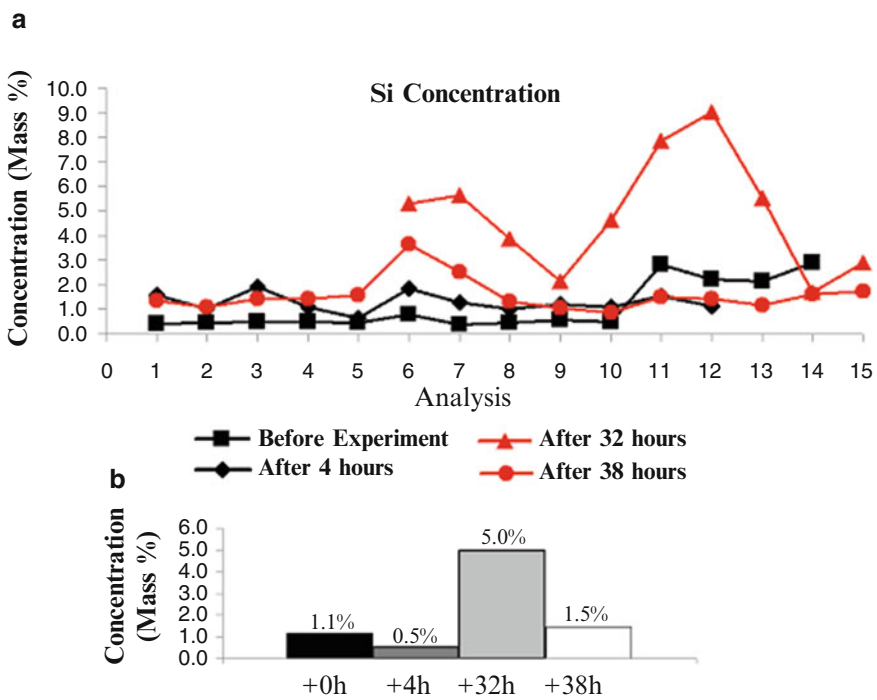

Fig. 46.9 Si concentration before the experiment, after 4 h, after 32 and 38 h (**a**). The mean values of Si concentration change from a mass percentage of 1.1 % and 0.5 % at the beginning of the experiment to 5.0 % and 1.1 % after 32 and 38 h respectively (**b**)

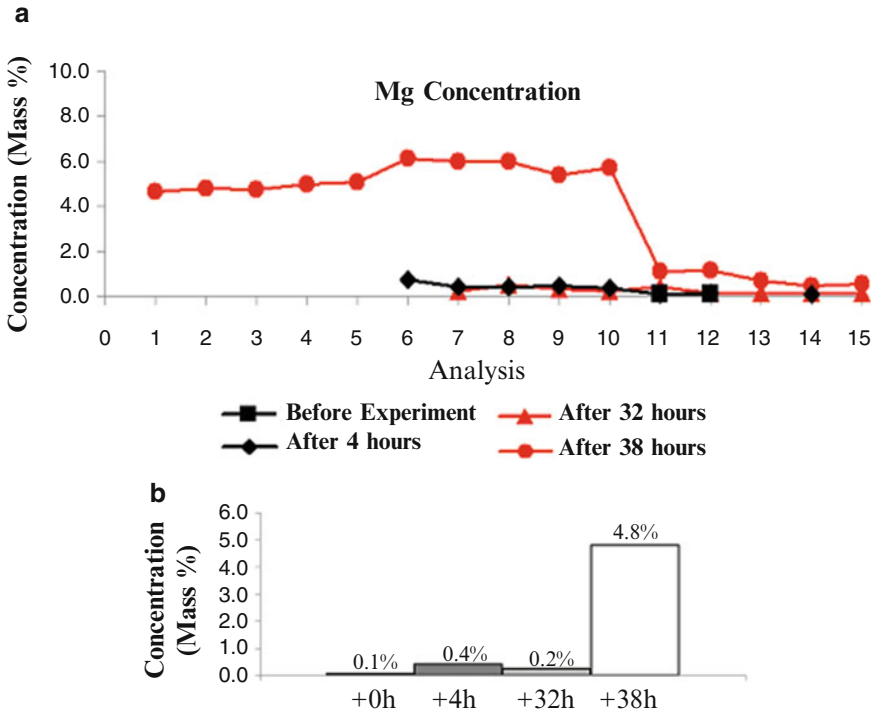

Fig. 46.10 Mg concentration before the experiment, after 4 h, after 32 and 38 h (**a**). The mean values of Mg concentration change from a mass percentage of 0.1 % and 0.4 % at the beginning of the experiment to 4.8 % after 38 h (**b**)

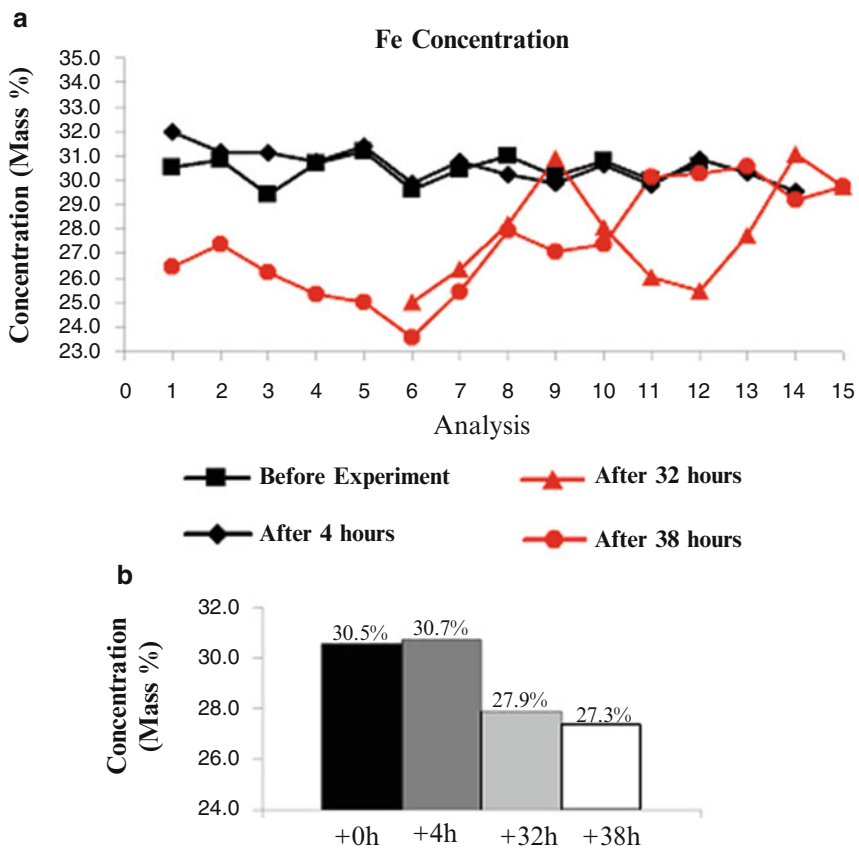

Fig. 46.11 Fe concentration before the experiment, after 4 h, after 32 and 38 h (**a**). The mean values of Fe concentration change from a mass percentage of 30.5 % at the beginning of the experiment to 27.9 % and 27.3 % after 32 and 38 h respectively (**b**)

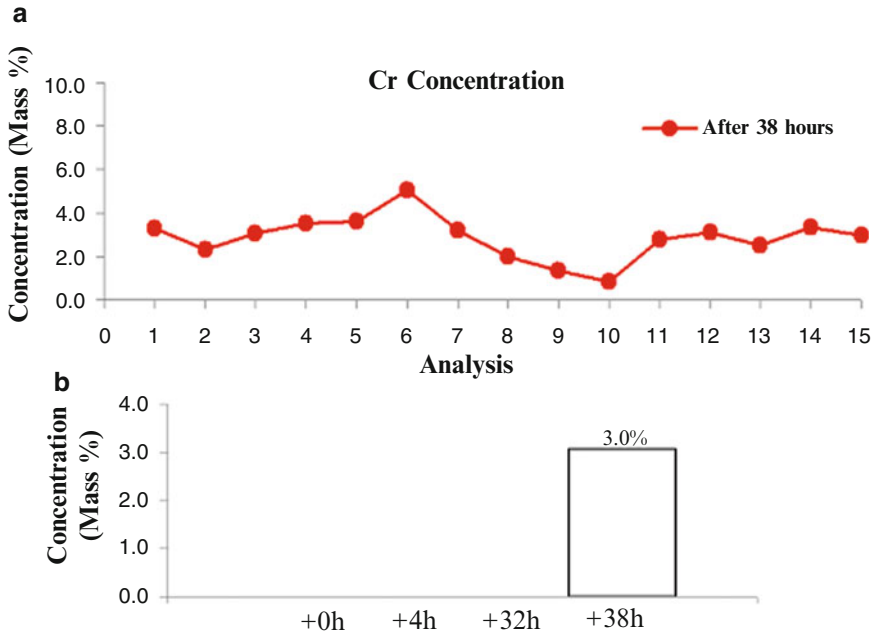

Fig. 46.12 Cr concentration after 38 h (**a**). The mean value of Cr concentration changes from 0 (absence of this element) to a mass percentage of 3.0 % after 38 h (**b**)

Table 46.3 Co-Cr electrode, element concentration before the experiment, after 4, after 32 and 38 h of the test

	Co(%)	Fe(%)	Cr(%)	K(%)
Before the experiment:	44.1	3.1	17.8	0.5
After 4 h	43.7	1.6	17.8	2.2
After 32 h	20.6	26.3	9.7	12.9
After 38 h	34.4	6.6	5.1	4.4

It is very interesting to notice that reactions (46.1) and (46.2) imply neutron emissions, as well as reaction (46.2) and (46.3) imply the emissions of alpha particles. From this point of view, the anomalous conjectured reactions could be used to interpret also the anomalous energy emissions in the form of neutrons and alpha particles reported in the previous section.

As far as the Co-Cr electrode is concerned, it is possible to observe variations even more evident in the concentrations of the most diffused constituting elements. In particular, the average Co concentration decreased of about 23.5 % from an initial percentage of 44.1 % to a weight concentration of about 20.6 % after 32 h (see Table 46.3 and Fig. 46.13a, b). At the same time an appreciable increment of 23.2 % can be observed in the Fe content after 32 h, changing from 3.1 % (concentration before the experiment) to 26.3 % at the end of the third phase (see Table 46.3 and Fig. 46.14a, b). It is rather impressive that the decrease in Co concentration and the increase in Fe are almost the same: Co (−23.5 %) ≅ Fe (+23.2 %). Similarly to the result of the Ni-Fe electrode, also in this case, according to the compositional direct evidence, the following reaction may be proposed:

$$\mathrm{Co}_{27}^{59} \rightarrow \mathrm{Fe}_{26}^{56} + \mathrm{H}_{1}^{1} + 2 \text{ neutrons}. \tag{46.4}$$

In Table 46.3 and in Figs. 46.15 and 46.16, Cr and K concentrations are reported for the different phases of the experiment. The mean Cr concentration decreases by 12.7 %, from 17.8 % to 5.1 % after 38 h (Table 46.3 and Fig. 46.15a, b). This decrease can be counterbalanced by the increase in K concentration from 0.5 % to 12.9 % after 32 h (Table 46.3 and Fig. 46.16a, b). Considering these variations also the following anomalous reaction, involving Cr as the starting element and K as the resultant could be considered:

$$\mathrm{Cr}_{24}^{52} \rightarrow \mathrm{K}_{19}^{39} + \mathrm{He}_{1}^{1} + 2\mathrm{He}_{2}^{4} + 4 \text{ neutrons}. \tag{46.5}$$

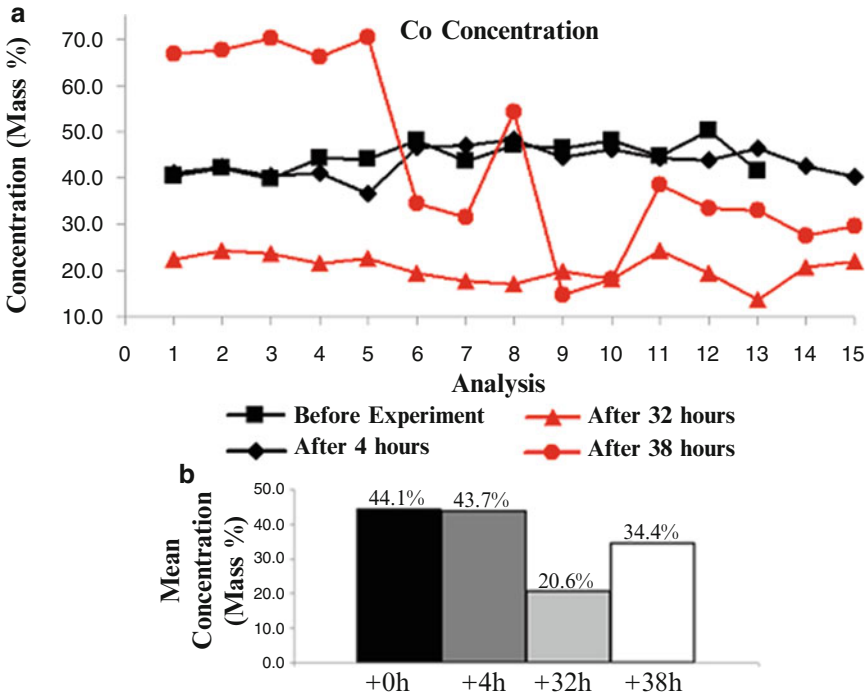

Fig. 46.13 Co concentration before the experiment, after 4 h, after 32 and 38 h (**a**). The mean values of Co concentration change from a mass percentage of 44.1 % at the beginning of the experiment to 20.6 % and 34.4 % after 32 and 38 h respectively (**b**)

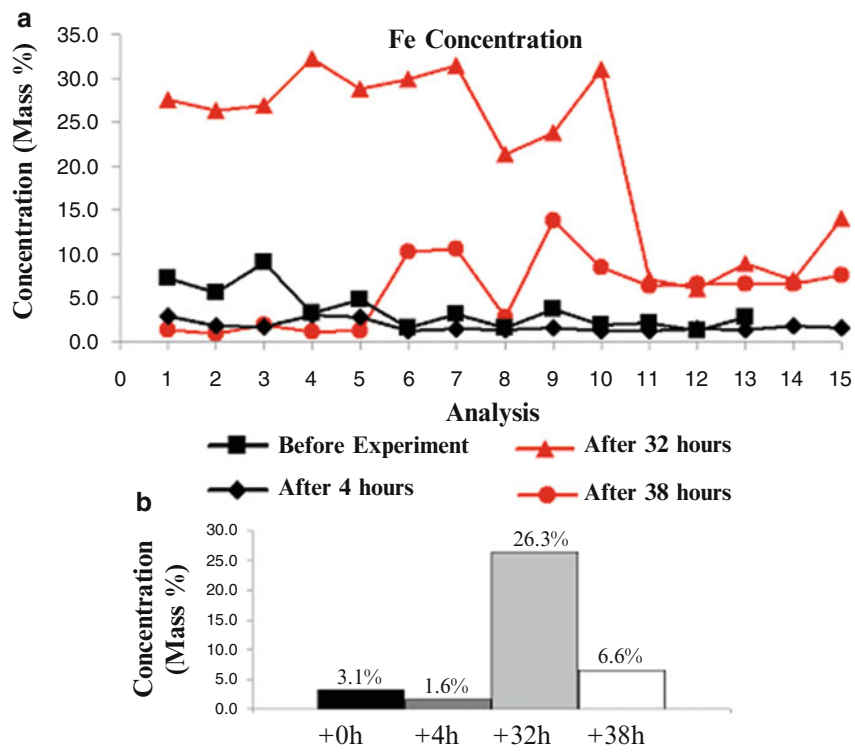

Fig. 46.14 Fe concentration before the experiment after 4 h and after 32 and 38 h (**a**). The mean values of Fe concentration change from a mass percentage of 3.1 % at the beginning of the experiment to 26.3 % and 6.6 % after 32 and 38 h respectively (**b**)

Also in this case, it is remarkable that both reactions (46.4) and (46.5) imply neutron emissions, while reaction (46.5) implies also the emission of alpha particles. The same considerations made for the first electrode may be repeated also in this case, where anomalous energy emissions and compositional variations seem to suggest the occurrence of fission reactions on the electrode surfaces.

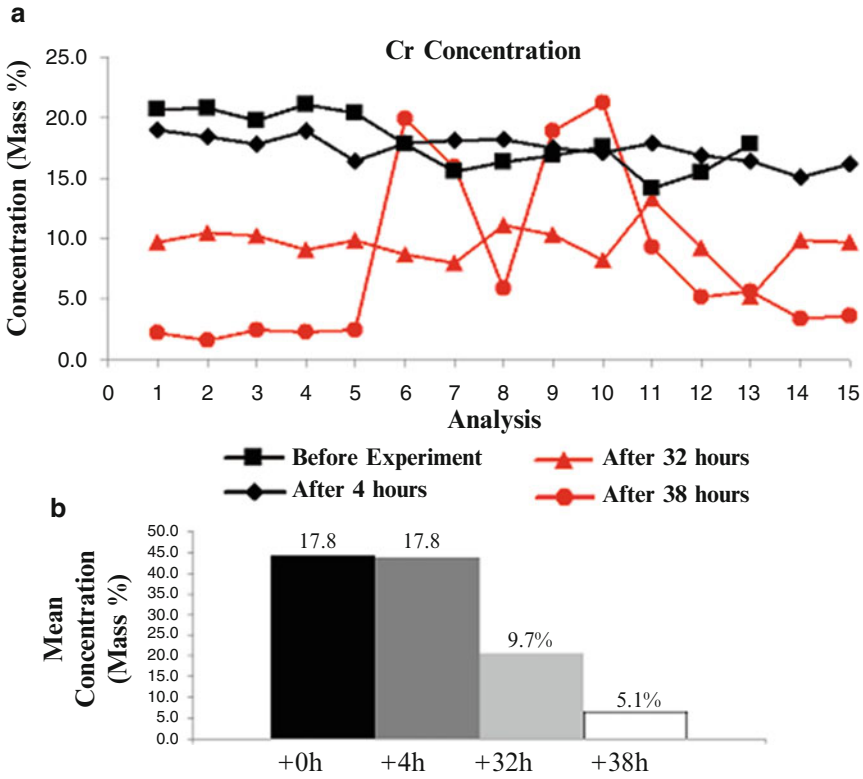

Fig. 46.15 Cr concentration before the experiment after 4 h, after 32 and 38 h (**a**). The Cr concentration changes from a mass percentage of 17.8 % to 9.7 % and 5.1 % after 32 and 38 h (**b**)

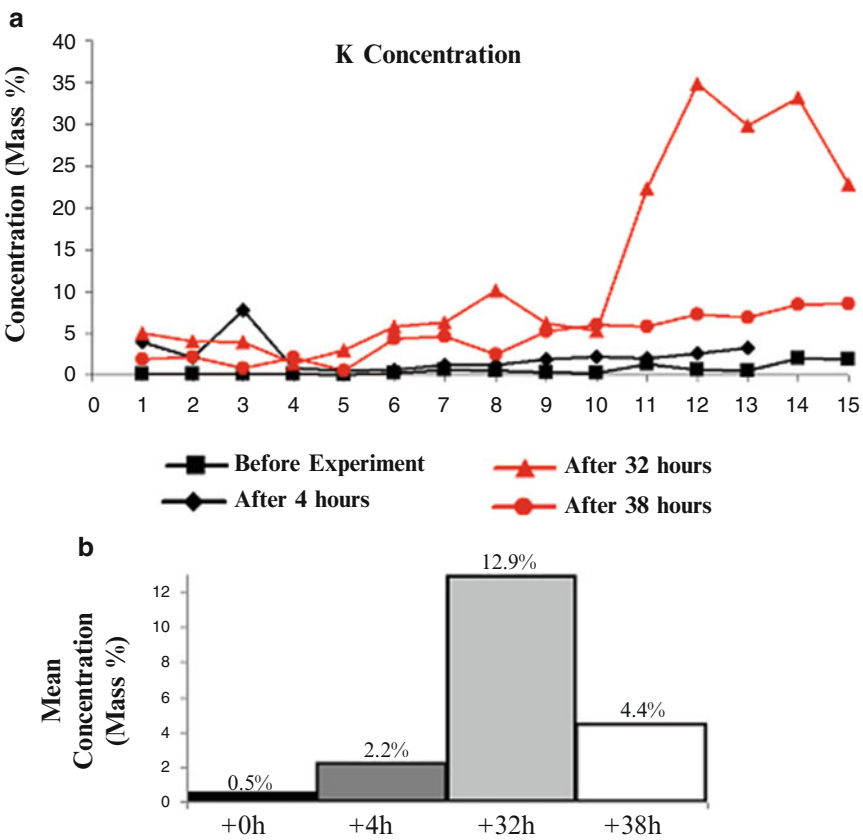

Fig. 46.16 K concentration before the experiment after 4 h, after 32 and 38 h (**a**). The K concentration changes from 0.5 % and 2.2 after 4 h to 12.9 % and 4.4 % after 32 and 38 h (**b**)

It is important to consider that the balances reported, for Ni-Fe electrode (reactions 46.1, 46.2, and 46.3) and for Co-Cr electrode (reactions 46.4, 46.5), were obtained considering the values of the third and the fourth steps corresponding to the larger variation for each element concentration (see Tables 46.2 and 46.3). Additional variations observed for some of these elements, such as Si, Co and Fe, between the third and the fourth step, may be explained considering other possible secondary piezonuclear fissions involving the electrode surfaces. Future works will be devoted to evaluate the evidence of these secondary piezonuclear fissions and ad-hoc experiments will be done to analyze the effects of the crusting layer, due to the salt solution deposition.

All these results suggest that during the gas loading, performed with deuterium (or hydrogen), the host matrix is subjected to mechanical damaging and fracturing due to atoms penetration. Evidences of a diffused cracking were recognized on the electrode surface after the experiments (see Fig. 46.7d). This would suggest that hydrogen, favoring crack propagation in the metal, came from the electrolysis of water. Being the electrodes immersed in a liquid solution, their surface is exposed to the formation of gaseous hydrogen due to the decomposition of water caused by the current passage.

46.4 Conclusions

Neutron emissions up to one order of magnitude higher than the background level were observed during the operating time of an electrolytic cell. In particular, after a time interval of about 3 h, neutron emissions of about 4 times the background level were measured. After 11 h, it was possible to observe a neutron emission level of about one order of magnitude greater than the background level. Similar results were observed after 20 and 25 h. When the cell was switched on, the mean value of the alpha emission was about 0.03 Cs^{-1} for 1 h of measurement; this value corresponds to an alpha emission of about three times the background level measured in the laboratory before and after the experiment (0.01 Cs^{-1}).

By the EDS analysis performed on the two electrodes in four successive steps, significant compositional variations can be recognized. In general, the decreases in Ni and Fe in the Ni-Fe electrode seem to be almost perfectly counterbalanced by the increases in lighter elements: Si, Mg and Cr. In fact, the balance Ni (−8.6 %) ≅ Si (+3.9 %) + Mg (+4.7 %) is satisfied by reactions (46.1) and (46.2). At the same time, the balance Fe (−3.2 %) = Cr (+3.0 %) may be explained considering reaction (46.3). As far as the Co-Cr electrode is concerned, the Co decrease is almost perfectly counterbalanced by the Fe increase: Co (−23.5 %) = Fe (+23.2 %). This last evidence, which is really impressive considering the amount of the mass percentage involved, seems to be explainable only considering reaction (46.4). Finally, the Cr decrease (−12.7 %) and the K increase (+12.9 %) may be explained by reaction (46.5).

Chemical variations and energy emissions may be accounted for direct and indirect evidence of *mechanonuclear fission reactions* correlated to microcrack formations and propagation due to *hydrogen embrittlement*. According to this interpretation of the so-called *Cold Nuclear Fusion*, hydrogen, which is imputed to favor the crack formation and propagation in the electrodes, comes from the metallic electrolysis of water. Being the electrodes immersed in a liquid solution, the metal surface is exposed to the formation of gaseous hydrogen due to the decomposition of water caused by the current passage. In addition, the high current density might contribute to the formation and penetration of hydrogen into the metal. The so-called *Cold Nuclear Fusion*, interpreted under the light of *hydrogen embrittlement*, may be explained by anomalous fission reactions (piezonuclear reactions) occurring in the host metal rather than by fusion of hydrogen isotopes dissolved in the metal lattice.

Aknowledgements Dr. A. Sardi and Dr. F. Durbiano are gratefully acknowledged for their help during the experimental set-up definition and for the assistance given during the measurements. Also Dr. A Chiodoni is acknowledged for the EDS measurements.

References

1. Arata Y, Zhang Y (1995) Achievement of solid-state plasma fusion ("cold-fusion"). Proc Jpn Acad 71:304–309, Ser. B
2. Bockris JO'M, Lin GH, Kainthla RC, Packham NJC, Velev O (1990) Does tritium form at electrodes by nuclear reactions?. In: The first annual conference on cold fusion, National Cold Fusion Institute, University of Utah Research Park, Salt Lake City
3. Borghi DC, Giori DC, Dall'Olio A (1957) Experimental evidence for the emission of neutrons from cold hydrogen plasma. CEN, Recife
4. Bush RT, Eagleton RD (1993) Calorimetric studies for several light water electrolytic cells with nickel fibrex cathodes and electrolytes with alkali salts of potassium, rubidium, and cesium. In: Fourth international conference on cold fusion, Lahaina, Maui, Electric Power Research Institute 3412 Hillview Ave., Palo Alto, p 13
5. Cardone F, Carpinteri A, Lacidogna G (2009) Piezonuclear neutrons from fracturing of inert solids. Phys Lett A 373:4158–4163

6. Cardone F, Mignani R (2004) Energy and geometry. World Scientific, Singapore, chap. 10
7. Carpinteri A, Cardone F, Lacidogna G (2009) Piezonuclear neutrons from brittle fracture: early results of mechanical compression tests. Strain 45:332–339, Atti dell'Accademia delle Scienze di Torino. 33, 27–42, (2009)
8. Carpinteri A, Cardone F, Lacidogna G (2010) Energy emissions from failure phenomena: mechanical, electromagnetic, nuclear. Exp Mech 50:1235–1243
9. Carpinteri A, Lacidogna G, Manuello A, Borla O (2012) Piezonuclear fission reactions: evidences from microchemical analysis, neutron emission, and geological transformation. Rock Mech Rock Eng 45:445–459
10. Carpinteri A, Lacidogna G, Manuello A, Borla O (2013) Piezonuclear fission reactions from earthquakes and brittle rocks failure: evidence of neutron emission and nonradioactive product elements. Exp Mech 53:345–365
11. Derjaguin BV et al (1989) Titanium fracture yields neutrons? Nature 34:492
12. Diebner K (1962) Fusionsprozesse mit Hilfe konvergenter Stosswellen – einige aeltere und neuere Versuche und Ueberlegungen. Kerntechnik 3:89–93
13. Fleischmann M, Pons S, Hawkins M (1989) Electrochemically induced nuclear fusion of deuterium. J Electroanal Chem 261:301
14. Fleischmann M, Pons S, Preparata G (1994) Possible theories of cold fusion. Nuovo Cimento Soc Ital Fis A 107:143
15. Fujii MF et al (2002) Neutron emission from fracture of piezoelectric materials in deuterium atmosphere. Jpn J Appl Phys 41:2115–2119
16. Kaliski S (1978) Bi-conical system of concentric explosive compression of D-T. J Tech Phys 19:283–289
17. Kanarev M, Mizuno T (2003) Cold fusion by plasma electrolysis of water. New Energy Technol 1:5–10
18. Liebowitz H (1971) Fracture an advanced treatise. Academic, New York
19. Little SR, Puthoff HE, Little ME (1998) Search for excess heat from a Pt electrode discharge in K_2CO_3-H_2O and K_2CO_3-D_2O electrolytes
20. Miles MH, Hollins RA, Bush BF, Lagowski JJ, Miles RE (1993) Correlation of Excess Power and Helium Production during D_2O and H_2O Electrolysis using Palladium Cathodes. J Electroanal Chem vol 346:99–117
21. Mills RL, Kneizys P (1991) Excess heat production by the electrolysis of an aqueous potassium carbonate electrolyte and the implications for cold fusion. Fusion Technol 20:65
22. Milne I, Ritchie RO, Karihaloo B (2003) Comprehensive structural integrity: fracture of materials from nano to macro, vol 6. Chapter 6.02, Elsevier, Amsterdam, pp 31–33
23. Mizuno T (1998) Nuclear transmutation: the reality of cold fusion. Infinite Energy Press, Concord, N.H., ISBN 1-892925-00-1
24. Mizuno T et al (2000) Production of heat during plasma electrolysis. Jpn J Appl Phys A 39:6055
25. Monti RA (1996) Low energy nuclear reactions: experimental evidence for the alpha extended model of the atom. J New Energy 1(3):131
26. Monti RA (1998) Nuclear transmutation processes of lead, silver, thorium, uranium. In: The seventh international conference on cold fusion, ENECO Inc., Vancouver
27. Mosier-Boss PA et al (2007) Use of CR-39 in Pd/D co-deposition experiments. Eur Phys J Appl Phys 40:293–303
28. Mosier-Boss PA et al (2010) Comparison of Pd/D co-deposition and DT neutron generated triple tracks observed in CR-39 detectors. Eur Phys J Appl Phys 51(2):20901–20911
29. Notoya R, Enyo M (1992) Excess heat production during electrolysis of H_2O on Ni, Au, Ag and Sn electrodes in alkaline media. In: Proceedings of third international conference on cold fusion, Nagoya Japan, Universal Academy Press, Tokyo
30. Ohmori T, Mizuno T (1998) Strong excess energy evolution, new element production, and electromagnetic wave and/or neutron emission in light water electrolysis with a tungsten cathode. Infin Energy 20:14–17
31. Ohmori T, Mizuno T (1999) Nuclear transmutation reaction caused by light water electrolysis on tungsten cathode under incandescent conditions. Infin Energy 5(27):34
32. Ohmori T, Mizuno T, Enyo M (1996) Isotopic distributions of heavy metal elements produced during the light water electrolysis on gold electrodes. J New Energy 1(3):90–99
33. Preparata G (1991) Some theories of cold fusion: a review. Fusion Technol 20:82
34. Preparata G (1991) A new look at solid-state fractures, particle emissions and «cold» nuclear fusion. Il Nuovo Cimento 104A:1259–1263
35. Ransford HE (1999) Non-stellar nucleosynthesis: transition metal production by DC plasma-discharge electrolysis using carbon electrodes in a non-metallic cell. Infin Energy 4(23):16
36. Storms E (2000) Excess power production from platinum cathodes using the Pons-Fleischmann effect. in: Eighth international conference on cold fusion, Lerici (La Spezia), Italian Physical Society, Bologna, pp 55–61
37. Storms E (2007) Science of low energy nuclear reaction: a comprehensive compilation of evidence and explanations about cold fusion. World Scientific, Singapore
38. Sundaresan R, Bockris JOM (1994) Anomalous reactions during arcing between carbon rods in water. Fusion Technol 26:261
39. Swartz M (2008) Three physical regions of anomalous activity in deuterated palladium. Infin Energy 14:19–31
40. Szpak S, Mosier-Boss PA, Smith JJ (1994) Deuterium uptake during Pd-D codeposition. J Electroanal Chem 379:121
41. Warner J, Dash J, Frantz S (2002) Electrolysis of D2O with titanium cathodes: enhancement of excess heat and further evidence of possible transmutation. In: The ninth international conference on cold fusion, Tsinghua University, Beijing, p 404
42. Winterberg F (1984) Autocatalytic fusion–fission implosions. Atomenergie-Kerntechnik 44:146

Chapter 47
Strain Decoupling for the Real Time Strains Measured During Welding Process

Liang Wang, Keyu Li, and Salahaddin Sanusei

Abstract Stress during welding is of high interest while complex due to the high gradient transient thermal effect. All published literatures studied it by finite element simulations. For the first time, the authors tried to derive the stress history based on measured temperature and in-plane strains. However, the measured strains were the total strains consisted of coupled thermal, elastic and plastic strains. To determine the stress based on the constitutive equations, measured total strains should be decoupled.

Three in-plane strain (strain X, strain Y and shear strain XY) histories which were general strain history during welding process were utilized for illustrating the strain decoupling process. Thermal strain was first determined by the measured temperature history. To separate the elastic strain and plastic strain, the sum of mechanical strain determined by subtracting thermal strain from total strain was divided into three stages: compression, recovery and tension. Yielding was detected at both the compression and tension regions using von Mises' yielding criteria. Similar to cyclic tension/compression testing, same amount of elastic strain will be recovered before the tension region starts. All material properties used were temperature dependent, and a plane stress condition was assumed since welding was applied on thin steel plates.

Keywords Strain • Stress • Welding • Strain decoupling • Thermo-elastic-plastic

47.1 Introduction

Welding is one of the most commonly used metal joining method in industry. However, due to the non-uniform temperature distribution with steep gradient near the weld, local deformations and distortions are induced causing products' poor quality, short fatigue life and durability. To diminish these side effects, studies were conducted for understanding the mechanism during welding such as investigating the dynamic strains, stresses and distortions through both analytical and experimental analysis [1–4]. Applying conventional residual stress measurement techniques, residual stress were studied for varied structures utilizing different welding methods [5, 6]. However, only limited experimental observations of welding strains have been proposed. The high temperature, steep temperature and strain gradient, and intensive welding light emission during the welding process make it challenging to measure the real time strains. In addition, no dynamic stress history during the welding process has been derived based on the experimental real time strains. With the development of modern computer technology, the transient strain/stress and residual stress were analytically examined using finite element simulation (FEM) in intensive literatures [7–9].

Three procedures are generally used for these finite element simulations. First of all, the temperature distribution is simulated for given welding parameters such as current and voltage. Different thermal models have been proposed [10], and the moving heat source model is highly recognized. Transient thermal analysis is conducted based on the temperature information for given thermal conductivity conditions. Dynamic thermal strains are obtained in this step. At last, by inputting the thermal strains, mechanical strains/stresses are simulated by solving the coupled thermo-mechanical models. Reasonable conclusions were drawn from these simulations, which however have un-neglected limitations. For example, material behavior at the weld pool is simplified without considering the thermal relaxation [11]. Rare simulations consider

L. Wang (✉) • K. Li • S. Sanusei
Department of Mechanical Engineering, Oakland University, Rochester, MI 48309, USA
e-mail: lwang@oakland.edu

H. Jin et al. (eds.), *Advancement of Optical Methods in Experimental Mechanics, Volume 3*,
Conference Proceedings of the Society for Experimental Mechanics Series,
DOI 10.1007/978-3-319-00768-7_47,

the strains due to creep, phase transformation or metallurgical structure changes. For some published works, the stress is assumed to be only contributed by the elastic strains [12, 13].

This paper will focus on the derivation of stresses during the welding process based on the field dynamic strains data acquired by a laser-based interference technique. Since the total strain measured during the welding process contains coupled thermal, elastic and plastic strains, strain decoupling is accomplished which requires determination of yielding and strain kinetics. Material properties such as Young's modulus, yield stress, Poisson's ratio, are temperature dependent. Following procedures described in this paper, the strain components can be decoupled and therefore the stress history can be determined. This procedure does not require the intensive work of solving the thermo-elastic-plastic model or partial differential equations in FEM. Also, procedures described in this paper will demonstrate how stresses are induced during the welding process.

47.2 Strain Decoupling Procedures

Dynamic strains during welding process were measured using a laser-based interferometric strain/slope rosette (ISSR) technique [14]. The ISSR is made of three pairs of optical gages which measures three in-plane strains (ε_{xx}, ε_{yy} and ε_{xy}) directly and simultaneously. More than 20 tests were conducted at different welding conditions such as varied temperature, material, plate thickness, and annealing condition. Depends on the welding conditions, the strain versus time may shift along the two axes. However, the overall strain trend is similar. For demonstrating purpose, one typical strain result is used for strain decoupling and stress determination. The temperature history and strain results are shown in Fig. 47.1. Strain X shown in Fig. 47.1 is along the welding direction, and strain Y is in transverse direction. In this test, the ISSR was installed 17 mm from the center of the weld line. Welding was continuously applied for 21 s, and the total weld length is 71 mm.

47.2.1 3D Strain/Stress Tensor Determination Based on Measured in-Plane Strains

Plastic deformation exists during the welding process. To check whether the material yields, the dynamic stress should be obtained in prior. On the other hand, the strain and stress tensor is of interest to be known in some applications. Therefore, determination of the strain and stress tensor in elastic region based on three measured in-plane strains is first presented in this paper.

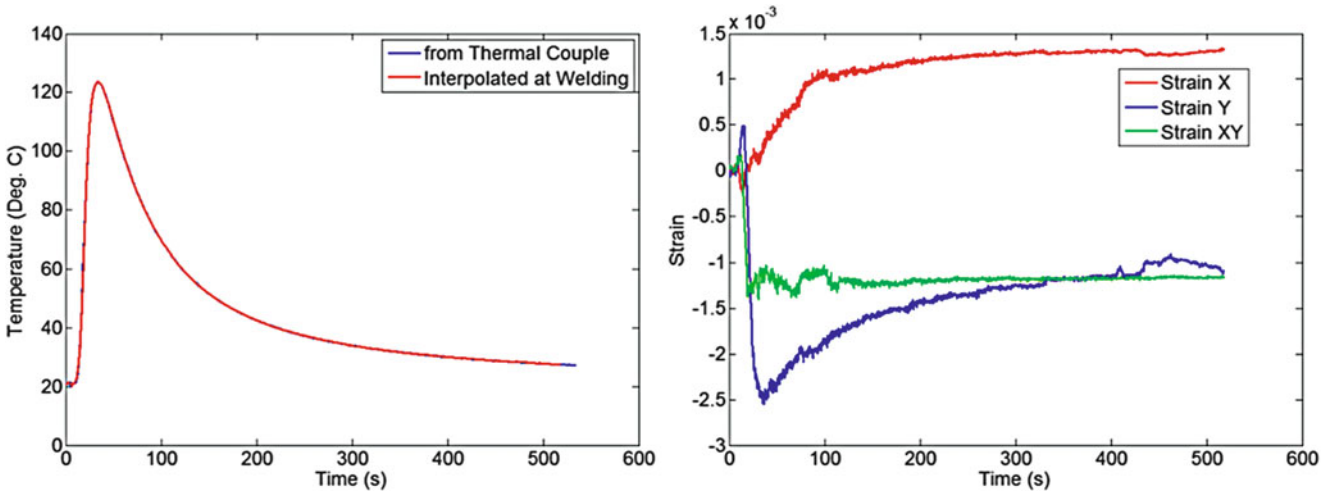

Fig. 47.1 Temperature and strain history for one typical welding test. The strains were measured from welding starts till temperature cools down to room temperature

Three in-plane strains ε_{xx}, ε_{yy} and ε_{xy} are measured experimentally. Assuming the plane stress condition since welding was applied on a thin steel plate, stress results in the following holds:

$$\sigma_{zz} = 0;\ \ \tau_{zx} = 0; \tau_{zy} = 0$$

Thus, the two shearing strains γ_{xz} and γ_{yz} equal to zero. Following the constitute equation in elastic region, the elastic strain in Z direction can be obtained by

$$\varepsilon_{zz} = -\nu\left(\frac{\sigma_{xx}}{E} + \frac{\sigma_{yy}}{E}\right) = -\frac{\nu}{1-\nu}(\varepsilon_{xx} + \varepsilon_{yy}) \tag{47.1}$$

Where ν is Poisson's ratio, E is Young's modulus. Therefore, the strain tensor in elastic region for isotropic material is determined as

$$\begin{bmatrix} \varepsilon_{xx} & \gamma_{xy} & \gamma_{xz} \\ \gamma_{yx} & \varepsilon_{yy} & \gamma_{yz} \\ \gamma_{zx} & \gamma_{zy} & \varepsilon_{zz} \end{bmatrix} = \begin{bmatrix} \varepsilon_{xx} & 2\varepsilon_{xy} & 0 \\ 2\varepsilon_{xy} & \varepsilon_{yy} & 0 \\ 0 & 0 & -\dfrac{\nu}{1-\nu}(\varepsilon_{xx} + \varepsilon_{yy}) \end{bmatrix} \tag{47.2}$$

Solving the constitute equations in elastic region, the corresponding stress tensor can be calculated by inputting the measured three in-plane strains:

$$\begin{bmatrix} \sigma_{xx} & \tau_{xy} & \tau_{xz} \\ \tau_{yx} & \sigma_{yy} & \tau_{yz} \\ \tau_{zx} & \tau_{zy} & \sigma_{zz} \end{bmatrix} = \begin{bmatrix} \dfrac{E(\varepsilon_{xx} + \nu\varepsilon_{yy})}{1-\nu^2} & \dfrac{E\varepsilon_{xy}}{1+\nu} & 0 \\ \dfrac{E\varepsilon_{xy}}{1+\nu} & \dfrac{E(\nu\varepsilon_{xx} + \varepsilon_{yy})}{1-\nu^2} & 0 \\ 0 & 0 & 0 \end{bmatrix} \tag{47.3}$$

From Eq. 47.3, the real time stresses before yielding can be obtained from dynamic measured strains. For situation where plane strain condition is concerned, the corresponding strain and stress tensor can be also obtained following same algorithm. Also, it should be mentioned that Eqs. 47.2 and 47.3 are applicable for elastic region only. The equations are not suitable for determining the stress directly by inputting the measured strains. However, stress in the elastic region can be solved which will be used for detecting the yielding.

47.2.2 Time Dependent Material Properties

Welding problem is challenging by its complex in high gradient transient thermal change and accompanying phase transformation, material microstructure and properties change, and mechanical deformations and distortions. To fully capture these factors, material properties used for determining the stress history has to be temperature dependent. For stainless steel 304 L where welding was applied on, the material properties such as yielding stress, Young's modulus, Poisson's ratio and thermal expansion coefficient are reported in literatures [7, 15]. In this paper, these material properties are adopted as shown in red empty circles shown in Fig. 47.2. To simulate the properties at each individual temperature, linear interpolation was conducted and the results are shown in the curves shown in Fig. 47.2. Unfortunately, temperature dependent plastic material properties are not found, which limits the derivation for only elastic-perfectly plastic material model.

Temperature changes during the welding process. In the later derivations, material properties at each individual time are required. Therefore, material properties in Fig. 47.2 are combined with Fig. 47.1 to generate the transient material properties as shown in Fig. 47.3. Using information in Fig. 47.3, thermal strain, stresses and accompanying derivations are ensured to be temperature dependent.

47.2.3 Strain Kinetics Model for the Welding Process

Cyclic loading which consists of tension and compression loading is well known. As shown in Fig. 47.4, when the material is continuously loaded by a tensile force, material stays in elastic before the stress reaches yield stress and in plastic region after that. If an unloading procedure is applied before the material reaches its ultimate strength, the elastic strain tends to

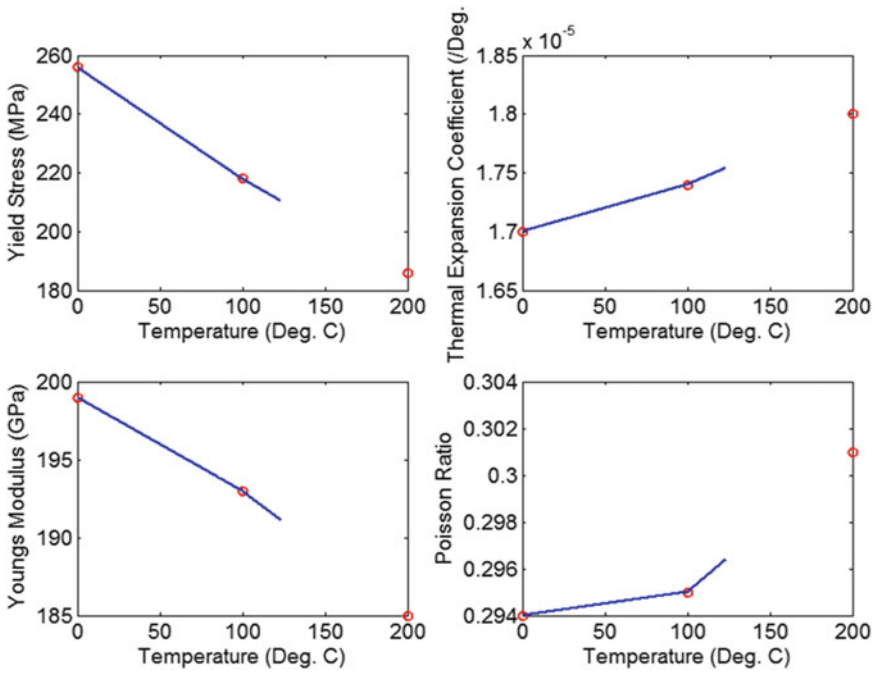

Fig. 47.2 Temperature dependent material properties

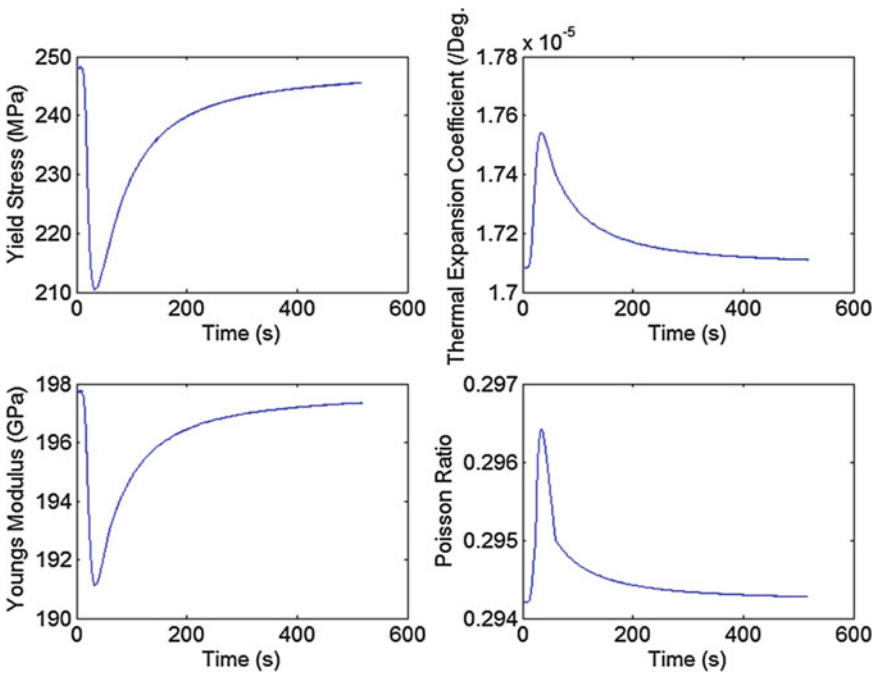

Fig. 47.3 Material properties versus time during the welding process

springback while the plastic strain remains. As the unloading goes, material will reach one stage that no load is imposed so that the elastic strain is fully recovered and purely plastic strain stores in the material. Following that, a compression load is applied so that the material also experience elastic and plastic stages. Note that, due to the Bauschinger effect, material will yield at lower stress than in tension. Similar process repeats during continuous unloading and loading.

To some extent, welding process is very similar to the simplified cyclic loading condition which only includes one compression and tension loading sequences. The algorithm is depicted in Fig. 47.5. As welding is imposed on the steel surface, the temperature increases and reaches peak at time t_2. When welding stops, the cooling process starts and the temperature drops gradually to room temperature. Due to the thermal expansion, material at weld pool is expanded and materials surrounding the weld pool are compressed. Similarly, at the cooling process, weld pool cools faster leading the adjacent material under tension.

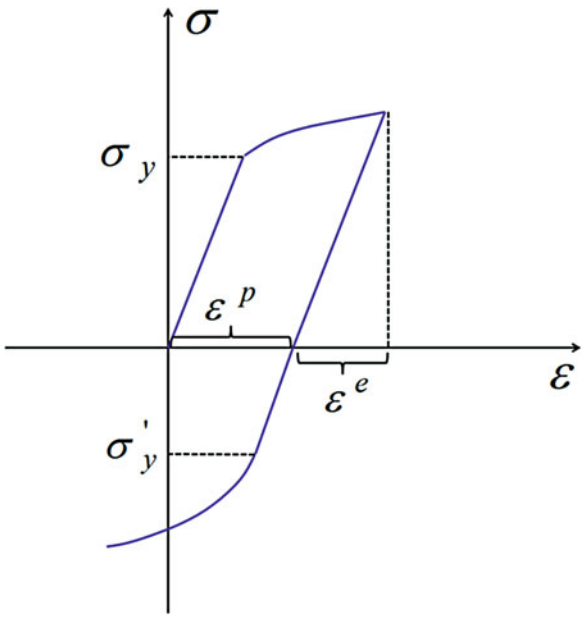

Fig. 47.4 Strain stress relationship during a tension and compression loading sequence

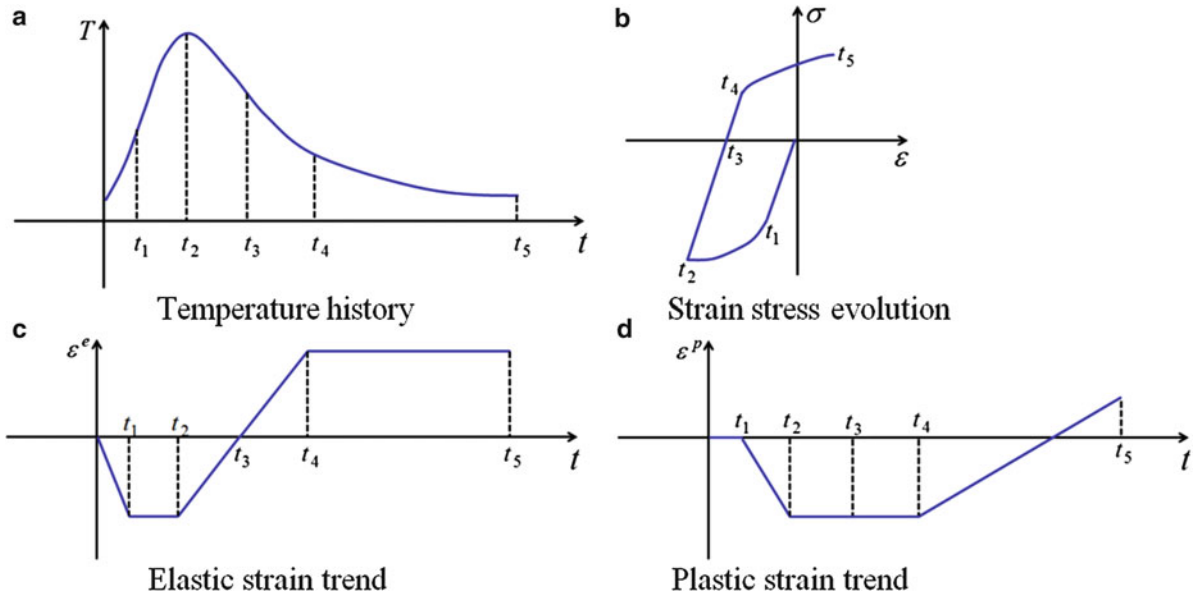

Fig. 47.5 Schematic strain kinetics during the heating and cooling process (**a**) Temperature history (**b**) Strain stress evolution (**c**) Elastic strain trend (**d**) Plastic strain trend

Therefore, as shown in Fig. 47.5b, when the temperature is increasing, material is under compression. At time t_1, the compression load is so high that material starts yielding. Plastic deformation dominants till the temperature reaches peak. After that, tensile stresses which contribute to the unloading and tension of the material are induced during the cooling process. At critical time t_3, the compression elastic strains are fully recovered and material starts the elastic deformation due to tension. Similar material yielding occurs when the tensile stress is higher than the yielding stress and plastic deformation cumulates till the material returns to room temperature.

The evolution of the elastic and plastic strains during this whole process is sketched in Figs. 47.5c, d. Increasing elastic strain is accumulated in the material before it yields at time t_1. Same amount of elastic strain stores in the material and stay same when the plastic strain increases as the material is continuously heated till time t_2. When the cooling process starts, the compression induced elastic strain decreases while the plastic strain remains. The inversing tensile loading leads to the recovery of the compression elastic strain at time t_3 and also the following tension yielding at time t_4.

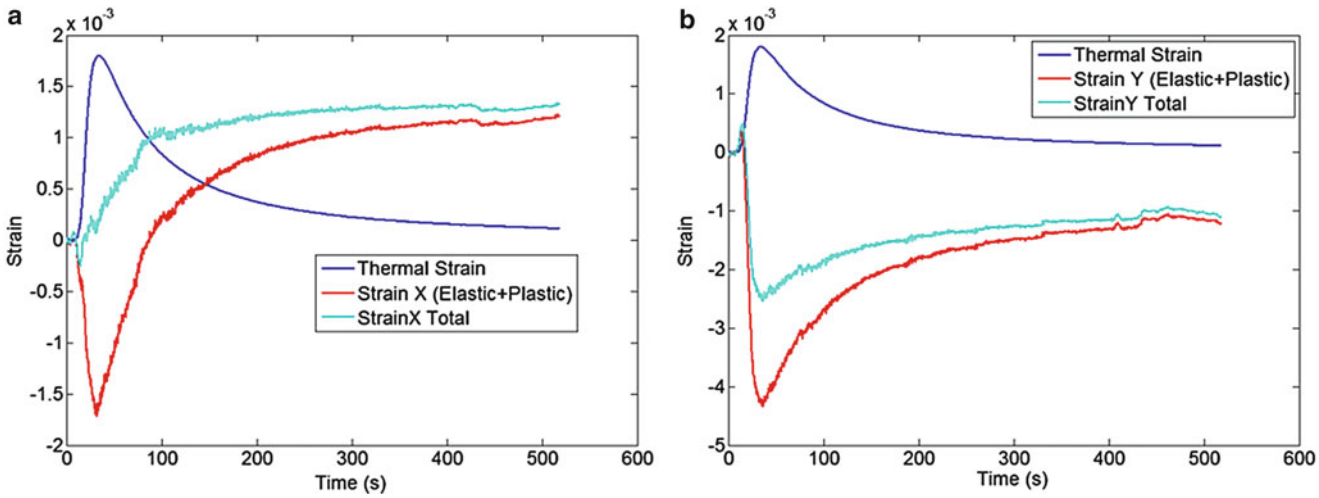

Fig. 47.6 Decomposition of measured strains which includes thermal strain and mechanical strains (**a**) strain X (**b**) strain Y

47.2.4 Elastic and Plastic Strain/Stress

Welding process induces a moving heat source which non-uniformly heats the material near the weld pool. Thermal strain is generated due to the temperature change. Also, due to the physical constraint of the plate, mechanical strains which include elastic and maybe plastic strains are also induced to balance the thermal strain. In addition, for some cases when welding is applied continuously for long time with high heating, creep strain and strain from phase transformation would occur. In this paper, since the welding process only takes around 21 s, the creep strain and phase transformation strain is neglected. For a plate which is fully constraint without external load, the thermal strain and mechanical strains are balanced such as

$$\varepsilon^{th} + \varepsilon^{e} + \varepsilon^{p} = 0 \tag{47.4}$$

Where ε^{th} denotes the thermal strain, ε^{e} and ε^{p} represents the elastic and plastic mechanical strains. However, since the plate was only constraint using moisture clay at plate's four corners during the welding process, which leads to a remain part of strains measured during the process such as [7–9]

$$\varepsilon^{th} + \varepsilon^{e} + \varepsilon^{p} = \varepsilon^{total} \tag{47.5}$$

Where ε^{total} is the strain measured during the welding process by the ISSR technique. Obviously, the measured strains are coupled with mechanical and thermal strains. Using the constitutive equations, the mechanical stress can be determined unless the mechanical strains are decoupled.

Thermal strain is readily dissolved by known thermal expansion coefficient and temperature history based on its definition in Eq. 47.6.

$$\varepsilon^{th} = \alpha \times \Delta T \tag{47.6}$$

Where α is thermal expansion coefficient whose value is shown in Fig. 47.3, and ΔT is the temperature difference which is known from the temperature history shown in Fig. 47.1. Assuming the thermal properties are isotropic in the measured steel material, the thermal strains in X and Y are identical during the test and are shown in Fig. 47.6.

Subtracting the thermal strains from the measured strains, the total mechanical strain (ε^{M}) consisted of elastic and plastic strains are determined as shown in Fig. 47.6a, b for strain X and Y.

Adopting the strain kinetics algorithm, the elastic and plastic strains are separated. Figure 47.7 shows the schematic timing when the material deforms differently as an example of mechanical parts of strain X. Several assumptions are made for this algorithm. First of all, due to the constrain effect of surrounding material, the recovery strain during unloading (or tension loading) may not be identical as the elastic strain in compression loading. However, in this paper, we assume same

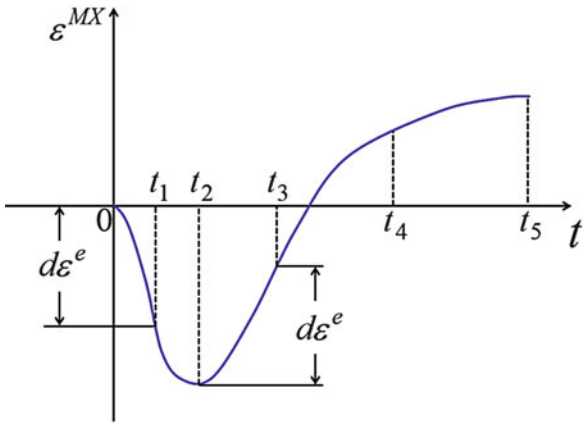

Fig. 47.7 Schematic decomposition of the strain history based on the strain kinetics

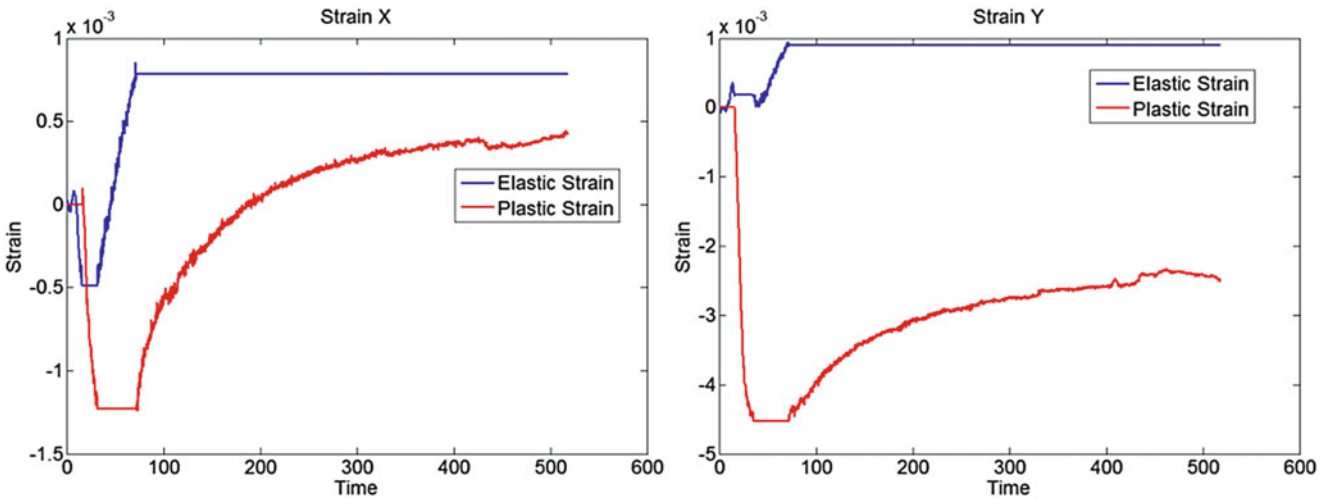

Fig. 47.8 Decoupled elastic and plastic strains for strain X and strain Y

amount of elastic strain will be recovered. Also, elastic strain and plastic strain are postulated to be independent. In the plastic range, the elastic strain is assumed to be constant. Similarly, plastic strain is treated stable during the elastic process. Due to the limitation of the temperature dependent plastic material properties, the elastic-perfectly plastic material model is used without considering the hardening. In addition, no Bauschinger effect is considered at this situation.

Von Mises yielding criteria was employed to detect the elastic and plastic stages. Since material at beginning of the welding is definitely in elastic, stresses are directly calculated using the stress tensor in Eq. 47.3. Von Mises effective stress can then be obtained. Note that all stresses are temperature dependent (time dependent). The yielding is also checked at real time base as shown in Eq. 47.7:

$$\sigma_X(T,t)^2 + \sigma_Y(T,t)^2 - \sigma_X(T,t) \times \sigma_Y(T,t) + 3\tau_{XY}(T,t)^2 \geq \sigma_y(T,t)^2 \tag{47.7}$$

Where σ_X, σ_Y and τ_{XY} are temperature and time dependent stresses, and σ_y is the yield stress. It should be mentioned that yielding is examined using stresses in both X and Y axes. Therefore, we assume that once the yielding criterion meets, material yields in all directions at same time. The decoupled elastic and plastic strains are shown in Fig. 47.8a, b for both strain X and strain Y. As shown, the elastic and plastic strains are comparable in magnitude. Also, positive elastic strains are remaining in both X and Y directions when the temperature cools to room temperature.

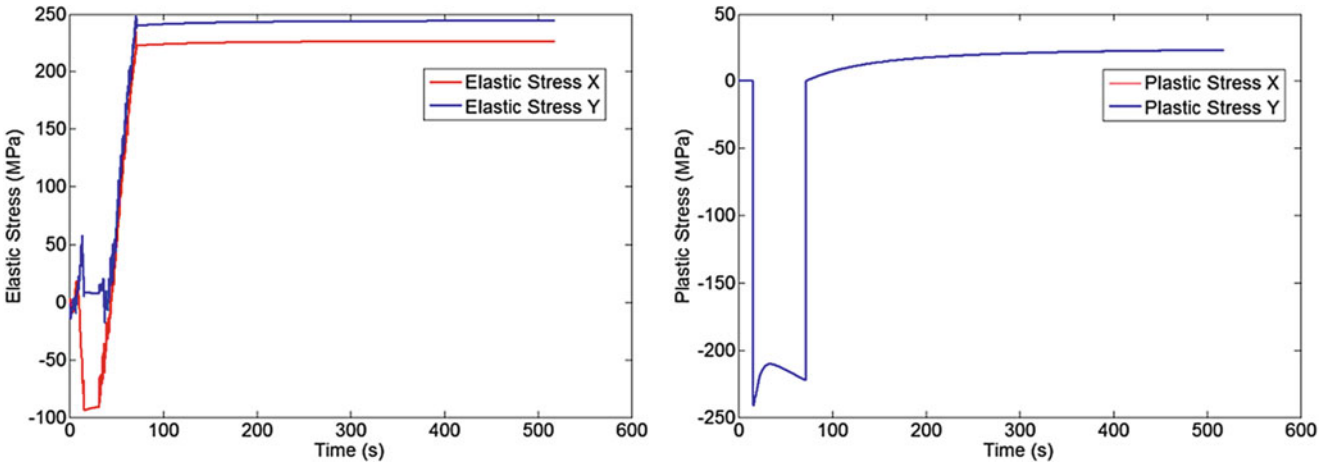

Fig. 47.9 Elastic and plastic stresses based on the decoupled strains

By inputting the elastic strains in Eq. 47.3, the elastic stresses are determined as shown in Fig. 47.9a. Because of the elastic-perfectly plastic model used in this paper, the stress at plastic region equals to the yield stress. Figure 47.9b shows the plastic stress changes versus time. Since we assume material yields in all directions once the yielding criterion meets, plastic strains X and Y are coincident. Based on the results in Fig. 47.9, the overall residual stress will be tensile in the material after the whole welding process.

47.3 Conclusions

Strain decoupling process is demonstrated in this paper for determining the thermal strain, elastic strain and plastic strain components of the real time welding strains. Strain stress tensor in elastic region is first determined for later yielding inspection using Von Mises criterion. A strain kinetics model is developed by adopting the algorithm of the cyclic tension compression loading test. Temperature dependent material properties are used in this model. Applying this model, the elastic and plastic regions are separated from the mechanical strain. Due to the limitation of the temperature dependent plastic material properties, the elastic-perfectly plastic material model is used to obtain the stress history. Methodology described in this paper is a much simpler approach for estimating the stress evolution during the welding process compared with solving the thermo-elastic–plastic models or partial differential equations in FEM.

References

1. Lundback A, Alberg H, Henrikson P (2003) Simulation and validation of TIG-welding and post weld heat treatment of an inconel 718 plate. In: Cerjak HK, Bhadeshia DH, and Kozeschnik E (eds) Proceedings of the 7th International Seminar on the Numerical Analysis of Weldability. Graz-Seggau, Austria
2. Muramatsu Y, Kuroda S (1996) In situ measurement of dynamic strain in welding by the laser speckle method: application of the laser speckle method to strain measurement in the welding process (2nd report). Weld Int 10:689–696
3. De Strycker M, Lava P, Van Paepegem W, Schueremans L, Debruyne D (2011) Measuring welding deformations with the digital image correlation technique. Suppl Weld J 90:107s–112s
4. Buster A, Lalbin X, Worswick MJ, Clarke JA, Altshuller B, Finn M, Jain M (2000) Prediction of strain distribution in aluminum tailor welded blanks for different welding techniques. Can Metall Q 39:493–502
5. Hwang JS (1976) Residual stress in weldments in high-strength steels, ocean. Engineer thesis, Massachusetts Institute of Technology
6. Wei R, Li KY (2004) An optical strain rosette/ring-core method applied on laser weld. In: Proceedings of the 21st international congress of theoretical and applied mechanics, Warsaw, 15–21 Aug, 2004
7. Ranjbarnodeh E, Farajpour M (2012) Evolution of plastic strians in dissimilar weld of strainless steel to carbon steel. Metall Mater Eng 18:19–27
8. Fang HY, Zhang XQ, Yang JG et al (2009) Discussion and calculation on welding residual longitudinal stress and plastic strain by finite element method. Front Mater Sci China 3:75–77

9. Jang CD (2007) Welding distortion analysis of hull blocks using equivalent load method based on inherent strain. Technical report SSC-453, Ship Structure Committee, Washington, DC
10. Mackwood AP, Crafer RC (2005) Thermal modelling of laser welding and related processes: a literature review. Opt Laser Technol 37:99–115
11. Feng ZL (2005) Processes and mechanisms of welding residual stress and distortion. Woodhead Publishing, Cambridge
12. Murakawa H (1997) Theoretical prediction of residual stress in welded structures. Weld Int 11:599–604
13. Williams JR, Lewis RW, Morgan K (1979) An elastic-viscoplastic thermal stress stress model with applications to the continuous casting of metals. Int J Numer Methods Eng 14:1–9
14. Wang L, Li KY, Sanusei S et al (2012) Welding strain/slope measurements using a laser-based technique. In: Proceeding of the 23rd international congress of theoretical and applied mechanics, Beijing, 19–24 Aug 2012
15. Nadimi S, Khoushehmehr RJ et al (2008) Investigation and analysis of weld induced residual stress in two dissimilar pipes by finite element modeling. J Appl Sci 8:1014–1020

Chapter 48
Thermal Output Observations from Fe-Ni-Cr Metal Foil Strain Gages

T.P. Kieffer and Y. Zhu

Abstract Fe-Ni-Cr alloys have been used for more than 40 years to manufacture metal foil strain gages for specific applications. The main characteristics of this metal are high gage factor, high fatigue strength, and high thermal output. To circumvent the effect of high thermal output, typical applications in stress analysis have involved dynamic loading where the high gage factor and fatigue strength could be used to advantage and the effect of thermal output could be minimized or ignored. Typical applications in precision transducers have also involved dynamic loading and/or careful exercise of Wheatstone bridge circuit cancelation of like-thermal output in adjacent arms. In this paper, we report uniform thermal output variation in Fe-Ni-Cr metal foil strain gages. Quarter bridge and half bridge thermal output data are presented, which illustrated the suitability of this type of strain gage for stress analysis and precision transducers even when loading conditions are not dynamic.

Keywords Thermal output • Fe-Ni-Cr • Strain gages • Stress analysis • Precision transducer

48.1 Introduction

The operating characteristics of resistive metal foil strain gages are influenced by many parameters, probably the most fundamental of which are the backing material (plastic insulator) and the resistive sensing material (metal conductor). While there are many other parameters including size, electrical resistance, orientation of sensing grid, etc., it is the backing material and the resistive sensing material which respond directly to the strain developed on the substrate [1]. Furthermore, it is the resistive sensing material which controls such factors as sensitivity (gage factor), cyclic endurance, elongation, temperature range, temperature sensitivity, and long-term stability, so many would say it is the most important consideration for making a strain gage selection decision [2].

The two most popular materials used for the resistive sensing element in metal foil strain gages are alloys of Cu-Ni and Ni-Cr. These materials have sufficient strain sensitivity for most applications (gage factor of approximately 2.0) and the temperature sensitivity can be minimized for a wide variety of substrate materials (steel, aluminum, ceramic, etc.). This latter characteristic is referred to as self-temperature-compensation and is a desirable characteristic when trying to determine mechanical strain when ambient temperature is not constant during strain measurement [3]. There is an alloy of Fe-Ni-Cr also used for the resistive sensing element in metal foil strain gages, but to a much lesser extent than either Cu-Ni or Ni-Cr. This material has desirable characteristics of high strain sensitivity (gage factor of approximately 3.2) and high fatigue strength. However, the temperature sensitivity is also high and the material is not capable of self-temperature-compensation.

A comparison of the temperature sensitivity of Cu-Ni (Constantan), Ni-Cr (Karma), and Fe-Ni-Cr (Isoelastic) alloys is given in Fig. 48.1 as plots of thermal output versus temperature [1]. The slope of the Fe-Ni-Cr thermal output curve is

T.P. Kieffer (✉)
Vishay Precision Group – Micro-Measurements, PO Box 27777, Raleigh, NC 27611, USA

North Carolina State University, 3238 Engineering Building III, Raleigh, NC 27695, USA
e-mail: tom.kieffer@vishaypg.com

Y. Zhu
North Carolina State University, 3238 Engineering Building III, Raleigh, NC 27695, USA

H. Jin et al. (eds.), *Advancement of Optical Methods in Experimental Mechanics, Volume 3*,
Conference Proceedings of the Society for Experimental Mechanics Series,
DOI 10.1007/978-3-319-00768-7_48,

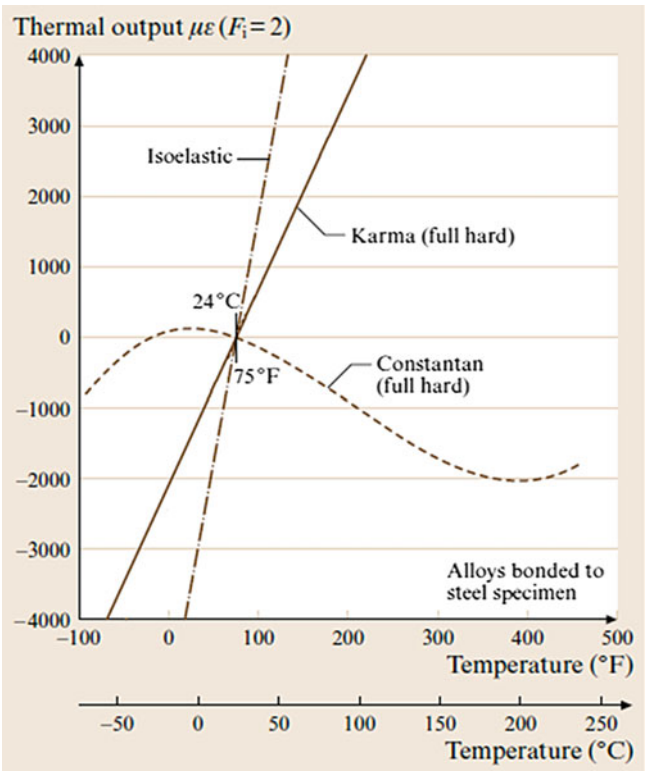

Fig. 48.1 Temperature sensitivity of Fe-Ni-Cr (Isoelastic), Ni-Cr (Karma), and Cu-Ni (Constantan) [1]

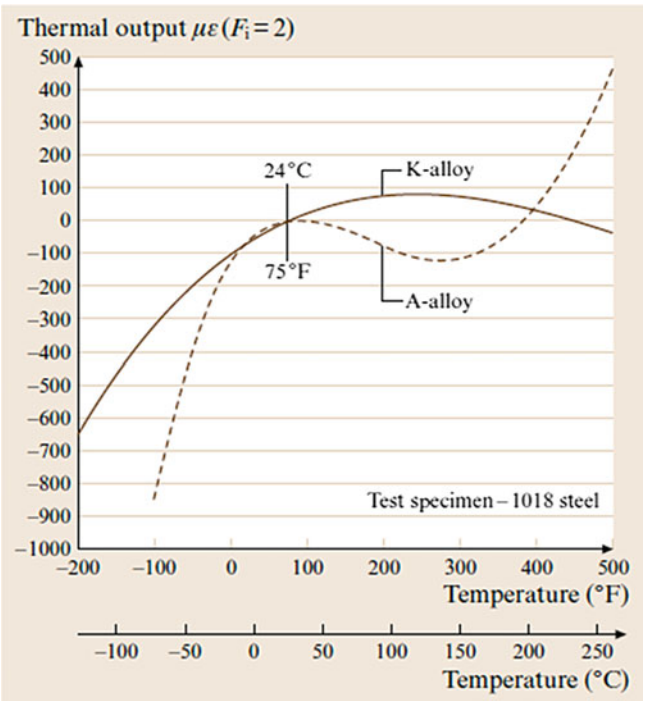

Fig. 48.2 Self-temperature-compensation characteristic for Cu-Ni (A-alloy) and Ni-Cr (K-alloy) [1]

approximately 80 με/°F (144 με/°C). Note the thermal output curves for Cu-Ni and Ni-Cr are for the full-hard condition. The thermal output for these two materials in self-temperature-compensated condition is given in Fig. 48.2. For temperatures of 0–400 °F (−18–204 °C) the thermal output of Cu-Ni (A-alloy) and Ni-Cr (K-alloy) is approximately ±100 με. Whereas the data in Fig. 48.1 suggest the thermal output of Fe-Ni-Cr would exceed ±4,000 με. Fatigue strengths are given in Fig. 48.3 for Cu-Ni (Constantan), Ni-Cr, and Fe-Ni-Cr (Isoelastic) [1]. The fatigue strength of Fe-Ni-Cr is about 20 % higher than Ni-Cr and more than double the fatigue strength of Cu-Ni (Constantan).

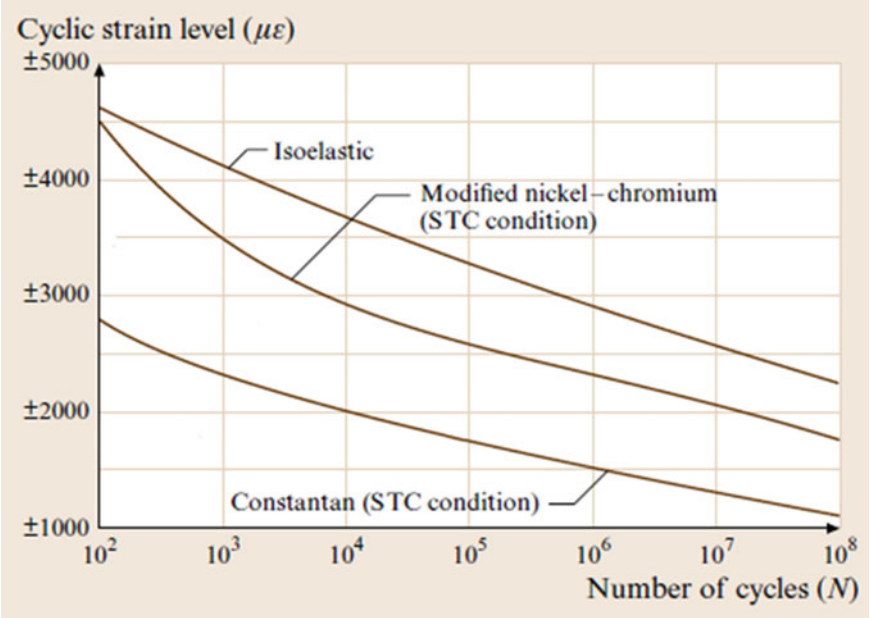

Fig. 48.3 Fatigue life of Fe-Ni-Cr (Isoelastic), Ni-Cr, and Cu-Ni (Constantan) [1]

Fe-Ni-Cr alloys have been used for more than 40 years to manufacture metal foil strain gages for both stress analysis applications like design validation and failure studies and for precision transducers sensing weight, pressure, displacement, etc. Historical use of Fe-Ni-Cr alloys for resistive sensing material has involved compromise. The high strain sensitivity and high fatigue strength are desirable characteristics but the high sensitivity to temperature must be carefully managed. Typical stress analysis applications involve dynamic loading where the high gage factor and fatigue strength can be used to advantage and the effect of thermal output can be minimized or ignored. Typical applications in precision transducers often involve dynamic loading also and/or careful exercise of Wheatstone bridge circuit cancelation of like-thermal output in adjacent arms. A review of the literature for materials used for the resistive sensing element in metal foil strain gages did not produce any data about the uniformity of thermal output in Fe-Ni-Cr alloys. Perhaps the conventional wisdom was the alloy had so much output due to temperature there was no incentive to try to use it for any applications other than those involving dynamic loading or specialized transducers.

The lack of experimental data on thermal output uniformity of Fe-Ni-Cr alloys appeared to be an opportunity for research which might quantitatively express the practical limits for use of Fe-Ni-Cr alloys in both experimental stress analysis and precision transducer applications. In this paper thermal output data are presented for Fe-Ni-Cr metal foil strain gages in quarter and half Wheatstone bridge configurations. An interesting finding is the high uniformity of thermal output from gage-to-gage which illustrates the possibility of using this type of strain gage for stress analysis and precision transducers even when loading conditions are not dynamic.

48.1.1 Initial Testing Considerations

Historical usage of Fe-Ni-Cr alloy had some influence on the direction of the test program. It was known that the thermal output would be high at approximately 80 με/°F (144 με/°C). Furthermore, it was believed that temperature compensation by Wheatstone bridge cancellation of like-strains in adjacent arms would probably be necessary [3]. Finally, it was believed that a practical application in static stress analysis would be unlikely. Consequently, a strain gage pattern with two grids in close proximity normally used for precision transducer applications was selected for testing. The plan was to acquire quarter bridge thermal output data on individual grids and then re-connect the grids in half bridge arrangements to acquire more thermal output data for comparison to the quarter bridge data.

Strain gages with two sensing grids (90º T-rosettes) were selected for initial thermal output testing (shown in Fig. 48.4). This type of strain gage is normally used for column load cells with one grid aligned in the direction of load application and the other grid aligned transverse to the loading direction. Materials of construction were polyimide film backing and encapsulation. The grid lengths were 0.080″ (2 mm) and the resistance was 1,000 Ω +/− 0.4 %.

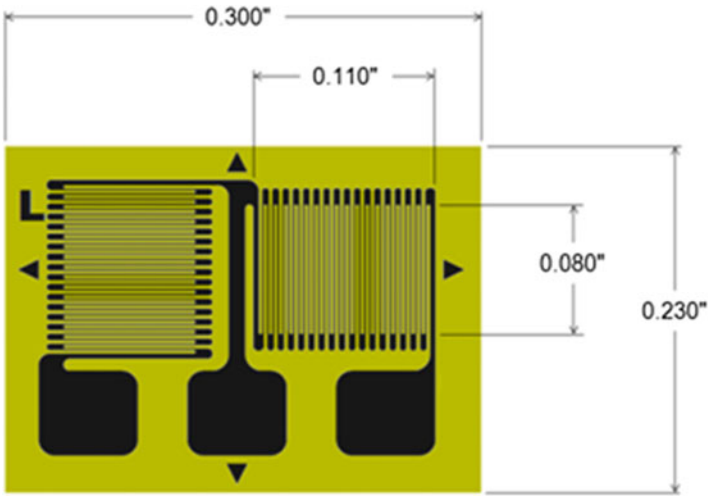

Fig. 48.4 T-rosette strain gage used for initial thermal output testing

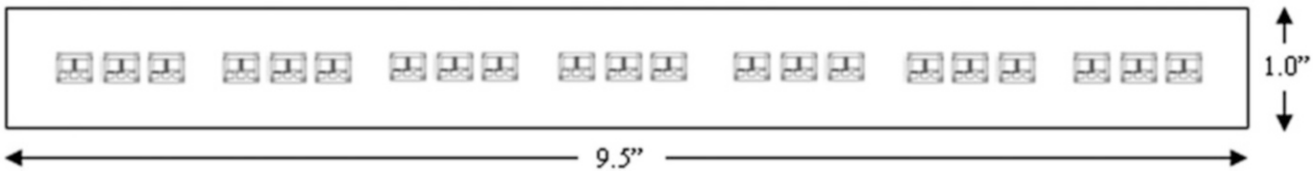

Fig. 48.5 Arrangement of 21 strain gages on 1/8″ (3 mm) thick aluminum beam

A total of 42 strain gages was used, which provided 84 grids – half in the longitudinal direction and half in the transverse direction. The strain gages were attached to two 2024-T4 aluminum beams approximately 1/8″ thick x 1″ wide x 9.5″ long (3 × 25 × 241 mm). The beams were attached to 10″ (254 mm) aluminum pans using drafting tape. The intention was to provide support for the weight of the lead wires without preventing the beams to expand and contract freely during the thermal output testing [4]. Both beams/pans were placed inside an oven with 1-in (25 cm) thermal (blanket) insulation above and below the pans. Temperature measurement was made using nickel RTD sensors attached to small aluminum blocks that were placed next to each test beam. System 5000 data acquisition instrument [5] was used to collect the data over the temperature range from 74 °F to 104 °F (23–40 °C). Quarter bridge data for individual grids was acquired first, and then half bridge data was obtained for three different grid pairings (transverse to longitudinal, longitudinal to longitudinal, and transverse to transverse). The arrangement of the strain gages on the beams, the beams on the pans, and the quarter and half bridge wiring connections are shown in Figs. 48.5, 48.6, and 48.7.[1]

48.1.2 Initial Test Results

The thermal output data for quarter bridge wiring connections is shown in Table 48.1. The longitudinal grids had a mean thermal output of 2,212 με at 104 °F (40 °C) with a standard deviation of 5.4 με and the transverse grids had a mean thermal output of 2,545 με with a standard deviation of 7.9 με. These values corresponded to chord slopes of 73.7 με/°F (132.7 με/°C) and 84.8 με/°F (152.7 με/°C) over the temperature range of 74–104 °F (23–40 °C). The measured thermal output agreed with the nominal value of 80 με/°F (144 με/°C) obtained for a variety of strain gage pattern geometries and backing materials over many years of manufacturing. The uniformity of the thermal output as indicated by the standard deviation of the mean was surprising given the high sensitivity to temperature and the fairly complex chemical composition of the Fe-Ni-Cr alloy.

[1] All strain gages, accessories, and instrumentation provided by Vishay Precision Group Micro-Measurements, Wendell, NC.

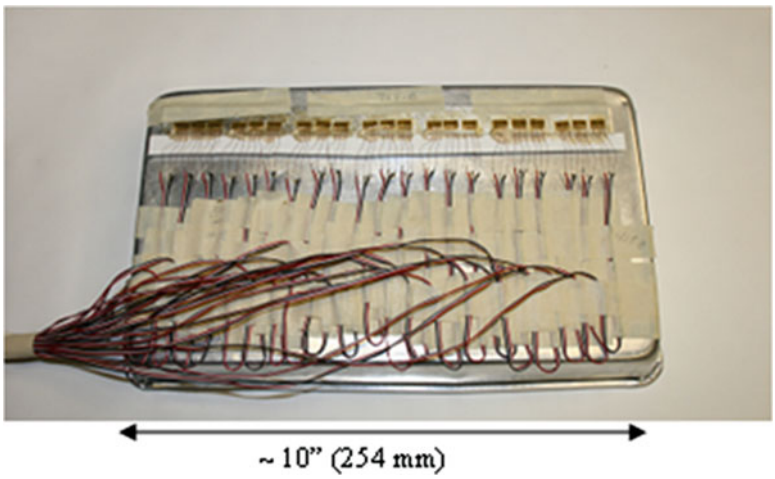

Fig. 48.6 Placement of 1/8″ (3 mm) thick aluminum beam on 10″ (254 cm) aluminum pan

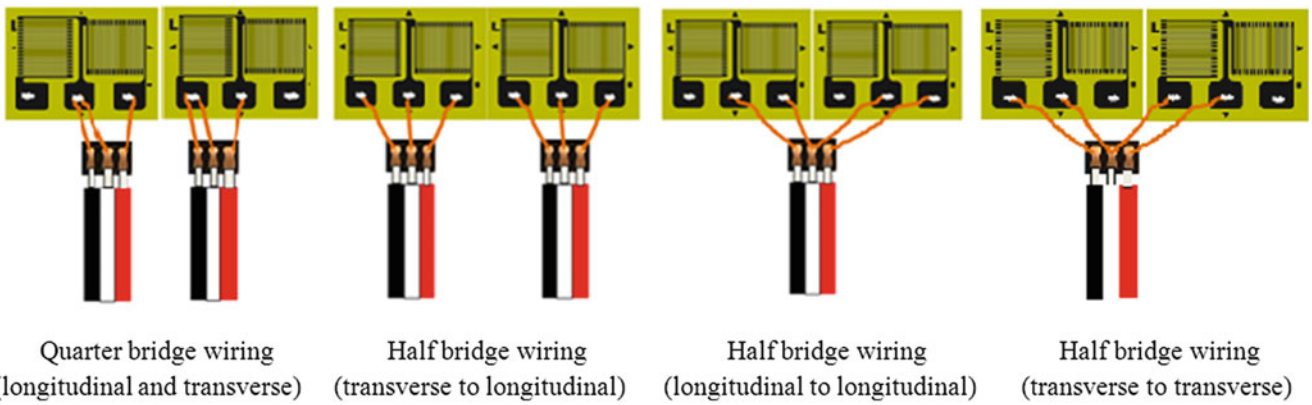

Fig. 48.7 Quarter bridge and half bridge wiring connections

Table 48.1 Quarter bridge thermal output for 90° T-rosette strain gages made with Fe-Ni-Cr alloy

	Mean thermal output @104 °F (40 °C)	Standard deviation of the mean	Chord slope 74–104 °F (23–40 °C)	Standard deviation of the chord slope
	με	με	με/°F(με/°C)	με/°F(με/°C)
Longitudinal grids	2,212	5.4	73.7 (132.7)	0.18 (0.32)
Transverse grids	2,545	7.9	84.8 (152.7)	0.26 (0.48)

The thermal output data for half bridge wiring connections is shown in Table 48.2. The mean thermal output for transverse-to-longitudinal grid pairings was 27 με at 104 °F (40 °C) with a standard deviation of 3.3 με. It is noted that this wiring would be typical when this 90° T-rosette strain gage was used for a column load cell transducer. The mean thermal output for longitudinal-to-longitudinal grid pairings was 2 με with a standard deviation of 0.3 με and the mean thermal output for transverse-to-transverse grid pairings was −2 με with a standard deviation of 0.4 με. These values corresponded to chord slopes of 0.9 με/°F (1.6 με/°C), 0.1 με/°F (0.1 με/°C), and −0.1 με/°F (−0.1 με/°C) over the temperature range of 74–104 °F (23–40 °C). Some reduction in thermal output was expected from Wheatstone bridge circuit cancelation of like-thermal output in adjacent arms. The uniformity of the thermal output seen in the quarter bridge results was extended here to yield the surprisingly low thermal output for same-grid pairings (longitudinal-to-longitudinal and transverse-to-transverse).

Table 48.2 Half bridge thermal output for 90° T-rosette strain gages made with Fe-Ni-Cr alloy

	Mean thermal output @104 °F (40 °C)	Standard deviation of the mean	Chord slope 74–104 °F (23–40 °C)	Standard deviation of the chord slope
	με	με	με/°F(με/°C)	με/°F(με/°C)
Transverse-longitudinal	27	3.3	0.9 (1.6)	0.11 (0.20)
Longitudinal-longitudinal	2	0.3	0.1 (0.1)	0.01 (0.02)
Transverse-transverse	−2	0.4	−0.1 (−0.1)	0.01 (0.02)

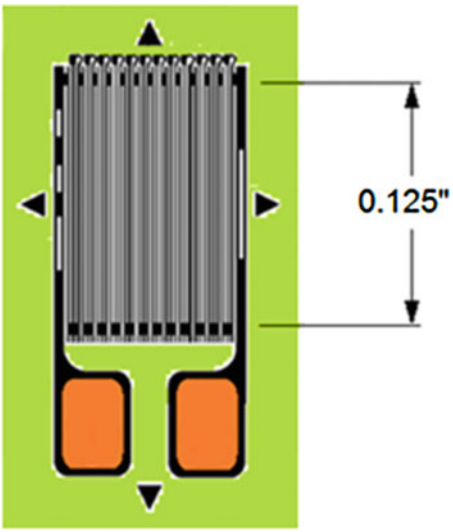

Fig. 48.8 Single element linear strain gage used for subsequent thermal output testing

48.1.3 Subsequent Test Considerations

The initial test results suggest refinements to further improve thermal output uniformity. Temperature compensation from Wheatstone bridge circuit cancelation of like-thermal output in adjacent arms could be used to greatest advantage if the strain gages in adjacent arms were at the same temperature and each had the same sensitivity to temperature [3]. In consideration of the need to have the strain gages at the same temperature, smaller test specimens were used. The need to have the strain gages respond the same to temperature prompted selection of strain gages which could be manufactured with process steps producing the highest gage-to-gage uniformity.

Single element linear strain gages without encapsulation were selected for thermal output testing (shown in Fig. 48.8). This type of strain gage is normally used for a wide variety of bending beam and single-point load cell transducers. The backing material was polyimide film and the solder pads were copper-coated to simplify soldering to the Fe-Ni-Cr alloy. The grid length was 0.125″ (3 mm) and the resistance was 1,000 Ω +/− 0.05 %.

A total of 24 strain gages was attached to six metal blocks, two each of 2024-T4 aluminum, 17-4PH stainless steel, and hot-rolled Fe-Ni-Cr alloy of the same material as the resistive sensing element of the strain gage. The blocks were approximately 1/8″ thick × 1″ wide × 1″ long (3 × 25 × 25 mm). The blocks were placed inside an oven with 1-in. (25 cm) thermal (blanket) insulation above and below the blocks. A type-J thermocouple was attached directly to the blocks for temperature measurement. P3 strain indicators [6] were used to collect data over the temperature range from 76 °F to 126 °F (24–52 °C).

Quarter bridge data for individual gages was acquired first, and then half bridge data was collected after rewiring the strain gages. The arrangement of the strain gages on the blocks and the quarter and half bridge wiring connections are shown in Figs. 48.9 and 48.10.

48.1.4 Subsequent Test Results

The thermal output data for quarter bridge wiring connections is shown in Table 48.3. The strain gages bonded to the aluminum blocks had a mean thermal output of 4,334 με at 126 °F (52 °C) with a standard deviation of 4.0 με. The strain gages bonded to the stainless steel blocks had a mean thermal output of 3,957 με with a standard deviation of 0.5 με.

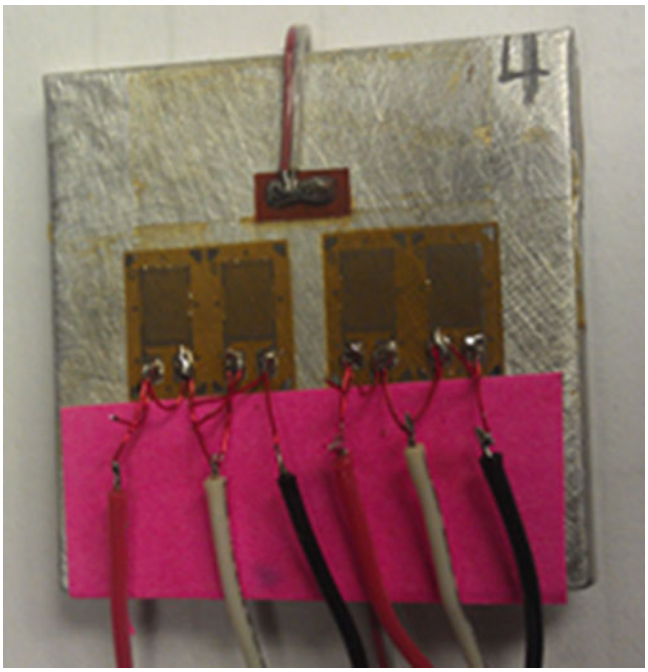

Fig. 48.9 Arrangement of four strain gages and type-J thermocouple on 1/8″ (3 mm) thick aluminum block

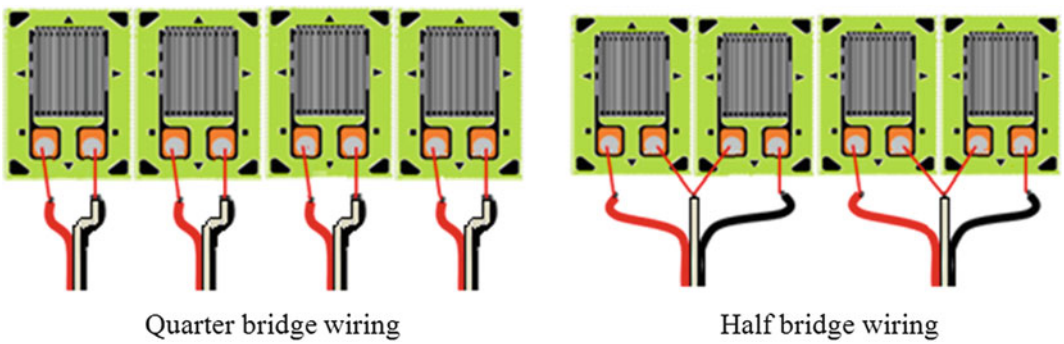

Fig. 48.10 Quarter bridge and half bridge wiring connections

Table 48.3 Quarter bridge thermal output for single element linear strain gages made with Fe-Ni-Cr alloy

	Mean thermal output @126 °F (52 °C)	Standard deviation of the mean	Chord slope 76–126 °F (24–52 °C)	Standard deviation of the chord slope
	με	με	με/°F(με/°C)	με/°F(με/°C)
Aluminum blocks	4,334	4.0	86.7 (156.0)	0.08 (0.14)
Stainless steel blocks	3,957	0.5	79.1 (142.5)	0.01 (0.02)
Fe-Ni-Cr blocks	3,855	0.4	77.1 (138.8)	0.01 (0.01)

Finally, the strain gages bonded to the Fe-Ni-Cr blocks had a mean thermal output of 3,855 με with a standard deviation of 0.4 με. These values corresponded to chord slopes of 86.7 με/°F (156.0 με/°C), 79.1 με/°F (142.5 με/°C), and 77.1 με/°F (138.8 με/°C) over the temperature range of 76–126 °F (24–52 °C). The uniformity of the thermal output as indicated by the standard deviation of the mean was better than the initial test data with 90° T-rosette strain gages, especially for the stainless steel blocks and the Fe-Ni-Cr blocks.

The thermal output data for half bridge wiring connections is shown in Table 48.4. The strain gages bonded to the aluminum blocks had a mean thermal output of 2.9 με at 126 °F (52 °C) with a standard deviation of 6.4 με. The strain gages

Table 48.4 Half bridge thermal output for single element linear strain gages made with Fe-Ni-Cr alloy

	Mean thermal output @126 °F (52 °C)	Standard deviation of the mean	Chord slope 76–126 °F (24–52 °C)	Standard deviation of the chord slope
	με	με	με/°F(με/°C)	με/°F(με/°C)
Aluminum blocks	2.9	6.4	0.058 (0.104)	0.128 (0.23)
Stainless steel blocks	0.3	0.8	0.006 (0.011)	0.016 (0.029)
Fe-Ni-Cr blocks	0.2	0.6	0.004 (0.007)	0.012 (0.022)

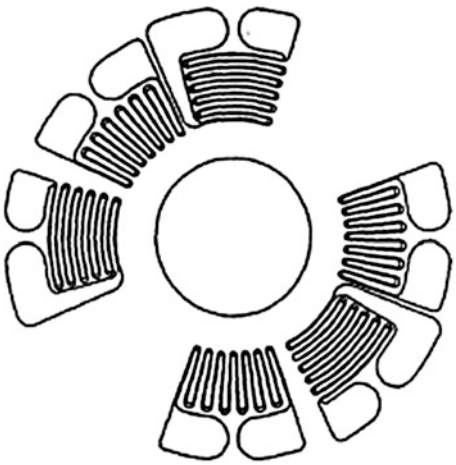

Fig. 48.11 Six-element strain gage proposed by Schajer and Tootooian [7]

bonded to the stainless steel blocks had a mean thermal output of 0.3 με with a standard deviation of 0.8 με. Finally, the strain gages bonded to the Fe-Ni-Cr blocks had a mean thermal output of 0.2 με with a standard deviation of 0.6 με. These values corresponded to chord slopes of 0.058 με/°F (0.104 με/°C), 0.006 με/°F (0.011 με/°C), and 0.004 με/°F (0.007 με/°C) over the temperature range of 76–126 °F (24–52 °C). The uniformity of the half bridge thermal output data was better than the initial test data with 90º T-rosette strain gages when comparing the mean values. However, the standard deviations of the means were comparable to the initial test data for the stainless steel and Fe-Ni-Cr blocks and worse for the aluminum blocks.

48.1.5 Discussion and Summary

This paper has confirmed the temperature sensitivity of Fe-Ni-Cr alloy is high at approximately 80 με/°F (144 με/°C), and it has revealed the temperature sensitivity is surprisingly uniform. Applications in stress analysis using quarter bridge circuits would appear to be the most challenging particularly if the temperature of the test article were to change during the measurement interval. However, due to the high uniformity in thermal output, it may be feasible to use Fe-Ni-Cr alloy strain gages for applications in stress analysis if half bridge circuits are suitable. Nevertheless, it is imperative for the strain gages to be at nearly the same temperature.

One such application may be for residual stress measurement using the six-element strain gage proposed by Schajer and Tootooian [7]. A sketch of the strain gage is shown in Fig. 48.11. The strain gage is wired as three separate half bridges each consisting of a radial and tangential grid. The strain gage was conceived to provide higher strain output when making residual stress measurements by hole-drilling technique. A secondary benefit was a reduction in thermal output and electrical noise. This may be an application suitable for Fe-Ni-Cr alloy strain gages, particularly since even higher output would be possible due the higher strain sensitivity compared to Cu-Ni or Ni-Cr alloys (gage factor of 3.2 versus 2.0). However, the difference in grid geometry (radial and tangential) and the separating distance across the hole would probably cause some temperature sensitivity perhaps on the same order of magnitude as shown in this paper with the 90° T-rosette strain gages (initial test results).

Applications for precision transducers appear to have the most promise for use of Fe-Ni-Cr strain gages since the spring element (counterforce) is typically designed to maximize mechanical strain output and minimize thermal strain output with

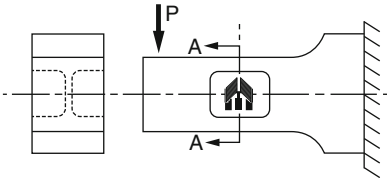

Fig. 48.12 Single-ended shear beam load cell with half bridge strain gage [8]

Wheatstone bridge combinations of multiple strain gages [8]. One example of a precision transducer possibly suited to strain gages manufactured with Fe-Ni-Cr alloy resistive sensing elements is the single-ended shear beam (see Fig. 48.12). This design often uses two strain gages bonded to opposite sides of the spring element with each strain gage having two grid elements oriented 45° to the sides. The grids are likely to have close tracking of thermal output because of the mirror symmetry and are likely to be at nearly the same temperature due to their close proximity.

The high sensitivity to temperature of Fe-Ni-Cr strain gages has historically limited their use to applications involving dynamic loading or for some specialized transducers where Wheatstone bridge cancellation of like-strain in adjacent arms was possible. Perhaps the uniformity in the temperature sensitivity of Fe-Ni-Cr strain gages presented in this paper will provide some encouragement for use in stress analysis and precision transducer applications that may have been previously dismissed.

References

1. Watson RB (2008) Bonded electrical resistance strain gages. In: Sharpe WN Jr (ed) Springer handbook of experimental mechanics. Springer, New York, pp 283–332
2. Strain gage selection: criteria, procedures, recommendations, Vishay precision group micro-measurements tech note 505, Vishay Measurements Group, P.O. Box 27777, Raleigh 27611, 2010
3. Strain gage thermal output and gage factor variation with temperature, Vishay precision group micro-measurements tech note 504, Vishay Measurements Group, P.O. Box 27777, Raleigh 27611, 2012
4. Watson RB, Perry CC, Harris SK (2004) Effects of material properties and heating/cooling rate on strain gage thermal output observations. In: Pappalettere C (ed) Advances in experimental mechanics. McGraw-Hill, New York
5. System 5000 StrainSmart® Data Acquisition System, Vishay precision group micro-measurements document no. 11269, Vishay Measurements Group, P.O. Box 27777, Raleigh 27611, 2011
6. P3 Strain indicator and recorder, Vishay precision group micro-measurements document no. 11102, Vishay Measurements Group, P.O. Box 27777, Raleigh 27611, 2011
7. Schajer GS, Tootoonian M (1997) A new rosette design for more reliable hole-drilling residual stress measurements. Exp Mech 37(3):299–306
8. Perry CC, Starr JE, Weidner JR (1992) Modern strain transducers: their design and construction. In: Hannah RL, Reed SE (eds) Strain gage users' handbook. Elsevier Applied Science, London/New York, SEM Edition, ISBN 0-912053-36-4 15; Society for Experimental Mechanco, Bethel